INTERWIRE CONTACT FORCES AND THE STATIC, HYSTERETIC AND FATIGUE PROPERTIES OF MULTI-LAYER STRUCTURAL STRANDS

by

MOHAMMED RAOOF
MSc, DIC

A Thesis submitted for the degree of Doctor of Philosophy in the Faculty of Engineering of the University of London

Imperial College of Science and Technology, London.

September 1983

To Mehdi

ABSTRACT

Analytical work backed by experimental studies on a long, 39mm., 91 wire strand with a nominal breaking load of 1.23MN is reported.

The theory involves a novel treatment of the layers of wires in a strand as a series of orthotropic sheets. The kinematics of a layer of helically laid wires have been used to predict the circumferential forces between wires in a given layer as a function of the radial movement of the layer. A non-linear compatability analysis is then used to determine the radial and circumferential distribution of the "clench" forces (induced in the helical wires by an axial load) between the layers of wires in the strand.

With this information, the initial loads on the contact patches are determined, and hence the compliances for a perturbation of a given type and size can be found, as can interwire movements and changes in wire strains. From the Properties of the sheets of wires, simple transformations and summation lead to estimates of axial and torsional tangent stiffnesses of the strand.

Using the above, the full slip histories on the interwire contact patches (from the micro-slips on the periphery at low loads, to the onset of gross slip at higher loads and beyond) are predicted. In addition, the hysteresis in the strand for axial and also torsional cyclic loading regimes is estimated.

For a given axial mean load, the response of strand to an applied bending moment is also considered in some detail. Two cases have been addressed, namely close to a termination

and (rather more simple) remote from the termination. To do this, the theoretical stiffness formulations describing the slippage between the various layers in the strand have been derived in an analytical form which are then used as an input to the differential equations describing the behaviour of individual wires. Using a simplified version of these equations, some light has been cast on an interesting phenomenon observed in previously reported bending fatigue experiments, where the first wire to fail was invariably the one which entered the socket on the bending neutral axis rather than (as might be expected) the wires in the "extreme fibre" positions.

The experimental work concentrated on measurements of wire stress, torsional and axial stiffness and related hysteresis and is in substantial agreement with the theory.

It is concluded that theoretical predictions of inter-wire forces and slippage and their associated energy dissipation in large strands such as those envisaged as tension leg members in buoyant platforms are feasible, and this information is of obvious value as an input to a fracture mechanics analysis of the fatigue behaviour of the strand away from its termination.

ACKNOWLEDGEMENTS

The investigation reported in this thesis was initiated by and carried out under the supervision of Dr.R. E. Hobbs, to whom the author expresses his deep gratitude for unfailing interest, constructive criticisms and valuable suggestions. The author is also grateful for the valuable suggestions of Dr.T. Wyatt about the damping measurements.

The major part of the work has been sponsored by the Marine Technology Directorate of the (U.K.) Science and Engineering Research Council, as part of the Wire Rope Programme. Their continuing support is gratefully acknowledged.

Thanks are also due to British Ropes, Doncaster, for their patient help with specimens and information.

Special thanks to Mr. J. Neale and other staff of the Engineering Structures Laboratories for their intensive efforts and willingness with which they participated in the experimental work. In particular Mr J. Neale suggested many and developed some of the features incorporated in the test rig.

Many thanks are due to my colleague P. Driver for reading the manuscript and to other colleagues; J. Herrera, C. Hargreaves and W. Fahy who so freely gave their time for various discussions over the period of this study.

The expertise and patience of Mr. A. Chipling who prepared the photographs, Mrs. A. Langford who traced the figures and Miss V.H.E. Collins who did the typing is also gratefully acknowledged.

To Shiva, my wife, goes my heartfelt appreciation for her support while this hang-up of mine worked itself out.

CONTENTS

		Page No.
ABSTRACT		3
ACKNOWLEDGEMENTS		5
CHAPTER 0	SOME PRELIMINARY DEFINTIONS AND REMARKS	12
	REFERENCES	19
CHAPTER 1	REVIEW OF CONTACT STRESS THEORIES	20
1.1	INTRODUCTION	20
1.2	BRIEF DISCUSSION OF HERTZIAN THEORY FOR NORMAL CONTACT	21
1.3	TANGENTIAL FORCES	39
1.4	CYCLIC TANGENTIAL LOADING WITH NORMAL LOAD KEPT CONSTANT	54
1.5	OBLIQUE FORCES	60
1.6	EXPERIMENTAL VERIFICATION AND PRACTICAL LIMITATIONS	63
1.7	CLOSURE	68
	REFERENCES	70
CHAPTER 2	STRAND THEORY	75
2.1	INTRODUCTION TO THE LITERATURE SURVEY	75
2.2	STRAND EXTENSIBILITY	75
2.3	REPEATED LOADING AND DAMPING	83
2.4	INTRODUCTION TO THE ANALYSIS	91
2.5	KINEMATICS OF HELIX	92
2.6	EQUILIBRIUM EQUATIONS FOR A HELICAL ROD	94
2.7	WIRE ACCOMMODATION IN EACH LAYER	96

CHAPTER 2 (cont.)

2.8 CONTACT FORCES IN A STRAND 98

2.9 PROPERTIES OF THE ORTHOTROPIC SHEET 100

2.10 TRANSFORMATION OF PROPERTIES 103

2.11 KINEMATICS OF THE WIRE LAYER CONTINUUM 104

2.12 METHOD OF SOLUTION 107

2.13 DETERMINATION OF RADIAL FORCE EXERTED ON THE RIGID CORE 109

2.14 RADIAL LOAD TRANSFER IN A MULTI-LAYERED STRAND 109

2.15 APPLICATION OF STRAND THEORY 111

REFERENCES 116

CHAPTER 3 THEORETICAL AXIAL AND TORSIONAL STIFFNESSES OF STRAND AND RELATED HYSTERETIC BEHAVIOUR 121

3.1 INTRODUCTION 121

3.2 COMMON METHODS OF MODELLING INTERNAL DAMPING 129

3.3 MECHANISM OF INTERNAL MATERIAL DAMPING 135

3.4 FRICTIONAL DAMPING 136

3.5 DAMPING OF REAL STRUCTURES 140

3.6 TORSIONAL STIFFNESS OF STRAND 142

3.6.1 Introduction 142

3.6.2 Analysis 144

3.7 AXIAL STIFFNESS OF STRAND 151

3.7.1 Introduction 151

3.7.2 Analysis 151

3.7.3 Results 154

CHAPTER 3 (cont.)

3.8	HYSTERESIS UNDER CYLIC LOADING	155
	3.8.1 Introduction	155
	3.8.2 Analysis	158
	3.8.2.1 Torsional Hysteresis	160
	3.8.2.2 Axial Hysteresis	162
	3.8.3 Results and Discussion	163
3.9	A NOTE REGARDING DAMPING IN THE SEVERN BRIDGE	170
3.10	THE EFFECT OF EXTERNAL HYDROSTATIC PRESSURE ON CABLE HYSTERESIS AND DAMPING	171
3.11	CONCLUSION	174
	REFERENCES	177
CHAPTER 4	FREE BENDING THEORY	180
4.1	INTRODUCTION AND LITERATURE SURVEY	180
4.2	SUMMARY OF THE LITERATURE SURVEY	193
4.3	KINEMATICS OF A HELICAL CURVE INSCRIBED ON THE SURFACE OF A CYLINDER BENT TO A CONSTANT RADIUS OF CURVATURE ρ	196
4.4	FREE FIELD BENDING OF A PRETENSIONED LARGE DIAMETER MULTI-LAYER STRAND IN REGIONS REMOTE FROM END RESTRAINTS	197
4.5	LOCAL PHENOMENA NEAR THE FIXED END OF THE STRAND	201
4.6	DETERMINATION OF THE SHEAR STIFFNESS COEFFICIENTS, κ AND G'	205
4.7	RESULTS FOR THE SHEAR STIFFNESS MODULI AND DISCUSSION	216

CHAPTER 4 (cont.)

4.8 SOLUTION OF THE DIFFERENTIAL EQUATION (4.20). 218

4.8.1 No-slip (Linear) Solution with $G_i' = 0$ 218

4.8.2 Free Field Solutions for the Two Extreme Cases of Zero and Infinite Friction 220

4.8.3 Results for Finite κ 222

4.8.4 Non-Linear Solution 224

4.8.5 Results for the Non-linear Case 227

4.9 LIMITATION OF THE PRESENT MODEL AND SCOPE FOR FUTURE WORK 230

4.10 CONCLUSIONS 233

REFERENCES 234

CHAPTER 5 EXPERIMENTAL WORK 239

5.1 INTRODUCTION 239

5.2 GENERAL ARRANGEMENT OF THE APPARATUS FOR AXIAL TENSIONING 242

5.3 AXIAL BEHAVIOUR 243

5.3.1 Stiffness and Hysteresis Results and Discussion 243

5.3.2 Strain Gauge Measurements on 39mm O.D. Strand in the Axial Mode 245

5.4 TORSIONAL BEHAVIOUR 249

5.4.1 Apparatus 249

5.4.2 Static Tests on 39mm O.D. Strand 250

5.4.3 Dynamic Tests on 39mm O.D. Strand 254

CHAPTER 5 (cont.)

5.4.4 Effect of Bedding-in on Strand Performance 259

5.4.5 Strain Gauge Measurements inthe Tonsion Mode 266

5.5 FREE BENDING 267

5.5.1 General Set-up 267

5.5.2 Scope of the Tests and Primary Objectives 269

5.5.3 Results and Discussion 271

5.6 CONCLUSIONS 277

REFERENCES 280

CHAPTER 6 STRAND FATIGUE PERFORMANCE 281

6.1 INTRODUCTION 281

6.2 LITERATURE SURVEY 283

6.2.1 Research on Single Wires 283

6.2.2 Research on Cable Fatigue in Air 287

6.3 PRESENTATION OF CONSTANT AMPLITUDE AXIAL FATIGUE DATA 296

6.4 CABLE MODELLING FOR FATIGUE STUDIES 303

6.4.1 Introduction 303

6.4.2 Development of a Simple Routine for Calculating the Interwire/ Interlayer Contact Forces and Displacements. 304

6.4.3 Effect of Strand Modelling on Axial Properties. 307

CHAPTER 6 (cont.)

6.5 FRETTING FATIGUE PHENOMENA AND STRAND FATIGUE PERFORMANCE 309

6.5.1 Introduction 309

6.5.2 A Brief Account of the Fretting-Fatigue Phenomenon 310

6.5.3 Fretting-Fatigue in Multi-Layer Strands 316

6.6 SUMMARY AND CONCLUSIONS 324

REFERENCES 326

CHAPTER 7 CONCLUSIONS 330

NOTATION 337

APPENDIX I 342

TABLES 344

FIGURES 358

CHAPTER 0

SOME PRELIMINARY DEFINITIONS AND REMARKS

In this thesis, a cable is defined as a flexible tension member consisting of one or more groups of wires, strands, or ropes. A single continuous length cold-drawn from rod is called a wire and an assembly of several layers of helically - laid wires with a common axis is referred to as a spiral strand. The term rope is applied to an assembly of a number of helical strands in one or more layers over a central core. Ropes are supplied either with fibre or with steel cores, the choice being largely dependent on the use for which the rope is intended.

In addition to helical strands there are also locked coil or parallel wire strands. In the latter individual wires are arranged in a parallel configuration without helical twist. In the former shaped wires of Full Lock Type (z section) are used to provide a final layer (or sometimes 2 final layers) over the basic spiral strand construction, resulting in a structure more resistant to corrosion at the cost of a slight reduction in the strength to weight ratio.

Ropes are produced with a wide variety of designs and reference to any manufacturer's rope list will show the arrangements which are considered to be standard. For example, Fig. (0.1) shows a variety of rope designs offered by British Ropes.

So-called non-rotating strands (and ropes) are designed and manufactured to be in a near balanced condition in a torsional sense. Obviously, ideal non-rotating strand (or rope) in the full sense of the term does not exist and the term is only a relative one. Non-rotating properties are obtained by counter laying two or more layers of wires in a strand or strands in a rope.

That distance in a strand or rope, measured parallel to the longitudinal axis, in which a wire in the strand (or a strand in the rope) makes one complete turn about the axis of the strand (or rope) is called the lay length or pitch. The lay angle or helix angle α_i for a given layer i is defined as: $\alpha_i = \tan^{-1}(\frac{2\pi r_i}{\ell_i})$, where ℓ_i is the pitch of the helix defined by the centre of a wire (or strand in that layer) and r_i corresponds to the helix radius.

Strands with equal lay construction are those in which all layers of wires have the same pitch, and hence on no occasion does a wire cross over the crown of an underlying wire as is the case in a cross-lay construction where wires in successive layers of the strand are spun at approximately the same lay angles with opposite sense. In the latter construction wires in successive layers make point contact that is liable to local crushing and cross-cutting which is detrimental to the strand fatigue properties.

Wire ropes can be made either in Lang's lay or in ordinary lay (regular lay). Lang's lay is one in which the

wires in the strand are laid in the same direction as the strands are laid into the rope, e.g. strand and rope both right hand helices. Ordinary lay construction is one in which the strand wires are laid in one direction, and the complete strands laid up into the rope in the opposite direction. Lang's lay rope has greater abrasive and fatigue resistance in comparison with the ordinary lay construction, and for applications where rotation or torque is not a problem, Lang's lay rope can be used with advantage.

The wires used are either ungalvanised (known as bright) or are covered by a layer of zinc coating. Hot dip galvanizing is the usual technique adopted. The quality of galvanizing is defined by its weight, evenness and adherence. Different classes are designated conventionally by letters A, B and C (0.1)*.

Wires in structural strands and ropes are not normally heat treated after drawing, although there could well be intermediate heat treatment during the drawing process depending on the amount of cold working involved. In some not atypical cases up to 95% of reduction of area is achieved. It follows that finished wires have highly anisotropic properties.

After the wire is drawn to a finished size, it undergoes a series of quality control tests. These include tests of strength, careful measurements of the diameter and a torsion test to determine uniformity and toughness.

---

* References in this thesis are denoted by Chapter number and sequence within the Chapter.

During the stranding process individual wires are subject to a number of direct forces accompanied by a combination of bending and torsional moments which result in a significant level of plastic (permanent) strains in the wire upon the removal of the external forces. The torsional twist fed into each wire during laying up of strands is controlled in the manufacturing process and influences the stability and ease of handling of the finished product. The torsion free outer wires of a locked coil strand are another example of this controlled process.

In equal lay construction several layers (or even the whole strand) can be put together in one operation which is of obvious commercial importance. The pattern depends mainly on the number of machine bobbins available - one bobbin for each individual wire. Such strands offer minimum possible diametral change under load and also have a greater strength/size ratio - that is more steel can be packed in when compared to the cross laid construction. The latter is often carried out by adding successive layers of wires in different operations (even for strands with small diameter). Many recent spiral strands are manufactured with an equal lay construction as their core which is then covered by a number of cross laid layers. Such strands offer an improved axial and transverse load carrying capacity necessary to meet the reaction from (e.g.) sheaves and pulleys and also have the often very desirable non-rotating properties. Figure (0.2) gives some examples of such constructions.

A rope is made in much the same manner as a strand except that strands replace wires in a larger machine.

For the process of closing strands and ropes a hot lubricant is applied, completely filling all the interstices. Lubricating ("blocking") compounds play an important role in assuring that a wire rope will give satisfactory service in the field. The type and the condition of the internal lubricant can have a marked effect on fatigue performance. During service a portion of the original lubricant oozes out due to heat or heavy radial pressures and is wiped away by abrasion and the washing action of rain and other elements. In such cases suitable service dressings are essential. These should be compatible with the manufacturing lubricant, and must be capable of penetrating into the strands and rope. It must be noted that apart from improving the rope's performance and safety, proper lubrication can save a considerable amount of time and/or money in the maintenance and replacement of not only the cable itself, but also the drums or sheaves on which it runs (0.2, 0.3).

End fittings are used to connect the cables to other parts of a structure . These fittings are of various shapes and sizes. Their selection, inspection and replacement criteria are based on past experience rather than comprehensive testing or analysis. In all cases the skill of the craftsman who makes the termination is an important factor in determining the strength of the termination. Ideally, the end fitting must be capable of transferring the breaking strength of the cable (under both the static and

dynamic conditions) without exceeding its own yield strength or significantly affecting the cable's mechanical properties such as its fatigue behaviour. Static tests are often used to check the efficiency of the end fitting, although (in most applications) the cable system is subject to fluctuating loads and its behaviour could differ from that observed during the static test.

For a given diameter, helical strands exhibit higher axial stiffness and ultimate strength than ropes. On the other hand they suffer from the drawback of a low bending flexibility. Strands usually have larger diameter wires than the ropes of the same size and the larger the zinc coated wires are, the smaller will be their rate of corrosion. Strands in general have less exposed surface area when they are placed in a corrosive environment and their outside surface is smoother than ropes. This makes them more amenable to the application of a plastic sheath for corrosion protection which can be very useful in,for example, offshore applications. It is because of these attractive properties that spiral strands have been used for a wide variety of structural purposes including hangers for suspension bridges, main cables in cable-stayed bridge designs and stays for guyed masts. Spiral strands are also considered as an attractive candidate for tension leg platform applications.

Cable design and manufacture is often considered to be an art rather than a science. The limits of validity of present design and calculating routines, largely based on

commercial experience, are far from clear. Simply scaling up cable diameters to meet the ever growing demands for stronger elements, via extrapolation of the orthodox designs, is a risky process. Model tests of the designs in the present state of understanding of cable behaviour are unacceptable while full-scale testing is very expensive. There is,therefore,a need to improve the methods of cable design, moving from craftsmanship and experience towards a more exact i.e. mathematical level.

A literature survey was carried out to establish the present state of the art. On both the experimental and theoretical sides, reliable information of direct practical use was found to be very scarce. In published work, there seemed to be an undue amount of prejudice, repetition and imprecise conclusion. The conflicting desires for publicity and commercial secrecy were also evident. Once fatigue is addressed, the number of variables involved makes the interpretation of the extensive work by manufacturers and technical societies rather difficult and divergence of opinion on various aspects of cable behaviour under even closely controlled laboratory conditions is not uncommon. It became clear that the physical behaviour of even the apparently simple spiral strand (much less a rope) was not well understood, and the analytical methods described had considerable shortcomings. The need for a stress analysis which takes the inter-wire contact forces and slip between wires into account became obvious and it is this aspect of the problem which is given much attention in what follows.

REFERENCES

0.1 ASTM Specification for Zinc-Coated Steel Structural Strand. ASTM A586-68 (Reapproved 1976).

0.2 KASTEN, R.O. Proper Wire Rope Lubrication. Lubrication Engineering. 1964: 20 (5) pp.180-183.

0.3 BURROUGHS, D.B. The Spray and Dip Methods of Applying Lubricant to Wire Rope. Lubrication Engineering. 1956: 12(3), pp.193-195.

CHAPTER 1

REVIEW OF CONTACT STRESS THEORIES

1.1 INTRODUCTION

In this chapter, the results of some generalizations of the classical Hertz theory of elastic contact are considered in detail. Particular attention is paid to cases involving cylinders in contact in view of their obvious relevance to the behaviour of individual wires in strands and ropes. The assumptions made and the consequent limitations on the use of the results are discussed in more detail than the particular solution techniques employed.

This section is followed by others dealing with contact due to force systems which do not act normally to the contact surface. In addition to the geometric non-linearity present in all contact problems, yielding and friction at the contact points give rise to further complications. Once slip develops, with its associated energy dissipation and permanent set, the changes in tractions and displacements are found to depend not only upon the initial state of loading, but also upon the entire history of loading and the instantaneous relative rates of changes of the normal and tangential forces.

The last section of this chapter is devoted to a survey of the available experimental work and its correlation with the theoretical results. The limitations of the

assumptions made in cases involving frictional phenomena are carefully examined.

1.2 BRIEF DISCUSSION OF HERTZIAN THEORY FOR NORMAL CONTACT

In two papers (1.1) published almost a century ago, Hertz reported his analysis describing the elastic stress system generated in two bodies(initially making a frictionless contact at a single point)upon being pressed together with a force p. His solution begins with a consideration of the geometry of two quadratic surfaces in the neighbourhood of the centre of contact. The bodies are assumed to be homogeneous and isotropic with their surfaces topographically smooth and continuous. The surface tractions are assumed to be due to contact forces only (adhesive forces are ignored), and the stresses and displacements are calculated according to small-strain theory of elasticity applied to a linear elastic half-space. The theory gives overall deformation, δ_n, the distance through which parts of the bodies remote from the contact point approach one another, magnitude and orientations of the principal axes of the ellipse bounding the contact interface,and the distribution of the normal tractions across the contact patch.

Numerous experiments have confirmed the essential validity of his results, specifically the shape and size of the contact region and aspects of the resulting stress field. Specific references may be found in Ref. (1.2).

Deviations from Hertz theory, for normal force, are generally small. Nonetheless in special circumstances physical conditions which were ignored by Hertz can be important. An extensive review of these aspects of the contact problem is outside the scope of this thesis. Representative results of, and references to, the extensions of the normal contact theory to non-Hertzian conditions may be found in the surveys by Johnson (1.3) and Deresiewicz (1.4). For the present purpose it suffices to touch upon a few particular aspects of such generalizations.

The quadratic representation of the surfaces in the neighbourhood of the centre of contact leads to no significant errors provided the dimensions of the contact region are much smaller than the radius of curvature at the contact. Attempts have been made to include terms higher than second order in the representation of surface profiles (e.g. see Ref.(1.5)). However, as pointed out by Johnson (1.3) the use of small-strain theory in conjunction with such generalizations makes the procedure generally unsatisfactory, because the errors associated with half space small-strain theory are often of the same order of magnitude as the corrections introduced by choosing a higher order surface profile.

In the normal contact of bodies, friction introduces a first order correction only when the two bodies have dissimilar elastic constants, whether or not their radii are equal (1.3).

Real surfaces are never perfectly smooth and it is now commonly accepted that when two supposedly 'flat' surfaces are placed together they touch only locally. The load is then transmitted across the interface through several contacts formed by the surface irregularities. This was first shown around 1940 by Holm (1.6) who was studying the properties of electric contacts, Ernst and Merchant (1.7) who were investigating the metal cutting process, and Bowden and Tabor (1.8) who dealt with surface chemistry.

Frictional behaviour is dominated by the properties of these small regions of contact. To have a clear picture of the friction and wear, it is, therefore, necessary to understand the physics of formation, deformation and subsequent breaking of these contact junctions. For example, it is important to know their number, size and distribution as well as their mode of deformation (how far it is elastic or plastic) and the extent of the adhesion at the interface. Both sliding and reciprocating sliding involve shearing of these contact regions and a knowledge of the effect of tangential displacements on their properties is of prime importance.

Because of the experimental difficulties of determining directly the true area of contact, a number of theoretical models have been developed showing how the true contact area may be expected to vary with load. Two extremes of deformation are employed in these models: either purely elastic or purely plastic.

Bowden and Tabor (1.9) have shown that, when metal surfaces rest on one another, the peaks of their asperities readily deform plastically, the mean pressure over the deformed areas being given by the relation:

$$P_m = C \quad Y$$

Y is the elastic limit of the deformed material at the tip of the asperities(work-hardening is ignored). The factor C , they suggest, depends on the shape and size of the surface irregularities, but for conical and pyramidal asperities of a wide range of angles and for hemispherical asperities C has a value of about three.

Thus

$$P_m \simeq 3 \; Y$$

The mode of deformation of the material around the asperity also appears to be very important. Samuels and Mulheam (1.10) and Mulheam (1.11) showed that for hardness test identations, material is often displaced radially outwards from the identations rather than towards the surface, as postulated in the rigid die theory. Mulheam assumes that the major deformation process is one of uniform radial compression, with the surfaces of equal displacement and equal strain being hemispheres. Marsh (1.12) used this mechanism in formulating a new theory for the identation hardness test, giving the equation:

$$\frac{P}{Y} = C+Bk \; \ell n \; Z$$

where C and K are constants,

$$B = \frac{3}{3-\lambda} \text{ and } Z = \frac{3}{\lambda+3\mu-\lambda\mu}$$

with $\lambda = 6(1-2\nu)\ {}^{Y}/_{E}$

and $\mu = (1+\nu)\ {}^{Y}/_{E}$

E is Young's modulus and ν is Poisson's ratio, Y being the flow stress of the material.

To test the validity of the above expression Marsh tested many materials. The results of these tests are shown in Fig.(1.1) where $\frac{P}{Y}$ is plotted against BℓnZ. Besides Tabor's line ($\frac{P}{Y} = 3$) the line predicted from Marsh's theory is inserted using "best fit" values for C= 0.28 and K = 0.60. The agreement of the lines with the experimental points is remarkable and the relations seem to have wide validity over their respective regimes, since materials as diverse as "Derlin" (nylon), a bearing steel, and soft lead alloys fall close to one line or the other.

Since it is reasonable to assume that the material behaviour during the identation test is similar to the behaviour of two asperities in contact, under load, the plasticity theory may be used to determine the real area of contact. For purely plastic deformation, therefore, the true area of contact A_r is directly proportional to the load; the mean pressure over each individual asperity being taken as $P_m = C.Y.$

In the practical problems for which Hertzian theory gives an elastic state of stress, two distinct regimes may actually occur within the stressed region - the main body of the material in which the deformation is elastic, and the surface asperities, where real contact occurs, in which the strains are plastic or partly so.

The second case to be considered is that in which shear forces, as well as normal forces, act on a junction. Owing to the discrete nature of the contact between rough surfaces the force of friction may be calculated by summing the individual frictional forces at the spots of real contact. Bowden and Tabor (1.9) suggest:

$$F = \sum_{k=1}^{n} \Delta\tau_k = \tau \sum_{k=1}^{n} \Delta A_r = \tau A_r$$

where F is the frictional force, n is the number of the elementary spots and A_r is the real area of contact which is equal to the sum of the elementary spots. τ is the shear stress at the contact point which is assumed to be a constant. Since A_r is assumed to be proportional to the load and independent of the size of the bodies, they then conclude that friction will also be proportional to the load, which is in accordance with Amonton's laws of friction.

For many years plasticity theory was considered justified because, based on over-simplified models similar to the type mentioned above, it provided an explanation for the generally accepted laws of friction, while, for a single elastic contact, the area of contact A is known to be proportional to the $^{2}/_{3}$ power of the load W. Since the

frictional force is generally assumed to be proportional to A_r, it was thought that in elastic deformation Amonton's law would not be obeyed.

More recently, Archard (1.13) considered the two extreme cases of either the number or the average size of multiple-contact areas to remain constant as the normal load W is increased. In the former case he suggested the area of contact to be proportional to the two-thirds power of the load, and in the latter case the area was taken to be proportional to the load. With real surfaces he suggested an intermediate behaviour. Consequently, for pure elastic deformation the true area of contact was found to be proportional to W^n, where n lies between $^2/_3$ and 1. If this is the only factor affecting the friction, the friction should also follow a relationship of this sort.

In a later paper, Archard (1.14) pointed out that although it is reasonable to assume plastic flow for the first few traversals of one body over another it is absurd to assume this for machine parts which may make millions of contacts during their life: the asperities may flow plastically at first, but they must reach a steady state in which the load is supported elastically. In the same paper he argued that in real life each asperity is covered with microasperities, and each microasperity with micromicro-asperities and so on. He then used a simple model in which a spherical surface was covered with smaller spherical protruberances upon it. For this case he showed the index of W is $\frac{8}{9}$ which is in agreement with the result obtained by

Lodge and Howell (1.15). For the case where these small spherical asperities were themselves covered by smaller spherical asperities the area of true contact based on elastic theory was shown to be proportional to $W^{26/27}$. In other words it was shown that as the scale of superimposed spheres is reduced, the index tends to unity. Thus he showed that a satisfactory explanation of Amonton's laws of friction is not dependent upon the assumption of purely plastic deformation.

Greenwood and Williamson (1.16) postulated a model, representing a rough nominally flat surface, consisting of a series of spherical peaks, each having the same radius of curvature, and having a Gaussian distribution of heights (note that in the model used by Archard the spherical asperities were assumed to be uniformly distributed). For their model, based on elastic theory, they also showed that the relation between A_r and W was close to linear proportionality.

Ling (1.17), Whitehouse and Archard (1.18), Nayak (1.19), Greenwood and Tripp (1.20), among others, have also proposed a number of other statistical models of nominally 'flat' elastic rough surfaces. The elastic contact of two parallel rough cylinders was investigated by Lo (1.21).

Although helpful, these models have serious limitations. For example, real asperities are not necessarily spherical: they may be of very varied shapes, and their distribution may be irregular. The diversity of the influencing factors makes it quite apparent that their

behaviour cannot be determined exactly by any generally valid law.

Surface defects are an ever present problem in all machine parts subject to cyclic loading. This aspect of the contact problem was considered analytically by Chiu (1.22) who investigated the static line contact of two elastic and topographically smooth cylinders under normal loading, one of which contains an idealized form of shallow longitudinal surface depression located symmetrically with respect to the centre of the contact region. His solution contains the surface contact pressure distribution but not the subsurface stresses. Moreover, it neglects effects of shear loading on these stresses which,in general,are very significant. Nevertheless, at least qualitatively, it is shown that these stresses deviate significantly from those of the normal Hertz problem. The sweeping assumptions made in idealizing such a complicated problem make the practical validity of the "stress - concentration factors" derived in the paper rather unlikely (see discussions to the paper).

The elastic contact problem of layered solids has also enjoyed some attention in recent years. Meijers (1.23) has presented asymptotic solutions to the plain strain problem of both very thin and thick elastic layers bonded to a rigid substrate. The particular problem tackled by him was the normal contact of a rigid cylinder on an elastic layer connected rigidly to a rigid base. Gupta and Wallowit (1.24) solved the more general problem of elastic

layers bonded to an elastic substrate and they have also discussed other available work on the subject. An important conclusion in (1.24) is that when the elastic behaviour of the layer and that of the substrate are substantially different, the contact problem is no longer Hertzian and the classical Hertzian stress analysis is generally not valid (a point to remember when calculating the contact stresses between galvanized wires in a wire rope).

Even apparently clean surfaces are still covered by a thin film of oxide, water vapour, and other adsorbed impurities. The contaminant film is usually at least several molecular layers in thickness, and may have significant effects on the friction (Bowden and Tabor (1.9)).

It is found experimentally that for surfaces without pronounced directional properties, the body moves in the direction of the applied tangential force, T, and from this it follows that the friction force is colinear with T. For such surfaces the instantaneous friction force may fluctuate by a degree or so from its assigned direction, changing direction continuously and in random fashion as sliding proceeds (1.25). If the surface has lapping marks or other scratches in one direction, or is the face of a crystal, the friction force may vary from its assigned direction by a few degrees if relative motion is at an angle to the "grain" of the surface (1.26). Hence, when we consider the shear interaction of various layers of a helical strand under bending, due to the orthotropic pattern of the

contact patches between the successive layers, the direction of the shear forces and their corresponding shear displacements do not in general coincide. A theoretical study of such effects will be presented later on (Ref. Chapter 4).

It is well known that the friction force required to start sliding is usually greater than the force required to maintain sliding, and this has given rise to the notion that there are two coefficients of friction - static (for surfaces at rest) and kinetic (for surfaces in motion). Fairly recent work has shown that this is a gross over-simplification, and the static coefficient of friction is a function of time of contact (1.27), whereas the kinetic friction coefficient is a function of velocity throughout the range of velocities.

Lubrication compounds play an important role in assuring that a wire rope will give satisfactory service in the field. Normal contact stress theory is not concerned with the influence of a lubricant between the surfaces, but in view of the practical importance of lubrication a few remarks must be made.

With extremely high local pressures at the contact points of the wires in association with their low relative speeds of movement there is little possibility of any significant elasto-hydrodynamic action.

For example, elasto-hydrodynamic action for stationary concentrated contact under vibrating load has been considered doubtful in the paper by Burton and Russell (1.28). They argue that although it is reasonable to assume

that for the first loading case a squeeze film will form as the load is applied, it is hard to believe that sustained support is possible under continuous cyclic loading as in this case the fluid would need to be drawn back into the contact zone every time the load is removed. As yet, no specific arguments in support of such a suction of fluid into the contact zone seem to have been put forward. However, not everybody in the field of lubrication agrees with them (see discussion to their paper).

In general,one may reasonably assume that the presence of a normal lubricating oil does not appreciably affect the normal stress problem except for the local value of the coefficient of friction,which is employed in the theory to determine the extent of micro-slip and the resulting tangential tractions over the contact region under the action of tangential forces (Vermeulen and Johnson (1.41)) it may be mentioned that the effect of minute quantities of lubricant trapped inside pits and surface irregularities (which usually exist in the surface of real materials) on the contact fatigue behaviour has been assumed to be significant. Under normal cyclic loads the lubricant trapped inside these surface defects may contribute significantly to the initiation and further propagation of fatigue cracks (Timoshenko (1.29)).

To conclude this section, results of the normal Hertzian theory for the case of non-spherical bodies as derived by Hertz and his successors will be presented. Particular attention will be given to the case of two

cylinders in contact as this is of obvious direct relevance to the investigation of contact forces and deformation patterns in a wire rope or strand.

When two curved bodies are in contact under normal load, the intensity of load across the contact area is given by the Hertzian solution:

$$p(x,y) = \frac{3P}{2\pi ab}\left(1 - \frac{x^2}{a^2} - \frac{y^2}{b^2}\right)^{\frac{1}{2}} \qquad (1.1)$$

where P is the total load acting on the body over the contact area, and a and b are the semi-major and semi-minor axes of the elliptical contact area respectively. It represents a pressure of $\frac{3}{2}\ \frac{P}{\pi ab}$ at the centre of the contact area (or 1.5 times the average pressure) and a zero pressure on the curve $\frac{x^2}{a^2} + \frac{y^2}{b^2} = 1$. In other words, the distribution of normal load takes the form of an ellipsoid whose three axes are $a > b$ and $\frac{3}{2}\frac{P}{\pi ab}$.

The formulae derived by Hertz give the maximum compressive stresses on the surface, but not the maximum shear stresses which occur in the interior of the compressed parts, nor the tensile stress which occurs at the boundary of the contact area and is normal to it (Timoshenko (1.30)).

In 1930, Thomas and Hoersch (1.31) discovered that the shearing stress on the axis of symmetry reaches a maximum at some distance underneath the centre of the contact area. Their computation of stresses was checked by experiment. Belajaf (1.32) calculated the stresses at any point in the infinite half-space and gave similar results on the axis of

symmetry to those obtained by Thomas and Hoersch. A tabulated summary of surface and subsurface stress distribution is given in Ref. (1.33).

For the case of two parallel cylinders Thomas and Hoersch give the following closed form expressions for the principal stresses for points on the axis of symmetry (z - axis) at various depths below the contact surface:-

$$\sigma_x = -2\nu \left[\sqrt{1+\left(\frac{z}{b}\right)^2} - \frac{z}{b} \right] \frac{b}{\Delta}$$

$$\sigma_y = -\left[\frac{\left(\sqrt{1+\left(\frac{z}{b}\right)^2} - \frac{z}{b} \right)^2}{\sqrt{1+\left(\frac{z}{b}\right)^2}} \right] \frac{b}{\Delta} \qquad (1.2)$$

$$\sigma_z = -\left[\frac{1}{\sqrt{1+\left(\frac{z}{b}\right)^2}} \right] \frac{b}{\Delta}$$

Where the quantity b is one-half the width of the rectangular area of contact between the cylinders and may be found from the equation:-

$$b = \left(\frac{2P\Delta}{\pi}\right)^{\frac{1}{2}} \qquad (1.3)$$

P is the load per unit length of the contact area and the value of Δ is given by:

$$\Delta = \frac{1}{\left(\frac{1}{2R_1}\right) + \left(\frac{1}{2R_2}\right)} \left(\frac{1-\nu_1^2}{E_1} + \frac{1-\nu_2^2}{E_2} \right)$$

Where R_1 and R_2 are the radii of the cylinders.

For two parallel cylinders, the maximum shear stress defined as $\frac{1}{2} |\sigma_z - \sigma_y|$ was then found to occur at $\frac{z}{b} = 0.7861$. Note, also, that the case of infinitely long cylinders under line - contact is one of plane strain resulting in the simple relation $\sigma_x = \nu(\sigma_z + \sigma_y)$.

Starkey and Cress (2.28) and Leissa (2.27) used the above expressions to investigate the contact stresses between wires of their model wire ropes.

The problem in using Equations (1.2) is that they only apply to the points lying on the z-axis. Simple closed expressions for the stresses throughout the infinite half-space for the case of long cylinders in line contact can be found in the work by Smith and Liu (1.34), who also consider the influence of frictional surface tractions. For a zero coefficient of friction they give:-

$$\sigma_y = -\frac{P_o}{\pi} z \left[\frac{b^2 + 2y^2 + 2z^2}{b} \psi^- - \frac{2\pi}{b} - 3y\psi \right]$$

$$\sigma_z = -\frac{P_o}{\pi} z \left[b\psi^- - y\psi \right] \qquad (1.4)$$

$$\sigma_x = \nu(\sigma_y + \sigma_z)$$

$$\tau_{yz} = -\frac{P_o}{\pi} z^2 \psi$$

where $P_o = \frac{2P}{\pi b}$ and $\psi = \frac{\pi}{K_1} \frac{1 - \sqrt{\frac{K_2}{K_1}}}{\sqrt{\frac{K_2}{K_1}} \sqrt{2\sqrt{\frac{K_2}{K_1}} + \frac{K_1 + K_2 - 4b^2}{K_1}}}$

$$\psi^- = \frac{\pi}{K_1} \frac{1 + \sqrt{\frac{K_2}{K_1}}}{\sqrt{\frac{K_2}{K_1}} \sqrt{2\sqrt{\frac{K_2}{K_1}} + \left(\frac{K_1 + K_2 - 4b^2}{K_1}\right)}}$$

$$K_1 = (b+y)^2 + z^2$$

$$K_2 = (b-y)^2 + z^2$$

Hamilton (1.35) combined these equations with the Von Mises yield criterion and, assuming $\nu = 0.3$, he showed that yielding first occurs on the centre line ($y=o$) at $\frac{z}{b} = 0.704$.

The reduction in distance between the centres of two parallel cylinders has been given in a closed form by (1.36):

$$\delta_n = \frac{2P(1-\nu^2)}{\pi E}\left(\frac{2}{3} + \ell n\,\frac{2R_1}{b} + \ell n\,\frac{2R_2}{b}\right) \qquad (1.5)$$

For the more general case of non-spherical bodies in contact the surface of contact will have an elliptical shape. The semiaxes of the elliptic boundary are:

$$a = \alpha\,(PK_D C_E)^{1/3} \qquad (1.6a)$$

$$b = \beta\,(PK_D C_E)^{1/3} \qquad (1.6b)$$

where $$C_E = \frac{1-\nu_1^2}{E_1} + \frac{1-\nu_2^2}{E_2} \qquad (1.6c)$$

and $$K_D = \frac{1.5}{\frac{1}{R_1} + \frac{1}{R_2} + \frac{1}{R_1'} + \frac{1}{R_2'}} \qquad (1.6d)$$

$\frac{1}{R_1}$ and $\frac{1}{R_1'}$ are the principal curvatures of body 1, and $\frac{1}{R_2}$ and $\frac{1}{R_2'}$ of body 2. R_1 and R_2 denote the minimum radii of curvature while R_1' and R_2' are the maximum radii of curvature. α and β are given in Table (1.1) in which:

$$\cos\theta' = \frac{K_D}{1.5}\sqrt{\left(\frac{1}{R_1}-\frac{1}{R_1'}\right)^2+\left(\frac{1}{R_2}-\frac{1}{R_2'}\right)^2+2\left(\frac{1}{R_1}-\frac{1}{R_1'}\right)\left(\frac{1}{R_2}-\frac{1}{R_2'}\right)\cos 2\phi} \tag{1.6e}$$

and ϕ is the angle between the plane containing curvature $\frac{1}{R_1}$ in body 1 and the plane containing curvature $\frac{1}{R_2}$ in body 2. P is the total load.

For the case of cylindrical surfaces the radii R_1' and R_2' are each indefinitely large so that $\frac{1}{R_1'}$ and $\frac{1}{R_2'}$ are each equal to zero. Then if $R_1 = R_2 = R$, $\theta' = \phi$.

The expression for the value of δ_n, the approach distance between the two bodies along the axis of loading is:

$$\delta_n = \lambda \left(\frac{P^2 C_E^{\,2}}{K_D}\right)^{1/3} \tag{1.7}$$

Values of λ as a function of $\cos\theta$ are also included in Table (1.1).

Thomas and Hoersch (1.31) and Foeppl (1.37) have found that in three dimensional contact stress problems the shearing stress on the axis of symmetry produced by a normal load is maximum at a distance below the surface. For a long time this discovery led engineers to believe that the failures which occurred in contacting parts, such as cracks and pits, are initiated in the interior of the body and spread towards the surface after a number of repetitions of loading. Recent investigations which have considered the influence of tangential forces on the contact surface indicate significant changes in the magnitude and general pattern of

stresses around the contact region and strongly suggest that the neglect of friction between two sliding bodies may give rise to somewhat misleading results. These ideas will be reviewed in the following sections.

1.3 TANGENTIAL FORCES

The initial situation considered is that of two metallic bodies pressed together by a force normal to their surface of contact and acted upon subsequently by a tangential force tending to cause one to slide upon the other. The three dimensional case has been solved independently by Cattaneo (1.38) and Mindlin (1.39).

Mindlin first considered the 'no slip' condition of two spheres pressed together under a normal force P and subsequently acted upon by a tangential force T parallel to the contact tangent plane. With the assumption that the surfaces adhere together without slip over the whole area of contact, and using small strain elastic theory applied to an infinite half-space, he found that the tangential traction on the circular contact area, with the same radius as determined by the Hertzian theory, is everywhere parallel to the direction of the tangential applied force and that contours of constant tangential traction are concentric circles. The magnitude of the traction rises from one half the average at the centre to infinity at the edge of the circle of contact and is given by:

$$\tau = \frac{T}{2\pi a}(a^2-\rho^2)^{-\frac{1}{2}} \quad , \quad \rho<a \qquad (1.8)$$

where a is the radius of the contact patch under normal load P , and T is the total tangential force.

The corresponding expression for the elliptic contact was found to be:

$$\tau = \frac{T}{2\pi ab}\left(1 - \frac{x^2}{a^2} - \frac{y^2}{b^2}\right)^{-\frac{1}{2}} \qquad \begin{matrix} x < a \\ y < b \end{matrix} \qquad (1.9)$$

where a and b are the semi-major and semi-minor axes of the ellipse of contact respectively. Equation (1.9) again indicates the existence of an infinitely large tangential traction on the edge of the contact patch.

Based on this tangential traction distribution, Mindlin found the 'no-slip' tangential compliances of two bodies to be constant,and for the practical range of the Poisson's ratio $0 < \nu < 0.5$ he obtained plots of the no-slip tangential compliance as a function of $(\frac{a}{b})^2$, for bodies having the same elastic properties (Fig.1.2).

According to these plots,the no-slip tangential compliance in the direction of the minor-axis is less than the initial tangential compliance, as it might alternatively be called, in the direction of the major-axis of the contact area. For the case of $\nu=o$, however, the initial tangential compliance is found to be isotropic.

Mindlin also gave plots of the ratio of initial tangential compliance to the normal compliance for bodies having the same elastic properties. These plots are

reproduced in Fig.(1.3). For the limiting case of two parallel cylinders, which is of direct relevance to the present work, the ratio takes the particularly simple form of:

$$\frac{S_{66}}{S_{22}} = \frac{1}{1-\nu} \tag{1.10}$$

where S_{66} and S_{22} are the initial tangential and normal compliances respectively of two bodies in contact.

The important assumption made by Mindlin is that the existence of the tangential surface tractions does not modify the Hertzian distribution of normal pressure. At the boundary of the contact region the Hertzian pressure distribution suggests the magnitude of the normal pressure to be zero so that slip must in fact occur regardless of how small the applied tangential force is. On the other hand, since in the absence of slip, the traction distribution is symmetric, slip will take place over an annular region.

Quite reasonably, it is assumed that the tangential traction τ at any point cannot exceed the product of a constant coefficient of friction and the normal pressure p, that is, $\tau < \mu p$, and that slip will continue until this condition is satisfied over the whole area of contact. Gross sliding, i.e. slip over the whole patch, takes place once we have $T = \mu P$. The addition of slip increases the relative displacement between points in one body remote from the contact with respect to similarly located points on the other body and for the case of two elastically similar spheres

Mindlin gives:

$$\Delta = \frac{3\mu P(2-\nu)}{16Ga}\left[1-(1-\frac{T}{\mu P})^{2/3}\right] \qquad (1.11)$$

where Δ is the displacement for one body. G is the shear rigidity and ν is Poisson's ratio, while a denotes the radius of the Hertzian contact circle.

The tangential compliance for one body is then given by Mindlin (1.39) as:

$$\frac{d\Delta}{dT} = \frac{2-\nu}{8Ga}(1-\frac{T}{\mu P})^{-1/3} \qquad (1.12)$$

Fig.(1.4) gives the distribution of tangential tractions due to a tangential force T across a circular contact area for both the no-slip and partial slip conditions.

For a pair of non-spherical bodies, tangential loading in the presence of constant normal load leads to results similar to those discussed above. Cattaneo (1.38) considered the case of a single force acting in the plane of contact and directed parallel to one of the principal axes of the contact ellipse. For a monotonically increasing force T, superposed on the constant normal force P , he found that slip in the direction of T takes place between the two bodies. Under the action of $T < \mu P$ the elliptical area of contact was shown to be divided into a central elliptical region, homothetic with the contact ellipse, where there was no relative slip between the surfaces and an annular region of slip. The distribution of tangential

traction in the slip region was again reasonably assumed to be equal to the normal pressure, as given by Hertz, multiplied by a constant coefficient of friction μ. The tangential surface tractions in the annulus of slip will then be:

$$\tau(x,y) = \frac{3\mu p}{2\pi ab} \left(1- \frac{x^2}{a^2} - \frac{y^2}{b^2}\right)^{\frac{1}{2}} \tag{1.13}$$

In the no-slip, inner, ellipse the traction is found to be

$$\tau(x,y) = \mu p(x,y) - \mu p_1(x,y)\left(1- \frac{T}{\mu p}\right)$$

where $$p(x,y) = \frac{3P}{2\pi ab}\left(1- \frac{x^2}{a^2} - \frac{y^2}{b^2}\right)^{\frac{1}{2}}$$

and $$p_1(x,y) = \frac{3P}{2\pi a_1 b_1}\left(1- \frac{x^2}{a_1^2} - \frac{y^2}{b_1^2}\right)^{\frac{1}{2}}$$

with a_1 and b_1 denoting the semi axes of the inner boundary of slip obeying the relations

$$\left(\frac{a_1}{a}\right)^3 = \left(\frac{b_1}{b}\right)^3 = 1- \frac{T}{\mu p} \tag{1.14}$$

Almost twenty years later Deresiewicz (1.40) evaluated the constant displacement of the adhered region for Cattaneo's problem in the form:

$$\Delta_\ell = \frac{3\mu p(2-\nu)}{16Ga}\left[1-\left(1- \frac{T}{\mu p}\right)^{2/3}\right]\phi$$

$$\text{where: } \phi = \begin{cases} \left[\frac{4a}{\pi b}(2-\nu)\right] \left[(1-\frac{\nu}{k^2})K + \frac{\nu E}{k^2}\right] & , a<b \\ 1 \ , a=b & \\ \left[\frac{4}{\pi}(2-\nu)\right] \left[(1-\nu+\frac{\nu}{k_1^2})K_1 - \frac{\nu E_1}{k_1^2}\right] & , a>b \end{cases} \qquad (1.15)$$

K and E are, respectively, complete elliptic integrals of the first and second kind of argument $k=(1-\frac{a^2}{b^2})^{\frac{1}{2}}$; K_1 and E_1 are similar integrals of argument $k_1=(1-\frac{b^2}{a^2})^{\frac{1}{2}}$

a is the half-width of the principal axis parallel to T and Δ_ℓ is the displacement per body in the direction of the applied tangential load of any point in the adhered region.

For the case of spherical bodies ϕ takes the value of unity and the resulting expression for Δ is identical to expression (1.11). In fact, Deresiewicz found that the relation between T and Δ is qualitatively the same for spherical and non-spherical bodies as well as for loading parallel to either principal axis of the contact patch. The quantitative difference between the various cases lies only in the constant factor ϕ which depends solely on the parameters of the normal Hertz problem.

The tangential compliance of <u>two</u> bodies is then:

$$\frac{d\delta_\ell}{dT} = \frac{2-\nu}{4Ga}\left(1-\frac{T}{\mu p}\right)^{-1/3} \phi \quad \text{where} \quad \delta_\ell = 2\Delta_\ell \qquad (1.16)$$

Gross slip occurs when $T=\mu p$. From Equation (1.15) it can be seen that at the onset of gross slip we have: $\Delta_{\ell_{max}} = \frac{3\mu p(2-\nu)}{16Ga}\phi$

However, for the **no-slip case**:

$$\Delta_\ell = \left(\frac{d\Delta_\ell}{dT}\right)_{T=o} . \ T \qquad (1.17)$$

i.e. when $T=\mu P$, we have $\Delta_\ell = \frac{2-\nu}{8Ga}(\mu P)\phi$

That is, the displacement before gross slip is 1.5 times greater than the elastic displacement calculated on the no-slip assumption.

For two cylinders in line contact with the tangential force directed along the line of contact the value of ϕ in (1.15) becomes indefinite and an alternative approach has been developed by the present author.

From (1.10) we have:

$$\frac{S_{66}}{S_{22}} = \frac{1}{1-\nu} \quad \text{as} \quad \frac{a}{b} \to \infty$$

on the other hand putting T=0 into (1.16) gives:

$$S_{66} = \frac{d\delta_\ell}{d(\frac{T}{a})} = \frac{2-\nu}{4G}\,\phi \tag{1.18}$$

where S_{66} is the tangential compliance for two bodies.
From (1.10) and (1.18) we finally get:

$$\phi = \frac{S_{22}(4G)}{(1-\nu)(2-\nu)} \tag{1.19}$$

Note that this value of "ϕ" only applies to the case of cylinders in line-contact with T parallel to the line of contact.

With the same general approach as in (1.40), Vermeulen and Johnson (1.41) used Cerruti's potential functions (see Love (2.56)) to find the tangential displacements on the contact surface, U and V, produced by the tangential tractions for the limiting case of $T = \mu P$. Using these they gave an expression for Δ, the displacement per body, in the form:

$$\Delta_\ell = \frac{p_o a}{2G}\left[1-(1-\frac{T}{\mu P})^{2/3}\right]\Gamma(\frac{a}{b}) \tag{1.20}$$

where $p_o = \frac{3\ \mu P}{2\pi ab}$ is the maximum tangential traction in the direction of T, and:

$$\Gamma(\frac{a}{b}) = \begin{cases} K-\nu D & a<b \\ \pi(2-\nu)/4 & a=b \\ \frac{b}{a}(K-\nu B) & a>b \end{cases} \qquad (1.21)$$

K, B and D are the complete elliptic integrals defined and tabulated by Jahnke and Emde (1.42) in terms of a modulus $k^2=1-\frac{a^2}{b^2}$ for a<b and $k^2=1-\frac{b^2}{a^2}$ for a>b. The tangential force T is directed along the principal axis of the ellipse of contact, and the semi-axis a is the one corresponding to the axis which is parallel to T. For ν= 0.3 a plot of $\Gamma(\frac{a}{b})$ versus $\frac{a}{b}$ is given in Fig. (1.5). Note that (1.21) is the result obtained by Deresiewicz presented in a different (more convenient) form.

For any given ratio $\frac{a}{b}$ as determined from Equations (1.6), the value of Γ can be found from either the expressions (1.21) or the plot in Fig. (1.5) (for ν=0.3). Care must be taken in the way a and b have been defined by their authors in (1.6) and (1.21). In expression (1.6) a is the semi-major axis; b corresponding to the semi-minor axis. On the other hand a in (1.20) and (1.21) always corresponds to the length of the semi-axis parallel to the applied load T.

For later use we derive the following formulations for S_{66}. The tangential compliance per body is obtained by differentiating Equation (1.20) with respect to T:

$$\frac{d\Delta_\ell}{dT} = \frac{1}{2G\pi b}\left[1-\frac{T}{\mu P}\right]^{-1/3}\Gamma(\frac{a}{b}) \qquad (1.22)$$

(1.20) can be put in the form:

$$\Delta_{\ell} = \Delta_{\ell max}\left[1-(1-\frac{T}{\mu P})^{2/3}\right]$$

where $$\Delta_{\ell max} = \frac{3}{4}\frac{\mu P}{\pi b G}\Gamma(\frac{a}{b}) \qquad (1.23),$$

$\Delta_{\ell max}$ corresponding to the case when $T=\mu P$ (i.e. onset of gross slippage).

From (1.23) we have: $$1-\frac{T}{\mu P} = (1-\frac{\Delta_{\ell}}{\Delta_{\ell max}})^{3/2} \qquad (1.24)$$

Substituting (1.24) into (1.22) we get:

$$\frac{d\Delta_{\ell}}{dT} = \frac{\Gamma(\frac{a}{b})}{2\pi b G}(1-\frac{\Delta_{\ell}}{\Delta_{\ell max}})^{-\frac{1}{2}} \qquad (1.25a)$$

The relations given for Δ_{ℓ} and $\Delta_{\ell max}$ apply to one body. For the compliance of two bodies we have:

$$\frac{d\delta_{\ell}}{dT} = \frac{\Gamma(\frac{a}{b})}{\pi b G}(1-\frac{\delta_{\ell}}{\delta_{\ell max}})^{-\frac{1}{2}} \qquad (1.25b)$$

where:

$$\delta_{\ell max} = \frac{3\mu P(1+\nu)}{\pi b E}\Gamma(\frac{a}{b}), \text{ taking } G=\frac{E}{2(1+\nu)}.$$

For the case of cylinders in line contact, Johnson's expressions for Δ_{ℓ} becomes indefinite. For this case one may use Equation (1.19).

Using the notation S_{66} for tangential compliance of two bodies we have:

$$\frac{d\delta_{\ell}}{d(\frac{T}{a})} = S_{66} = \frac{2-\nu}{8G}(1-\frac{T}{\mu P})^{-1/3}. \ (2\phi) \qquad (1.26)$$

Again using (1.24). (1.19) and (1.26) we get:

$$S_{66} = \frac{S_{22}}{1-\nu}(1-\frac{\Delta_{\ell}}{\Delta_{\ell max}})^{-\frac{1}{2}} \qquad (1.27a)$$

where $\Delta_{\ell max} = \frac{3}{4} \frac{\mu P}{1-\nu} S_{22}$ (1.27b)

P is the normal load per unit length, S_{22} is the normal compliance for two cylinders in line contact defined as:

$S_{22} = \frac{d\delta_n}{d(\frac{P}{a})}$.

Using the boundary conditions suggested by Cattaneo - i.e.

$$\tau_{zx} = p_o\left(1 - \frac{x^2}{a^2} - \frac{y^2}{b^2}\right)^{\frac{1}{2}}$$

and $\tau_{yz} = \sigma_z = o$

where $p_o = \frac{3\mu P}{2\pi ab}$

Vermeulen et.al. (1.41) found the complete stress - tensor at any point in the contact surface for the limiting case when T= μp to be:

$$\sigma_x = \frac{-p_o}{1-\nu}\left[2\phi - \nu\,\frac{a}{b}\theta\right]\frac{x}{a}$$

$$\sigma_y = \frac{p_o}{1-\nu}\left[\frac{a}{b}\,\theta - 2\nu\phi\right]\frac{x}{a} \qquad (1.28)$$

$$\tau_{xy} = -p_o\left[\frac{a}{b}\,\psi - \frac{1}{2}\,\theta\right]\frac{y}{b}$$

where $\phi(\frac{a}{b}) = \begin{cases} B - \nu(D-C) & a<b \\ \pi(4-3\nu)/16 & a=b \\ \frac{b}{a}\left[D - \nu(D-C)\right] & a>b \end{cases}$

$$\psi(\frac{a}{b}) = \begin{cases} D - \nu C & a<b \\ \pi(4-\nu)/16 & a=b \\ \frac{b}{a}\left[B - \nu\,\frac{b^2}{a^2}\,C\right] & a>b \end{cases}$$

$$\theta(\frac{a}{b}) = \begin{cases} 2\nu\,\frac{a}{b}C & a<b \\ \pi\nu/8 & a=b \\ 2\nu\,\frac{b^2}{a^2}C & a>b \end{cases}$$

B, C and D are complete elliptic integrals defined and tabulated by Jahnke and Emde (1.42) in terms of modulus $k^2 = 1 - \frac{a^2}{b^2}$ for $a<b$ and $k^2 = 1 - \frac{b^2}{a^2}$ for $a>b$. Note again that the x-axis is taken to be the one parallel to T. These stresses are due to pure tangential loading, and for the combined action of normal and tangential loading the final state of stress at any point on the contact patch may be found by direct addition of the stress due to normal load to the corresponding one as given in (1.28). An interesting consequence of including friction in the analysis is that the point of initial yielding (based on the Mises or Tresca criteria) moves up to the contact surface even for relatively moderate values of μ (very roughly about 0.3). The appearance of a high tensile stress at the end of the axis parallel to the tractive force under pure tangential loading, often considered important in connection with fatigue studies of brittle materials, is the other important result coming to light from their work. This stress acts along the same line as the tensile stress created under pure normal loading i.e. for combined tangential and normal loading the resultant stress is additive.

The case of long or short cylinders in line contact under combined normal and tangential loading for the case when the tangential load is parallel to the minor axis of the contact patch has been solved independently by Poritsky (1.43) and Smith and Liu (1.34) . Following Mindlin and Cattaneo they both assume that sliding occurs when shearing

stresses on the contact area due to the frictional force T are distributed as ordinates to an ellipse. With the pressure distribution between two cylinders pressed together given by:

$$p(y) = \frac{2P}{\pi b}\left(1 - \frac{y^2}{b^2}\right)^{\frac{1}{2}} \qquad (1.29),$$

the shear stresses on the surface $\tau_{zy}(y)$ for the limiting case of gross sliding will be:

$$\tau_{zy}(y) = \frac{2\mu P}{\pi b}\left(1 - \frac{y^2}{b^2}\right)^{\frac{1}{2}} \qquad (1.30)$$

where P is the load per unit length and b represents the half width of the contact patch.

Closed form solutions for the state of stress throughout the body for the plane-strain case are given in both references.

For the case of pure tangential loading Ref.(1.34) gives:

$$\sigma_y = -\frac{q_o}{\pi}\left[(2y^2-2b^2-3z^2)\psi + 2\pi\frac{y}{a} + 2(b^2-y^2-z^2)\frac{y}{b}\,\bar{\psi}\right]$$

$$\sigma_z = -\frac{q_o}{\pi}\, z^2\psi \qquad (1.31)$$

$$\sigma_x = \nu(\sigma_y+\sigma_z)$$

$$\tau_{yz} = \frac{-q_o}{\pi}\left[(b^2+2y^2+2z^2)\,\frac{z}{b}\,\bar{\psi} - 2\pi\frac{z}{b} - 3yz\psi\right]$$

where ψ and $\bar{\psi}$ are defined in (1.4) and $q_o = \mu P_o = \mu\,\frac{2P}{\pi b}$ The final stress distribution in the body is obtained by adding the normal and tangential contributions together.

Hamilton (1.35) used these expressions in conjunction with the Mises yield criterion to investigate the

effect of varying the coefficient of friction μ on the magnitude of the normal load P at which yield will first occur (note that Equations (1.31) apply only to the case when $T = \mu P$). His results are shown in Fig.(1.6) for the three cases of $\mu = 0$, 0.25 and 0.50. Table (1.2) shows the fraction of the original load P at which yielding first occurs under pure normal loading.

From the plots we see that at first the maximum stress remains below the surface but as the friction is increased a subsidiary maximum begins to develop in the surface and at $\mu \simeq 0.25$ they become equal in value. Thereafter the value at the surface is the greater and by $\mu \simeq 0.4$ the original maximum has reached the surface and lost its identity.

A further effect of the surface traction is to induce a large tensile stress in the surface. Fig.(1.7) gives a plot of σ_y for $\mu = 0$, 0.25, 0.50. It is seen that in the region $\frac{y}{b} \simeq -1.0$, σ_y (a tension) rises rapidly to the same magnitude as the maximum compressive stress at the centre.

In connection with fatigue failures, the range of stresses is often considered as being of prime importance. The critical type of stress is either taken to be the octahedral shear or the principal tension. For a quantitative description of these stresses one must know the magnitude, line of action and sense (whether tensile or compressive) of the stress at a given point on a given plane throughout one cycle of application and release of the load. In order to do this one must compute the stresses at a given point for several positions of the loads relative to the

location of the given point.

This aspect of the contact problem was investigated quantitatively in (1.34). For illustrative purposes they have used $\mu = \frac{1}{3}$ and $\nu = 0.25$ throughout their parametric study.

By superimposing the results from Equation (1.4) and (1.31) for a large number of points in the vicinity of the contact patch they found the stress distribution under combined normal and tangential loading. By drawing contour lines that represent constant values of principal stress, they found that maximum values of the three principal stresses occur at the point A($z=0$, $y = +0.3b$) - see Fig.(1.8). Table (1.3) gives their results for both the case of combined normal and tangential loading and also for pure normal loading providing a means of comparison between the two cases. They then calculated the magnitude, direction and sign of the three principal stresses at a given point for different positions of the load - see Figs.(1.9) and (1.10). The load is assumed to start from a far distance from the fixed point o , designated as " $+\infty$"; pass over it and finally move to a far distance on the other side of the fixed point, taken as "$-\infty$". In Fig.(1.10) the symbol σ_1^* is always given to the principal stress having the largest magnitude, σ_3^* to the one of least magnitude and σ_2^* is the intermediate principal stress. The interesting point coming out of this figure is that unlike the more usual cases of fatigue in members where the direction of each of the principal stresses remains fixed during the load cycle and only their magnitude and sign changes, in the particular problem considered the

directions of the two principal stresses that lie in the x-z plane rotate through 90^{o} as the load moves form "+ ∞" to "- ∞".

They then calculated the range of critical stresses on three different fixed planes through the point 0. The fixed planes chosen are the plane of maximum shear stress, plane of maximum octahedral shearing stress and plane of normal stress σ_y^*. σ_y^* is chosen because from their work they found it to have a greater change in magnitude than the normal stress on any other fixed plane through a fixed point either on or underneath the surface (at least for the case of $\mu = \frac{1}{3}$).

The final result is:

max range of $\sigma_y^* = 1.87\ P_o$ (see Fig.(1.10))

Range of shearing stress on plane of maximum shear $= 0.53P_o$

Range of shearing stress on plane of octahedral shearing stress $\approx 0.63p_o$

for $\mu = \frac{1}{3}$, $\nu = 0.25$, $E = 30{,}000{,}000$ psi, $P_o = \frac{2P}{\pi b}$

Comparing these with the results for normal contact in Table (1.3) reveals the importance of including tangential forces in any stress analysis associated with the sliding contact problem. Of course these quantitative results only apply to two cylinders in line contact with T parallel to the minor-axis of the contact patch, However, at least qualitatively, the same conclusions may be expected to hold for the more general cases of contact problems for which (at least for the present) no analytical solutions exist.

Although in Ref.(1.34) the stress range is found for the case when the load travels from "+ ∞" to "- ∞", it does not however explain what happens when the load reverses its direction of movement subsequently and travels back from "- ∞" to "+ ∞". This additional result would be of considerable practical interest for repeated loading/fatigue analysis.

1.4 CYCLIC TANGENTIAL LOADING WITH NORMAL LOAD KEPT CONSTANT

Equation (1.13) gives the distribution of tangential traction on the contact surface for the case when the normal force is applied first, following which the tangential force T increases monotonically from zero-see Fig.(1.11). When $T= \mu P$, the adhered portion of the contact surface has shrunk to zero and the displacement Δ has reached the value given by Equation (1.17). Any further increase in T will then result in a rigid body sliding over the whole contact surface. That is, after the point F in the figure the displacement becomes indeterminate.

In the following, the case when the tangential force T is reduced after having reached a value T^*, where $0<T^*<\mu P$, is considered.

The unloading problem of two like spheres has been dealt with by Mindlin, Mason, Osmer and Deresiewicz (1.44). The unloading case is taken to be the result of superposing a tangential force of magnitude $\Delta T = T^*-T$ in the direction

opposite to that of T^*, on the system of forces P and T^*. Again the assumption is made that the tangential tractions do not affect the distribution of normal stresses, as determined by the classical Hertzian solution.

If slip is prevented, the tangential traction on the boundary of the contact patch is found to tend to negative infinity (the direction of initial slip is taken as positive). Hence slip, opposite in sense to the initial slip, is presumed to start at the edge of the contact surface resulting in the formation of an annulus of counter-slip which grows radially inwards as the tangential force continues to be reduced. The tangential traction on the annulus is taken as equal to μp, where p is defined in Equation (1.13), but its sense is now opposite to that of the initial traction. Hence the change of traction over the annulus is $-2\mu p$.

The resultant tangential traction on the contact patch and the corresponding relative displacement of distant points in the two spheres during unloading were obtained in Reference (1.44). They also considered the case when T oscillates between $\pm T^*$, $|T^*| < \mu P$, and found that the plot of T against Δ after the first quarter of cycle forms a closed loop, see Fig. (1.12), whose area represents the frictional work done during each cycle. Closed form solutions were then obtained for the area enclosed in the loop.

The work in (1.44) was later extended by Deresiewicz (1.40) to the contact of nonspherical bodies. He gave the resultant tangential component of traction at level T during unloading as:

$$\tau(x,y) = -\mu p \qquad a_2 \leqslant x \leqslant a, \quad b_2 \leqslant y \leqslant b$$

$$\tau(x,y) = -\mu p + 2\mu p_2 \left[1-(T^*-T)/2\mu p\right] \qquad a_1 \leqslant x \leqslant a_2, b_1 \leqslant y \leqslant b_2$$

$$\tau(x,y) = -\mu p + 2\mu p_2 \left[1-(T^*-T)/2\mu p\right] + \mu p_1 (1-T^*/\mu p) \qquad x < a_1, y < b_1$$

where $p = \frac{3P}{2\pi ab}\sqrt{(1-\frac{x^2}{a^2}-\frac{y^2}{b^2})}$

$$p_1 = \frac{3P}{2\pi ab}\sqrt{(1-\frac{x^2}{a_1^2}-\frac{y^2}{b_1^2})} \qquad (1.32)$$

$$p_2 = \frac{3P}{2\pi ab}\sqrt{(1-\frac{x^2}{a_2^2}-\frac{y^2}{b_2^2})}$$

a and b are semi-axes of the ellipse for normal Hertz theory under load P . a_1 and b_1 denote the semi-axes of the inner boundary of slip during the initial loading, case (1), while a_2 and b_2 are the semi-axes of the inner boundary of the annulus of counter-slip. They are given by:

$$(\frac{a_1}{a})^3 = (\frac{b_1}{b})^3 = 1-\frac{T^*}{\mu p}$$

$$(\frac{a_2}{a})^3 = (\frac{b_2}{b})^3 = 1-(\frac{T^*-T}{2\mu P}) \qquad (1.33)$$

The corresponding relative displacement of distant points in the two bodies during unloading is:

$$\delta_u = 2\Delta_u = \frac{3\mu P(2-\nu)}{8Ga}\left[2(1-\frac{T^*-T}{2\mu P})^{2/3}-(1-\frac{T^*}{\mu P})^{2/3}-1\right]\phi \qquad (1.34)$$

where ϕ is given by Equation (1.15). Yet again tangential force is assumed to be parallel to one of the principal axes of the contact patch, whose semi-axis is of length a.

The results in Ref. (1.40) indicate that the expressions for the displacement, compliances, and energy

loss for non-spherical bodies under constant normal load P and cyclic tangential load T^* may be obtained from the corresponding expressions in Ref. (1.44) simply by multiplying the latter by the constant ϕ. For a varying normal load, however, the situation is not quite so simple, as is discussed later.

The tangential compliance, for two bodies, during unloading is:

$$\frac{d\delta_u}{dT} = \frac{2-\nu}{4Ga}\left(1-\frac{T^*-T}{2\mu P}\right)^{-1/3}\phi \qquad (1.35)$$

From Equation (1.34) it is seen that due to the presence of an initial state of stress and relative displacement at the outset of the unloading phase, the reduction of T from T^* to zero will result in a permanent set given by OR, in Fig. (1.12), the magnitude of which is obtained by setting T=0 in Equation (1.34). Moreover, complete removal of T does not result in total disappearance of tangential surface tractions over the contact patch but merely causes a self-equilibrating distribution of these tractions. Their distribution is obtained by putting T=0 in Equation (1.32). As T is further reduced to the value $-T^*$ Equations (1.33) give: $a_2 = a_1$ and $b_2 = b_1$.

Putting $T = -T^*$ into (1.34) also shows that the displacement at this stage is equal to minus the displacement at $T=T^*$. Furthermore, the compliance of the unloading curve at the point corresponding to T^* is identical to that of the loading curve at $T=T^*$. In other words, the entire situation at $T= -T^*$ is identical with that at $T=T_1^*$ except for reversal of signs assigned to δ and T. A subsequent increase of T from

$-T^*$ to T^* will be accompanied by the same events as occurred during the decrease from T^* to $-T^*$, except for reversal of sign. The displacement along the loading curve S-U-P in Fig.(1.12) is then:

$$\delta_i = -\delta_u(-T) = -\frac{3\mu P(2-\nu)}{8Ga}\left[2\left(1-\frac{T^*+T}{2\mu P}\right)^{2/3} - \left(1-\frac{T^*}{\mu P}\right)^{2/3} - 1\right]\phi \qquad (1.36)$$

The area enclosed in the loop is also calculated in Ref.(1.44) as:

$$E = \int_{-T^*}^{T^*} (\delta_u - \delta_i)\, dT \qquad (1.37)$$

or:

$$E = \frac{9(2-\nu)\mu^2 P^2}{5Ga}\left\{1-\left(1-\frac{T^*}{\mu P}\right)^{5/3} - \frac{5}{6}\frac{T^*}{\mu P}\left[1+\left(1-\frac{T^*}{\mu P}\right)^{2/3}\right]\right\}\phi$$

where E is energy dissipation per cycle for two bodies. For small $\frac{T^*}{\mu P}$ we have:

$$E = \frac{(2-\nu)T^{*3}}{18Ga\mu P}\phi \qquad (1.38)$$

That is for small amplitudes of loading the energy loss per cycle varies as the cube of the maximum tangential force.

Keer and Goodman (1.45) used an arbitrary function, in place of the Amontons-Coulomb law of friction, to represent resistance to slip for the case of two identical spheres in contact. For small amplitudes of loading they showed that the nature of the frictional resistance function affects Equation (1.38) only to the extent of a multiplicative constant and the energy loss is always proportional to the cube of the maximum tangential force.

It is interesting to note that the initial tangential compliance on first loading (T=0 in Equation (1.16)) is the same as the initial compliance on unloading from the

state $T=T^*$ ($T=T^*$ in Equation (1.35)) or the initial compliance on loading from the state $T=-T^*$. In other words the initial tangential compliance is independent of the initial state of stress and relative displacement at the onset of movement. The independence of the initial tangential compliance of the value assigned to μ, the coefficient of friction, is the other important point to be borne in mind.

Comparing Equations (1.34) and (1.36) shows that the theoretical hysteresis loop is diagonally skew-symmetric. For the position $T=0$ the width of the hysteresis loop corresponding to a cyclic maximum tangential force T^*, the distance $\overline{UR}$ in Fig.(1.12), is given by:

$$(\delta_u-\delta_i)_{T=o} = 2\delta_{max}\left[2\left(1-\frac{T^*}{2T_{max}}\right)^{2/3}-\left(1-\frac{T^*}{T_{max}}\right)^{2/3}-1\right]$$

where $\delta_{max} = \frac{3\mu P(2-\nu)}{8Ga}\phi$ and $T_{max}=\mu P$ (1.39)

For the particular case of $T^* = T_{max} = \mu P$ we have:

$$\frac{(\delta_u-\delta_i)_{T=0}}{2\delta_{max}} \simeq 0.26 \qquad (1.40)$$

Although in principle the onset of gross slip is defined as the instant when $T=\mu P$, it is difficult experimentally to detect accurately the onset of rigid body movement between two surfaces in contact. Equation (1.40) provides an alternative definition of δ_{max}: i.e. it corresponds to a hysteresis loop for which the ratio of width to amplitude is 0.26. By plotting experimental hysteresis loops δ_{max} may then be determined accurately (Ref.(1.47)).

Finally, Fig.(1.13) taken from Ref.(1.53), gives the energy dissipation, ΔE, per loading cycle as a function of friction coefficient, μ, for various values of T^*/P. In the computation the normal force P, contact area a, and elastic properties G and ν for the spheres in contact are held constant. The striking conclusion from these plots is that decreasing the coefficient of friction for partial slip conditions will result in an increase in energy loss ΔE.

1.5 OBLIQUE FORCES

The discussion so far has been restricted to a contact in which the oscillating force acts tangentially to the interface. Mindlin and Deresiewicz (1.46) have extended their analysis to the more general situation of identical spheres subjected to an oscillating force which acts obliquely at an arbitrary angle β to the common normal. The very important difference between this case and the case of pure tangential loading is that in the former due to the normal component of the oscillating force, the area of contact fluctuates in size. By studying a variety of special cases they showed that the changes in stress and displacements, and hence the tangential compliances, not only depend upon the initial state of loading, but also upon the entire history of loading and the instantaneous relative rates of change of the normal and tangential forces. Among other cases, they studied the case of an initial normal load followed by an oblique force whose inclination remains constant while its

magnitude varies. The force first increases, then decreases, and finally, oscillates. With the tangential component of the additional oscillating force varying between the limits $\pm T^*$, the normal component changes such as to maintain the ratio $\beta = \frac{dT}{dP}$ a constant. For $\beta > \mu$ the force-displacement relation reaches a steady state after one and three-quarter cycles - Fig.(1.14). During the first loading from $(P_o\ 0)$ to (P_o+P^*, T^*) the displacement will be given by (see curve OP, Fig.(1.14))

$$\delta_\ell = \frac{3(2-\nu)\mu P}{8Ga}\left\{(1+\theta L)^{2/3} - \left[1-(1-\theta)L\right]^{2/3}\right\}, 0<L<L^* \qquad (1.41)$$

where δ_ℓ is the displacement for two bodies,
$L = \frac{T}{T_o^*}$ (where $T_o^* = \mu P_o$), $L^* = \frac{T^*}{\mu P_o}$ and $\theta = \frac{\mu}{\beta} \leq 1$ with $\beta = \frac{dT}{dp}$.
The radius of the contact surface a corresponding to the normal load $(P_o + \Delta P)$ is given by:

$$a = a_o(1+\theta L)^{1/3}$$

where a_o is the radius corresponding to the load P_o.
The tangential compliance in this load interval is then given by:

$$\frac{d\delta_\ell}{dT} = \frac{2-\nu}{4Ga}\left[\frac{\mu dP}{dT} + \left(1-\frac{\mu dP}{dT}\right)\left(1-\frac{T}{\mu P}\right)^{-1/3}\right] \quad \theta<1 \qquad (1.42)$$

It is interesting to note that the initial tangential compliance (T=0 in Equation (1.42)) is again independent of the coefficient of friction μ. Moreover, its magnitude is the same as in the case of pure tangential loading (c.f. Equation (1.16)) for the case $\phi=1$ and T=0.

The tangential compliance of the contact in the stabilized cycle during loading (curve SUV) is:

$$\frac{d\delta_r}{dT} = \frac{2-\nu}{4Ga}\left\{\theta+(1-\theta)\left[1-(1+\theta)\frac{L^*+L}{2(1+\theta L)}\right]^{-1/3}\right\} \quad \theta\leq 1 \qquad (1.43)$$

The compliance during unloading (curve VWS) is given by the same expression but in this case one must reverse the signs of θ and L.

The area enclosed in the stabilized loop was also calculated in a closed form. For the sake of brevity only the simple expression applying to small values of L* will be given here:

$$\Delta E = \frac{(2-\nu)T^{*3}}{36Ga_o\mu P_o}(1-\theta^2) \qquad (1.44)$$

For the case $\theta\geq 1$ (i.e. $\beta\leq\mu$) the situation was found to be quite different. In this case, slip is no longer possible for any magnitude of tangential component of the force. Putting it in other words, no slip at all occurs if the angle of obliquity of the oscillating force is less than the angle of limiting friction for the two surfaces. In this case the load - displacement relation is as shown in Fig.(1.15), where for the stabilized condition the displacement retraces its path in loading and unloading (curves S-U-V and V-U-S) so that no loop is formed, i.e., there is no frictional energy loss involved. The trace OPOS in the figure corresponds to the initial loading and unloading paths. The tangential compliance for the stabilized situation is:

$$\frac{d\delta}{dT} = \frac{2-\nu}{4Ga} \qquad (1.45)$$

Although the work in (1.46) is restricted to the

contact of two spheres,the conclusions throw considerable light on the mechanism of slip, energy dissipation and fretting between engineering surfaces. For the case of non-spherical bodies in contact, Deresiewicz (1.40) pointed out that "as in the Hertz problem a change in the normal contact force gives rise to an area of contact whose bounding ellipse is homothetic with that of initial contact, the results obtained by Mindlin and Deresiewicz (1.46) for the contact of two spheres subjected to simultaneously varying normal and tangential force maybe extended immediately to the case of contact between non-spherical bodies". However, he did not illustrate this point quantitatively by developing formulae for any specific cases.

1.6 EXPERIMENTAL VERIFICATION AND PRACTICAL LIMITATIONS

The analytic solutions given in this chapter have been the subject of a large number of experimental checks. Mindlin, Mason, Osmer, and Deresiewicz (1.44) verified the occurrence of the annulus of slip as well as the relation between the size of the inner radius of the annulus and the magnitude of T^*, by observing the wear pattern between two glass lenses in contact. They also made some measurements of the energy dissipation and found that for amplitudes of motion near the gross slip amplitude (that is for magnitudes of $T^*/\mu P$ close to unity), the area of the stabilized hysteresis loop agreed closely with that calculated from Equation (1.37). However, for very small $T^*/\mu P$ the measured areas were nearly

proportional to the square of the maximum tangential force T* rather than the cube of T* as predicted by the theory (see Equation (1.38)). The findings of Mason and White (1.48) also confirmed the results given in Reference (1.44). Duffy and Mindlin (1.49) used $\frac{1}{8}$ -in diameter stainless-steel spheres as part of a study of the stress-strain relation for a medium composed of a face centered cubic array of elastic spheres in contact. By measuring the decay of vibrations, the rate of energy dissipation was found to be proportional to the square of the maximum tangential contact force, as was the case for the previous experiments with single contact in (1.50). The work done by Klint (1.51) also provides some experimental evidence in support of Mindlin's theory. Hetenyi and McDonald (1.52) used photo-elastic tests to investigate the distribution and magnitude of the tangential surface tractions for the case of an elastic sphere pressed against an elastic half-space and twisted until complete slip occurs. They found the assumption of a constant coefficient of limiting friction all over the contact patch as being compatible with their experimental results. Both static and dynamic tests on steel balls in contact with a steel sphere were conducted by Johnson (1.50). Figs.(1.16) and (1.17) show his results for static tests which show a very close agreement with Mindlin's theory.

The results for dynamic tests are given in Fig.(1.18) which substantiates the force - displacement relationship obtained in static tests. Johnson also measured energy dissipation using a vibration decay method. By varying the ball diameter,

he produced a sequence of experimental curves of energy dissipation versus peak tangential force, one curve for each sphere size, when only a single theoretical curve would have been anticipated. Goodman and Brown (1.47) eliminated this discrepancy between theory and experiment by noticing that the appropriate value of μ, the coefficient of friction, to insert in the theoretical equations remains a very unpredictable and variable "constant". Consequently they presented their experimental data in such a way as to eliminate this variation from their comparison between theory and experiment. This was achieved by writing Equation (1.37) in the form:

$$\frac{\Delta E}{T_{max}\delta_{max}} = \frac{24}{5}\left\{1-\left(1-\frac{T^*}{T_{max}}\right)^{5/3} - \frac{5}{6}\frac{T^*}{T_{max}}\left[1+\left(1-\frac{T^*}{T_{max}}\right)^{2/3}\right]\right\} \qquad (1.46)$$

where $\delta_{max} = \frac{3(2-\nu)\mu P}{8Ga}$ and $T_{max} = \mu P$

Also from (1.15) with $\phi=1$ and $\delta_{max} = 2\Delta_{max}$:

$$\frac{\delta^*}{\delta_{max}} = 1-\left(1-\frac{T^*}{T_{max}}\right)^{2/3} \qquad (1.47)$$

Equations (1.46) and (1.47) define a curve for $\frac{\Delta E}{T_{max}\delta_{max}}$ against $\frac{\delta^*}{\delta_{max}}$ which is independent of material properties and geometry and only depends on the measured quantity $\frac{T^*}{T_{max}}$. A comparison between their experimental results, for a sphere between two flat plates, and theory is shown in Fig.(1.19). The agreement between theory and experiments is good and the size effect noticed in earlier work by Johnson ("Johnson Scatter") has obviously disappeared. Goodman and Brown then suggest that this was only a consequence of random variation in μ

from experiment to experiment. Fig.(1.20) gives a comparison between actual and theoretical hysteresis loops for a single test as given in (1.47). The agreement between theory and experiment is striking and, at least for any particluar sphere, it seems as if the assumption of a constant μ over the whole contact patch, as assumed in the theory, is a reasonable one. In the discussion of Ref.(1.47), Johnson (1.53) suggests that as a result of repeated slip, the rupture of oxide films and the development of strong metallic cold-welded junctions will lead to the development of a coefficient of friction which varies throughout the annulus of slip. In support of this view he also provided some experimental evidence (Ref. to the discussion and also Ref.(1.54)). He then argues that the variation of the coefficient of limiting friction accounts for the overestimation of the theoretical energy loss, based on a constant near-gross-slip value of μ, at intermediate amplitudes of oscillation in his own experiments. The use of stainless steel, he continues to say, for which change of μ by abrasive breakdown of oxide films is less marked, has minimized this effect in the work in (1.47) - although it still has not entirely disappeared as seen in Fig.(1.19). The theory may then be said to provide an upper limit to the damping capacity of the contact, for the cases when the amplitudes are not very small. An alternative explanation is put forward by Bowden and Tabor (1.9) who, following Mindlin's results for the case of single contact, argue that under sustained cyclic loading the load-displacement

cycle for a given asperity is as shown in Fig.(1.21a) and during a complete cycle of tangential force, the energy dissipated is equal to the area of the loop ABCD which for large values of relative displacement x is not greatly different from Mindlin's idealized behaviour shown in Fig.(1.21b). However, for smaller tangential displacements this is no longer so. In this case, the force-displacement cycle for an individual asperity is GHKL and the area enclosed by the loop is appreciably less than the corresponding loop in Mindlin's idealized model which is based on the ordinary coefficient of friction as suggested by Coulomb.

O'Connor and Johnson (1.55) have investigated the role of surface asperities in transmitting normal and tangential forces. They conclude that the contribution of the displacements of the individual asperities to the overall compliance of multi-junction contact is small, even when plastic flow of the junction takes place in the first loading. In subsequent loadings the asperity displacements were found to be elastic and negligible. Consequently,the tangential compliance of a multi-junction contact is primarily controlled by the elastic deformation of the bulk of the material near the contact surfaces which is in accordance with the assumptions made in Mindlin's analysis,and it is not surprising to find close agreement between all the reported experimentally determined values of tangential compliance and the corresponding theoretical predictions.

Johnson (1.54) also made an experimental investigation of Mindlin's theoretical values for the energy dissipation at the contact of two spheres under oblique oscillating force. In particular, Johnson was interested in the effect of the angle of obliquity of the oscillating force on the energy dissipation and associated surface damage over the annulus of slip. Fig.(1.22) gives his results in terms of non-dimensional energy loss against amplitude of oscillating force for different angles of obliquity. Yet again, for the intermediate amplitudes of vibration the theoretical results give an upper bound to the damping capacity of the contact. As shown in the plots, at small amplitudes of oscillation the energy dissipation does not fall to zero but to a small constant value. The curve corresponding to $\alpha=o$ denotes the case when the normal load alone fluctuates so that in this case it is reasonable to assume that the energy loss is due to internal hysteresis rather than slippage at the contacts (assuming that experimental errors were not significant). Moreover, for values of α less than the angle of limiting friction, which in this case is about 29^{o}, the energy dissipation measurements hardly differ from the case when $\alpha=o$. At angles of obliquity greater than the angle of friction energy dissipation, and surface damage, was found to increase rapidly and the over all agreement between theory and experiment was close.

1.7 CLOSURE

The available theoretical information on contact

stresses (including, most importantly, the effect of friction at the interface) has been critically reviewed. Particular attention has been paid to the case of cylinders in contact because of its direct relevance to the behaviour of wires in cables. It has been shown that the neglect of friction can lead to serious errors in contact stress calculations. The variations of the contact stresses and their associated displacements have been shown to be dependent on the entire past history of loading and the instantaneous rates of change of the normal and tangential forces.

This work is of obvious direct relevance to the formulation of the interwire contact problem in multi-layered strands which is presented in the next chapter.

REFERENCES

1.1 HERTZ, H. Miscellaneous papers (translated by JONES D.E., and SCHOTT, G.A.). London: Macmillan and Co.,Ltd, 1896, pp.146-183. Translated from Journal Reine und Angewandte Mathematik (Crelle). 1881:92, pp.156-171 and, Verhand Vereins Beforder Gewerbefleisses Nov.1882.

1.2 LUBKIN, J.L. Contact problems, Handbook of Engineering Mechanics, edited by W.Flugge. New York: McGraw-Hill, 1962. Chapter 42.

1.3 JOHNSON, K.L. Non-Hertzian Contact of Elastic Spheres. Proceedings, Symp.Int.Union. of Theor.& Appl. Mechanics. Edited by A.D. de Pater & J.J.Kalker. Enschede Netherlands, Aug.,1974. Delft Univ.Press: 1975.

1.4 DERESIEWICZ, H. Bodies in Contact with Applications to Granular Media. R.D. Mindlin and Applied Mechanics, edited by G.Herrmann. Pergamon, 1974.

1.5 MOW, V.C., CHOW, P.L., and LING, F.F. Micro-slips Between Contacting Paraboloids. Journal of Applied Mechanics, Transactions of the ASME. 1967: 34, pp.321-328.

1.6 HOLM, R. The Friction Force Over the Real Area of Contact (in German). Wiss.Veröff.Siemens-Werk. 1938: 17, no.4, pp.38-42.

1.7 ERNST, H., and MERCHANT, M.E. Surface Friction between Metals -A Basic Factor in the Metal Cutting Process. Proceedings, Special Summer Conference on Friction and Surface Finish. M.I.T., 1940. pp.76-101.

1.8 BOWDEN, F.P., and TABOR,D. The Theory of Metallic Friction and the Role of Shearing and Ploughing. Comm. of Australian Council Sci. and Ind.Research, 1942. Bulletin 145.

1.9 BOWDEN, F.P., and TABOR, D. The Friction and Lubrication of Solids. 2nd ed. Oxford (1954) Part I, and (1964) Part II.

1.10 SAMUELS, L.E., and MULHEAM, T.O. An Experimental Investigation of the Deformed Zone Associated with Indentation Hardness Impressions. Journal of the Mechanics and Physics of Solids. 1950: 5,pp.125-134.

1.11 MULHEAM, T.O. The Deformation of Metals by Vickers-type Pyramidal Indenters. Journal of the Mechanics and Physics of Solids. 1959:7, pp.85-96.

1.12 MARSH, D.M. Plastic Flow in Glass. Proceedings of the Royal Society. 1964: A279, pp.420-435.

1.13 ARCHARD, J.F. Elastic Deformation and the Contact of Surfaces. Nature. 1953: 172, pp.918-919.

1.14 ARCHARD, J.F. Elastic Deformation and the Laws of Friction. Proceedings of the Royal Society of London. 1957, A243, pp.190-205.

1.15 LODGE, A.S., and HOWELL, H.G. Friction of an Elastic Solid. Proceedings, Physical Society. 1954: B67, pp.89-97.

1.16 GREENWOOD, J.A., and WILLIAMSON, B.P. Contact of Nominally Flat Surfaces. Proceeding, Royal Society of London. 1966: A295, pp.300-319.

1.17 LING, F.F. On Asperity Distributions of Metallic Surfaces. Journal of Applied Physics. 1958: 29, pp.1168ff.

1.18 WHITEHOUSE, D.J., and ARCHARD, J.F. The Properties of Random Surfaces of Significance in their Contact. Proceedings of the Royal Society of London. 1970: A316, pp.97-121.

1.19 NAYAK, P.R. Random Process Model of Rough Surfaces. Journal of Lubrication Tech., Transactions of ASME. 1971: 93, pp.398ff.

1.20 GREENWOOD, J.A., and TRIPP, J.H. The Elastic Contact of Rough Spheres. Journal of Applied Mechanics, Transactions of the ASME. 1967: 34, pp.153-159.

1.21 LO, C.C. Elastic Contact of Rough Cylinders. International Journal of Mechanical Sciences. 1969: 11, pp.105-115.

1.22 CHIU, Y.P. On the Contact Problem of Cylinders Containing a Shallow Longitudinal Surface Depression. Journal of Applied Mechanics, Transactions of the ASME. 1969: 36, pp.852-879.

1.23 MEIJERS, P. The Contact Problems of a Rigid Cylinder on an Elastic Layer. Appl.Sci.Res. 1968: 18, pp.353-383.

1.24 GUPTA, P.K., and WALLOWIT, Contact Stresses between an Elastic Cylinder and a Layered Elastic Solid. Journal of Lubrication Technology, Transactions of the ASME. 1974, 96, pp.

1.25 RABINOWICZ, E. Direction of the Friction Force. Nature. 1957: 179, p.1073.

1.26 HALAUNBRENNER, M. Directional Effects in Friction. Wear. 1960: 3, pp.421-425.

1.27 DOKOS, S.J. Sliding Friction Under Extreme Pressures. Journal of Applied Mechanics, Transactions of the ASME. 1946: 13, pp.A148-A156.

1.28 BURTON, R.A., and RUSSELL, J.A. Lubrication Effects on Fatigue in a Stationary Concentrated Contact Under Vibrating Loading. Journal of Basic Engineering, Transactions of the ASME, 1966: 88, pp.573-582,

1.29 TIMOSHENKO, S.P. Strength of Materials; Part II: Advanced Theory and Problems. 3rd ed., D.Van Nostrand Company, 1956. pp.505-509.

1.30 TIMOSHENKO, S.P., and GOODIER, J.N. Theory of Elasticity. 3rd ed. McGraw-Hill, 1970.

1.31 THOMAS, H.R., and HOERSCH, V.A. Stresses Due to the Pressure of One Elastic Solid Upon Another. Eng.Exp. Sta. Univ.Ill.: 1930. Bulletin 212.

1.32 BELAJAF, N.M. On the Problem of Contact Stresses. Bull. Eng.Ways Commun.: St. Petersburg,1917. Also see, Computation of Maximal Stresses Obtained from Formulas for Pressure in Bodies in Contact. Bull.Eng. Ways Commun.: Leningrad, 1929.

1.33 LUNDBERG, G., and SJOVALL, H. Stress and Deformation in Elastic Contacts. Institution of Theory of Elasticity and Strength of Materials, Chalmers University of Technology: Gothenburg, 1958.

1.34 SMITH, J.O. and LIU, C.K. Stresses due to Tangential and Normal Loads on an Elastic Solid with Application to Some Contact Stress Problems. Journal of Applied Mechanics, Transactions of the ASME. 1953, 20, pp.157-166.

1.35 HAMILTON, G.M. Yielding in Contact Stress Problems. A.E.I. Research Laboratory: Aldermaston Court, Berks, England, 1963. Technical Report: A.1374.

1.36 ROARK, R.J. and YOUNG, W.C. Formulas for Stress and Strain. Fifth ed. International Student Edition, McGraw-Hill International, 1975.

1.37 FOEPPL, A. Technische Mechanik, 4th ed.Vol.5.

1.38 CATTANEO, C. Sul Contatto di Due Corpi Elastici. Accademia dei Lincei. Rendiconti, Series 6, Fol.27, Part I, pp.342-348, Part II, pp.434-436, Part III, pp.474-478.

1.39 MINDLIN, R.D. Compliance of Elastic Bodies in Contact. Journal of Applied Mechanics, Transactions of the ASME. 1949: 16, pp.259-268.

1.40 DERESIEWICZ, H. Oblique Contact of Non-Spherical Bodies. Journal of Applied Mechanics, Transactions of the ASME. 1957: 24, pp.623-624.

1.41 VERMEULEN, P.J. and JOHNSON, K.L. Contact of Non spherical Elastic Bodies Transmitting Tangential Forces. Journal of Applied Mechanics, Transactions of the ASME. 1964: 31, pp.338-340.

1.42 JAHNKE, E., and EMDE, F. Tables of Functions. New York, Dover Publications Inc., 1945. (also Sixth ed. JAHNKE, EMDE and LÖSCH. Tables of Higher Functions. McGraw-Hill, 1960).

1.43 PORITSKY, H. Stresses and Deflections of Cylindrical Bodies in Contact with Application to Contact of Gears and Locomotive Wheels. Journal of Applied Mechanics, Transactions of the ASME. 1950. 17, pp.191-201.

1.44 MINDLIN, R.D., MASON, W.P., OSMER, T.F., and DERESIEWICZ, H. Effects of an Oscillating Tangential Force on the Contact Surfaces of Elastic Spheres. Proceedings, First National Congress of Applied Mechanics, 1951, pp. 203-208.

1.45 KEER, L.M., and GOODMAN, L.E. Tangential Loading of Two Bodies in Contact. Journal of Applied Mechanics, Transactions of the ASME. 1976: 98, pp.513-514.

1.46 MINDLIN, R.D., and DERESIEWICZ, H. Elastic Spheres in Contact Under Varying Oblique Forces. Journal of Applied Mechanics, Transactions of the ASME. 1953: 75, pp.327-344.

1.47 GOODMAN, L.E., and BROWN, C.B. Energy Dissipation in Contact Friction: Constant Normal and Cyclic Tangential Loading. Journal of Applied Mechanics, Transactions of the ASME. 1962: 29, pp.17-22.

1.48 MASON, W.P. and WHITE, S.D. New Techniques for Measuring Forces and Wear in Telephone Switching Apparatus. Bell System Technical Journal. 1952: 31, pp.469-503.

1.49 DUFFY, J., and MINDLIN, R.D. Stress-Strain Relations and Vibrations of a Granular Medium. Journal of Applied Mechanics, Transactions of the ASME. 1957: 24, pp.585-593.

1.50 JOHNSON, K.L. Surface Interaction Between Elastically Loaded Bodies Under Tangential Forces. Proceedings of the Royal Society of London. 1955: A230, pp.531-548.

1.51 KLINT, R.V. Oscillating Tangential Forces on Cylindrical Specimens in Contact at Displacements Within the Region of No Gross-slip. Transactions of the ASME. 1960, 3, pp.255-264.

1.52 HETENYI,M., and McDONALD, P.H. Contact Stresses Under Combined Pressure and Twist. Journal of Applied Mechanics, Transactions of the ASME. 1958: 25, pp.396-401.

1.53 JOHNSON, K.L. Discussion to Ref. (1.46). Journal of Applied Mechanics, Transactions of the ASME. 1962: 29, pp.763-764.

1.54 JOHNSON, K.L. Energy Dissipation at Spherical Surfaces in Contact Transmitting Oscillating Forces. Journal of Mechanical Engineering Science. 1961: 3, pp.362-367.

1.55 O'CONNOR, J.J., and JOHNSON, K.L. The Role of Surface Asperities in Transmitting Tangential Forces Between Metals. Wear. 1963: 6, pp.118-139.

1.56 HAMILTON, G.M., and GOODMAN, L.E. The Stress Field Created by a Circular Sliding Contact. Journal of Applied Mechanics, Transactions of the ASME. 1966: 33, pp.371-376.

CHAPTER 2

STRAND THEORY

2.1 INTRODUCTION TO THE LITERATURE SURVEY

At first glance the analysis of a helical strand seems straightforward, and the derivation of the properties of a group of such strands laid up as a wire rope only slightly more onerous. However, appearances are deceptive, and the rational analysis and design of this important group of components for engineering structures is far from simple, and many unresolved problems remain in the field.

There are relatively few theoretical references on the static and dynamic behaviour of spiral strand and ropes. In the main, strands consisting of only six or seven wires or ropes consisting of six such strands have been considered, and even for these simplified configurations the analyses have had to include further sweeping assumptions.

2.2 STRAND EXTENSIBILITY

Hruska (2.1) assumed that each wire in a multi-layered strand was subjected to tension alone, and demonstrated that (for small deformations) the tensile stresses in each layer vary in proportion to the square of the cosine of the lay angle. He also derived a relationship between the radial clench forces and the axial force in the strand (2.2), ignoring the slight changes in the lay angle, α, and changes in

diameter. The proportion of the radial clench forces resisted by hoop stresses in individual layers was not considered in any detail. The importance of friction and its effect on the interaction of individual wires in strands and ropes was emphasized. In a later paper,Hruska (2.3) discussed the origin and consequences of the torque induced in a helical strand (or rope) by an axial load. It was mentioned that rotation causes some changes in the lay angle, resulting in some bending and torsion in individual wires. No quantitative data was given on the magnitude of these moments.

Chi (2.4, 2.5) extended the linear (small deformation) kinematic relations derived by Hruska to include changes in the lay angle and strand radius. The importance of the changes in strand diameter was pointed out,but no theoretical estimates or experimentally derived data were given for such changes. Theoretical elongations and strains were compared with some experimental results for single layered steel helical strands.

The work of Gibson et.al.(2.6) also followed essentially the same approach as Hruska (2.3). They calculated torsional properties of wire ropes, and obtained an encouraging comparison between their experiments and theory. Bowers (2.7, 2.8) also suggested a similar theory and discussed some relevant aspects of marine operational problems.

Studies by Durelli et al.(2.9, 2.10) which included experimental work on an oversized epoxy resin model of a six wire strand emphasized the importance of bending and twisting

moments in the six individual wires of steel strands which were assumed to undergo zero diametral changes. Considerable scatter was observed in the strain measurements on the individual wires. The final linearized theoretical constitutive equations for the seven wire model were:

$$N = A_1\varepsilon + A_2\gamma$$
$$T = A_3\varepsilon + A_4\gamma \qquad (2.1)$$

where A_1, A_2, A_3 and A_4 are constants depending on cable geometry and material properties. N is the external axial force and T represents the external torque on the cable; ε and γ represent the corresponding axial and torsional strains.

An experimental method was developed by the Naval Research Laboratory (2.11) to verify Equation (2.1) as applied to a large diameter rope. The agreement between theory and experiment in the range of loads considered was fairly satisfactory, although high non-linearities were observed at the onset of loading (Fig.2.1).

Samras et al. (2.12) used Equations (2.1) and developed an analytical model for the analysis of coupled torsional - extensional vibrations of wire ropes moored to the ocean floor.

Owada (2.13) used Kirchoff's equations for twisted rods to calculate torsional and axial stiffnesses of a single-layer strand with a steel core. Normal contact forces between the side wires and the core were calculated assuming zero friction inside the cable. Some experimental

results for the axial stiffness are provided which appear to support the theoretical findings. His analysis is,however, rather difficult to follow.

Phillips and Costello (2.14) also used the Kirchoff equations to analyse the contact stresses in highly idealized single layered helical strands with no (or a very soft) core. The wires were assumed to be just in contact at the onset of loading and friction was completely ignored. They examined the non-linearity of strands as a function of very large load - induced changes in the helix angle. Contact deformation between the wires was ignored, while, changes in strand diameter due to changes in the lay angle were taken into account. The wire material was assumed to be inextensible (rigid). Torsional and bending moments in individual wires were considered as first order factors in determining the overall mechanical behaviour. However, it is doubtful whether these effects would be significant in a practical strand (which might have 90 wires or more) where the wire diameter to strand diameter ratio is much smaller. Moreover, neglecting the substantial frictional forces which must certainly be present if the helix angle changes significantly is rather unrealistic. In a series of papers, Phillips and Costello (2.15, 2.16), Costello and Sinha (2.17, 2.18) and Costello and Miller (2.19) used the above approach to determine the geometrical non-linear behaviour of such over-simplified models in a variety of applications. The only major improvement made to the original model (Phillips

and Costello (2.14)) was the removal of the wire inextensibility assumption.

Huang (2.20) employed the theory of slender curved rods to analyse the geometrical non-linearities due to changes in the lay-angle and diameter of a single layered steel strand with a central core. He took friction into account. According to his theoretical findings, as a result of the contact between the central core and helical wires, a separation can occur between helical wires in a strand subject to axial deformation. Conditions of torsionally fixed and free ends were both considered in some detail.

Nowak (2.21) and Knapp (2.22, 2.23) addressed the problem of the frictionless but geometrically non-linear properties of strands with compressible cores. Nowak made a detailed analysis of the relations between geometric parameters governing the problem of wire accomodation around the core. He then used Kirchoff's thin rod theory to analyse the forces between the individual elements of electromechanical cables. The presence of hoop stresses inside the various layers was ignored. Nowak used Von Mises' yield criterion to develop a rather over-simplified model for determining the cable's ultimate load carrying capacity, defined in his work as the load at which first wire breakage occurs. The model only applies to wires with elasto-plastic material properties and ignores the very important localized effects of contact stresses where wires touch each other. Knapp placed no limit on the number of layers in his model

and by linearizing his equations showed that Equation (2.1) could be applied to multi-layered strands. He also derived theoretical equations for determining the constants A_1 to A_4. The presence of hoop stresses was again ignored. Good correlation was obtained between theory and experiment. However, the experiments were carried out on strands with only two layers of armouring wires. As pointed out by Knapp, the theory is only strictly applicable if the deflections of the armour wires are geometrically compatible.

Although such a case may hold in strands with one or two layers of wires,it is doubtful if it will be the case in large diameter, multi-layered structural strands where the interaction of wires in the individual layers will surely affect the radial movements in the various layers.

Kasper (2.24, 2.25) used finite element techniques to analyse multi-conductor armoured electrical cables ignoring friction. An attempt was made to determine the interaction between the cable components with little success, as the computer costs turned out to be rather high for every-day practical applications.

By the analysis of experimental data, Drucker and Tachau (2.26) demonstrated the importance of stresses at the contact points between wires in a strand. Their work was followed by Leissa (2.27), Starkey and Cress (2.28) and Bert and Stein (2.29) who attempted theoretical studies of interwire contact stresses. All of these theoretical works ignored friction effects.

Leissa only considered the case of wires in a strand (or a rope) making a line-contact. Hertzian theory was used to calculate the local stresses between the wires under normal loads, which were determined using the method suggested by Hruska (2.2). By superimposing the mean axial tensile stresses in the wires on these local stresses they showed the seriousness of the contact stresses. Two failure criteria were applied - the maximum shear-stress criterion and the maximum normal-stress criterion-to investigate the effects of such stresses on cable ultimate strength. The existence of fretting corrosion and its significant role in determining the cable's fatigue life was noted,although no mention was made of the order of magnitude of the interwire tangential forces and relative displacements.

Starkey and Cress extended the work of Leissa (2.27) to the case when wires cross each other at an angle. Incredibly high values of theoretical elastic contact stresses were obtained,which indicated that plastic deformation (at least for the first loading case) was inevitable. The importance of fretting and its possible contribution to fatigue crack initiation and propagation was stressed. A number of interesting discussions to the paper brought out the principal shortcomings of their highly idealized model in practical applications. The work by Bert and Stein is similar to these two papers.

Jones and Christodoulides (2.30) concentrated on the theoretica elastic-plastic behaviour of a single layered strand with no

core. They used the equations developed by Phillips and Costello (2.14) to calculate static plastic collapse of an unrealistic frictionless cable composed of wires which did not have a work-hardening characteristic. It is interesting to note that Jones found the practical utility of the theoretical elastic results presented by Phillips and Costello (2.14) to be restricted to the immediate vicinity of the origin of the graphs presented in their paper. Thus the change in the helix angle,even for a single layered strand with practical lay angles and realistic material properties,was found to be very much less than implied by Phillips and Costello.

The initial plastic strains, first in wire drawing, and then in spinning a strand are also important. Schinke (2.31) discussed methods of determining the level of twist in the wires,while Yoshida (2.32) analysed the plastic strains developed in individual wires during strand laying on a theoretical basis. Yoshida did not take work hardening into account. Winkelman (2.33), in a remarkable theoretical study of the manufacturing process, investigated the residual plastic strains in practical strands and ropes composed of wires with bi-linear stress-strain properties. The degree of back-twist and changes in the wire's geometry during stranding were taken into account in this investigation. Kirchoff's equations were employed in deriving the equilibrium equations linking the forces and the moments acting on each wire,with the twisting and bending moments considered as the obvious primary factors in determining the final helical shape of the originally straight wires.

Strain gauging of individual wires in the outer layer of small steel strands has been carried out by Durelli et.al. (2.10) and Smislova et.al. (2.34). Durelli et.al. found that for a seven wire steel strand strains in some wires were not linearly proportional to load,and considerable variation was observed in the axial strains in the outer wires at any transverse cable section. Repetition of load did not appreciably alter the non-linear behaviour of the wires or the uneven distribution of axial strains between them. Application of a brittle lacquer coating to an oversized epoxy model indicated an irregular stress pattern with stresses varying over the exposed surface by as much as a factor of two.

2.3 REPEATED LOADING AND DAMPING

Wilson (2.35) discussed the elastic characteristics of mooring ropes and by analysing the manufacturers' data for various constructions suggested a square-power law relating the weight per unit length, w, for steel and fibre ropes (under wet and dry conditions) to nominal diameter d:

$$w = c.d^2$$

where c is a constant. Different constants are used for dry or wet conditions. A similar empirical relationship was put forward linking ultimate strength, T_u, and diameter. These constants were later used by Skop and Samras (2.36) in an extension of their original work (2.12) on coupled extensional-rotational vibrations of mooring lines. Wilson also conducted some interesting repeated static tensile tests

on both new and old ropes with fixed ends. The centre-lines of stable hysteresis loops for any given rope type were found to have the same shape regardless of the age of the rope. Elastic axial tension-elongation plots for the fully bedded-in ropes were shown to be non-linear (Fig.2.2) and axial stiffness was shown to be a function of the elastic perturbation axial strain. Using a semi-empirical approach the following relationship between the rope axial elastic modulus, E, and elastic strain, $\frac{\Delta S}{S_o}$, was obtained for ropes under repeated loading:

$$E = \frac{\frac{\Delta T}{A}}{\frac{\Delta \zeta}{S_o}} = \frac{mC_e}{C_A} \left(\frac{\Delta S}{S_o}\right)^{m-1} \qquad (2.2)$$

where S_o is the original length, and C_e,C_A and m are experimentally determined constants depending on the type of rope material and construction. $\frac{\Delta T}{A}$ is the perturbation axial stress on the cable (equal to range/2) with a mean axial load, T. $\frac{\Delta \zeta}{S_o}$ is the corresponding perturbation axial elastic strain.

Bechtloff (2.37) introduced an empirical constant, the Poisson number m (not to be confused with m in Equation (2.2)) to represent the diametral contraction of the cable. Only six wire strands or six strand ropes (both without steel cores) were analysed with the effect of bending and twisting moments in individual wires included. Even for these simple models the ratio of hoop to radial forces on individual wires could not be determined and only the extreme case of pure arch action was considered, Fig.(2.3). This is similar to

the work in the series of papers by Costello and his co-workers (2.14 - 2.19) in analysing single layer strands with no core and also along the same lines as in (2.27-2.29) where only the two extreme cases of either zero hoop (arch) action or zero radial resistance for seven wire strand models were considered. Bechtloff derived theoretical expressions for strand and rope axial stiffness and damping behaviour. However, the agreement between his theory and experimental results was not very satisfactory.

Ridley (2.38) also attempted to predict axial damping in structural strands from first principles with little success. By pulling out individual wires of a pretensioned cable he obtained values for the coefficient of friction, μ, between the wires which lay between 0.14 and 0.19. Because of the uncertainties about the theoretically derived values of the clench and hoop forces, the estimates of μ may have contained significant errors. Because of the short length of the specimens used, his experimental results for cable damping may also be wrong.

Kawashima and Kimura (2.39) used the decay of vertical oscillations of a mass suspended from a fairly long (ca. 4m). cable to obtain experimental data on cable damping properties. The frequency of vibration was about 10 Hertz. Tests were done on steel and copper wires, as well as a copper strand and four different steel rope constructions. All of the ropes used were ordinary lay with a hemp core. Three of them were galvanized and preformed while the fourth was neither galvanized and nor preformed. Their tests gave good straight lines (over their full range)

for the log decrement, δ, versus the amplitude, A, represented by:

$$\delta = \delta_o + kA \qquad (2.3)$$

where δ_o is the logarithmic decrement for zero amplitude.k is a constant for a given rope and suspended mass - i.e. mean tension. δ_o was obtained by extrapolation to zero amplitude. The logarithmic decrement, over their limited experimental load range, was found to decrease with increases in the mean axial tension, Fig. (2.4a). The tests on steel wires at similar tensions and amplitudes gave log. decrements increasing linearly with amplitude from $\delta \simeq 0.001$ to $\delta \simeq 0.003$ at 1mm amplitude. Therefore, it may safely be assumed that there was no sign of hysteresis from outside elements such as supports,etc. It is important to note that the 7-wire copper strand showed δ similar to that for a single copper wire for a mean stress $>100N/mm^2$: for single wires δ appeared to be a function of the amplitude alone and independent of the mean tension, and the same was true for the 7-wire copper strand at higher ranges of axial tension, Fig.(2.4b). They also found that the dynamic modulus of elasticity, for the relatively limited load range covered in their experiments, was greater than the static modulus of cables which is compatible with the observations by Wilson (2.35). In a later work, Kimura (2.40) reported experimental data on log. decrement, δ, and dynamic stiffness of a variety of new and not fully bedded-in ropes. The experimental technique was the same as in (2.39). Plots of δ versus amplitude of vibration (Fig.(2.4c)) over a wider

range of amplitudes than those in (2.39) were found to be non-linear,with δ varying in proportion to about $\frac{1}{4}$th to $\frac{1}{3}$rd power of the amplitude. The history of loading appeared to affect the results significantly.

Yu (2.41) performed dynamic decay and comparable static tests on a number of 7-wire and single wire specimens under pure bending. The close agreement between the static and dynamic energy dissipation quotients indicated that the strand damping mechanism was loading rate-independent. Comparison of the results on single wires and stranded cables confirmed that, over the range of deflections considered, the solid internal friction of the wire materials was much less than the energy dissipation due to interwire dry friction. Increasing the lay angle, while keeping other parameters constant , was shown to lead to higher damping.

Vanderveldt, Chung and Reader (2.42) also performed some experiments to investigate the damping mechanism in transverse vibration with a variety of ropes of different constructions. Coulomb damping was identified as the primary source of energy dissipation. Their rather simple analysis of ropes under longitudinal or transverse vibrations employed models with a single lumped mass and lumped damping coefficient and could only predict the longitudinal (or transverse) frequencies of the rope,which agreed with the experimental results.

Analytical and experimental studies of wave propagation in steel wire rope subject to an impulsive velocity at its end has also received some attention. For example, Kawashima, Kimura and their co-workers at

Kyushu University (2.43-2.46) modelled the cable as a semi-infinite rod and demonstrated the importance of including the effects of cable hysteresis in the analysis. Modelling the cable as a visco-elastic rod of Kelvin-Voigt material (2.44) did not give satisfactory agreement between theory and experiments. By incorporating a speed independent lumped damping force (structural damper) with its magnitude proportional to the elastic force, but with 90 degrees phase difference, Kimura (2.47) obtained a better comparison between his theoretical results and earlier experiments. He concluded that both the structural and also viscous damping effects must be included in the model.

Ringleb (2.48) analysed the response of cables to oblique impact. He did not consider the possible rotational motion of the ends and ignored the energy absorption and also diametral changes under the transient response. He gave the longitudinal sound velocity, v, in a cable under mean tensile stress, σ_o, prior to the application of a longitudinal shock as:

$$v = \sqrt{(1+\frac{\sigma_o}{E})\ \frac{E}{\rho}} \qquad (2.4)$$

Note that in plane rod theory which applies to the propagation of waves the lengths of which are large compared with the diameter of the elastic bar, the wave velocity is $\sqrt{\frac{E}{\rho}}$. For operative wavelengths of the same order as the diameter, a non-uniform distribution of stress develops in the cross-section of the bar and plane transverse sections are distorted (Ref.2.49).

Ringleb also provided some experimental data for the case of transverse impact which appeared to match the theoretical predictions very favourably, Fig.(2.5a). However, Vanderveldt and Gilheany (2.50) did not achieve agreement between their experimental data on wire ropes and theoretical data based on Equation (2.4), Fig.(2.5b). In their tests, the velocity of longitudinal waves was found to increase with increasing tension, approaching the velocity in a solid bar.

Phillips and Costello (2.51) also used a highly idealized frictionless model of a single layer strand with no core to investigate the axial (and associated rotational) response of the cable to impact loading. No experiments were performed to check the validity of the theoretical predictions. Leech and Overington (2.52) used a different technique to solve the basic equations derived in (2.51). They also conducted some experiments on single layer strands which appeared to support their theory in a qualitative manner.

Experimental and theoretical work on the bending of cables and the related problem of the fatigue lives of strands under various loadings is reviewed in Chapters 4 and 6.

Hobbs and Ghavami (2.53) and Hobbs and Wyatt (2.54) conducted a number of fatigue and dynamic tests on long specimens of a 39mm diameter structural strand. The dynamic tests included measurements of stable cyclic axial stiffness and hysteretic behaviour of old and fully bedded -

in specimens. A significant variation was observed in the magnitude of effective dynamic axial stiffness as a function of the ratio of the range of axial load perturbation to steady mean axial force. Hysteresis measured under a single hand controlled loading was roughly ten times the steady-state values obtained after several thousand cycles at uniform amplitude. On the other hand, the steady state damping measurements turned out to be much less than had been believed previously by perhaps as much as a factor of four. Considerable confidence was placed in the hysteretic measurements as these were obtained by two quite independent methods, namely the rate of heat loss to the surroundings and the relations between axial forces and corresponding axial displacements. The frequency of loading used for all the tests was about four Hertz.

The axial dynamic stiffness and the related hysteretic behaviour are important in structures as diverse as guyed towers or tension leg platforms and cable stayed bridges. Any analytical work with the ultimate aim of predicting these properties from first principles must include the means of determining interwire contact forces (both in the hoop and also radial directions) and relative displacements with friction included.

Of course,no theory can be used with confidence without appropriate experimental support which should reveal possible real life limitations of idealizations inevitably adopted in the course of developing the mathematical model.

In what follows, a theory backed by a number of experimental checks is developed which takes into account

the details of interwire contact force and displacements in a practical multi-layer large diameter strand. The final results include axial and torsional stiffnesses plus their corresponding hysteretic characteristics. The magnitude of the theoretically obtained interwire forces and slip is of obvious value as an input to a fracture mechanics analysis of the fatigue behaviour of the strand away from its terminations, while the axial and torsional dynamic properties are pertinent to a number of aero- and hydrodynamic problems in, for example, bridge and guyed tower design.

2.4 INTRODUCTION TO THE ANALYSIS

In both torsional and extensional regimes, two limiting cases can be identified: for small perturbations no interwire slip occurs, while for large enough disturbances where slip occurs interwire friction forces become negligible compared to force changes in the wires themselves. In what follows it is postulated that each layer of wires in a strand has enough wires for the properties to be averaged so that the layer can be treated as an orthotropic sheet. The elastic properties of the sheet are then derived (as a function of the perturbation) with reference to principal axes parallel and perpendicular to the wires. It is then simple (Hearmon (2.55)) to transform them to values parallel and perpendicular to the strand axis. Along the axis of the wires, the Young's modulus for the material applies, subject to an allowance for the net area of the circular wire being $\pi/4$ times the elemental area. Perpendicular to the wire

axis, it is necessary to allow for the overall stiffness between wires in line contact. This problem was solved by Hertz (Roark and Young (1.36)) as a function of the mean load on the contact line. This mean load can be estimated from the mean axial load in the wire. The shear stiffness is obtained from other results in contact stress theory.

Unfortunately, there are uncertainties in calculating the line contact stress even on a nominal basis, and additional variability due to irregularities in the fit of the wires in the strand must be expected. A discussion of the contact stresses thus precedes detailed analysis of the anisotropic sheet, the assembly of several shells of wires into a strand, and predictions of strand axial and torsional stiffness and associated damping characteristics.

2.5 KINEMATICS OF HELIX

The parametric representation of a helix is as follows:

$$x = r\,\mathrm{Cos}\phi$$

$$y = r\,\mathrm{Sin}\phi$$

$$z = (r\mathrm{Cot}\alpha) \qquad (2.5)$$

where α is the lay angle, ϕ the polar angle and r is the helix radius. It is assumed that the centre-line of a wire in a strand forms a helix both before and after axial or torsional deformation. Opening out the helix, a right-angled triangle is formed (Fig.2.6). The deformation of a wire in a strand with a free end will be composed of an axial extension, a radial contraction and a rotation (Knapp (2.23)).

Treating a strand length δ, these components are $\varepsilon_c\delta$, $\phi\Delta r$ and $\Delta\phi(r-\Delta r)$, where ε_c is the strand axial strain, $\Delta\phi$ the end rotation and Δr the change in the radius. ε_h denotes the wire axial strain.

Before and after deformation, Equation (2.5) gives:

$$\phi = \delta/r\text{Cot}\alpha$$
$$\phi' = \delta'/r'\text{Cot}\alpha \qquad (2.6)$$

Assuming that all the wires are the same length and that plane sections remain plane which, at least, is reasonable for sections remote from the ends of the strand

$$\delta' = \delta(1+\varepsilon_c) \qquad (2.7)$$

Combining Equations (2.6) and (2.7)

$$\frac{\Delta\phi}{\delta} = \frac{1+\varepsilon_c}{r'\text{Cot}\alpha'} - \frac{1}{r\text{Cot}\alpha} \qquad (2.8)$$

an expression for the rotation per unit length of strand.

In the case of a strand subjected to pure tension whose ends are not permitted to rotate, $\Delta\phi/\delta$ is zero and Equation (2.8) yields:

$$\frac{\tan\alpha'}{\tan\alpha} = \frac{r'}{r(1+\varepsilon_c)} \qquad (2.9)$$

From Fig.(2.6)

$$\text{Cos}\alpha = \frac{\delta}{\ell} \quad \text{and} \quad \text{Cos}\alpha' = \frac{\delta(1+\varepsilon_c)}{\ell(1+\varepsilon_h)}$$

where ℓ is the undeformed wire length and hence

$$\frac{\text{Cos}\alpha'}{\text{Cos}\alpha} = \frac{1+\varepsilon_c}{1+\varepsilon_h} \qquad (2.10)$$

For a strand with non-rotating ends (Chi (2.5))

$$\varepsilon_h = \frac{\ell'-\ell}{\ell} = \text{Cos}\alpha\ ((1+\varepsilon_c)^2+(\frac{r'}{r}\tan\alpha)^2)^{\frac{1}{2}}-1 \qquad (2.11)$$

Assuming $\frac{r'}{r}=1$ and using a binomial expansion, Equation (2.11) is simplified to:

$$\varepsilon_h = \varepsilon_c\ \text{Cos}^2\alpha \qquad (2.12)$$

which is the expression first derived by Hruska (2.1).

Substituting (2.12) into (2.10) we have:

$$\text{Cos}(\alpha-d\alpha) = \text{Cos}\alpha(1+\varepsilon_c)(1+\varepsilon_c\text{Cos}^2\alpha)^{-1} \qquad (2.13)$$

From (2.13), ignoring second order terms, it is possible to obtain the simple relation:

$$d\alpha \simeq \varepsilon_c\ \text{Sin}\alpha\ \text{Cos}\alpha \qquad (2.14)$$

where $d\alpha$ is the change in the lay angle due to axial cable strain, ε_c.

A more exact method for determining the change in the lay angle including the effects of changes in radius will be presented later.

2.6 EQUILIBRIUM EQUATIONS FOR A HELICAL ROD

The force and moment equilibrium equations for a curved rod are given by Love (2.56). For the final state of equilibrium they are:

$$\begin{aligned}
&\frac{dN}{ds} - N'\tau_1 + T\kappa_1' + X = 0\\
&\frac{dN'}{dS} - T\kappa_1 + N\tau_1 + Y = 0\\
&\frac{dT}{ds} - N\kappa_1' + N'\kappa_1 + Z = 0\\
&\frac{dG}{ds} - G'\tau_1 + H\kappa_1' - N' + K = 0\\
&\frac{dG'}{ds} - H\kappa_1 + G\tau_1 + N + K' = 0\\
&\frac{dH}{ds} - G\kappa_1' + G'\kappa_1 + \theta = 0
\end{aligned} \qquad (2.15)$$

in which T, N, N', G, G' etc. are the external and internal force and moment resultants in the normal, binormal and tangential directions (Fig. 2.7). For a helical wire, the initial curvatures and twist are:

$$\kappa_o = 0, \quad \kappa_o' = \frac{\sin^2\alpha}{r}, \quad \tau_o = \frac{\sin\alpha\cos\alpha}{r} \tag{2.16}$$

Once the strand is loaded, the new wire geometry is given by:

$$\kappa_1 = 0, \quad \kappa_1' = \frac{\sin^2\alpha'}{r'}, \quad \tau_1 = \frac{\sin\alpha'\cos\alpha'}{r'} \tag{2.17}$$

For wire cross sections remote from the clamping points, it is assumed that simple bending and torsion theory holds and

$$G = A(\kappa_1-\kappa_o), \quad G' = A(\kappa_1'-\kappa_o'), \quad H = C(\tau_1-\tau_o) \tag{2.18}$$

where A and C are the bending and torsion moduli for the wire.

Durelli et al. (2.9) were the first to emphasize the importance in a six wire strand of bending and twisting moments in the individual wires, as defined by Equations (2.18). Phillips and Costello (2.14) ignored friction between the wires, and assuming K, K' and dT/ds to be zero, used Equations (2.15), (2.18) to show that

$$X = \left[C(\tau_1-\tau_o)\kappa_1'-A(\kappa_1'-\kappa_o')\tau_1\right]\tau_1-T\kappa_1' \tag{2.19}$$

However, for large diameter steel strands under working loads the changes in the lay angle and radius are extremely small and Equation (2.19) may be simplified to:

$$X = -T\sin^2\alpha/r \tag{2.20}$$

This is the relation obtained by Hruska (2.2) using hoop tension formulae.

2.7 WIRE ACCOMMODATION IN EACH LAYER

This problem has been addressed by several authors. Nowak (2.21) considered n wires of identical circular cross section wound helically on a cylindrical core. He showed that for large n and small lay angles, it is reasonable to assume that, on a transverse section of the strand itself, wire cross-sections are elliptical. However, for small n and for large lay angles, the wire section is kidney shaped, as Fig.(2.8), an enlarged section of a five wire strand, shows.

Nowak also took into account the gaps between the wires in each layer and derived analytical expressions for their size. However, he assumed a uniform distribution of gaps, and inspection of well bedded-in strand samples suggests that this may be an unrealistic assumption. Indeed, the gaps seem to accumulate as one or two large gaps with the other wires in a layer in contact.

For an idealized strand,it is now assumed that the wires in each layer are just touching in the unstressed configuration, and as the theory is developed for strands with a large number of wires it is further assumed that wire cross sections in a normal section of the strand may be treated as ellipses (Fig.2.9).

Following Phillips and Costello (2.14), for a single layer of wires.

$$\frac{r}{R} = \left[1 + \frac{\tan^2(\pi/2 - \pi/n)}{\cos^2\alpha} \right]^{\frac{1}{2}} \qquad (2.21)$$

where R is the wire radius, and there are n wires in the layer. For the loaded configuration

$$\frac{r'}{R} = \left[1 + \frac{\tan^2(\pi/2 - \pi/n)}{\cos^2\alpha'} \right]^{\frac{1}{2}} \tag{2.22}$$

or

$$r' = r(1 + S'_{2R}) \tag{2.23}$$

where S'_{2R} is the radial strain in the strand cross section due to change of lay angle, with compression regarded as negative. From Equations (2.21) to (2.23)

$$1 + S'_{2R} = \left[\frac{\cos^2\alpha(\cos^2\alpha' + \tan^2(\pi/2 - \pi/n))}{\cos^2\alpha'(\cos^2\alpha + \tan^2(\pi/2 - \pi/n))} \right]^{\frac{1}{2}} \tag{2.24}$$

For n large,

$$\tan^2(\pi/2 - \pi/n) >> \cos^2\alpha', \cos^2\alpha \tag{2.25}$$

and using Equations (2.10) and (2.25), Equation (2.24) reduces to:

$$1 + S'_{2R} = \frac{1 + \varepsilon_h}{1 + \varepsilon_c} \tag{2.26}$$

and ignoring second order terms

$$S'_{2R} = -(\varepsilon_c - \varepsilon_h) \tag{2.27}$$

For a single layer strand with a hemp core, or no core wire, the change in diameter under load is composed of three separate mechanisms:

i) the Poisson's ratio effects in the wire material,

ii) deformation due to contact stresses between individual wires in line contact, and

iii) reduction in radius due to changes in lay angle as defined in Equation (2.24).

In a multi-layered strand, effects (i) and (ii) are operative, but (iii) is assumed to be negligible. Moreover, the diametral contraction of individual layers due to (i) is believed to be fairly uniform over the cable cross-section and hence it is postulated that (i) does not affect the contact stresses between individual wires in different layers.

In what follows the large diameter strand is modelled as an assembly of a number of concentric partly self-prestressed orthotropic cylinders. The prestress in each layer is partly due to the body forces in the wires composing the cylinder and partly due to the clenching forces acting on the cylinder from the neighbouring cylinders. While it is recognised that the problem is essentially three-dimensional, the simplifying assumptions made are supported by the favourable agreement found later between experimental and theoretical results.

The main assumption is that twisting and bending moments in individual wires are negligible, i.e., that the wire carries a pure tension, or G, G' and H as defined in Equations (2.18) are all zero. Plane sections are assumed to remain plane during strand deformation. In consequence the analysis is applicable only to sections remote from the clamping points. Nearer the clamps, shear deformations between cable layers may be significant.

2.8 Contact Forces in a Strand

Using the notation of Fig.(2.10), consider a wire element of length dL, mean radius in the strand r, subtending an angle $d\phi$ on a perpendicular cross-section of the strand.

For a mean axial stress F_o, and effective radial and circumferential contact stresses F_R and F_N based on gross elemental areas (e.g. $r\Delta r\Delta\phi$), the radial inward equilibrium equation becomes:

$$\frac{F_o}{\cos\alpha}\ \frac{\sin^2\alpha}{r}\ \frac{dL}{\cos\alpha}\ rdrd\phi + F_N\cos\alpha\frac{dL}{\cos\alpha}\ drd\phi$$

$$- (F_R + r\frac{dF_R}{dr})dLdrd\phi = o \qquad (2.28)$$

$$\text{or} \quad F_o\tan^2\alpha + F_N - (F_R + r\frac{dF_R}{dr}) = 0 \qquad (2.29)$$

F_o is positive while F_N and F_R are expected to be negative (compressive).

In normal cable constructions, the lay angles in different layers are very similar and the assumption of a uniform F_o over the whole cross-section is a reasonable initial approximation. Moreover, changes in α and r can be assumed to be very small. However, in Section 2.9 onwards a method will be proposed which takes variations of F_o over the cross-section and changes in α and r into account. For the time being Equation (2.29) can be used to explain some of the essentials of the interwire/ interlayer contact problem.

The first term represents the clench force generated by tension in the layer, the other two the circumferential and radial reactions to this force. The strand make-up includes a subtle variation of r and α in the various layers based on commercial experience, and the proportion of the clenching effect resisted by circumferential contact forces to radial contact forces has not previously been obtained either by theory or experiment.

In contact problems,stresses are not in general linearly proportional to the load and consequently the ratio F_N/F_R for a given layer is not a constant and varies as a function of the axial load on the cable. For a given axial load various layers inside the strand are expected to have different F_N/F_R ratios.

Although it is reasonable to assume plastic flow at the contact points between individual wires for the first few cycles of loading, it is unrealistic to assume this for cases when the elements make a large number of contacts during their life: plastic flow may occur at first, but this is followed by a steady state in which the load is supported elastically - ref. to Chapter 1 .

The ideal elastic stiffness in the radial direction across the trellis crossing of cylinders (wires) is clearly smaller than in the hoop direction across line-contact between cylinders. It is further assumed that F_N and F_R are of the same order of magnitude. Consequently, the radial movements of different layers due to contact forces will be governed by the interaction of wires in line-contact in individual layers. The interactions between different layers will then take place in such a way as to be compatible with those in the hoop direction.

2.9 PROPERTIES OF THE ORTHOTROPIC SHEET

Using Hearmon's (2.55) notation,stresses T_i and engineering strains S_i referred to the axes of orthotropy are related by compliances S_{ij} where:

$$S_1 = S_{11}T_1 + S_{12}T_2$$

$$S_2 = S_{12}T_1 + S_{22}T_2$$

$$S_6 = S_{66}T_6 \qquad (2.30)$$

Taking axis 1 parallel to the wire axis,

$$S_{11} = {}^{4}/\pi E \qquad (2.31)$$

and

$$S_{12} = -\nu s_{11} \qquad (2.32)$$

where ν is Poisson's ratio. The other two compliances may be obtained from contact stress theory.

For the line contact of two equal diameter cylinders, made from the same material, the total width of the contact area, 2b, is (Section 1.2):

$$2b = 1.6\ \left(\frac{PD(1-\nu^2)}{E}\right)^{\frac{1}{2}} \qquad (2.33)$$

where P is the load per unit length, and D the wire diameter. The diametral deflection, δ_n, is obtained by setting $2R_1 = 2R_2 = D$ in Equation (1.5):

$$\delta_n = \frac{4P(1-\nu^2)}{\pi E}\left(\frac{1}{3} + \ell n\ \frac{D}{b}\right) \qquad (2.34)$$

Substituting for P and b, using $\nu = 0.28$ again, and rearranging

$$\delta_n = \frac{P}{E}\left[0.39 + 1.17\ell n\left(\frac{2}{1.54}\sqrt{\frac{ED}{P}}\right)\right] \qquad (2.35)$$

Then the compliance in the diametral direction of the equivalent orthotropic sheet, S_{22}, is given by:

$$S_{22} = \frac{1}{D}\ \frac{d\delta_n}{d({}^{P}/_{D})} = \frac{1}{E}\ (0.11 + 0.59\ell n\ \frac{ED}{P}) \qquad (2.36)$$

For cylinders in line contact, the author used the equation derived by Mindlin (1.39) and Deresiewicz (1.40) for the constant displacement of the adhered region in Cattaneo's problem to obtain expressions for the tangential compliance covering the no-slip to full-slip regime. Details and references are given in the previous chapter (Section 1.3) and Appendix (A.1). For pure tangential loading (i.e. with zero perturbation of normal load) the following applies:

For the first application of load

$$S_{66} = \frac{d\delta_\ell}{d(\frac{T}{a})} = \frac{S_{22}}{1-\nu}\left(1- \frac{\delta_\ell}{2\Delta_{\ell max}}\right)^{-\frac{1}{2}} \qquad (2.37)$$

where

$$\Delta_{\ell max} = \frac{3}{4}\ \frac{\mu P}{1-\nu}\ S_{22}$$

$\Delta_{\ell max}$ denotes the limiting tangential displacement per body at which rigid-body movement just starts. $\Delta_{\ell max}$ applies to the first quarter of the first application of loading, i.e., with initial tangential force and displacement equal to zero. The work in Appendix (A.1) shows that for the case when the tangential force oscillates between $\pm$ T*, $|T^*|<\mu P$, Equation (2.37) may be modified to:

$$S_{66} = \frac{S_{22}}{1-\nu}\left(1- \frac{\delta}{v}\right)^{\frac{1}{2}} \qquad (2.38)$$

where

$$v = \frac{3\lambda\mu P}{2(1-\nu)}\ S_{22}$$

'$\lambda\mu$' is called the pseudo-coefficient of friction. λ is a co-efficient whose magnitude is determined by the

conditions of stress and displacement at the onset of the current loading change. For the ideal model of Mindlin λ is equal to 2.

Note that the initial tangential compliance is always given by Equation (2.38) with δ=o, irrespective of the initial state of stress and relative displacement, so long as we change direction cf. the previous increment.

2.10 TRANSFORMATION OF PROPERTIES

Using Hearmon's notation again, the stresses T_i' and strains S_i' referred to arbitrary axes aligned at an angle α to the axes of orthotropy are related by

$$\begin{aligned} S_1' &= S_{11}'T_1' + S_{12}'T_2' + S_{16}'T_6' \\ S_2' &+ S_{12}'T_1' + S_{22}'T_2' + S_{26}'T_6' \\ S_6' &= S_{16}'T_1' + S_{26}'T_2' + S_{66}'T_6' \end{aligned} \qquad (2.39a)$$

where, denoting cos α by m and sin α by n

$$\begin{aligned} S_{11}' &= m^4S_{11} + 2m^2n^2S_{12} + n^4S_{22} + m^2n^2S_{66} \\ S_{12}' &= m^2n^2S_{11} + (m^4+ n^4)S_{12} + m^2n^2S_{22} - m^2n^2S_{66} \\ S_{16}' &= -2m^3nS_{11} + 2mn(m^2- n^2)S_{12} + 2mn^3S_{22} + mn(m^2- n^2)S_{66} \\ S_{22}' &= n^4S_{11} + 2m^2n^2S_{12} + m^4S_{22} + m^2n^2S_{66} \\ S_{26}' &= -2mn^3S_{11} - 2mn(m^2- n^2)S_{12} + 2m^3nS_{22}- mn(m^2- n^2)S_{66} \\ S_{66}' &= 4m^2n^2S_{11} - 8m^2n^2S_{12} + 4m^2n^2S_{22} + (m^2- n^2)S_{66} \end{aligned}$$

(2.39b)

2.11 KINEMATICS OF THE WIRE LAYER CONTINUUM

Following Section 2.7, each layer of wires in the multi-layered strand may be treated as an anisotropic cylinder. The diametral contraction caused by axial load is partly due to the Poisson's ratio of the wires and partly caused by deformations on the line contacts between the wires. As regards the magnitude of the changes in cable diameter, both of these effects are of the same order of magnitude. However, the Poisson effect is believed (Section 2.7) to be secondary when calculating the magnitude of the interwire/interlayer contact forces and will be ignored. As argued in Section 2.8, the line contact effects control the "trellis point" interactions between the different layers.

In the absence of an inner core, there is a stress-free radial inward rigid body motion, S'_{2R}, associated with changes in the lay angle (Equation 2.24), which is a part of the total radial movement, S'_{2C}. For a multi-layered strand, however, all layers will have a core which prevents the stress-free motion. In other words, in the absence of interwire contact deformations, a decrease in the lay angle α, should, in the presence of the core, lead to creation of gaps between the wires in a given layer.

In a multi-layered strand, the cylinder will then act as a two-dimensional continiuum whose kinematics may properly be treated by tensorial methods*.

---

*Later numerical invariance checks (see Section 2.15) confirmed the tensorial nature of these continuum strains.

Thus, for a given cable axial strain, ε_c, the core may initially be removed, and the rigid body motion, S'_{2R}, and total radial movement, S'_{2C}, calculated. Replacing the core, and enforcing compatibility of radial movement, the deformations in the hoop direction and the line contact forces may then be computed as functions of the net radial strain.

Working with the unwrapped centres of the layer of wires, consider a rectangular element ABCD in the unstressed condition, Fig.(2.11). A'B'C'D' corresponds to the deformed state of ABCD under the axial cable strain S'_1. As discussed above, in the absence of the core, the wires would experience a rigid body movement, S'_{2R}, given by Equation (2.24). Due to this radial strain, wires in the corresponding layer experience a slight decrease in their longitudinal strain $d\varepsilon_h$ which may be found by setting $\varepsilon_c=0$ and $r' = r(1+S'_{2R})$ in Equation (2.11).

This leads to:

$$d\varepsilon_h = \cos\alpha \sqrt{1+(1+ S'_{2R})^2 \tan^2\alpha}-1 \qquad (2.40)$$

From Fig.(2.11), the slip between two wires, u, in the presence of the core is, therefore:

$$u = D \left[\tan\alpha(1+\varepsilon_h - d\varepsilon_h)- \tan\alpha'\right] \qquad (2.41)$$

For the orthotropic membrane $S_1=\varepsilon_h$ and from (2.10)

$$1+ S_1 = \frac{\cos\alpha(1 + S'_1)}{\cos\alpha'} \qquad (2.42)$$

Thus, inclusion of the core will result in a slight increase in the axial wire strain, since α' is increased slightly.

The tensorial shear strain S_{6T} will then be:

$$S_{6T} = \tfrac{1}{2}\gamma$$

$$= u/_{2D'}$$

$$= \frac{1}{2(1+S_2)} \left[\tan\alpha(1+S_1-d\varepsilon_h)-\tan\alpha'\right] \qquad (2.43)$$

where γ is the engineering strain and $S_2 = \frac{D'-D}{D}$ corresponds to the approaching strain between distant points in two wires in line contact.

Returning to the diametral strains, from Equation (2.9)

$$S'_{2C} = (1+S'_1)\frac{\tan\alpha'}{\tan\alpha} - 1 \qquad (2.44)$$

S'_{2C} is the total magnitude of the radial strain in the layer with the core removed. With the core included, the compatibility of movements in the radial direction gives

$$S'_2 = S'_{2C} - S'_{2R} \qquad (2.45)$$

where S'_2 is the radial strain in the cable cross-section used for the orthotropic sheet.

The two dimensional element in its final deformed state may always be rotated through an angle α' with the strains on it considered as a second order tensor.

Thus

$$S_2 = -\frac{S'_1-S'_2}{2}\,\mathrm{Cos}(2\alpha') + \frac{S'_1+S'_2}{2} \qquad (2.46)$$

Moreover, for a cable with rotationally fixed ends, $S_6=0$. In other words the cable axis is coincident with the principal axis of the element, hence:

$$S_{6T} = \left(\frac{S_1' - S_2'}{2}\right) \mathrm{Sin}(2\alpha') \qquad (2.47)$$

2.12 METHOD OF SOLUTION

For a cable strain S_1', Equations (2.24), (2.40) and (2.42)-(2.47) may be solved as a set of non-linear simultaneous equations to yield values of S_1, α', S_{2C}', S_{2R}', S_2', S_2, S_6 and $d\varepsilon_h$ - providing a set of compatible strains in the anisotropic cylinder with the core. The method adopted involves treating S_1 as the primary unknown and using a Newton iteration with the derivative approximated by a central finite difference form. First rearrange Equation (2.43) in the form:

$$F(S_1) = \frac{1}{2(1+S_2)} \left[\tan\alpha(1+ S_1 - d\varepsilon_h) - \tan\alpha' \right] - S_{6T} \qquad (2.48)$$

so that a zero of $F(S_1)$ is to be found. Then for an initial estimate:

$$(S_1)_o = S_1' \, \mathrm{Cos}^2\alpha \qquad (2.49)$$

of the strain S_1, compute estimates of $(\alpha')_o$, $(S_{2R}')_o$, $(d\varepsilon_h)_o$, $(S_{2C}')_o$, $(S_2')_o$, $(S_2)_o$ and $(S_6)_o$ of α', S_{2R}', etc., using Equations (2.42), (2.24), (2.40), (2.44), (2.45), (2.46) and (2.47) respectively.

The Newton iterative technique could then be used to compute an improved estimate $(S_1)_1$ of S_1 using:

$$(S_1)_1 = (S_1)_o - \frac{F\left[(S_1)_o\right]}{F'\left[(S_1)_o\right]} \qquad (2.50)$$

where $F'\left[(S_1)_o\right]$ is the derivative $\left[\frac{dF}{dS_1}\right]_{S_1=0}$ of Equation (2.48). Obtaining an analytical expression for $F'(S_1)$ is not easy. Alternatively, express $F'(S_1)$ in a central finite difference form. Taking an arbitrary mesh length of 0.001

$$F'\left[(S_1)_o\right] \approx \frac{F\left[1.001(S_1)_o\right] - F\left[0.999(S_1)_o\right]}{0.002} \tag{2.51}$$

where $F\left[1.001(S_1)_o\right]$, for example, represents the value of the function $F(S_1)$ for $S_1 = 1.001(S_1)_o$.

Using (2.51), (2.50) may be replaced by:

$$(S_1)_1 = (S_1)_o \left[1 - \frac{0.001\ F\left[(S_1)_o\right]}{F\left[1.001(S_1)_o\right] - F\left[0.999(S_1)_o\right]}\right] \tag{2.52}$$

This value of S_1 is used to calculate better approximations of α', S'_{2R} etc. and thus leads to a further improved approximation $(S_1)_2$ to S_1.

Once convergence has occurred, values of α', S'_{2R}, $d\varepsilon_h$, S'_{2C}, S'_2, S_2 and S_6 are known. Using Equation (2.20) with the wire force $T=EAS_1$, the clench force may be found. Additionally, the diametral deflection δ_n in Equation (2.34) is very nearly:

$$\delta_n = S_2 D \tag{2.53}$$

where D is the wire diameter.

Equations (2.33), (2.34) and (2.53) may then be solved by a Newton iteration to give values of the contact force P_{RC} per unit length between wires in the layer as a function of S'_1, for this rigid core configuration. The initial guess for P_{RC} may be taken as:

$$(P_{RC})_o = EA\,\frac{S_1\,\sin^2\alpha}{r}$$

where $A = \pi D^2/4$.

2.13 DETERMINATION OF RADIAL FORCE EXERTED ON THE RIGID CORE

The angle, β, (Fig.2.9) which locates the lines of action of the line contact loads, P, is (Phillips and Costello (2.15)).

$$\cos\beta = \frac{1}{\sin^2\alpha}\left(\sqrt{1+\frac{\tan^2(\pi/2-\pi/n)}{\cos^2\alpha}}\right.$$

$$\left.-\sqrt{\tan^2(\pi/2-\pi/n)\left[1+\frac{1}{\cot^2\alpha\cos^2(\pi/2-\pi/n)\left[\cos^2\alpha+\tan^2(\pi/2-\pi/n)\right]}\right]+\cos^4\alpha}\right) \tag{2.54}$$

The net normal force per unit length of the wire carried by the core is, Fig. (2.9).

$$X_R = X_{RC} - 2P_{RC}\cos\beta$$

$$= \frac{EAS_1\sin^2\alpha}{r} - 2P_{RC}\cos\beta \tag{2.55}$$

Note that in Equations (2.54) and (2.55), changes in the lay angle, α, and helix radius, r, due to axial cable strains, S_1', are assumed small enough to be ignored.

2.14 RADIAL LOAD TRANSFER IN A MULTI-LAYERED STRAND

Until now, a single layered cylinder with an inner core has been considered. If α, n, and R are specified, it is then possible to determine all the deformations and forces in the membrane for any given cable axial strain S_1' using the above analysis. In particular, it is possible to obtain line contact forces between the individual wires in the

layer, P_{RC}, and radial body forces, X_{RC}, for different strains, S_1'.

In a multi-layered strand, part of the radial force exerted on any layer is due to the radial body forces in that layer and the rest is due to the clenching effects of the outer layers (see Section 2.8). These effects grow radially inwards and may be simply described starting from the outermost layer, layer 1. Noting that the relationship between line contact force P_{MS} and radial force X_{MS} in the outer layer is identical to that between P_{RC} and X_{RC}, it is possible to calculate the line contact forces in the other layers as follows (subscript MS stands for multi-layered strand): for a given cable strain S_1' the clenching force provided by each wire in layer i acting on layer i+1 is given by, Fig.(2.9)

$$X_{Ri} = EA_i \frac{S_{1i} \, Sin^2\alpha_i}{r_i^2} - 2P_{MSi}Cos\beta_i \qquad (2.56)$$

where the subscript i refers to the i th layer and $A_i = \frac{\pi D_i^2}{4}$.

Each wire in layer j= i+1 thus experiences a total radial force

$$X_{MSj} = EA_j \frac{S_{1j} \, Sin^2\alpha_j}{r_j^2} + X_{Ri} \frac{n_i}{n_j} \cdot \frac{Cos\alpha_j}{Cos\alpha_i} \qquad (2.57)$$

where n_i and n_j are the numbers of wires in two layers (Ref.Sect.4.6)

Using the previously calculated P_{RC}/X_{RC} data for layer i+1, it is then possible to find corresponding values for P_{MS} and X_{MS} for layer i+1. The process is then repeated, moving in another layer each time until the whole strand has been analysed.

2.15 APPLICATION OF STRAND THEORY

Table (2.1) gives details of a 92 wire 39mm diameter strand used for experimental studies. Column (6) of the table gives results from Equation (2.22) for the theoretical radius at which n wires just touch and should be compared with the fully bedded-in measurements in Column (7). Column (8) gives the net wire area for layer i in the cable transverse section based on:

$$A_{ni} = n_i \text{ Sec } \alpha_i \frac{\pi D_i^2}{4} \tag{2.58}$$

The gross area used for the orthotropic sheet model, A_{gi}, is simply:

$$A_{gi} = 4 A_{ni}/\pi \tag{2.59}$$

Apart from the 39mm O.D. strand, numerical studies were conducted on 16mm, 51mm and 127mm O.D. strands whose details are given in Tables (2.2-2.4). All of these strands are of realistic constructions and are composed of galvanized high tensile steel wires. Fatigue results on 39mm and 16mm strands have already been reported by Hobbs and Ghavami (2.53). These two constructions consist of a number of layers covering a central core which consists of one single wire- the king. The other two strands are of equal lay core construction (Ref. Chapter 0).

Using the methods described in Section 2, results have been obtained for the wire axial and shear strains, S_1 and S_{6T}, for strand axial strains S_1' up to 5×10^{-3} for the

layers of each strand. The relations are essentially linear up to this level and on this basis slip between the wires may be obtained from :

$$\delta_S = 2DS_{6T} = 2DkS_1' \tag{2.60}$$

where the constant k can be taken from the graphs of S_{6T} versus S_1'.

Results for interwire contact forces P_{RC} and radial body forces X_{RC} for a layer of wires on a rigid core are presented in Fig. (2.12) which gives the results for the various layers in the 39mm O.D. strand. The line contact forces P_{MS} in the multi-layer strand (from Section 2.12) are shown in Figs. (2.13) and (2.14) as a function of cable axial strain. Plots of radial contact force X_{MS} for various strand constructions as a function of cable axial strain are given in Figs.(2.15) and (2.16).

It is reassuring to note that the analysis of the final results always confirmed the invariance properties of tensor coefficients - ie:

$$S_{1T} + S_2 = S_1' + S_2'$$

where

$$S_{1T} = S_1 - d\varepsilon_h \tag{2.61}$$

and

$$-S_{6T}^2 + S_2 \cdot S_{1T} = S_2' S_1' \tag{2.62}$$

A comparison of the theoretical contact stress distributions in the various constructions reveals significant changes in the pattern of internal radial and hoop stress distribution across the cable cross section. This is

especially important in the case of the outer layers. It therefore confirms (if confirmation was needed) that the linear scaling up of conventional strand (or rope) design involves significant changes in the state of internal contact forces and hence fatigue behaviour. The estimation of the fatigue life of large diameter cables by the use of small diameter models at the present state of knowledge is therefore risky,and could give misleading results. There are obviously other complications such as the limitations on the size of wires because of manufacturing constraints and the relevant metallurgical factors.

The geometrical non-linearities within the practical working range of strand axial strains ($\varepsilon_c < 4000\times10^{-6}$ or so) are not believed to be significant,and the non-linear relationship between cable axial strain (and/or axial tension) and contact forces between wires (even for the limiting case when the coefficient of friction, μ, is zero) is almost entirely due to the non-linear nature of the elastic contact problem. Further material non-linearities due to the presence of friction in the cable will be considered in considerable detail later on.

It is worth noting in view of the original assumptions that the theoretical results show that the bending and twist in individual wires within the normal working strand axial strains are insignificant. For example, consider the 39mm strand under a fairly high cable axial strain of 4000×10^{-6}, which corresponds to a cable axial load of about 0.6MN or roughly half of its breaking strength. The difference between the theoretical values of clench force

on individual wires as calculated from the simple linearized Equation (2.20) (which ignores both geometrical non-linearities and friction) and Equation (2.19) (which also ignores friction but takes geometrical non-linearities into account), for the wires situated in the outer layer, is only about 0.04%. It appears that the inclusion of bending and twisting terms for individual wires in calculations for a practical multi-wire strand under normal working loads merely adds to the complexity of the work without making a significant contribution to the accuracy of the final results. However, it should be borne in mind that this has only been formally demonstrated for the case of a strand with both ends fixed against rotation.

For any strand construction, specifying ε_c automatically leads to the determination of interwire forces and displacements throughout the strand cross-section. With the fatigue life of strands mainly governed by the degree of fretting between the wires, cable cyclic axial strain, ε_c, appears to be the obvious parameter to use when presenting fatigue data. For the case when cable axial stiffness is a constant, plotting load range versus fatigue life is equivalent to plotting cable axial strain against fatigue life. However, as shown by Hobbs and Wyatt (2.54) cable axial stiffness is dependent on the ratio of range of load perturbation to mean axial load and significant variation has been observed between the limits of no-slip and full-slip cable stiffness.

In the presence of such variations in the axial stiffness it is reasonable, when covering the full range of the cable's fatigue life from very small (no-slip) to very large (full-slip) load perturbations, to adopt ε_c versus number of cycles to failure as the basis for fatigue plots. Obviously, ε_c is not the only parameter governing a cable's fatigue life (although it is the most important one) and, for example, the level of mean axial load must also be taken into account.

Interwire normal contact forces for large diameter and multi layer strands (away from the terminations) can now be predicted for the ideal case when with zero tensile force on the cable the individual wires in each layer just touch each other. This assumption is not strictly true for the usual practical strand constructions and experimental checks of its limitations will be discussed in the next chapter, which also gives methods based on the work of this chapter for incorporating frictional forces between the wires into theoretical predictions of the torsional and axial stiffnesses of the cable and their associated damping characteristics.

REFERENCES

2.1 HRUSKA, F.H. Calculation of Stresses in Wire Ropes. Wire and Wire Products. 1951: 26, pp.766-767, 799-801.

2.2 HRUSKA, F.H. Radial Forces in Wire Ropes. Wire and Wire Products. 1952: 27, pp.459-463.

2.3 HRUSKA, F.H. Tangential Forces in Wire Rope. Wire and Wire Products. 1953: 28, pp.455-460.

2.4 CHI, M. Analysis of Multi-Wire Strands in Tension and Combined Tension and Torsion. Catholic University of America: 1971. Technical Report 71-9.

2.5 CHI, M. Analysis of Operating Characteristic of Strands in Tension Allowing End-rotation. Catholic University of America: 1971. Technical Report 71-10.

2.6 GIBSON, P.T., CRESS, H.A., KAUFMAN, W.J., and GALLANT,W.J. Torsional Properties of Wire Rope. ASME Paper No. 69-DE-34, May, 1969.

2.7 BOWERS, W.E. High Strength to Weight Cable for Deep Ocean Projects. Proceedings, 22nd International Wire and Cable Symposium. Atlantic City,NJ, 1973, pp.279-285.

2.8 McLOAD, K.W., BOWERS, W.E. Torque Balanced Armored Cables. Marine Tech. Soc. Buoy Technology Symp.Trans. Washington D.C., March, 1964. pp.341-357.

2.9 DURELLI, A.J., MACHIDA, S., and PARKS, V.J. Strains and Displacements in a Steel Wire Strand. Naval Engineering Journal. 1972: 84, pp.85-93.

2.10 DURELLI, A.J., and MACHIDA, S. Response of Epoxy Oversized Models of Strands to Axial and Torsional Loads. Experimental Mechanics. 1973: 13, pp.313-321.

2.11 NAVAL RESEARCH LABORATORY. Testing Wire Rope: Measurement System and Experimental Study: 1974. Technical Report AD-782 515.

2.12 SAMRAS, R.A., SKOP, R.A., and MILBURN, D.A. An Analysis of Coupled Extensional- Torsional Oscillations in Wire Rope. Journal of Engineering for Industry. Transactions of the ASME. 1974: 96, pp.1130-1135.

2.13 OWADA, SHIN. Calculation of Tensile and Torsional Stiffnesses of Single-Lay Cables. Proceedings, 2nd Japan National Congress for Applied Mechanics. 1952: pp.159-164.

2.14 PHILLIPS, J.W., and COSTELLO, G.A. Contact Stresses in Twisted Wire Cables. Journal of the Engineering Mechanics Division, ASCE. 1973: 99, pp.331-341.

2.15 COSTELLO, G.A., and PHILLIPS, J.W. A More Exact Theory for Twisted Wire Cables. Journal of the Engineering Mechanics Division, ASCE. 1974: 100, pp.1096-1099.

2.16 COSTELLO, G.A., and PHILLIPS, J.W. Effective Modulus of Twisted Wire Cables. Journal of the Engineering Mechanics Division, ASCE. 1976: 102, pp.171-181.

2.17 COSTELLO, G.A., and SINHA, S.K. Static Behaviour of Wire Rope. Advances in Civil Engineering Through Engineering Mechanics, Proceedings Second Annual Engineering Mechanics Division Specialty Conference. North Carolina State University, Raleigh, N.C. 1977. pp.475-478.

2.18 COSTELLO, G.A., and SINHA, S.K. Torsional Stiffness of Twisted Wire Cables. Journal of the Engineering Mechanics Division, ASCE. 1977: 103, pp.766-770.

2.19 COSTELLO, G.A., and MILLER, R.E. Lay Effect of Wire Rope. Journal of the Engineering Mechanics Division, ASCE. 1979: 105, pp.597-608.

2.20 HUANG, N.C. Finite Extension of an Elastic Strand with a Central Core. Journal of Applied Mechanics, Transactions of the ASME. 1978: 45, pp.852-858.

2.21 NOWAK, G. Computer Design of Electromechanical Cables For Ocean Applications. Proceedings, 10th Annual MTS Conference. Washington D.C., 1974. pp.293-305.

2.22 KNAPP, R.H. Non Linear Analysis of Helically Armored Cable with Non Uniform Mechanical Properties in Tension. Proceedings, IEEE/MTS Conference: Engineering in the Ocean Environment. 1975: pp.155-164.

2.23 KNAPP, R.H. Derivation of a New Stiffness Matrix for Helically Armoured Cables Considering Tension and Torsion. International Journal for Numerical Methods in Engineering. 1979: 14, pp.515-529.

2.24 KASPER, R.G. A Structural Analysis of Multiconductor Cable. Naval Underwater Systems Centre, Distributed by National Technical Information Service, 1973. Technical Report AD-767 963.

2.25 KASPER, R.G. Cable Design Guidelines Based on a Bending, Tension and Torsion Study of an Electro-mechanical Cable. Naval Underwater Systems Centre, Distributed by National Technical Information Service, 1973. Technical Report AD-769 212.

2.26 DRUCKER, D.C., and TACHAU, H. A New Design Criterion for Wire Rope. Journal of Applied Mechanics, Transactions of the ASME. 1945: 12, pp.A.33-A.38.

2.27 LEISSA, A.W. Contact Stresses in Wire Ropes. Wire and Wire Products. 1959: 34, pp.372-373.

2.28 STARKEY, W.L., and CRESS, H.A. An Analysis of Critical Stresses and Modes of Failure of a Wire Rope. Journal of Engineering for Industry, Transactions of the ASME. 1959: 81, pp.307-316.

2.29 BERT, C.W. and STEIN, R.A. Stress Analysis of Wire Rope in Tension and Torsion. Wire and Wire Products. 1962: 37, pp.769-770, 772, 816.

2.30 JONES, N., and CHRISTODOULIDES, J.C. Static Plastic Behaviour of a Strand. International Journal of Mechanical Sciences. 1980: 22, pp.185-195.

2.31 SCHINKE, H.W. Variable Back-Twist in Rope Making Machinery. Wire. 1961: Oct., pp.1398-1402, 1441-1442.

2.32 YOSHIDA, S. On the Moments Applied to Wires During the Stranding Process. Proceedings, 2nd Japan National Congress for Applied Mechanics. 1952: pp.109-112.

2.33 WINKELMANN, W. Beitrag Zur Berechnung der Verseilspannungen Wissenschaftliche Zeitschrift der Technischen Hochschule Otto von Guericke Magdeburg. 1972, 16, Heft 4.

2.34 SMISLOVA, A., LOEWER, A.C., and ENEY, W.J. Using SR-4 Gages to Measure Strains in Wire Strand. Product Engineering. 1953, 24, p.214.

2.35 WILSON, B.W. Elastic Characteristics of Moorings. Journal of the Waterways and Harbours Division, ASCE. 1967: 93, pp.27-55.

2.36 SKOP, R.A., and SAMRAS, R.K. Effects of Coupled Extensional-Torsional Oscillations in Wire Rope During Ocean Salvage and Construction Operations. Journal of Engineering for Industry, Transactions of the ASME. 1975: 97, pp. 485-492.

2.37 BECHTLOFF, G. Longitudinal Elongation and Transverse Contraction of a Six-Stranded Wire Rope Under Tensile Load. Wire World International (English Translation from DRAHT-WELT). 1963, 5, pp.247-252.

2.38 RIDLEY, S.A. The Damping Capacities of Helically Wound Multi-Strand Steel Cables. Imperial College, Department of Civil Engineering. M.Sc.Thesis, 1973.

2.39 KAWASHIMA, S., and KIMURA, H. Measurements of the Internal Friction of Metal Wire Ropes Through the Longitudinal Vibration. Memoirs of the Faculty of Engineering, Kyushu University. 1952: 13 (1), pp.119-130.

2.40 KIMURA, H. A Viscoelastic Consideration of the Dynamic Behaviour of Wire Ropes. Workshop on Marine Wire Rope, Catholic University of America. Washington D.C.: 1970.

2.41 YU, Ai-Ting. Vibration Damping of Stranded Cables. Proceedings, The Society for Experimental Stress Analysis. 1952: 9, pp.141-158.

2.42 VANDERVELDT, H., CHUNG, B, and READER, W. Some Dynamic Properties of Axially Loaded Wire Ropes. Experimental Mechanics. 1973: 13, pp.24-30.

2.43 KAWASHIMA, S., KIMURA, H., and HAN, N. On the Longitudinal Waves Transmitted Through Steel Wire Ropes. Kyushu University: 1958. Technical Report. 31, No.3-4.

2.44 KAWASHIMA, S., KIMURA, H., and FUGITA, N. Wave Propagation in Steel Ropes. Memoirs of the Faculty of Engineering. Kyushu University. 1961: 21(1), pp.69-80.

2.45 KIMURA, H. Measurement of Longitudinal Waves in Steel Wire Ropes. (I) Technical Report. Kyushu University. 1962: 35 (4) (II)Technical Report, Kyushu University. 1963: 36(1).

2.46 KIMURA, H. Measurement of Dynamic Stress in Steel Wire Ropes. Proceedings, 7th Japan Congress for Testing Materials. 1964.

2.47 KIMURA, H. A Study on the Propagation of Waves in Wire Rope as Affected by Structural Damping. Proceedings, 14th Japan National Congress for Applied Mechanics. 1944: pp.236-241.

2.48 RINGLEB, F.O. Motion and Stress of an Elastic Cable Due to Impact. Journal of Applied Mechanics, Transactions of the ASME. 1957: 24, pp.417-425.

2.49 KOLSKY, H. Stress Waves in Solids. New York: Dover Publications, Inc., 1963.

2.50 VANDERVELDT, H., and GILHEANY,J., Propagation of a Longitudinal Pulse in Wire Ropes Under Axial Loads. Experimental Mechanics. 1970: 10, pp.401-407.

2.51 PHILLIPS, J.W., and COSTELLO, G.A. Axial Impact of Twisted Wire Cables. Journal of Applied Mechanics, Transactio of the ASME. 1977: 44, pp.127-131.

2.52 LEECH, C.M., and OVERINGTON, M.S. The Dynamics of Wire Rope Subjected to Shock Axial Loads. Proceedings, 14th Annual Offshore Technology Conference. Houston, Texas: 1982.

2.53 HOBBS, R.E., and GHAVAMI, K. Fatigue of Socketed Cables: In-Line and Transverse Tests on 38mm Specimens. Imperial College, Civil Engineering Department, Ceslic Report SC2, 1978.

2.54 WYATT, T.A. Internal Damping in 38mm (nominal) Specimens. Imperial College, Civil Engineering Department, Ceslic Report SC2, 1978.

2.55 HEARMON, R.F.H. Applied Anisotropic Elasticity, Oxford: Oxford University Press: 1961.

2.56 LOVE, A.E.H. Treatise on the Mathematical Theory of Elasticity. 4th ed. Cambridge: 1927. (and Dover Publications, New York: 1944).

CHAPTER 3

THEORETICAL AXIAL AND TORSIONAL STIFFNESSES OF STRAND AND RELATED HYSTERETIC BEHAVIOUR

3.1 INTRODUCTION

It has long been appreciated that spiral strand exhibits significant hysteresis in its longitudinal load/displacement behaviour. It also (3.1) exhibits significant damping of torsional oscillations in the presence of an axial load. This dissipation of energy is potentially a major contribution to the overall damping of the structure supported by the strands.

Since the failure of the Tacoma Narrows Bridge, the importance of the capacity of suspension bridges to dissipate energy imparted by wind action and its bearing on the dynamic stability of the structure have been fully recognized. In the case of cable stayed bridges about 70% of the energy of oscillation is stored in the cables (3.2), and it follows that with their relatively high specific loss values these elements contribute significantly to the total damping capacity of the structure.

Examining some existing bridges in Norway, Selberg (3.3) reported logarithmic decrements, δ, for composite steel and concrete structures between 0.05 and 0.15. For bridges with timber flooring, the value of δ was between 0.12 and 0.22. Several of the bridges were believed to be stable

only because of the benefit of high damping. Bleich, et.al. (3.4) also carried out some theoretical and experimental work on the damping of suspension bridges and, in particular, pointed out the importance of the damping in black bolted or riveted joints, friction between stringers and floor beams, and the energy dissipation in the bearings, parapets and other components. It was concluded that more attention should be paid to the utilization of the potential sources of friction in floor systems. Tang (3.5), based on tests on Norderelbe Bridge and elsewhere, suggested logarithmic decrements between 0.05 and 0.08 for normal cable stayed bridges.

As pointed out by Wyatt (3.6, 3.7), recent "fully participating" designs have largely eliminated the above sources of damping in bridges and have reduced the logarithmic decrements to potentially dangerous levels. Incorporating external dampers into the system is one possible option for increasing the overall damping capacity of the structure. However, their effective and economic use is not always possible. For example, it is not always easy to find a location with significant relative movements and enough space to accommodate these dampers. In the case of suspension bridges, increased hysteretic damping at a reasonable increase in constructional costs has been obtained by the use of inclined hanger systems. The Severn and Bosporus Bridges both employ this concept.

The problems of oscillating stacks and guyed towers

have also enjoyed considerable attention,and a number of methods for preventing their wind-excited oscillations have been suggested - for example, (3.8) and (3.9). The most common cause of oscillations is vortex-excitation leading to movements in a direction transverse to the flow. This problem has assumed greater importance with the construction of light-weight stacks with very low structural damping. The general nature of this type of aero- or hydro-dynamic instability is well-known and is widely cited in the literature.

Very briefly, when air (or water) flows past the object, vortices are shed alternately from the sides of the body, which creates a harmonic force acting in the direction normal to the flow. Significant transverse oscillations may result, particularly if the frequency of vortex shedding coincides with a natural frequency of the structure. The frequency of generation of these vortices has been measured for a variety of cylindrical shapes and is expressed in terms of the non-dimensional Strouhal number, $S = \frac{f.D}{V}$, where f is the frequency of shedding of vortex pairs, V is the speed of the fluid and D is a typical length. In general the value of S depends on the shape of the object and is also a function of the Reynolds number, $R = \frac{V.D}{\nu}$, of the flow,where ν is the kinematic viscosity of the fluid.

Thus, in the absence of coupled motions, the critical wind speed at which vibrations due to vortex

excitation occur is a function of the shape of the structure, its natural frequency, and its capacity to dissipate vibrational energy (3.10). Modification of one or more of these factors is generally employed as a remedial measure against this type of aerodynamic instability. One of the methods employed involves the addition of guys to the free-standing structure. These guys will not only increase the stiffness (and hence the natural frequency) but can also contribute to the overall damping capacity of the system, which is highly desirable. However, it must be noted that due to the sag in the cables their force-displacement behaviour involves geometrical non-linearities, with their effective stiffness increasing with deflection (if the mast goes the right way). It then follows that the effective axial load range in the cables between operational limits on deflection may not be sufficiently large to ensure maximum utilization of the cable's damping capacity. Moreover, as pointed out by Wyatt (2.54), the gravitational movements of the stays may take up a significant proportion of the stored energy of oscillation in the system, and hence reduce the effectiveness of damping in the cables as regards the total system damping behaviour. In addition, the cables which are used to ensure aerodynamic stability of the structure may under certain conditions become aerodynamically unstable within themselves, and undergo aeolian vibrations similar to those experienced in connection with the transmission line cables. Two distinctly different types of

wind-induced oscillations of overhead lines can be identified, both of which are caused by steady transverse winds. In either case, energy is extracted from the flow, and the amplitude of oscillation builds up until the energy input matches the system energy dissipation. The high frequency, low amplitude (generally less than one cable diameter) vibrations are often referred to as vortex excitations, and for the usual overhead line design result in the formation of 30 or more standing waves along the cable (3.11). On the other hand the low frequency / large amplitude (much larger than the cable diameter) disturbances are referred to as galloping, which generally occur in the first harmonic modes. Unlike the vortex induced vibrations which can even occur with a smooth cylinder, galloping instability has almost always been reported to occur when the cross section of the cable lacks symmetry. By far the most common cause is the non-uniform accumulation of ice leading to the formation of an asymmetric cross-section, but asymmetric corrosion of the cable has also been reported to lead to conductor galloping (3.12). In one case, the stranded nature of a newly fabricated ice-free conductor was reported to have caused serious galloping problems (3.13). It appears that for this to happen the direction of the wind must not be normal to the axis of the cylinder. In this case, the problem was eliminated by wrapping the conductor with adhesive P.V.C. tape which effectively formed a smooth surface for the conductor.

In cases when the direction of wind is at right angles to the axis of the conductor, galloping can sometimes be prominent in only the vertical direction (for a horizontal wind direction) and in other cases instability may be associated with the coupling of two or three degrees of freedom which, individually, may be quite stable. The three degrees of freedom are the two components of translation and the rotation. Essentially, what happens is that due to the complex movement of the non-symmetrical cross-section, the angle of attack changes continuously, as a result of which the body experiences an aerodynamic lift in the direction of its movement. For instability to occur the energy input into the system per cycle by the wind forces must exceed that dissipated by the internal damping.

The torsional stiffness of conductors and their damping characteristics have been investigated experimentally by Hogg and Edwards (3.12), who concluded that substantial torsional movements of conductors may in some cases significantly modify the angle of attack and set an otherwise aerodynamically stable system into galloping excitation. However, they did point out that in many cases the involvement of torsional motion in the galloping movements is incidental rather than essential. Richardson, et.al. (3.14) made a theoretical study (coupled with some experiments) of the conductor galloping problem taking vertical, horizontal and torsional degrees of freedom into account. They emphasized the importance of torsional movements for the

initiation of galloping in some cases. They showed that it is possible for a conductor with a non-symmetrical cross-section which is positioned at an aerodynamically stable angle of attack to become statically unstable for some values of wind speed, and hence rotate towards a position of dynamic instability and stay there. This, obviously, increases the chances of galloping instability. They also conducted some experimental measurements of the no-slip torsional modulus of the conductor. Their attempt to measure torsional damping was, however, not successful.

Wind-induced oscillations have been the cause of numerous fatigue failures in transmission lines. The cure adopted for the high frequency, low amplitude, vortex-induced vibrations has, in many cases, involved increases in the level of damping in the system by the use of external dampers such as Stockbridge dampers (3.15). A damping device, making use of the large dynamic tension loads associated with the galloping vibrations, was also suggested by Richardson et.al. (3.14). The suppression of galloping by increasing the degree of system damping is not, however, thought to be very effective by Scruton et.al. (3.8).

Similar vibrational problems can be experienced by underwater cables; these are discussed by Poffenberger and Capadona (3.16) and Capadona (3.17). In deep water applications, the cable tension under its own weight (of course corrected for the bouyancy effects), flow direction, and flow intensity vary with depth. Many experimental results for relatively short, flexible cylinders positioned

in steady and uniform currents are available - see, for example, the paper by Sarpkaya (3.18). Hydrodynamic models of cable strumming and galloping in deep water applications are, however, far from complete (3.19).

Among their various applications, cables have been considered as attractive candidates for the design of tension leg platform (TLP) tethers. These tethers may experience vortex-induced or even galloping instabilities, which may significantly influence the fatigue life of the tethers, and the overall dynamic stability and fatigue life of the structure. When dimensioning the tether groups, attention must be given to the possibility of tether collision within a group, which will determine the choice of distance between individual tethers. Hydrodynamic instability of tethers may be also influenced by the presence of marine growth in long term applications in a way similar to the ice accretion problem in transmission lines.

For very small motions, the effect of the hydrodynamic damping is of the same order as the effect of the structural damping, i.e. the system is rather lightly damped. Cable strumming may be considered as the limit cycle of a lightly damped non-linear system (3.20): in this case a knowledge of the structural damping characteristics of the cable becomes important. The clench force due to the hydrostatic water pressure in very deep water applications (for which TLP or guyed tower designs are often proposed) becomes comparable with, or even larger than, the clench force effects

in an axially loaded cable at normal atmospheric external pressure. Such external pressure will tend to suppress the slippage of wires in the cable by increasing the frictional forces between them. This will obviously lead to higher cable stiffness which may have significant design implications.

To summarize, it appears that theoretical predictions of the axial and torsional stiffnesses of large diameter multilayered strands and their corresponding damping characteristics are of considerable practical importance. The rest of this chapter will be devoted to the development of an analytical technique capable of predicting these properties. As a first stage, a brief introduction will be given to the essentials of the various damping models used in dynamic analysis. An understanding of these concepts should prove useful in approaching a rather more complicated system, the spiral strand , which follows. In particular, it is intended to demonstrate the sometimes very serious limitations of some of the classical damping models in correctly interpreting real life observations.

3.2 COMMON METHODS OF MODELLING INTERNAL DAMPING

The most direct method of defining internal friction is as the ratio $\psi = \frac{\Delta U}{U}$, where ΔU is the energy dissipated per cycle and U is the strain energy corresponding to the energy of oscillation. This ratio is sometimes called the specific damping capacity or the specific loss. It can be measured for a stress cycle without any assumptions being made about the nature of internal friction. When the

loop width is large some difficulty may arise in defining the idealized stored energy,U, but in practice taking ψ as the quotient of the stippled to shaded areas in Fig.(3.1) is satisfactory even when ψ appears large, at least up to the order of unity (3.6). The value obtained is generally found to depend on the amplitude and the speed of the cycle, and often also on the past history of the specimen.

The classical model of damping in solids is often assumed to be related to the behaviour of a viscous fluid. In such a model the restoring forces are proportional to the amplitude of vibration, whilst the dissipative forces are proportional to the velocity. When these conditions apply, the plot of the dissipative force against displacement for a single degree of freedom system subjected to a harmonic motion is an ellipse whose enclosed area is equal to $\pi a^2 c\omega$, Fig.(3.2),where a is the maximum displacement amplitude, c is the viscosity coefficient and ω is the vibration frequency of the system.

It then follows that energy dissipation per cycle is proportional to the square of the displacement amplitude, and hence for the case of free vibrations of a viscously damped system the energy loss per cycle is a constant proportion of the energy of motion. In this case the vibration decays exponentially with the successive amplitudes having a constant logarithmic relation with one another. The logarithmic decrement, δ, is a constant property of the system defined as:

$$\delta = \ln \frac{a_n}{a_{n+1}} \qquad (3.1)$$

where a_n and a_{n+1} refer to two successive displacement amplitudes.

For a viscously damped single degree of freedom system there is a "critical" damping coefficient, c_c, which is the minimum damping at which the mass, released from a displaced position, will just return to its equilibrium state without passing through it. For a system with less than critical damping the damped vibration frequency, ω_D, is related to the undamped vibration frequency, ω, by:

$$\omega_D = \omega \sqrt{1-\zeta^2} \tag{3.2}$$

where $\zeta = \frac{c}{c_c}$ is called the damping ratio. It is then easy to show

$$\delta = \ln \frac{a_n}{a_{n+1}} = 2\pi\zeta \frac{\omega}{\omega_D} \tag{3.3}$$

For low damping $\omega \simeq \omega_D$, and so, $\delta \simeq 2\pi\zeta$. In such cases Equation (3.3) can be written as a series expansion:

$$\frac{a_n}{a_{n+1}} = e^{\delta} \simeq e^{2\pi\zeta} = 1+2\pi\zeta + \frac{(2\pi\zeta)^2}{2!} + \tag{3.4}$$

For low values of ζ, sufficient accuracy can be obtained by retaining only the first two terms in the series, in which case:

$$\zeta \simeq \frac{a_n - a_{n+1}}{2\pi a_{n+1}}$$

or

$$\delta \simeq \frac{a_n - a_{n+1}}{a_{n+1}} \tag{3.5}$$

In general for any damped system, whether it is viscous or not, the energy stored in the specimen is

proportional to the square of the amplitude, so that if a_n and a_{n+1} are successive amplitudes on the same side of the equilibrium position the specific loss $\frac{\Delta U}{U}$ will be given by $\frac{a_n^2 - a_{n+1}^2}{a_n^2}$. This of course assumes low damping, and when it is small compared to unity we have:

$$\psi = \frac{\Delta U}{U} \simeq \frac{a_n^2 - a_{n+1}^2}{a_n^2} \simeq \frac{2(a_n - a_{n+1})}{a_n}$$

and by Equation (3.5)

$$\simeq \frac{2(a_n - a_{n+1})}{a_{n+1}} \simeq 2\delta \qquad (3.6)$$

That is, for very low damping, by considering the maximum amplitudes reached, an equivalent logarithmic decrement, δ_{eq}, may be defined for any damped system as:

$$\delta_{eq} = \frac{a_n - a_{n+1}}{a_n} = \frac{\Delta U}{2U} \qquad (3.7)$$

The relation $\delta_{eq} = \frac{\psi}{2}$ is approximate and only applies when $\delta_{eq} << 1$. For a viscously damped system the decay is exponential and ψ is a constant throughout the cycles. In non-viscous damping the decay is no longer exponential and ψ will be amplitude dependent. Nevertheless, the relation $\delta_{eq} = \frac{\psi}{2}$ also holds in cases of varying ψ since this parameter can reasonably be considered as invariant during one cycle. It can be found experimentally or numerically by considering successive amplitudes during the natural decay of a freely vibrating system, and evaluating $\delta_{eq} = \frac{\Delta a}{a}$. Alternatively $\delta_{eq} = \frac{\Delta U}{2U}$ can be used and applied to a system which is undergoing steady state motion, since in this case, the energy input to the system per cycle must be equal to ΔU, the energy dissipated.

Even when undergoing harmonic motion, the shape of the force-displacement diagram of a non-viscous damping system will not be elliptical. In this case an equivalent viscous damping coefficient, c_{eq}, may be defined which would cause the same energy loss per cycle as in the observed force - displacement plot:

$$c_{eq} = \frac{\Delta U}{\pi \omega a^2} \tag{3.8}$$

The criteria for equivalence are (1) equal energy dissipation per cycle, and (2) the same harmonic relative displacement, a, Fig. (3.3). The assumption of harmonic motion is reasonable only for small non-viscous damping.

The viscous model is extremely convenient mathematically as in this case the resulting equations of motion become linear and, during harmonic motion, the damping forces themselves vary harmonically. However, it has got major shortcomings; for example, experiments have often shown that the energy loss per cycle is independent of frequency and that, as explained above, amplitude does not always decay exponentially with time.

In real problems,it is rare for the magnitudes of the damping forces to be known with anything like the same accuracy as the elastic and inertia forces. It is therefore pointless to attempt to construct a detailed mathematical treatment of the damping effects. Rather, the treatment adopted should be chosen for its simplicity and convenience of use, provided that it gives a reasonable estimate of the damping effects. For example, to cater for the limiting case of frequency independence of the energy loss one

possibility is to retain the concept of a frictional force proportional to the velocity but to discard that of a viscosity constant, c, and to replace it by a factor which is an appropriate function of the frequency such that the total energy loss is independent of the frequency, ω. A damper with this characteristic will be called a hysteretic damper, and its dissipative force is obtained by writing $\frac{h}{\omega}$ for c in the previous model. Thus, the enclosed area within the force- displacement loop becomes $\pi h a^2$, which is independent of ω. h is called the hysteretic damping coefficient. Note that hysteretic damping has been defined for steady harmonic motion. With such a damping model, the equations of motion remain linear and a harmonic excitation produces a harmonic response. This is again consistent with the statement that the fractional loss of energy per cycle is constant and a constant logarithmic decrement, δ, exists. In certain problems notably where dissipation of energy is due to imperfect elasticity, hysteretic damping is a better approximation than viscous damping.

In a system composed of a number of elements with different damping capacities Bleich and Teller (3.4) suggest:

$$\psi = \frac{\Delta U_1 + \Delta U_2 + \cdots\cdots}{U} \tag{3.9}$$

where ΔU_1, ΔU_2, ... are energy losses per cycle in the various elements and U is the energy of oscillation of the entire system. Hence:

$$\psi = \sum_i r_i \psi_i$$

where

$$\psi_i = \frac{\Delta U_i}{U_i} \quad \text{and} \quad r_i = \frac{U_i}{U} \tag{3.10}$$

ψ_i represent the individual damping capacities of the elements and r_i correspond to their relative energy storage capacity.

3.3 MECHANISM OF INTERNAL MATERIAL DAMPING

In spite of numerous experimental investigations of the internal friction in solids, the mechanism of internal friction is not at all well understood. The ignorance as to its mechanism is due partly to the fact that no one mechanism is responsible for the energy losses in all cases of vibrating solids (3.21). Although ultimately all these different mechanisms result in the mechanical energy loss being transformed to other energy types (mainly heat), two different processes are involved. The first type of process depends directly on the inelastic behaviour of the solid under a static stress cycle, with a certain amount of energy being dissipated which will appear as part of the specific loss when the specimen is vibrating. Gemant and Jackson (3.22) found that for many materials the logarithmic decrement is in fact constant over a considerable range of frequencies. Similar results have been obtained by Wegel and Walter (3.23) at higher frequencies. However, not all materials exhibit rate-independent hysteresis. For example, Zener (3.24) discusses the importance of local fluctuations in temperature within a vibrating solid in relation to its internal friction. According to his work, if the period of the cyclic stress is comparable with the time required for significant heat flow along the temperature gradients produced (from one

part of the specimen to the other), an irreversible conversion of mechanical energy into heat takes place and damping occurs. For the two extreme cases of very slow and very fast vibrations, the heat transfer mechanism is considered to be isothermal and adiabatic respectively and there will be no loss of mechanical energy. Zener considered the temperature difference between the tension (expanded) and compressed sides of a beam under flexural vibrations, and the validity of Zener's theory was later demonstrated by the favourable agreement between his theoretical predictions and experimental results obtained by Bennewitz (3.25). Local temperature gradients can also occur even under macroscopically uniform axial stress because of the anisotropic mechanical and thermal properties of the individual crystals in the body. Such micro-thermoelastic mechanisms can also lead to flow of thermal energy and damping (3.21). Loss of mechanical energy can similarly occur due to the presence of different types of imperfections such as impurities, grain boundaries and dislocations, among others. In particular, note that dislocation motions can occur even at low stress (local microscopic stress may be large enough even though macroscopic stress is small). Lazan (3.21) gives a detailed discussion of such mechanisms and refers to a large body of literature on this topic.

3.4 FRICTIONAL DAMPING

In many structures, a number of mating surfaces (interfaces) are maintained in contact during the cyclic movements. In the case of, for example, bolted joints,

particulate materials such as soils, and multi-layered spiral strands the frictional loss of energy caused by relative movements at such interfaces appears to be the dominant source of damping.

Available experimental and theoretical findings regarding the contact of bodies acted upon by inclined forces were discussed in some detail in Chapter 1. In particular, it was shown that theoretical methods of calculating steady-state hysteresis between non-spherical (as well as spherical) bodies acted upon by pure tangential forces are available and have been verified experimentally. Some progress has also been made towards calculating the hysteresis of a system subjected to inclined force perturbations superimposed upon a mean normal load. However, the present quantitative solutions are only applicable to the contact of two spheres subjected to an inclined perturbation of force whose inclination remains constant throughout the cycle. The importance of past history of loading was also emphasized.

Familiar classical models of friction, namely the rigid-plastic, ideal single elasto-plastic, and multiple elasto-plastic, have been used extensively in attempts to describe (qualitatively or quantitatively) the observed behaviour of a wide variety of systems. As a prelude to the analysis presented in this chapter, their essentials and terminology are reviewed here.

The classic Coulomb rigid-plastic model is shown in Fig.(3.4), with energy dissipation per cycle at amplitude a equal to $4F_f a$. With restoring energy in the system, U,

proportional to the square of the amplitude of motion, specific damping capacity, ψ, will be inversely proportional to a:

$$\psi = \frac{\Delta U}{U} \propto \frac{1}{a} \qquad (3.11a)$$

In general, with low damping we have, Equation (3.6)

$$\psi \simeq 2\,\frac{\Delta a}{a} \simeq 2\delta \qquad (3.11b)$$

In such a case Δa (the absolute loss of amplitude in each cycle) is a constant, that is the decay of the amplitude to zero is in the form of a straight line and the corresponding logarithmic decrement, δ, is a parabolic function of the amplitude. Note that in this model the motion can only start when the force on the damper exceeds F_f. However, in real life no system is perfectly rigid and a more realistic model is suggested in Fig.(3.5). Again, movement of the damper only takes place if the force acting on it reaches the force of limiting friction F_f. Before this can occur the damper spring must be extended by an amount $\pm\,\Delta$, where $\Delta = \frac{F_f}{K_f}$ and K_f is the spring stiffness. Hence, if the amplitude, a, of the mass is less than Δ, the damper will remain stationary and no energy will be dissipated (i.e. a critical amplitude exists below which δ=o). When the amplitude of the mass is greater than Δ, slip will occur, but the amplitude at the dashpot will be less than the amplitude of the mass. This phenomenon of a proportion of amplitude being taken up by elastic deflection of the system rather than it all being transmitted to the sliding surfaces of the damper, has been termed "elastic kick-back" by Wyatt (3.7). Energy dissipated per cycle

is therefore:

$$\Delta U = 4F_f.a - 2\left(\frac{1}{2} \cdot \frac{2F_f}{K_f} \cdot 2F_f\right) \tag{3.12a}$$

while the maximum stored strain energy is:

$$U = \frac{1}{2} Ka^2 + \frac{1}{2} \frac{F_f^2}{K_f} \tag{3.12b}$$

$$\therefore \quad \delta = \frac{\Delta U}{2U} = \frac{4\left(\frac{aK}{F_f} - r\right)}{\frac{aK}{F_f} + r} \tag{3.12c}$$

where $r = \frac{K}{K_f}$

Wyatt gives plots of δ versus the non-dimensionalized amplitude $\frac{aK}{F_f}$. These are reproduced in Fig.(3.6).

It can be seen that the critical amplitude at which δ=o is different for each value of r and also that for each r there exists a value of $\frac{aK}{F_f}$ at which maximum damping can be obtained. This model is relevant for cases where homogenous shear displacement takes place over the entire surface between two bodies.

However, for cases with progressive slip phenomena (partial to full-slip transition) one must use an assembly consisting of many individual Coulomb spring-dashpot units, Fig.(3.7). For example, Whiteman (3.26) used this type of model to formulate the stress-strain properties of materials, and Goodman and Klumpp (3.27) analyzed the slip damping occurring at the interface of a pair of clamped cantilever beams subject to static and dynamic load at the tip. For such cases the contribution from each of the spring-dashpot units to the total specific capacity, ψ, of the system is

dependent on the ratio of the elastic energy stored in the unit to that of the total system (Ref. Equations (3.9) and (3.10)) and different units will begin sliding (dissipating energy) at different system amplitudes.

Mindlin's theoretical model for calculating the frictional hysteresis at the contact patch of two bodies is also based essentially on the above approach (Ref. Chapter 1). In his model he assumed that the tangential traction, τ, at any point in the contact patch cannot exceed the product of a constant coefficient of friction and the normal pressure, p, that is, $T<\mu p$, and that slip will continue until this condition is satisfied over the whole area of contact. Gross sliding, i.e. slip over the whole of the contact patch, takes place as soon as $T=\mu P$, where T and P are the total tangential and normal forces on the contact region respectively.

The energy dissipation in spiral strands mainly arises from the frictional effects at the contact patches between wires in the same layer which, under the action of a mean tension on the cable, are subjected to radial (clench) and hoop forces as discussed in the previous chapter. In such a case the theoretical model essentially consists of the assemblage of a number of contact patches which can be treated individually as Coulomb dashpot units.

3.5 DAMPING OF REAL STRUCTURES

In structures as built there may be damping from aerodynamic sources (air and/or water), radiative and dissipative

effects in the foundations and from the internal hysteresis in the materials and interface slip. The total value of the equivalent logarithmic decrement of the structure is often impossible to estimate and its prediction normally relies on data from tests on previous structures. Once the structure is complete, it is often possible to measure its total damping by setting the structure into vibration and recording the decay of its amplitude with time. The nature of the foundations can significantly influence the total damping and similar structures behave differently on different sites (3.8). For the present work (calculation of damping in straight multi-layered strands) we are only concerned with material and slip damping. The interest in material hysteresis will only be to the extent of comparing the amount of energy loss available from this source with the loss from slip at the interfaces.

For strands subject to load ranges within normal operational limits, internal material damping capacity of the wires and lubricating compounds filling the gaps is in general negligible in comparison with the frictional work done at the contact regions between individual wires. However, with high enough mean axial load and small enough axial load perturbations, elastic "kick-back" action (Ref. Sections 1.5 and 3.3) may suppress the relative movement between the wires and the whole strand will then behave very nearly like a solid bar (allowing, of course, for the voids between the wires). In such a case, the only operative

source of damping will be a very small amount of the internal material type.

In the following treatment, a theoretical analysis of a strand using orthotropic sheet theory with appropriate compliances derived from results in contact stress theory is developed for axial and torsional loadings. The theory is developed for a fully bedded-in strand and is based on a rate-independent multi-assembly frictional model with elastic "kick-back" action accounted for.

3.6 TORSIONAL STIFFNESS OF STRAND

3.6.1 Introduction

A direct experimental check of the interwire contact forces in a strand is probably impossible, and indirect measurements must be made. One relatively straight-forward approach is via the torsional stiffness in the presence of a steady axial load on the strand. As explained in Section 3.1, the torsional stiffness is also of practical interest in certain aero-and hydrodynamic problems. It also offers the possibility of deducing realistic in-situ values of the coefficient of friction between wires comprising the strand in contrast to the more orthodox but less reliable methods of sliding tests between two individual wires in air whose surface conditions (especially their state of lubrication) need not necessarily resemble that of the wires when lying inside the heavily lubricated cable. In-situ friction tests in the form of pulling single wires out

of pretensioned cables have been used in the past (2.38) with little success. The uncertainties about the distribution about the mean of normal contact forces between the wires in the strand has made realistic estimates of the coefficient of friction, μ, from these tests rather difficult. Accurate values of μ are of direct use in any fracture mechanics analysis of the fatigue behaviour of the strand (Ref. Section 1.3) and are of obvious value in the prediction of the strand's axial hysteresis under regularly varying axial load.

The mathematical theory developed in Chapter 2 assumes an ideal multi-layered strand model with no gaps between the wires in a layer. The theory ignores the presence of residual contact stresses in the hoop direction, and also uses the theoretical relationships for normal and shear compliances between wires in line contact which have strictly been developed for the case of bare steel wires. In most practical strand constructions, consisting of galvanized wires, none of the above assumptions are likely to be strictly true. However, using the following theoretical results in conjunction with experimental checks (to be discussed in Chapter 5), it is possible to throw considerable light on the validity and limitations of these simplifying assumptions. By employing the so-called in-situ coefficient of friction an attempt will be made to adjust the ideal theoretical model to match the properties of real life practical strand construction. These properties are a function of the imperfections and misfits inside the strand which are bound to be of a random nature depending,

inter alia, on the method of manufacture and past history of the strand. They are obviously extremely difficult to measure by presently available experimental techniques. A statistical treatment of these problems also appears fraught with difficulties.

3.6.2 Analysis

Intuitively, the tangent torsional stiffness of a strand would be expected to fall as the applied torque increases, because at small torques interwire friction would suffice to prevent interwire movements, while at higher torques this friction would be overcome leading to greater flexibility. Indeed, this degradation of stiffness is progressive as slipping starts in the outer layer and spreads towards the core at higher torques.

It is postulated that in each layer of wires the perturbation axial and hoop strains S_1' and S_2' on applying the torque to the axially preloaded strand are zero. Using the first and second of Equations (2.39a), T_1' and T_2' can be expressed in terms of T_6' and hence the shear flexibility, S_6'/T_6', can be obtained:

$$\frac{S_6'}{T_6'} = S_{66}' + \frac{2S_{26}'S_{12}'S_{16}' - S_{22}'S_{26}'^2 - S_{11}'S_{26}'^2}{S_{11}'S_{22}' - S_{12}'^2} \qquad (3.13)$$

The strains may be considered as a second order tensor, and with $S_1'=S_2'=0$

$$S_6=S_6' \cos(2\alpha) = r \frac{d\phi}{d\ell} \cos(2\alpha) \qquad (3.14)$$

where $\frac{d\phi}{d\ell}$ is the twist per unit length in the strand which is assumed to be the same for all layers. Equation (3.14)

may alternatively be derived using linearized kinematical relations for helices: from Equation (2.10), taking $\varepsilon_c=0$

$$\text{Cos } \alpha' = \frac{\text{Cos}\alpha}{1+\varepsilon_h}$$

or for $\varepsilon_h<<1$

$$\text{Cos}(\alpha-d\alpha) = \text{Cos}\alpha(1-\varepsilon_h) \tag{3.15}$$

which gives:

$$d\alpha = -\varepsilon_h \text{ Cot}\alpha \tag{3.16}$$

For a helix which is allowed to rotate, Chi (2.5) used the kinematics of a helix (similar to those given in Section 2.3) to show:

$$\varepsilon_h = \text{Cos}\alpha\left((1+\varepsilon_c)^2+\left(\frac{r'}{r}\right)^2\left(\tan\alpha-r\,\frac{d\phi}{d\ell}\right)^2\right)^{\frac{1}{2}}-1 \tag{3.17}$$

With $\frac{r'}{r}=1$, Equation (3.17) may be linearized (using a binomial expansion of the radical) to give:

$$\varepsilon_h \simeq \text{Cos}^2\alpha(\varepsilon_c-r\,\frac{d\phi}{d\ell}\tan\alpha) \tag{3.18}$$

which was first obtained by Hruska (2.3). For the case of $\varepsilon_c=o$:

$$\varepsilon_h \simeq -\text{Cos}^2\alpha(r\,\frac{d\phi}{d\ell})\tan\alpha \tag{3.19}$$

Using Equations (3.16) and (3.19)

$$d\alpha = S_6' \text{ Cos}^2\alpha \tag{3.20}$$

Moreover, the longitudinal length of two adjacent wires in a given layer at a given cable transverse section is equal to D tanα, Fig.(2.11). The change in this length under the application of a torsional shear strain $S_6'= r\,\frac{d\phi}{d\ell}$ is:

$$\eta = D\tan\alpha \cdot \varepsilon_h \tag{3.21}$$

Using Equations (3.19) and (3.21)

$$\eta = D\tan\alpha \cdot \left(-r \frac{d\phi}{d\ell} \cos^2\alpha \tan\alpha\right)$$

$$= - DS_6' \sin^2\alpha$$

$$\text{or } \eta/D = - S_6' \sin^2\alpha \tag{3.22}$$

The shear strain, S_6, is then given by adding together the contributions from the change in the lay angle and the axial strain in the wires. Using Equations (3.20) and (3.22):

$$S_6 = d\alpha + \frac{\eta}{D}$$

$$= S_6'(\cos^2\alpha - \sin^2\alpha)$$

$$= S_6' \cos 2\alpha \tag{3.23}$$

which is the result obtained before - Equation (3.14).

Slip over one wire diameter is then given by:

$$\Delta = D\, S_6' \cos 2\alpha \tag{3.24}$$

In the fully bedded-in condition, for a mean axial load, T, one can determine S_1' in the cable. P_{MS} versus S_1' plots (Ref. Section 2.13) may then be used to find the normal contact forces between wires in various layers. Substituting $p = P_{MS}$ in Equation (2.36) gives the normal compliance in individual layers. Equations (3.14), (2.38), (3.13) and (3.24) are then used to express T_6' as a function of the variable $\frac{d\phi}{d\ell}$ alone (for a given mean axial load on the cable). Integration of T_6' with respect to $\frac{d\phi}{d\ell}$ will finally

lead to theoretical plots of shear stress in a cable transverse section, τ, against twist per unit length $\frac{d\phi}{d\ell}$, Fig.(3.8). For any particular twist per unit length the total torque on the cable may be obtained from:

$$M = \sum_i (\tau A_g r)_i \qquad (3.25)$$

where A_g is given by Equation (2.59) and all layers are included. Plots of M versus $\frac{d\phi}{d\ell}$ for various possible values of the coefficient of friction are given in Fig.(3.9). As an alternative to the zero perturbation strain condition, the conditions $T'_1=0$ and $T'_2=0$ lead to:

$$\frac{S'_6}{T'_6} = S'_{66} - \frac{S'^2_{16}}{S'_{11}} \qquad (3.26)$$

Table (3.1) gives the no-slip and full-slip shear moduli applicable to the net area (i.e. $\frac{\pi}{4}$ times gross cross-section area), based on Equations (3.13) and (3.26), of various layers of the 39mm. strand used in the experiments. Results are given for two cable mean axial loads of 0.41MN and 0.10MN. Of course, the value of the no-slip torsion modulus is independent of the value assigned to the coefficient of friction.

Examination of the no-slip figures suggests that the effect of direct stress perturbations on the shear behaviour is small, apart from the primary influence of the clench effect due to the application of a mean axial load . It is interesting to note that the magnitude of the full-slip shear modulus appears to be insensitive to the magnitude of the mean axial load.

As a further option in the large slip regime, it is therefore reasonable to postulate that a layer of wires deformed in shear has the same stiffness as the set of tension members which would be created by "unwrapping" the layer. In this case inter-wire forces become negligibly small by comparison with force changes in the wires.

The effective shear modulus for the full-slip case is therefore related to Young's modulus, E, of the wires by:

$$G = E \, Sin^2\alpha \, Cos^2\alpha \qquad (3.27)$$

where α is the lay angle.

Note that Equation (3.27) applies to cases where changes in α are very small (i.e. geometrical non-linearity is assumed to be absent). The form of (3.27) differs from the more familiar $Sin^2\alpha \, Cos\alpha$ because the reference area is the area of metal exposed in a strand cross-section, equal to the sum of the wire areas times $Sec\alpha$. For very large disturbances, changes in α become significant and the non-linear kinematical relations developed in Section 2.3 may then be used to cater for the geometrical non-linearities in the model. Approximate full-slip G-values based on Equation (3.27), which is independent of mean axial load, are also included in Table (3.1).

Note that the high degree of non-linearity in the torque-twist behaviour for the range of twist investigated is due to contact patch non-linearity (inter-wire friction forces) rather than the secondary effects of geometrical non-linearities such as changes of lay angle. The linear

nature of full slip modulus and associated changes in wire axial strains for the range of twist considered here will later on be demonstrated experimentally (Ref. Chapter 5).

Although the spiral strand construction with alternating lay directions is only weakly rotation-extension coupled, it is useful to have some idea of the magnitude of the perturbation axial forces induced in individual layers by an externally applied torque. The algebraic sum of these axial perturbations over the whole cable cross-section will, of course, give the mean axial perturbation over the whole cable section. However, it is clear that even for a weakly rotation-extension coupled construction, very low magnitudes of total perturbation axial load on the cable do not necessarily mean that the axial perturbations in individual layers are equally insignificant. If the magnitude of the latter become comparable to the magnitude of the steady tensile axial mean load on the particular layer, they can alter significantly the magnitude of the normal contact pressures between the wires in line-contact. For the working ranges of axial load on the cable, such effects should not affect the no-slip torsional modulus of the strand, but may prove important in the theoretical hysteresis calculations. To investigate this effect, substitute $S'_1=S'_2=0$ into Equations (2.39a) to obtain $\frac{S'_6}{T'_1}$:

$$\frac{S'_6}{T'_1} = \frac{S'^{2}_{16}S'_{22}-2S'_{16}S'_{26}S'_{12}+S'^{2}_{26}S'_{11}+S'^{2}_{12}S'_{66}-S'_{66}S'_{22}S'_{11}}{S'_{16}S'_{22}-S'^{2}_{26}S'_{12}} \qquad (3.28)$$

Note that changing the sign of α in Equations (2.39) will only change signs of S'_{16} and S'_{26}, which when used in Equation (3.28) will result in a change in the sign of T'_1 (S'_6 has the same sign for all the layers). Consequently, depending on the direction of the externally applied torque, some layers experience compressive forces while the others, with opposite lay, will be subject to tensile axial perturbations.

With S'_6 and S_{66} written in terms of $\frac{d\phi}{d\ell}$, it is once again possible to express T'_1 as a sole function of the variable $\frac{d\phi}{d\ell}$. Numerical integration of the right hand-side of Equation (3.28) with respect to $\frac{d\phi}{d\ell}$ will yield the level of axial load perturbation in various layers. Summation of these stresses over the whole cable section will lead to plots of total axial perturbation versus $\frac{d\phi}{d\ell}$.

Figs.(3.10) and (3.11) present plots of axial perturbations in individual layers as a function of $\frac{d\phi}{d\ell}$, for two different mean axial loads on the cable. The coefficient of friction is assumed to be $\mu = 0.115$ (i.e. pseudo-coefficient of friction = 0.23). This has been found to be the appropriate one for the galvanized 39mm strand used in the experiments (Ref. Chapter 5). The plot of total perturbation axial load versus $\frac{d\phi}{d\ell}$ is given in Fig.(3.12).

At least for the present strand construction, and realistic (e.g. one third of ultimate tensile strength) operational levels of mean axial load on the cable, it appears that such disturbances will have negligible effect on the magnitude of the steady normal contact force between the wires.

3.7 AXIAL STIFFNESS OF STRAND

3.7.1 Introduction

Another indirect test of the theory of Chapter 2 is to use it to predict the perturbation axial stiffness of strand. This, too, has obvious practical utility. For example, the legs of a T.L.P. or the hangers of a suspension bridge are both subject to relatively small variations of axial load superimposed on the mean axial tension, and a knowledge of this stiffness as a function of the perturbation size is a useful input to the dynamic response analysis of the platform or bridge. Again, the stiffness is larger for small perturbations which do not initiate interwire slip than for larger perturbations which are associated with slippage on the contact lines.

3.7.2 Analysis

It is postulated that a change in the axial stress T_1' is associated with a perturbation of the hoop stress T_2' where:

$$T_2' = T_1' \frac{T_2}{T_1} \tag{3.29}$$

If it is further assumed that the shear strain S_6' is zero, then the first and third of Equations (2.39a) lead to the desired axial flexibility of the membrane

$$\frac{S_1'}{T_1'} = S_{11}' + kS_{12}' - \frac{S_{16}'}{S_{66}'}(S_{16}' + kS_{26}') \tag{3.30}$$

where $k = \frac{T_2}{T_1}$. k is a function of the cable axial strain S_1' and for a given S_1' is equal to the tangent to the plots of $(\frac{P_{MS}}{D})$ vs $(\frac{\pi}{4} \cdot ES_1)$, an example of which is given as Fig.(3.13).

Numerical differentiation has been used to obtain plots of k versus S_1' for different layers of the 39mm O.D. strand: these are presented in Fig.(3.14) which also gives similar plots for the 16mm O.D. strand for comparison.

Equation (2.38) only gives the tangential compliance between two cylinders in line contact with the oscillating force acting along the interface. With an axial load perturbation on the strand, the oscillating force is actually at an angle to the common normal to the wires. The angle of inclination in itself is a function of S_1'. It is, however, thought that the problem of contact of non-spherical bodies subject to an oblique oscillating force whose inclination to the common normal changes during each cycle has not yet been solved theoretically (Ref. Section 1.4).

The energy dissipation measurements reported by Wyatt (2.54) indicate a peak in the energy dissipation quotient at a load range of about 0.15 times the mean load, with slow fall away from the peak. He pointed out that this is compatible with the frictional basis of the energy dissipation in view of the large number of potential slip surfaces (Ref. Section 3.3). The onset of full slip on these surfaces was expected to occur at a relatively small ratio of load to mean axial load (supporting evidence for this expectation is provided by the theoretical results). It then follows that, as a first approximation, it is reasonable to assume the normal component of the oscillating force to be negligible in comparison with the

constant mean normal load between the wires throughout the partial slip regime. Equation (2.38) may then be used to describe the gradual degradation of the shear stiffness between the wires in a given layer.

The limiting case of full interwire slip is addressed first. In this situation, the shear compliance S_{66} for each sheet of wires tends to infinity. The relationship between cable tension and axial strain is obtained by the following procedure:

(i) For a known cable axial strain S_1', calculate the interwire forces, P_{MS}, by the method of Chapter 2. The value of k for each S_1' is obtained from k versus S_1' plots for various layers - Ref. Fig.(3.14) .

(ii) Calculate S_{22} by Equation (2.36).

(iii) Using Equations (2.39b) and then (3.30), values of the changes in S_1'/T_1' can be obtained for various strains S_1'.

(iv) Integration of T_1' with respect to S_1' leads to values of cable axial stress for each layer as a function of the changes in S_1', and summation over the layers gives cable axial force change as a function of S_1'.

For the experimental (i.e. 39mm O.D.) strand over the working range, this last relationship was very nearly linear. Consequently, rather than using different k and S_{22} values for different cable axial strains, it was possible and easier to choose a constant k and corresponding S_{22} value and compute the full slip stiffness of the cable associated with them.

Then, for perturbations of the mean axial load it is still reasonable to use constant k and S_{22} values corresponding to the mean cable axial strain.

Turning now to the calculation of the degradation of the perturbation axial stiffness as the size of the disturbance increases, i.e. following the development of slip in the various layers, a slightly different procedure is necessary:

(i) For a given mean axial cable strain find the ratio k and hence S_{22}.

(ii) for a range of perturbations of cable axial strain, calculate values of S_{66} using Equations (2.38) and (2.60).

(iii) and (iv) as above for the full slip calculation.

3.7.3 RESULTS

A plot of total axial force versus cable axial strain for the 39mm O.D. strand under a mean axial load of 0.41 MN is presented in Fig.(3.15). The pseudo-coefficient of friction assumed is 0.23. Assuming that the tensile stress-strain hysteresis loop is skew-symmetric, it is then possible to define an effective Young's modulus (axial stiffness) of the strand which varies as a function of range/mean of the axial load. Fig. (3.16) presents and correlates theoretical and experimental values reported by Hobbs (3.28) and Wyatt (2.54) for the perturbation axial stiffness of the 92 wire, 39 mm strand. The effective Young's modulus of

the strand is based on net wire area and assumes E_{steel}= 207 KN/mm^2. Experimental work by Montague (3.29) on both stranded and straight (unstranded) wires has shown that the cold work experienced in the stranding process does not significantly change the Young's modulus of the wire material. In his experiments Montague considered aluminium as well as steel wires.

Axial stiffness results for various cable constructions whose details are given in Tables (2.1) to (2.4) are presented in Fig. (3.17). A coefficient of friction equal to 0.115 has been assumed for all the plots. It is interesting to note that for the present ideal model with no gaps between the wires in the same layer, increasing the lay angle (keeping other parameters roughly constant) may lead to significant increases in the ratio of no-slip to full-slip cable axial stiffness. Plots of cable axial stiffness for 16 and 51mm O.D. strands, however, clearly indicate that the difference between the no-slip and full-slip axial stiffness is not always significant, and depends on the type of cable construction. Finally, the value of the full-slip modulus was found to be independent of the mean axial load on the cable.

3.8 HYSTERESIS UNDER CYCLIC LOADING

3.8.1 Introduction

In the following, the rubbing movement between the parallel wires in each layer is assumed to absorb much more energy than the rotational movement on the "trellis" contact

points between (counter-laid) wires in different layers. As a first approximation, the trellis movement is equal to the sum of the changes in the lay angles, which can be calculated by the methods developed in the previous chapter. Note that Equation (2.14), although approximate, gives a reasonable estimate of changes in the lay angle,and may be used as a first order approximation as a substitute for the rather more involved method which takes the changes in the cable diameter and other geometrical non-linearities into account. It is further assumed that the friction between wires within a given layer is controlled by the clenching action of the mean load. No distinction is drawn between static and dynamic coefficients of friction,which are also assumed to be independent of the normal load on the contact patch. Clearly, the different layers will have different magnitudes of hoop forces and it is assumed that the coefficient of friction is the same anywhere in an individual contact patch and, moreover, is a constant for all the contact patches throughout the strand. The hysteresis within the body of the wires themselves and also the blocking lubricant are neglected. The lubricant is assumed to merely act for boundary lubrication with no elasto-hydrodynamic action. In other words, it only affects the magnitude of the coefficient of friction and is not carrying any normal loads (Ref. Section 1.2). The analysis is developed for a fully bedded-in condition, i.e. regular repeated oscillations, although it is known from torsional experiments that the damping might be as much as twice as

large for the first application of a given disturbance. It is further assumed that damping is independent of the speed of loading and also the temperature of the cable. This last assumption is supported by the experimental observations of Wyatt (2.54), who (by measuring the initial rate of rise of temperature and also the rate of cooling of the strand from a range of steady state temperatures) deduced the rate of heat generation and therefore hysteresis in the cable. The steady state temperature in his in-line tests, which were all conducted at a constant frequency of 4.4 Hz, was obviously dependent on the level of range of load/mean ratio. For his experimental range of about 50°C over the ambient temperature, hysteresis was not significantly affected by the temperature of the strand. Finally, the theory treats the cable sections away from the terminations and therefore the end effects are ignored. For practical applications, the length of the strand is very much greater than its diameter and these effects (due to, e.g., restrained torque actions and/or warping tendencies between successive layers) will have no significant bearing on the overall hysteretic performance.

The analysis is developed for both the torsional and the axial loading cases, and should provide another indirect check of the interwire contact theory developed in the previous chapter. Its practical applications in the field of structures have already been discussed - Ref. Section 3.1. It also throws some light on the mechanism of

fretting initiated fatigue failures in individual wires.

3.8.2 Analysis

For both the torsional and axial regimes, the load-displacement plots for the loading and subsequent unloading phases form a hysteresis loop which is very nearly skew-symmetric. It then follows that energy dissipation per cycle for each level of loading may simply be obtained by finding the area enclosed by the loading curves (which can be obtained by the methods suggested in Sections 3.6 for the torsional case and 3.7 for the axial case) and their unloading skew-symmetric counterparts. This is called method (a).

Alternatively, solutions may be obtained by considering the problem from first principles - i.e. calculating the overall hysteresis by summing the contributions of the individual slip surfaces to the overall strand hysteresis. This will be referred to as method (b).

Agreement between the outcomes of these two methods will then provide a theoretical double-check.

Method (a) only takes the rubbing movement of wires in line-contact into account and does not see the energy dissipation of the trellis points at all. The "trellis" intersections of wires in successive layers are presumed to have a relatively high threshold, and their contribution to the overall damping for practical ranges of range of load/mean ratio is probably rather insignificant. Method (b), however, has the possibility of being extended to cater

for this effect if the need arises although again this will not be easy. This is so because a full analysis of the situation when the oscillating force (under cable axial perturbations) is inclined at an angle to the common normal between the wires is not,as yet,available.

Method (b):-

For pure tangential loading of two non-spherical bodies in contact, energy dissipation per cycle for one body, ΔE, in the partial slip regime is (Ref. Chapter 1):

$$\Delta E = \frac{9(2-\nu)\mu^2 p^2}{10Ga}\left[1-\left(1-\frac{T^*}{\mu p}\right)^{5/3}-\frac{5}{6}\frac{T^*}{\mu p}\left[1+\left(1-\frac{T^*}{\mu p}\right)^{2/3}\right]\right]\phi \qquad (3.(1.37))$$

where $T^*<\mu p$, using the notation defined previously.

For two parallel cylinders ϕ is given by Equation (1.19), and inserting this value in (3.(1.37)) gives:

$$\Delta E = \frac{18}{5}\frac{\mu^2 p^2}{1-\nu} S_{22}\left[1-\left(1-\frac{T^*}{\mu p}\right)^{5/3}-\frac{5}{6}\frac{T^*}{\mu p}\left[1+\left(1-\frac{T^*}{\mu p}\right)^{2/3}\right]\right] \qquad (3.31)$$

where p is the normal contact force per unit length of the contact line, and hence ΔE corresponds to the dissipation per unit length of contact. From Equation (1.24)

$$\frac{T^*}{\mu p} = 1-\left(1-\frac{\Delta_\ell}{\Delta_{\ell max}}\right)^{3/2} \qquad (3.(1.24)$$

where

$$\Delta_{\ell max} = \frac{3}{4}\frac{\mu p}{(1-\nu)} S_{22} \qquad (3.(1.27b)$$

Once $\frac{T^*}{\mu p}$ reaches unity, gross sliding takes place between the wires and the force displacement loop is as shown in Fig.(3.18) - this of course assumes zero change in the magnitude of the normal load, p, on the contact patch during the cycling process. For the partial slip regime, the change in p is sufficiently small to be ignored (Ref. Section 3.7.1). For the full-slip regime, however, the normal load may change by quite a significant amount depending on the load range/mean ratio. But if we assume zero non-linearity in the way normal load changes with cable axial strain, then p increases, in one half cycle, to $p+\Delta\bar{p}$ and decreases in the other half to $p-\Delta p$. The average value of the normal force is equal to p, and for a constant coefficient of friction, μ, energy dissipation during gross-sliding is:

$$(\Delta E)^{gross} = 4\mu p(\Delta_\ell - \Delta_{\ell max}) \qquad (3.32)$$

At the onset of gross-sliding substitute $\frac{T^*}{\mu p} = 1$ in Equation (3.31) to obtain:

$$(\Delta E)^{partial}_{max} = \frac{3}{5}\frac{\mu^2 p^2}{(1-\nu)} S_{22}$$

During gross-sliding (i.e. $\Delta_\ell > \Delta_{\ell max}$):

$$\Delta E = (\Delta E)^{partial}_{max} + (\Delta E)^{gross} \qquad (3.33)$$

3.8.2.1 Torsional hysteresis

Here slip over one body is given by Equation (3.24):

$$\Delta_\ell = DS_6' \cos\alpha$$

where $S_6' = r \frac{d\phi}{d\ell}$ (3.24)

In this case $\frac{d\phi}{d\ell}$ corresponds to half of the perturbation range.

The energy dissipation in the strand per unit length, is:

$$\Delta U = \sum_i \left(\frac{N\Delta E}{\cos\alpha}\right)_i \tag{3.34}$$

summing over all layers i, with N effective slip surfaces in layer i. The number of effective slip surfaces for the torsional mode will be shown to be half the number of wires in the layer. For the axial mode, however, N will be the same as the total number of wires in the layer. This will be demonstrated later on by matching the two theoretical results derived by methods (a) and (b).
The energy input per cycle per unit length is:

$$U = \frac{1}{2}\left(\frac{M}{2}\right) \frac{d\phi}{d\ell} \tag{3.35}$$

Thus, the energy dissipation may be found by the following procedure:

i) for the mean axial load, use the procedure in Section 3.6 to find the change $2\frac{d\phi}{d\ell}$ (corresponding to the full range of twist perturbation) corresponding to any assumed torque perturbation, M.

ii) Use Equations (3.(1.27b)) and (3.24) to check whether $\frac{\Delta\ell}{\Delta_{\ell max}}$ is greater or less than one, corresponding to full or partial slip cases respectively.

iii) In the partial slip regime, use Equations (3.31) and (3.(1.24)), or otherwise use Equations (3.33) and (3.24) to determine the energy dissipated per millimetre of a wire in layer i.

iv) Use Equations (3.34) and (3.35) to obtain the energy loss ratio as a function of half of the full twist perturbation range.

3.8.2.2 Axial hysteresis

In this case slip over the contact patch is determined by Equation (2.60)

$$\Delta_{\ell} = 2KDS_1' \qquad (3.(2.60))$$

where S_1' is half the total cable axial strain perturbation.

The energy input per cycle per unit length is:

$$U = \frac{1}{2}\left(\frac{\text{load range}}{2}\right)S_1' \qquad (3.36)$$

The procedure for calculating cable hysteresis is then as follows:

i) For a given mean axial load, use the procedure in Section 3.7 to find the change in S_1' (corresponding to half the load perturbation) for any assumed axial load perturbation.

ii) Same as (ii) for torsion case

iii) Same as (iii) for torsion case but now use Equation (3.(2.60)) instead of Equation (3.24).

iv) Use Equations (3.34) and (3.36) to obtain the energy loss ratio as a function of the load range to mean ratio.

3.8.3 Results and Discussion

i) Axial hysteresis

Fig. (3.19) gives theoretical values for the energy dissipated in each layer of the 39mm O.D. strand. Similar plots for the 127mm O.D. cable are presented in Fig. (3.20), for comparison. Both of these strands are assumed to sustain a mean axial load of about 35% of their ultimate capacity, in an axially fully bedded-in condition. Method (a) has been used for both plots. Note the significant contribution of the inner layers to the overall hysteresis, especially at higher ratios of load range/mean. Overall (i.e. total) theoretical axial hysteresis plots based on method (a) as well as method (b), for both of these cable constructions and also constructions with 16 and 51mm O.D. are given in Figs. (3.21) to (3.25). In addition, Figs. (3.21) and (3.22) compare experimental data on the 39mm O.D. strand due to Wyatt (2.54) with the present theory, for two mean axial loads, 0.42MN and 0.105MN. The agreement between experiment and theory is encouraging. Because of the non-linear nature of the contact problem, the plots appear to be dependent on the level of mean axial load on the strand.

Agreement between methods (a) and (b) is satisfactory and, in the present example, appears to improve with decreasing level of mean axial load. The discrepancy between the two methods is believed to be mainly a result of assuming zero change in the size of the line contact

patches during the axial cycling. This is specially important in the partial-slip regime.

As shown in Tables (2.3) and (2.4), the 51mm and 127mm strands have an equal lay core construction. The present theory is strictly speaking applicable to multi-layered counter laid strands with a single central wire (the king), and does not predict the interwire contact forces and hence the hysteresis within an equal lay core construction (which is composed of wires with different diameters in a given layer, in order to have higher rigidity). The contribution of the core to overall cable hysteresis is, however, thought to be insignificant and has been ignored in the hysteresis plots. On the other hand, the contribution of the core to cable overall axial stiffness is very significant and cannot be ignored. The lay angles of such equal lay constructions are in general very small and the simple formula $\varepsilon_h = \varepsilon_c \cos^2\alpha$ of Hruska may be used to obtain the core axial stiffness with minimal loss of accuracy. This has been done in the axial stiffness plots, Fig. (3.17).

The change in the fully bedded-in axial damping characteristics with the type of cable construction is significant. It appears to be mainly governed by the choice of the lay angle in various layers. Increasing the lay angles will, in general, increase the capability of an orthotropic layer to generate contact forces in the hoop direction, as well as increasing the rate of relative

slippage (for a given axial cable strain) between its component wires in line-contact. As there is usually little practical scope for modifying other geometrical parameters (e.g. the strand outer diameter which is generally determined on the basis of design ultimate load and/or sizes of individual wires), high hysteresis values could most easily be achieved by increasing the lay angles. However, this must be done with caution, so as to guard against adverse effects (such as reduced fatigue life) on the strand properties. It is comforting to note that small changes in lay angle would induce large variations in the level of hysteresis. Therefore, higher damping could be obtained by changing values of α within the usual manufacturers' design limit of say $\alpha < 25^{\circ}$.

Cables are always heavily lubricated during their manufacture and, in some applications, relubricated during their life to compensate for the loss of the lubricants in service. The surface texture of the wires will also change during the cable's life. Consequently, the coefficient of friction, μ, will probably remain a very unpredictable parameter, even for a given cable. However, one can reasonably expect it to change within certain limits. Figs. (3.26) and (3.27), show the variations in axial damping characteristics over possible practical ranges of μ. The plots are given for 39mm as well as 127mm O.D. strands. The rather unexpected result is that the maximum value of $\frac{\Delta U}{2U}$ appears to be independent of the value assigned to μ, for

any given construction and mean axial load. For the present idealised model, changes in the coefficient of friction will merely change the value of load range to mean load ratio at which maximum axial damping occurs. In other words, an increase in the coefficient of friction does not by itself indicate an increase in the level of axial damping. The damping also depends on the ratio of range to mean axial load. In some structural applications where strand axial damping is an important design factor (such as inclined-hanger systems in suspension bridges), it may be that the critical load range/mean ratio falls on the ascending part of the damping curves, and an increase in μ causes a decrease in $\frac{\Delta U}{2U}$. This is obviously a consequence of including elastic kick-back in the model.

The theory has only been developed for a repeated loading/fully bedded-in condition, and the variations in strand damping coefficients under a more realistic random loading situation may be significantly different. Moreover, real strands may have additional variability due to, for example, irregularities in the fit of the wires and variations in μ at various locations inside them. These effects will be discussed later (see Chapter 5).

As discussed in Section 1.5, various measurements of energy dissipation on single contacts between spheres have indicated that although the assumption of Coulomb friction is a reasonable approximation over that portion of the annulus of slip where relative displacement is large, it is a poor approximation for small relative displacements. For very small tangential force changes, the latter regime

predominates,and the present theory fails to predict the energy dissipation at low perturbations at all well. If the damping forces were viscous rather than frictional in nature, the energy loss expressed as $\frac{\Delta U}{2U}$ would be constant. Experiments on the decay of free torsional oscillations in a fully bedded-in condition (see Chapter 5), have confirmed that the logarithmic decrement for the cable falls with decreasing amplitude of oscillations, reaching a constant for very small amplitudes. This value was found to be very nearly independent of the axial load on the cable. This is obviously an example of the well known property of viscously damped systems, where $\delta \simeq \frac{\Delta U}{U}$ for very small oscillations was about 0.05 and constant. However, this figure may change from one cable to another.

The careful experimental works of Kawashima et.al. (2.39), and Kimura (2.40) who measured the logarithmic decrement, δ, of cables (ropes as well as strands and also single wires) by measuring the decay of their vertical oscillations, has been discussed in Section 2.3. In particular, they showed that with high enough tension on a 7-wire copper strand, δ appeared to be a function of the amplitude alone and independent of the level of mean axial load. The magnitude of δ for the strand was then found to be similar to that for a single copper wire, Fig. (2.4b). It is interesting to note that even for a single copper wire, logarithmic decrement was found to be a function of the amplitude and not a constant, as is the case for an ideal

viscous model. Moreover, Fig. (2.4a) shows that over their limited experimental range of amplitudes, increases in the level of mean axial load led to significant reductions in damping. The present theory suggests that their ratio of load range/mean was small enough to lie on the ascending part of the damping curves where the elastic kick-back action predominates.

ii) Torsional hysteresis

Method (a) may be used to follow the non-linear torque-twist relation for the strand and hence, assuming a skew-symmetric torsional hysteresis loop, plots of energy dissipation, $\frac{\Delta U}{2U}$, against half range of twist, $\frac{d\phi}{d\ell}$, can be obtained. $\frac{d\phi}{d\ell}$ will, then, correspond to the amplitude on one side of the dynamic free decay curves, from which

$$\delta = \frac{1}{m}\log_e \frac{(\frac{d\phi}{d\ell})_n}{(\frac{d\phi}{d\ell})_{n+m}} \simeq \frac{\Delta U}{U} \qquad (3.37)$$

This, of course, assumes small damping (see Section 3.2) but experiments (see Chapter 5) have confirmed that this is the case. Theoretical energy dissipation quotients based on method (b), were, however, found to almost identically (within normal accuracies of the numerical calculations) match those based on method (a), only when N in Equation (3.34) is taken as half of the number of wires in each layer. A possible reason for this is as follows. A close examination of the equations in Section 3.8.2 suggests that simple

linear scaling of methods (a) and (b) to give identical results in both the partial and the full-slip regimes and throughout the strand, is only possible by manipulating the factors U and/or N. U represents the maximum elastic energy in a cycle and there is little doubt about its magnitude. The remaining factor, N (which is essentially governing the number of "effective" slip surfaces) must therefore be the one to be divided by two.

Theoretical values for the torsional energy dissipation in each layer of the 39mm O.D. strand are given in Fig.(3.28). The assumed mean axial load is 0.420MN. The inner layers of wires contribute very little to torsional damping. The dependence of the overall hysteresis on mean axial load (for the same strand) is examined in Fig.(3.29). This figure suggests that over a large range (in terms of practical torsional vibration amplitudes) of $\frac{d\phi}{d\ell}$, increasing the mean axial load on the cable will lead to a reduction in damping. This is again due to elastic kick-back action between the wires. As discussed before, for very low amplitudes viscous damping takes over and invalidates the interwire friction theory. Finally, Fig.(3.30) shows the dependence of torsional hysteresis upon the value assigned to μ. Decreasing the coefficient of friction over the practical ranges of $\frac{d\phi}{d\ell}$ can lead to a decrease in the damping quotient. The practical limitations on the torsion results are similar to those associated with the axial problem.

3.9 A NOTE REGARDING DAMPING IN THE SEVERN BRIDGE

Inclined hangers have been used to damp out the residual deck motions of this suspension bridge, where the deck consists of an all-welded streamlined box girder. This "fully participating" design was thought to have a potentially dangerous low level of damping and the designers exploited the hysteresis by inclining the hangers to achieve a truss action. As discussed by Roberts (3.30), the hanger manufacturers were asked to carry out hysteresis measurements on both small (model) and full sized ropes for which few data were then available. The general conclusions were:

" (a) hysteresis is slightly increased by a shorter lay (i.e. a steeper spiral) in the strand or rope;

(b) there is no significant difference between wire rope and bridge strand;

(c) hysteresis is greater for small stress cycles than larger ones;

(d) hysteresis is much greater for short time cycles (10 s) than for longer cycles (say 10 min.)"

Cyclic tests with a seven seconds period and typical service stress ranges gave a minimum logarithmic decrement of 1.5, a value which greatly exceeds the present theoretical estimations for damping of various cable constructions. The first antisymmetric torsion mode of oscillation was identified as the most damaging to the structure. For this mode, 7% of the energy of oscillation was calculated to be stored in the hangers, at the instant of maximum displacement. The

logarithmic decrement of the whole structure was then calculated with the assumption that the inclined hangers were the only sources of energy dissipation. Based on this assumption, the logarithmic decrement for the bridge as a whole is equal to 0.07 x 1.5 = 0.105 (Ref. Equation (3.10)). In spite of this alarming calculation, the structure has been in service for nearly 20 years, with no sign of dynamic instability, although some hanger fatigue problems have been widely reported.

The present theoretical results, and the carefully conducted fully bedded-in axial hysteresis measurements reported in (2.54), do seem to substantiate each other, but not the manufacturers' general recommendations regarding cable hysteresis, reported in (3.30). The difference is alarmingly large (i.e. a factor of seven or so). Admittedly, all of the results developed here are concerned with the fully bedded-in condition, under uniform cyclic loading, and it is likely (as is experimentally demonstrated later on, for the torsion case) that under random loading conditions, the energy dissipation quotient may be significantly higher. Nevertheless, it is felt unlikely that it increases the axial damping by as much as a factor of seven.

3.10 THE EFFECT OF EXTERNAL HYDROSTATIC PRESSURE ON CABLE AXIAL STIFFNESS AND DAMPING

The clench forces due to the hydrostatic water pressure in very deep water applications (for which TLP or guyed tower designs are often proposed) may become

significant compared with the clench forces inside the cable caused by the mean axial load. Unlike our ideal model in which it is assumed that no gap occurs between the wires, the pre-stressed wires in the outer layer of real strands (where the size of gaps between wires depends on the manufacturing process and is hard to quantify) may not seal the interior of the strand from the outside. It is thus possible that water pressure gets all around the wires and consequently no significant clench force due to the external pressure will develop . This situation is analogous to that treated by the effective stress concept in soil mechanics.

However, high density, supposedly impermeable polythene sheaths have been offered by cable manufacturers for corrosion protection. For such a "sealed construction", it is then reasonable to assume that the plastic sheath causes full hydrostatic pressure to act as a clench force on the outer layer of the strand. A similar situation arises in the case of sealed electro-mechanical cables with soft cores and/or gas filled voids. In the presence of substantial airfilled voids, the inner wires will experience some extra clench force due to the external water pressure. It is also noted that the agreement between theory and experiments in air (Ref. Chapter 5) suggests that internal pressure in the blocking lubricant does not act to reduce the effective stress on the wire contact points, at least for low external pressures.

The following solutions should prove useful in giving an insight into the manner in which the effect of hydrostatic force from outside is determined as one moves nearer to the centre of the cable, when at the same time there will be a build up of clench forces due to the mean axial load. Deep water applications are obviously taken as an example from a variety of applications in which cables may reasonably be assumed to be subjected to uniform external pressure.

The method of calculating the radial and hoop forces

in various layers follows that set out in Section 2.14, but in this case X_{RC} and X_{MS} (and hence P_{RC} and P_{MS}) are no longer the same for the outer layer, and

$$X_{MS1} = X_{RC1} + X_H \tag{3.38}$$

where X_H corresponds to the magnitude of the hydrostatic pressure from the outside, per unit length of the wire in the outer layer. X_{MS1} and X_{RC1} are defined as before. Equations (2.56) and (2.57) are then used in exactly the same way as explained in Section 2.14.

Fig. (3.31) gives variations of the line-contact forces in various layers of the 39mm O.D. strand as a function of water depth (i.e. hydrostatic pressure). The mean axial load in this case is assumed to be zero. On the other hand, Fig. (3.32) shows the way in which the line contact forces, P_{MSi}, in various layers i (outer layer: i=1) vary as a function of cable axial strain, S_1' (representing the axial force on the strand). The 39mm O.D. cable is assumed to be subjected to 400 metres of external water pressure. At zero cable axial tension, P_{MS} is highest in the outer layer and lowest in the innermost one (i=5). As the cable axial force increases, the internal clench forces grow in magnitude. This in turn increases the level of the line-contact forces in the inner layers at a higher rate than that in the outer ones. With high enough tension on the cable, the outer layer will have the lowest P_{MS} among all the other layers in the strand.

Based on these contact force distributions, one may calculate the variation of the cable Young's modulus as a

function of range of axial load to the mean, for various water depths. The results are given in Fig. (3.33), which shows that external pressure on a sealed strand will tend to suppress the slippage of wires in the cable by increasing the frictional forces between them. A higher cable axial stiffness then follows.

Finally, Fig. (3.34) shows the way in which the theoretical fully bedded-in cable axial hysteresis may vary with water depth. It is especially noteworthy that increases in the level of external hydrostatic pressure appear to lead to large variations in the magnitude of range to mean axial load at which maximum damping takes place. In the present example, 1600 m of water will double this ratio. This will obviously have a significant bearing on the overall structural damping characteristics of the moored system.

3.11 CONCLUSION

The theoretical analysis of a strand using orthotropic sheet theory with appropriate compliances derived from results in contact stress theory has been developed for axial and torsional loadings. In each case, predictions of wire strains, interwire forces and slippage, strand tangent stiffness and hysteresis have been made.

A new feature in theoretical work has been to treat the layers of wires in a strand as orthotropic sheets - and if the method is to be applicable there must be enough wires in a layer to avoid serious effects from the magnitude of

the polar angle between wires, or other inaccuracies. However, in the kind of large strands used for bridge hangers (and even more so for the tethers in a TLP or TBP), it appears that the orthotropic sheet approach is a valid and useful one.

For a given mean axial load, the torsional and axial stiffnesses have been found to be functions of the applied torque and axial load perturbations, respectively. The stiffness for small load changes was found to be larger than for large perturbations, because small disturbances do not induce interwire slippage. The theory predicts the bounds to the stiffnesses and describes the variation between the limits.

Prediction of the energy dissipation quotient, $\Delta U/_U$, under continued uniform cyclic loading is now possible and is in satisfactory agreement with the results reported in (2.54). It is much lower than previously believed. However, in a more realistic random loading situation it is reasonable to expect rather higher values. The effect of external hydrostatic pressure on cable axial stiffness and hysteresis, has been discussed and may have significant design implications. The practical applications of the theoretical results have been discussed in some detail.

Finally, with the present model it would be economically possible to run the hundreds of cases necessary for a proper parametric study which should then lead to further valuable design recommendations. The two independent methods, namely (a) and (b) are both incorporated in the computer

program in order to guard against possible data preparation mistakes which might occur in future runs.

REFERENCES

3.1 WYATT , T.A. Personal Communication. Department of Civil Engineering, Imperial College.

3.2 BARON, F., and SHEN-YING LIEN. Analytical Studies of a Cable Stayed Girder Bridge. Computers and Structures. 1973: 3, pp.443-465.

3.3 SELBERG, A. Dampening Effect in Suspension Bridges. Int.Assoc. Bridge Struct. Engr. Zürich: 1950, 10.

3.4 BLEICH, F., and TELLER,L.W., Structural Damping in Suspension Bridges. Transactions, ASCE. 1952: 117 (March), pp.165-203.

3.5 TANG, MAN-CHUNG. Design of Cable Stayed Girder Bridges. Journal of the Structural Division, Proceedings of the ASCE. 1972: ST8 (Aug.), pp.1789-1802.

3.6 WYATT, T.A. On the Dynamic Properties of Cable-Stayed Bridges. Journal of Constructional Steel Research. 1980: 1(1), pp.10-17.

3.7 WYATT, T.A. Mechanics of Damping. Symposium on Dynamic Behaviour of Bridges. Crowthorne, Berks, U.K., 1977. Transport and Road Research Laboratory Supplementary Report. 275, pp.10-21.

3.8 SCRUTON, C., FLINT, A.R. Wind-excited Oscillations of Structures. Proceedings, Institution of Civil Engineers. 1964: 27 (April) pp.673-702.

3.9 WALSHE, D.E., WOOTON, L.R. Preventing Wind-induced Oscillations of Structures of Circular Section. Proceedings, Institution of Civil Engineers. 1970: 47, pp.1-23.

3.10 SCRUTON, C. Wind-Excited Oscillations of Tall Stacks. The Engineer. 1955:10 (June), pp.806-808.

3.11 RICHARDS, D.J.W. Discussion to 3.8. Proceedings, Institution of Civil Engineers. 1965: 31 (Aug.), pp.384-403.

3.12 HOGG, A.D., and EDWARDS, A.T. The Status of the Conductor Galloping Problem in Canada. International Conference: Wind Effects on Buildings and Structures. National Physical Laboratory. Teddington, Middlesex, 1963, pp.562-580.

3.13 DAVIS, D.A., RICHARDS, D.J.W., and SCRIVEN, R.A. Investigation of Conductor Oscillation on the 275kv Crossing Over the Rivers Severn and Wye. Proceedings, I.E.E. 1963: 110(1), pp.205-219.

3.14 RICHARDSON, A.S., MARTUCCELLI, J.R. and PRICE, W.S. Research Study on Galloping of Electric Power Transmission Lines. International Conference: Wind Effects on Buildings and Structures. National Physical Laboratory, Teddington, Middlesex, 1963, pp.612-686.

3.15 DEN HARTOG, J.P. Mechanical Vibrations. 4th ed. New York: MacGraw-Hill, 1956.

3.16 POFFENBERGER, E.A., CAPADONA, E.A., and SITER, R.B. Dynamic Testing of Cables. Transactions, 2nd Annual Marine Technology Society Conference: Exploiting the Ocean. Washington, D.C., 1966. pp.485-523.

3.17 CAPADONA, E.A. Dynamic Testing Predicts Failures. Undersea Technology. 1967: (Oct.), pp.26-29.

3.18 SARPKAYA, T. Vortex-Induced Oscillations, A Selective Review. Journal of Applied Mechanics. 1979: 46(2), pp.241-258.

3.19 KENNEDY, M., and VANDIVER, J.K. A Random Vibration Model for Cable Strumming Prediction. Proceedings, Civil Engineering in the Ocean IV, ASCE, 1979. pp.273-292.

3.20 BELVINS, R.D. Flow-Induced Vibrations. New York: Van Nostrand Reinhold, 1977.

3.21 LAZAN, B.J. Damping of Materials and Members in Structural Mechanics. Oxford: Pergamon Press, 1968.

3.22 GEMANT, A., and JACKSON, W . The Measurement of Internal Friction in Some Solid Dielectric Materials. Philosophical Magazine and Journal of Science. 1937: XXIII, pp.960-983.

3.23 WEGEL, R.L., and WALTER, H. Internal Dissipation in Solids for Small Cyclic Strains. Physics, 1935:6, p.141.

3.24 ZENER, C. Internal Friction in Solids. I. Theory of Internal Friction in Reeds. Physical Review. 1937: 52, pp.230-235.

3.25 BENNEWITZ,K. and RÖTGER, H. Internal Friction in Solids, Part II. Zeits. f. Techn.Physik. 1938: 19, pp.521-526.

3.26 WHITEMAN, I.R. On the Derivation of the Stress-Strain Diagram from a Statistical Approach. Aero.Eng. 1962: 21 (10), p.56.

3.27 GOODMAN, L.E., and KLUMPP, J.H. Analysis of Slip Damping with Reference to Turbine Blade Vibration. Journal of Applied Mechanics, Transactions of the ASME. 1956: 23 (Sept.), pp.421-429.

3.28 HOBBS, R.E. Personal Communication. Department of Civil Engineering, Imperial College.

3.29 MONTAGUE, P. Load Distribution in Overhead Strand Conductors. International Journal of Mechanical Sciences. 1961: 2(3), pp.277-293.

3.30 ROBERTS, G. Severn Bridge-Design and Contract Arrangements. Proceedings, The Institution of Civil Engineers. 1968: 41, pp.1-48.

CHAPTER 4

FREE BENDING THEORY

4.1 INTRODUCTION AND LITERATURE SURVEY

In offshore applications, platform drift and yaw and possible hydrodynamic effects such as vortex excitation will be responsible for a restrained bending action near the end fittings of, for example, TLp's in the inevitable presence of bearing friction at the terminations. This chapter is particularly concerned with these bending effects in spiral strands in the absence of sheaves, fairleads or other formers, so that the radius of curvature of the strand is not pre-determined. These conditions will be referred to as "free bending".

Closely related free bending problems are a source of concern (and not infrequent failures) in other structures ranging from suspension and cable-stayed bridge hangers and the stays for guyed masts to electro-mechanical cables where fatigue failures near partially restrained terminations caused by aero-or hydrodynamic loading are not uncommon.

Despite the efforts of research workers which date back to the early years of this century, little light has been cast on this important problem. The approaches have mostly been purely experimental in nature, and the results have been restricted in application in the absence of any soundly based theoretical interpretation which would permit predictions of the performance of other strands to be made. Fatigue tests on large diameter strands are, however, so

exceptionally expensive that the pressing need for proper design and later interpretation of such tests gives a fresh urgency to the search for a better theoretical understanding of the underlying phenomena of strand behaviour.

For the free bending of long cables under an approximately steady axial load it is common to introduce a mathematically convenient constant effective bending rigidity $(EI)_{eff}$ for the cable, from which the radii of curvature at the points of restraint are calculated. The maximum bending strains in individual wires are then found on the basis of a variety of, frankly, sweeping assumptions: these strains are further assumed to govern the strand bending fatigue life. However, this last assumption is not supported by the experimental evidence where it is often found that the primary mode of wire fatigue failure is associated with interlayer or interwire fretting action very close to the usually partially restrained terminations of various types.

An interesting survey of the state of the art prior to 1920 is given by Scoble (4.1) who also made an extensive series of tests on rope fatigue behaviour (4.2). Howe (4.3) assumed plane sections in bending to remain plane and developed a method for determining the moduli of elasticity of both helical strands and ropes. He pointed out the need to take the helical arrangement, as opposed to the parallel wire case, into account. Chapman (4.4) attributed the significant hysteresis in rope load-deflection plots to interwire friction, and took the inclination of the loop's centreline as a measure of the rope's flexibility. Scoble used 9 inch (229mm) long specimens which were firmly clamped at one end and were subsequently bent to a constant radius of curvature

to obtain static hysteresis loops. These tests led to no definite result. Carstarphen (4.5) assumed the wire rope to be an assemblage of open-coiled helical springs and proposed a method for determining the bending stresses in individual wires. Strum (4.6), Ikeda and Ueno (4.7) and Glushko (4.8) are among those who have attempted to analyse the problem of a single layered cable in bending assuming zero interaction between the component wires. In particular, Glushko emphasized the importance of the asymmetrical distribution of the axial stresses in individual wires in any given cross-section of the strand which led to a "corkscrew" effect in the cable. Costello and Butson (4.9) tackled the problem of friction-less, single layered strand wrapped around a sheave with geometrical non-linearities taken into account.

Nowak (4.10) investigated the behaviour of friction-less multi-layered strands with compressible cores in bending. The constraints on the cable, free from any pretension, in bending were considered not only from the view point of equilibrium but also from bending kinematics. The approach adopted by Mitchell and Woodall (4.11) was essentially along the same lines as Nowak: in the absence of friction and in the presence of gaps between individual wires in each layer, wires were assumed to undergo individual bending like free helical coils. However, the presence of other wires in the same layer meant that there existed a minimum cable bending diameter at which interference between neighbouring wires was inevitable. Beyond this point, wire interaction was treated by means of displacement boundary conditions implying rigid bodies in contact. Kasper (4.12) also considered the problem of friction-less wires of a multi-conductor armoured electrical cable in bending. He used finite element techniques to determine the inter-

action between cable components.

Steidel (4.13, 4.14) addressed the problem of wind-induced vibrations of cables. In his first paper, he reported the experimental measurement of strains in a vibrating cable and also discussed the causes of Aeolian vibrations. In the second paper, analytical solutions for the dynamic bending stress in the outer layer were obtained using the methods of standard beam theory. In this solution he incorporated a factor ζ which represented how closely the suspension clamp approached the ideal pinned (or rigid) state. In a discussion to Steidel's second paper, Elton (4.15a) reported the occu rrence of inner-layer strand fatigue damage in ACSR unarmoured conductors which was verified by x-ray examination. In a separate discussion on the same paper, Hard (4.15b) also pointed out the greater tendency of wires in a multi-layer conductor to fail in the second rather than outer layer; this view was also supported by Capadona and Colletti (4.16) and Hondalus (4.17). Hondalus, working with 25-38 mm specimens, reported wire failures occurring at a distance of usually no more than 25mm from the mouth of the clamp. Fretting corrosion appeared to be the main cause of wire failures although some outer wires were fatigued because of striking the mouth of the clamp. Damage due to fretting was greatest at the mouth of the clamp and decreased in intensity out to about 300mm from the clamp ,where it vanished altogether. In addition, no evidence of fretting was found between the wires at nodal or antinodal areas along the vibrating cable.

This work is an example of the interest in predicting the properties of electrical cables which has been the subject of rather extensive research in the past.

Poffenberger and Swart (4.18) gave historical background coupled with a number of references to a variety of approaches for investigating conductor vibration. They formulated a mathematical solution defining the relationship between conductor outer-wire strain and the measured bending amplitude, called the differential displacement, of the short but critical segment of the deflected curve near the clamp. In experiments, account was taken of possible joint flexibility by rigidly extending a displacement transducer from the suspension clamp body on a deflection arm which rotates with the clamp. The relative (effective bending) displacement of the cable at a point situated about 75mm from the edge of the support was then measured. Their analysis was that of a statically loaded cable of uniform bending stiffness with one fixed and one pinned end subjected to a sinusoidally distributed transverse loading. The final theoretical relationship between maximum outer fibre strain, ε, at clamp and the differential displacement, $y(x_a)$, of a point situated at a distance x_a away from the clamp was:

$$\varepsilon = \frac{d}{2j^2\left(e^{\left(-\frac{x_a}{j}\right)} - 1 + \frac{x_a}{j}\right)}\, y(x_a) \qquad (4.1)$$

where $j = \sqrt{\frac{EI}{T}}$,

d is the wire diameter, T denotes the tension in the cable and EI corresponds to the cable stiffness in bending. Note that in Equation (4.1) it was assumed that:

$$\varepsilon = \frac{d}{2 \times \text{radius of curvature}}$$

Laboratory data for solid single wire specimens supported the theoretical results. However, experimental plots of outer fibre strain against differential displacement for a number of ACSR conductors were found to be non-linear, the degree of non-linearity depending on the level of mean tension in the strand, Fig.(4.1). Such deviations from the linear theory were thought to be the result of assuming a constant bending stiffness throughout the bending cycle. In a discussion to (4.18), Hondalus applied the above theory to his experimental results and found the linear (i.e.: low displacement) experimental results to be significantly higher than the theoretical predictions. In response to this Poffenberger et.al. agreed that their own experimental results, as well as Hondalus' , showed that their theory is invalid for low displacements particularly for large diameter conductors.

Scanlan and Swart (4.19) extended the quasi-static theory derived in (4.18) to cover the case of vibrating cables. Yet again they used the classical beam theory. Following a number of reasonable simplifying assumptions compatible with common practical vibration situations, they finally arrived at the same expression for the extreme fibre strain obtained in Ref.(4.18) for a static loading.

By integration of the fourth order differential equation for cable deflection, the so-called constant cable bending stiffness was expressed as a sole function of the variable u, the cable deflection, and its derivatives. Numerical differentiation of the experimentally determined cable deflection curves, with different peak (mid span) amplitudes, was then employed to get semi-empirical values of cable bending rigidity. Significant scatter was observed in the final plots,but most importantly, cable EI values appeared to vary spanwise as a function of cable configuration and load which was obviously not compatible with the original assumptions in the theory. Their specimen had an outer diameter of 35.1mm with a total of 54 wires of 3.90mm diameter in its three outer layers (24, 18, 12).

In theoretical calculations of bending rigidity (EI) two limiting cases can be considered: either full or zero shear interaction of the wire elements of a cable. In the former case the cable acts as a 'solid bar' whose modulus differs from the material Young's modulus only by an allowance for the helical voids and the effects of the helical arrangement of the wires. In the latter,wires are assumed to act individually and bend about their own neutral-axis. For large diameter, multi-layered strands the difference between the two limits is unacceptably large, being given approximately by the square of the strand/wire diameter ratio. Based on their experimental EI values,Scanlan and Swart suggested that all but a very few wires must be considered as acting

together. In fact they argued that the experimental strain confirmations of Komenda and Swart (4.20) and Poffenberger and Swart (4.18) of Equation (4.1) are only applicable to the outer wires which appear to undergo individual bending.

Claren and Diana (4.21, 4.22) and McConnel and Zemke (4.23) have also made measurements of cable bending stiffness. In their first paper Claren and Diana analysed the problem of cable lateral vibrations under a harmonically varying force with damping included. The theoretical damping model employed was hysteretic,that is energy dissipation per cycle is independent of frequency. Their analytical results were backed by favourable experimental data on long span conductors. The frequency independence of damping was demonstrated experimentally. The negligible effects of frequency on dynamic wire strains over a wide range of frequencies has also been demonstrated by the I.E.E.E. Committee Report (4.24). In their second paper Claren and Diana investigated outer wire strains near the clamps of vibrating conductors both by experiment and by theory. Yet again their theory was shown (see discussion to the paper by Poffenberger and Komenda) to give almost identical wire strain results to those derived by Equation (4.1). For bending rigidity significant scatter between theory and experiment was observed. Neither of the two extreme values of EI, namely the no-slip and the independent wire action limits,appeared to give any reasonable theoretical predictions. In a discussion to the paper

Poffenberger attributed this to the fact that the average value of the authors' displacement near the clamp had been less than half of those employed in Ref.(4.18) and that the theory breaks down for displacements below a certain level. Poffenberger suggested 10 to 15 mils of deflection at a distance of about 100 mils from the clamp as the order of deflection for which their theory worked.

Pankratov and Volkov (4.25) made a theoretical investigation of bending stresses in a pretensioned rope without sag subjected to vibration without damping. They also made experimental measurements of wire rope radius of curvature at the anchorage points as a function of the imposed axial tension on the cable. The following empirical equation was suggested for determination of the second moment of area, I:

$$I = 0.7 \frac{\pi d^4}{64}\left(1-\exp\left(-k_1 \frac{\sigma^{k_2}}{q^{k_3}}\right)\right) \qquad (4.2)$$

where d is the rope diameter, q is the uniformly distributed static load on the rope and σ is the tensile stress in the rope based on net steel area. k_1, k_2 and k_3 are coefficients determined by the geometrical parameters of the wire rope and the loading conditions. For calculating the stresses it was assumed that the rope consists of two separate layers: the upper layer in which the strands stick together like a solid bar and the lower layer in which wires act individually. Some graphs were presented which showed significant variation of bending stresses near the anchorage point. However, these were not supported by any clear indication of the type

of calculations involved.

Lutchansky (4.26) used the kinematical relations derived by Zhadnov (4.27) and developed an analytical model of the wire-core shear interaction in single lay helical armour wires of a large diameter submarine cable. Lutchansky assumed the core to undergo zero shear distortion and used a constant distributed shear stiffness, K, to define the interaction shear force between the outer layer wires and the core. Only tentative values were quoted for K and the model could not predict the interwire slippage phenomena which are of prime importance in the analysis of the fatigue behaviour of strands near terminations. For a helical cable bent to a constant curvature and clamped at one end it was shown that for a constant K, the highest wire axial strains do not occur at the extreme fibre position, which is of course different from the classical results of the familiar Euler-Bernoulli beam theory. For the limiting case of zero helix angle (i.e. a cable composed of parallel straight wires) maximum direct stresses were obviously at the extreme fibre position.

In the field of structures, Wyatt (4.28) investigated the occurrence of secondary stresses, as he called them, in parallel wire suspension cables. In the case of suspension bridges, such stresses are created in the vicinity of end fittings when restraint is provided to changes in end slope by friction in pins, or by fixity produced by clevis end fittings. Wyatt analysed the variation of stresses across the cable section caused by deflection of the cable, with frictional shear interaction between the wires included.

The frictional model used was a Coulomb rigid-plastic one.

There is surprisingly very little information publicly available on fatigue performance of structural cables in free bending. The majority of the published work concentrates on the influence of pulleys and sheaves as sources of wear and fatigue damage: Scoble(4.2), Edgar (4.29), Drucker and Tachau (2.26) and Gibson et.al. (4.30) are among those who have attempted to analyse experimental and field data on wire ropes running over sheaves. In particular, Drucker and Tachau pointed out the importance of considering bearing pressure at the contact points in rope fatigue studies and by the analysis of experimental data, found a dimensionless parameter:

$$B = \frac{2T}{UdD} \qquad (4.3)$$

called the bearing-pressure variable,which appeared to be of prime importance in controlling rope fatigue life in bending over sheaves, where T is tensile force in the rope, d denotes the rope diameter, D gives the pitch diameter of the sheave and U is the ultimate tensile strength of wires. In discussion to Ref.(2.26), Hardesty (4.31) and Lonngren (4.32) transformed $B = \frac{2T}{UdD}$ to const.$(\frac{T}{U'})(\frac{d}{D})$ where $\frac{T}{U'}$, is the ratio of tension in the rope to rope breaking strength and $\frac{d}{D}$ is the rope to sheave diameter ratio. In other words they argued that the dimensionless ratio, B, is an alternative way of catering for the combined effect of the two (often thought of as separate) factors traditionally used for designing ropes over sheaves. A modified version of the factor B is proposed in the later work of Rice (4.33).

Dong and Steidel (4.34) used techniques of photo-elasticity to investigate the interwire contact stresses existing in a double-layered (cross-laid) strand while it rested in a supporting clamp. Based on the normal Hertzian theory (with friction ignored) they suggested the maximum shear stress under static loads to be the basis for design. The most important factor in any strand fatigue study, namely the fretting action at the contact points, was not mentioned in their work.

Experience at British Ropes (4.35) has shown that in the repeated bending fatigue of strands, bends in excess of about 10 degrees are just as detrimental as a right angle deflection, again substantiating the argument that fretting between wires is the primary cause of fatigue. It follows that in any meaningful analysis of the experimental fatigue data one must not only consider the magnitude of interwire stresses in the strand but also the range of movements and slip threshold between them.

Hobbs and Ghavami (2.53) carried out a limited series of six bending tests on 8.5 metre long, 39mm specimens carrying a steady axial load while pulsating lateral movements were applied. Details of the 92 wire strands are given in Table (2.1). The end terminations used were zinc metal filling in sockets to BS463 except for an elongated jaw. The end conditions of the strand were nominally the same as those assumed in the mathematical model developed in (4.18) - ie.:- fixed-pinned, Fig.(4.2). The nature of the imposed lateral loading was, however, different. In

this case point loads were applied via an opposed pair of jacks acting on curved aluminium formers resting on the strand. Table (4.1) gives details of the test parameters adopted. Bending fatigue results covering the gradual fracture of wires until final failure are summarized in Fig. (4.3). Note that the maximum deflection angle, θ, at the socket employed in the tests is only about 1.4 degrees which is much lower than the nominal figure of 10 degrees suggested by British Ropes. It follows then that although within the particular range of deflection angles, θ, investigated one can reasonably draw straight lines to represent θ versus cycles to first (and last) wire failure; it would be imprudent to predict strand fatigue lives for values of θ outside the experimental range. All wire failures occurred adjacent to the socket, and based on visual observations and the use of a shock contact device they suggested that first wire failures occurred in the outer layer rather than the inner ones. Considerable fretting damage between the two outer layers of wire with opposite lay was observed and most importantly first wire fractures were invariably located not on what would be the "extreme fibre" (in bending terms) but rather near the neutral axis.

Hobbs and Smith (4.36) suggested that the end moment, M_o, given by:

$$M_o = \pm 1.1 \tan\theta \sqrt{\frac{T}{(EI)_{eff}}} \qquad (4.4)$$

dictates the cable's fatigue life. Note that the above formula is only approximate and strictly applies to a cable

without any sag under a transverse point load. Certain outer layer stresses were calculated using a number of tentative empirical factors and these were correlated with the limited experimental data. It was emphasized that the curves produced were to be used with caution until further theoretical work, taking the helical arrangement of the wires into account, was developed.

4.2 SUMMARY OF THE LITERATURE SURVEY:

Fatigue damage in free bending is concentrated in the vicinity of end fittings and places where an abrupt change of slope is imposed on the cable. It follows that the degree of imposed bending restraint is of prime importance and any reduction in its intensity can prove beneficial to cable fatigue performance (4.14, 4.18, 4.24, 2.53 , 4.36).

At least for the case of cross-laid, large diameter strands fretting between the two outermost layers is the prime initiator of fatigue cracks leading to wire failure, although some outer wires may fail due to other causes such as the presence of defects acting as stress raisers, or fretting between the outer wire and the mouth of the clamp (4.17, 4.18,2.53 ,4.36).

Wire failures occur very close to the restraint point, at a distance of no more than a few wire diameters. For example, examination of fatigue specimens has revealed that damage due to fretting is greatest near the clamp and decreases in intensity within a very short distance from

the termination so that away from the fixed end (in the free-field cable zone) it vanishes altogether (4.18). It follows that away from terminations it is reasonable to assume that during bending plane sections remain plane. In other words the effective shear stiffness between individual layers of a strand away from terminations may be taken to be infinite. Note that even for this limiting situation slip between wires in each layer can still take place, i.e.: the shear stiffness within the layer is finite.

Depending on the level of mean axial load on the cable, increasing cable bending deflection near the clamp will lead to inter-wire/inter-layer slip in due course, and the notion of a constant bending stiffness throughout the span, analogous to classical beam theories, is not realistic. Even for very small bending deflections for which inter-wire/inter-layer slip does not exist the constant stiffness concept based on 'solid-bar' approach appears to fail (4.18). The work of Lutchansky (4.26), which takes the helical arrangement of the wires into account, appears to offer the most satisfactory approach. This will be considered in some detail below.

The work of British Ropes (4.35) indicates that slip between the two outermost layers must take place even at rather large radii of curvature and small angular offsets.

Although outer wire strain measurements show that maximum strain occurs at the extreme fibre position (in bending terms), the work in (2.53) demonstrates that first wire fractures are located near the neutral axis.

In the following, two different cases are addressed, namely (i) bending well away from terminations and indeed any other sources of an abrupt change in curvature (for example, concentrated loads), and (ii) the more difficult problem of bending within the zone of influence of a termination. Although it is recognised that the radius of curvature in, for example, Fig.(4.2) changes rapidly along the length of the cable in the near vicinity of the clamping position, case (ii) will be developed for a constant curvature imposed on a cable fixed at one end, as a reasonable first step.

In Fig.(4.2) the curvature is obviously most severe at the rotationally restrained end, and hence interlayer wire slippage must start at this section. Two factors then combine to ensure that this slippage will be made easier to initiate between the outer and penultimate layers of wires than elsewhere, deeper, in the strand. The first factor is the build-up of "clench" (radial) forces towards the centre of the pre-tensioned strand in response to the axial load. The second factor is the reduction in plane section bending strains towards the neutral axis. Thus the interlayer shear stiffness κ between the two outermost layers, whose initial no-slip value is probably only slightly lower than the value for a pair of deeper layers, will diminish much more rapidly due to the development of slippage than is the case in the core layers. It then follows that, at least for the purposes of investigating the initiation stages of interlayer and interwire slippage near the clamp, it is reasonable to model the strand as a single layered cable with finite κ over a solid core which undergoes plane section bending.

In contrast, the free field section of the cable is modelled

as a multi-layered strand in which (for reasons of symmetry) a uniform radius of curvature is associated with plane section bending.

Finally the frequency independence of wire strains (4.24) and cable damping during lateral vibrations (4.21) is compatible with the properties of the classical Coulomb frictional model and it appears that time - dependent viscoelastic effects may be ignored.

4.3 KINEMATICS OF A HELICAL CURVE INSCRIBED ON THE SURFACE OF A CYLINDER BENT TO A CONSTANT RADIUS OF CURVATURE ρ :

This problem has been considered by Zhadnov (4.27) and solved by Lutchansky (4.26). These authors assumed that plane cross sections of the cylinder normal to the original axis remain plane and normal to the deformed axis. For the case when the radius of the cylinder, R, (which is the same as the helix radius) is much less than the toroid radius ρ it is shown that the plane section displacement along the path of the helix on the surface of the toroid, u^P, may reasonably be expressed as:

$$u^P = U(\mathrm{Sin}\theta - \mathrm{Sin}\theta_o) \qquad (4.5)$$

where $$U = \frac{k^2 R}{\rho\sqrt{R^2+k^2}}$$

The notation used is identical to that adopted by Lutchansky, Fig. (4.4). k is the pitch of the helix divided by 2π, and θ is the polar angle of the helix measured from the point at which the helix first crosses the extreme fibre position of the bent cylinder. θ_o denotes the helix

polar angle at which the toroidal section starts. Note that for the helix which starts at the tensile extreme fibre position θ_o is equal to zero; otherwise θ_o is always negative.

The total undeformed length of the helix from the start of the toroid to the position with polar angle θ is given by:

$$S_T = (\theta-\theta_o)\sqrt{R^2+k^2} \qquad (4.6)$$

4.4 FREE FIELD BENDING OF A PRETENSIONED LARGE DIAMETER MULTI-LAYER STRAND IN REGIONS REMOTE FROM END RESTRAINTS

In the light of the conclusions in Section 4.2 no-slip shear interaction is assumed between the layers. As a first approximation the effective shear stiffness between layers is assumed infinite, i.e. plane sections remain plane during bending. Later on the effect of a finite shear stiffness between layers will be considered in some detail. It is further assumed that the perturbation in axial force due to lateral movements is negligible when compared to the pretension in the strand, and that the stresses and movements are time-independent. The perturbation contact forces between wires in line-contact in each layer due to bending of the cable (and hence the change in wire axial strain) are also ignored when compared to the mean radial contact forces created by the steady pretension.

Yet again, it is postulated that each layer of

wires in the strand has enough wires for the properties to be averaged so that the layer can be treated as an orthotropic membrane. As with the cable axial stiffness calculations, two limiting cases can be identified: for small perturbations no interwire slip occurs, while for large enough disturbances full sliding can occur between the wires in line-contact in a given layer. Note that this is fully compatible with the assumption that plane sections remain plane during bending.

To demonstrate this, consider the two adjacent wires a and b in Fig.(4.5). In the undeformed state, it can easily be shown that:

$$\theta_A^a - \theta_C^a \simeq - \frac{D}{k} \operatorname{Sin}\alpha \tag{4.7}$$

where θ_A^a and θ_C^a are the polar angles of the points A and C respectively. D is the wire diameter, and α is the helix lay angle.

After the cable is bent to a radius of curvature, ρ, Equations (4.5) and (4.6) may be used to show that the changes in the lengths along the helices to A and B are:

$$\begin{aligned} dS_A^a &= U \left[\operatorname{Sin}(\theta_B^b - d\theta_o - \frac{D}{k} \operatorname{Sin}\alpha) - \operatorname{Sin}(\theta_o^b - d\theta_o) \right] \\ dS_B^b &= U \left[\operatorname{Sin}(\theta_B^b) - \operatorname{Sin}(\theta_o^b) \right] \end{aligned} \tag{4.8}$$

where $d\theta_o = \frac{-2\pi}{n}$ and n is the number of wires (helices) in the layer.

The slip S between wires a and b is then defined as:

$$S = dS_B^b - dS_A^a \tag{4.9}$$

It is seen that the kinematics of slip between two adjacent wires in a given layer is a function of cable construction (D, $\frac{k^2 R}{\sqrt{R^2+k^2}}$), toroidal radius of curvature (ρ), and the wires' position in the cross-section where the restraint (clamp) is (θ_o^b) and the section under consideration away from the termination (θ_B^b).

For $\alpha = 17.74^o$, $\frac{S}{U}$ is plotted against θ_B^b for different values of θ_o^b in Fig.(4.6). It is clear that the maximum and minimum amounts of slip occur near to the "extreme fibres" of the toroid. Given these slip data, it is possible to use the methods described in Chapters 2 and 3 to predict the axial moduli of individual layers and hence the contribution of each layer to the total bending stiffness. Maximum variation of the axial stiffnesses corresponding to the range of slip values is only about 15 percent or so. The axial stiffnesses are also very nearly independent of the mean axial load on the cable (Ref. Section 3.7). It was considered reasonable to work only with the limiting cases of no-slip and full-slip line-contact of wires in individual layers and, as a first approach, to avoid the rather tedious process of calculating the gradual variation between them which seemed to be of limited practical relevance. This is so partly because of the limitations of the present analytical techniques for cable lateral vibrations (e.g. 4.14, 4.18, 4.19, 4.21, 4.22) which

only use the concept of a constant bending rigidity.

For either the no-slip or full-slip line-contact of wires, the overall bending rigidity with plane sections remaining plane is then expressed in the form $E_{eff}I$, where $I = \frac{\pi}{4} \cdot \frac{\pi d^4}{64}$ if d is the strand outer diameter. Then, E_{eff} is a weighted mean of the layer stiffnesses:

$$E_{eff} = \sum_i E_i \lambda_i \tag{4.10}$$

where $$\lambda_i = \frac{I_{ni}}{I_o}$$

with $$I_{ni} = \frac{\pi}{4} \cdot \frac{\pi}{64} \left[(2r_i+D)^4-(2r_i-D)^4\right] \tag{4.11}$$

and $$I_o = \sum_i I_{ni} \tag{4.12}$$

where r_i is the theoretical radius for the layer calculated by Equation (2.17) and D is the wire diameter.

Note that the axial flexibilities in the individual layers, $\frac{1}{E_i}(=\frac{S_1'}{T_1'})$, (as given by Equation (3.30)) are based on the gross cross-sectional area which is very nearly $4/\pi$ times the net steel area in the strand normal cross-section. I_{ni} in the above is, then, the corresponding second moment of area of the individual layers, i, whose helix radius is r_i. Because of the slight bedding-in at the interlayer contact points, I_o is slightly different from I.

No-slip and full-slip values of E_i for the various layers of the 39mm strand (Ref.Table (2.1)) are given in Table (4.2), with the corresponding E_{eff} values for the strand in both regimes. The difference between the no-slip

and full slip free field cable bending moduli for this construction is about 13%.

4.5 LOCAL PHENOMENA NEAR THE FIXED END OF THE STRAND

Following the observations in (4.18, 4.19, 2.53), interlayer shear stiffness near the clamp changes during bending, with consequent fretting marks at the trellis points of contact.

The pretensioned large diameter strand is modelled as being composed of a solid core, which undergoes plane-section bending, covered by a single layer of helical wires whose shear interaction with the core for any given strand geometry is a function of the mean axial load on the strand and the imposed radius of curvature in the vicinity of the point of restraint. Small variations of the radius of curvature along the cable in the very close vicinity of the clamp are ignored (for a strand under free bending, radius of curvature is obviously greatest at the fixed end and is reduced fairly rapidly, as one moves away from the point of restraint). Outer wire diameters are assumed to be much less than the core diameter. The magnitude of the normal load between the outer wires and the core is assumed to stay constant throughout the bending cycle. Changes of strand diameter during bending are ignored. Furthermore, the strand axis is assumed to coincide with the neutral-axis in bending, i.e. it experiences no change of length.

Interaction of the outer wires in line-contact is modelled in a way analogous to a thin sheet with longitudinal

stringers, Fig. (4.7). Wire-core interaction is treated as an extended version of the model suggested by Lutchansky (4.26). In this work Lutchansky assumed that the interface shear was linearly proportional to the difference between the local movements of the outer wire, u, and the underlying core particle, u^p, adjacent to the wire surface. However, he did not put any experimental or theoretical values to the constant of proportionality. In what follows, his theoretical work is extended to include a quantitative treatment of the transition between no-slip and full-slip frictional interaction between the wires.

Considering the longitudinal equilibrium of stringer 2 in Fig.(4.7) gives:

$$\frac{dN_2}{dS_{c2}} = q_1 - q_2 + \kappa_2(u_2 - u_2^p) \qquad (4.13)$$

where N_2 is the axial force in the stringer (wire) number 2, dS_{c2} denotes the length of the element, q_1 and q_2 are the shear forces per unit length on either side of the element, u_2 is its stretch and u_2^p is the corresponding core particle movement under core (plane-sections) bending. κ_2 is the outerwire-core shear stiffness. For a given geometry, κ_i is a function of $(u_i - u_i^p)$ and the radial force between the outer layer and the core, which in turn is related to mean axial tension on the strand.

From Fig.(4.7b), assuming a state of pure shear in each panel

$$\gamma_1 = \frac{u_2 - u_1}{g} \qquad (4.14)$$

where γ_1 is the shear strain in panel 1 and g is the panel width. For a large number of wires in the unwrapped layer the effect of polar angles can be ignored and we can assume $g \simeq D$. It then follows that:

$$\frac{q_1}{D} = G_1'\gamma_1 = \frac{G_1'(u_2-u_1)}{D} \tag{4.15}$$

where G_1' is the shear stiffness between the wires in line-contact. For a given strand geometry G_1' is a function of (u_2-u_1) and the mean axial load on the strand.

In addition, the wire force/strain relation gives:

$$N_2 = AE \frac{du_2}{dS_{c2}} \tag{4.16}$$

where A is the wire normal cross-sectional area (assumed concentrated at the centre of the wire) and E is Young's modulus of the wire.

Using Equations (4.15) and (4.16), Equation (4.13) can be rearranged to give:

$$\frac{d^2u_2}{dS_{c2}^2} = \frac{G_1'}{AE}(u_2-u_1) - \frac{G_2'}{AE}(u_3-u_2) + \frac{\kappa_2}{AE}(u_2-u_2^P) \tag{4.17}$$

From Equation (4.5):

$$u_2^P = U(\sin\theta_2 - \mathrm{Sin}\theta_{02}) \tag{4.18}$$

where $\theta_2 = \frac{S_{c2}}{a}$, $\theta_{02} = \frac{S_{c02}}{a}$

and $a = \sqrt{R^2+k^2}$ = constant

The total undeformed length of the wire between the clamping position and position θ_2 , S_{T2} , is

$$S_{T2} = S_{c2} + |S_{c02}| \qquad (4.19)$$

S_{c02} is the length of the wire between the clamping position and the tensile extreme-fibre position (S_{c02} always negative) and S_{c2} gives the undeformed length of the wire from the extreme-fibre position to the position with the polar angle equal to θ_2.

Substituting for u_2^P as given by (4.18) into (4.17), the following differential equation is found for any wire i in the outer layer:

$$\frac{d^2u_i}{d^2S_{ci}} = \frac{G'_{i-1}}{AE}(u_i - u_{i-1}) - \frac{G'_i}{AE}(u_{i+1} - u_i) + \frac{\kappa_i}{AE}\left(u_i - U\left(\mathrm{Sin}\,\frac{S_{ci}}{a} - \mathrm{Sin}\,\frac{S_{coi}}{a}\right)\right) \qquad (4.20a)$$

Thus, if there are n wires in the outer layer, a set of n simultaneous differential equations can be established. Because of the nature of κ_i and G'_i these coupled equations are non-linear. For the limiting case of no-slip between the wires, G'_i and κ_i do not vary from one wire to another and in this case Equation (4.20a) may be rewritten as:

$$\frac{d^2u_i}{d^2S_{ci}} - \left(\frac{2G'+\kappa}{AE}\right)u_i + \frac{G'}{AE}(u_{i-1} + u_{i+1}) = \frac{\kappa U}{AE}\left(\mathrm{Sin}\,\frac{S_{ci}}{a} - \mathrm{Sin}\,\frac{S_{coi}}{a}\right) \qquad (4.20b)$$

where: $G'_i = G' = \text{Constant}$

$\kappa_i = \kappa = \text{Constant}$ for all i

4.6 DETERMINATION OF THE SHEAR STIFFNESS COEFFICIENTS, κ and G':

In a cross-laid construction, the outer layer wires touch the underlying core at a number of isolated points (contact patches) in a trellis pattern, Fig.(4.8). In the usual strand constructions the lay angles of the two outermost layers are of very similar magnitudes with opposite sense. Therefore, it is reasonable to assume that one of the two principal axes of the orthotropic pattern of the contact ellipses is parallel to the cable axis. It is further assumed that the number of such projections is large enough that any local effects can be ignored. This is analogous to the concept of contact between two bearing surfaces occurring at the tips of their surface asperities. In the light of the results presented in Chapter 1, Hertzian normal contact theory is used to compute the sizes of the contact areas and the distribution of the normal contact stresses over the individual contact regions. This, coupled with the work of Mindlin (1.39) and Vermeulen et.al. (1.41), provides an analytical frictional model which gives the shear stiffness of the individual contact patches along their principal axes. Determination of the overall shear stiffness of a large number of isolated ellipses of contact will then follow.

In Chapter 1, the present author used the relation obtained by Vermeulen et.al (1.41) to evaluate the compliance of two non-spherical bodies in contact along one of the principal axes of their elliptic contact area.

The final result, Equation (1.25b), is reproduced here:

$$\frac{d\delta_{\ell}}{dT} = \frac{\Gamma(a/b)}{\pi b G}\left(1 - \frac{\delta_{\ell}}{\delta_{\ell max}}\right)^{-\frac{1}{2}} \qquad (4.(1.25b))$$

where $G = \frac{E}{2(1+\nu)}$

$$\delta_{\ell max} = \frac{3\mu P_R(1+\nu)}{\pi b E}\,\Gamma(a/b)$$

and

$$\Gamma(a/b) = \begin{cases} K-\nu D & \text{for } a<b \\ \pi(2-\nu)/4 & a=b \\ \frac{b}{a}(K-\nu B) & a>b \end{cases} \qquad (4.(1.21))$$

This result only applies to the first application of load with zero residual tangential stresses and displacements at the onset of movement.

For two straight cylinders in contact the ratio $\frac{a}{b}$ is a function of the angle between the crossed cylinders alone (Ref. Section 1.2). The wires in a strand are of helical shape with curvatures, κ', equal to $\frac{\sin^2\alpha}{r}$ - Ref. Equation (2.16). It then follows that strictly speaking $\frac{1}{R'_1}$ and $\frac{1}{R'_2}$ in Equations (1.6) are not equal to zero. In such a case, substituting for

$$R_1 = D/2 \quad , \qquad R'_1 = \frac{r}{\sin^2\alpha_1}$$

$$R_2 = D/2 \quad , \qquad R'_2 = \frac{r}{\sin^2\alpha_2}$$

into Equations (1.6d) and (1.6e) will lead to the magnitude of the parameters K_D and θ' which are then used to determine the size of the contact patch between the two helical

cylinders - Equations (1.6a) and (1.6b). In the above, D is the diameter of the wires, α the helix angle with subscripts 1 and 2 denoting the layer number. r is the radius of the cylinder on which the contact patches between the two outermost layers lie. It is reasonably given by

$$r = r_1 - \frac{D}{2}$$

where r_1 is the helix radius of the outer layer.

Table (1.1) only covers the range $0<\cos\theta'<0.99$. An extension for $0.99<\cos\theta'<1$ is given by Kornhauser (4.37) and his results are quoted in Table (4.3).

The method described in Chapter 2 may be used to obtain reasonable estimates of the magnitude of hoop and radial forces induced in the cable under the action of a steady mean axial load. However, it must be noted that the formulation for interwire contact forces was, strictly speaking, developed only for strand sections away from the end-effects.

The magnitude of b (which can be either the semi-major or the semi-minor axis depending on the direction of the tangential force T) may be obtained by using Equations (1.6) with the proviso that in Equations (1.6), a represents the major semi-axis and b is the minor semi-axis.

Following Kelsey, Gellatly and Clark (4.38), let the direction of the applied shear force be denoted by subscript 1 and the direction normal to it (in the plane of the contact patch) by subscript 2. Due to the orthotropic

nature of the problem, the direction of the resultant shear displacement, Δ, does not coincide with the direction of the applied shear force, Fig.(4.9). The displacement Δ can then be resolved into two components along directions 1 and 2. The shear along directions 1 and 2 can be expressed for the shear strains as:

$$\begin{bmatrix} \gamma_1 \\ \gamma_2 \end{bmatrix} = \begin{bmatrix} f_{11} & f_{12} \\ f_{21} & f_{22} \end{bmatrix} \begin{bmatrix} \tau_1 \\ \tau_2 \end{bmatrix} \tag{4.21}$$

where F_{ij} is the flexibility matrix, or alternatively by:

$$\begin{bmatrix} \tau_1 \\ \tau_2 \end{bmatrix} = \begin{bmatrix} k_{11} & k_{12} \\ k_{21} & k_{22} \end{bmatrix} \begin{bmatrix} \gamma_1 \\ \gamma_2 \end{bmatrix} \tag{4.22}$$

where K_{ij} is the stiffness matrix, and

$$\mathbb{F} = \mathbb{K}^{-1} \tag{4.23}$$

Treating the stiffnesses as a second order tensor

$$\begin{aligned} k_{11} &= k_{xx}\,\mathrm{Cos}^2\alpha + k_{yy}\mathrm{Sin}^2\alpha \\ k_{22} &= k_{xx}\,\mathrm{Sin}^2\alpha + k_{yy}\mathrm{Cos}^2\alpha \\ k_{12} &= k_{21} = \frac{k_{xx}-k_{yy}}{2}\,\mathrm{Sin}2\alpha \end{aligned} \tag{4.24}$$

where α is the lay angle (assumed to be the same in the two cross-laid outer layers). k_{xx} and k_{yy} denote the shear stiffness of the contact patch along its principal directions (axis X is parallel to the direction of the strand axis).

For the no-slip case Mindlin (1.39) was the first

to show that with $\nu=o$, the shear compliance across the contact patch is isotropic. To demonstrate this, set $\nu=o$ into expressions (1.21)

$$\Gamma(a/b) = K \quad \text{for} \quad a<b$$

$$\Gamma(a/b) = \frac{b}{a}K \qquad a>b \tag{4.25}$$

That is for the no-slip case with $\nu=o$; $k_{xx}=k_{yy}$ and hence $k_{21}= k_{12}= 0$.

For the present problem, $\tau_2=0$. Using Equations (4.22) with $\tau_2=0$ and $k_{12}= k_{21}= 0$ we get:

$$\tau_1 = k_{11}\,\gamma_1$$

and $$\gamma_2 = 0 \tag{4.26}$$

where $$k_{11} = k_{xx}$$

$$= \left(\frac{d\delta_\ell}{dT}\right)_{xx}$$

$$= \frac{K}{\pi aG}\left(1- \frac{u-u^P}{\delta_{\ell max}}\right)^{-\frac{1}{2}} \qquad \text{for} \quad \Gamma\left(\frac{a}{b}\right)=K$$

a is the length of the semi-major axis and direction 1 is coincident with the wire axis.

Poisson's ratio for steel is, however, about 0.28, therefore, $k_{xx} \neq k_{yy}$. In this case the problem is not isotropic. The exact distribution of shear stress or strain at the points of contact presents a very complex problem. The elastic shear modulus in any direction may be obtained by the use of the method used by Kelsey et.al. (4.38) and Ueng, Underwood, and Liu (4.39) who were interested in the

theoretical determination of the elastic shear modulus for formed sandwich cores.

With $\tau_2=0$ and γ_2 free to develop , Equations (4.21) and (4.22) give:

$$\tau_1 = \frac{1}{f_{11}} \gamma_1$$

where

$$\frac{1}{f_{11}} = k_{11} - \frac{k_{12}^2}{k_{22}} = I \qquad \text{(say)} \qquad (4.27)$$

Note that for $0<\nu<0.5$, the stiffness in the direction of the major axis, k_{xx}, is less than the stiffness in the direction of the minor axis, k_{yy} (Ref.Section 1.3) and $\frac{k_{12}^2}{k_{22}} \neq 0$.

The overall effect of the outer wire to core shear interaction for a large number of contact points may reasonably be taken into account by expressing the interaction coefficient, κ, as, Fig.(4.8)

$$\kappa = \frac{I}{x} \qquad (4.28)$$

where x is the spacing between the contact patches along the outer layer.

In general, x may reasonably be expressed as (Phillips, Miller and Costello (4.40)), Fig. (4.10)

$$x \simeq \frac{2\pi r}{n_2} \frac{\text{Cos } \alpha_2}{\text{Sin}(\alpha_1-\alpha_2)} \qquad (4.29a)$$

where α_1 and α_2 are lay angles in layers 1 (outer) and 2, respectively. n_2 denotes the number of wires in the second

layer. $r = r_1 - \frac{D}{2}$, where r_1 is the helix radius in the outer layer and D is the wire diameter in that layer.

It is also worth noting that the spacing of the contact points on the convex side of the wires in the second layer, x', is in general given by

$$x' = \frac{2\pi r}{n_1} \quad \frac{\mathrm{Cos}\alpha_1}{\mathrm{Sin}(\alpha_1 - \alpha_2)} \tag{4.29b}$$

where n_1 is the number of wires in the outer layer.

Using Equations (4.29a) and (4.29b):

$$\frac{x}{x'} = \frac{n_1}{n_2} \cdot \frac{\mathrm{Cos}\alpha_2}{\mathrm{Cos}\alpha_1} \tag{4.29c}$$

The original theoretical work of Mindlin and his successors concentrates on the case when the tangential force is directed along one of the principal axes of the ellipse of contact. The extension of their work to predict the variation in the tangential force, T, making an angle, α, with the major axis of the contact patch is discussed below.

Equation (4.28) gives the no-slip tangential stiffness along any arbitrary direction, α. As a first approximation, the familiar spring and dashpot model with its bi-linear elasto-plastic characteristics (Fig.4.11) may be used to predict the onset of full-slippage. In this model, shear deformation between the two surfaces is elastic until $T=\mu P$, when full sliding at constant T takes place. It then follows that κ for $u-u^P < \frac{\mu P_R}{I}$ is calculated from Equation (4.28). Once $u-u^P = \frac{\mu P_R}{I}$, gross sliding takes place, and

$$\kappa = \frac{\mu P_R}{x(u-u^P)}$$

where x is as defined in Equation (4.28). Note that κ is a secant modulus.

As shown in Section 1.3, the gradual transition from the no-slip regime to the full-slip regime in Mindlin's model leads to a theoretical shear displacement at the onset of full-slippage which is 1.5 times greater than the elastic displacement calculated on the no-slip assumption. In other words, the neglect of partial-slip phenomena will lead to rather significant errors in the predicted value at full-slip initiation. Therefore, the gradual non-linear transition from the no-slip to full-slip threshold must be taken into account.

From Equation (1.20) the relationship between shear deformation, δ, and tangential force, T, is of the form:

$$\delta = C \frac{\Gamma(\frac{a}{b})}{b} \left[1-(1- \frac{T}{\mu P_R})^{2/3}\right]$$

where $C = \frac{3(1+\nu)}{\pi E} \mu P_R$

and $C \frac{\Gamma(\frac{a}{b})}{b} = \delta_{max}$

For a given material (i.e. known μ, ν and E) and normal contact force, P_R, the difference between the circular contact between two spheres (an axi-symmetric problem), and that of two non-spherical bodies, lies in the value assigned to the parameter $\frac{\Gamma(a/b)}{b}$. This parameter is a function solely of the dimensions of the contact patch as determined by the normal Hertzian solution.

The above equation has been shown to apply for the case of $\alpha=0$ and/or $\alpha=90^{o}$. For the case of $0<\alpha<90^{o}$, it is still reasonable to assume that

$$\delta^{\alpha}= \delta^{\alpha}_{max} \left[1-(1- \frac{T}{\mu P_R})^{2/3}\right] \tag{4.30}$$

where δ^{α} denotes the shear displacement in the direction of the applied tangential force T which is directed at an angle α to the major principal axis of the contact patch. δ^{α}_{max} corresponds to the displacement at the onset of sliding.

Using the method described before (Ref. Section 1.3), Equation (4.30) leads to:

$$\frac{d\delta^{\alpha}}{dT} = \frac{2\delta^{\alpha}_{max}}{3\mu P_R} (1- \frac{\delta^{\alpha}}{\delta^{\alpha}_{max}})^{-\frac{1}{2}} \tag{4.31}$$

The no-slip tangential compliance is then found by setting $\delta^{\alpha}=0$ in Equation (4.31):

$$(\frac{d\delta^{\alpha}}{dT})_{no\text{-}slip} = \frac{2}{3} \frac{\delta^{\alpha}_{max}}{\mu P_R} \tag{4.32}$$

where

$$\frac{1}{I} = (\frac{d\delta^{\alpha}}{dT})_{no\text{-}slip} \tag{4.33}$$

From Equations (4.32) and (4.33)

$$\delta^{\alpha}_{max} = \frac{3}{2} \frac{\mu P_R}{I} \tag{4.34}$$

Using Equations (4.24) and (4.27), the no-slip stiffness in direction α, I, is found by assuming:

$$K_{xx} = \left(\frac{dT}{d\delta^{\alpha}}\right)_{\text{no-slip}}^{\alpha=0}$$

$$K_{yy} = \left(\frac{dT}{d\delta^{\alpha}}\right)_{\text{no-slip}}^{\alpha=90^{o}} \qquad (4.35)$$

where K_{xx} and K_{yy} are the no-slip tangential stiffnesses along the major and minor axes of the ellipse of contact, respectively. These may be calculated from Equations (1.25b) and (1.21).

It is interesting to note that from Equation (4.34) with a constant μP_R, the ratio of initial tangential compliance, $\left(\frac{d\delta^{\alpha}}{dT}\right)_{\text{no-slip}}$ to δ^{α}_{max} is in general a constant, and independent of α.

Substitution of δ^{α}_{max} from Equation (4.36) into Equation (4.30) leads to:

$$\delta^{\alpha} = \frac{3}{2}\,\frac{\mu P_R}{I}\left[1-\left(1-\frac{T}{\mu P_R}\right)\right]^{2/3} \qquad (4.36)$$

Calculation of the Secant modulus, κ, is then as follows:

i) For a mean axial load on the strand, obtain the corresponding cable axial strain, ε_c.

ii) Use the method developed in Chapter 2 to compute the distribution of radial and hoop forces.

iii) Knowing P_R, calculate the size of major and minor principal axes of the contact patch (Equations 1.6) and use Equations (1.25b) and (1.21) to compute no-slip values of the tangential stiffnesses K_{xx} and K_{yy}.

iv) From Equations (4.24) and (4.27), find the no-slip tangential stiffness, I, at a direction α to the principal major axis and calculate δ^{α}_{max} from Equation (4.34).

v) For any given slip, $(u-u^P)$, check whether the slip is less or greater than δ^{α}_{max}. If $(u-u^P) < \delta^{\alpha}_{max}$ use Equation (4.36) to compute the corresponding tangential force, T. κ will then be:

$$\kappa = \frac{T}{(u-u^P)x} \tag{4.37a}$$

If $u-u^P \geqslant \delta^{\alpha}_{max}$

$$\kappa = \frac{\mu P_R}{(u-u^P).x} \tag{4.37b}$$

where x is defined by Equation (4.29a).

Theoretical calculations of the shear interaction between adjacent wires are fully dealt with in Section 1.3. For cylinders in line-contact:

$$\delta_{\ell} = \delta_{\ell max}\left[1-(1-\frac{T}{\mu P})\right]^{2/3}$$

where $\delta_{\ell max} = 2\Delta_{\ell max} = \frac{3\mu P S_{22}}{2(1-\nu)}$ (4.(1.23))

$\delta_{\ell max}$ is the relative displacement at the onset of full slippage for two cylinders in line contact. Equations (4.(1.23)) apply to the first quarter of the first cycle of a repeated tangential movement. Note that P and T in the above. are normal and tangential forces per unit length, respectively.

For the present bending model:

$$G_i' = \frac{\left(\frac{q_i}{D}\right)}{\left(\frac{u_{i+1}-u_i}{D}\right)} \qquad (4.38)$$

Taking $q_i=T$ and $(u_{i+1}-u_i)=\delta_\ell$, Equations (4.(1.23)) give

$$\frac{q_i}{\mu p} = 1-(1-\frac{u_{i+1}-u_i}{\delta_{\ell max}})^{-\frac{1}{2}} \qquad (4.39)$$

Note that the quantity $\frac{u_{i+1}-u_i}{\delta_{\ell max}}$ in the above is always greater than or equal to zero.

For each given ratio of $\frac{u_{i+1}-u_i}{\delta_{\ell max}}<1$ the secant modulus, G_i', may easily be obtained by Equations (4.39) and then (4.38). For $\frac{u_{i+1}-u_i}{\delta_{\ell max}}>1$

$$G_i' = \frac{\mu p}{(u_{i+1}-u_i)}$$

4.7 RESULTS FOR THE SHEAR STIFFNESS MODULI AND DISCUSSION

The variation of the theoretical shear stiffness, κ, along the direction $\alpha\simeq 17.7^o$, is given as a function of relative slippage between the outer wire and the core of the 39mm O.D. strand in Fig.(4.12). Similar predictions for $\alpha\simeq 17.7^o$ from the simple (but less accurate) bi-linear model, plus the two limiting cases of $\alpha=0$ and $\alpha=90^o$ as calculated by Equations (4.(1.25b)) and (4.(1.21)), are also included in this same figure. The assumed mean axial load for all these plots is 0.410MN.

In practice, there is considerable uncertainty about the exact value assigned to the parameter μ. Moreover, the predicted magnitude of the normal contact force between the two layers is strictly speaking derived for sections away from the terminations. It then follows that, at least for the present example, the difference between the two cases of $\alpha \simeq 0$ and $\alpha \simeq 17^{o}$ may not be of practical significance. However, in view of the vast variety of cable constructions, it is imprudent to generalize the conclusion.

In the present work, the transformation of the shear stiffness between the outer wire and the underlying core has been formulated for the special case of equal lays of opposite signs in the two outermost layers. Exploiting symmetry then leads to the convenient result that the principal axis of orthotropy on the contact patch is parallel to the axis of the cable. Extension of the method to the case of a strand with unequal lay angles with general direction (i.e. not necessarily of opposite sense) is straightforward. The only major modification required involves the determination of β, the angle between the major principal axis of the contact patch and the axis of the strand, since these are no longer parallel. This can be done, using the classical Hertzian geometrical relations for the three dimensional contact problem (e.g. Ref.(4.41)). α in Equations (4.24) is replaced by β, and the appropriate value for the parameter x, which defines the spacing of the contact patches along the outer wires as given by Equation (4.29a), must also be used.

4.8 SOLUTION OF THE DIFFERENTIAL EQUATION (4.20)

Equations (4.20) represent a system of non-linear ordinary differential equations where the number of the equations is the same as the number of wires in the outer layer. The linear solution to these equations only applies to position $\theta_i=\theta_{Oi}$ (i.e. at the mouth of the clamp), where it may reasonably be assumed that there can not be any relative slippage between the outer wires in line-contact, or between the outer wires and the core. For any other θ, these equations are all non-linear and coupled. The solution of such a system of equations is discussed later but,as a first step, the interference of wires in line contact was ignored (i.e. it was assumed that $G_i'=0$). This greatly simplifies the problem; the resulting system of equations becomes uncoupled, and numerical solutions have been obtained.

4.8.1 No-Slip (linear) solution with $G_i'=0$

With zero shear stiffness between wires in the outer layer and a constant κ, Equation (4.20) reduces to the one obtained by Lutchansky (4.26):

$$\frac{d^2u}{dS_c^2} - \frac{\kappa u}{AE} = -\frac{\kappa U}{AE}\left(\mathrm{Sin}\,\frac{S_c}{a} - \mathrm{Sin}\,\frac{S_{co}}{a}\right) \qquad (4.40)$$

In the derivation of Equation (4.40), no distinction was made between the core outer radius and the distance between the outer wire centres and the core centre. In practical strand constructions, wire diameters are significant compared with the cable diameter and to take this into account, we still assume

wire diameters to be very small fractions of the cable diameter, but take

$$a = \sqrt{R^2 + k^2}$$

with

$$R \simeq r_1 - \frac{D}{2}$$

or

$$a \simeq \sqrt{(r_1 - \frac{D}{2})^2 + k^2} \qquad (4.41)$$

R in the above denotes the radius of the ideal core over which the outer wires of (now) finite diameter D and helix radius, r_1, are sliding. R corresponds to the radius of the cylinder whose outer surface is covered by the contact patches. Outer wire diameters should, obviously, be small enough, so that the bending strains at their extreme fibre positions remain insignificant compared with the corresponding bending strains on the core surface.

For a strand rigidly clamped at one end and bent to a constant radius of curvature, Lutchansky showed that

$$\frac{du}{dS_c} = \frac{U\acute{a}\kappa}{1 + \frac{a^2\kappa}{AE}} \left[-\frac{1}{a} \sqrt{\frac{1}{\kappa AE}} \cdot \exp\left(\sqrt{\frac{\kappa}{AE}}\, a(\theta_o - \theta)\right) . \mathrm{Sin}\theta_o + \frac{1}{AE}\mathrm{Cos}\theta \right] \qquad (4.42)$$

where $\frac{du}{dS_c}$ is the strain in any chosen wire (depending on the value assigned to θ_o) at any position along the strand-determined by the parameter θ. With slip between layers included in the model, expression (4.42) only applies to the clamping point - i.e. $\theta = \theta_o$. At this section no inter-layer slip can take place and κ can be determined by Equation (4.28).

4.8.2 Free Field Solutions for the Two Extreme Cases of Zero and Infinite Friction

With finite but constant κ for all θ and θ_o, the oscillatory free field wire axial strain (obtained by letting $\theta \to \infty$ in Equation (4.42)) is:

$$\frac{du}{dS_c} = \frac{\kappa k^2 R \cos\theta}{\rho\left[AE+\kappa(R^2+k^2)\right]} \tag{4.43}$$

For the extreme case of plane-section bending (i.e. $\kappa \to \infty$):

$$\left.\frac{du}{dS_c}\right|_{\kappa\to\infty} = \frac{k^2 R \cos\theta}{\rho(R^2+k^2)} \tag{4.44a}$$

by definition

$$\frac{k^2}{R^2+k^2} = \cos^2\alpha$$

hence

$$\left.\frac{du}{dS_c}\right|_{\kappa\to\infty} = \left(\frac{R\cos\theta}{\rho}\right)\cos^2\alpha \tag{4.44b}$$

From classical beam theory, the first term (in the brackets) represents the direct (i.e. parallel to the cable axis) strain , ε_c, at position θ.

In other words

$$\left.\frac{du}{dS_c}\right|_{\kappa\to\infty} = \varepsilon_c \cos^2\alpha \tag{4.44c}$$

which is similar to the equation derived by Hruska (2.1) for a helical strand under uniform axial tension. (Ref. Equation (2.12)). Hruska assumed the changes in the lay angle and helix diameter to be very small and, hence, was able to

linearize the kinematics of the helix. In recent work, Knapp (4.42), who only considered the bending of strands in the free field (i.e. away from the terminations), obtained a more accurate version of Equation (4.44c), which in the present notation is:

$$\left.\frac{du}{dS_c}\right|_{\kappa\to\infty} = \left[1+\left(2\,\frac{R}{\rho}\,\cos\theta + \frac{R^2}{\rho^2}\cos^2\theta\right)\cos^2\alpha\right]^{\frac{1}{2}} - 1 \qquad (4.44d)$$

Equation (4.44d) was obtained by a minor manipulation of the original kinematical relationships derived by Lutchansky. For $\frac{R}{\rho} \ll 1$, Equations (4.44c) and (4.44d) give almost identical answers.

With $\kappa = 0$ (i.e. no frictional shear interaction), Equation (4.43) gives $\frac{du}{dS_c} = 0$. Thus for this case, the outer wires will have no axial strain, and only bend about their own axes. Significant slippage will then take place between the outer wire and the core, which is assumed to undergo plane section bending. The total length of an outer wire's axis will remain unchanged simply because there are no external forces acting along the wire.

The mathematical theory of open coiled helical springs has been covered by an enormous body of literature. Modelling of helical strands (as well as ropes) in bending as an assemblage of a number of frictionless helical wires, all bent to the same radius of curvature, dates back nearly eighty years to a classic paper by Chapman (4.43). Bending of the cable will lead to slight changes in cable diameter and lay angle of individual wires. The individual frictionless

wires will be subjected to bending as well as torsional loading. There is also the possibility that the frictionless wires within a layer will interact with each other at a low enough radius of curvature (Ref. Mitchell and Woodall (4.11)). In Lutchansky's model, the cable neutral axis is assumed to coincide with the centre-line of the strand. It also ignores changes in the cable diameter. Glushko et.al. (4.44), on the other hand, argue that in the presence of changes in cable diameter, this is not strictly true. Glusko's rather oversimplified model, however, is not relevant to the case of multilayered helical strands subjected to a high level of pretension before the radius of curvature is imposed on it. In this case the wires are firmly locked in their position by the external axial force and are unlikely to undergo the type of deformation as considered by Glushko.

4.8.3 Results for Finite κ

For the no-slip case, Lutchansky used Equation (4.42) to show that the highest stress occurring at the clamp is in the wire with:

$$\theta_o^{max} = \tan^{-1}\left(-\frac{1}{a}\sqrt{\frac{AE}{\kappa}}\right) \qquad (4.45)$$

Variation of κ with shear displacement for various mean axial loads on the 39mm O.D. strand is presented in Fig.(4.13). Figs.(4.14) to (4.16) include plots of wire axial strains at the clamp versus the change in the radius of curvature in this same strand. These plots cover three mean axial loads of 0.410, 0.205 and 0.103 MN. Wire strains are

only plotted for the range $-180 \leq \theta_o \leq 0$; as for $-360^o \leq \theta_o \leq -180^o$ the pattern repeats itself with a mere change in the sign of wire strains.

From the figures it is concluded that, for the present strand, wire axial strains at the clamp are greatest in the neighbourhood of the extreme fibre position (in terms of the classical plane section bending theory). Their exact location is determined by the no-slip value of κ in Equation (4.45) which, in turn, is dependent on the level of mean axial load on the strand. Variation of no-slip κ over the full practical range of cable axial loads is not very significant. It then follows that, θ^o_{max} for the present steel strand construction does not vary significantly with the level of mean axial load on the cable. On the other hand the level of wire axial strains near the neutral axis is much less than those near the θ^o_{max} position. According to Hobbs et.al. (2.53) , however, first wire fractures in free bending tests were invariably located near the neutral axis. It then follows that the no-slip wire axial strains at the fixed termination, by themselves, cannot be the true underlying factor dictating the cable's fatigue life. In the next section, it will be demonstrated that the primary mechanism for fatigue initiation must be the fretting action between the outer wires and the underlying core. To do this, it is necessary to consider the gradual transition from no-slip to full-slip and beyond, as a function of the level of mean axial load and imposed radius of curvature on the strand in the vicinity of the clamp.

4.8.4 Non-linear Solution

The non-linear version of Equation (4.20) with proper (variable) κ values has been solved by a numerical NAG routine with $G_i'=0$. The routine integrates a system of first-order ordinary differential equations over a range with suitable initial conditions, using a variable-order variable-step Adams method (4.45) and returns the solution at points specified by the user.

To use the routine, substitute

$$y_1 = u$$

$$y_2 = \frac{du}{dS_c} \qquad (4.46)$$

Using the above transformation in Equation (4.20a) with $G_i'=0$ for all i

$$\frac{dy_1}{dS_c} = y_2$$

$$\frac{dy_2}{dS_c} = \frac{\kappa y_1}{AE} - \frac{\kappa U}{AE} \cdot \left(\sin\left(\frac{S_c}{a}\right) - \sin\left(\frac{S_{co}}{a}\right)\right) \qquad (4.47)$$

where the subscript i is dropped, because the equation is the same for all the wires. Equations (4.47) are two simultaneous first order differential equations of the form:

$$y_i' = F_i(S_c, y_1, y_2), \quad i=1,2 \qquad (4.48)$$

Note that κ in Equation (4.47) is itself a non-linear function of y_1. The NAG routine integrates the system of Equations (4.48) from $S_c=S_{co}$ to $S_c= S_{CF}$ (subscript F stands for final) as an initial value problem. The system is defined by a subroutine

FCN supplied by the user, which evaluates F_i in terms of S_c, y_1 and y_2. The initial values for our present problem are:

$$\text{at } S_{co} = a\theta_o$$

$$\begin{cases} y_1 = o \\ y_2 = \dfrac{Ua\kappa_{ns}}{1+\dfrac{a^2\kappa_{ns}}{AE}} \left[-\frac{1}{a}\sqrt{\frac{1}{\kappa_{ns}AE}}\,\mathrm{Sin}\theta_o - \frac{1}{AE}\mathrm{Cos}\theta_o \right] \end{cases} \qquad (4.49)$$

where κ_{ns} is the no-slip value of κ, which represents the shear stiffness between the outer wire and the core at the clamp (i.e. position $\theta=\theta_o$). For all other θ, κ is a non-linear function of slip between the two elements, $(u-u^P)$. The last expression in Equations (4.49) is obtained by setting $\theta=\theta_o$ in Equation (4.42).

The present bending model only covers the case of a monotonically increasing radius of curvature, ρ, from a state of zero curvature, with zero residual stresses and/or displacements at the contact patches (i.e. first quarter of the first cycle of a repeated bending movement). An interesting feature of the model is that even for this loading case, changes of slip direction between the outer wire and the core may take place at various positions along the length of the wire. Alternatively, because of the helical nature of the wires and consequent periodic changes in the parameter u^P, which is a function of the polar angle, θ(Ref.Equation (4.5)), plots of the variable $(u-u^P)$ as a function of the length

of the wire from the clamp are not monotonically increasing (or algebraically decreasing as the case may be) and exhibit turning points. These turning points obviously cause sudden changes of the shear stiffness, κ, to the no-slip value.

The computer program, for its initial run, ignores such sudden changes in the shear stiffness and assumes the secant modulus, κ, to decrease monotonically from its no-slip value at the clamp to its final "reduced" magnitude at position S_{cf}. The integration is carried out for a total undeformed length of the helix from the start of the toroid to the position with polar angle θ_f. Values of u, $\frac{du}{dS_c}$ and $(u-u^P)$ at a number of equally spaced mesh points along the wire, as specified by the user, are stored in the memory. Subsequent systematic search through stored values of $(u-u^P)$ starting from the clamp, reveals the possible occurrence of a turning point in the wire section under consideration. If no turning points are found, the results are printed and program is terminated. On the other hand, if a turning point is identified, its position along the wire, S_{TP}, and corresponding $(u-u^P)$ is established by the simple interpolation formula (4.46)

$$x_m \simeq (\tfrac{1}{2} - \frac{\Delta y_o}{\Delta^2 y_o})h \qquad (4.50a)$$

$$y_m \simeq y_1 - \frac{(\Delta y_1 + \Delta y_o)^2}{8\Delta^2 y_o} \qquad (4.50b)$$

where x_m is the abscissa of the maximum (or minimum) and y_m represents the corresponding maximum (or minimum) ordinate while readings are taken at equally spaced points x=o, h, 2h near the maximum (or minimum) of the function y=f(x) and

$$\Delta y_o = y(x_o+h) - y(x_o) \tag{4.50c}$$

$$\Delta^2 y_o = y(x_o+2h) - 2y(x_o+h) + y(x_o) \tag{4.50d}$$

For the present problem a spacing of 2mm. was used throughout the computer runs.

The NAG Library may now be used to integrate the differential Equation (4.20) from position $S_c = S_{TP}$ to position with polar angle θ_f, as an initial value problem. The shear stiffness at position $S = S_{TP}$ is that of no-slip, and initial values of u and $\frac{du}{dS}$ for the second run are equal to the results from the previous run at this same position. Slip between the wire and the core, δ^α, is, however, not equal to $(u-u^P)$ but is given by:

$$\delta = |u-u^P| - |u-u^P|_{TP} \tag{4.51}$$

where $|u-u^P|_{TP}$ corresponds to that obtained at position S_{TP} from the first run. δ^α in Equation (4.36) is now the incremental slip over that at position S_{TP}. The process is repeated until the whole region $S_{co} < S_i < S_{cf}$ is analysed.

4.8.5 Results For the Non-linear Case

Fig. (4.17) gives the variation of $(u-u^P)$ along the wire with $\theta_o = -108^o$ of the 39mm O.D. strand under a mean axial load of 0.410 MN and subjected to a uniform radius of curvature equal to 20m. The corresponding variations of the shear stiffness, κ, along the length of the wire are also included. At the clamp, $S_c = -108.83$mm and $(u-u^P) = \delta^\alpha = 0$. As we move along the wire away from the clamp, $(u-u^P)$ increases

in magnitude while its associated value of κ decreases monotonically from the no-slip magnitude at the clamp. Once a turning point in the variation of the parameter $(u-u^P)$ occurs, a sudden jump takes place in the magnitude of κ to its no-slip level and δ^α for the second computer run is set to zero. Further variations of δ^α with S_c from this position are given by the curve labelled (a) which is obtained from Equation (4.51).

In a discussion to (4.26), Poffenberger and Komenda (4.47) argued that the rub marks at the trellis points between the wires show that the wires must have slipped relative to each other and, in consequence, they concluded that, at some point in time there must have been zero shear interaction. The present analysis confirms the occurrence of full-sliding of wires over each other, for certain combinations of mean axial load and imposed radius of curvature, as suggested by (4.47). However, full sliding under a given normal load is not a zero shear interaction condition, although it is a condition with zero tangent shear modulus. Shear forces between the two surfaces do exist and will change the state of the axial stress in the outer layer wires. The clue lies in the way Equation (4.13) is set up. κ in this equation represents a secant (and not a tangent) shear modulus. For the special case of a straight wire resting on a substrate with friction included, mobilization of these frictional stresses (i.e. full-sliding condition), will, obviously, lead to a linear increase of the axial force along the wire's length. On the other hand, in the case of wires with helical shapes, the full-sliding situation leads to a

non-linear transfer of axial forces to the wires, with possible reversal in the direction of relative slippage.

Variations of wire axial stresses (along the element with $\theta_o = -108^o$ of the 39mm O.D. strand) as a function of the distance from the clamp are presented in Figs.(4.18) and (4.19). These plots cover a wide range of changes in the radius of curvature, ρ, and correspond to two mean axial loads of 0.410 and 0.205 MN. These figures also give the position along the wire where a change occurs in the direction of slip. The location of such points, for a given mean axial load and strand construction, is a function of the radius of curvature, ρ.

Changes of $(u-u^P)$ along the length of various wires with $0 < \theta_o < -180^o$ are given in Figs.(4.20) and (4.21). Mean axial load is taken as 0.410MN, and a radius of curvature equal to 20m has been assumed for all the plots. It is most interesting to note that maximum slippage between the outer wires and the core occur in the neighbourhood of the neutral-axis (in the present example: $\theta_o \simeq -108$). The locations along the individual wires where the turning points (i.e. jumps in the shear stiffness coefficient, κ, to the no-slip value), in the $(u-u^P)$ versus S_T plots occur, are different for different wires. Corresponding plots for the range $-360^o < \theta_o < -180^o$ are not all included, as the pattern repeats itself with a mere change in the sign of the parameter $(u-u^P)$.

Finally, the plots in Figs. (4.22) and (4.23) confirm that the magnitude of the relative slippage is

invariably greatest in the neighbourhood of the neutral axis for all values of the radius of curvature and mean-axial loads of 0.410 and 0.205 MN. These plots are given for points at a fixed distance of 2mm from the clamp.

For practical mean axial loads, and moderate radii of curvature, it appears that a rapid transition from the no-slip to full-slip regime and beyond can take place in the near vicinity of the clamp. This will obviously be of prime importance in the fatigue analysis of the strand in free bending. The most probable mode of fatigue failure under this type of loading mechanism, has in practice been identified as that of fretting at the trellis points between the wires (Ref. Section 4.1). In particular, the present model can successfully explain the observations regarding the location of first wire failures in the free bending tests reported by Hobbs et.al. (2.53). These were all invariably located near the neutral-axis, which according to the present analysis is the location where maximum slippage (and hence fretting) takes place. The non-linear theory in its present form, gives quantitative answers at positions other than $\theta=\theta_o$ for only the first quarter cycle of a repeated bending process. However, the qualitative conclusions should hold in general.

4.9 LIMITATION OF THE PRESENT MODEL AND SCOPE FOR FUTURE WORK

The multi-layered large diameter strand has been modelled as a solid core, undergoing zero shear deformation

(i.e. infinite interlayer shear stiffness),covered by a layer of wires whose shear stiffness with the solid core is finite. In Section 4.6 a method is proposed for calculating the shear stiffness in any direction on the contact patch. Although only the case of cross-laid outermost layers with equal lay angles has been considered in extenso, the method may easily be extended to the case of a strand with unequal lay angles with general direction (i.e. not necessarily of opposite sense) as discussed in Section 4.7. Moreover, using the theoretically derived values of interwire contact forces in the normal and hoop directions throughout the strand, it is straightforward to calculate the finite values of the interlayer shear stiffnesses throughout the cable in any desired direction on the individual contact patches. Calculation of the secant shear stiffness for wires in line-contact can also be easily carried out for all the individual layers. Theoretical normal interwire contact forces have, however, been calculated for cable sections away from the terminations. Their application to cable sections near the end fittings will probably not be free from errors. It is extremely difficult to quantify the extent of the error either experimentally or by theory. Such errors should not, however, invalidate the qualitative conclusions from the model, and in fact are probably less significant than those due to uncertainties in choosing the correct value for the coefficient of friction, μ.

Before making an attempt to analyse the whole cable with finite shear stiffness between all its layers, it would be reasonable to carry out the following:

i) The differential equations taking the effect of inter-wire interaction in the outer layer into account, have already been set up (Ref. Equation (4.20a)), and they may be solved using the same NAG routine as before. The number of equations in this case is, however, n times that in the previous problem, where n is the number of wires in the outer layer. A difficulty may arise in determining the initial conditions for the equations, at position $\theta=\theta_o$. As a first approximation, it is believed reasonable to assume that, at the mouth of the clamp (only) the wires do not touch each other in line contact. This assumption is felt to be reasonable for zinc poured sockets, where at the mouth of the socket, wires are embedded in a zinc matrix. The initial conditions will then be of the same form as before.

ii) Only the first quarter of the first cycle in a repeated bending movement has been solved in this thesis. Extension of the model to cover the case of repeated bending would be most useful for fatigue analysis of the strand. Finally, the outer wires touch the core at a number of isolated contact patches whose shear transfer mechanism has, for analytical convenience, been modelled as a contineous function all along the wire. It then follows that the present model is more capable of demonstrating the general overall characteristics of the system, rather than its exact detailed behaviour at the contact regions. For example, for a contact patch spacing of x=7mm, the theory may, for

certain values of mean axial load and radius of curvature, predict the onset of full-slippage between the wire and the core at a position 2mm from the clamp, which may not physically be possible. It is some comfort to know that the true distance of the fixed end from the nearest contact patch in strands as terminated is in general unknown, and difficult to assess, so that an improved analysis would not of itself be very useful.

4.10 CONCLUSIONS

A simple bending model has been proposed which offers a means of determining the strand behaviour both near and (more simply) away from the terminations. The theory is capable of exploring the variations of the secant shear stiffness between the outer wires and the central core, from the no-slip to full-slip regime and beyond. It is developed for a multi-layered large diameter steel helical strand under a mean axial tension, and with one end fixed against rotation and translation. For an assumed constant state of curvature near the clamp, results are obtained for outer wire axial stresses and associated extent of relative slippage between the wires and the core. The theoretical results explain the experimental observations reported by Hobbs.et.al. (2.53), that the first wire fractures in bending fatigue tests are located near the neutral axis (in terms of plane bending theory). The limitations of the present simplified model and its scope for further improvement has been discussed in some detail.

REFERENCES

4.1 SCOBLE, W.A. Wire Rope Research. Proceedings, The Institution of Mechanical Engineers. 1920, Oct., pp.835-867.

4.2 SCOBLE, W.A. Second, Third and Fourth Reports of the Wire Rope Research Committee. Proceedings, The Institution of Mechanical Engineers, 1924: Dec.; 1928: April; and 1930: June.

4.3 HOWE, J.F. Determination of Stresses in Wire Rope As Applied to Modern Engineering Problems. Journal of the American Society of Mechanical Engineers. 1918: 40, pp.1016-1020.

4.4 CHAPMAN, R.W. Flexibility of Wire Ropes. Engineering. 1910: (Jan), p.25.

4.5 CARSTARPHEN, F.C. Effects of Bending Wire Rope. Transactions of the American Society of Civil Engineers. 1931: Dec., pp.562-589.

4.6 STRUM, B.G. Vibration of Cables and Dampers. I Electrical Engineering. 1936: 55 (May), pp.455-465; II, 1936: (June), pp.673-688.

4.7 IKEDA, S., UENO, I. Equivalent Bending and Torsional Rigidity of Wire Rope and Stress Induced in Elementary Wire of Wire Rope when it is Bent Along the Sheave. Proceedings, 1st Japan National Congress for Applied Mechanics, 1951, pp.199-208.

4.8 GLUSHKO, M.F. Non-Symmetrical Tension and Corkscrew Effect in Steel Wire Rope. Prikladnaya Mekhanika, Otdelenie Matematiki, Mekhaniki i Kibernetiki, AN Ukr. SSR. 1965: 1 (5), pp.72-78. (translated by CEGB information services. C.E. Trans. 4615).

4,9 COSTELLO, G.A., BUSTON, G.J. Simplified Bending Theory for Wire Rope. Journal of the Engineering Mechanics Division, Proceedings of the ASCE. 1982: 108 (April), pp.219-227.

4.10 NOWAK, G. Computer Design of Electromechanical Cables for Ocean Applications. Proceedings, 10th Annual MTS Conference. Washington D.C., 1974. pp.293-305.

4.11 MITCHELL, L.A., WOODALL, D. Failure of Helically Wound Cables in High Friction Environments. Proceedings, The Institution of Mechanical Engineers, Nuclear Energy Group. 1972, 186 43/72, pp.491-498.

4.12 KASPER, R.G. Cable Design Guidlines Based on a Bending, Tension and Torsion Study of an Electro-mechanical Cable. Naval Underwater Systems Centre, Distributed by National Technical Information Service, 1973, Technical Report, AD-769 212.

4.13 STEIDEL, R.F. Strains Induced in Transmission-Line Cables by Aeolian Vibration. Proceedings, Society For Experimental Stress Analysis. 1959: 16(2), pp 109-118.

4.14 STEIDEL, R.F. Factors Affecting Vibratory Stresses in Cable Near the Point of Support. Transactions of AIEE, Part IIIB. 1959: 78, pp.109-118.

4.15a ELTON, M.B. Discussion to 4.14. Transactions of AIEE, Part III B. 1959: 78.

4.15b HARD, A.R. Discussion to 4.14. Transactions of AIEE, Part III B. 1959: 78.

4.16 CAPADONA, E.A., COLLETI, W. Establishing Test Parameters for Evaluation and Design of Cable and Fittings for VDS Towed Systems. The New Thrust Seaward, Transactions, 3rd Marine Technology Scoiety Conference, 1967. pp.641-675.

4.17 HONDALUS, B. Comparative Vibration Fatigue Tests 84/19 ACSR "Chukar" Versus 61-Strand 5005. IEEE. Winter Power Meeting, New York. N.Y. Feb.1964.

4.18 POFFENBERGER, J.C., SWART, R.L. Differential Displacement and Dynamic Conductor Strain. IEEE Transactions Power Apparatus and Systems. 1965: Vol. PAS-84 (April), pp.281-289.

4.19 SCANLAN, R.H., SWART, R.L. Bending Stiffness and Strain in Stranded Cables. IEEE Winter Power Meeting, New York, N.Y. 1968, 68 cp 43-PWR.

4.20 KOMENDA, R.A., SWART, R.L. Interpretation of Field Vibration Data. IEEE Summer Power Meeting, 1967, 31 TP 67-462.

4.21 CLAREN, R., DIANA, G. Mathematical Analysis of Transmission Line Vibration. IEEE Transactions of Power Apparatus and Systems. 1969: PAS-88 (12), pp.1741-1771.

4,22 CLAREN, R., DIANA, G. Dynamic Strain Distribution of Loaded Stranded Cables. IEEE Transactions of Power Apparatus and Systems. 1969: PAS-88 (11), pp.1678-1686.

4.23 McCONNELL, K.G., ZEMKE, W.P. The Measurement of Flexural Stiffness of Multistranded Electrical Conductors while Under Tension. Experimental Mechanics. 1980: 20 (June), pp.198-204.

4.24 IEEE Committee Report. Standardization of Conductor Vibration Measurements. IEE Transactions of Power Apparatus and Systems. 1966: PAS-85 (Jan.), pp.10-22.

4.25 PANKRATOV, S.A., VOLKOV, B.N. Calculation of Tensions in Long Ropes and Suspensions. Russian Engineering Journal (Translation of Vestnik Mashinostroeniya). 1966: 46 (12), pp.29-32.

4.26 LUTCHANSKY, M. Axial Stresses in Armor Wires of Bent Submarine Cables. Journal of Engineering for Industry, Transactions of the ASME. 1969: 91 (Aug.), pp.687-693.

4.27 ZHADNOV, G.P. Bending Stresses in Steel Wire Ropes. Nauchnye Trudy Karkov, Gornogo Inst. 1955: 2, pp.127-135.

4.28 WYATT, T.A. Secondary Stresses in Parallel Wire Suspension Cables. Journal of the Structural Division, Proceedings of the ASCE. 1960: ST7 (July), pp.37-59.

4.29 HELLER, S.R., Jr. The Contact Pressure Between Rope and Sheave. Naval Engineers Journal. 1970.

4.30 GIBSON, P.T., WHITE, L.A. SCHALIT, THOMAS, R.E., COTE, R.W., and CRESS, H.A. A Study of Parameters that Influence Wire Rope Fatigue Life. Battelle Columbus Laboratories, Long Beach Research Facility, California, 1974. Technical Report, AD/A-001 673.

4.31 HARDESTY, S. Discussion to (2.26). Journal of Applied Mechanics. 1946: 68 (March), P.A-75.

4.32 LONNGREN, B.L. Discussion to (2.26) Journal of Applied Mechanics. 1946: 68 (March), p.A.75-A.76.

4.33 RICE, R.C. The Correlation of Large and Small Diameter Wire Rope Bending Fatigue Behaviour. Proceedings, First Annual Wire Rope Symposium, 1980. pp.43-72.

4.34 DONG, R.G., STEIDEL, R.F. Contact Stress in Stranded Cable. Experimental Mechanics. 1965: 5, pp.142-147.

4.35 BRITISH ROPES. Ropes for Deep Water Moorings, Pub. No.1156, 1979.

4.36 HOBBS, R.E., and SMITH, B.W. The Fatigue Performance of Socketed Terminations to Structural Strands. Proceedings, Institution of Civil Engineers, Part II. To be published.

4.37 KORNHAUSER, J. A Note on Elastic Surface Deformation. Journal of Applied Mechanics, Transactions of the ASME. 1951: 18, pp.251-252.

4.38 KELSEY, S., GELLATLY, R.A., and CLARK, B.W. The Shear Modulus of Foil Honeycomb Cores. Aircraft Engineering. 1958: 30, pp.294-302.

4.39 UENG, C.E.S., UNDERWOOD, E.E., and LIU, T.L. Shear Modulus of Superplastically Formed Sandwich Cores. Computers and Structures. 1979: 10, pp.393-397.

4.40 PHILLIPS, J.W., MILLER, R.E., and COSTELLO, G.A. Contact Stresses in a Straight Cross-lay Wire Rope. First Annual Wire Rope Conference, Denver, Co., March 1980. pp. 177-200.

4.41 BORESI, A.P., SIDEBOTTOM, O.M., SEELY, F.B., and SMITH, J.O. Advanced Mechanics of Materials. New York: John Wiley and Sons, 1978.

4.42 KNAPP, R.H. Simple Bending Models for Helically Armored Cables. Proceedings of the Second International Offshore Mechanics and Arctic Engineering Symposium. Presented at Energy Sources Technology Conference and Exhibition, Houston, Texas, 1983. pp.360-364.

4.43 CHAPMAN, R.W. The Stress in Wire Ropes due to Bending. The Engineering Review. 1908: 29 (July-Dec.), pp. 258-269.

4.44 GLUSHKO, M.F., DROSDOV, N.Y., and KONONYENKO, P.F. Calculation of Curvatures and Gaps between Wires in Lifting Ropes Bent by Design (In Russian). Stal. 1972:3, pp.276-278.

4.45 HALL, G., and WATT, J.M. eds. Modern Numerical Methods For Ordinary Differential Equations. Oxford: Clarendon Press, 1976.

4.46 WYLIE, C.R., and BARRETT, L.C. Advanced Engineering Mathematics. 5th ed. McGraw Hill, Inc., 1951. p.262.

4.47 POFFENBERGER, J.C., and KOMENDA, R.A. Discussion to Ref. (4.26) above. Journal of Engineering for Industry. Transactions of the ASME. 1969: 91 (Aug.), pp.691-693.

CHAPTER 5

EXPERIMENTAL WORK

5.1 INTRODUCTION

Chapters 2 and 3 discuss experimental checks of previously reported linear and non-linear theoretical models. In many cases, these checks have been limited to a comparison of measured linear overall characteristics (such as the axial and/or torsional stiffnesses) with theoretical predictions, and very small (six or seven wire) strands have been used. Such small models are not, however, representative of the much larger (e.g. 127mm O.D.) strands for which the theoretical and/or experimental results have sometimes been extrapolated. The influence of bending and torsion in the individual wires on the overall cable performance diminishes very rapidly with increasing ratio of the strand to wire diameter, while the interwire frictional forces gain more importance. Strain gauging of the individual wires has been carried out only on small size strands, and the results, in general, have shown a large degree of scatter. There has been an attempt to measure the interwire contact forces directly, using photo-elastic techniques (4.34). This approach is not thought to be satisfactory because it involved the use of transparent model strands with very different material and structural characteristics from a real strand. On the other hand,

the direct measurement of interwire contact forces in a steel wire strand is clearly extremely difficult, and probably impossible, so that indirect approaches must be used. No-slip axial stiffness and, in particular, axial hysteresis of cables under a steady mean axial load are much more sensitive to interwire forces than the full-slip axial stiffness. The accurate measurement of the former parameters in conventional testing equipment is by no means easy, as has been pointed out in Ref.(3.7). Friction and backlash of the loading system can easily invalidate the hysteresis measurements unless especial precautions are taken. Moreover, short (say, 20d) specimens suffer to an intolerable degree from end effects so that reliable hysteresis measurements can only be carried out on significantly longer ($\frac{\ell}{d}$ = 70, say - refer to Section 6.3) specimens.

As noted in Chapter 3, the torsional hysteresis of strands under a mean axial load is significantly larger than the axial damping and, hence, is much easier (although hardly easy) to measure experimentally. It, therefore, provides a relatively convenient and reliable indirect check of the theoretical predictions for interwire contact forces.

In view of these factors, the experimental work carried out for this thesis concentrated on long specimens of multi-layered spiral strands the size of which was as large as could be accommodated in the laboratory.

Two different strands were used: 39mm and 41mm O.D., Tables (2.1) and (5.1). Both of them had zinc poured sockets to BS463 at each end. As noted earlier, the 39mm specimen had seen service as part of a 170m long guy to a television

mast for over 15 years, and hence its characteristics should closely resemble those of strands in long term applications: under service conditions, the external loads of a random nature do (over a number of years) cause a significant degree of interwire abrasion and compaction which is not easy to simulate in newly manufactured strands under laboratory conditions. Even then, Wyatt (2.54) found that this supposedly well bedded-in strand took a rather large number of cycles (around 20000) of uniform axial loading to reach a steady condition. As regards the 41mm construction, it was delivered in as-manufactured (new) condition with some noticeable gaps in its outer layer. It would have been desirable to work with two specimens with nominally identical constructions but of different age (i.e. degree of bedding-in), however, practical constraints did not allow this.

The main thrust of the present experiments was on torsional and bending measurements on these substantial strands under various steady mean axial loads. The available equipment proved unsuitable for axial hysteresis measurements as will be discussed later. Instead, a comparison is given between the present analytical predictions and some previously reported experimental data. On the other hand, strain gauge measurements on the individual wires under the axial (as well as the torsional and bending) modes were carried out with encouraging results.

5.2 GENERAL ARRANGEMENT OF THE APPARATUS FOR AXIAL TENSIONING

The specimens were subjected to varying tensile loads superimposed on a mean load using the apparatus shown in Fig. (5.1), which was a modified version of that used in the previous fatigue tests (2.53). In this equipment, one end of the specimen was restrained some 350mm above a 900mm prestressed strong floor by a hold-down bolted to the floor. The other end of the specimen was loaded, via a cross-head moving on roller bearings, by two 0.5 MN dynamic capacity jacks. These jacks reacted on a robust frame also bolted to the strong floor, and were supplied with oil from a small servo-controlled system with a low rate of oil delivery so that only very slow cycling was possible. The axial load in the cable was monitored at the dead end by a very sensitive 1MN capacity quartz load washer. The electric charge from this piezoelectric force transducer was fed into a so-called "charge amplifier" which converted the signal into a voltage. This could then be displayed on a digital voltmeter or, alternatively, on an X-Y plotter. The load washer could measure a change in force of the order of 1N under a preload of several tons. Installation of this highly sensitive load cell in the existing rig was found to demand very special precautions, and a satisfactory arrangement was finally achieved by prestressing the washer to about 0.2MN between two very heavy steel blocks. This sandwich assembly was then connected via a central shaft in tension to the test specimen so that the compression load cell reacted against a heavy steel block spanning across the hole

in a 100mm thick frontal plate. This 100mm thick plate was itself prestressed via a heavy box against a cross beam by four bolts each of which carried a pretension of 0.25MN. A general view of the test rig (including a frame with a system of pulleys which was used for the torsion tests discussed later) is given in Fig.(5.2). Fig.(5.3) gives a close-up of the fixed end.

5.3 AXIAL BEHAVIOUR

5.3.1 Stiffness and Hysteresis Results and Discussion

Theoretical values of the axial stiffness for the 39mm strand have already been compared with experimental results in Fig.(3.16), where the significant theoretical effect of varying the value of Young's modulus taken for the individual wires is also shown: for the galvanized wires used in this strand the lower value (200 KN/mm^2) is thought more appropriate. The influence of mean axial load (which, as might be expected, dies away as slipping develops) is also indicated.

Table (5.2) compares theoretical predictions of the full-slip effective Young's modulus for four different strand constructions (including one very large strand) with experimental data obtained by British Ropes. Except for the 39mm strand, the experimental values were obtained on freshly manufactured specimens and they might be expected to rise a little in service as the strand is bedded-in.

The batch effect for the new specimens is also indicated for two of these constructions. A very encouraging level of agreement between experiment and theory has thus been found.

Turning to hysteresis, Fig.(5.4) compares theoretical predictions for two different mean axial loads with some measurements by Wyatt (2.54). The agreement between theory which (as explained in Section 5.4.2) assumes $\mu = 0.115$, and experiment even in an area where experimentation is notoriously difficult is encouraging. The constant lower bound to the $\frac{\Delta U}{U}$ quotient in the small range/mean region is related to the predominance of the no-slip condition over the major part of the contact region, for which Mindlin's theory breaks down (Ref.Section 1.6). This lower bound has been estimated using the torsion results as its determination in the axial mode was found to be almost impossible. In the present test rig with the specimen lying horizontally, minute inevitable (Routh (5.1)) vertical movements of the specimen due to the application of an axial load perturbation were found to spoil the mechanical (i.e. force-deflection) measurements which were carried out during very slow (e.g. 30 sec.) cycles. Wyatt's experiments with long horizontal specimens were carried out at a frequency of 4.4 Hz which allowed him (in view of the high rate of energy input) to obtain axial hysteresis data by thermal measurements. In this way, the serious problems associated with the alternative mechanical techniques were bypassed. Heat generation

measurements are not, however, reliable for very small range/mean ratios where the rise in temperature is small and large errors can occur. Such near no-slip damping quotients, $\frac{\Delta U}{U}$, could best be obtained by mechanical measurements on vertical long specimens; either by plotting force-displacement loops or simply by measuring the phase difference between force and extension at the instant of zero crossing. In the latter case, reduction of data to estimate logarithmic decrement involves the assumption that the hysteresis loop is elliptical. Alternatively, damping quotients at small amplitudes of movement might be obtained by recording the decay of free axial vibrations. Despite its shortcomings for the axial hysteresis experiments, the present apparatus was further modified to allow successful hysteresis measurements (both static and free-decay) in the torsional mode as will be described later.

5.3.2 Strain Gauge Measurements on 39mm Strand in the Axial Mode

20mm long electric resistance strain gauges were placed on the thirty individual outer wires of the 39mm construction (one gauge on each wire) at each of two cable sections (i.e. sixty gauges in total). One section was about 2 metres away from the face of the socket (i.e. in the cable's free field) and the other section was positioned as close as possible to the socket. The galvanizing was carefully removed prior to the application of strain gauges

which were then placed on bare steel.

Incremental (static) strain gauge readings were taken by a computer controlled data logger with a high level of minimum axial load in the cable in order to reduce the secondary effects due to lateral deflections. The range of axial load was 0.10MN with a base (minimum) load of 0.50MN. The cable was cycled over this range one hundred times. Significant scatter was still observed in the readings as would be expected in view of the quasi-random nature of effects of interlayer contacts on outer wire strains. Histograms of typical results at each cable section are presented in Fig.(5.5). The large number of results at each cable cross-section offered (irrespective of the type of probability distribution for the test data) the possibility of obtaining reliable arithmetic mean axial wire strains for comparison with theoretical predictions. Variation of the strain along an individual wire was also monitored (in a preliminary test) with 5 gauges placed on the same wire at intervals of one lay length: the scatter in the results was not very different from that among the 30 free field readings. The log-normal distribution is used as a convenient model for presenting the degree (band) of scatter in the experimental results for both of the cable sections, Figs.(5.6) and (5.7). Fig.(5.8) gives a comparison between the data from these two locations in the cable, while, comparison of Figs.(5.7) (0.5MN base load) and (5.9) (0.15MN base load) throws some light on the effect of cable sag on the strain gauge readings. A comparison between the theoretical results of Hruska (Equation (2.12)), the present theory (taking the influence

of the Poisson's ratio for steel, ν = 0.28, into account), and the mean of the free field data is also made, Fig.(5.10). Recalling that for the present theory, part of the cable's lateral contraction is due to the presence of interwire contact deformations and part due to the Poisson's effect of the wire material itself, a theoretical line assuming ν=o is also included in Fig.(5.10). This line demonstrates the influence on $S_1(\varepsilon_h)$ of the interwire contact deformations alone.

The agreement between the experimental mean curve and the present theory with ν = 0.28 appears to be very satisfactory, Fig.(5.10). However, it should be borne in mind that possible experimental errors are of the same order of magnitude as the difference between the predictions based on Hruska's linearized theory and the predictions of the present model.

The prime use of the strain gauge results (for the axial and torsional modes) is not to verify the theory, as this is more efficiently done via other methods such as torsional stiffness and hysteresis measurements to be discussed later. Rather, these results are primarily intended to provide a comparison between the free field and close-to-socket behaviour. They also highlight the limitations of assuming a uniform state of axial strain in all the wires.

Although further cycling of the cable (up to say 20000 times) might somewhat reduce the degree of scatter in the results, there are other factors which may also be

responsible for such deviations from the mean. The counter-laid construction of the two outermost layers must have some influence on the results as in this case the individual wires span (under the radial loads) across the interlayer trellis points of contact. There is, therefore, some degree of bending in the individual wires which are, further, subjected to rather severe states of local lateral pressure immediately over the regions of contact. The accuracy of placing strain gauges on these small diameter wires is also a factor, although the success of the strain gauging operation is, in fact, demonstrated later on in connection with the free bending tests using this same system of strain gauges (Ref. Section 5.5.3).

It has, in the past, been suggested that the scatter in the measured axial strains in various wires may have significant implications in terms of cable axial fatigue performance. From the axial fatigue tests, wire failures invariably occurred close to the socket in spite of the observed close agreement between the strain gauge readings in the free field and at the mouth of the socket. Hence it is felt that the wire strain scatter is <u>not</u> significant in this context. It may, therefore, be concluded that the measurement of individual wire axial strains alone is unlikely to be of much use when addressing the problem of cable <u>axial</u> fatigue.

5.4 TORSIONAL BEHAVIOUR

5.4.1 Apparatus

Fig.(5.11) shows the general arrangement of a system of pulleys through which a pure external torque was applied at any position along the test specimen. The torque was generated by placing the appropriate weights on the load hanger; three different load hangers (with self-weights of 2.9, 19.9 and 60.1N) were used. In this way it was possible to apply very small as well as rather large ranges of external torque. A thin sheet of copper was placed between the split torque clamp and the surface of the strand providing a good grip while avoiding cross cutting. The lever arm on the torque clamp was 0.516m. The gallows shown in Fig.(5.11) were used to support the weight of the cable under no tension and were removed after the cable was axially loaded. The torsion tests were carried out with the strand kept under a steady mean axial load. Both ends of the specimen were closely restrained against rotation. Nevertheless, the small levels of end twist were carefully measured throughout the tests and were taken into account in the data resolution stages. The presence of a steady mean axial load was ensured by preloading the cross-head against the robust frame. Using the pair of 0.50MN jacks, the cable was initially tensioned to a level slightly higher than that required, while the axial load was (in the presence of a rather significant level of friction at the moving end) carefully monitored by the load cell positioned at the fixed hold-down. The cross-head was then propped in position

using a simple adjustable nut and bolt arrangement, Fig.(5.12), so that on removal of the load from the jacks, the cross-head was preloaded against the robust frame. The final slightly reduced (by 3-8% say) value of the strand axial load was then recorded. For the initial torsion experiments, this preload was monitored over many days without significant apparent reduction.

5.4.2 Static Tests on 39mm O.D. Strand

Fig.(5.13) compares the theoretical predictions (using μ=0.115) with static torque-twist results on the 39mm strand under a mean axial load of 0.414MN. The coefficient of friction μ=0.115 was obtained from the match of theory and experiments at a mean axial load of 0.410MN and was kept as a constant for the comparison of theoretical predictions and test data under other levels of mean axial load and even modes of external loading (axial, torsional and bending). The external torque was applied at the centre of the specimen with the twist initially measured by four low sensitivity electro-level transducers fitted at positions A, B (2 instruments) and C and D, Fig.(5.13). The two halves of the specimen had very similar twist per unit length and it was assumed that each carried very nearly half of the total external torque. Obviously, on the application of the external central twist one end of the outermost layer of wires tightened-up while the other end untightened. This, however, did not seem to cause unequal division of the external torque

between the two halves of this internally torque balanced strand with weak rotation-extension coupling (Ref.Section 3.6.2). Hence, apart from these initial tests, the rest of torsion experiments were carried out using only two transducers on one half of the strand.

Some of the scatter in these initial experiments was due to the unbedded nature of the strand under the axial loading: more consistent results were later obtained by axial cycling of the strand between 0.10 and 0.41 MN over 500 times prior to the static torsion tests which, in turn, consisted of 30 applications of the full-range torque which was found to lead to a good approximation to a steady-state cyclic load response. Incremental readings were then taken over the next four torsion cycles to ensure repeatability of the results. Even after 30 cycles the static hysteresis loop (especially for large torque perturbations) showed a definite if very small residual deformation on removal of the torque, Fig.(5.14). In an attempt to reduce the observed creep (probably associated with the interwire friction interaction in the presence of the zinc coating) the static test was followed by a set of so-called "dynamic" (i.e. fast) experiments in which only peak to peak values of the torque-twist results were recorded: for a given torque range, the strand was twisted for 30 cycles, and then the peak to peak twist under quick manual application of the external torque was recorded. As a check it was found that given sufficient delay the "dynamic" readings were very close to the corresponding incremental test data, Fig.(5.15), which gives a comparison between the experiments and theory at a mean

axial load of 0.590MN. The agreement between theory and experiment at 0.105MN axial load, Fig.(5.16), is also very satisfactory.

Figs.(5.17) to (5.19) compare the measured static torsional hysteresis (presented as equivalent logarithmic decrement, $\delta_{eq} = \frac{\Delta U}{2U}$) with the theoretical predictions over a range of mean axial loads, 0.105, 0.210 and 0.415MN. Static hysteresis values were obtained by the numerical integration of torque-twist loops similar to those in Figs. (5.14) and (5.16). It should be noted that different calibration factors were used in the various tests, depending on the full range of twist. In particular, for very small ranges in the vicinity of the origin, readings as fine as one digit per each 0.4×10^{-6} rad/m were used in order to reliably calculate the enclosed area in the hysteresis loop. Of course, such measurements were repeated many times in order to ensure repeatability. For such fine measurements the electro-levels were not very reliable and an alternative arrangement was used as discussed in the next section. Further, because of the creep problem at the large ranges of twist, the hysteresis values showed more scatter with increasing level of torque perturbation.

The theoretical predictions at large twist appear to overestimate the steady state measurements. This is believed to be a consequence of neglecting variations in the magnitude of the normal interwire line-contact forces which become more pronounced (compared to the corresponding steady values under zero external twist) with increasing

levels of twist and decreasing levels of sustained mean axial load. The discrepancy is particularly marked in Fig. (5.17) where the mean axial load is only 0.105MN. For this case, even the variations due to irregularities in the fit of the strand are likely to have some significance.

The load cell was, according to its manufacturers, capable of detecting 1N variation in the axial load over a mean of many tons. In practice this resolution was not, at least for the present test set-up, achieved, although very reasonable estimates of small axial perturbation could certainly be made. For example, in the above tests with torque applied to the centre of the strand, it was found that the axial load perturbation was extremely small. With the cable under a mean axial load of 0.590MN, the torque frame was then moved away from the mid-point (i.e. placed at the 1/3rd point) and new results for total torque, T, against twist on either side of the clamp, $(\frac{d\phi}{d\ell})_a$ and $(\frac{d\phi}{d\ell})_b$, were obtained, Fig.(5.20). Approximate estimates of variations in the axial load of about 250N at total torque range of 200N-m were also obtained by the load cell. Fig. (5.19) was then used to obtain the estimates of internal torques, T_a and T_b, in segments a and b of the specimen which under a given total external torque, T, gave the measured twists per unit length $(\frac{d\phi}{d\ell})_a$ and $(\frac{d\phi}{d\ell})_b$. The so-obtained estimates of the total internal (reactive) torque $T_e (= T_a + T_b)$ were then plotted against the corresponding values of the external torque, T, Fig.(5.21), where for the

elastic part a line very nearly at 45° to either axis was found, as would be expected. Once the experimental results became non-linear this technique for resolving the data became unworkable and significant errors occurred as is shown in the figure. The negligible influence of the axial perturbation, T, on strand no-slip torsion modulus is nevertheless demonstrated.

5.4.3 Dynamic Tests on 39mm O.D. Strand

The electro-levels were not sensitive enough for measuring strand hysteresis at small torque ranges, nor was their response fast enough for truly dynamic measurements. Instead, the twist was measured by monitoring the deflection at the tip of a lever clamped to the cable with a displacement transducer. Fig. (5.22) shows the alternative arrangements: the electro-level and the $\pm 5_{mm}$ range displacement transducer with a flat anvil resting on the ball head placed at the tip of the 349.6mm lever arm. All of the dynamic tests were of the free decay type with the initial steady torque applied to the centre of the specimen. Transducer readings were taken at two locations on the same side of the clamp. One transducer was placed at about 60mm from the face of the socket and the other one was located at about 100mm from the face of the torque clamp. The difference of their outputs was automatically obtained by feeding the readings from the individual transducers (which had been carefully checked to have almost identical calibration factors) into an (a-b) function module. The

signal was then amplified either through another module into a digital display or by using the amplifier in the fast response X-Y plotter which had a minimum range of 0.05 mv/cm. Fig. (5.23) shows some of the electronic equipment. The digital display was used for plotting the static hysteresis loops which were all drawn by hand. A fully automated static torsion set-up was, at one stage, tried with no success in view of the intolerable level of jerkiness and backlash present at the very small levels of load and displacement involved. The fast X-Y plotter was, on the other hand, extremely useful for recording the free decay response which could be carried out at great amplification covering an A3 size sheet. In this way, the presence of minute levels of undesired harmonics could be detected. In addition, variations of the equivalent logarithmic decrement, δ_{eq}, with amplitude to a very high degree of accuracy, even in the notoriously difficult area of the no-slip regime at vanishingly small levels of twist, could be obtained with ease. This set-up was also suitable for monitoring the influence of the degree of bedding-in and unsteady loading on hysteresis.

The torque frame used in the static tests was modified to include a quick release system. This release consisted of the simple soldered lap joint, indicated (by an arrow) in Fig.(5.11). By heating the joint with a torch the initial static torque was suddenly removed and the free decay response in the free field was recorded as in, for example, Fig.(5.24) which is a photocopier reduction of the original recording on A3 size paper.

The torsional natural frequency of the cable is (for given boundary conditions) a function of its length and the torsion modulus, GJ. The latter is a non-linear function of the mean tension with two limiting values of no-slip and full-slip as has been discussed in Chapter 3. The torsional natural frequency of the test specimen was too high for immediate recording by the X-Y plotter. Therefore, an approximately 2.5m long 34mm diameter solid bar was clamped to the middle of the cable: this added polar inertia reduced the natural frequency of the system to a level within the range of the X-Y plotter.

Fig.(5.25) concentrates on the torsional hysteresis measurements at low levels of twist. Within the range considered, static and dynamic δ_{eq} declined as the twist amplitude fell, being effectively constant at very small ranges of $\frac{d\phi}{d\ell}$. The mean axial load was 0.410MN.

The agreement between the theory, which is based on a rate independent Coulomb frictional model (with internal material damping ignored), and the static results is very encouraging for longer ranges of twist, but breaks down for very small movements at which the no-slip condition predominates on the line-contact patches throughout the strand. The presence of a finite constant δ_{eq} at very small amplitudes has been reported previously in connection with hysteresis measurements on single contact patches. A fairly detailed review of their results has been presented in Chapter 1.

As shown in Fig.(5.25), the fully bedded-in dynamic hysteresis data with various initial static torques were (for the given mean axial load of 0.410 MN) invariably higher than the corresponding static values, except at very small magnitudes of twist where, as explained above, δ_{eq} was found to be rate-independent and also a constant.

The higher level of observed dynamic δ_{eq} is believed to be due to variations in the coefficient of friction as a function of the relative speed of interfacial movement. As discussed in Section 1.2, the static coefficient of friction is a function of time of contact, whereas the kinetic friction coefficient is a function of velocity throughout the range of velocities. The decrease in damping with increasing μ for the present range of cable twist has already been demonstrated theoretically, and is compatible with the present experimental observations in which the so-called dynamic μ must have been smaller than the static one. (i.e. for a given range of twist, a smaller log.dec. would be expected for static (high μ) than dynamic (low μ) measurements).

Further tests were carried out at a mean axial load of 0.59MN for which static and dynamic δ_{eq} under steady conditions were found to be very nearly the same, Fig.(5.26), with the constant near-origin value nearly equal to that in the previous tests with 0.41MN of mean tension. Some disturbed dynamic results are also presented in Fig.(5.26), which will be discussed later.

Overall, the match of static and dynamic experimental

results (especially at small twist) indicate that there was no significant damping from outside elements such as supports and that aerodynamic damping at the experimental range of frequencies (roughly 2 Hz) was minimal. The increase in the mean axial load to 0.590 MN has, obviously, further delayed the progress of slip within the strand and it is postulated that the appropriate value of the coefficient of friction at this high load is near to the static value, not so much because μ is a function of the imposed normal load on the contact patches, but because the full-slip interfacial distance (and hence relative speed for comparable twist and frequencies of cable vibration) has been reduced. The agreement between theory and static δ_{eq} over the large range of mean axial loads (0.20 to 0.59MN) may be taken as indicating the independence of μ and the normal contact force. However, it should be noted that (5.2) μ can (for sufficiently small p) be a function of the normal load, Fig.(5.27): in these experiments on lubricated wires, no significant difference was found between galvanized and bare wires.

The mechanism of friction interaction is very much dependent on the past history of loading. Service loads are invariably of a random nature and estimation of the average in-service cable hysteresis from steady state experimental results is not easy. It was postulated that random loading gave a higher average energy dissipation. In order to examine this assumption, a series of dynamic torsion tests

were carried out in which the 39mm O.D. cable was disturbed to various degrees prior to each free decay experiment. Some tests were also carried out on the newly manufactured 41mm O.D. strand through which the effect of age on strand characteristics was briefly examined. The results of these trials are discussed in the following section.

5.4.4 Effect of Bedding-in on Strand Performance

Starting with the 39mm O.D. strand, Fig.(5.28) compares some dynamic δ_{eq} measurements under torsionally fully bedded-in and under disturbed conditions at a mean axial load of 0.410MN. Firstly, though, Fig.(5.28) also presents a comparison between the fully bedded-in dynamic torsion δ_{eq} with values obtained from a free decay curve logged immediately after the application of 70 cycles of manual peak to peak unidirectional, $0 < d\phi < \theta_o^+$, (as opposed to reversed, $\theta_o^- < d\phi < \theta_o^+$) torque applications. There does not appear to be any significant difference between the results of these last two cases; indicating that the pattern of frictional contact stresses can,at least for the present cable, adapt itself fairly quickly to a reversal in the direction of the externally applied disturbance with a fixed peak value, $|\theta_o|$. As regards the influence that a change in the magnitude of the disturbance may have on hysteresis, the torsionally fully bedded-in strand was then subjected to a series of sequentially disturbed experiments. The magnitude of the initial static torque in these

sequential tests was changed in an ascending order: every decay test was followed by an immediate change of the level of static (initial) torque and the system was released again with no intermediate static or dynamic torsional bedding-in. Fig.(5.29) shows how the strand twist amplitude in various tests fell with increasing number of cycles. The corresponding estimated values of δ_{eq} are plotted in Fig.(5.28) which clearly indicates the significant increase in the level of hysteresis as a consequence of changes in the magnitude of the external disturbance as well as the great increase in log.dec. associated with lack of bedding-in. It is most interesting to note that all of the sequentially disturbed results converged (with increasing number of cycles) to a single curve, which at very small levels of twist very sharply approached the constant supposedly no-slip value of δ_{eq} which was obtained from the fully bedded-in tests. It is, therefore, demonstrated that the presence of an apparently amplitude independent (constant) logarithmic decrement under steady fully bedded-in conditions is not sufficient grounds for the assumption that no-slip interaction exists at the points of contact. As discussed by Wyatt (3.7) superposition of frictional hysteresis from a large number of Coulomb spring-dashpot units (Ref.Section 3.4) may lead to an observed (apparent) constant value for δ_{eq} with the underlying cause different from that of internal material damping (often modelled with viscous dashpots alone) for which δ_{eq} is always a constant (i.e. amplitude independent).

Sequentially disturbed tests were also carried out at a mean tension of 0.590MN. The (disturbed) values of

δ_{eq} so-obtained for the full range of dynamic experiments hardly differed (considering the acceptable degree of scatter in hysteresis measurements) from the fully bedded-in results, Fig.(5.26). It, therefore, follows that the presence of random loading does not necessarily guarantee a significant increase in the level of cable hysteresis over the average steady state values. It is thought that under a sufficiently high level of mean axial load,interwire slippage and hence frictional damping can be suppressed altogether even at the tips of the surface asperities. The only source of damping will then be that due to internal hysteresis of the wire material and the blocking lubricant.

In the past, hysteresis measurements have almost always been carried out on newly manufactured specimens. However, cables under service conditions may undergo significant internal changes due to interwire abrasion and compaction with age. The following experiments on the newly manufactured 41mm O.D. strand were designed to cast some light on this important aspect of cable behaviour. It is noteworthy that in practice cable manufacturers work-in new cables for at most a few tens of cycles prior to each test. The following torsional experiments demonstrate that although such a procedure is fairly satisfactory for the full-slip cable axial stiffness measurements, it is far from reliable for in-service hysteresis estimation.

The new cable was worked-in (i.e. its initial permanent constructional stretch was taken up) by an initial series (called case (i)) of axial loadings: fifty 0.10-0.60MN axial cycles followed by around two hundred and fifty cycles

from 0.60-0.70MN. It was then locked-up in the rig at a mean axial load of 0.410MN. Static torque-twist measurements were obtained, Fig.(5.30), with the external torque applied to the middle of the specimen. After a number of dynamic (free decay) experiments whose results are reported later on, the steady mean axial load was increased to 0.697MN and the static torque test was repeated: the results of this test are also presented in Fig.(5.30). Both of these static tests gave very nearly identical straight lines indicating that the torsional stiffness is (in this new cable) independent of the level of mean axial load. It is, therefore, safe to assume the absence of any significant line-contact normal forces in, at least, the outermost layers which provide the major part of the strand's resistance to torsion. On the other hand, according to the theory in Chapter 3, the full-slip strand torsional stiffness is, for all practical purposes, independent of the level of steady mean axial load and, as shown in Fig.(5.30), the theoretical predictions of the full-slip stiffness are substantiated by the experimental data.

This new strand is of an equal lay core construction which, as explained in Chapter 0, is very stiff in the radial direction. Moreover, the lay angles in the various layers are considerably smaller than those in the 39mm strand (Ref. tables (2.1) and (5.1)), so that even the limiting theoretical predictions of the hoop forces in the latter are considerably smaller than those for the old 39mm strand.

Thus, even with no gaps between the wires, the influence of interwire friction on the torsional stiffness of the 41mm strand would be considerably less than on the 39mm construction. Proper (long-term) bedding-in of this new strand is likely to involve many tens of thousands of cycles and only a rough indication of such effects could be obtained using the available slow equipment.

The new strand was (over about two weeks of continuous cycling) subjected to a few thousand axial cycles, referred to as Case (ii): 3560 cycles with 0.050-0.250MN, 28690 cycles with 0.45-0.65MN and finally 2510 cycles with 0.65-0.70 MN. Static and dynamic torsion tests were then carried out over a wide range of mean axial loads, namely 0.10, 0.40 and 0.70 MN.

The results of the static torsion tests at two mean axial loads, 0.40 and 0.70MN, are shown in Fig.(5.31) which clearly indicates the presence of some line-contact friction interaction which has apparently been generated by extra, Case (ii), axial cycling.

As regards the dynamic experiments, Fig.(5.32) gives torsionally fully bedded-in dynamic δ_{eq} on the new strand following case (i) axial bedding-in. At large twist, δ_{eq} was found to be independent of the mean tension and also the levels of twist amplitude; while at sufficiently small levels of twist, there was a significant increase in δ_{eq} with decreasing deflection amplitude and increasing level of mean axial load. Comparison of these results with

the corresponding plots of δ_{eq} which were obtained after case (ii) of axial bedding-in, Fig.(5.33), is very interesting as even the general shape of the δ_{eq} versus twist curves appears to have changed.

In Fig.(5.33), δ_{eq} is nearly independent of the level of mean axial load. There does not appear to be any amplitude independent (constant) lower bound to δ_{eq} near the origin (unlike that associated with the old 39mm strand). Instead, for $\frac{\text{range of twist}}{2} < 0.2 \times 10^{-3}$ rad/m, say, the plot of δ_{eq} against $\frac{d\phi}{d\ell}$ is almost linear; with a zero-twist intercept of $\delta_{eq} \simeq 0.012$, which is about half of the constant no-slip logarithmic decrement for the 39mm construction.

Figs.(5.34) to (5.36) present further data regarding the torsional damping of the new strand: in the top half of each figure, the variations of δ_{eq} against $\frac{d\phi}{d\ell}$ in the course of the dynamic bedding-in process under a constant initial torque are presented, with test number 1 denoting the first free decay experiment. These plots are coupled with others in the lower half of the figure involving a series of sequentially disturbed tests. The results clearly demonstrate the amplitude insensitivity of δ_{eq} for this particular (new) specimen subjected to a given degree of axial bedding-in to quasi-random torsional loading. Only at very small levels of twist does δ_{eq} change by a factor of two or so depending on the level of mean axial load and degree of bedding-in.

Finally, the 41mm strand was further cycled between 0.65 and 0.70 MN around 55000 times and, then, dynamic steady state logarithmic decrement was measured over a much wider range of twist than in the above tests, Fig.(5.37), where an upper plateau with $\delta_{eq} \simeq 0.09$ was obtained at larger ranges of movement. In particular, the shape of the δ_{eq} versus $\frac{d\Phi}{d\ell}$ plots was, as a whole, similar to those for the 39mm strand, Figs. (5.17) to (5.19).

It is therefore concluded that new strands change their internal hysteresis very drastically with age in a rather complex way, and estimation of in-service hysteresis from tests on new strands can be misleading. The effectiveness of random-loading in increasing the level of average damping is very much dependent on the level of mean axial load and the age of the strand. In new strands the gap between the wires is determined by the manufacturer and if large enough can lead to insignificant levels of within-layer hoop forces and hence much reduced hysteresis. Nevertheless, under service conditions the interwire fretting movements do, over a sufficiently long period of time, close the gaps between the wires so that they eventually behave along the same lines as has been proposed by the interwire contact theory of Chapters 2 and 3.

The very encouraging agreement between the experimental data on the old and well bedded-in 39mm construction and theory appears to support the validity of this argument. In particular, it is noted that the value for the coefficient of friction used in the theory has been kept constant (at

μ = 0.115) throughout the present work so that the use of this parameter as a convenient "fiddle factor" to match theory with experiments has been avoided.

5.4.5 Strain Gauge Measurements in the Torsion Mode

Using the strain gauges installed for the axial load case, the axial strains in the individual wires caused by the application of an incremental external torque to the midpoint of the 39mm strand were measured. The mean axial load was 0.410MN, and the cable was torsionally bedded-in for fifty cycles prior to taking measurements over two cycles. Significant scatter was again found in the results, Fig. (5.38), both close to and remote from the termination. Figs.(5.39) and (5.40) give the arithmetic mean and band of scatter (assuming a log-normal distribution) of the wire strain, ε_h, versus $\frac{d\phi}{d\ell}$ plots at these two locations. A comparison between the mean curves is made in Fig.(5.41), which indicates the significantly higher level of average wire axial strain at the mouth of the socket compared with that in the free field. The theoretical predictions based on Equation (3.19) are also included in Fig.(5.41). There is some uncertainty about the appropriate value of r: in the torsion theory of Chapter 3, r of the outer layer, r_1, is taken as the radius of the helix (i.e. distance between the outer wire centre and the centre of the strand), while in the experiments the strain gauges were, obviously, placed on the outer surface of the wires at a nominal radius of

$r = r_1 + \frac{D}{2}$ (= 17.73 + $\frac{3.53}{2}$ mm). The average experimental curve for the free field lies in-between the theoretical predictions based on the above two extreme values for the parameter r.

The limitations of the present strain gauge measurements are similar to those already discussed in connection with the axial mode, with the difference that the torsion experiments did not suffer from the undesirable influence of the minute but inevitable lateral deflections present in the axial case.

5.5 FREE BENDING

5.5.1 General Set-up

The 39mm specimen was subjected to lateral cyclic movements while sustaining a nominally constant mean axial load using apparatus shown in Fig.(5.42). The mean axial load was applied in exactly the same way as in the torsion experiments discussed before. Lateral concentrated loads were then imposed by a pair of 0.10MN dynamic capacity jacks of 55 mm maximum dynamic stroke. The lateral exciter consisted of a light alloy clamp block with internal radii to reduce stress concentrations at the clamping points and was already available from the previous fatigue tests reported in (2.53). As shown in Fig.(5.43), this block ran horizontally on four ball races on a machined steel table which was clamped to the laboratory floor. A top plate over the ball races prevented the clamp from lifting.

One jack was supplied from the servo-controlled system while the second was provided to act as a constant force return spring being connected to an Amsler accumulator (the large cylinder in Fig.(5.43)) which contained pressurized nitrogen over hydraulic oil and provided a nominally constant force.

The movement of the exciter (clamp) in a horizontal plane was continuously monitored by a displacement transducer which provided a feedback signal to the servo system. This arrangement, then, allowed the tests to be carried-out under displacement-controlled conditions. Force-controlled tests were not considered to be satisfactory in view of the significant level of friction in the lateral-displacement jacks which were to experience small loads.

The socket at the fixed hold-down was mounted with its pin vertical. The lateral exciter was placed 2530mm from the face of the other socket (whose pin was horizontal) at the cross-head position. This distance was very nearly equal to that used in the fatigue experiments of Ref.(2.53). In all the bending experiments, the longitudinally (i.e. parallel to the cable) preloaded cross-head was further immobilized laterally by packing it against the robust frame.

Four substantial box-sections were welded to the base-plate as shown in Fig.(5.44) so that the slightly flexible socket with a horizontal pin could be propped against them. The fatigue tests of Ref.(2.53) employed an "unpropped" socket with a horizontal pin.

Further, following Poffenberger and Swart (4.18), a rigid arm was extended from the socket along which a series of ± 5mm range displacement transducers were positioned. Each transducer had a flat end which rested on a ball head mounted on the cable. The transducer positions were chosen as close as was physically possible. Following the discussion of Section (4.1), this arrangement was designed to provide reliable estimate of net cable lateral deflections, free from rigid body effects.

5.5.2 Scope of the Tests and Primary Objectives

The next section describes the results of a series of free bending experiments on the 39mm strand which had already been strain gauged for the axial and torsion tests. The free bending modes are classified as $-\delta$, $+\delta$ and $\pm\delta$ where the modes $-\delta$ and $+\delta$ correspond to cases where the cable is cycled to only one side while type $\pm\delta$ identifies a reversed bending process. The +ve sign represents the case when the lateral cable deflection at the fixed socket is in the same direction as the lay angle when looking along the cable from the cross-head position and looking from above.

The tests were carried out under mean axial loads of 0.205, 0.410 and 0.615 MN and strain gauge readings at the mouth of the socket were obtained under the three modes of bending with the socket nominally fixed against lateral movements. In addition, for the mean axial loads of 0.205 and 0.41MN, the lateral restraint on the socket from the box sections was removed and $\pm\delta$ results were obtained, reproducing the conditions under which the earlier free

bending fatigue experiments were carried out. As a prerequisite to a consideration of the results of these tests, it is instructive to note the following points.

The behaviour of practical sockets (as opposed to purpose-built alternatives which provide convenient limiting boundary conditions) is highly complex and depends on the method of manufacture. It is not easy to accurately quantify the degree of end fixity on the individual wires which are collectively (i.e. as a bunch) embedded in the relatively soft zinc matrix. Furthermore, the exact location of the cable/zinc interface is unknown, occurring inside the conical housing at an indeterminate distance from the face of the socket. Fig.(5.45) shows the detail at the socket face where there may be quite significant levels of eccentricity as the cable enters the cone, depending on the skill of the craftsman.

Fig.(5.46) shows some deflected shapes for the cable at the propped socket under modes ($-\delta$) and ($+\delta$) of bending. The mean axial load was 0.410MN and the deflected shapes were obtained using Poffenberger's differential displacement method. The lack of symmetry in these results is not due to plasticity (as was confirmed by strain measurements discussed later). Instead it is believed to be partly due to the presence of external rigid body movements, as is demonstrated in Fig.(5.47). Here, the <u>total</u> deflection range of each transducer under modes ($-\delta$) and ($+\delta$) (i.e. 2δ) is plotted against the total rigid body movement of the light

split clamp. On these are superimposed the corresponding points for the ($\pm\delta$) mode. All of these plots can be linearly extrapolated to very nearly a single point on the horizontal axis with an intercept of about 1mm. In other words, there appears to be an initial offset (probably due to slight clearance problems) between the lateral cable deflection and rigid body movement of the clamp. This, however, is not a serious pitfall and as shown in the following, it may safely be bypassed for the present purposes. The plots of Fig.(5.46) clearly demonstrate that, irrespective of this secondary clearance problem, the strand lateral deflection at the face of the socket (i.e. at x=o) is not zero and, in fact, the point of zero lateral net deflection is somewhere well inside the conical housing. Taken with the rapid decrease in curvature away from any fixed point, this implies that too much should not be expected of the strain gauge readings from the wires at the face of the socket. Rather than exact correlations with the theory, which assumes a definite end fixity, rather more qualitative results can be expected. For example, the strain gauges could be expected to provide an experimental means of confirming the theoretical predictions that contact point slippage is greatest near the neutral axis, and that slippage can become significant at rather small levels of curvature.

5.5.3 Results and Discussion

The wire strains around the outer layer in the vicinity of the socket are plotted for various levels of imposed lateral

displacement, $+\delta$, with the cable under a mean axial load of 0.615MN, in Fig.(5.48). For each level of δ, the cable was laterally cycled between $\delta=o$ and $\delta = +\delta$ for a number of times, following which peak to peak strain gauge readings were obtained (using an automatic data logging system) over two consecutive stages. Zero readings were taken with the cable at $\delta=o$ following which the strand was moved to the other extreme position $\delta= +\delta$ where the change in wire strains was recorded. Strain gauge readings were then zeroed and the process was repeated by returning the cable back to the $\delta=o$ configuration. The final plots in Fig. (5.48) employ the average of the above peak-peak readings. It was very encouraging to find a minimal degree of scatter in the results at small δ – this is shown more clearly in the enlarged plots for $\delta=5$ and 10mm presented as Fig.(5.49). Apart from locations 1 and 2, the other 28 gauges (locations 3 to 30) were, thus, found to give reliable answers. At small levels of δ, the distribution of wire strains in the outer layer appears to be symmetrical about the neutral axis, but this symmetry is lost fairly rapidly with increasing levels of lateral deflection. The rather erratic changes of axial wire strains near the extreme fibre (gauges 13 and 29) and neutral axis (gauges 6 and 21) positions as a function of δ are not believed to be due to shortcomings of the method of strain gauging. Rather, they are considered to be a characteristic of the cable itself.

Similar results have been obtained for lower mean axial loads (0.410 and 0.205MN, respectively) where, as expected, deviations from a plane bending response were

initiated at even lower levels of δ, Figs.(5.50) and (5.51). Note that based on elastic theory, the radius of curvature, ρ, at the ideal fixed end of a cable subjected to boundary conditions and loading similar to the present set-up is given by

$$\frac{1}{\rho} = 1.1 \frac{\delta}{x} \sqrt{\frac{T}{(EI)_{eff}}} \qquad (5.(4.4))$$

where the no-slip and full-slip limits to $(EI)_{eff}$ for the cable in its free field are given in Table (4.2). $(EI)_{eff}$ is fairly insensitive to the level of mean axial load on the cable and, hence, the radius of curvature for given δ and x is only dependent on the square root of the mean axial load T. In turn,T is theoretically assumed to remain constant and independent of the imposed level of lateral deflection.

The present apparatus allowed reliable measurements of changes in the axial tension at the fixed hold down. Fig.(5.52) shows the small variations of the axial load in the cable as a function of the lateral movement at the jack position with a steady mean axial load of about 0.51MN when δ=o. The rate of change in the level of mean axial load, increases with increasing δ (due to the membrane action). For a maximum range of δ = 55mm (corresponding to an estimate of minimum ρ at the socket of 6.9m, based on Equation (5.(4.4)) with the full-slip $(EI)_{eff}$), the axial load changed by 0.147MN (i.e. by about 3%) which can probably be ignored.

The plots of Figs.(5.48) to (5.51) are not suitable for identifying the locations in the strand outer layer where interlayer slippage (and hence non-linearity in the wire strains) is greatest. Based on the theory of Chapter 4, interlayer slippage should start around the neutral axis. The magnitude of, at least, the initial $(EI)_{eff}$ of the cable is, on the other hand, a function primarily of the stresses at the extreme fibre positions where the onset of variations in the interlayer shear stiffness against the imposed radius of curvature is expected to lag considerably behind those around the neutral axis. It then follows that, by plotting the variations of strain gauge readings against cable lateral deflection for all the wires at the mouth of the socket, it should be possible (as is discussed below) to detect the regions in the outer layer where interlayer slippage is greatest. Figs.(5.53) present a series of such plots for a mean axial load of 0.410 MN and three modes of bending, $-\delta$, $+\delta$ and $\pm\delta$. Modes $+\delta$ and $\pm\delta$ were carried out under the peak to peak (fast) procedure described previously while mode ($-\delta$) was (for this particular mean axial load) obtained under incremental static loading. The servo-controlled system provided a reliable control over the jack displacements, as shown in Fig.(5.54), which is a reduced version of the original X-Y plotter record on A3 size paper in which peak to peak (fast) plots of jack displacement from δ=o position against cable lateral displacement at a distance of around 150mm from the mouth of the socket are

superimposed on the static response curve. All of the "fast" curves follow the static response curve over the full range with minimal deviation so that it is acceptable to compare static and dynamic data. For Fig.(5.54) the mean axial load was 0.205MN and the (+δ) mode of bending was used. The two stage (averaging) peak to peak type of bending was, nevertheless, preferred and adapted for the next two series of tests under mean axial loads of 0.410 and 0.615MN.

Figs. (5.53) clearly support the theoretical predictions that interlayer slippage is greatest around the neutral axis (gauges 6 and 21) and least around the extreme fibre position (gauges 13 and 28) where over a considerably larger range of δ, the wire strain against range of lateral displacement plots appear to be linear and independent of the mode of bending. It is also demonstrated that the no-slip to full-slip transition does initiate at alarmingly small levels of curvature as was suggested by the simple theoretical plots of Fig.(4.22).

Figs.(5.55) and (5.56) present similar plots of wire strain against cable lateral deflection for two other mean axial loads, 0.205 and 0.615MN, respectively. Yet again, local non-linear response is found to initiate near the neutral axis.

All of the above tests were carried out with the socket propped against lateral deflections. A comparison between the maximum wire strain readings under unpropped and propped conditions for a mean axial load of 0.410MN is made

in Fig. (5.57). Similar results are given for a mean axial load of 0.205MN in Fig.(5.58). The unpropped results represent the conditions under which the free bending fatigue results of Ref.(2.53) were obtained. The possibility of correlating strand fatigue life and the maximum wire strains obtained here is discussed in Section 6.5.3. For the time being, it is interesting to note the rather high levels of wire strain which can be produced under ranges of bending movement which could occur in TLP applications. In view of the practical problems outlined at the beginning of Section 5.5.2 as regards the inaccessibility of the cable/zinc interface where the curvature reaches a maximum, and also the fast rate of decrease in cable curvature away from the so-called fixed end, the encouraging comparisons of theoretical predictions using no-slip κ and experimental data in Figs.(5.57) and (5.58) are rather striking (note that the theoretical plots have ignored bending of the wires about their own axes). Maximum cable curvature for the theoretical curves was obtained by employing a full-slip value of $(EI)_{eff}$ in equation (5.(4.4)). A further plot at a mean cable tension of 0.615MN, Fig.(5.59), clearly demonstrates that the discrepancy between theoretical and experimental curves increases with increasing T. This may be attributed to the more rapid decrease in curvature from the inaccessible so-called fixed end to the position where strain gauging was carried out at large tensions.

The primary function of the 20mm long strain gauges in the free bending tests was to identify the location where interwire slippage is greatest and the level of strand curvature at which it becomes significant. The averaged out figures for wire strains over the 20mm gauge length need not accurately represent the maximum wire strain in that locality which should perhaps have been measured by a more sensitive system of (say) four or five closely spaced 5mm long gauges on each of the wires near the extreme fibre position. Trials with a number of shorter gauges will be undertaken in a future programme.

5.6 CONCLUSIONS

A very encouraging level of agreement has been obtained between the theoretical predictions of axial and torsional stiffnesses and hysteresis and the results of carefully conducted experiments using a substantial (39mm), long and fully bedded-in old specimen over a wide range of steady mean axial loads. The coefficient of friction taken for the theoretical work was 0.115 throughout, that is for all mean axial loads and both modes (axial and torsion) of superimposed loading.

For sufficiently small levels of movement, the theoretical model of cable hysteresis based on a rate-independent Coulomb friction idealization breaks down, and the internal damping of the wire material and the blocking lubricant become important. This finding is in accordance with the results of earlier work on single contacts between elastic bodies.

For old strands, there can be significant increases in the level of cable hysteresis due to random loading, provided that the interfacial movements are large enough to overcome the predominance of the no-slip condition.

The tests on a newly manufactured 41mm O.D. spiral strand demonstrate that, depending on the method of manufacture, new strands may need a very lengthy period of axial bedding-in for their internal structure to become stable. During this period complex changes occur in the hysteretic behaviour. Consequently, hysteresis measurements on newly manufactured strands can be misleading for long term applications since they are not representative of in-service conditions. The unsteady nature of real loading in the absence of significant hoop stresses in newly manufactured cables does not cause any significant increases in cable hysteresis. In long term applications, however, interwire/interlayer abrasion leads to increased level of hoop forces with a consequent increased sensitivity of cable damping to random disturbances. These conclusions may have a significant bearing on, for example, the dynamic stability of structures supported by spiral strands, as discussed in Chapter 3.

Unlike cable hysteresis, the full-slip torsional and axial stiffnesses are for all practical purposes insensitive to age and bedding-in, and the agreement between theory and experiment even on brand new strands is very satisfactory. In particular, the theory was able to predict accurately the axial stiffness of a very large 127mm O.D. strand.

Strain gauging of the individual wires was carried out satisfactorily. For the axial case, no significant differences were observed between the pattern of wire strains in the very near vicinity of the socket and in the free field, although both locations showed considerable scatter in the results for various wires which are theoretically assumed to carry a uniform strain.

Free bending tests were also conducted on the 39mm strand under various levels of mean axial load and modes of bending. Using the strain gauges next to the socket face, the theoretical prediction that local interlayer slippage is greatest near the neutral axis was confirmed experimentally. As predicted by the theory, the onset of deviations from no-slip interlayer shear interaction was found to occur at rather small levels of bending rotation at the fixed end, and the consequent fretting movements may have important implications in, for example, TBP applications where the bending loads with highest number of occurrences are those with the smallest magnitudes. This problem is discussed in the next chapter, which also examines the possibility of correlating cable bending fatigue life with the maximum levels of wire strain.

REFERENCES

5.1 ROUTH, E.J. Analytical Statics. Vol.1. Cambridge: Cambridge University Press, ch.10: 1891.

5.2 RECKNAGEL, G. Untersuchungen an Aufzugtreibscheiben mit Sitzrillen Unter Verwendung von Drahtseilen Verschiedener Litzenzahi Dissertation Universität Karlsruhe, 1972.

CHAPTER 6

STRAND FATIGUE PERFORMANCE

6.1 INTRODUCTION

The safety of the many deepwater platform concepts is, among other considerations, strongly dependent on the reliability of the anchoring systems. In a tethered buoyant platform (T.B.P.), the floating hull is fixed to the sea bed by vertical mooring lines (tethers). The excess buoyancy of the hull maintains a mean tensile force in the tethers, on which is superimposed a variable component resulting from movements of the hull in response to hydrodynamic (waves, currents and tides) and aerodynamic forces as well as variations in the deck loading. Thus during the operational life of the platform the mooring lines will experience significant axial and free bending stress perturbations (the latter in the vicinity of the end terminations) with a consequent danger of fatigue failure. The induced axial load changes may be due to platform surge or heave, while platform drift or yaw and possible hydrodynamic effects in the individual mooring lines (such as tether strumming or buffeting) will be responsible for the restrained bending action in the absence of perfect frictionless bearings near the end fittings.

The loading spectrum on the individual tethers is obviously very complex; it depends mainly upon the type of platform, its location, and the type of tethering system adopted. The most significant aspects of the service

conditions are long lives (in excess of maybe twenty years) and the random nature of the imposed loading. A collection of examples which demonstrate the level of loads and their frequency of occurrence, is given in a recent report for the U.K. Department of Energy (6.1). This report is concerned with a feasibility study for the three primary types of tether design (wire strands of parallel or spiral lay, thin wall tubular steel, and thick wall tubular steel and shaped forgings) which are, at present, believed to be the strongest candidates for T.B.P. applications. Among other priorities, this report identifies an urgent need for a better understanding of the axial and free bending performance of large diameter (e.g. 127mm O.D. or greater) strands, for which at present there seems to be very little available information of direct practical relevance. Obviously, before these strands can be used with confidence, reliable performance data for large diameter constructions under realistic conditions must be obtained. Experimental data will be expensive and time consuming to acquire for these large strands, and the results will be of restricted application in the absence of adequate theoretically based interpretation. For example, even for the same diameter and loading, different cable constructions may have significantly different fatigue lives.

Many of the factors affecting the service life of large diameter cables could be studied much more economically and quickly by using smaller scale model strands, provided only that the results so obtained could be extrapolated to

those for the prototype size with sufficient confidence. To do this, a sound understanding of the fundamental factors influencing cable fatigue performance is necessary.

The work reported here may be regarded as a first step towards this goal. In the following, a brief survey of the available literature on cable fatigue performance under axial and free bending conditions is given. A discussion of the influence of interwire contact forces and displacements on strand fatigue life, with special emphasis on the problem of cable modelling, then follows. The correlation of the fatigue lives of the individual components (wires) and the complete structure (the spiral strand) is obviously highly desirable. However, to achieve this, a clear picture of the mechanism of fretting corrosion and its associated (and usually very significant) reductions in wire fatigue life must be formed. This aspect of the problem is fraught with difficulties, one of the major problems being the absence of relevant experimental data on fretting of wires against each other, while subjected to the appropriate modes of loading (e.g. twist and/or sliding). This area is briefly discussed and experimental routines with appropriate load and displacement inputs for various strand constructions are recommended for future application.

6.2 LITERATURE SURVEY

6.2.1 Research on Single Wires

Extensive experimental studies of individual wire fatigue have been carried out by many investigators, and

the effects of parameters such as the carbon content, method of manufacture (e.g. heat treatment and the percentage reduction in wire diameter), surface condition and surface coatings, on wire fatigue life have been widely reported (Refer, e.g., to the surveys by Hempel (6.2) and Bahke (6.3)). As pointed out by Hempel, the direct application of fatigue studies on single wires to the evaluation of cable fatigue life is a very difficult procedure, and fatigue tests on rope sections are absolutely essential. Nevertheless, tests on isolated wires are generally believed to provide valuable quality control information.

Using such tests, it has been shown that galvanizing generally reduces the fatigue strength of wires when they are tested in air, by significant margins (Bahke (6.3) and Watt (6.4)), and that wires with different diameters exhibit significant variations in their fatigue performance depending on the degree and rate (i.e. the number of steps) of diameter reduction by cold drawing. The endurance limit of smaller diameter wires (with other parameters kept constant) is generally found to be greater than for larger sizes, while, at the same time, the ratio of the endurance limit to ultimate tensile strength appears to decrease.

Significant variations of fatigue life with wire (and, indeed , cable) temperature (in the range +20 to -50 ^{o}C) are reported by Korbin (6.5), who also gives a number of references on this topic.

The occurrence of martensitic areas, which favour the formation of fatigue cracks because of their very brittle nature, has been discussed by Mc Clellan (6.6) and

Williams (6.7), who have investigated the corrosion problems associated with colliery haulage ropes. The danger of stress-corrosion, on the other hand, is discussed by Spare (6.8). A full discussion of the topic of wire (and cable) corrosion is outside the scope of the present thesis: the interested reader may refer to references (6.1) and (6.9) for some fairly recent information on this topic.

The available fatigue data generally exhibit a very large degree of scatter even for apparently very similar materials and types of tests. S-N curves and fatigue envelopes are generally thought to be over-simplified representations of fatigue properties, and it is better to use statistical techniques to control the selection of samples, the testing method and (ultimately) the reduction and presentation of the results. An attempt on these lines was made by Birkenmaier (6.10), who performed fatigue tests on individual 7mm diameter wires whose average breaking strength as obtained from 1800 static tests was 1733 N/mm^2 with a standard deviation of only 33 N/mm^2. From a very limited number of fatigue tests on single wires in a preliminary trial, he concluded that, for a value of maximum stress less than half the ultimate static value, the stress range sustained by the wire (for a given number of cycles of survival-in his case, $N=2x10^6$) is almost independent of the level of maximum and also mean stresses. A similar conclusion, again based on very limited data, was obtained by Shelton and Swanger (6.11). Dillmann and Gabriel (6.12) used a similar technique to Birkenmaier but with a larger

number of samples and produced "Smith diagrams", Fig.(6.1), for 6mm diameter wires and wires with Z profiles, used for locked coil strand construction. The probability of rupture, P_r, for the round wire results is 5%.

Birkenmaier also tested a total of 210 7mm diameter wire specimens taken from 116 different coils of wires and assumed a log-normal distribution for fatigue failures, with the probability of rupture, P_r, calculated according to the formulae first suggested by Weibull (6.13), who argued that although the log-normal distribution may fit the fatigue data reasonably well in the region around the mean-value, it may not be a satisfactory representation of the two extremes. S-N curves with a constant upper stress (σ_{max}= 750 N/mm^2) for P_r= 5%, 16% and 50% were then obtained, Fig.(6.2), which clearly indicate the very significant scatter in the fatigue results for single wires whose static ultimate strength tests showed a much smaller standard deviation. This immediately suggests that a small scatter in the usual simple quality control test data (concerned with conventional static property characteristics such as tensile and torsion strength,elongation at rupture, etc.) should not be taken as a reliable indicator of a negligible degree of scatter in the fatigue data for wires.

Gabriel and his co-workers have performed extensive tests on various mechanical properties of individual wires as well as their response to lateral static pressure from, for example, neighbouring wires in a cable or a clamp.

Reference (6.12) contains a vast body of such information. The fatigue of wires under pulsating axial tension and sustained lateral pressure is discussed by Pantucek (6.14).

6.2.2 Research on Cable Fatigue in Air

For parallel wire strands, Birkenmaier (6.10) suggests a empirical factor γ equal to 1.6 by which the S-N curves for the wires, Fig.(6.2), must be reduced to give the corresponding S-N curves for the whole tendon (in its free field). The factor γ is assumed to represent the collective effect of two separate factors $\gamma_1 = 1.3$ and $\gamma_2 = 1.25$ (with $\gamma \simeq \gamma_1 \cdot \gamma_2$). γ_1 represents the reduction in the basic wire fatigue strength due to stranding of wires, unequal distribution of axial stress among them, etc., and γ_2 is a safety factor. For $\sigma_{max} < 0.45\beta_z$ (where σ_{max} is the maximum axial external stress on the tendon and β_z the ultimate strength of the wire material) it is claimed that tests on long (e.g. 6 metre) tendons have confirmed the reliability of the suggested method. The fatigue curve for the strand with P_r=5%, assumes that static rupture load after the fatigue test will reach at least 95% of the theoretical ultimate load of the tendon (defined as $Z_u = 0.98.\beta_z.f_s$, where f_s is the net steel area). It should be noted that Birkenmaier has ignored the effect of mean stresses on the fatigue life of the wires and the tendon. The correlation between the data for single wires and for the multi-wire assembly (the strand) is also discussed by Gabriel (6.15).

To the present author's knowledge, there is no available information on the free bending fatigue performance of parallel wire strands.

The criterion of fatigue failure for wire rope is of necessity more complex than that applied to continuous structures where crack length measurements or a simple observation of loss of integrity may suffice. Discard criteria are based on a mixture of past experience, personal preferences, and prejudice, for each particular type of rope application. The occurrence of an unacceptable number of wire breaks is by far the most common measure adopted for wire rope fatigue damage assessment. This, however, is not free from serious pitfalls. Wire breakages can both be internal and/or external, and reliable methods for detecting internal wire failures (under service conditions, especially in under-water applications) have still to be developed, although some progress has been made (e.g. see Refs. (6.16) and (6.17)). The percentage of wire breaks over the whole cross-section per lay (say) of the strand (in applications where wire breaks occur away from the termination) can, obviously, be measured by subsequent dismantling of the specimens. The use of a standard length is essential because multiple breaks can take place along any individual wire due to significant levels of interwire friction, especially in spiral constructions. Non-destructive wire breakage detectors may then be calibrated against such data (Hanzawa.et.al.(6.16)).

In the case of parallel-wire strands, Birkenmaier found (from a limited number of tests) that the percentage of wire breaks gives a safe estimate of the reduction in static strength. In other words, he found that the reduction of static strength caused by fatigue damage to unbroken wires is negligible. No such simple relationship between the number of wire breaks and the residual strength has, as yet, been demonstrated for spiral strands. In fact, the work of Stonesifer and Smith (6.18) and also Smith et.al. (6.19) indicates that wire break density in ropes is not a simple indicator of residual tensile strength,and prior knowledge of load history (and associated rope axial compliance at various stages) is necessary for a reasonable estimation of the residual strength. Their work, however, was only concerned with ropes (mainly 12.7mm and 6.3mm diameter) and not spiral strands.

Very often, ropes are kept in service until they either break or are rejected by visual inspection. Even under laboratory conditions, external wire breakages have sometimes been assumed to reflect the degree of actual fatigue damage. The work of Refs. (6.16), (6.18) and (6.19) confirms that the number of inner wire breaks can be a very significant proportion of the total wire breakage density. Unfortunately, none of these references mention whether the first few wire breakages were internal or external. This is, obviously, important for cable fatigue initiation studies.

Due to the possible premature occurrence of wire breaks caused, for example, by the incidental presence of surface defects acting as stress raisers, life to first wire break, N1, is not, in general, considered as a satisfactory method for presenting (or analysing) fatigue data for endurance limit estimations. However, in the case of small diameter strands such as the very common 7-wire specimens, this may be the only way - one wire break represents about 14 percent loss of steel area. Therefore, if the purpose is to use data from small scale models to predict the performance of larger diameter prototypes, it is more reasonable to use life to five percent (say) wire breakage and use specimens with at least 100 or so wires. In the 39mm nominal diameter strand with 92 wires (see Table 2.1) this corresponds to the presence of five broken wires. Hobbs and Ghavami (2.53) performed axial fatigue tests on 16 and 39mm strands and found that, in their load controlled tests, the increase in cable diameter led to an increase in the life from first wire break until final failure (as more wires were able to share the load). Their tests were performed on 6m long specimens with zinc poured sockets to BS463, and all failures were found to occur at the cable/socket interface. First wire breaks all took place in the outermost layer. However, this finding was only based on visual checks, and discussion of the paper by Hobbs and Smith (4.36) drew attention to the possibility of inner layer failures particularly in strands whose outer layers were of locked coil construction.

For free field fatigue tests of cables (i.e. tests arranged so that the occurrence of failures in the vicinity of the terminations is eliminated), the present author believes that displacement controlled tests are probably more relevant to possible future attempts to correlate interwire fretting fatigue, corrosion and strand life. This is because, based on the findings of the interwire/interlayer contact force theory presented in Chapter 2, cable perturbation axial strain, ε_c (for a given strand construction), determines the magnitude of contact forces and the degree of movement (line-contact slippage and cross-wire twist) between the component wires. Coupled with the individual perturbation axial wire strains, such information should throw considerable light on the fretting-fatigue mechanism of the individual elements, and hence the cable.

On the other hand, even for a fully bedded-in condition,cable axial stiffness has already been shown in Chapter 3 to depend on the level of load range/mean ratio. Additional significant variations in cable axial stiffness are also expected in the initial stages of the bedding-in process and in the very important time interval between the first wire fracture and final failure. In the former, cable stiffness is increased with time (becoming effectively constant after say 40000 cycles). In the latter, there exists a gradual increase in strand compliance, the rate of increase being dependent on cable diameter (the larger the diameter, the lower the rate).

Thus, displacement controlled tests,while perhaps less relevant to in-service conditions, will effectivley

bypass the effects of such difficult to monitor (and later on, to account for) variations in cable axial movements during a load controlled test.

End terminations with 100% efficiency in static ultimate tests are often found to concentrate very significant numbers of wire fatigue breakages in their vicinity. As a result of this, dramatic reductions occur in the fatigue life of the cable. Metcalf, Maryland and Matanzo (6.20) have performed fatigue tests on various rope constructions with different terminations. In particular, they emphasize the importance of the quality of workmanship and the relative insensitivity of cable fatigue life to wire rope construction and diameter. Hanzawa, et.al.(6.16) also carried out axial fatigue tests on large diameter ropes and locked coil strands with zinc and epoxy- filled sockets. Both of these references illustrate the generally,but not infallibly,superior fatigue performance of epoxy resin compared with zinc. As pointed out by Ref.(6.16), the epoxy resin filling allows less slip-out of the rope from the socket and is very suitable for applications with high density polythene sheaths for corrosion prevention.

Stripping and re-capping of ropes (fixing a new termination) after certain periods of application, is currently required by National Coal Board regulations (6.21). In this way, the NCB make use of the significantly greater fatigue life of the free-field rope sections. The occurrence of premature failures such as socket eye breakage and sudden pull-out is reported in Ref.(2.53).

For parallel-wire strands, Ref. (6.10) suggests a new method of wire anchorage which is claimed to eliminate the problem of wire fatigue damage (under axial loading) at the end fittings.

As discussed previously (Chapter 4), wire fatigue breaks under cable free bending, always occur at the end terminations. Possible preventive (or remedial) measures will, obviously, depend on the type of application. Reinforcing (strengthening) the critical section of the cable near the supports has been tried by several investigators in order to reduce the effective radius of curvature at these critical positions. Swart (6.22) and Stange (6.23) have explored this idea in connection with electromechanical cable applications. The use of high quality bearings to eliminate any degree of end restraint, is often considered financially (as well as technically, because of, for example, corrosion problems in long term applications) unrealistic. On the other hand, the use of bend limiting fairleads placed at a distance form the socket has been envisaged for guyed tower and T.L.P. mooring systems. At present, the only fatigue results for the free bending of helical strands are those reported by Hobbs and Ghavami (2.53). Bend-over-sheave fatigue data on 76mm O.D. ropes are reported by Beeman (6.24), who tried to correlate fatigue results on 76mm O.D. ropes with those for 9mm O.D. samples via the very popular Drucker-Tachau ratio (Ref. Section 4.1). The correlation between the two sets of results was not satisfactory.

However, it is important to note that the core of the smaller ropes was made of fibre as opposed to the IWR core used for the larger diameter specimens. As pointed out by Beeman, this will obviously make direct comparisons rather difficult. For the larger diameter ropes, internal wire fractures (especially where outer strands touched the IWRC) were frequent, and dramatic reductions in fatigue life were observed (cf. the smaller sized ropes) at higher levels of mean axial load.

Significant improvements in the constant amplitude axial fatigue life of ropes have been achieved by applying periodic overloads of various magnitudes and frequencies of application in the course of cycling (Smith et.al. (6.19) and Kies (6.25)). Such substantial extensions in cable fatigue life (cf. constant amplitude results) are particularly relevant to offshore guyed platform applications where for the greater part of the cable's life the imposed loads are of low magnitude and high frequency of occurrence with occasional significant overloading during storm conditions. Smith et.al. attribute the increase in fatigue life to possible crack tip blunting, increase of cable stiffness (and hence reduction in axial extension in the load controlled tests) and possible rearrangement of contact regions, as a consequence of which fresh points of contact will form with subsequent displacement of already initiated cracks from the most critical regions. These phenomena will, obviously, have an important bearing on the behaviour of cables under

random loading which has recently attracted much attention. Very little work has previously been conducted in the area of non-uniform loading: Cullimore (6.26) carried out a large number of constant amplitude tests on small (15mm O.D.) concrete prestressing strands from which he concluded that there was no obvious "endurance limit" i.e. no limit below which no damage would occur. He also performed a limited number of two step loading tests from which Miner's damage factor, $D = \sum_i \frac{n_i}{N_i}$, was found to range from 0.592 to 1.276 with an average of 0.948. Warner and Hulsbes (6.27), on the other hand, found extreme values of 0.48 and 1.65 with a population mean of 0.97 for this same factor. Their work was also concerned with prestressing strand. In general, however, there are quite important structural as well as metallurgical differences between prestressing strands and the type of multi-layered cables which forms the subject of the present thesis.

Random block loading of ropes under sheave bending fatigue conditions have been carried out by Rosetti (6.28), Dragone and Rosetti (6.29), and Rosetti (6.30). For bending fatiuge tests, Ref. (6.29) found the mean of Miner's damage factor to lie inside the limits 0.951-1.045, with a 95% probability. The two extremes of the factor D reported were 0.60 and 1.60. Of course, the linear damage theory of Miner ignores the interaction effect between the fatigue damage caused by repeated load cycles of different magnitudes. This assumption is obviously not compatible with the significant

overload effects on cable fatigue life discussed previously. However, despite its limitations, the conceptually simple "Miner's rule" has been the only cumulative damage formulation adopted by the limited number of investigators working on this aspect of rope performance.

6.3 PRESENTATION OF CONSTANT AMPLITUDE AXIAL FATIGUE DATA

Axial fatigue loading on cables is generally in the form of a nominally sinusoidal load perturbation with an amplitude $S_a = \frac{1}{2}(S_{max} - S_{min})$, superimposed on a steady mean load S_m. The results are usually presented in terms of two variables, for example, S_{max}-N (or S_a-N, where $S_a = S_{max} - S_{min}$) curves for various values of the ratio R, which is defined as $R = \frac{S_{min}}{S_{max}}$. Rather than plotting a separate curve for each value of R, Birkenmaier (6.10) used a single plot of S_a-N for all values of R, but kept the upper stress, S_{max}, constant throughout his tests which were conducted on parallel wire tendons (see Section 6.2). In connection with spiral strands, Hobbs and Ghavami (2.53) used two base (i.e. S_{min}) stresses of 10% and 30% of the nominal ultimate strength, S_u, with rather arbitrary S_m and R values covering a large range of strand life, and reported near independence of the fatigue life and the mean axial load, Fig.(6.3). Their conclusion, however, is not substantiated by the findings of British Ropes (6.31), who suggest that fatigue is not only a function of stress range but also (albeit to a lesser degree) the mean axial load.

In the absence of any other information, British Ropes has suggested the use of a Goodman treatment of the fatigue data (through which "least square" lines are drawn), in order to interpolate or extrapolate into regions for which no data exists.

In view of the discussions in the previous section, the definition of cable fatigue "failure" is, at least for the present, rather arbitrary,and the use of the fairly well established techniques of Goodman and/or Greber for displaying fatigue data of plain specimens under various mean loads in connection with rope fatigue analysis is not as yet completely justified. Despite possible major shortcomings, in the absence of any other more reliable technique, the present author has used equations of the form

$$\frac{S_{eq}}{S_u} = \frac{\frac{S_a}{S_u}}{1-\left(\frac{S_m}{S_u}\right)^n} \qquad (6.1)$$

in replotting some of the limited available data on spiral strand fatigue life, with a view to reducing some of the scatter in composite plots of the experimental results from different sources. In Equation (6.1), S_a is the range of applied stress (i.e. twice the amplitudes) and S_m is the mean. S_{eq} is an equivalent stress analogous to those defined by Goodman and Greber. In Equation (6.1), Goodman used n=1 and Greber took n=2. Obviously, Equation (6.1) attempts to obtain a single curve for all possible combinations of S_m and S_a, for each given strand construction.

Figs.(6.4) to (6.6) present some fatigue results obtained from British Ropes, Ltd., on wire ropes of various constructions and from different batches. An examination of these curves is very instructive. Unfortunately, only fatigue lives to final (complete) failure were available and, hence, no information could be given for the fatigue initiation stages. Equivalent stresses are calculated based on Equation (6.1) with n=2, which was, in general, found to give less scatter than n=1.

Fatigue results for a 32mm 6x25 rope of right hand ordinary lay (R.H.O.) construction with an IWR core are presented in Fig.(6.4). Three different axial load ranges were used. For two of these ranges the mean axial load level was itself varied widely in order to throw some light on the effect of mean load on cable fatigue life, which was found to be significant. Some of the tests were carried out under nominally identical conditions (i.e. same S_a and S_m and batch) a number of times in an attempt to assess the degree of variability in the results. Moreover, for the stress range of 20% of ultimate breaking load, U.B.L., and a mean of 50% U.B.L., nineteen test results were obtained on the 6x25 construction from six different batches (three tests on each of five batches and four tests on the sixth one). The histogram for the results is given in Fig.(6.4a), while the lower and upper bounds plus the mean of these results is included in Fig.(6.4). The degree of scatter even for nominally identical tests (i.e. from the same batch)

is quite significant. The importance of batch effect is also evident. These conclusions are further reinforced by the similar fatigue results obtained from seven batches of a 22mm O.D. rope of R.H.O. lay construction with an IWR core, presented in Fig. (6.5b). Finally, fatigue results on a number of rope constructions subjected to a variety of axial load ranges and steady mean axial forces are superimposed on the 32mm fatigue results of Fig.(6.4), as presented in Fig. (6.6). The effect of rope construction on fatigue life (in this case to complete failure) is, obviously, also important.

The present thesis is, however, more concerned with the behaviour of spiral strands. Their "fatigue life" will be expressed in terms of life to first wire break (for the data for 16mm diameter strands) or life to 5% wire fractures (for larger diameter specimens) following the argument of Section (6.2). Thus, only the problem of strand fatigue initiation will be addressed, for which it may reasonably be assumed that the difference between load-controlled and displacement- controlled tests is not significant. As noted above, the differences would be more marked if the period from first wire break to total failure were considered.

The plots of $(\frac{S_{eq}}{S_u})$ against N1 obtained in this way for the 16 and 39mm strand of Ref.(2.53) are presented in Fig.(6.7). N1 is taken as the life to first wire break. A smaller scatter was obtained by setting n in Equation (6.1)

equal to 2. All of the specimens had zinc poured sockets and the 16mm specimens were from two batches which, it was noted, looked very different. Tests were carried out with a variety of R and S_m values, Tables (6.1). All failures occurred at the mouth of the socket including some pull-out failures (in 16mm specimens) of wires sliding from the zinc matrix. It appears from Fig.(6.7) that conservative estimates of the life of 39mm strand could be made from the results for the smaller strand. Moreover, there seems to be a sharp reduction in the rate of fatigue damage for values of $\frac{S_{eq}}{S_u} < 11\%$. These conclusions were supported by a sight of some commercially confidential data for large (> 39mm) diameter epoxy resin socketed strands which invariably exhibited longer lives to first wire fracture than the 16mm specimens (but, on the other hand, showed more scatter). Unfortunately, these results could not be made publicly available and are not included in the figure.

The next move was to replot the 39mm and also the confidential larger diameter results in the form of $\frac{S_{eq}}{S_u}$ against life to 5% wire fracture (N5), Fig. (6.8). The scatter in the results for the larger strand was then found to be very small and it became obvious that some of the first wire fractures were premature and due to other effects. The data from the 16mm specimens were excluded from this second set of plots because one wire fracture (which may be premature) represents about 5% loss of strength. A least squares curve (with no extrapolation) is plotted through the confidential data which covers a wide range of fatigue

life and is, most importantly, concentrating on fatigue life of strands in the low stress (long life) region which is relevant to offshore applications. The S_{eq} versus N5 may be expressed analytically as:

$$\left(\frac{S_{eq}}{S_u}\right)^m . N5 = C \qquad (6.2)$$

where m and C are constants depending on the type of cable construction. Equation (6.2) is the same as that suggested by Ref.(6.29) for the resolution of rope bending fatigue results. The most important conclusion is the apparent lack of any endurance limit over the large range of life considered. In view of the previous results for the 16mm strand, Fig.(6.7), with an apparent fatigue limit, it then follows that the estimation of endurance limits for larger sized ropes from smaller scale models could be misleading. The data for the 39mm diameter strand are very limited (only three values) but its fatigue life is obviously inferior to the other construction which is of the same order of magnitude in diameter. A tentative straight line (analytically expressed in the form of Equation (6.2)) may be drawnthrough the 39mm data points and cautiously extrapolated into regions for which no results are available. It is important to remember that the 39mm diameter strand had been in service as a single 170m stay for about fifteen years before it was cut into 6m long specimens for the fatigue tests. This prior service can only have reduced its fatigue life, which

may also have been reduced because of the relatively long length of the specimens tested. As pointed out by Edwards and Picard (6.32) in connection with concrete prestressing strands, the dominant mode of failure may be significantly affected by the presence of the end effects and increasing the length of short test samples (in their case, $\frac{d}{\ell} \simeq 20$) lead to significant reductions in the apparent strand axial fatigue life. These conclusions are also supported by the findings of Gabriel (6.15), who worked on parallel wire tendons. However, neither of these references discuss an appropriate lower bound to the required $\frac{d}{\ell}$ ratio.

Wyatt (2.54) took detailed temperature measurements on 6m long 39mm strands which were terminated by zinc poured sockets to BS463, and found that under steady state conditions achieved by uniform axial cycling at 4.4HZ for about two hours, the average temperature at either end of the specimen was significantly higher than that in the central (i.e. free field) portion of the cable. This zone of end effects appeared to extend about 15% of the cable's length, i.e. about 23d, from either end. It then follows that at least for this particular strand and type of socketing a specimen with $\frac{d}{\ell}$ ratio equal to $46 (= \frac{39}{2 \times 0.15 \times 6000})$ will have hardly any central portion free from end effects and, intuitively, a $\frac{d}{\ell}$ ratio of say 70 is suggested as a reasonable guide for future tests whose aim is to predict the life of long strands in service.

The proposed method for presenting the very limited available experimental data on strand axial fatigue

performance appears reasonably satisfactory. However, it has of course been the case with fatigue studies that such encouraging results are merely fortuitous rather than representative of the true underlying behaviour. The method's immediate predictive use is thus unsafe, and a more fundamental approach than mere curve fitting is very desirable.

As one possibility, the use of model strands in the form of geometrically scaled down versions of the prototype is currently being considered for fatigue life evaluation of the full scale cables by rope manufacturers. It is, obviously, important to know how closely the geometrically scaled down models duplicate the pattern of interwire fretting actions in the larger diameter versions, upon which (at least in the free field, and in the case of axial load) the strand's fatigue life depends. This topic forms the subject of the next few sections.

6.4 CABLE MODELLING FOR FATIGUE STUDIES

6.4.1 Introduction

The method developed in Chapter 2 involves the solution of a set of non-linear equations and is not suitable for hand calculations. The results of the inter-wire contact theory are, however, of prime importance as an input to interwire fretting experiments such as those which are at present in progress at a number of institutions. Easy-to-use charts of the theoretical results are, therefore,

desirable and will be presented in the following section. This section is,in turn, followed by others dealing with the implications of such results in terms of cable fatigue life estimation from geometrically scaled down models.

The correlation of individual wire fretting fatigue results with cable fatigue life is thought to be a difficult problem. However, single or twin wire experiments (carried out under realistic conditions of imposed magnitudes and modes of interwire forces and displacements) should cast some light on the validity of extrapolating fatigue results for model strands to predict the fatigue life of the prototypes. This is so because model and prototype use a different wire diameter and, hence, are likely to suffer from significantly different rates of fatigue damage as discussed in the following sections.

6.4.2 Development of a Simple Routine for Calculating the Interwire/Interlayer Contact Forces and Displacements

Recalling the results of Section 2.7, it has already been shown that for a large number of wires, n, Equation (2.24) may be replaced by the much simpler equation

$$S'_{2R} \simeq \varepsilon_h - \varepsilon_C \qquad (6.(2.27))$$

Careful examination of Equations (6.(2.27)), (2.40) and (2.42)-(2.47) then reveals that the set of compatible strains in the anisotropic cylinder with the core included

become a function of the parameters α (the lay angle) and ε_c (the cable axial strain) alone, and that it is independent of the cable diameter. In other words, for a large number of wires in a layer, specifying α and ε_c leads to a very reasonable prediction of the other quantities S_1, α', S'_{2c}, S'_{2R}, S'_2, S_2, S_{6T} and $d\varepsilon_h$. Hence, using the method of solution outlined in Section 2.12, a set of curves for S_2, $d\alpha$, S_{6T} and S_1 can be produced which depend only on α and ε_c, Figs.(6.9) to (6.12). Fig.(6.12) also gives a plot of $\frac{d\alpha}{\varepsilon_c}$ against α, based on the very simple Equation (2.14) which ignores the changes in cable diameter and is derived assuming small deformations. The two approaches appear to give very close agreement for small values of α, although the inaccuracies involved in the simple method appear to grow fairly rapidly with increases in the lay angle. This is believed to be due to neglecting the effect of the normal strain S_2 which, as shown in Figs. (6.9) and (6.10), is very small (compared with ε_c) for small α, but appears to gain significance in relation to ε_c (and hence S_1) for greater values of the lay angle. It is also worth noting that for $S'_2 << S'_1$ and $\alpha' \simeq \alpha$, Equations (2.47) and (2.14) give $S_{6T} \simeq d\alpha \simeq \varepsilon_c \, Sin\alpha Cos\alpha$

However, as α grows, S_2 (and hence S'_2) grow fairly rapidly, Figs.(6.9) and (6.10), and hence the effect of S'_2 on S_{6T} and $d\alpha$ becomes significant. The effect of the Poisson's ratio of the wire material on the cable diametral contraction has been ignored in these plots, although it is taken into account in the constitutive relation-

ships for the orthotropic membrane which may be used later to obtain the cable tangent moduli and the total lateral contraction in various layers. This, however, is not believed to be necessary for the determination of input parameters for the interwire fretting experiments which, after all, need the right order of magnitude rather than so called "exact" answers.

Thus, by specifying α and ε_c, one can easily obtain the corresponding values of S_2 from Figs. (6.9) or (6.10). Moreover, once the wire diameter, D, in the given layer is specified, Equations (2.53), (2.33) and (2.34) may be used to calculate the magnitude of the line contact force, P_{Rc}, for the assumed single layer strand with the core included. Similarly, for a given α and ε_c, S_1 may be obtained from Fig. (6.11), which is then substituted, with the appropriate values of D and r, into Equation (2.20) to give the magnitude of the radial force, X_{Rc}. The procedure is repeated for a number of different ε_c values and for all the layers in the strand, in order to produce P_{Rc} against X_{Rc} plots for various layers. The simple method outlined in Section 2.14 may then be used to obtain the $P_{MS}-\varepsilon_c$ and $X_{MS}-\varepsilon_c$ curves for various layers, which represent the hoop and radial forces, respectively, of the multi-layered strand as a function of the cable axial strain. The rotational movement between wires, on the other hand, is easily obtained from the $d\alpha$ against ε_c plots (rotation $= \sum_{i=1}^{2} d\alpha_i$, where α_1 and α_2 are the lay angles in the two touching layers), while the sliding distance between wires in line contact in various layers is equal to $2S_{6T} \cdot D$, where

S_{6T} for a given ε_c and α may be obtained from Fig.(6.12).

6.4.3 Effect of Strand Modelling on Axial Properties

The above results also throw some light on the reliability of the current practice among cable manufacturers of evaluating the axial fatigue life of large diameter (e.g. > 100mm O.D.) strands from tests on smaller diameter model cables (which are made as geometrically scaled down versions of the prototype).

As a pre-requisite to the discussion on cable modelling for fatigue investigations, it is instructive to check that the geometrical scaling of cables work broadly in the same way as for straightforward conventional structures where the same non-dimensional geometrical ratios lead to the same levels of stresses and their associated strains, while deflections are increased by the linear ratio.

The only subtlety in the present case is the presence of geometrical and material out-of-scale effects inherent in the problem of contact between the wires.

The invariance of the average radial and hoop stresses, $\frac{X_{MS}}{D}$ and $\frac{P_{MS}}{D}$, respectively, in the geometrical scaling process becomes evident through examining the appropriate equations in Chapter 2 with the proviso that for given α's in various layers, S_1 and S_2 are functions of the cable axial strain alone. Equations (2.33) and (1.6) with the appropriate values of the contact forces then suggest that the area of the contact patches throughout the

strand are changed by ζ^2. For given ε_c, S_{6T} (line-contact shear strain) and $d\alpha$ (interlayer trellis rotation) are constants and independent of the wire diameter (i.e. scaling ratio), while the line-contact and rotational relative slippages over the contact patches obey the linear scaling law. As regards the cable axial stiffness and axial hysteresis, the present theory suggests that they are both independent of the scaling ratio.

Table (6.2) gives construction details for one third scale model of the 127mm O.D. strand (Ref. Table 2.4). This is a realistic version of the prototype except that because of manufacturing constraints it has 37 (as opposed to 36 in the prototype) wires in its 4th layer. Figs. (6.13) and (6.14) show the very close agreement between the calculated variation of the effective E value and the axial hysteresis of the two constructions as a function of the $\frac{\text{range}}{\text{mean}}$ ratio.

It is therefore clear that for the axial fatigue case, the magnitude of the average (and hence maximum normal Hertzian) stress remains constant and independent of the strand scaling ratio, over both the line-contact regions and also the interlayer elliptic patches. On the other hand, the magnitude of the slip over the regions of contact changes in proportion to the wire diameters. It is known that fretting fatigue life is, among other things, dependent on the magnitude of the normal forces and the size of relative movements and, hence, the small scale model need not necessarily be a reliable representative, in terms of axial fatigue (much less the free bending) performance, of

the prototype. The situation is further complicated by the well known fact that wires with different diameters (other parameters kept constant) generally exhibit significantly different lives under even plain fatigue conditions - Ref. Section (6.21). The scaling process for fatigue modelling may, therefore, suffer from serious pitfalls and a critical examination of the fretting problem over the contact patches is necessary. This follows next.

6.5 FRETTING FATIGUE PHENOMENA AND STRAND FATIGUE PERFORMANCE

6.5.1 Introduction

The fretting problem is an extremely difficult one and in the absence of relevant experimental results, it is not easy to draw any reliable conclusions from purely analytical techniques. Nevertheless, careful examination of the literature in the general field of fretting fatigue, coupled with the type of contact stress theories discussed in Chapter 1, and load and displacement values as obtained from the present chapter, should at least help to design (and, later on, interpret the results of) interwire fretting fatigue tests. A detailed discussion of the mechanism of fretting fatigue is outside the scope of the present thesis. It is extensively documented elsewhere (e.g. Waterhouse (6.33), (6.34)). For the present purpose, a few introductory remarks may give a feeling for the complexities involved

and provide a few clues as how to tackle the problem.

6.5.2 A Brief Account of the Fretting-Fatigue Phenomenon

It is now well established (e.g. Uhlig (6.35)) that fretting damage is caused by a combination of mechanical and chemical effects. The magnitude of relative slippage, size and distribution of the normal contact pressure, the surface condition and subsurface state of stress, and, obviously, type of material as well as the environment, the testing frequency, and the level of temperature rise at the contact regions can all affect the fretting fatigue life significantly. It is also accepted that the amount of fretting wear is not a good indicator of the reduction in fatigue life (Waterhouse (6.34)). Because of the partly chemical nature of fretting phenomena, predictions of the state of stress in the contact regions are not necessarily sufficient for fatigue life assessment. Moreover, as pointed out in Chapter 1, real surfaces are never smooth and despite the enormous body of literature on the subject, the available analytical techniques are unable to predict sufficiently accurately the true nature of stresses (including the interface friction interaction) at the tip of surface asperities. However, the importance of the frictional shear stresses has been repeatedly emphasized. Despite these problems, attempts have been made to correlate the theoretical predictions of Mindlin-type topographically smooth models with fretting fatigue results and, indeed, some progress has been made. For

example, Nishioka and Hirakawa (6.36) have proposed a semi-empirical expression for the alternating stress σ_{fw1} to initiate fretting fatigue cracks in a fatigue specimen in contact with a cylindrical pad:

$$\sigma_{fw1} \geq \sigma_{w1} - 2\mu P \left[1-\exp(-\frac{S}{k})\right] \qquad (6.3)$$

where σ_{w1} is the fatigue strength in the absence of fretting, μ the coefficient of friction and the mean pressure over the contact area is denoted by P. S is the relative movement of distant points in the two bodies (gross relative slippage) and k an empirical constant. They showed an encouraging agreement between their theory and experiments. However, as pointed out by Waterhouse (6.33), the above relationship suggests that an increase in plain fatigue life, σ_{w1}, should lead to an increase in the fretting fatigue life, and this is not always true. Waterhouse argues that because of the formation and subsequent breakage of intermetallic welds, fretting is a high strain fatigue phenomena (as regards initiation of the cracks) and notes that the performance of materials under high strain and normal strain fatigue is not always comparable. The above equation takes the partial slip phenomena into account and, most importantly, assumes that crack initiation starts at the outer contact boundary where, as discussed in Chapter 1, a high tensile stress, σ_x, exists at the end of the axis parallel to the external tangential force, Fig.(1.35). The magnitude of this stress for the general case of non-spherical bodies subjected to $T=\mu p$ (i.e. at the onset of

sliding) may be estimated by Equations (1.28). These equations also give an upper bound to the magnitude of such tensile stresses under partial slip conditions. For the two-dimensional problem of a cylinder in contact with a plane, the magnitude of the tensile stress is given by (Johnson and O'Conner (6.37))

$$\sigma_x^{max} = 2\mu p_o \left[1-\left(\frac{b}{a}\right)^2\right]$$

where

$$1-\left(\frac{b}{a}\right)^2 = \frac{T}{\mu p}$$

$$= \phi', \quad \text{say}$$

or

$$\sigma_x^{max} = 2\mu p_o \phi' \qquad (6.4)$$

p_o is the maximum Hertzian pressure and the situation at full sliding is that $\phi'=1$. For an alternating shear force, $\pm$ T, σ_x^{max} will alternate through a range $\pm 2\mu p_o \phi'$. The argument put forward by Nishioka and Hirakawa (6.36) is that the magnitude of the gross relative slippage, S, determines the magnitude of ϕ', and hence σ_x^{max}. For their particular (two dimensional) loading mechanism, they proposed the following empirical formula

$$S = - k \log_e(1-\phi') \qquad (6.5)$$

If the above argument is correct, it may then be inferred that it is not just the absolute magnitude of gross relative movement which is important. Due account should also be taken of the actual mode of loading, which determines the way the partial slip to full slip transition (and hence

build-up of σ_x) takes place.

As discussed in Chapter 1, the coefficient of friction, μ, is a very unpredictable quantity, which in many applications varies over the annular region of slippage and in the case of repeated loading, varies significantly in the course of cycling.

The magnitude of the micro-slip in the annular region of contact (for the case of spherical bodies and constant μ) has been calculated by Johnson (1.50). He found that the maximum level of relative local (interfacial) slippage occurs at the edge of the contact area and is given by:

$$\frac{\alpha}{a} = \frac{\pi(2-\nu)}{8} \frac{\mu p_o}{G} \left\{ \left[1- \frac{2}{\pi} \mathrm{Sin}^{-1}\left(\frac{a'}{a}\right) \right] \left[1-2\left(\frac{a'}{a}\right)^2 \right] + \frac{2}{\pi}\left(\frac{a'}{a}\right) \left[1-\left(\frac{a'}{a}\right)^2 \right]^{\frac{1}{2}} \right\}$$

where $$\frac{a'}{a} = \left[1-\left(\frac{T}{\mu p}\right) \right]^{1/3} \qquad (6.6)$$

Fig.(6.15) shows the variation of $\frac{\alpha}{\Delta_{\ell max}}$ and also $\frac{\Delta}{\Delta_{\ell max}}$ (where Δ is the relative movement of distant points) as a function of $\frac{T}{\mu p}$. Even the maximum value of the local (interfacial) slippage is considerably less than the overall displacement between the two bodies. It is regrettable that fretting experiments invariably seem to record only the overall displacement.

Johnson and O'Connor (6.38), among others, have also emphasized the importance of the alternating tensile stresses at the edge of the contact patch on which is

superimposed a local state of steady tensile stress due to the Hertzian normal pressures as a possible cause of fretting fatigue crack initiation, although, as reported by Waterhouse (6.34), for example, cracks can also develop (and subsequently propagate) at the interface between the no-slip and full-slip regions. The above discussions are for the case $|T| < \mu p$, and the picture of the fretting fatigue mechanism where $|T| > \mu p$ is even less clear. It is certain merely that there is plenty of scope for future research in this area.

Fretting fatigue cracks may initiate at a very early stage. Their initial rate of propagation is dependent on the extent and severity of the subsurface stresses in the vicinity of the region of contact. The variable component of these stresses is a function of the alternating interfacial shear stress (as well as the free field external cyclic forces) and, hence, the magnitude of the coefficient of friction. Experimentally, it is found that, once initiated, the cracks propagate at an oblique angle to the surface until they extend beyond the influence of the fretting action when they change direction and become perpendicular to the direction of the external (free field) alternating tensile stresses. The occurrence of multiple cracks and gradual movement of the boundary of no-slip and partial slip regions have also been widely reported.

Fairly recently, fracture mechanics has been applied in order to predict fretting fatigue life under both steady and also random loading conditions with some success (Edwards and Cook (6.39), (6.40)). However, its applicability

to the case of interwire fretting fatigue phenomena has not, as yet, been satisfactorily demonstrated. The problem is complicated by the highly anisotropic nature of the wire material and (perhaps) by its small diameter.

Finally, of particular importance to our present wire rope problem are the findings of Ref.(6.41). These experiments considered the two-dimensional line-contact situation of two cylinders pressed against a flat specimen which was subjected to alternating external axial loading, $\pm \sigma$. The material used throughout the experiments was B.S. L65 aluminium alloy. The contact stress problem was the same as that analysed by Smith and Liu (1.34) and Poritsky (1.43). The cylinders were of various diameters, D, while the ratio $\frac{p}{D}$, where p is the normal force per unit length, was held constant. Hence the maximum as well as the average normal Hertzian stress was constant. Moreover, by careful adjustments to the ratio $\frac{T}{p}$ (where T is the alternating tangential force on the cylinder) a reasonably successful attempt was made to keep the maximum amplitude of the alternating tensile stresses (at the edge of the contact region) a constant, while varying the volume of material comprising the subsurface zone of induced contact stresses. For given values of $\frac{p}{D}$ and σ, it was found that there was a certain critical value of D, and hence contact width, above which a sharp reduction in fatigue life took place. This phenomenon was apparently associated with the initiation of <u>propagating</u> cracks, Fig. (6.16). The critical size was strongly dependent on the parameter μ and, for a given $\frac{p}{D}$ and μ, decreased with increasing σ. It was suggested, yet

again, that the magnitude of the alternating tensile stress at the trailing edge of the contact patch (in this case equal to $\sigma + 2\mu p_o$) may be taken as a rough and ready measure of the maximum stress in the specimen, and based on very limited experimental data, the following relationship was tentatively proposed

$$(\sigma + 2\mu p_o)^3 . (2b_{crit}) = \text{constant} \qquad (6.7)$$

where $2b_{crit}$ is the critical width.

6.5.3 Fretting-Fatigue in Multi-Layer Strands

The conclusions of the last section (although based on tests with an aluminium alloy rather than high tensile steel) may have a significant bearing on the validity of the cable modelling process for fatigue life evaluation, since the characteristics of the interwire/interlayer contact problem in the strand modelling exercise discussed previously follow broadly similar patterns to the invariant fretting parameters in the course of the above experiments. At least for the case of strand axial fatigue away from the terminations, the magnitude of the average normal Hertzian pressure over the contact patches and the axial tensile stresses in the wires (for a given ε_c) are kept constant, while the invariance of the $\frac{T}{p}$ ratio in the two-dimensional tests is comparable with the invariance of the interlayer rotation and interwire shear deformations in a given layer in the three dimensional contact situations which exist in the helical strand. The possible occurrence of critical size effects associated with such interwire fretting mechanisms should, therefore, be

checked, as their presence may invalidate the cable modelling process. Fretting experiments on individual wires under appropriate normal forces and tangential displacements (as given by the now available "easy to use" routines of Section 6.4.2) are, therefore, strongly recommended. These experiments should be carried out under constant average normal stress and (for the axial case) constant wire axial strain perturbation covering the appropriate ranges of wire diameters. The use of the same modes of interwire contact deformation as those in the strand is also strongly recommended (in the present state of knowledge in the field of fretting). The two modes in the axial case are the line-contact sliding movements of the wires in any given layer and the interwire twist at the trellis points of contact between wires in different layers. It is important to remember that in both cases the magnitude of the normal forces on the contact patches vary continuously during cycling and, as discussed in Chapter 1, such variations in the normal Hertzian pressure can have a significant influence on the shear compliance and interwire fretting mechanism. Therefore, these effects should also be studied in the interwire fretting mechanism.

Alternatively, by removing a number of the outer layers from the prototype and the scale model such that at least two crossing layers (and preferably more) are left over the central core, two small diameter strands (called A1 and A2) can be produced. The diameter of the type A strands must be chosen to accord with the capacity of the

available fatigue test equipment. Comparative testing of these type A strands may then be used (with acceptable cost) for investigating the possible occurrence of critical contact patch effects. It would, at least, be possible to obtain an empirical correction factor which could then be applied to the results of the fatigue tests on the scale model of the larger diameter prototype. In this way, the very considerable cost and difficulty of fatigue tests on the prototype can be reduced to a minimum or perhaps avoided altogether. The method has the added advantage that fatigue testing is carried out on as-manufactured cable with a representative state of internal lubrication. Lubrication is an important factor in cable fatigue performance and is not easy to reproduce reliably in single or twin wire tests. Using such tests on cables, it is fairly straightforward to investigate possible variations in cable fatigue life with changes in wire diameter over a wide range of fretting conditions which can, in turn, be controlled by varying the imposed $\frac{\text{range}}{\text{mean}}$ ratio of the axial load. In addition, by varying the length of the test specimens, which should use realistic terminations, one can investigate the possibly significant influence that the ever present end effects may have on cable fatigue life and find the minimum $\frac{d}{\ell}$ ratio necessary to predict fatigue life with $\ell = \infty$.

For the axial case, the work of chapters 3 and 5 has already demonstrated that the full-sliding threshold of the line-contact patches is significantly lower than that of the trellis points of interlayer contact. Full sliding

on the line-contact patches occurs throughout the helical strand at rather low values of the $\frac{\text{range}}{\text{mean}}$ ratio (very roughly around 0.1 - 0.15 depending on the type of construction and also the degree of bedding-in (age)). The presence of frictional interaction at very small levels of interwire movement (small enough to result in an observed constant logarithmic decrement under steady state conditions)has also been identified by the free decay torsion experiments. In view of the apparently low sensitivity of the axial fatigue life to the magnitude of the mean axial load, and the relatively low levels of the $\frac{\text{range}}{\text{mean}}$ ratio for the line-contact full-sliding threshold throughout the strand, it is tempting to suggest that the primary cause of interwire fretting fatigue failures in the axial case (away from the end effects) is the torsional movements at the interlayer trellis points. However, particularly in offshore applications, the externally applied forces with the highest number of occurrences are those with very small amplitudes (i.e. very low $\frac{\text{range}}{\text{mean}}$ ratios, where the mean level may typically be taken as about 20% of the U.B.L.). Under such conditions it is not unreasonable to assume that with the high threshold level for the interlayer contact patches, the line-contact fretting action may become important. In other words, the mode of fatigue failure may depend on the spectrum of applied forces in particular applications. The above arguments also suggest that the overall hysteresis of the cable, even if it could be measured accurately, is unlikely to be of any direct relevance to fatigue life evaluation which is a <u>local</u> rather than an overall feature

of the structure. Thus, monitoring of the variations in cable hysteresis with number of applied load cycles is unlikely to provide a good measure of internal damage as has been suggested by Hochrein and Thiruvengadam (6.42).

As regards the free bending fatigue of helical strands, the observed occurrence of the initial wire fatigue fractures near the neutral axis position (reported in Ref.(2.53)) has been shown, via a simple theoretical model whose predictions are reasonably supported by experiments, to be due to the interwire fretting action between the layers in close proximity to the clamping position. The mode of interwire fretting for the strand bending fatigue process is, however, one of a sawing action at the trellis points of the interlayer contact patches as opposed to the rotational mode for the axial case. For the average strand construction subjected to typical working axial loads, interwire fretting appears to reach a significant level at rather small values of the angle of rotation at the restrained socket. For example, for the 39mm strand under mean axial load of about 33% of the U.B.L., interwire slippage between the outer wire and the underlying core could be identified at as low an angle of rotation at the restrained socket as, say, 0.3^{o}. Slippage and hence fretting fatigue of internal (invisible) wires under service conditions is, therefore, quite likely to occur. As remarked earlier, these internal failures cannot yet be reliably detected.

As in the axial case, the invariance with model scale of the average pressure over the trellis points of interlayer contact (for a given steady axial strain on the strand) leads

to an invariant value for the wire to core no-slip shear stiffness κ (as may easily be verified by examining the appropriate equations in Section 4.6). For a constant no-slip κ, Equation (4.42) then suggests that for a given $\frac{R}{\rho}$ ratio, the wire axial strain, $\frac{du}{dS_c}$, remains unchanged. Moreover, by analysing the simple non-linear single layer bending models corresponding to the 127mm strand construction and its 45mm geometrically scaled down version, it was found that the onset of wire to core full-slip page and also the pattern of the axial wire strains near the clamp are functions of the $\frac{R}{\rho}$ ratio and the mean cable axial strain alone, and are independent of the scaling ratio. In other words, the present idealized model suggests that for the free bending fatigue tests, the imposed radius of curvature on the geometrically scaled down model must follow the same scaling law,while the mean axial strain on the strand must be kept constant. Therefore, for modest scale ratios, for example, of the order of $\frac{1}{2}$,the modelling process should give reasonable answers provided that contact patch (i.e. wire size) effects are carefully checked using techniques similar to those suggested for the axial case.

It has, in the past, been suggested that the maximum level of axial stress at the extreme fibre position may be taken as an indicator of strand fatigue life to first wire breakage. This view, however, is incompatible with the present work which suggests that the interlayer fretting near the neutral axis is the primary cause of fatigue initiation. The lack of correspondence between maximum axial wire strain and fatigue initiation is also illustrated by a comparison of the

wire strains obtained from the static bending experiments (which used a set-up which was practically identical to that used by Hobbs and Ghavami (2.53)) and the life to second wire failure reported in Ref. (2.53). There is no apparent correlation, Fig. (6.17). Note that the position of the wire with the maximum axial strain, θ_o^{max}, is slightly dependent on the level of the mean axial load. Fig.(6.17) also gives maximum axial wire strain versus fatigue life to total failure (i.e. total breakage of the strand) where there appears to be the possibility of a correlation. The very limited nature of the experimental fatigue data must, however, be borne in mind.

The significant influence that external hydrostatic pressure in deep water applications may have on the pattern of interwire contact forces in sealed strands (e.g. spiral strands covered by high density polythene sheaths for corrosion protection) has already been discussed in Section 3.10. Assuming that interwire fretting is the prime cause of fatigue failure, the increased levels of contact forces especially in the case of free bending fatigue at the sea-bed termination, may have a significant bearing on the cable's fatigue performance. It is, therefore, recommended that the fatigue tests should be carried out at a mean axial load rather larger than at the 20% of U.B.L. considered as the typical in-service value to cater for the loss of fatigue life due to the above source.

Table (6.3) gives theoretical values for the stress tensor on the surface of the interlayer "trellis" contact patches of the 39mm O.D. strand between the outer and

penultimate layers for two mean axial loads, 0.410 and 0.205MN. The coefficient of friction, μ, was taken as 0.115, which was found to be a realistic value from the torsional and axial tests. The calculations are based on Equations (1.28), which give the state of stress at the onset of sliding (i.e. $T = \mu p$) and assume the tangential force, T, to act along one of the principal axes of the contact region. Noting that for the free bending case these contact stresses are the most significant variable stresses in the wire (since the mean axial and bending strains in the individual critical wires near the neutral axis have been shown to be relatively small), it is reasonable (in the absence of any other information) to consider using them as a criterion in future work on the cable free bending problem. In particular, the theoretical tensile stress at the trailing edge of the contact region (i.e. σ_{max} at $\frac{x}{a} = -1$) is the one often referred to in fretting studies, as discussed in the previous section.

Finally, for applications in which strands undergo restrained bending and tensile movements of a random nature, it would be ideal to carry out fatigue tests which combined the two modes of loading. Under such conditions, it would probably be the interlayer contact patches which were likely to suffer most, under the rotational and sawing movements of the wires relative to each other. Hence, significant damage might occur due to the very frequent occurrence of small amplitude movements which are often neglected in the usual single mode (either tensile or bending) fatigue tests.

6.6 SUMMARY AND CONCLUSIONS

A literature survey on cable fatigue presented in the opening section of the present chapter points out the need for an improved understanding of cable fatigue behaviour. This is especially true for offshore applications which use very large strands for which full size model fatigue testing is very expensive, so expensive that scale model testing is envisaged. A fairly detailed study of the various modes of interwire fretting action under axial and free bending cyclic movements then follows, with an emphasis on the possible shortcomings of current practice among cable manufacturers regarding the estimation of prototype fatigue life from model fatigue tests.

It is concluded that geometrical scaling of cables works broadly in the same way as for conventional structures. The same non-dimensional geometrical ratios lead to the same levels of stresses and strains, while deflections are increased by the linear ratio. Predictions of cable axial stiffness and hysteresis from the scaled down models is possible, as one would expect, but fatigue life prediction is not so straightforward and the following cautionary notes must be borne in mind.

The geometrical scaling process will inevitably lead to the use of different diameter wires in the prototype and model. Even under plain fatigue conditions, wires with different diameters (other parameters kept constant) exhibit significantly different fatigue lives. The modelling situation is further complicated by the possible existence of critical size effects

associated with changes in the fretting-fatigue mechanism at the interwire contact patches. Such effects have been reported in connection with fretting fatigue tests on an aluminium alloy under comparable conditions. These effects could invalidate the modelling process.

Simple graphs have been produced for use in future interwire testing on wires with different diameters in order to examine the relevance of such contact patch effects. The use in single wire tests of the same magnitudes and modes of interwire fretting as occur inside a strand, is, in the present state of knowledge in the field of fretting, also strongly recommended. An alternative routine for contact patch investigations, employing small diameter strands with appropriate wire sizes, is proposed. This routine is fairly straightforward and is thought to be practical using existing equipment.

The present chapter has also demonstrated that there is unlikely to be a "fatigue limit" stress range below which no damage occurs. This is of particular importance in offshore applications where the small amplitude forces are the ones with the highest number of occurrences. Therefore, it is concluded that small amplitude/long life testing is necessary for these applications: this is another area for which hardly any fatigue results are currently available.

REFERENCES

6.1 WEBSTER, S.E., RUDD, W.J., and COOK, W.T. Review of Information on the Fatigue of Tethering Systems for Tethered Buoyant Platforms. Report by BSC Research Services for the U.K. Department of Energy, 1982.

6.2 HEMPEL, M. Fatigue Tests on Steel Wire. Draht (English Edition No.22). 1956: (April), pp.11-33.

6.3 BAHKE, E. Principles Defining the Strength of Wire Ropes and Chains. Wire. Part I, 1980: 29(2), pp.54-61. Part II, 1980: 30(3), pp.168-176.

6.4 WATT, D.G. Fatigue Test on Zinc-Coated Steel Wire. Wire and Wire Products. 1941: 16(May), pp.280-285, 294, 295.

6.5 KORBIN, M. Low Temperature Fatigue Tensile Tests of High Strength Wire and Wire Tendons. Wire. 1977: 26 (March-April), pp.59-63.

6.6 McCLELLAND, A.E. Failures of Wire Rope. Iron and Coal Trades Review. 1951: 162 (432), pp.387-394.

6.7 WILLIAMS, A.E. Steel Wire Ropes, Some Factors Influencing Their Life. Iron and Coal Trades Review. 1952: 164 (4372), pp.187-191.

6.8 SPARE, G.T. Prestressing Wire:Stress- Relaxation and Stress-Corrosion Up to Date. Wire and Wire Products. 1954: 29(12), pp.1421-24 and 1492-93.

6.9 WOOD, H.T. A Survey of Publications Dealing with Corrosion in Wire Rope. Catholic University of America, Washington D.C., Report No.AD 725 134, 1971.

6.10 BIRKENMAIER, M. Fatigue Resistant Tendons for Cable-Stayed Construction. IABSE Proceedings P-30/80. 1980, pp.65-79.

6.11 SHELTON, S.M., SWANGER, W.H. Fatigue Properties of Steel Wire. Journal of Research of the National Bureau of Standards. 1935: 14, pp.17-32.

6.12 DILLMANN, U., and GABRIEL, K. High-Strength Steel Wire for Ropes and Bundles for Structural Engineering-A Sequence of Publications in the Archiv für das Eisenhüttenwesen, Düsseldorf. 1980-82 (in German).

6.13 WEIBULL, W. A Statistical Representation of Fatigue Failures in Solids. Transactions of the Royal Inst. of Technology, Stockholm, 1949, No .27.

6.14 PANTUCEK, P. Pressung von Seildraht unter Statischer und Dynamischer Beanspruchung. Doktordissertation Universität Karlsruhe, 1977.

6.15 GABRIEL, K. Anwendung von Statisticschen Methoden und Wahrscheinlichkeitsbetrachtungen auf das Verhalten von Seilen und Bündeln aus vielen und Langen Drähten. Vorberichte zum 2. Internationalen Symposium des Sonderforschungsbereiches 64, Universität Stuttgart, 1979.

6.16 HANZAWA, M., YOKOTA, H., TODA, Y., and YOKOYAMA,K. Fatigue Behaviour of Large Diameter Wire Ropes. Proceedings, 8th Annual Offshore Technology Conference, Houston, Tex. 1981, pp.435-442.

6.17 LAURA, P.A., VANDERVELDT, H.H., and GAFFNEY, P.G. Mechanical Behaviour of Stranded Wire Rope. Marine Technology Society Journal. 1970: 4(3), pp.19-32.

6.18 STONESIFER, F.R., and SMITH, H.L. Tensile Fatigue in Wire Rope. Proceedings, 11th Annual Offshore Technology Conference, Houston, Tex.1979, pp.539-545.

6.19 SMITH, H.L., STONESIFER, F.R., SEIBERT, E.R. Increased Fatigue Life of Wire Rope Through Periodic Overloads. Proceedings, 10th Annual Offshore Technology Conference, Houston, Tex.1978, pp.1771-1778.

6.20 METCALF, J.T., and MATANZO, F. Wire Rope Terminations, Selection and Replacement Criteria. Proceedings, 12th Annual Offshore Technology Conference, Houston, Tex.1980, pp.517-524.

6.21 The Wire Rope Handbook. NCB, 1980.

6.22 SWART, R.L. Bend Limiters Improve Cable Performance. Oceans 77, 3rd Annual Combined Conference IEEE. Marine Technology Society, Los Angeles, 1977. pp.24D1-24D9.

6.23 STANGE, W.F. Laboratory Testing for Enhanced Undersea Cable Survivability. Proceedings, 2nd International Offshore Mechanics and Arctic Engineering Symposium. Presented at Energy Sources Technology Conference and Exhibition, Houston, Texas,1983. pp. 347-353.

6.24 BEEMAN, G.H. Factors Affecting the Service Life of Large Diameter Wire Rope. Pacific Northwest Laboratory, Richland, Washington 99352, 1978.

6.25 KIES, J.A. Overload Effects on Fatigue Damage on Wire-Rope Pendants. Journal of Engineering Materials and Technology, Transactions of the ASME. 1977: 99(July) pp.277-278.

6.26 CULLIMORE, M.S.G. The Fatigue Strength of High Tensile Steel Wire Cable Subjected to Stress Fluctuations of Small Amplitude. International Association for Bridge and Structural Engineering, Zurich, Publication 32-I, 1972, pp.49-56.

6.27 WARNER, R.F., and HULSBOS, C.L. Fatigue Properties of Prestressing Strand. PCI Journal.1966: 11 (Feb.), pp.32-54.

6.28 ROSETTI, U. Application of the Cumulative Damage Theory to the Endurance Test of Wire Ropes by the Progressive Load Method. Proceedings, 3rd Conference on Dimensioning, Budapest, 1968.

6.29 DRAGONE, G., and ROSETTI, U. Recent Investigations into Wire Rope Fatigue. Wire Industry. 1976: 43 (Mar.), pp.185-189.

6.30 ROSETTI, U. New Methods for Ropes Calculation Based on Fatigue Cumulative Damage. New Ways for Rope: OIPEEC Conference, Luxemburg, 1977.

6.31 BRITISH ROPES. Ropes for Deep Water Moorings. Pub.No.1156, 1979.

6.32 EDWARDS, A.D., and PICARD, A. Fatigue Characteristics of Prestressing Strand. Proceedings, Institution of Civil Engineers, Part 2. 1972: 53 (Sept.), pp.323-336.

6.33 WATERHOUSE, R.B. Fretting Corrosion. Oxford, Pergamon, 1972.

6.34 WATERHOUSE, R.B. (editor). Fretting Fatigue. Applied Science Publishers Ltd., 1981.

6.35 UHLIG, H. Mechanism of Fretting Corrosion. Journal of Applied Mechanics, Transactions of the ASME. 1954: 21 (Dec.), pp.401-407.

6.36 NISHIOKA, K., and HIRAKAWA, K. Fundamental Investigations of Fretting Fatigue. Bulletin of JSME. 1969, 12 (52), pp.692-697.

6.37 JOHNSON, K.L., and O'CONNOR, J.J. Mechanics of Fretting. Applied Mechanics Convention: Proceedings of the Institution of Mechanical Engineers, 1963-64, vol.178, pt 3J.pp.7-21.

6.39 EDWARDS, P.R., and COOK, R. Frictional Force Measurements on Fretted Specimens Under Constant Amplitude Loading. Royal Aircraft Establishment, Technical Report. 78019, 1978.

6.40 EDWARDS, P.R., and COOK, R. Frictional Force Measurements on Fretted Specimens Under Variable Amplitude Loading. Royal Aircraft Establishment, Technical Report 78059, 1978.

6.41 O'CONNOR, J.J. The Role of Elastic Stress Analysis in the Interpretation of Fretting Fatigue Failures. Reference (6.34) above, pp.23-66.

6.42 HOCHREIN, A.A., THIRUVENGADAM, A.P., and SHERRARD,J.R. Application of Internal Friction Damping as a Nondestructive Evaluation Technique for Wire Rope. 15th Annual Offshore Technology Conference, Houston, Tex., 1983. pp.447-454.

CHAPTER 7

CONCLUSIONS

A survey of previous work on spiral strands showed that on both the experimental and the theoretical sides, reliable information of direct practical use was very scarce. The impression gained was that the analyses and techniques had paid too little attention to the effects of interwire contacts on overall strand behaviour,and rather too much attention to small (six or seven wire) strands. Accordingly, a substantial effort has been put into assessing contact forces and the associated relative displacements between wires, taking full account of frictional effects, in large spiral strands.

The other novelty in the study reported here is the treatment of the layers of wires in a strand as a series of cylindrical orthotropic sheets (one per layer). Thus each layer of wires, although discontinuous, has its elastic properties "averaged" in a way familiar in the analysis of stiffened plating for bridge decks and ship structures. Results from contact stress theory are used to determine the properties of the orthotropic sheets, whose principal axes run parallel and perpendicular to the individual wire axes. The chief advantage of this approach is that its accuracy improves as the number of wires in a given layer increases, i.e. for practical wire sizes, as the size of

strand considered grows. This desirable situation may be contrasted with the decreasing accuracy and increasing complexity as the number of wires increases associated with certain previously available methods of analysis.

For a multi-layered strand with its ends fixed against rotation, the build-up of clench forces from the outside layer inwards can now be estimated by a sequence of non-linear compatibility conditions, which are based on the main assumption that with no gaps between the wires in each layer, the stiffness on the trellis contact patches is very much less than that between the wires in line contact in a given layer. For an assumed level of strand mean axial strain, then, it is possible to assess the distribution of the reaction to the clench forces between hoop and radial components, and hence to calculate the stiffnesses of the various orthotropic sheets (layers of wires) as a function of these forces. No such results have previously been available for multi-layered strands, either by theory or experiment.

For a given mean axial load, the orthotropic sheet theory yields estimates of the torsional and axial stiffnesses, which are found to be functions of the applied torque and axial load perturbations, respectively. The stiffnesses for small load changes can be much larger than for large perturbations, because sufficiently small disturbances do not induce interwire slippage. The theory predicts the bounds to the stiffnesses and describes the variation between them.

It is now possible to predict the energy dissipated under continued uniform cyclic axial or torsional loading in two ways, which provide a mutual check. The first assesses energy dissipation per cycle on each of the contact patches within the strand: summation yields a value for strand hysteresis which should closely match that given by the second method, which integrates the area under the overall strand force-displacement curve, whose tangent slope was found earlier using the orthotropic sheet transformations.

The match between carefully conducted axial and torsional stiffness and hysteresis experiments on an old and fully bedded-in large diameter strand subjected to uniform cycling and theory is very encouraging. The axial damping quotient has been found to be much lower than previously believed. A series of torsionally disturbed experiments, however, demonstrated that under more realistic quasi-random loading situations rather higher values can be expected depending on the level of mean axial load and range of load perturbations. Even so, long term cable damping is unlikely to be as large as has, for example, been assumed in connection with the dynamic stability calculations for the Severn bridge.

The present work has also provided an insight into the effect of high external hydrostatic pressures on cable axial stiffness and hysteresis, which may have significant design implications in, for example, deep water tension leg platform applications.

Tests on a newly manufactured 41mm strand demonstrated that hysteresis data obtained from new specimens (even after a few thousand cycles of axial bedding-in) are unlikely to provide a realistic estimate of cable damping performance in long-term applications. Due to the very gradual nature of interwire/interlayer fretting, cables may need (depending on their construction) a very lengthy period of working-in for their internal structure to become reasonably stabilized. In this period hysteresis will change in a very complex way. Full-slip axial and torsional tangent stiffnesses are not, however, so sensitive to age. Neither are these properties as sensitive to the size of the gaps between the wires in the individual layers as has been widely assumed in previous studies.

The effect of random loading, as regards increases in cable hysteresis, was experimentally found to be less pronounced for the new specimen. Because of the frictional nature of damping, a cable's hysteresis depends on the level of mean axial load. It is also amplitude dependent. Due to elastic kick-back action, the predominant mode of damping can, for sufficiently large levels of mean axial load, and small load ranges, change from the frictional to the internal hysteresis type, where the primary source of damping is the energy dissipation in the wire material and the blocking lubricant. If internal hysteresis becomes dominant, an apparently amplitude independent logarithmic decrement is obtained.

The problem of the bending of a spiral strand is also addressed, with particular reference to the "free bending" situation where pulleys or other restraints are absent. The analysis treats the "free field" bending, remote from the termination, as well as the situation close to a termination. In the former case, limiting values for the effective bending stiffness of the strand are presented; in the latter case a treatment of the behaviour of an outer layer of wires sliding (with known frictional behaviour) over an assumed solid core leads to predictions of the strains and movements between the individual wires and the core as a function of wire position in the strand. The results offer an explanation of some experimental observations from fatigue tests on a large (39mm) strand under combined steady axial load and lateral movements causing bending adjacent to the restrained termination. In particular, the observation that wire failures close to the socket occur not at the extreme fibre position, but at the neutral axis, can be explained in terms of the much larger slip on the interlayer contact points there. A series of free bending experiments on the 39mm specimen were also carried out, which supported the theoretical predictions regarding the location where highest interwire slippage takes place. These experiments employed a series of electrical resistance strain gauges, which gave further valuable data for axial and torsional modes.

No correlation was found between the cable fatigue life to initial wire breakages and the measured maximum wire bending stresses. It is concluded that future free bending fatigue initiation studies should, therefore, concentrate on the interwire fretting phenomena. To assist such studies (as well as those on the axial mode) simple approximate charts have been produced for the calculation of contact forces and interwire/interlayer displacements. Such information should prove to be of interest and value to others working on, for example, the fretting behaviour of individual wires.

The reliability of current practice among cable manufacturers in evaluating the axial and free bending fatigue life of large diameter (e.g. 100mm O.D.) strands by using tests on smaller diameter model cables (which are made as a geometrically scaled down versions of the prototype), has been critically reviewed. Three primary cautionary notes must be made: firstly, the geometrical scaling process will inevitably lead to the use of different diameter wires in the prototype and model and even under plain fatigue conditions, wires with different diameters (other parameters kept constant) exhibit significantly different fatigue lives. Secondly, the geometrical modelling process may suffer from serious contact patch size effects, as regards the mechanism of interwire fretting-fatigue phenomena. Thirdly, short specimens can give unreliable results. Practical and, it is hoped, economically viable

suggestions have been made in order to guard against such possible pitfalls, while still avoiding the need for the very expensive alternative of full-scale testing.

Finally, the need for long-life fatigue testing of substantial spiral strands, especially under free-bending conditions, is emphasized. These tests would be particularly relevant to offshore applications since here the loads with the highest number of occurrences are those with smallest magnitude. According to the present theoretical and experimental work, free bending fatigue damage can occur at very small levels (say, 0.2^{o}) of bending rotation at the terminations. The apparent lack of an endurance limit for the axial case, and the consequent need for small amplitude in-line fatigue testing, is also identified. Because of the very significant hydrostatic clench forces generated on sealed strands in deep water applications, the level of mean axial load for the fatigue tests should be increased appropriately over the typical operational mean axial tension of, say, 20% U.B.L. The necessary increase can be calculated using simple design charts based on the results of the interwire/interlayer contact force theory presented here.

NOTATION

A	Cross sectional area of wire
A_r	Real area of contact
A_{gi}	Gross area of layer i
A_{ni}	Net area of layer i
a	Semi-axis of the ellipse of contact, radius of contact circle
a_n, a_{n+1}	Consecutive amplitudes in free decay curves
B	Complete elliptic integral
b	Semi-axis of the ellipse of contact, half-width of the line-contact patch
C	Complete elliptic integral
c	Viscous damping coefficient
c_c	Critical viscous damping coefficient
c_{eq}	Equivalent viscous damping coefficient
D	Wire diameter, sheave diameter, constant of the Miner's formulae, complete elliptic integral
d	Cable (wire, strand or rope) outer diameter
E	Young's modulus, energy dissipation, complete elliptic integral of second kind
F	Frictional force
F_o	Assumed uniform stress on gross cable cross-section
F_f	Limiting frictional force in the dashpot unit
F_N, F_R	Circumferential and radial reactions to clench forces, respectively
f_{ij}	Elliptic contact patch flexibility coefficients
G	Shear modulus of steel $E/(2(1+\nu))$, cable shear modulus

G, G', H	Components of moment on the wire cross section
h	Hysteretic damping coefficient
I	Second moment of area, no-slip contact patch shear stiffness at an angle α to the major principal axis
K	Complete elliptic integral of first kind
K, K_1, θ	Components of moment per unit length on the wire
K_f	Spring stiffness in frictional dashpot model
k	Helix pitch/2π
k, k_1	Arguments of the elliptic integrals
k_{ij}	Contact patch shear stiffnesses
k_{xx} & k_{yy}	Contact patch shear stiffnesses along principal directions
ℓ, ℓ'	Undeformed and deformed lengths of wire, respectively
M	Internal torque
M_o	Maximum moment in strand under free bending
N	Number of cycles in fatigue tests
N, N', T	Components of force on the wire cross-section
Ni	Number of fatigue cycles to ith wire fracture
N_i	Axial force in a wire in layer i
n	Number of wires in a layer
P	Total normal load on a contact patch
P_m	Mean pressure over surface asperities
P_{MS}	Circumferential force in a multi-layered strand
P_{RC}	Circumferential force in a single layer strand with a solid core
p	Normal pressure, normal load per unit length of line-contact patch
q	Uniformly distributed static load

q_i	Line-contact shear force per unit length for wire i
R	Wire radius, ratio of minimum to maximum axial perturbation in uniform cyclic loading
R_i, R_i'	Principal radii of curvature in body i
r, r'	Helix radii before and after deformation, respectively
r_i	Helix radius of layer i
S	Amplitude of axial load perturbation $\frac{1}{2}(S_{max}-S_{min})$, relative gross slippage
S_i	Strain component (transformation denoted by Superscript ",")
S_{eq}	Equivalent range of stress
S_m	Mean of axial perturbation $\frac{1}{2}(S_{max}+ S_{min})$
S_u	Nominal ultimate strength
S'_{2C}	Total radial strain in a layer with core removed
S'_{2R}	Radial strain due changes of lay angle
S_{6T}	Tensorial shear strain
S_c	Coordinate along wire
S_{ij}	Compliance (transformation denoted by superscript ",")
T	Tangential force, tension in wire or strand
T_i	Stress component (transformation denoted by Superscript ",")
T_u	Ultimate strength
T*	Peak tangential force in cyclic partial slip regime
U	Maximum stored energy during vibration
u	Displacement along wire
u^p	Displacement on a core under plane section bending
X	Radial force per unit length of wire in a given layer
X_R	Radial clench force transferred from one layer to another

X_{RC}	Radial force in a single layer strand with rigid core
X_{MS}	Radial force in a multi layered strand
x	Spacing between the contact patches along the outer layer
x'	Spacing of contact points on the convex side of wires
Y	Elastic limit

α, α'	Lay angle before and after deformation
α, β, λ	Constants in the Hertz problem
γ	Engineering shear strain, torsional strain
Δ	Tangential displacement per body
δ	Tangential displacement per two bodies 2Δ, underformed length of cable, logarithmic decrement
$\delta_{\ell \max}$	Displacement between two bodies at the onset of full sliding when $T_{max} = \mu p$
δ_n	Normal approach of distant points in the Hertz problem
δ_s	Interwire slippage
δ^{α}	Contact patch displacement at an angle α to the principal axis.
δ_{eq}	Equivalent logarithmic decrement
δ'	Post deformation length of cable
ε	Axial strain
ε_c	Cable axial strain

ε_h	Wire axial strain
ξ	Damping ratio, geometrical scaling factor
θ	Rotation at fixed end of a strand under free bending, polar angle in strand
θ'	Parameter in the Hertz problem
κ	Interlayer shear stiffness
κ_o, κ_o'	Components of wire curvature in undeformed condition
κ_1, κ_1'	Components of wire curvature after deformation
μ	Coefficient of friction
ν	Poisson's ratio
ρ	Radius of curvature, density of cable
σ	Direct stress
$\sigma_x, \sigma_y, \sigma_z$	Direct stresses along x,y and z directions, respectively
σ_o	Mean tensile stress on the cable
σ_{wl}	Plain fatigue strength
σ_{fwl}	Stress to initiate fretting fatigue cracks
τ	Shear stress
τ_o, τ_1	Twist of the wire for the undeformed and deformed configurations, respectively
ϕ	Angle between planes with curvature $1/R_1$ and $1/R_2$ in bodies 1 and 2, a constant in the Hertz problem, polar angle in the strand
ψ	Specific damping capacity
ω	Frequency of vibration, weight per unit length
ω_D	Frequency of vibration with damping included

APPENDIX I

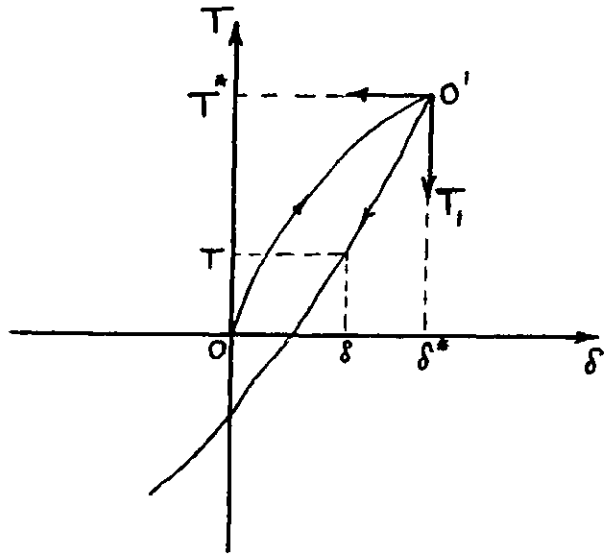

For the first loading curve Equation (1.15) gives:

$$\delta^* = 2\Delta^* = \delta_{max}\left[1-(1-\frac{T^*}{\mu P})^{2/3}\right] \qquad (A1.1)$$

where $\delta_{max} = \frac{3\mu P(2-\nu)}{8Ga}\,\phi$

For the unloading curve Equation (1.34) is:

$$\delta_u = \delta_{max}\left[2(1-\frac{T^*-T}{2\mu P})^{2/3} - (1-\frac{T^*}{\mu P})^{2/3} - 1\right]$$

Transforming the centre of the coordinate-axis from O to O' as shown in the figure gives:

$$\delta_1 = 2\left[1-(1-\frac{T_1}{2\mu P})^{2/3}\right]\delta_{max} \qquad (A1.2)$$

where $\begin{cases} \delta_1 = \delta^* - \delta \\ T_1 = T^* - T \end{cases}$

(A1.2) can be put in the form:

$$(1- \frac{\delta_1}{2\delta_{max}})^{-\frac{1}{2}} = (1- \frac{T_1}{2\mu P})^{-\frac{1}{3}} \qquad \text{(A1.3)}$$

The tangential compliance for the unloading curve can then be written as:

$$\frac{d\delta_1}{dT_1} = - \delta_{max} \left[-2 \times \frac{1}{3\mu P} (1- \frac{T_1}{2\mu P})^{-1/3} \right] \qquad \text{(A1.4)}$$

Using (A1.3) we can then put (A1.4) in the following form:

$$\frac{d\delta_1}{dT_1} = \frac{2\delta_{max}}{3\mu P} (1- \frac{\delta_1}{2\delta_{max}})^{-\frac{1}{2}} \qquad \text{(A1.5)}$$

The corresponding expression for the loading curve is given by:

$$\frac{d\delta_\ell}{dT} = \frac{2\delta_{max}}{3\mu P} (1- \frac{\delta_\ell}{\delta_{max}})^{-\frac{1}{2}} \qquad \text{(A1.6)}$$

Table 1.1 - After Ref.(1.36)

$\cos\theta'$	0.00	0.10	0.20	0.30	0.40	0.50	0.60	0.70	0.75	0.80	0.85	0.90	0.92	0.94	0.96	0.98	0.99
α	1.000	1.070	1.150	1.242	1.351	1.486	1.661	1.905	2.072	2.292	2.600	3.093	3.396	3.824	4.508	5.937	7.774
β	1.000	0.936	0.878	0.822	0.769	0.717	0.664	0.608	0.578	0.544	0.507	0.461	0.438	0.412	0.378	0.328	0.287
λ	0.750	0.748	0.743	0.734	0.721	0.703	0.678	0.644	0.622	0.594	0.559	0.510	0.484	0.452	0.410	0.345	0.288

Table 1.2 - After Ref.(1.35)

Coefficient of friction	Fraction of original Po
0	1
0.25	0.84
0.50	0.32
1.00	0.09

Table 1.3 After Ref.(1.34)

	Combined normal and tangential loading	pure normal loading	Increase in critical stress due to tangential load
σ^*_{1max}	$-1.39\ P_o$	$-P_o$	39%
σ^*_{2max}	$-0.72\ P_o$	$-P_o$	-
σ^*_{3max}	$-0.53\ P_o$	$-0.5\ P_o$	6%
max shear stress τ_{max}	$0.43\ P_o$	$-0.3\ P_o$	43%
max octahedral shear stress	$0.37\ P_o$	$-0.27\ P_o$	37%
location of critical point	z=o y=+0.3b	y=o z=0.78b	

$P_o = \frac{2P}{\pi b}$. $\mu = \frac{1}{3}$, $\nu = 0.25$

- ve stress denotes compression

$$\tau_{max} = \frac{1}{2}(\sigma^*_1 - \sigma^*_3)$$

$$\text{max. octahedral shear stress} = \frac{1}{3}\sqrt{(\sigma^*_{1max}-\sigma^*_{2max})^2+(\sigma^*_{2max}-\sigma^*_{3max})^2+(\sigma^*_{3max}-\sigma^*_{1max})^2}$$

Table 2.1 1 x 92 wire strand, 39.0mm O.D

Ultimate tensile strength = 1.23 MN

(1) Layer	(2) number of wires	(3) lay direction	(4) wire diameter D(mm)	(5) lay angle (degrees)	(6) pitch circle radius (theo) r(mm)	(7) pitch circle radius (prac) r(mm)	(8) net steel area A_n (mm^2)
1	30	RH	3.54	17.74	17.73	17.75	308.4
2	24	LH	3.54	16.45	14.10	14.35	245.0
3	18	LH	3.54	15.93	10.57	10.95	183.2
4	12	RH	3.54	14.90	7.04	7.54	121.6
5	7	RH	3.54	15.42	4.19	4.17	71.08
King	1	-	5.05	-	-	-	20.00

Note: Column (7), measured outside radius = 19.5mm.

Direct addition of wire diameters give 20.2mm.

Thus bedding at each interface = (20.2 - 19.5)/5 = 0.14.

Then data in column (7) built-up from centre using 0.14mm bedding at each interface.

Table 2.2 1 x 19 wire strand, 16.4mm O.D.

Ultimate tensile strength = 0.234 MN

(1) Layer	(2) Number of wires n	(3) Lay direction	(4) Wire diameter D (mm)	(5) Lay angle α (degrees)	(6) Pitch circle radius (theo.) r(mm)	(7) Net steel area A_n (mm^2)
1	12	RH	3.25	11.91	6.41	101.69
2	6	LH	3.25	11.42	3.30	50.75
King	1	-	3.594	-		10.14

Table 2.3 1 x 139 wire strand, 51.0mm O.D.

Ultimate tensile strength = 2.16MN

(1) Layer	(2) Number of wires n	(3) Lay direction	(4) Wire diameter D(mm)	(5) Lay angle α(degrees)	(6) Pitch circle radius (theo.) r(mm)	(7) Net steel area A_n(mm^2)
1	36		4.01	12.83	23.59	466.06
2	30		4.01	12.63	19.65	388.08
3	24		4.01	12.35	15.72	310.13
4	18		4.01	11.94	11.79	232.24
5	12		4.01	11.14	7.89	154.38
Core	6		2.31	7.74		24.45
	6		3.00	6.71		41.53
	6		2.84	4.05		37.71
	1		3.00	-		7.07

(net Core area)

Table 2.4 1 x 291 wire strand, 127mm O.D.

Ultimate tensile strength = 13.35MN.

(1) Layer	(2) Number of wires n	(3) Lay direction	(4) Wire diameter D(mm)	(5) Lay angle α(degrees)	(6) pitch circle radius (theo.) r(mm)	(7) Net steel area A_n(mm^2)
1	54	RH	6.55	18.01	59.22	1912.30
2	48	LH	6.55	18.01	52.64	1699.85
3	42	LH	6.55	18.01	46.07	1487.37
4	36	RH	6.55	18.01	39.50	1274.89
5	31	LH	6.55	18.01	34.02	1097.82
6	25	RH	6.55	18.01	27.46	885.34
7	19	LH	6.55	18.01	20.90	672.86
8	14	RH	6.30	18.01	14.85	458.66
Core	7		3.90	13.07		net core area 85.80
	7		5.10	12.20		146.23
	7		5.25	7.62		152.80
	1		7.00	-		38.47

Table (3.1) Variation of Effective Shear Modulus in Various Layers of 39mm Strand for Two Mean Axial Loads as Determined from Various Approximations.

		Full Slip					No Slip			
Equation		(3.27)	(3.26)		(3.13)		(3.26)		(3.13)	
mean axial load/MN		-	0.10	0.41	0.10	0.41	0.10	0.41	0.10	0.41
non-dimensionalized	5	0.0655	0.0705	0.0710	0.0720	0.0734	0.1638	0.1831	0.1729	0.1928
effective shear	4	0.0621	0.0667	0.0671	0.0686	0.0696	0.1681	0.1870	0.1768	0.1961
modulus G/E	3	0.694	0.0754	0.0754	0.0768	0.0778	0.1696	0.1879	0.1797	0.1981
in layer:	2	0.0738	0.0802	0.0807	0.0812	0.0826	0.1686	0.1870	0.1792	0.1981
	1	0.0842	0.0913	0.0928	0.0918	0.0937	0.1599	0.1836	0.1734	0.1966

Table (4.1) - After (4.38)

Test No.	Axial Load tons	Exciter CL to Socket face (m)	Exciter Amplitude (Stroke) mm	Nominal Amplitude at Socket face degrees
4	41	4.30	±40.5 (81)	±0.539
5	41	2.44	±40.5 (81)	±0.952
6	20.5	2.44	±40.5 (81)	±0.952
7	20.5	2.44	±55 (110)	±1.29
8	41	2.44	±55 (110)	±1.29
9	41	2.44	±33.8 (67.6)	±0.794

For the definition of above terms refer to Fig.(4.2)

Table 4.2 Calculation of no-slip and full-slip E_{eff} for the 39mm strand under free field bending.

Layer	$\frac{E_i}{E_{steel}}$		$\frac{I_{ni}}{I_o} \cdot \frac{E_i}{E_{steel}}$	
	full-slip	no-slip	full-slip	no-slip
1	0.711	0.850	0.382	0.456
2	0.743	0.866	0.211	0.246
3	0.754	0.872	0.097	0.112
4	0.781	0.884	0.0336	0.0380
5	0.770	0.879	0.00624	0.00713
	$\therefore E_{eff}/E_{steel} = \Sigma$		0.730	0.859

Table (4.3) - After (4.37)

θ	0	½°	1°	1½°	2°	3°	4°	6°	8°	10°	20°
α	∞	61.40	36.89	27.48	22.26	16.50	13.31	9.790	7.860	6.604	3.813
β	0	0.1018	0.1314	0.1522	0.1691	0.1964	0.2188	0.2552	0.2850	0.3112	0.4123

Table 5.1 1x73 wire strand, 41mm O.D.

(1) Layer	(2) Number of Wires n	(3) Lay direction	(4) Wire diameter D(mm)	(5) Lay angle α(degree)	(6) Pitch circle radius (theo.) r(mm)	(7) Net steel area A_n(mm^2)
1	24	LH	4.57	12.45	35.84	403.15
2	18	RH	4.57	11.96	26.88	301.80
3	12	LH	4.57	11.25	17.98	200.69
	12(6+6)	LH	3.43 & 2.67	7 & 7.7		Net 89.76
Core	6	LH	3.38	4		core 53.97
	1	-	3.38	-		area 8.973

Table 5.2 Comparison of theoretical and measured full slip strand stiffnesses.

Cable diameter (mm)	Effective strand modulus (kN/mm^2) for wire modulus of:		Mean Experimental moduli (kN/mm^2)
	207 kN/mm^2	201 kN/mm^2	
39	154.6	150.1	155
41	183.0	177.7	172.5*
51	179.9	174.7	169.7+
127	143.4	139.2	142.0

*Mean of values for 3 manufacturing batches (172.0, 174.1, 171.4 kN/mm^2)

+Mean of values for 2 batches

Table 6.1 Parameters for axial fatigue tests on 16 and 39mm O.D. strands.

Strand diameter (mm)	Test No	S_a/S_u %	S_m/S_u %	$R=\frac{S_{min}}{S_{max}}$
16	1	40.6	50	0.42
	2	40.6	50	0.42
	3	23.3	41.5	0.56
	4	23.3	41.5	0.56
	5	10.2	35	0.75
	6	10.6	35	0.74
	7	30.4	25	0.24
	8	30.4	25	0.24
	9	20.2	20	0.33
	10	20.2	20	0.33
	11	10.6	15	0.48
	12	14.8	17	0.39
39	1	10	35	0.75
	2	27.8	25.9	0.30
	3	28.5	44.3	0.51

Table 6.2 1x 292 Wire Strand, 45mm O.D.

Calculated ultimate tensile strength =1.72 MN.

(1) Layer	(2) Number of wires n	(3) Lay direction	(4) Wire diameter D(mm)	(5) Lay angle α (degrees)	(6) Pitch circle radius (theo.) r(mm)	(7) Net Steel area A_n (mm^2)
1	54	RH	2.36	18.01	21.34	248.38
2	48	LH	2.36	18.01	18.96	220.79
3	42	LH	2.36	18.01	16.60	193.19
4	37	RH	2.36	18.01	14.63	170.19
5	31	LH	2.36	18.01	12.26	142.59
6	25	RH	2.36	18.01	9.89	114.99
7	19	LH	2.36	18.01	7.53	87.39
8	14	RH	2.28	18.01	5.37	60.10
	7		1.44	13.07		net 11.70
	7		1.88	12.20		core area 19.88
Core	7		1.96	7.62		21.31
	1		2.65	-		5.52

mean axial load (MN)	0.410	0.205
a(mm)	0.2705	0.2175
b(mm)	0.0613	0.0493
$X_o = \frac{3\mu p}{2\pi ab}(N/mm^2)$	425	342
σ_x	$= -1.011\ X_o \cdot \frac{x}{a}$	
σ_y	$= -0.116\ X_o \cdot \frac{x}{a}$	
τ_{xy}	$= -0.933\ X_o\ \frac{y}{b}$	

where symbols are defined in Section 1.3; Equation (1.28) and $\mu = 0.115$.

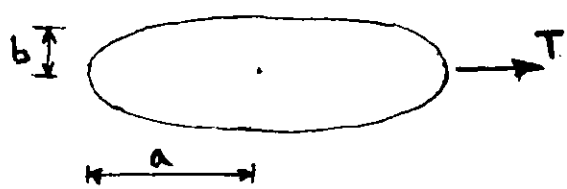

Table 6.3 Calculation of surface stress tensor over the trellis contact points with T directed along the major principal axis of the contact patch.

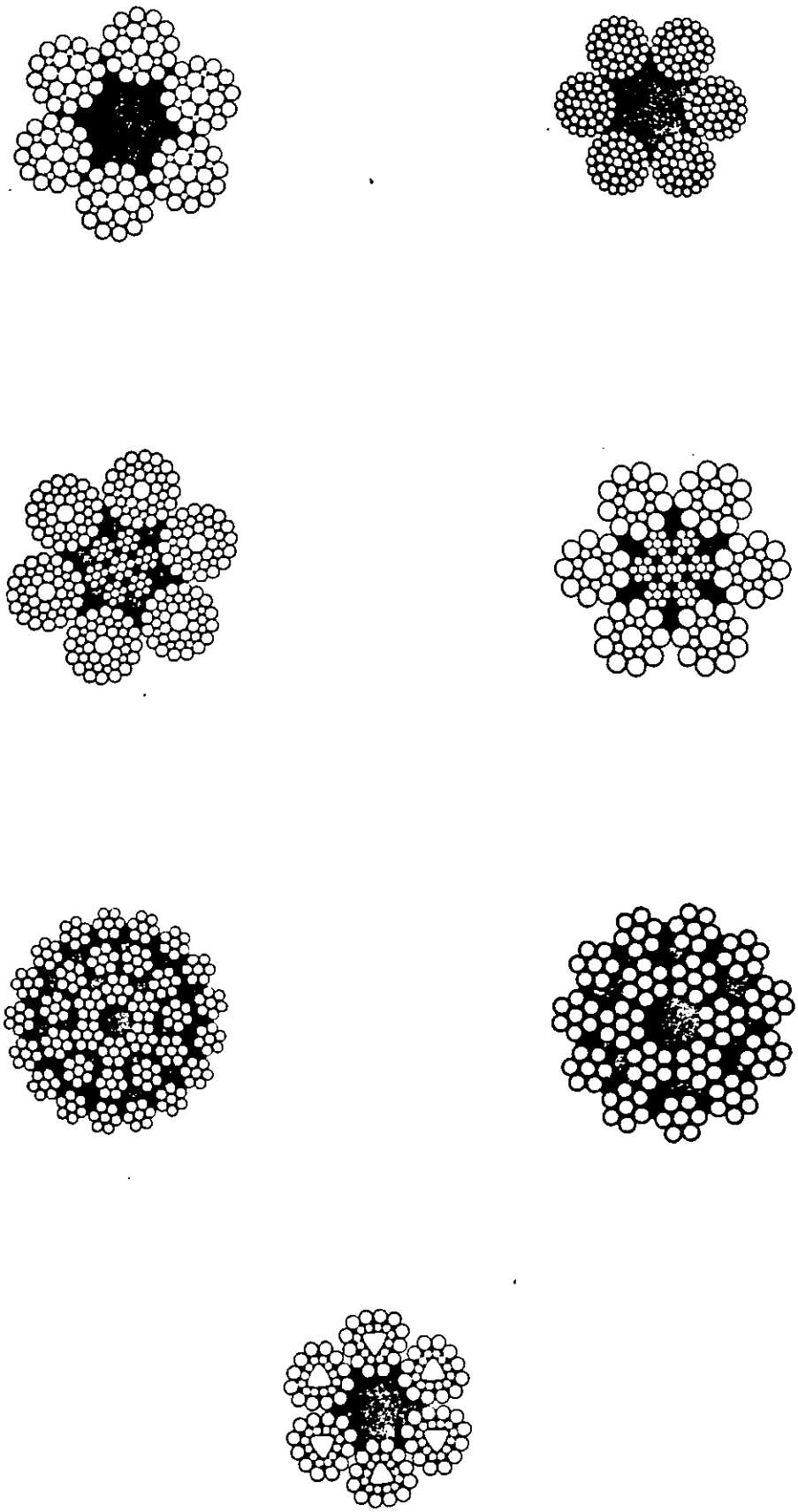

Fig. 0.1 Some examples of rope construction

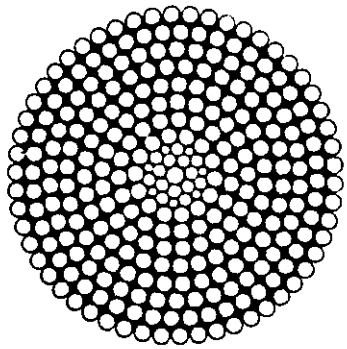

Spiral strand with no outer layer coating

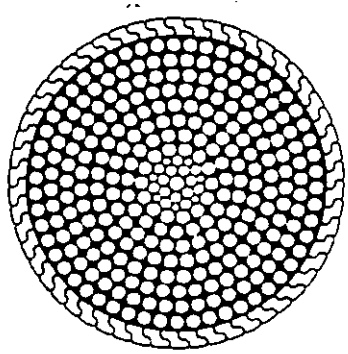

Locked coil construction

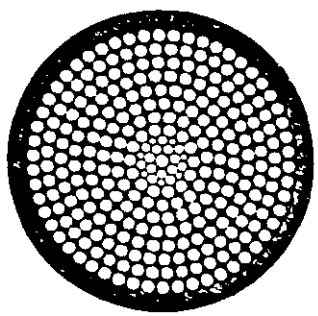

Spiral strand covered by high density polythene sheathing

Fig. 0.2 Spiral strands with an equal lay construction as their core

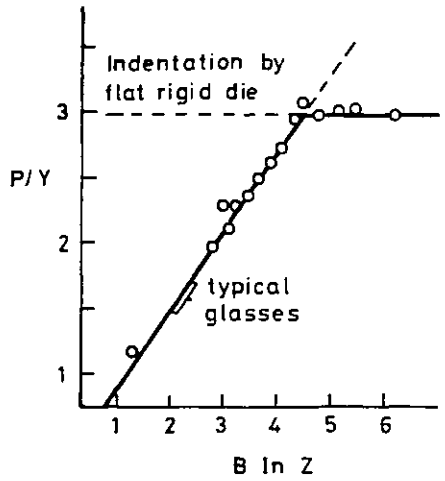

Fig 1·1 After Ref (1·12)

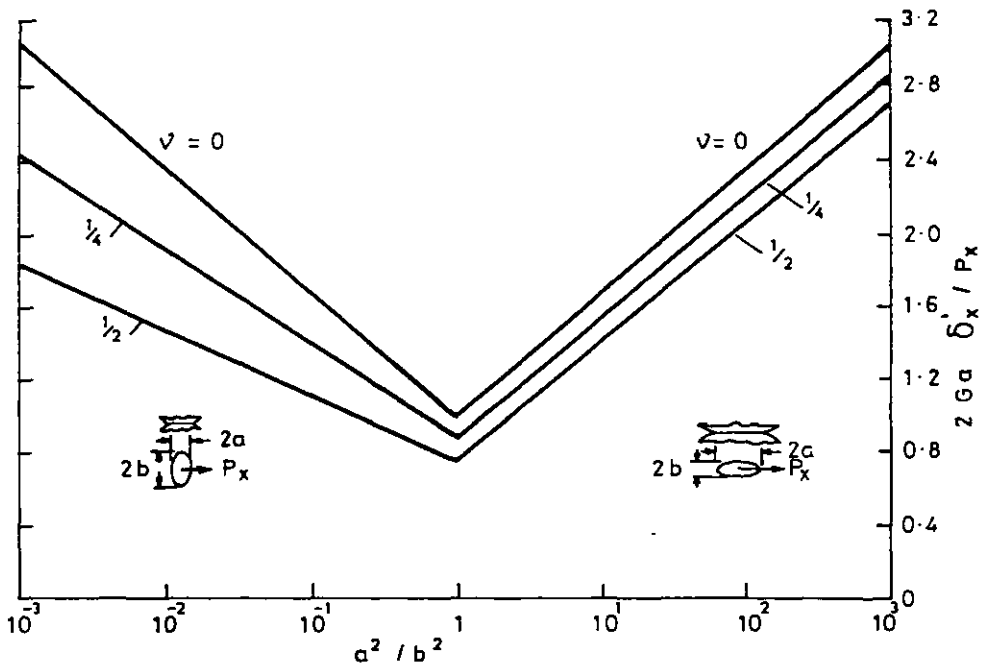

a, b = principal semi-axes of elliptic contact surface
P_x = force in direction of axis a
δ'_x = relative displacement in direction a
G = modulus of rigidity
ν = Poisson's ratio

INITIAL TANGENTIAL COMPLIANCE OF ELASTIC BODIES IN CONTACT

Fig 1·2 After Ref (1·39)

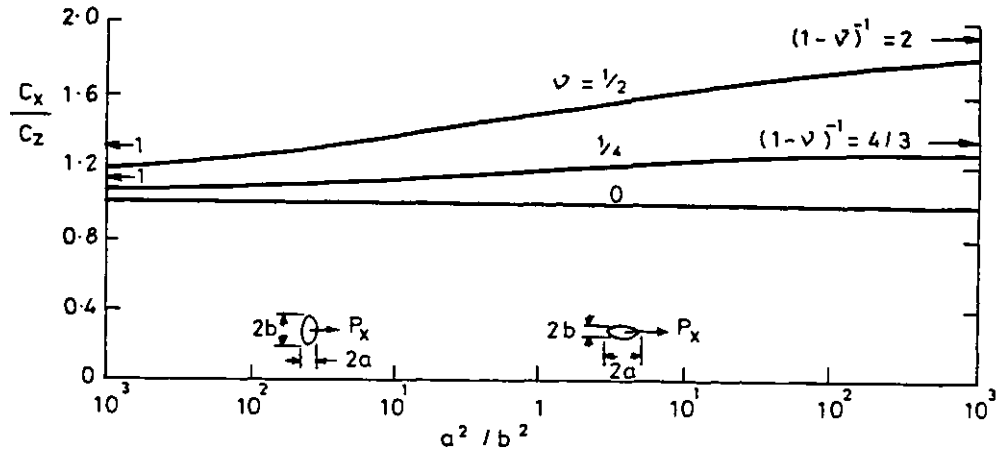

RATIO OF INITIAL TANGENTIAL COMPLIANCE C_x TO NORMAL COMPLIANCE C_z OF BODIES WITH LIKE ELASTIC CONSTANTS

Fig 1·3 After Ref (1·39)

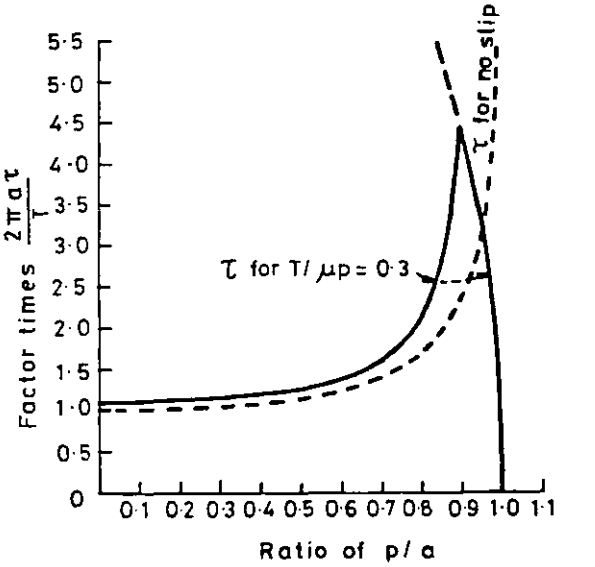

Traction plotted against radius for elastic displacement and modification introduced by the effect of slip

Fig 1·4 After Ref (1·39)

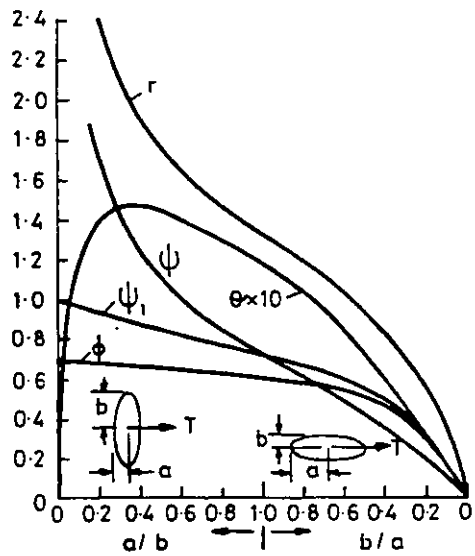

Fig 1·5 After Ref (1·41)

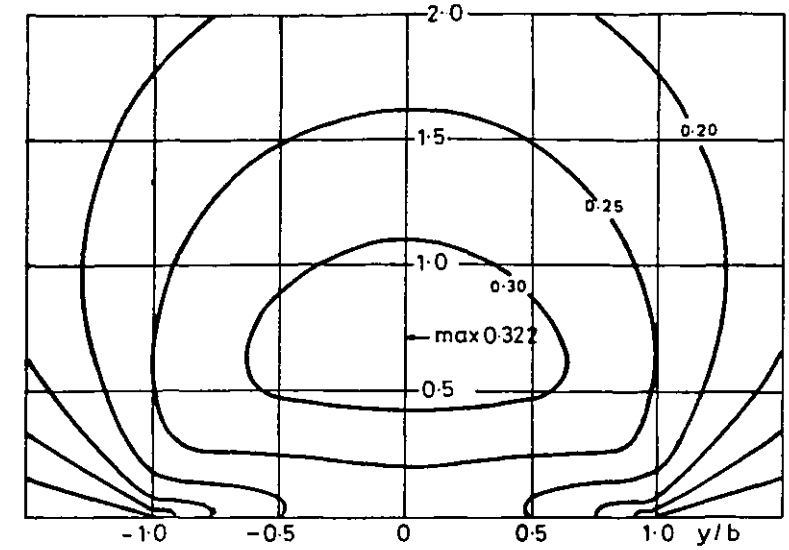

Lines of constant $J_2^{1/2}/p_o$ beneath contact between normally loaded cylinders

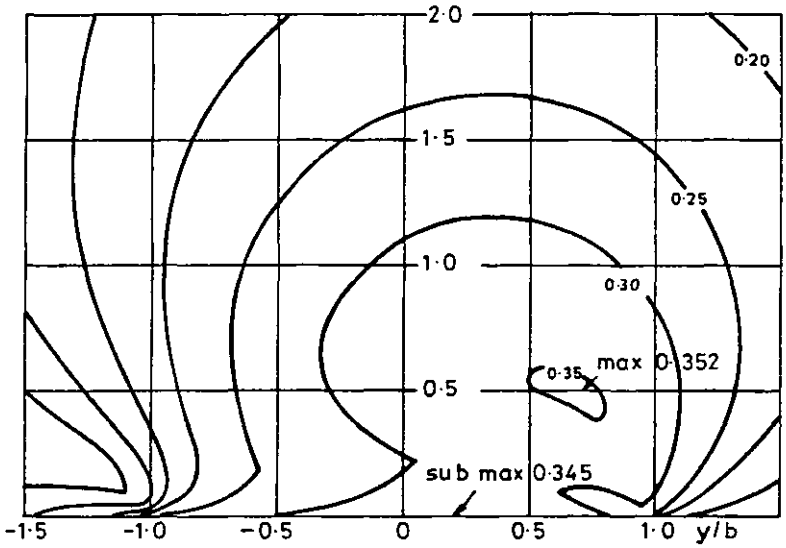

Lines of constant $J_2^{1/2}/p_o$ beneath contact between cylinders $\mu = 0.25$

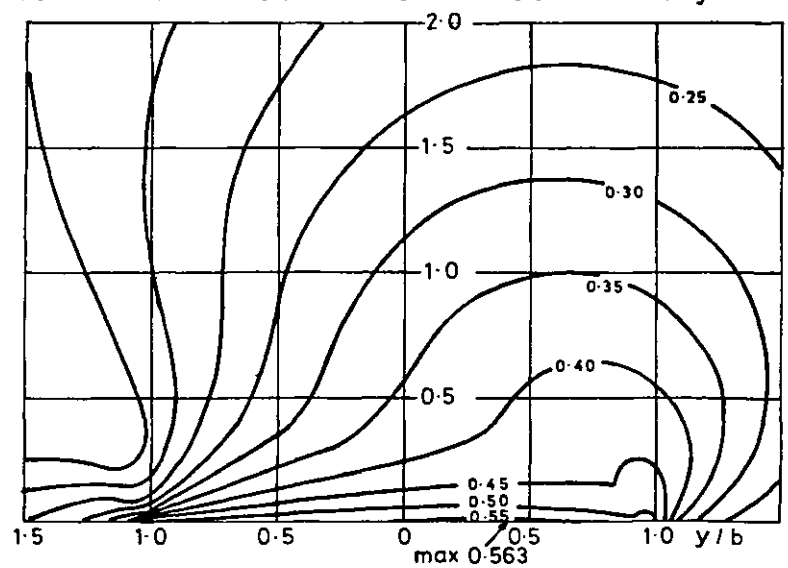

Lines of constant $J_2^{1/2}/p_o$ beneath contact between cylinders $\mu = 0.50$

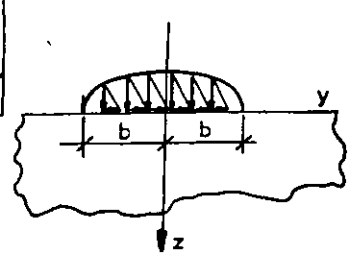

Fig 1·6 After Ref (1·56)

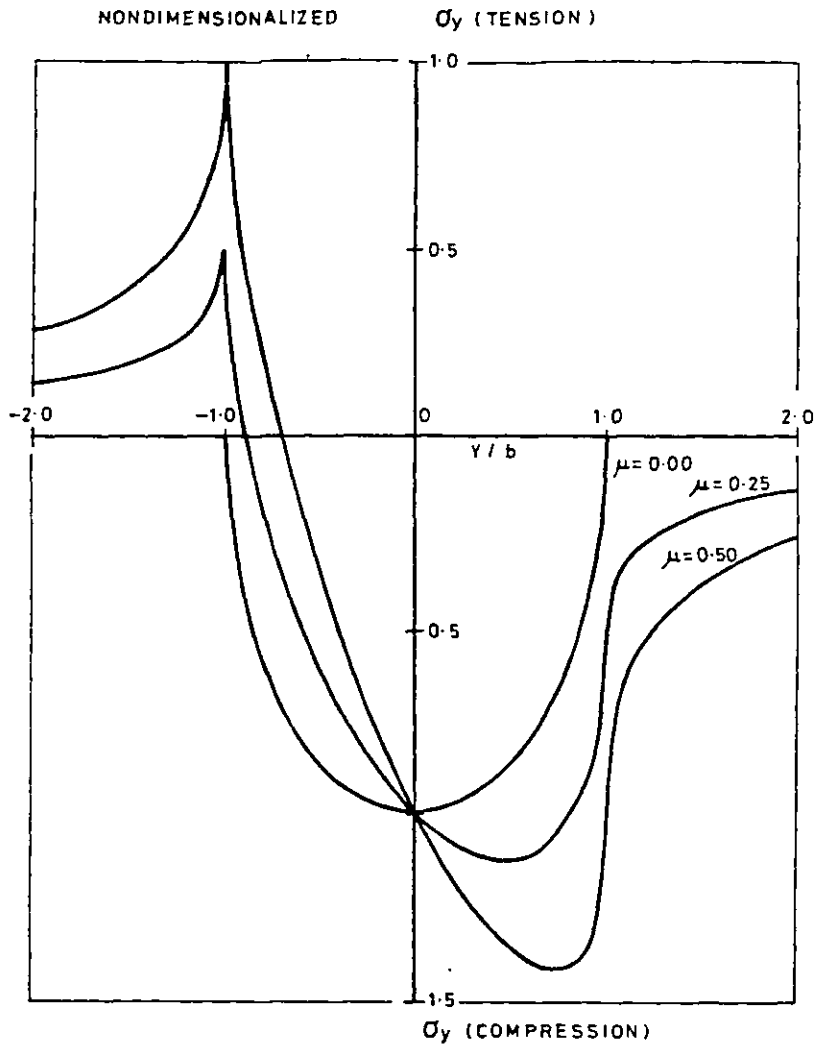

TENSILE STRESS IN SURFACE OF A CYLINDRICAL CONTACT

Fig 1·7 After Ref. (1·35)

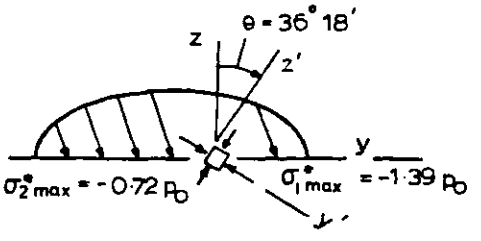

Fig 1.8 After Ref (1·34)

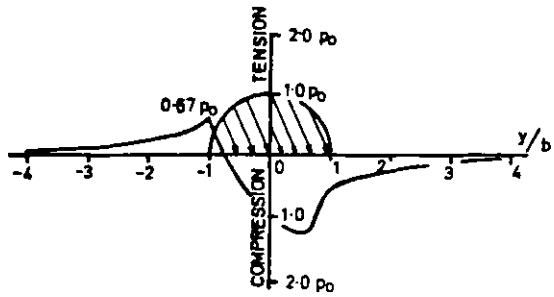

Range of values of σ_y^* at a point O (fixed) as load moves past point

Fig. 1.9 After Ref. (1·34)

Table showing changes in magnitude sense and direction of principal stresses at a fixed point O in surface, as load moves past it

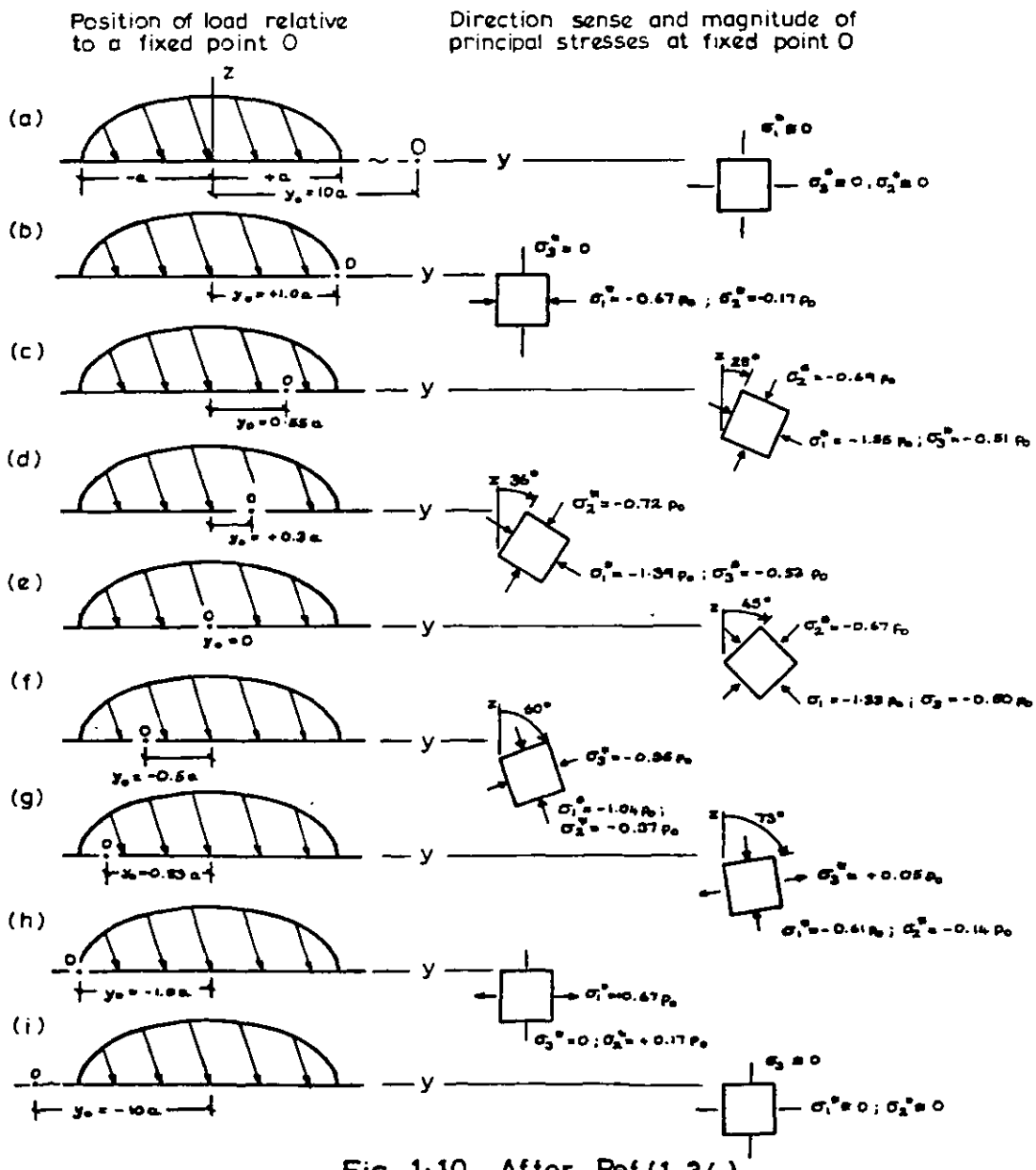

Fig 1·10 After Ref (1·34)

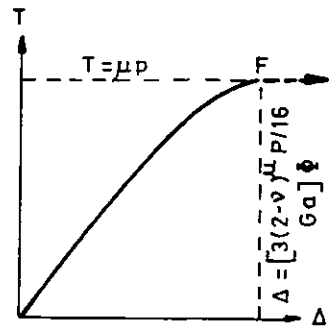

Fig 1·11

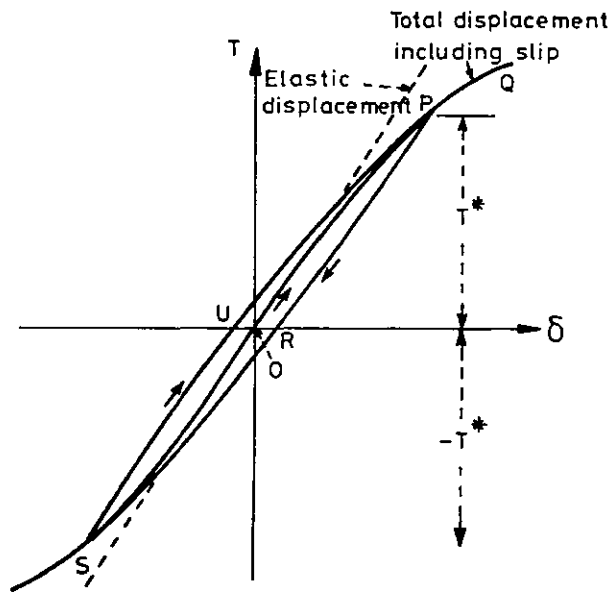

Fig 1·12 After Ref (1·44)

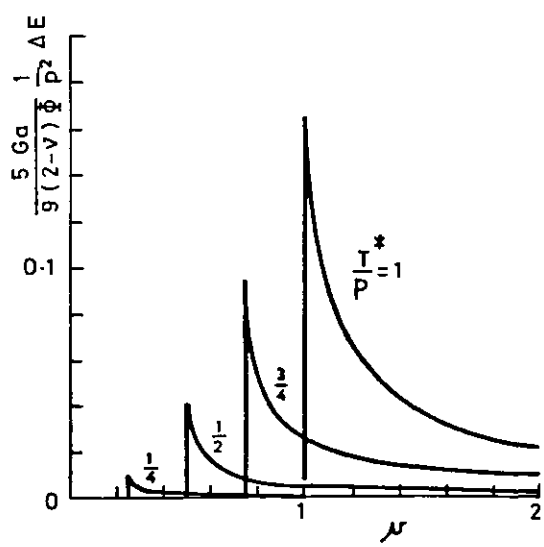

Energy loss in contact friction: constant normal and cyclic tangential loading

Fig 1·13 After Ref (1·53)

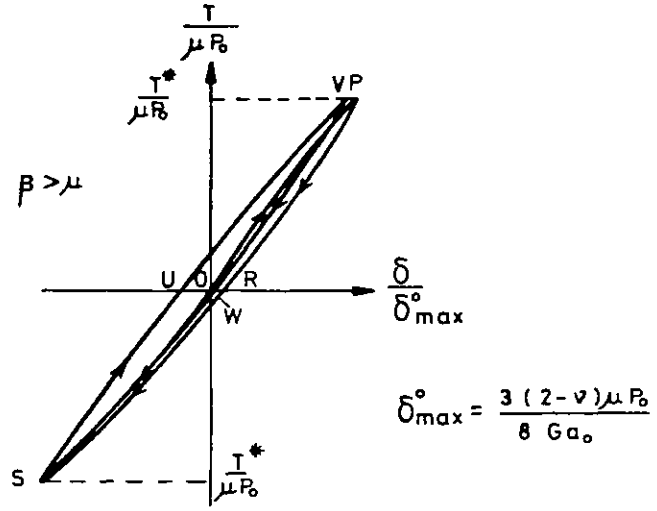

Fig 1·14 After Ref (1·46)

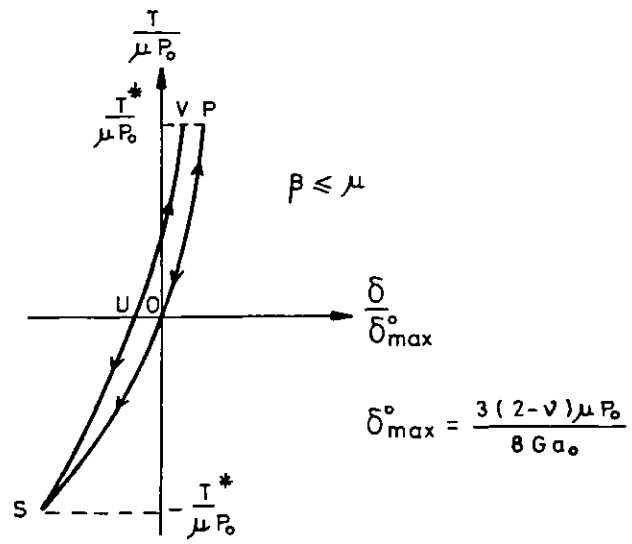

Fig 1·15 After Ref (1·46)

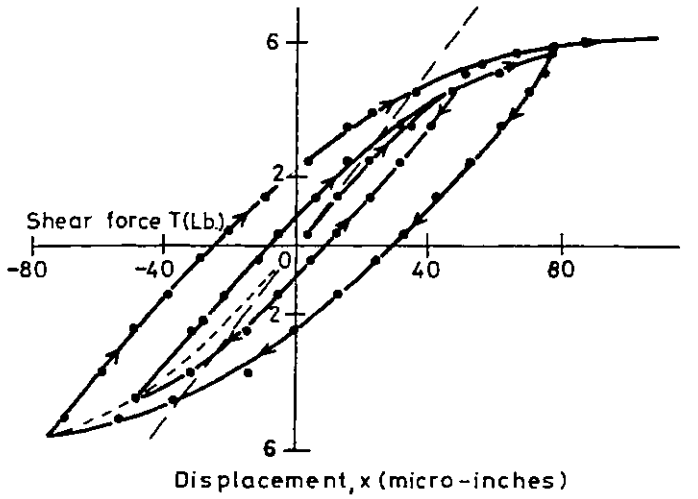

STATIC HYSTERESIS LOOP FROM STATIC TESTS

Fig 1·16 After Ref (1·50)

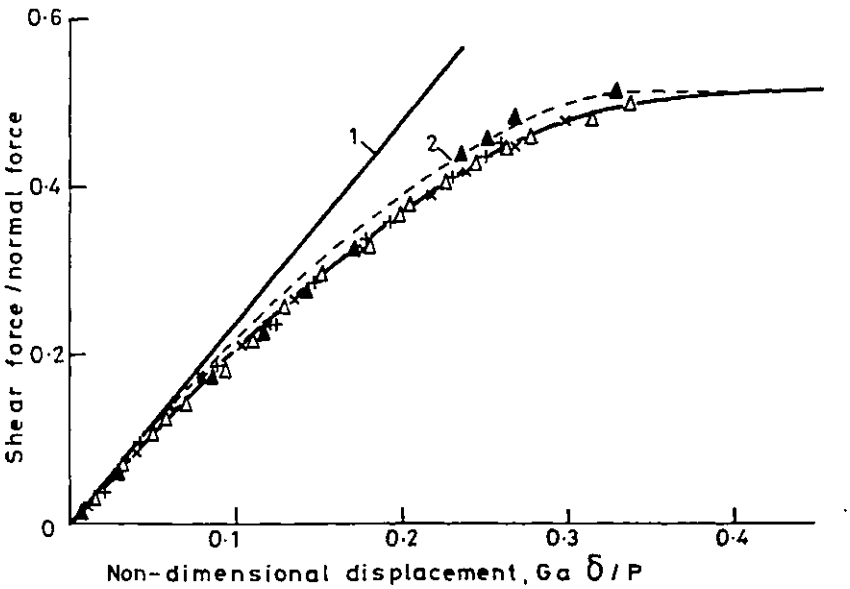

STATIC FORCE-DISPLACEMENT TESTS
Broken curve shows Mindlin's theoretical relationship

Fig 1·17 After Ref (1·50)

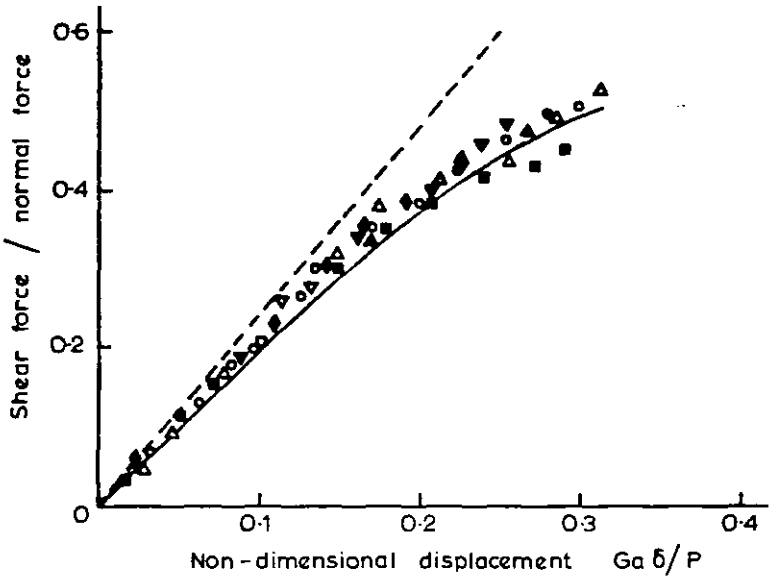

Dynamic displacement tests Non-dimensional correlation of results for range of ball diameters and normal loads compared with Mindlin's theoretical relationship taking $\mu = 0.5$

Fig.1·18 After Ref (1·50)

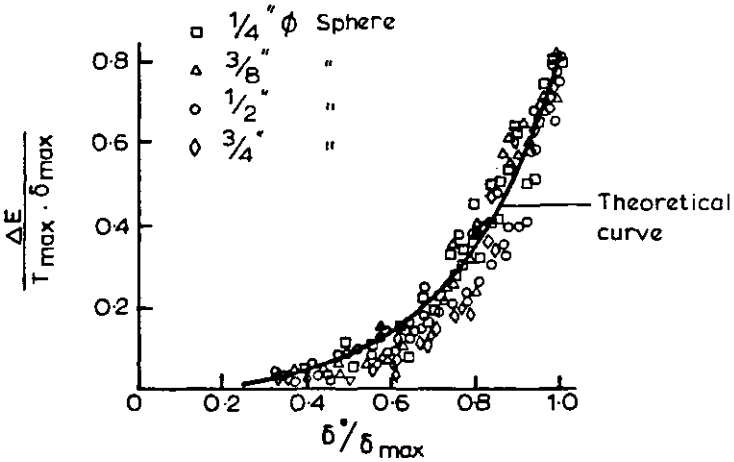

Comparison between experiment and theory of the dimensionless energy dissipation per cycle ($\Delta E / T_{max} \cdot \delta_{max}$) versus ($\delta^* / \delta_{max}$) for various sphere diameters

Fig.1·19 After Ref (1·47)

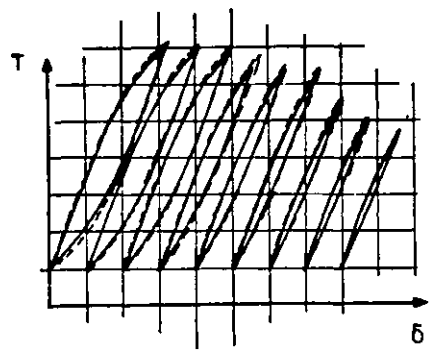

Experimental and theoretical hysteresis loops
(1/4" diam. sphere ; N = 0·573 lb ; T : 1 division = 0·0743 lb
δ : 1 division = 4·82 x 10^{-6} in)

Fig.1·20 After Ref. (1·47)

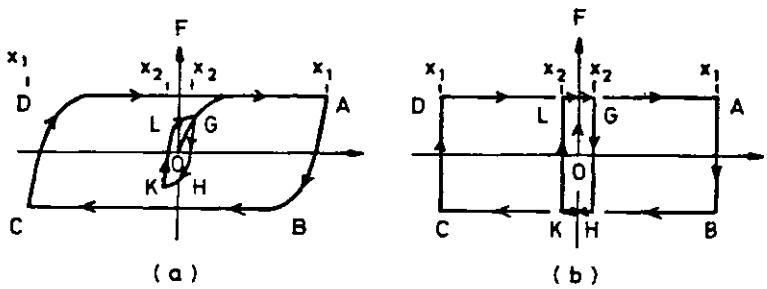

TANGENTIAL DISPLACEMENT OF CONTACTING SURFACES SUBJECTED TO TANGENTIAL FORCES. a) REAL BEHAVIOUR OF INDIVIDUAL ASPERITY; b) IDEALIZED BEHAVIOUR ASSUMED IN MINDLIN'S THEORETICAL TREATMENT.

Fig 1·21 After Ref (1·9)

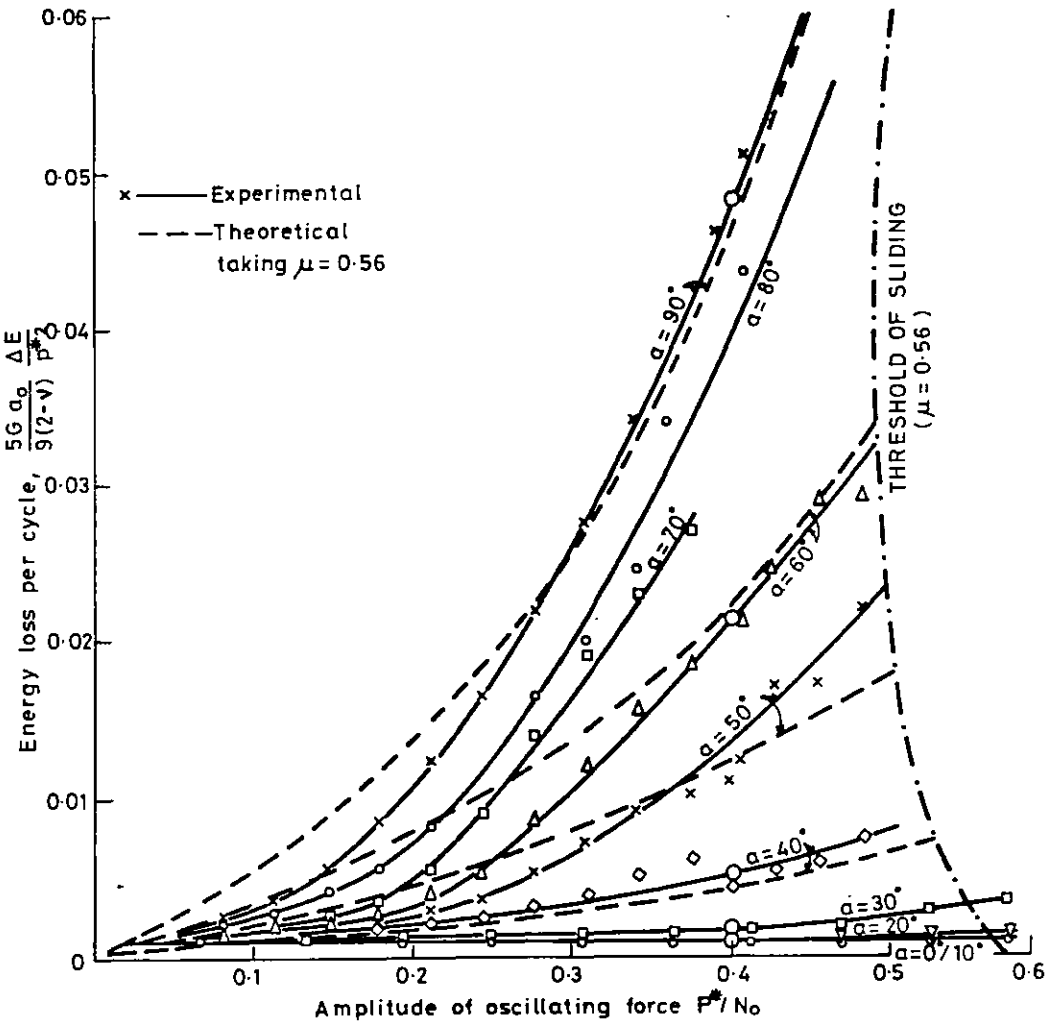

RESULTS OF ENERGY DISSIPATION MEASUREMENTS AT VARIOUS ANGLES OF OBLIQUITY

FIG 1·22 After Ref. (1·54)

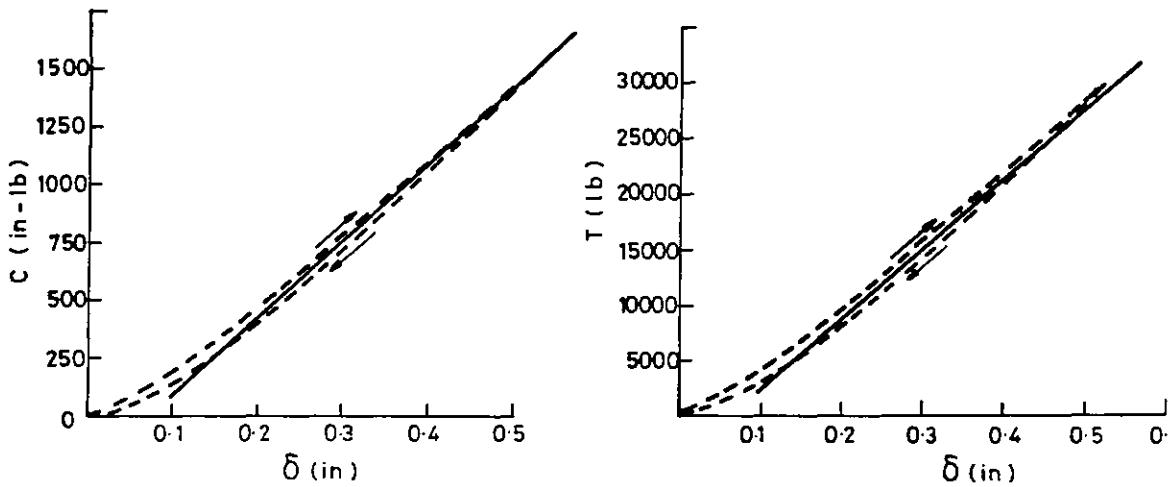

a) Torque C vs elongation δ

b) Tensile load T vs elongation δ

DATA FROM THE CLAMPED-END ROPE TEST

FIG 2·1 After Ref (2·11)

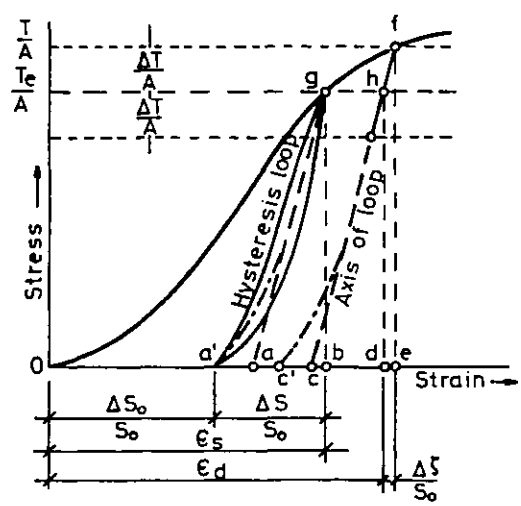

SCHEMATIC DIAGRAM OF STRESS-STRAIN RELATIONSHIPS FOR A TYPICAL MOORING ROPE

FIG 2·2 After Ref (2·35)

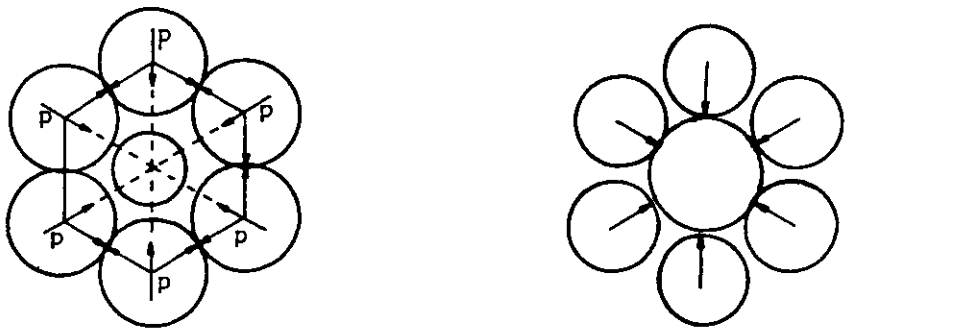

FIG 2·3 After Ref (2·37)

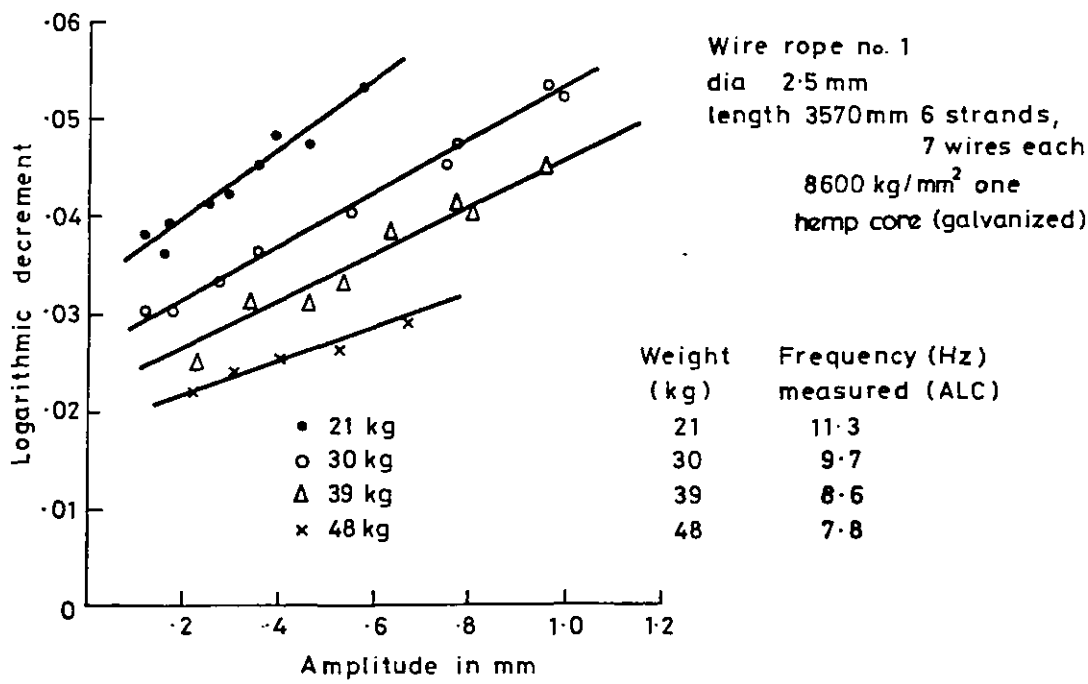

FIG 2·4(a) After Ref (2·39)

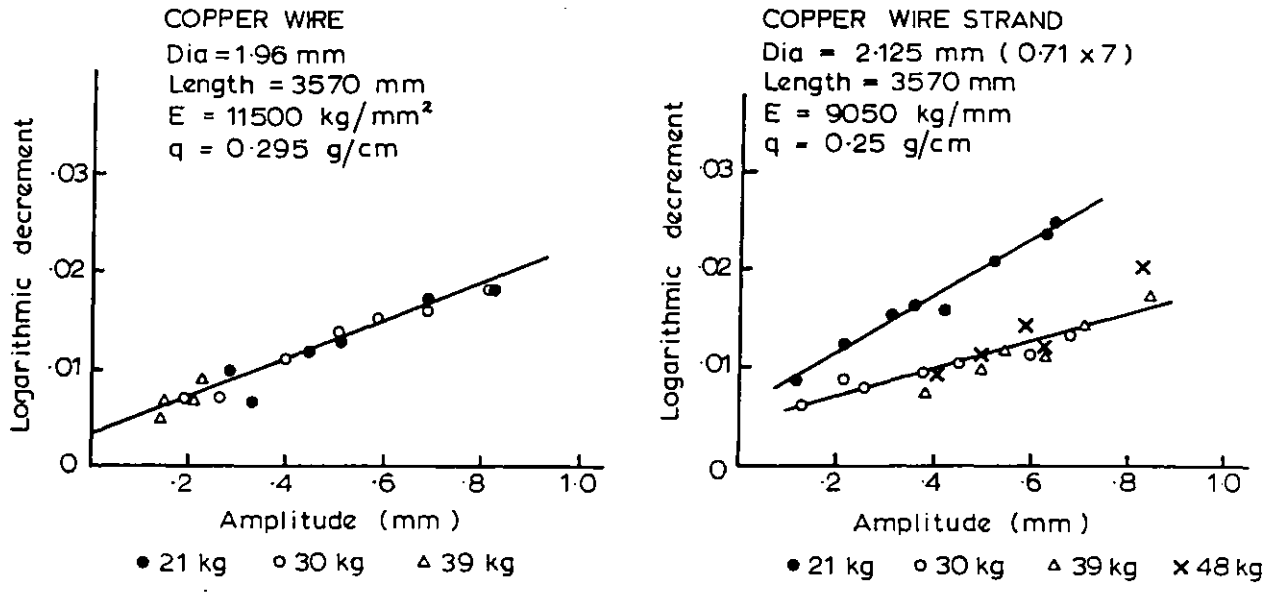

Fig. 2.4(b) After Ref. (2·39)

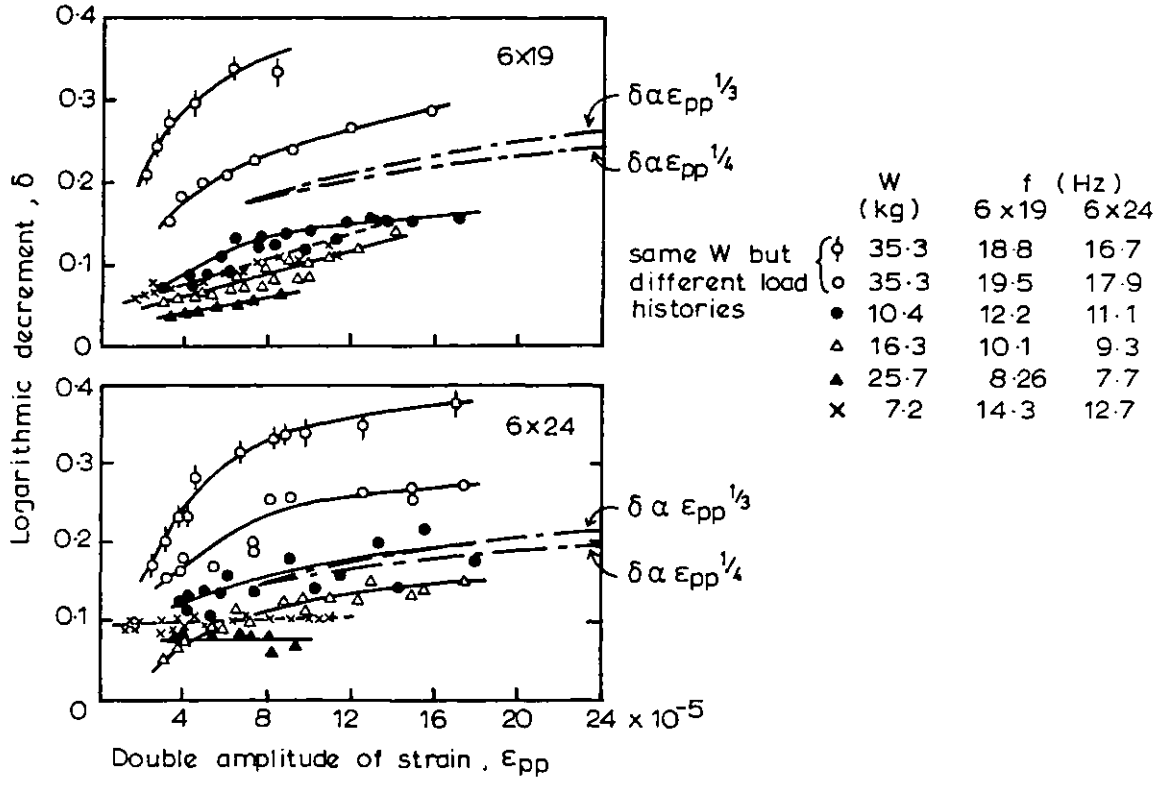

Fig 2.4 (c) After Ref. (2·40)

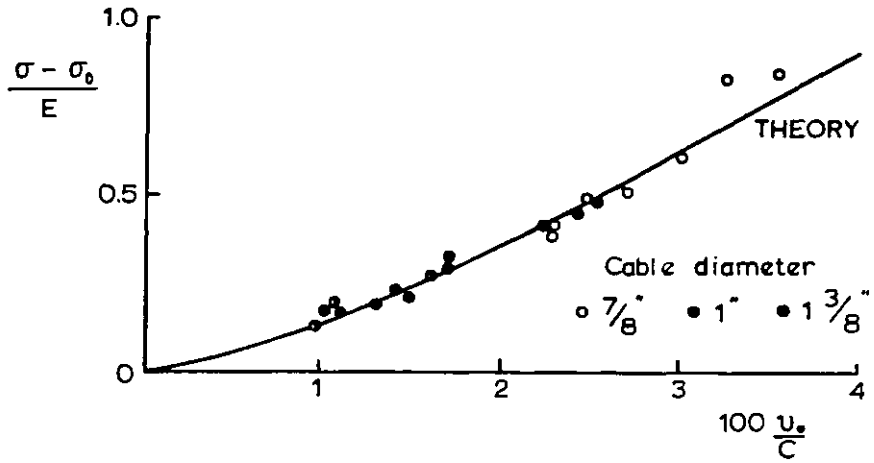

Fig 2.5a Comparison of theory and experiment for perpendicular impact
(After Ref 2·48)

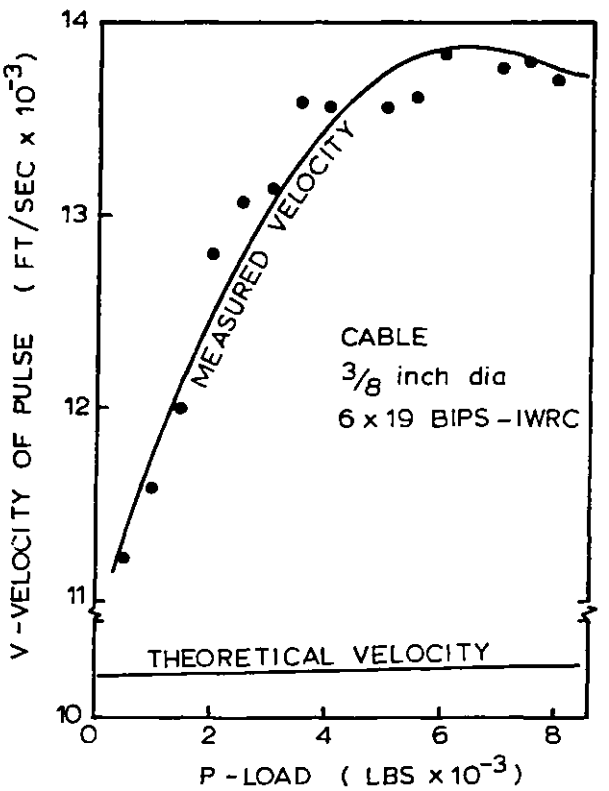

Fig 2·5.b Comparison of theory [e.q. (2.4)] and experiment for longitudinal impact
(After Ref 2·50)

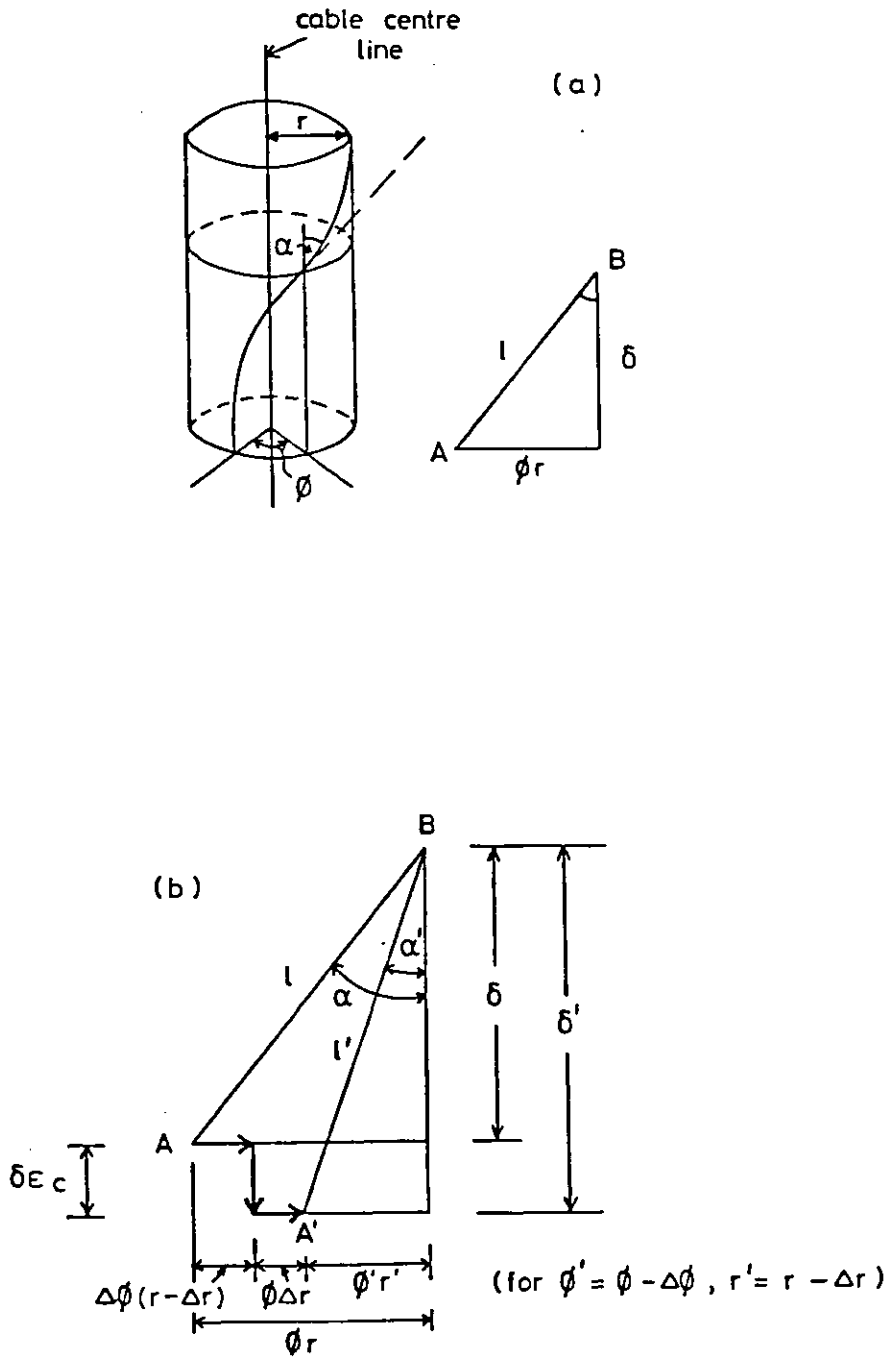

Fig 2.6 Helix geometry before and after cable deformation

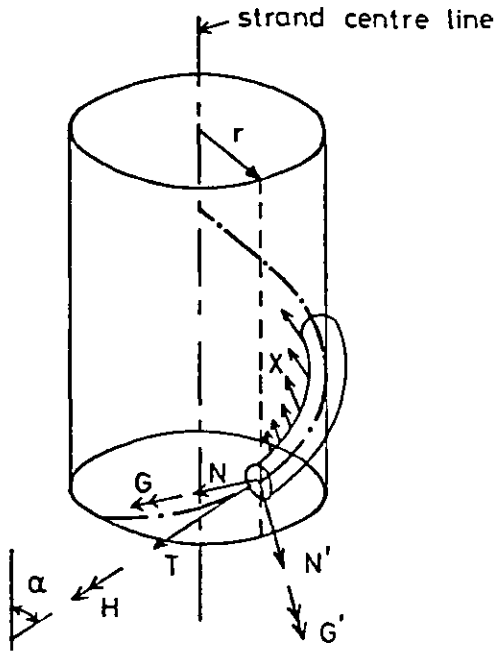

Fig. 2.7 Force resultants acting on a single wire

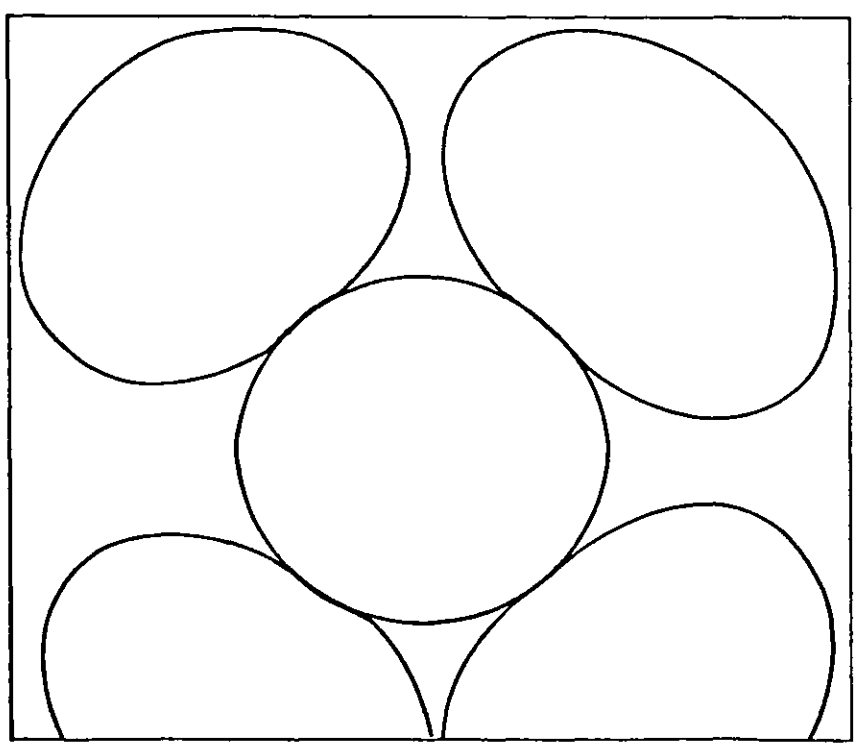

Fig. 2.8 Enlarged wire cross sections in a five wire strand

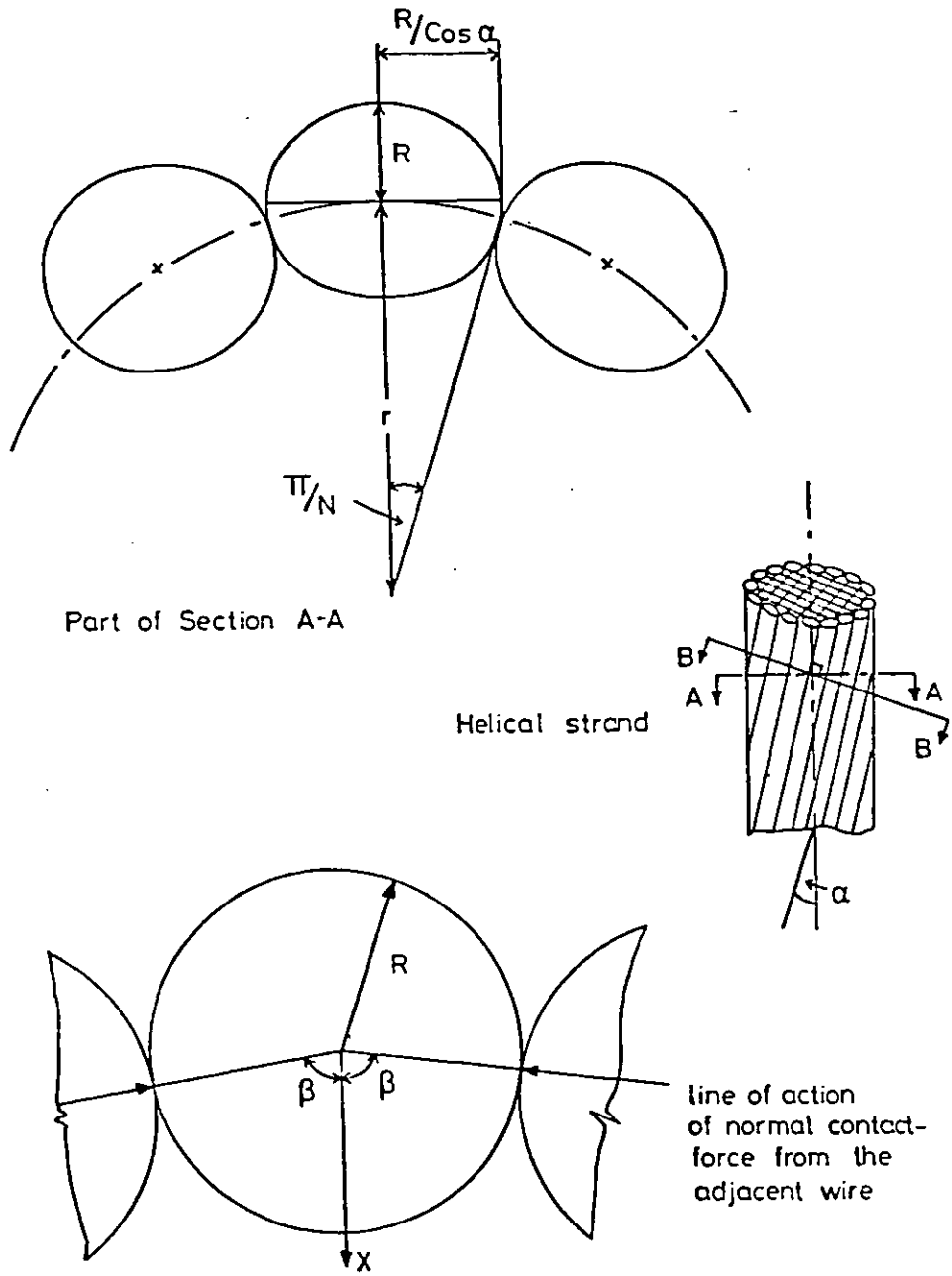

Fig. 2.9 Single layered strand with N wires

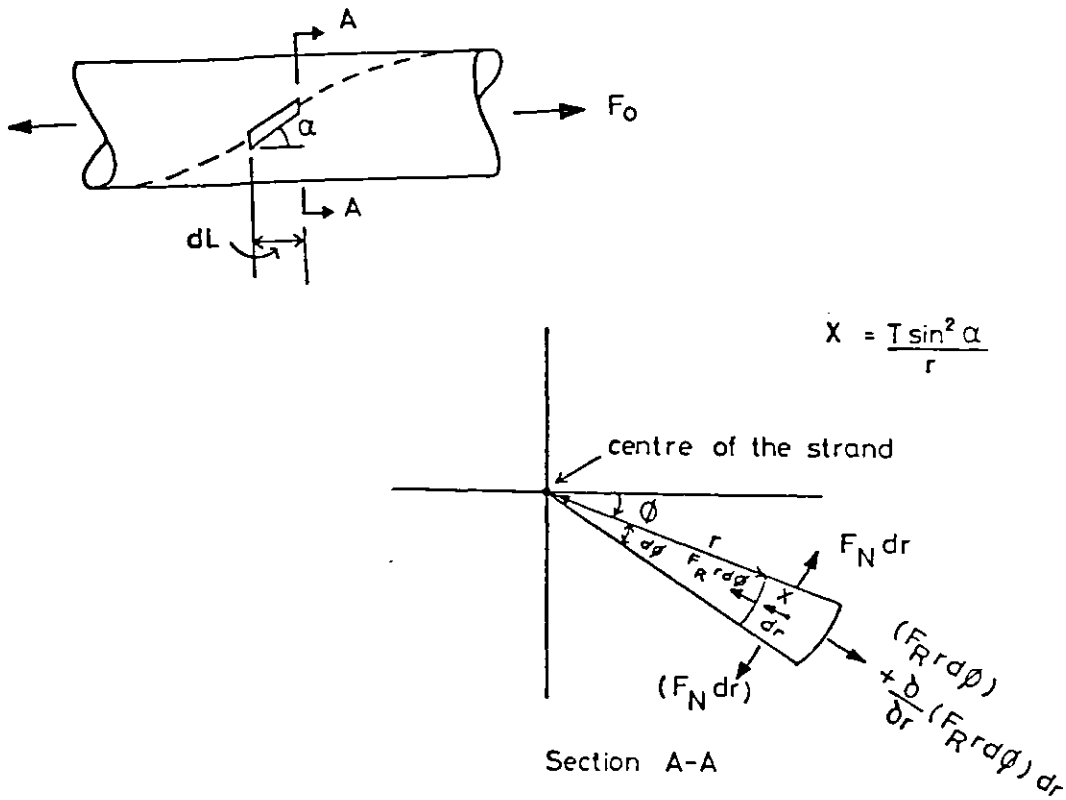

Fig. 2.10 Strand under pure tension treated as an axially symmetrical plane strain problem

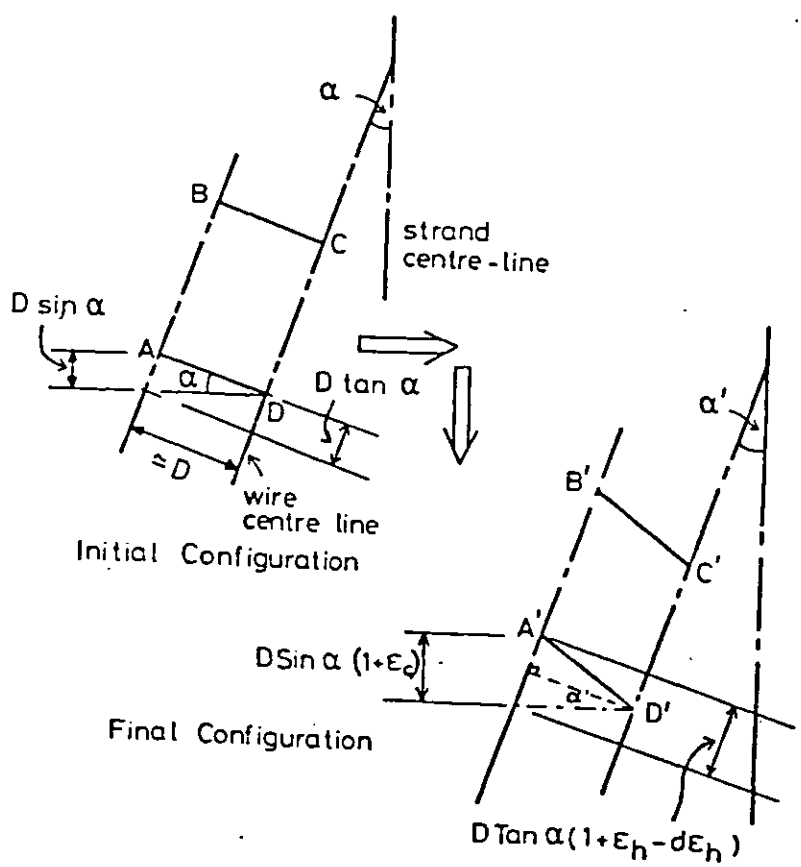

Fig. 2.11 Compatibility of wire movements in a layer

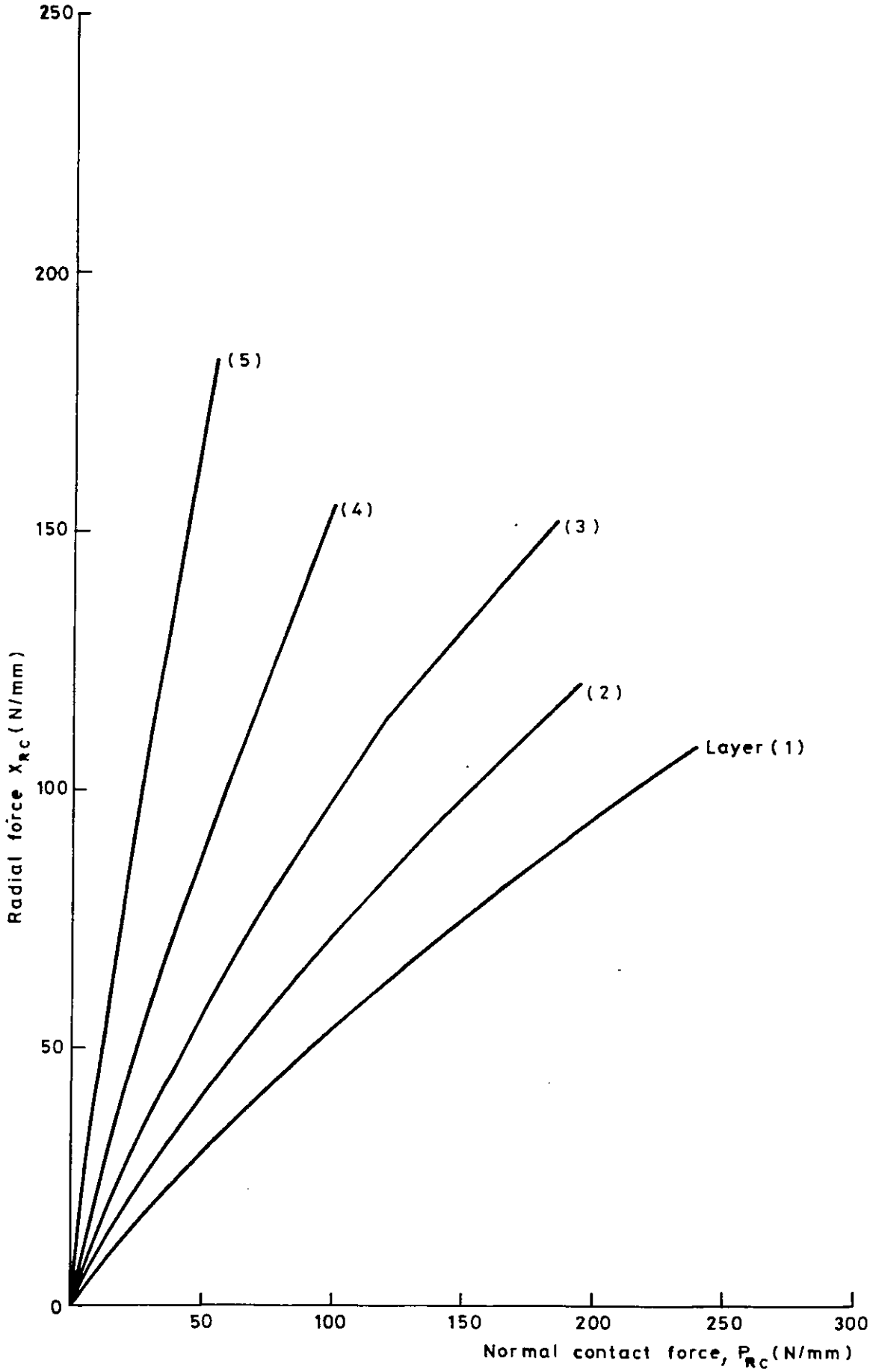

Fig 2·12 Contact forces in layers on rigid core - 39mm O·D· strand

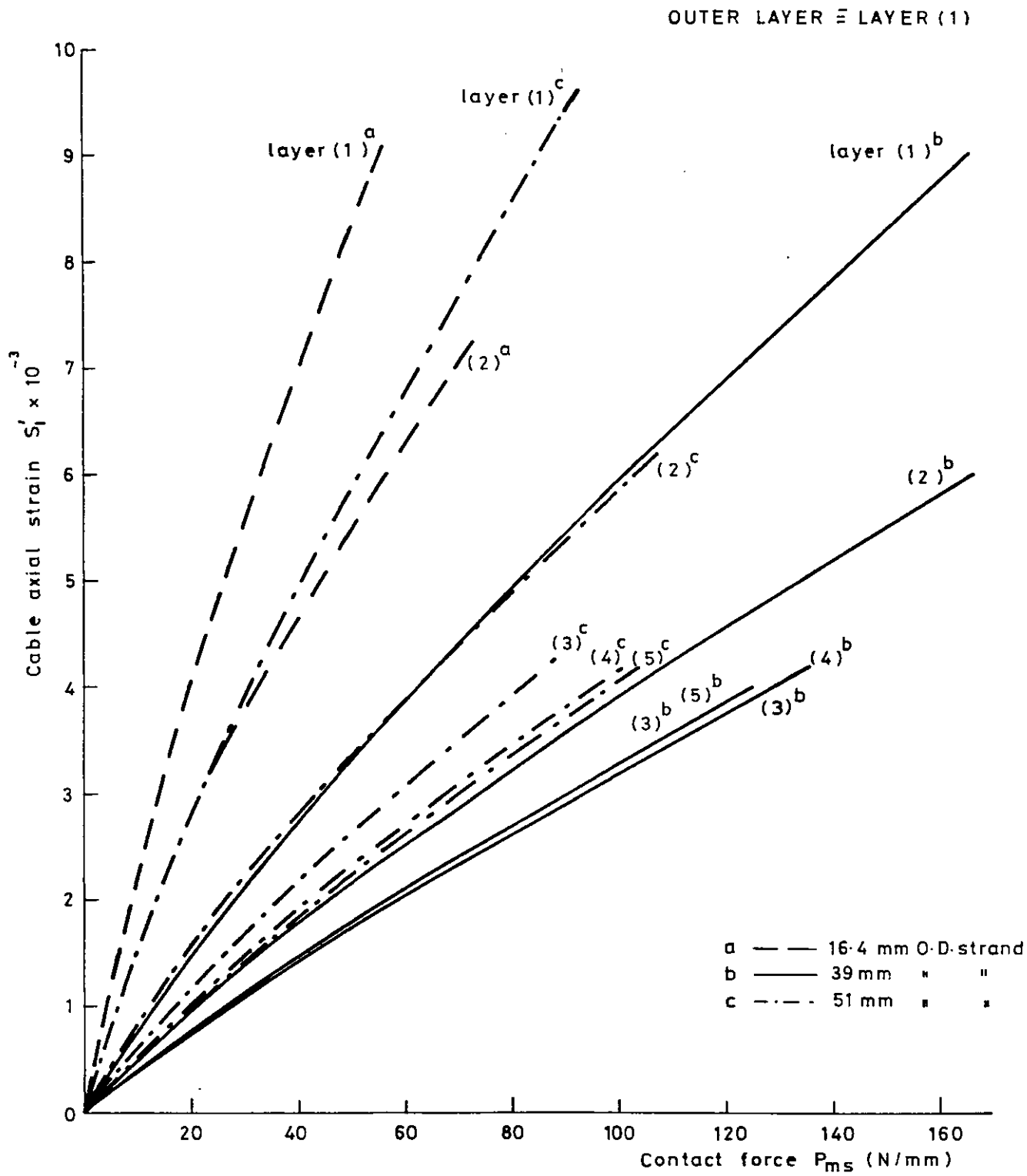

Fig 2-13 Line contact forces in assembled strands for three different constructions

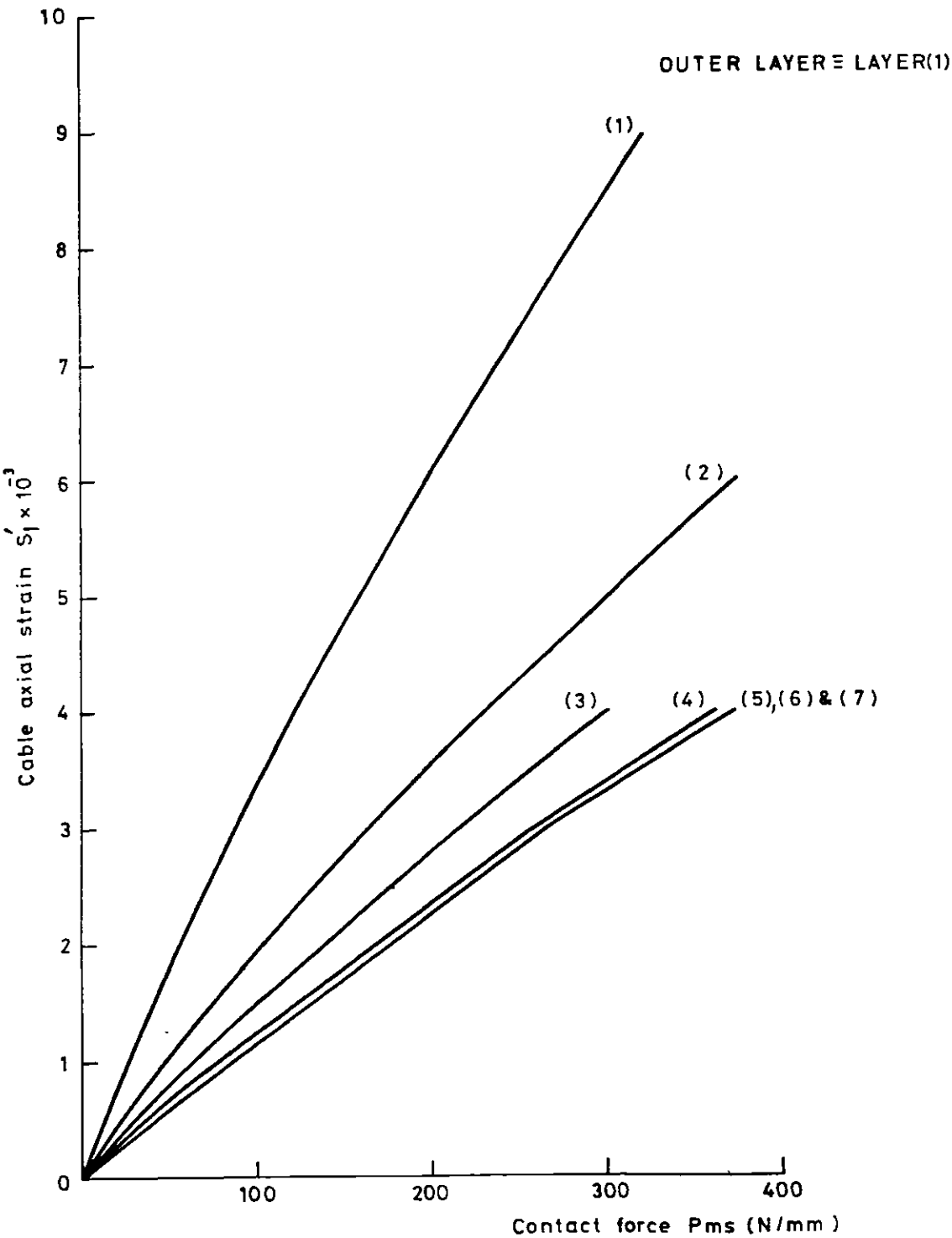

Fig 2·14 Line contact forces in assembled strand -127mm O·D·

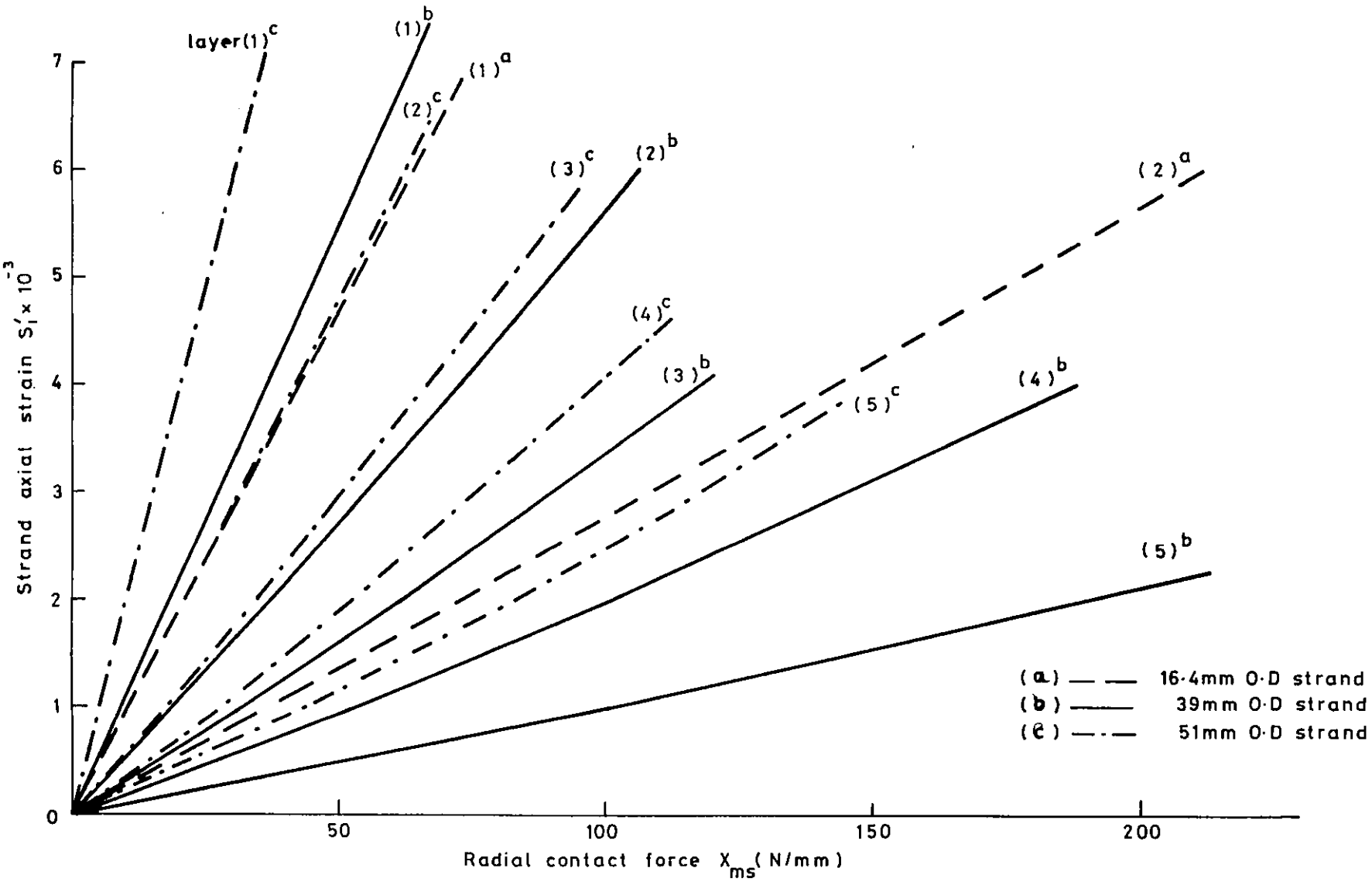

Fig 2·15 Plot of radial contact force per unit length X_{ms} versus cable axial strain

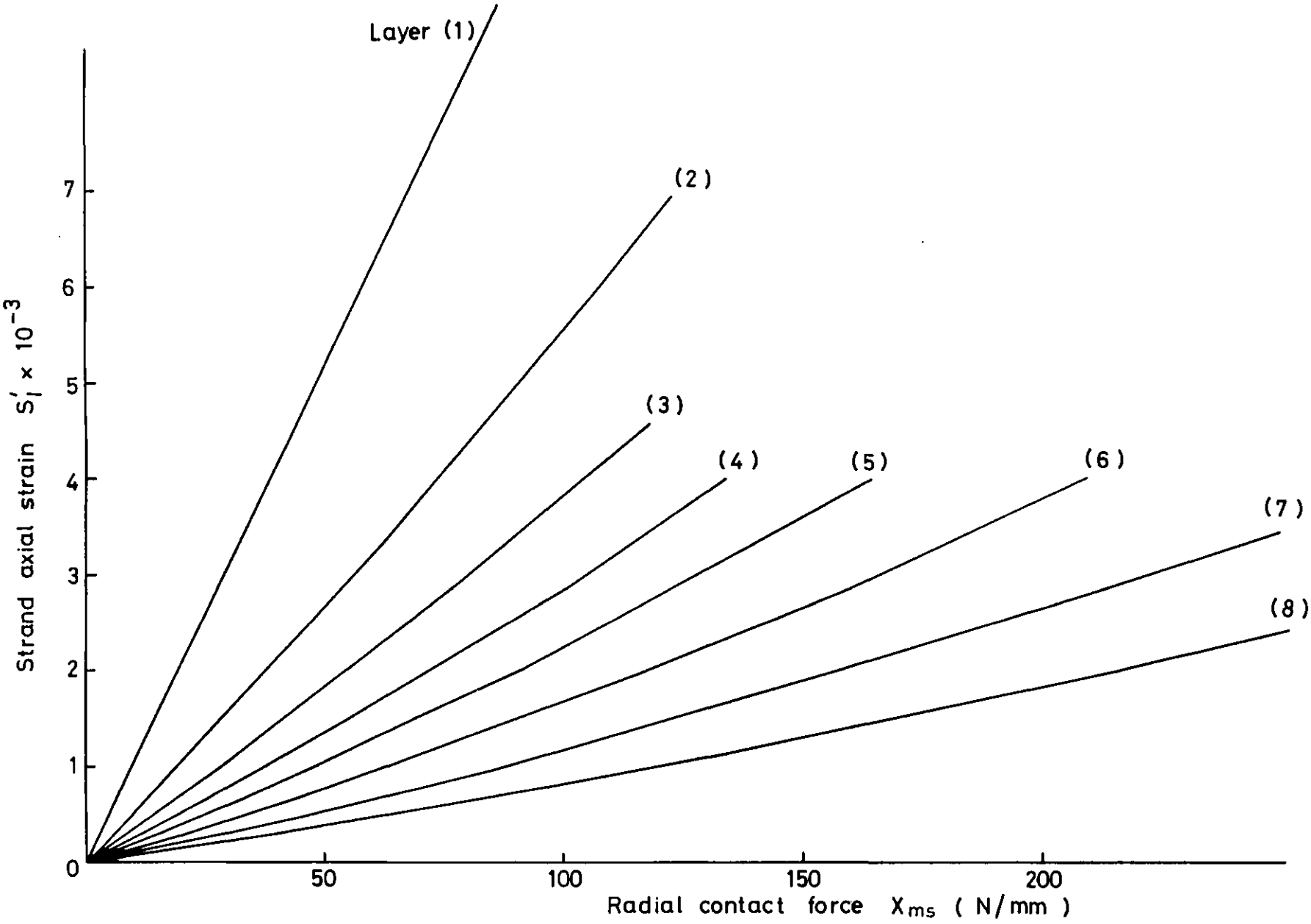

Fig. 2.16 Plot of radial contact force per unit length X_{ms} versus cable axial strain for the 127 mm O.D. strand

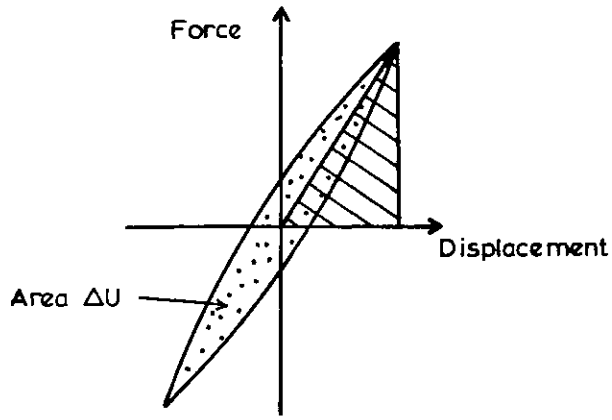

Fig 3.1

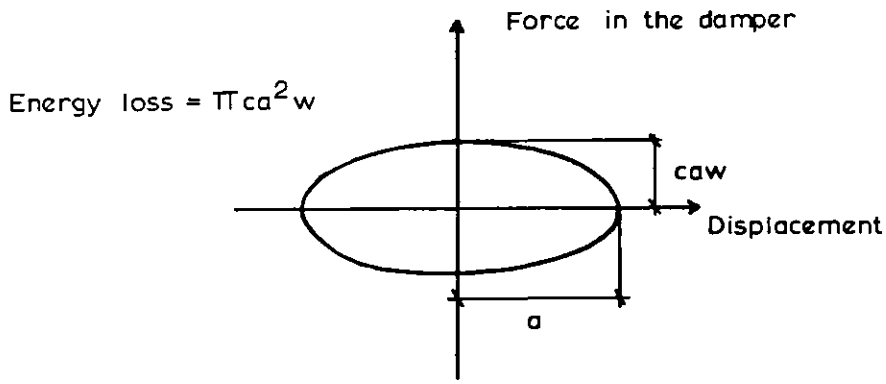

Fig 3.2

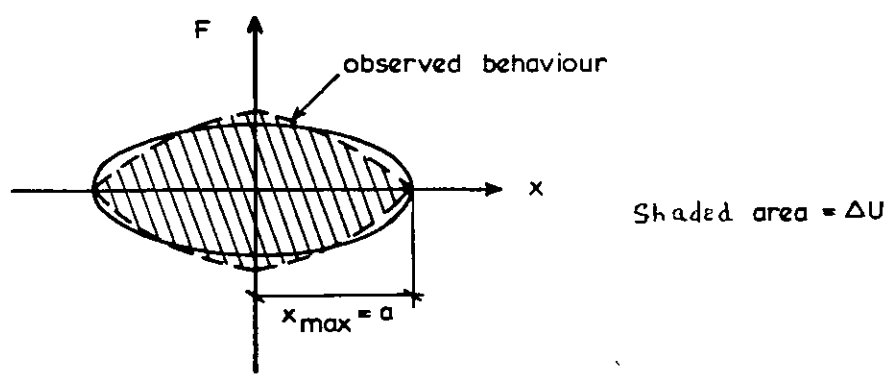

Fig 3.3

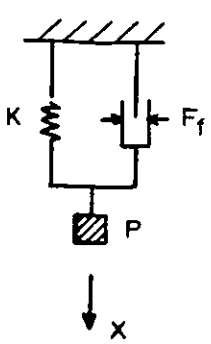

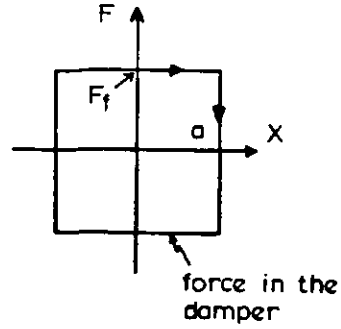

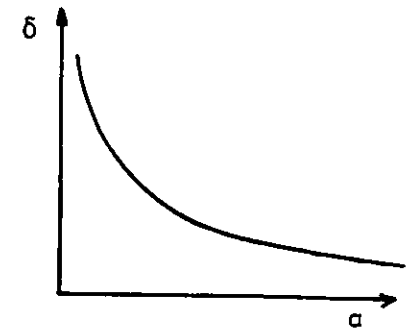

Variation of equivalent log.dec. with amplitude for the case of no elastic kick-back

Fig. 3.4

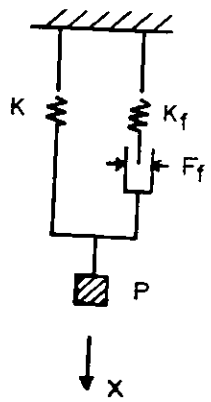

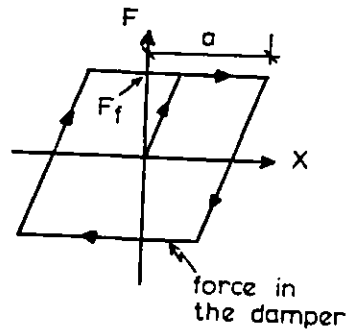

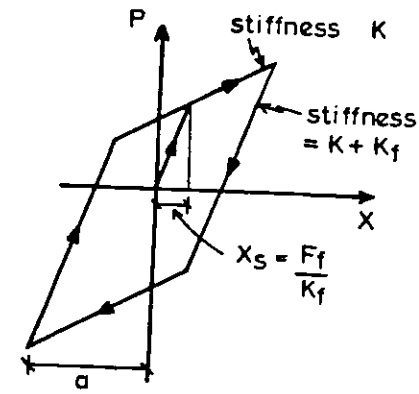

Hysteresis loop of the whole system

Fig. 3.5

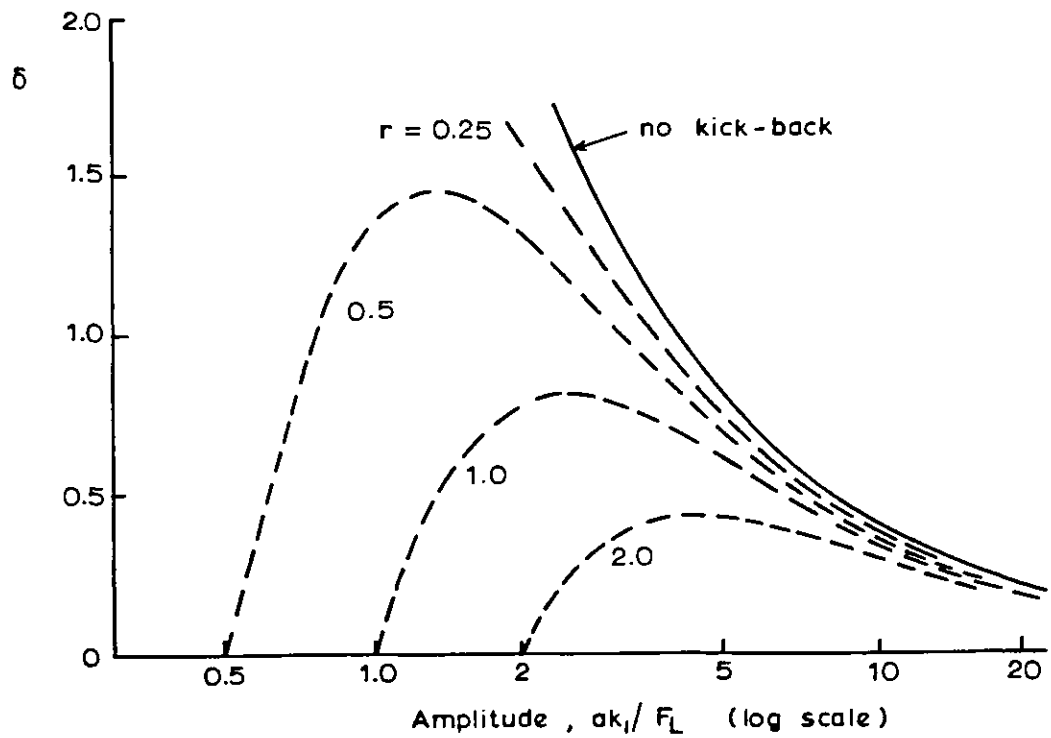

Fig. 3.6

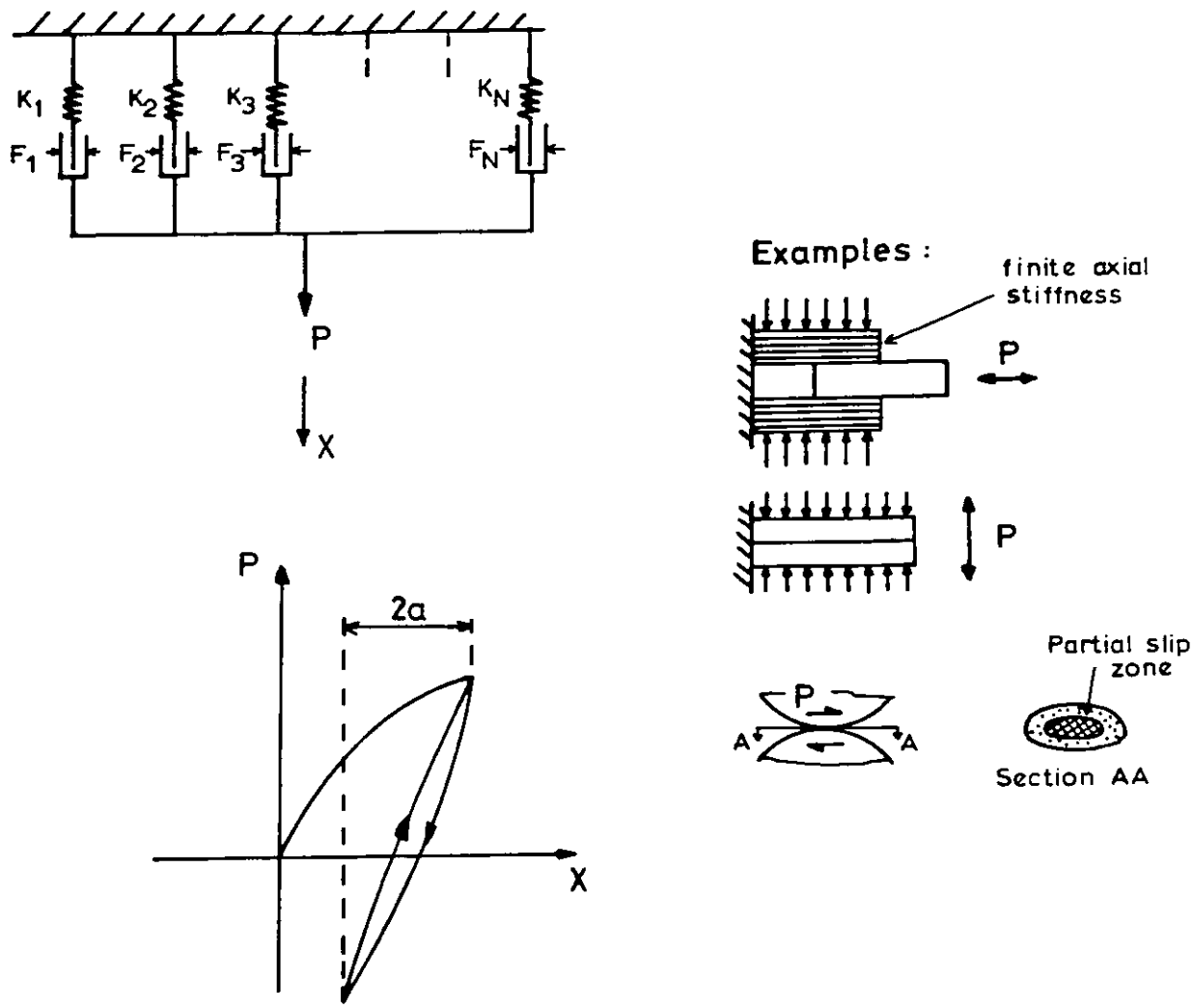
K1
K2
K3
KN
F1
F2
F3
FN
P
X
P
2a
X
Examples :
finite axial stiffness
P
P
P
A
A
Partial slip zone
Section AA

Fig. 3.7

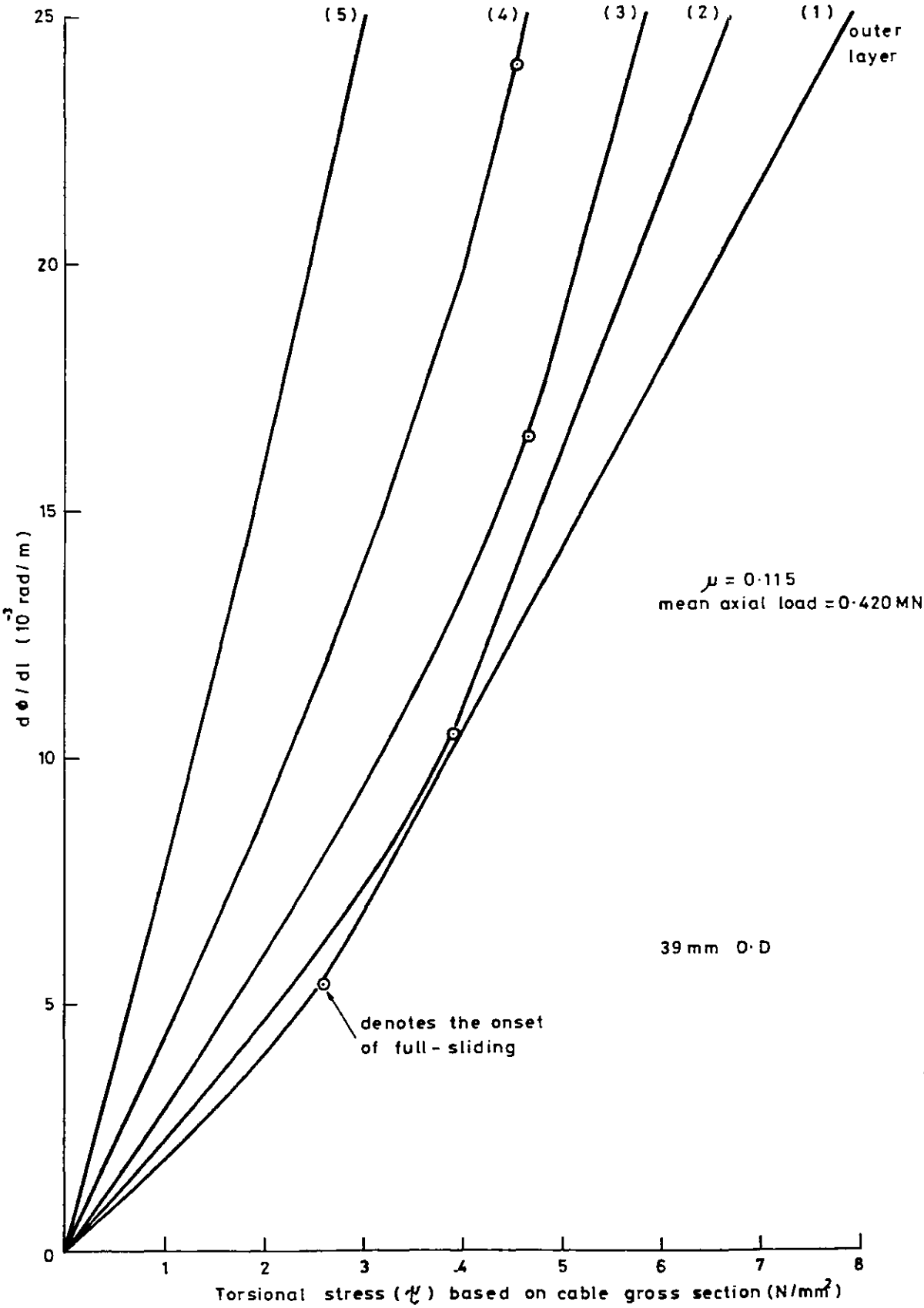

Fig 3·8 Plot of torsional stress in each layer versus twist

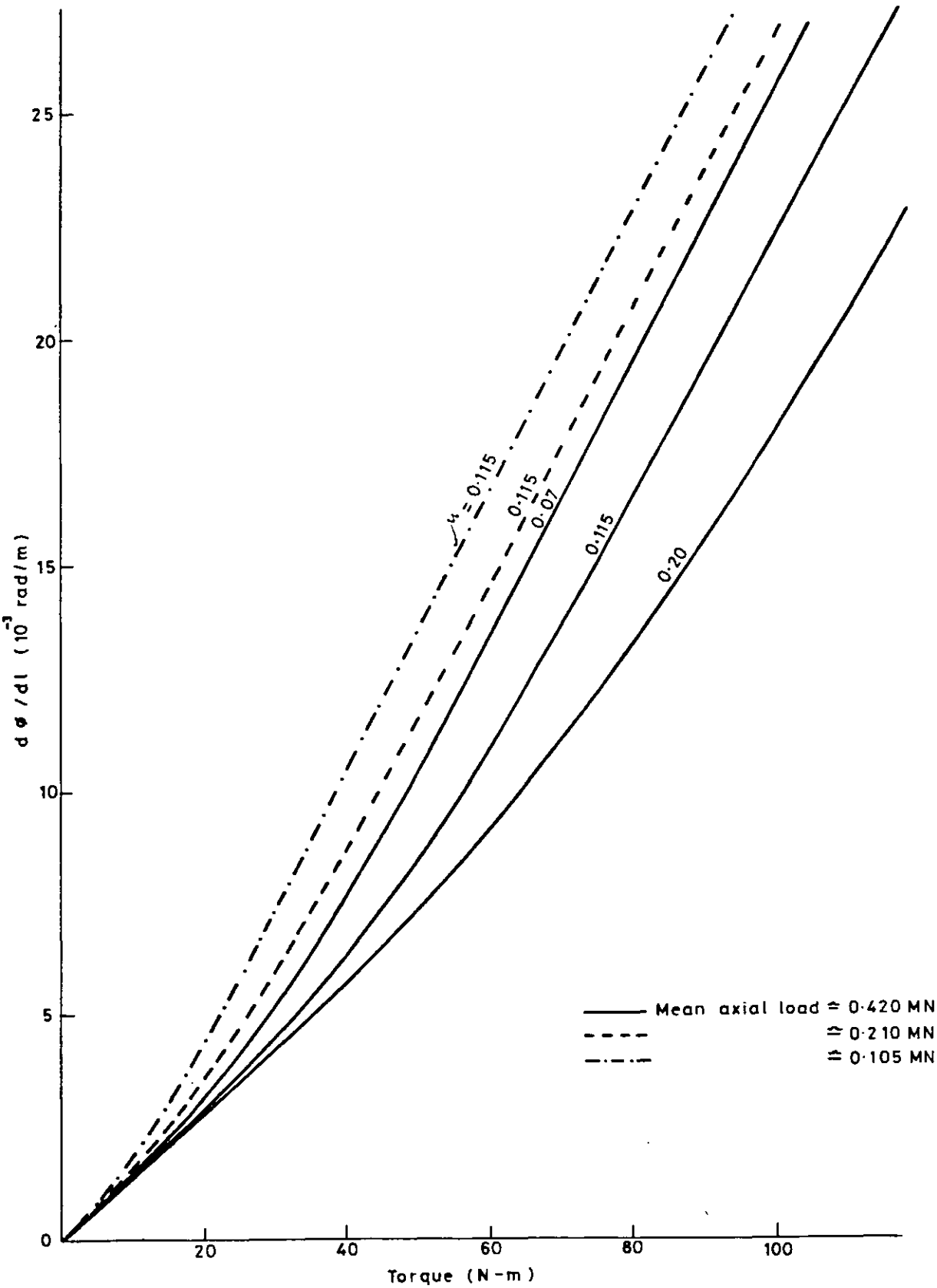

Fig 3·9 Variation of torque-twist results with changes in mean axial load and coefficient of friction - 39mm O·D strand

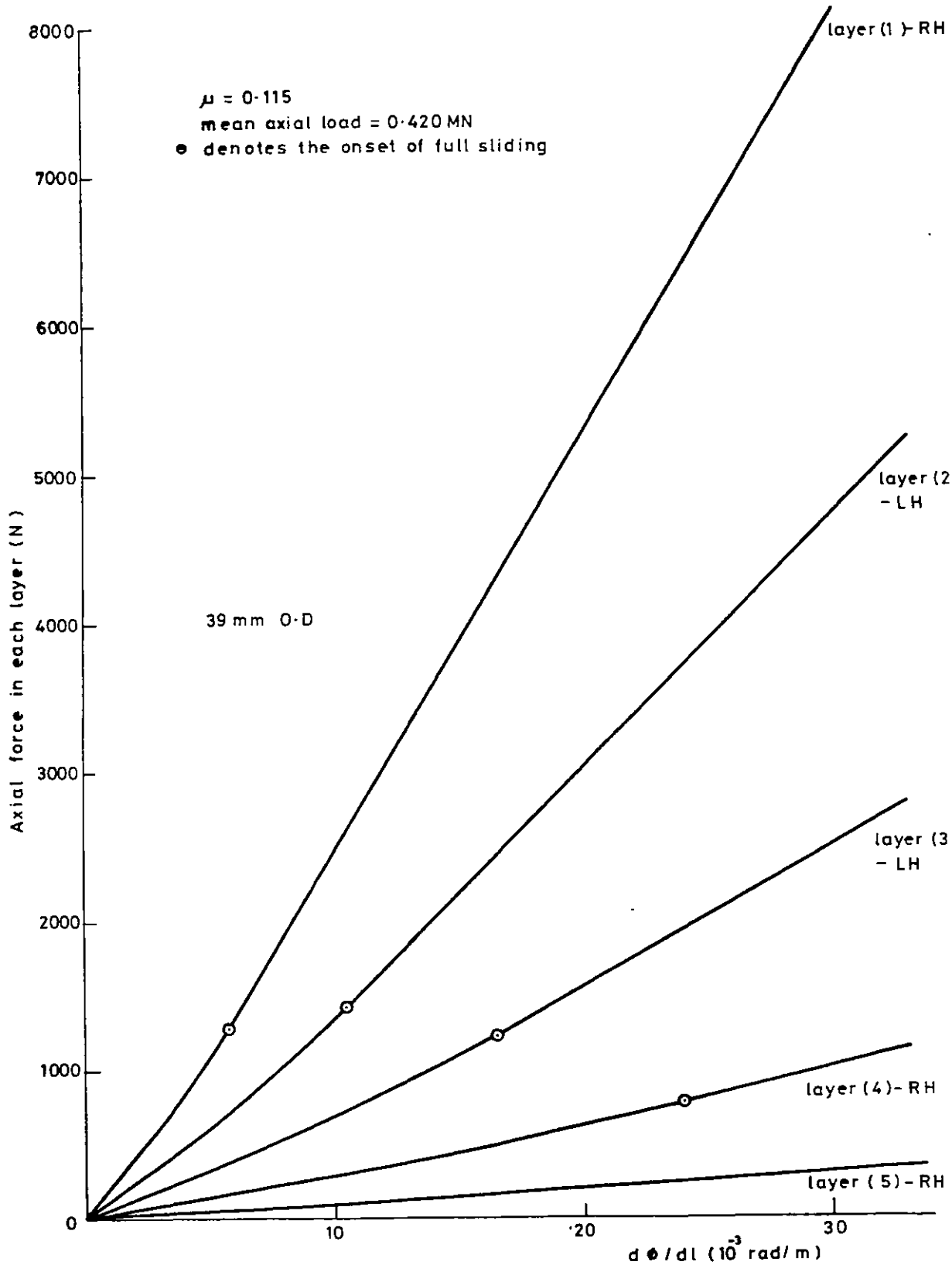

Fig 3·10 Variation of axial perturbations in individual layers as a function of twist in the cable

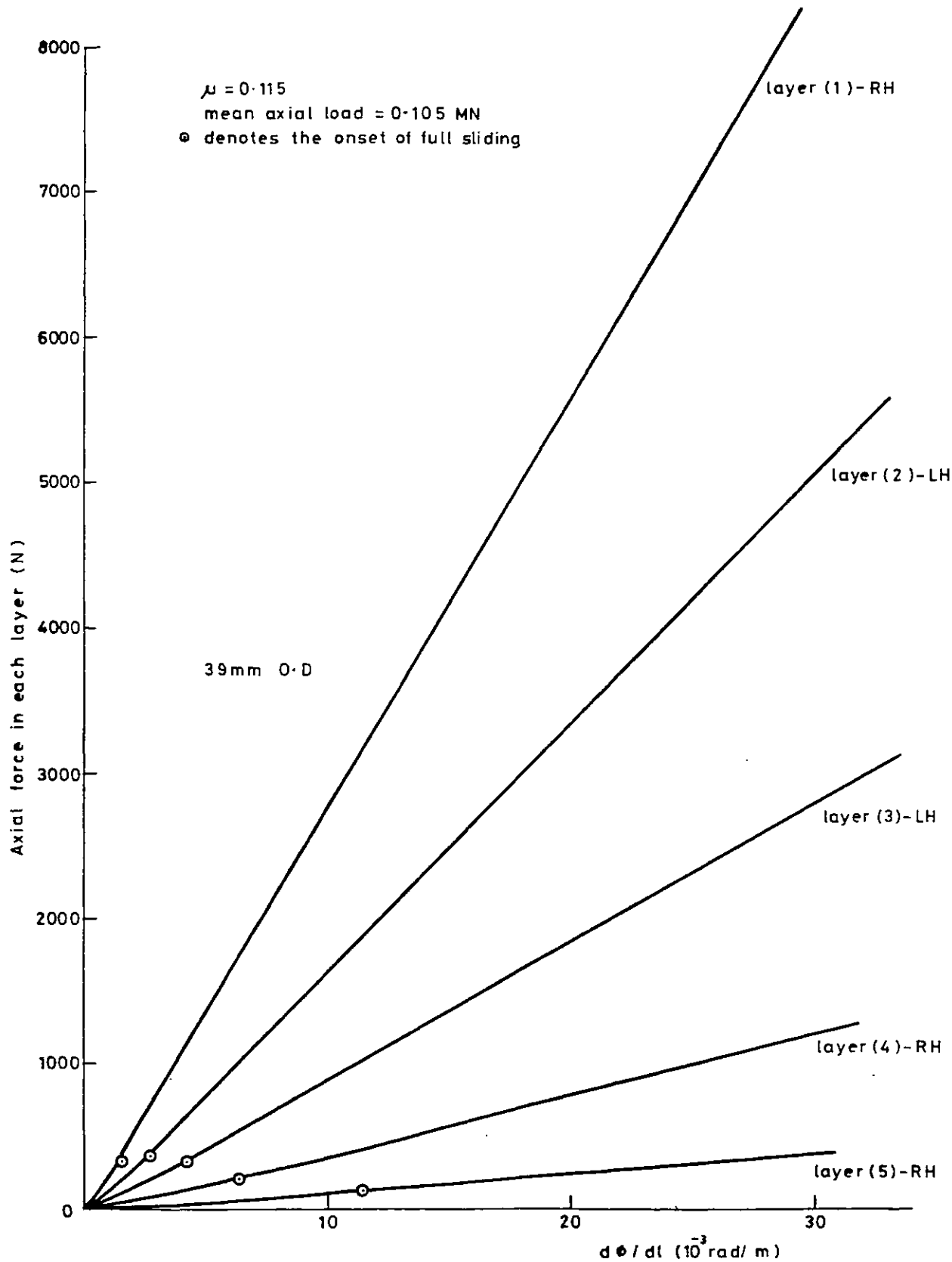

Fig 3·11 Variation of axial perturbation in individual layers as a function of twist in the cable

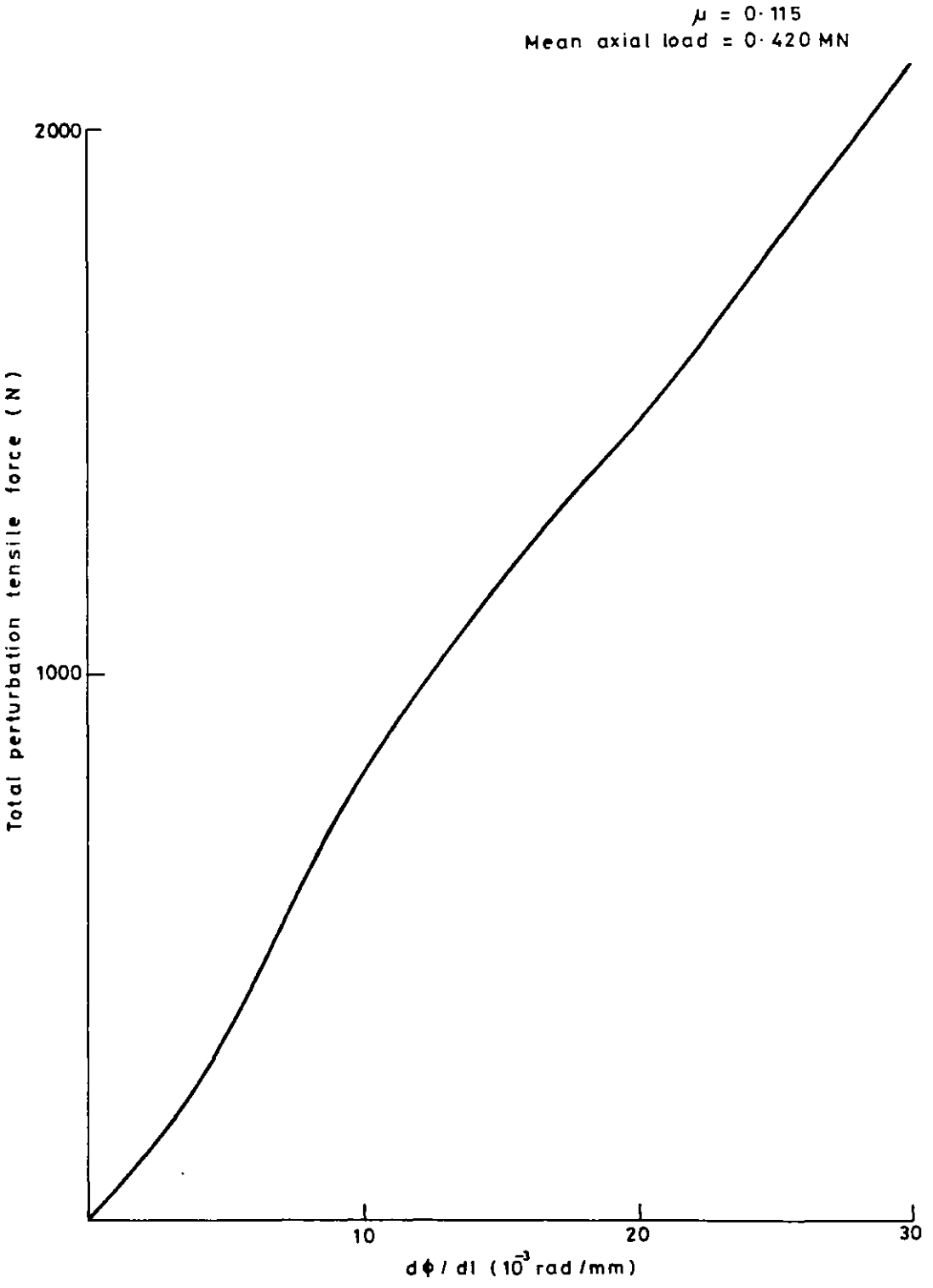

Fig 3·12 Plot of total perturbation tensile force in the cable as a function of twist

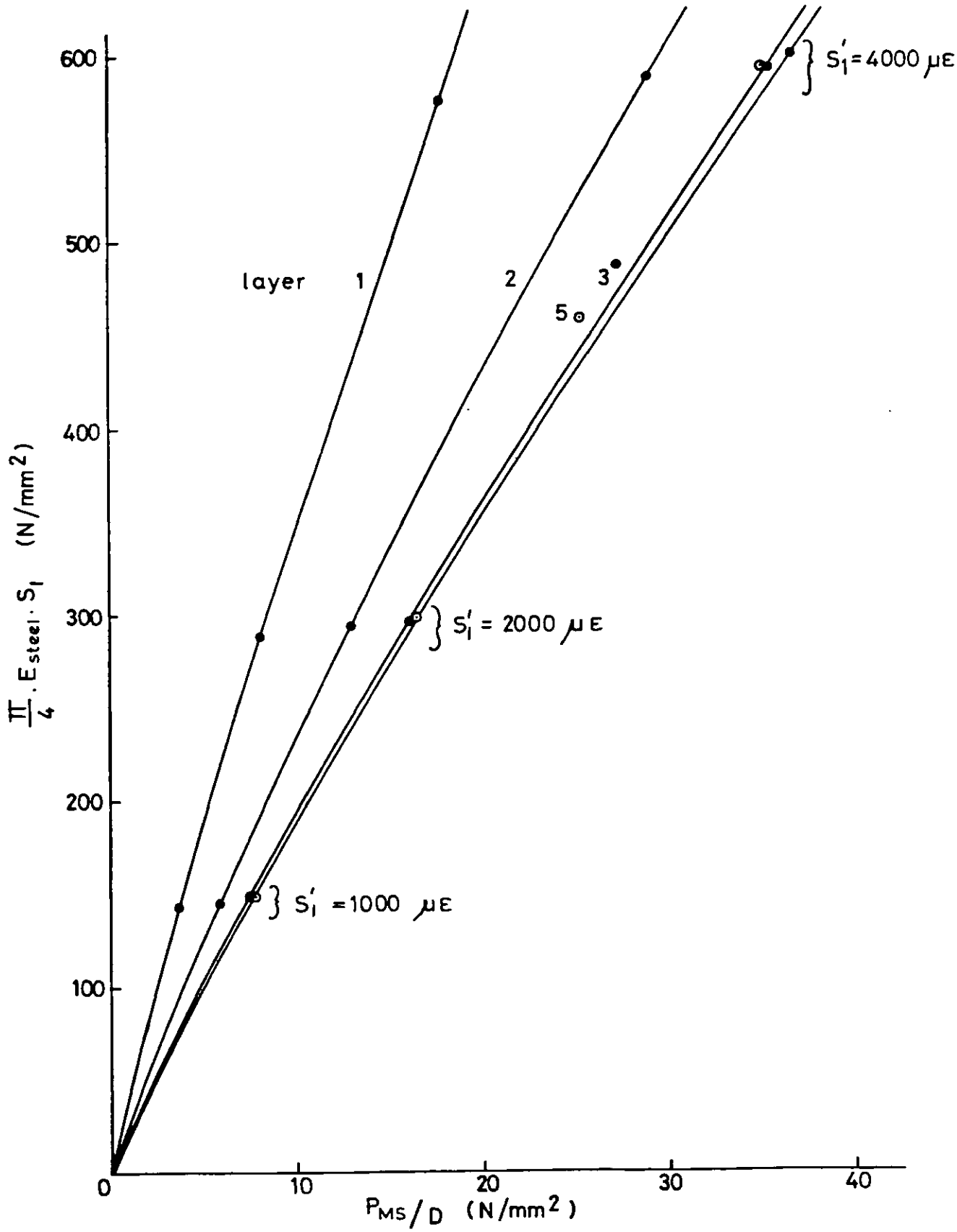

Fig 3·13 Theoretical plots of stresses in the directions of orthotropy

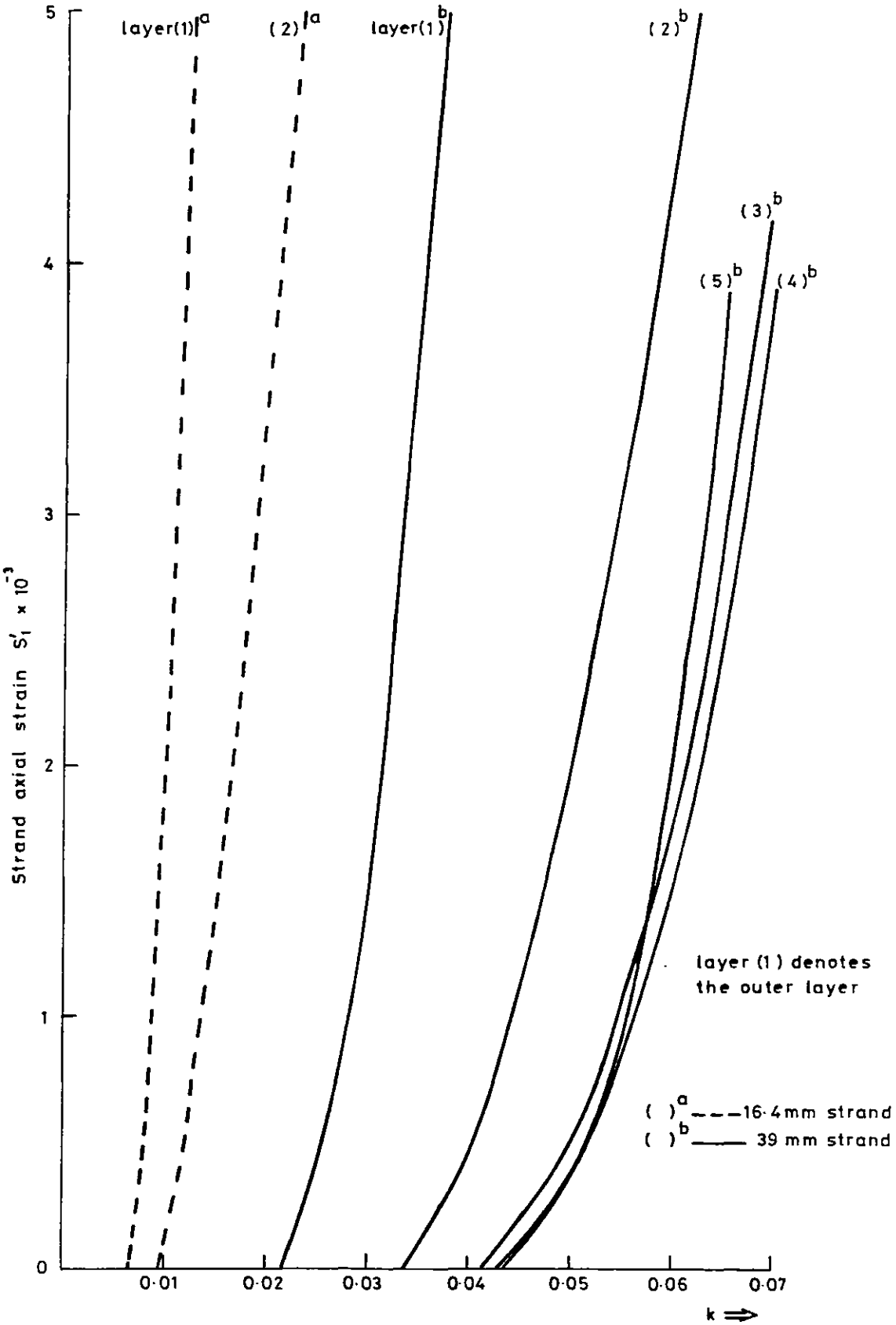

Fig 3·14 Plot of k as a function of strand axial strain – for two different constructions

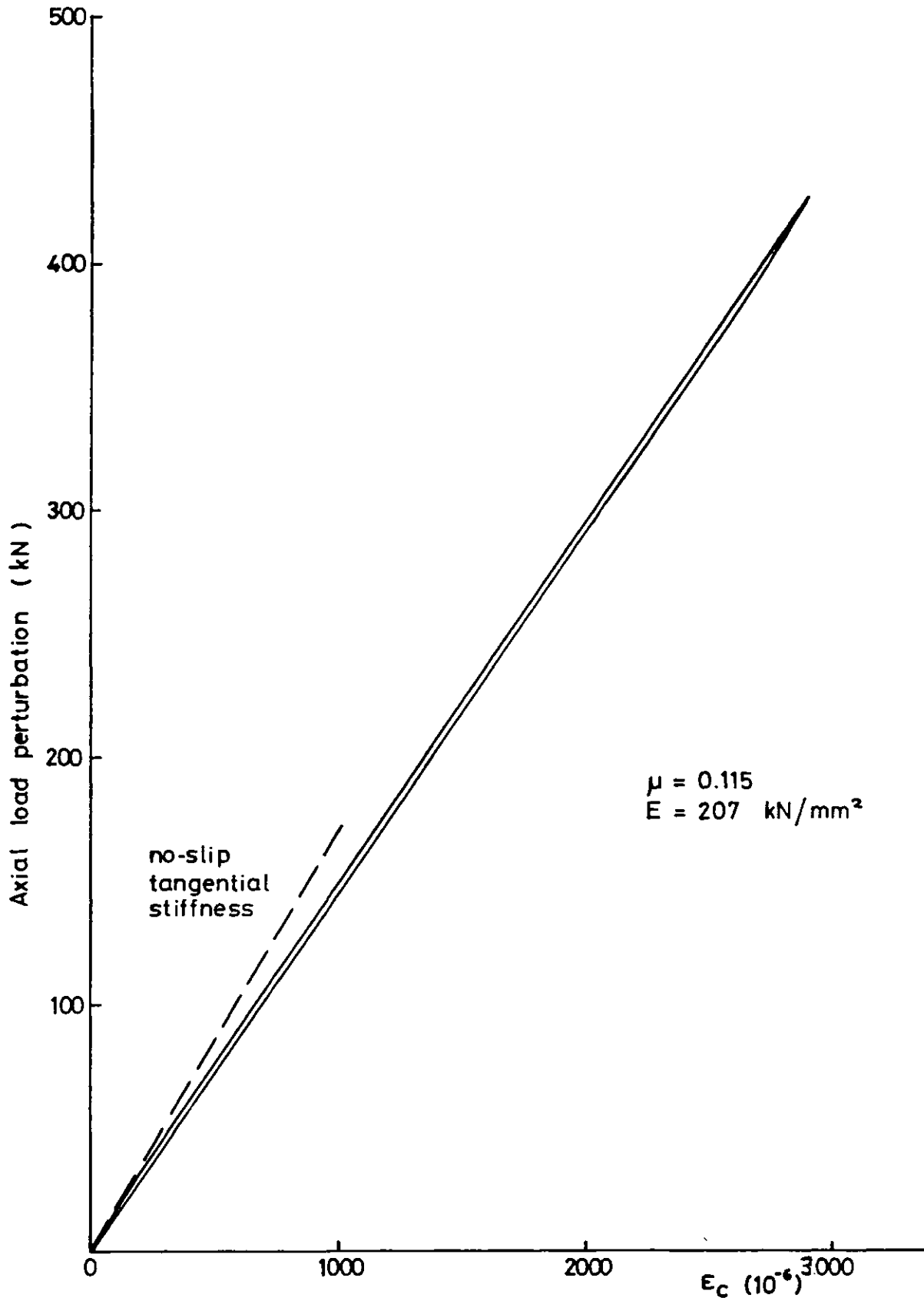

Fig 3.15 Theoretical plot of axial hysteresis loop of 39 mm O.D. strand, under a mean axial load of 0.41 MN

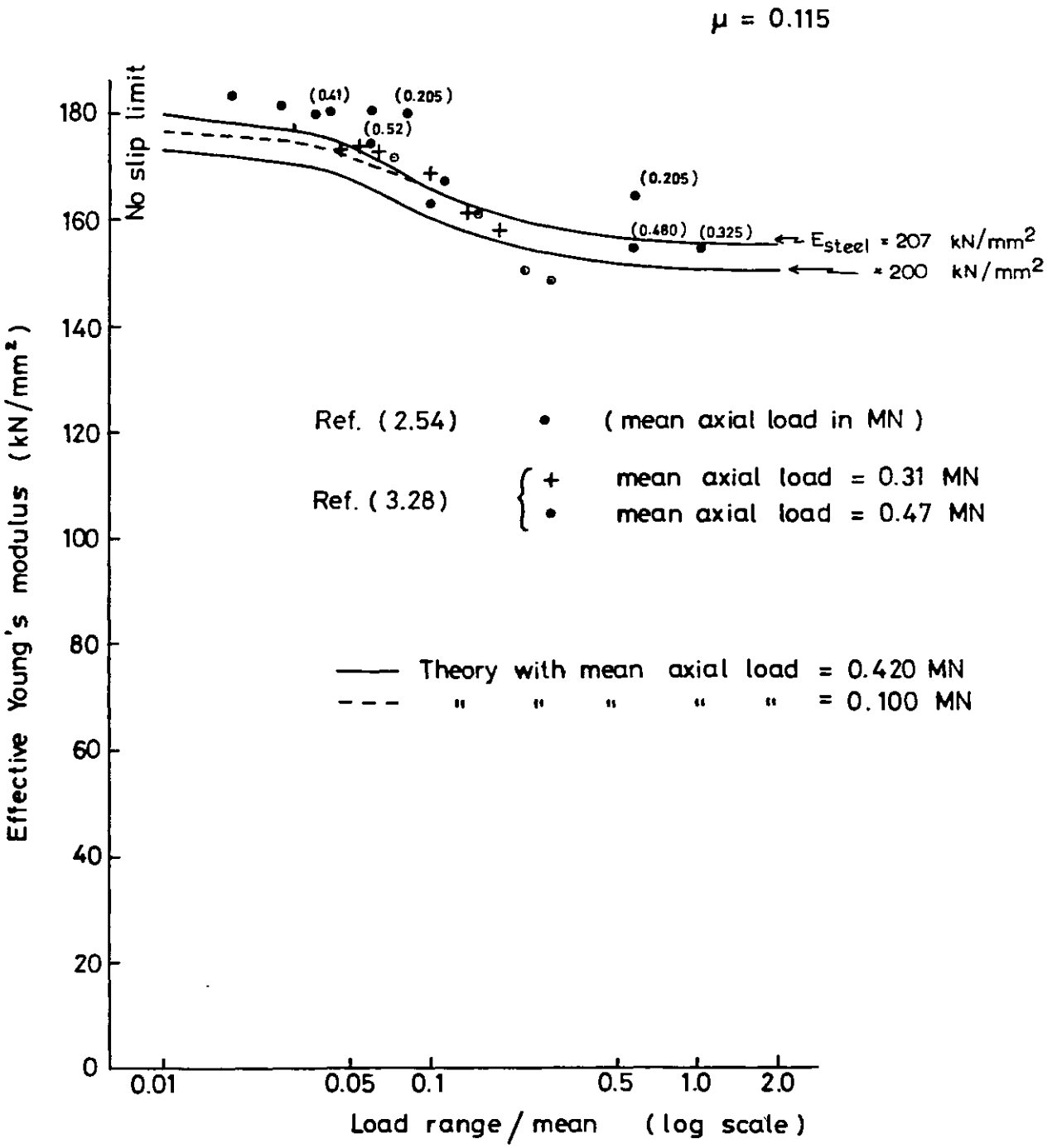

Fig 3·16 Axial stiffness results for 39 mm O.D. strand

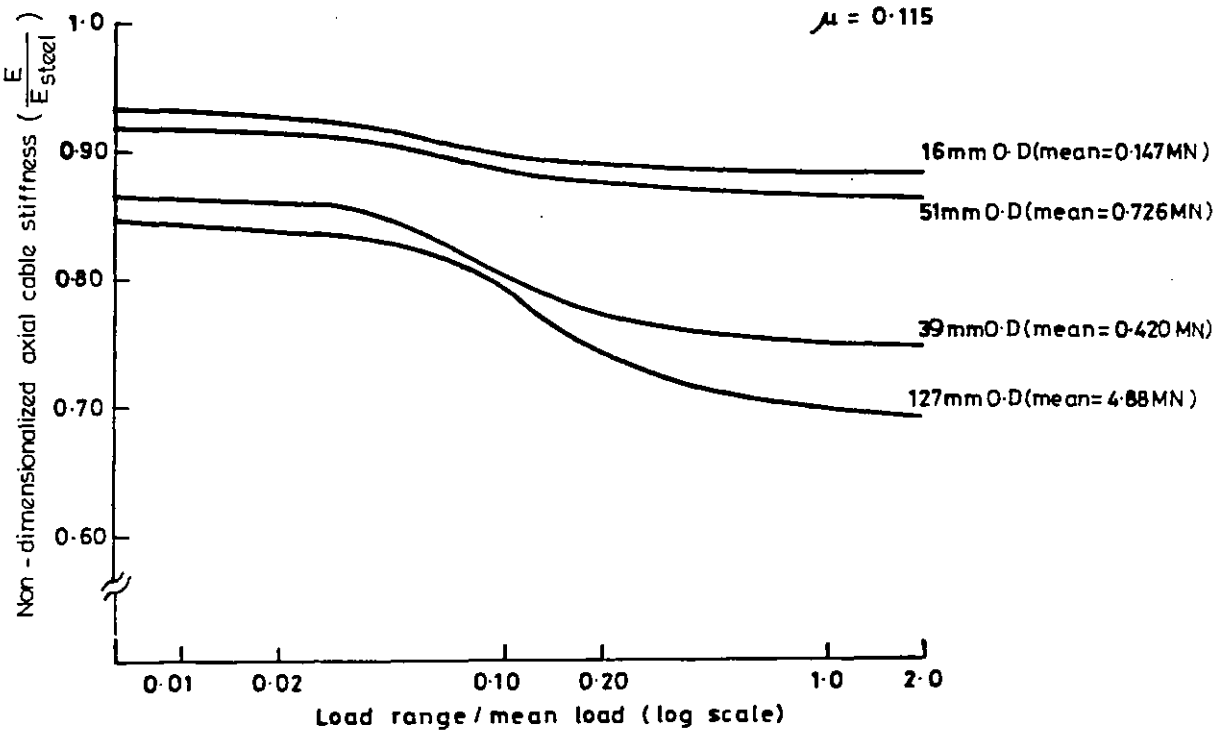

Fig 3·17 Axial stiffness results for various cable constructions

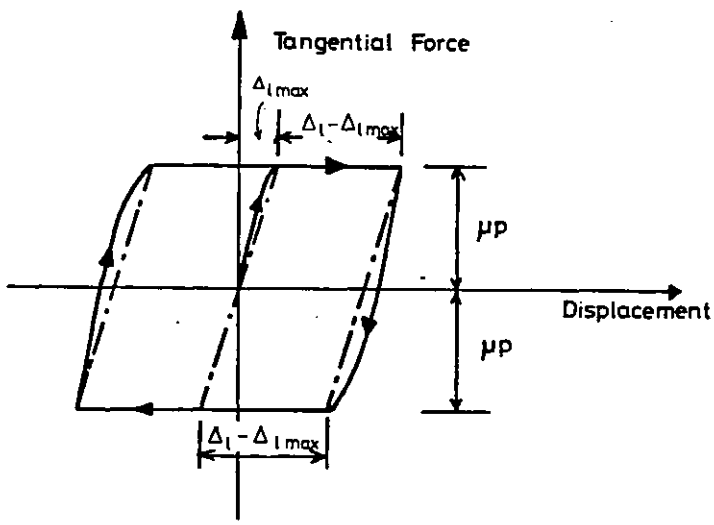

Fig 3.18 Hysteresis loop in gross slip regime

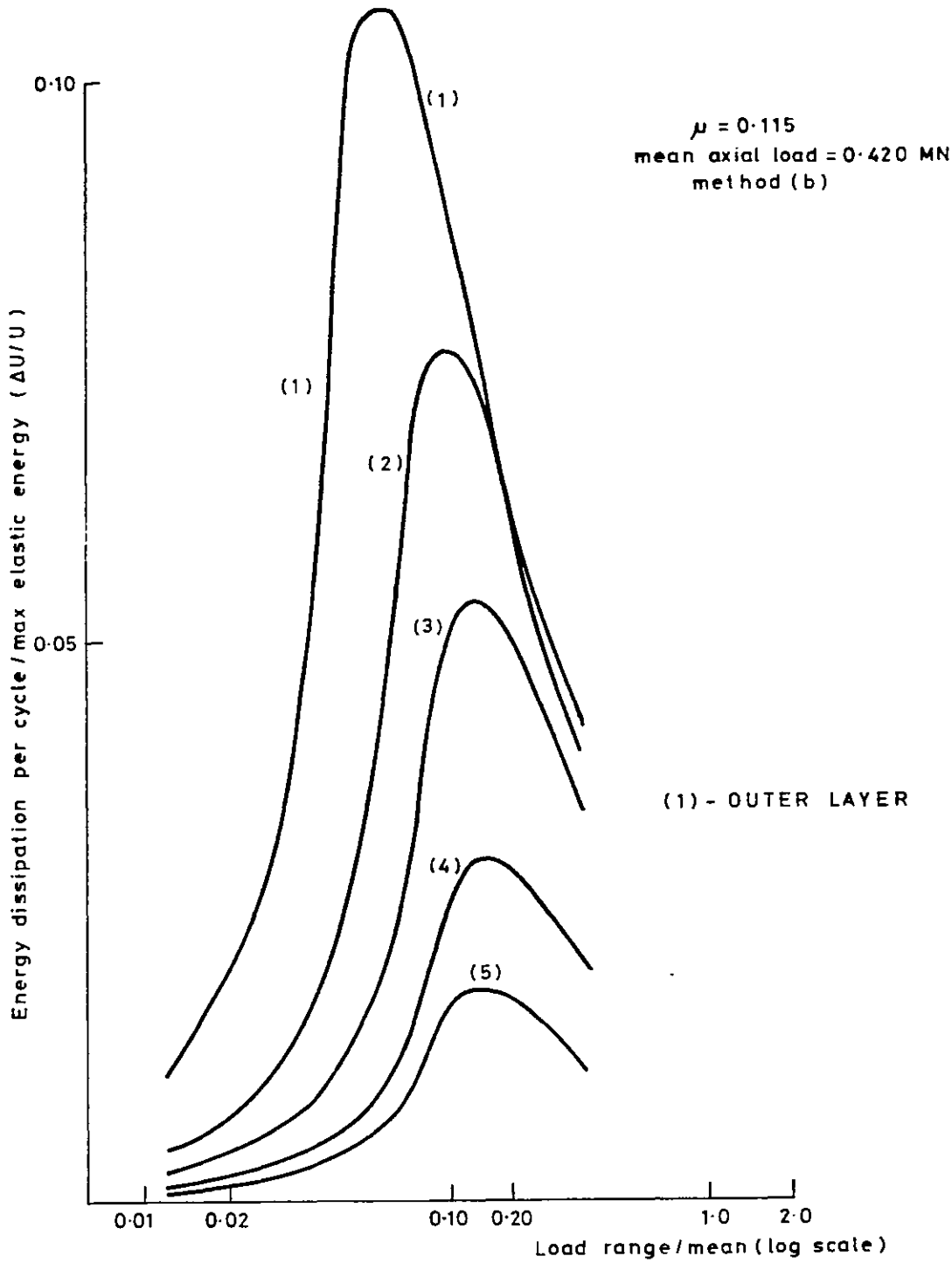

Fig 3.19 Theoretical energy dissipation in each layer of 39mm O·D strand

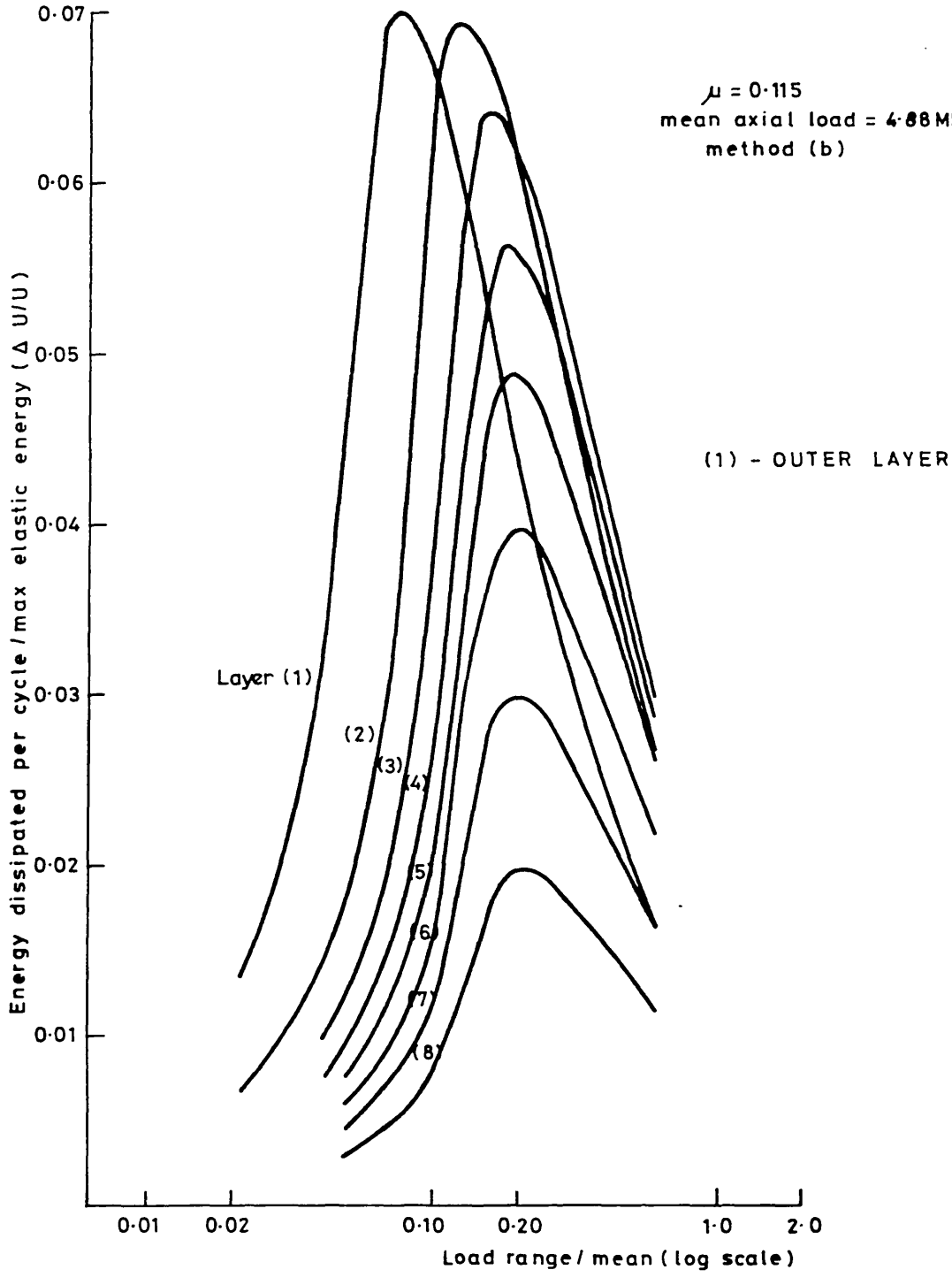

Fig 3·20 Theoretical energy dissipation in each layer of 127mm O.D. strand

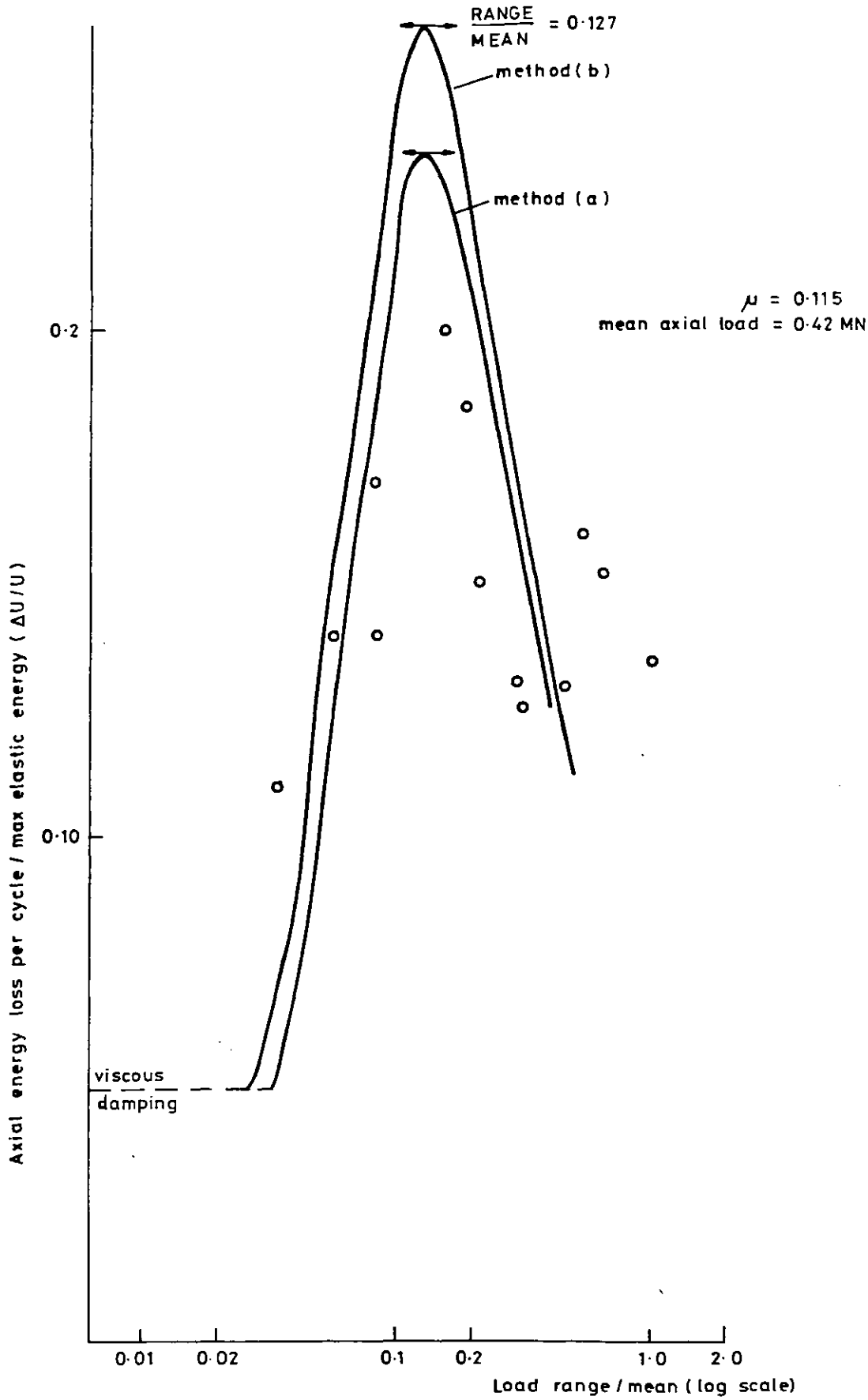

Fig 3·21 Axial energy dissipation in 39 mm O.D. strand — Comparison of theory and experiment

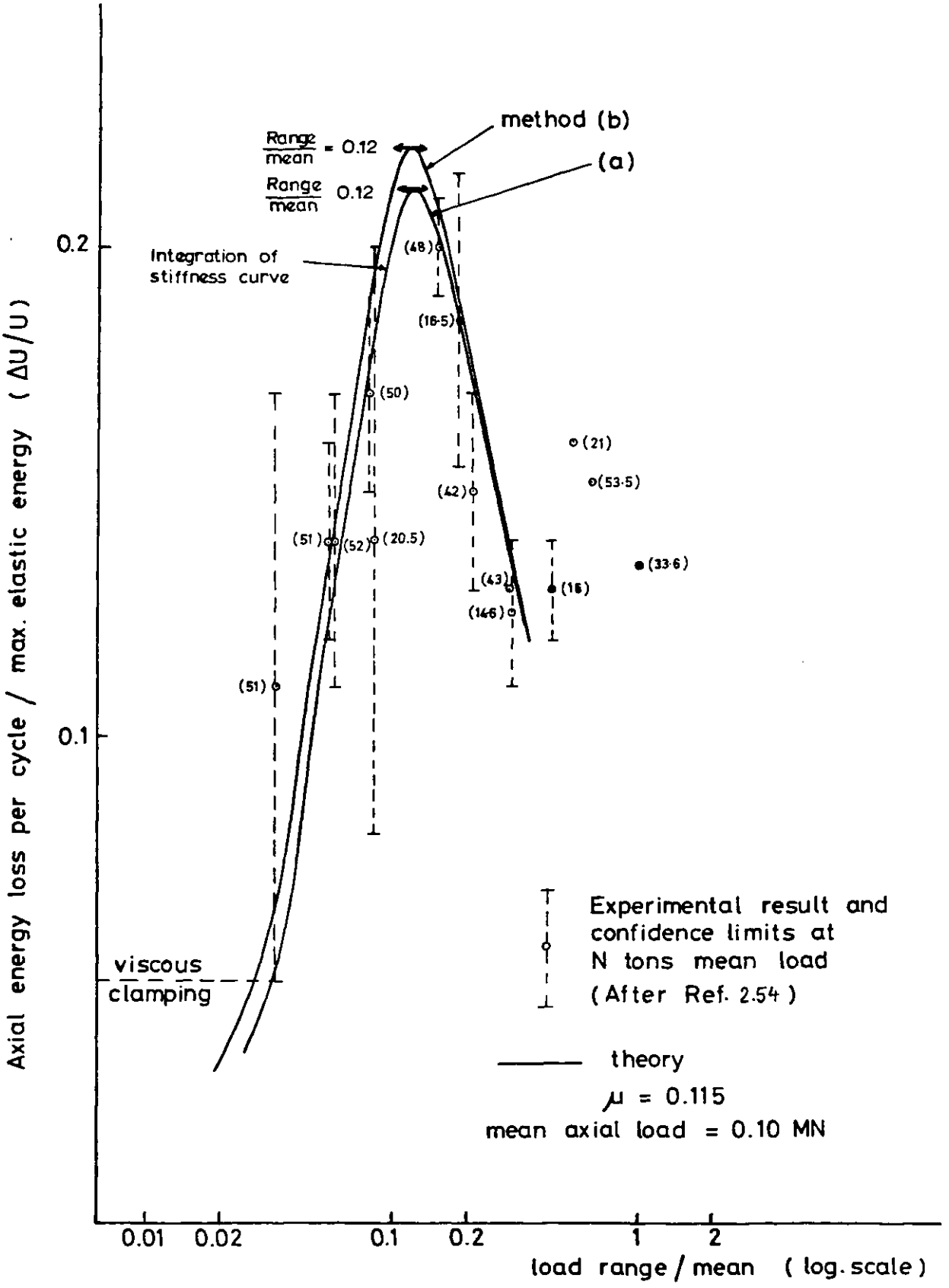

Fig 3.22 Axial energy dissipation for the 39 mm O.D. strand

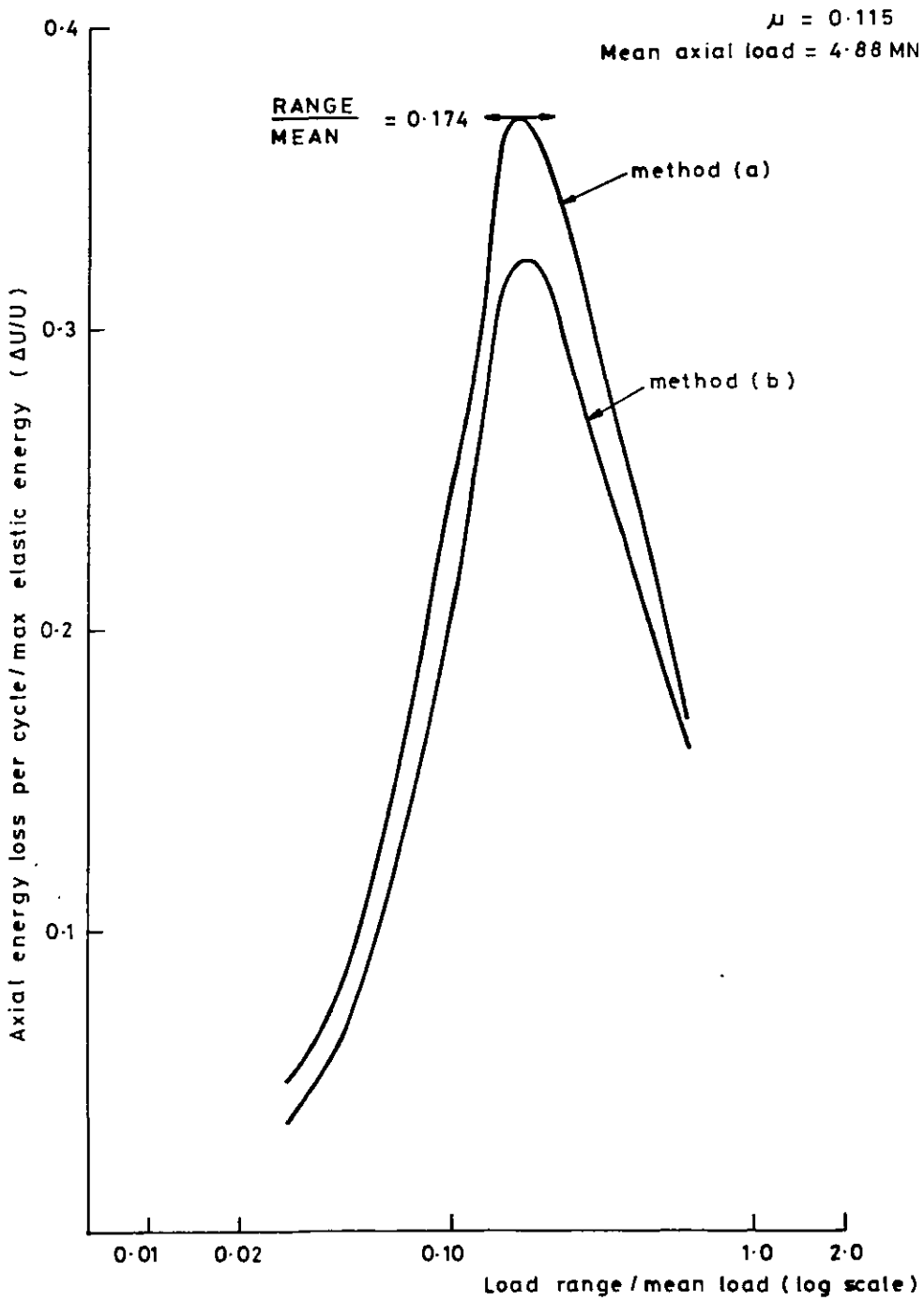

Fig 3·23 Theoretical axial energy dissipation in 127mm O.D. strand

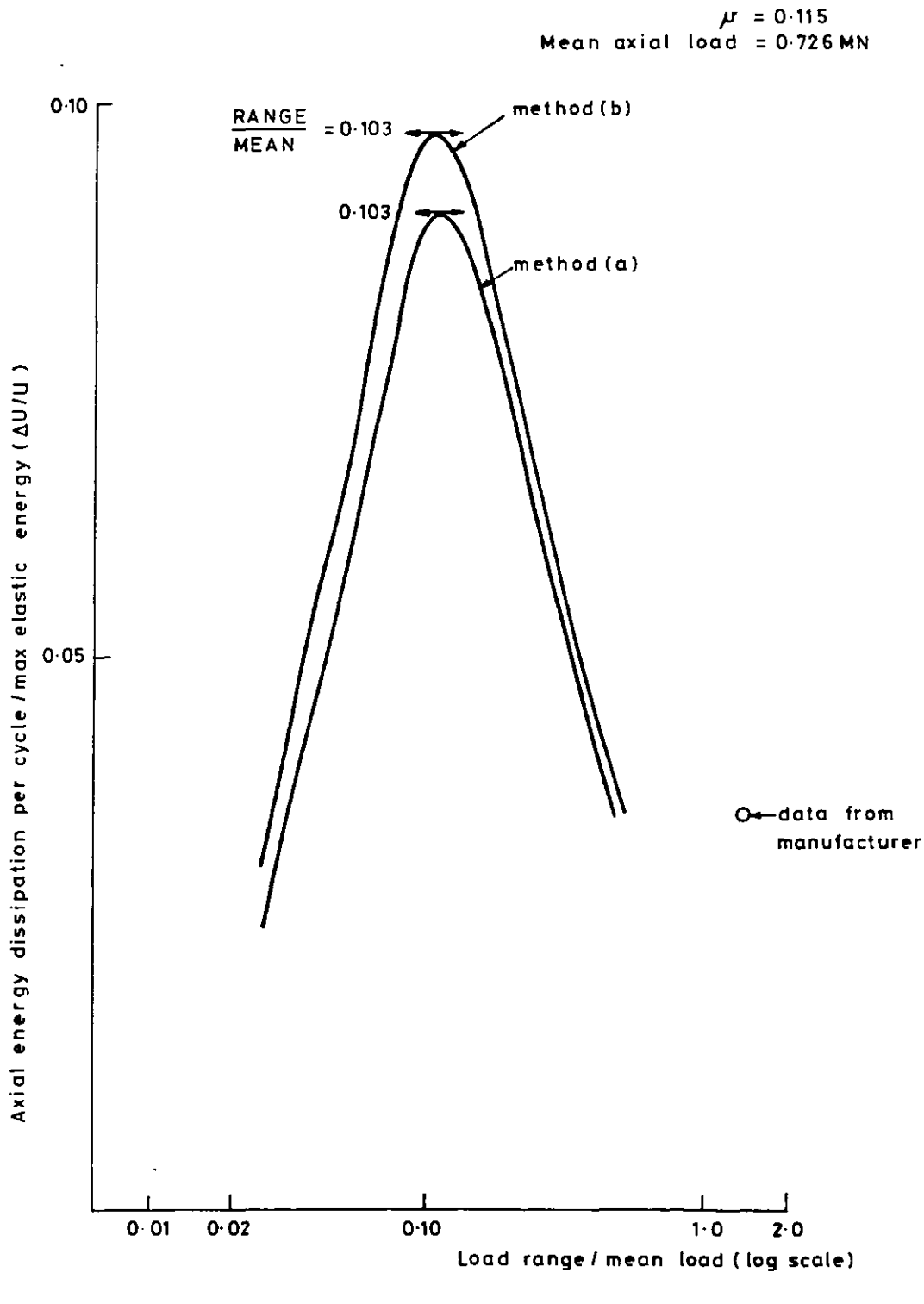

Fig 3·24 Theoretical axial energy dissipation in 51mm O.D strand

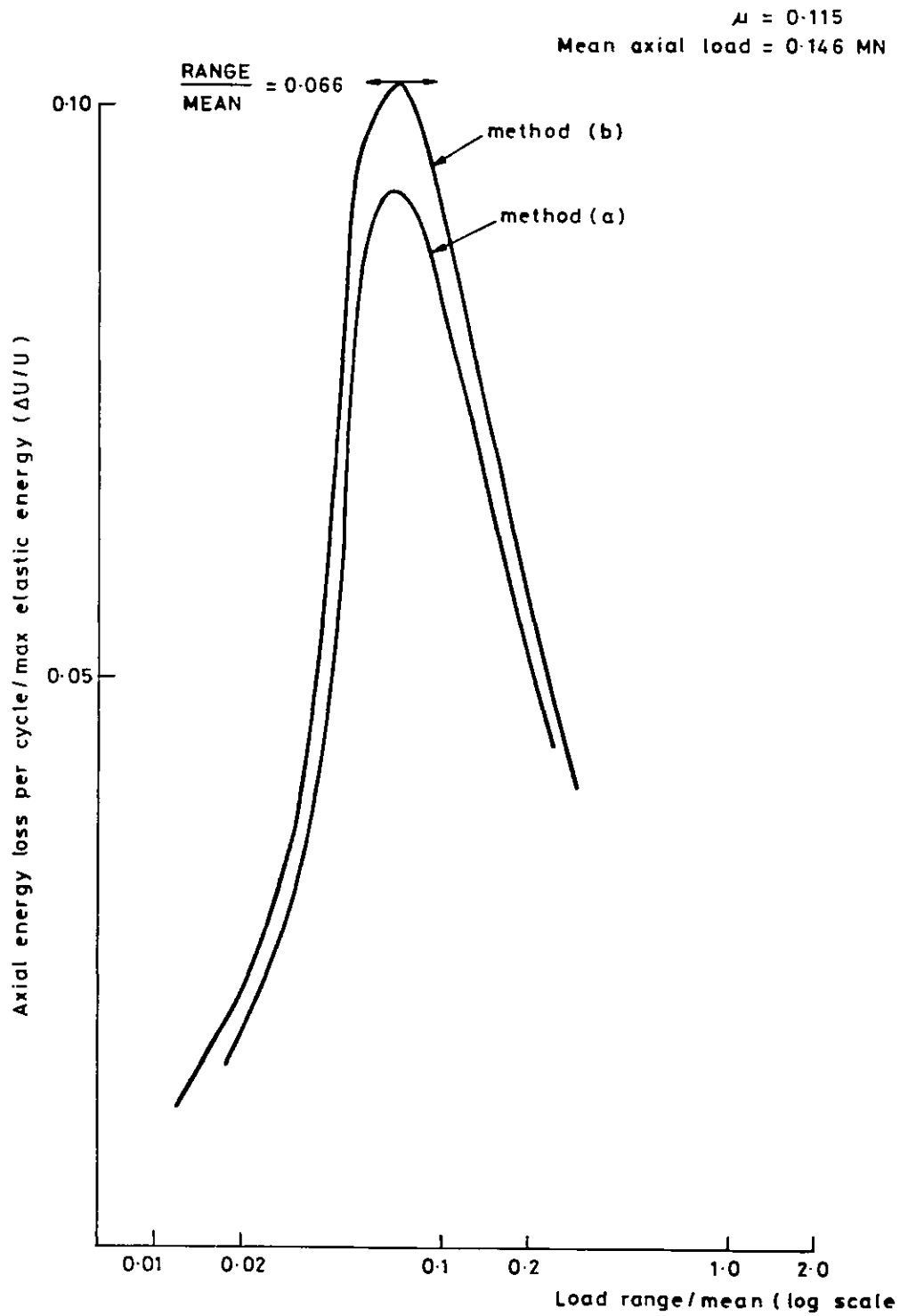

Fig 3·25 Theoretical axial energy dissipation in 16mm O·D strand

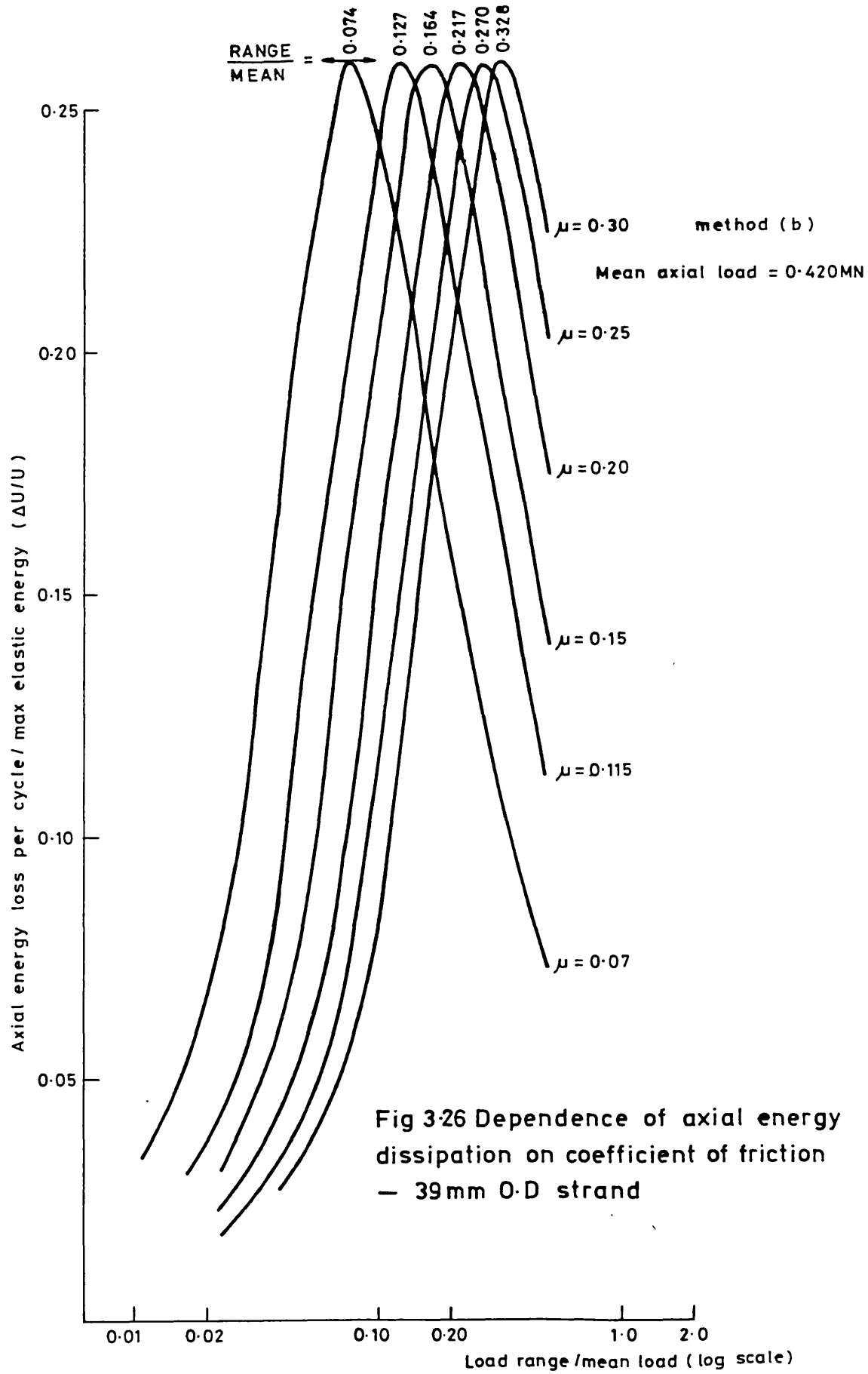

Fig 3·26 Dependence of axial energy dissipation on coefficient of friction — 39mm O·D strand

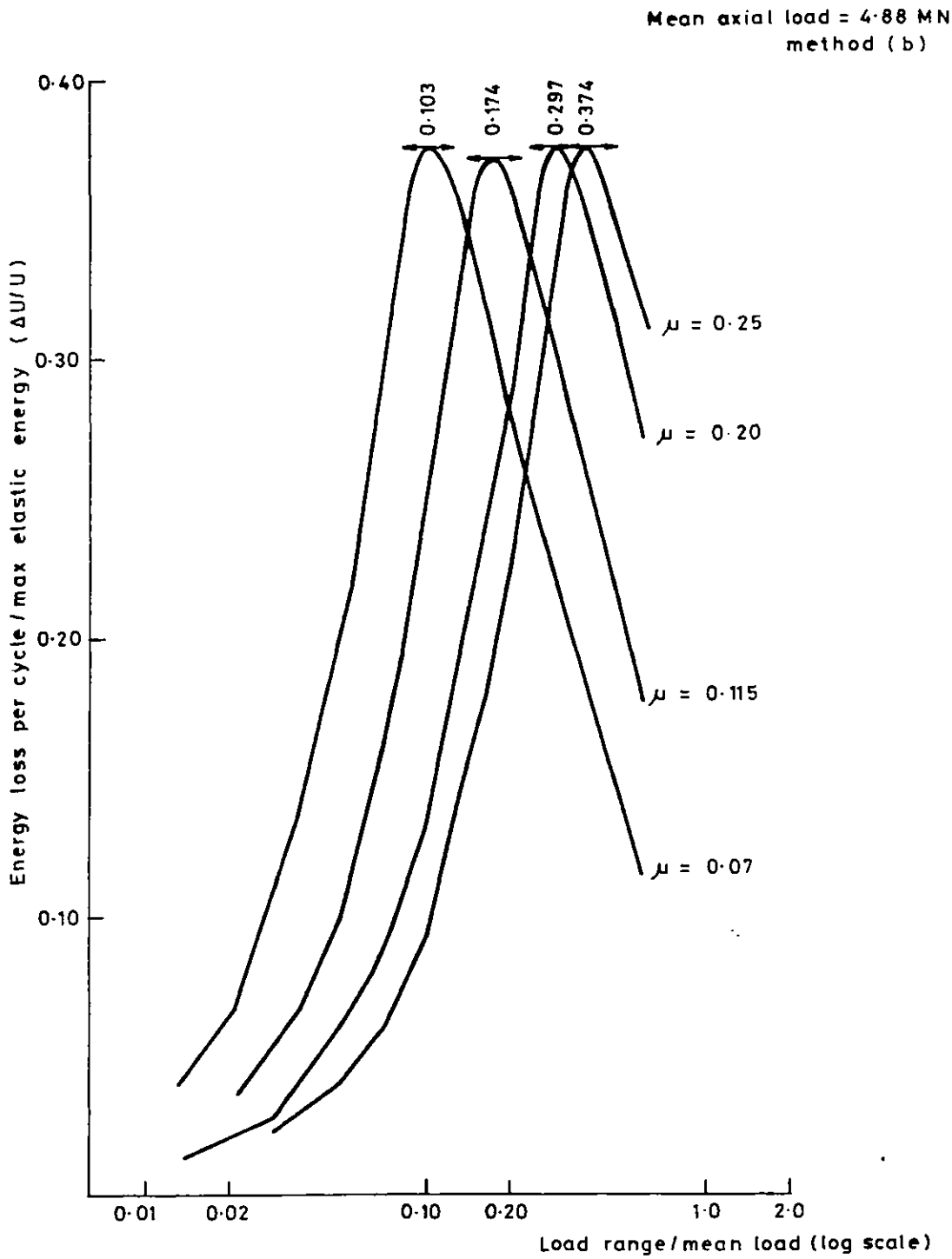

Fig 3·27 Dependence of axial energy dissipation on coefficient of friction - 127mm O·D strand

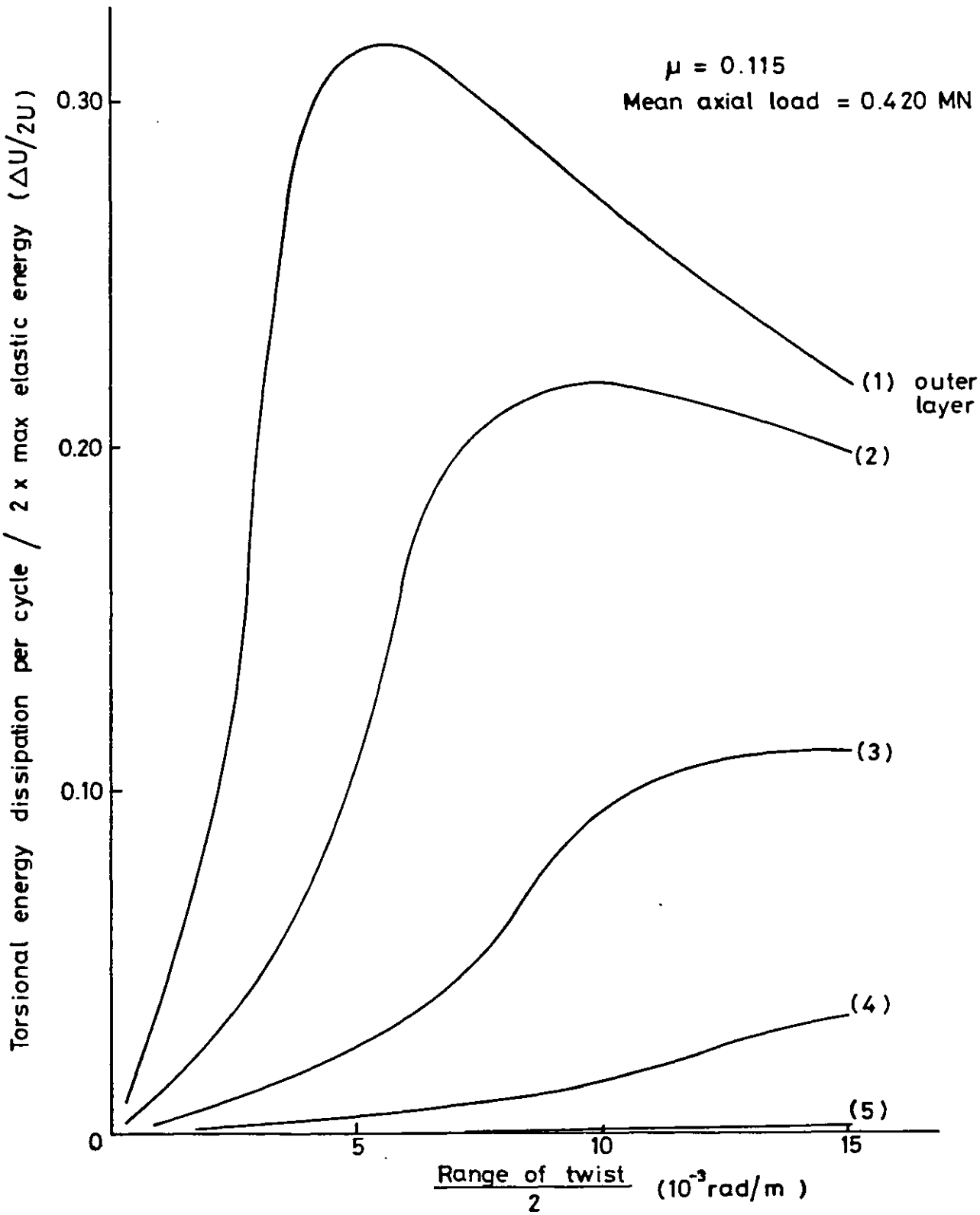

Fig 3·28 Theoretical energy dissipation in each layer of 39 mm O.D. strand

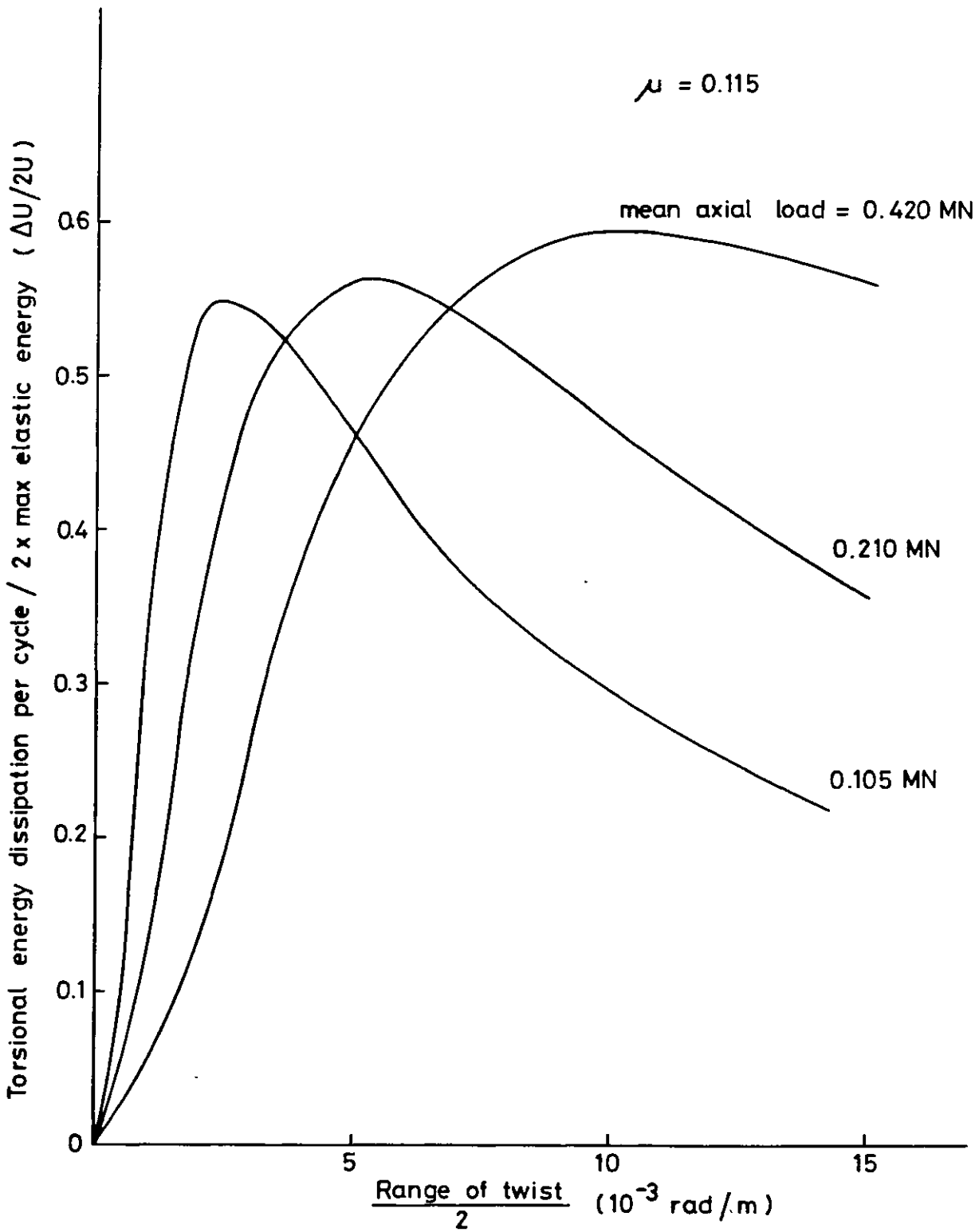

Fig 3·29 Theoretical plots of torsional energy dissipation in 39 mm O.D. strand under various mean axial loads

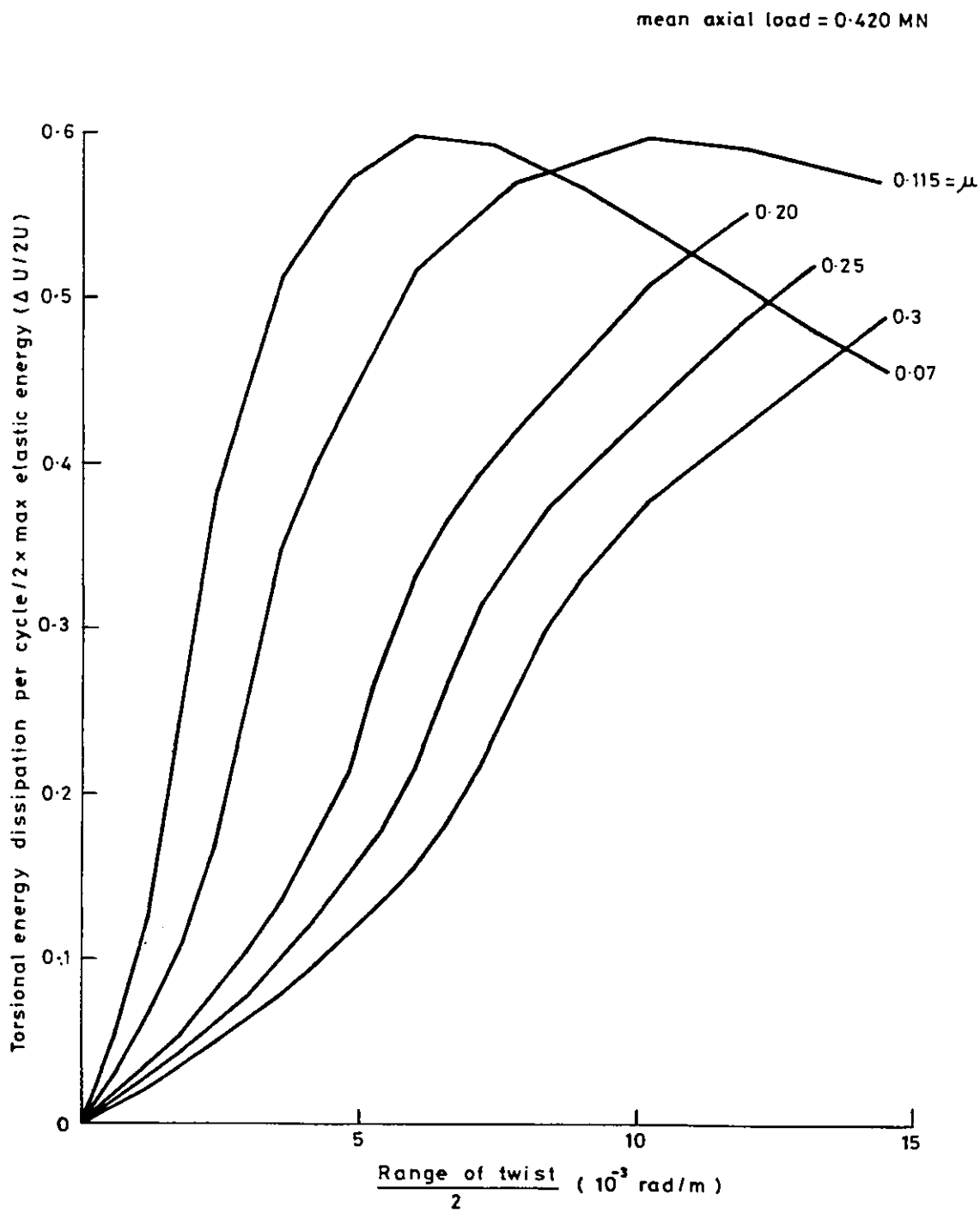

Fig 3·30 Theoretical torsional energy dissipation per cycle for 39mm O·D. strand for various μ

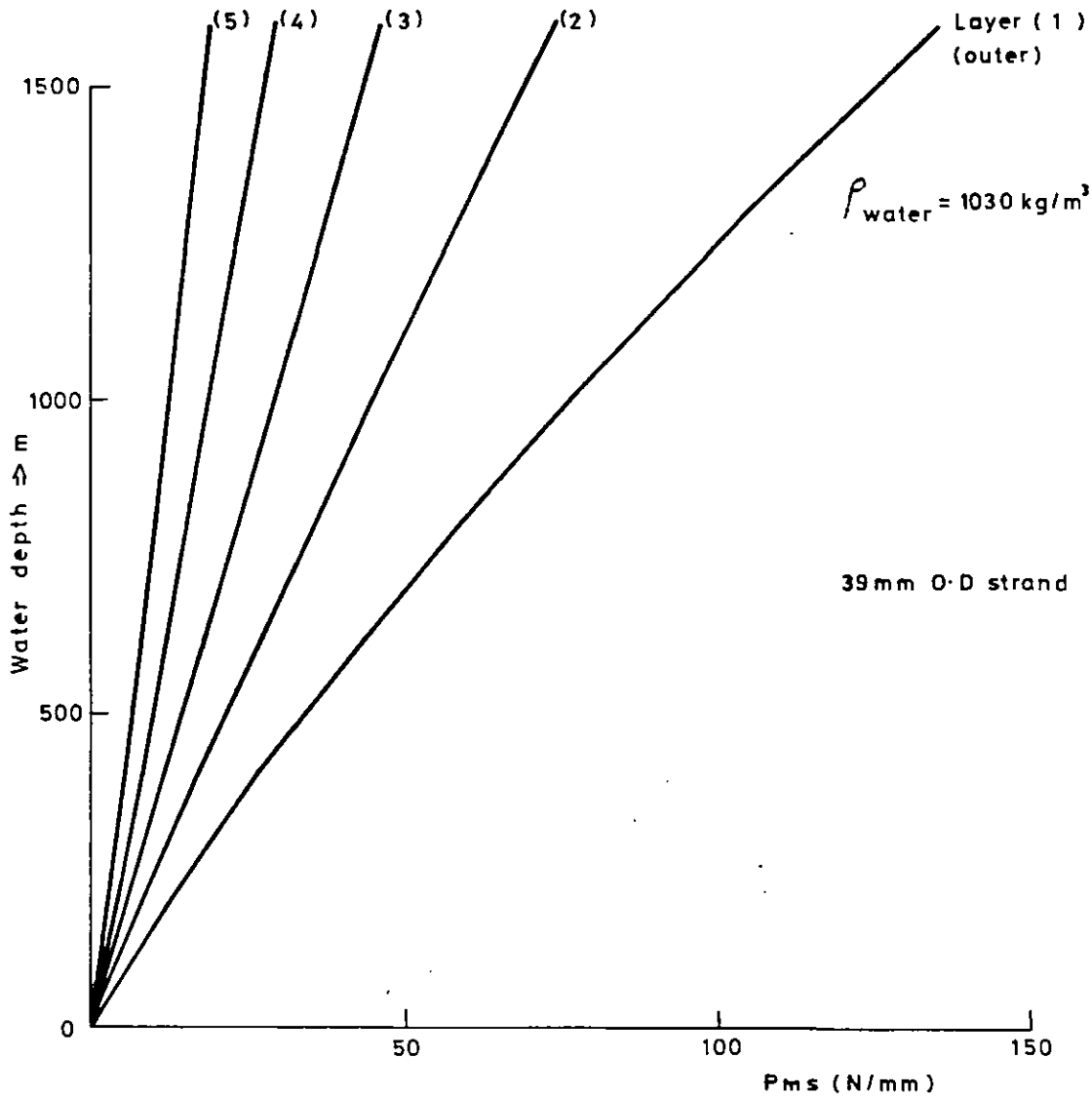

Fig 3·31 Variation of hoop contact force in individual layers as a function of water depth - zero mean tension is assumed in the cable

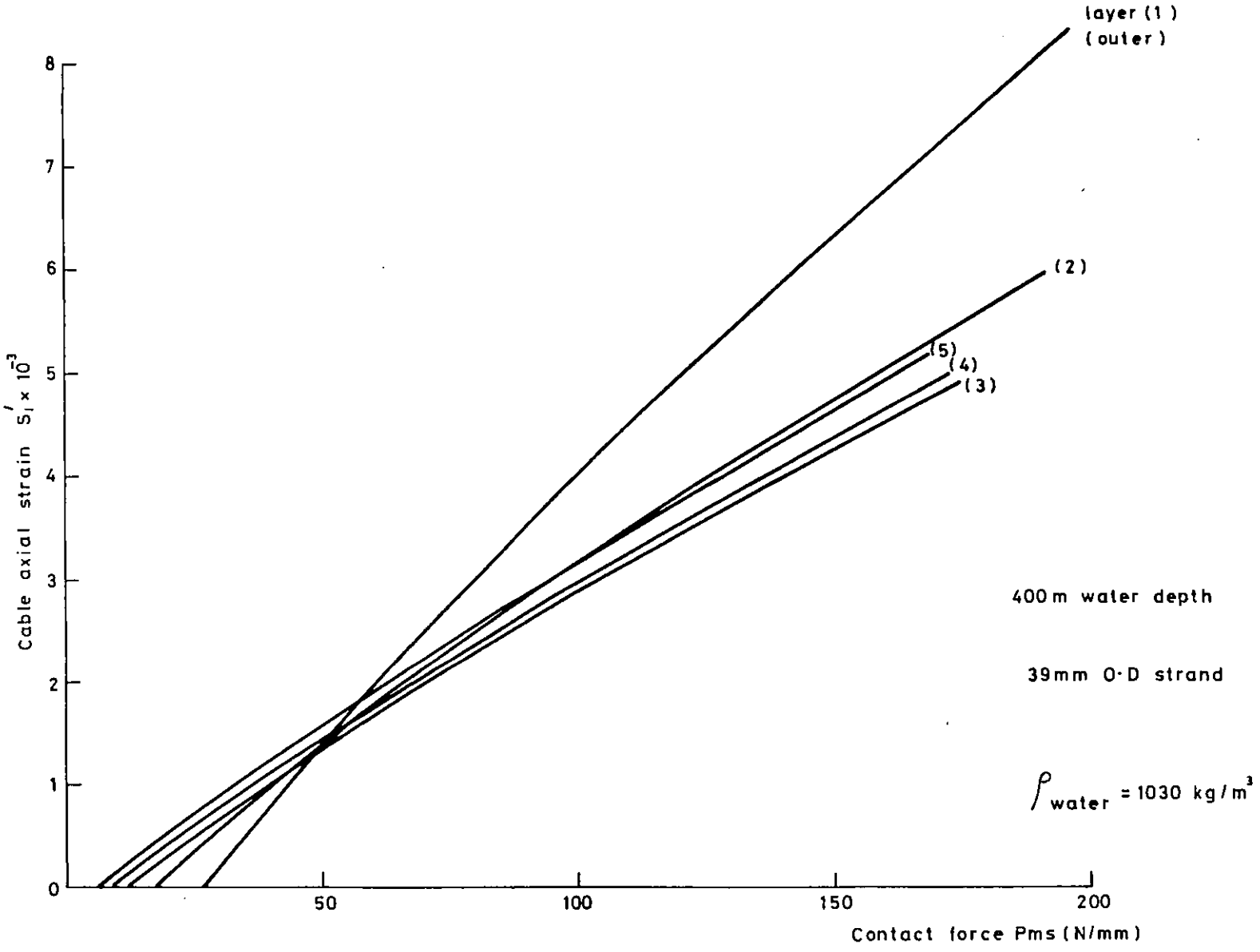

Fig 3·32 Line contact forces in assembled strand subject to hydrostatic water pressure

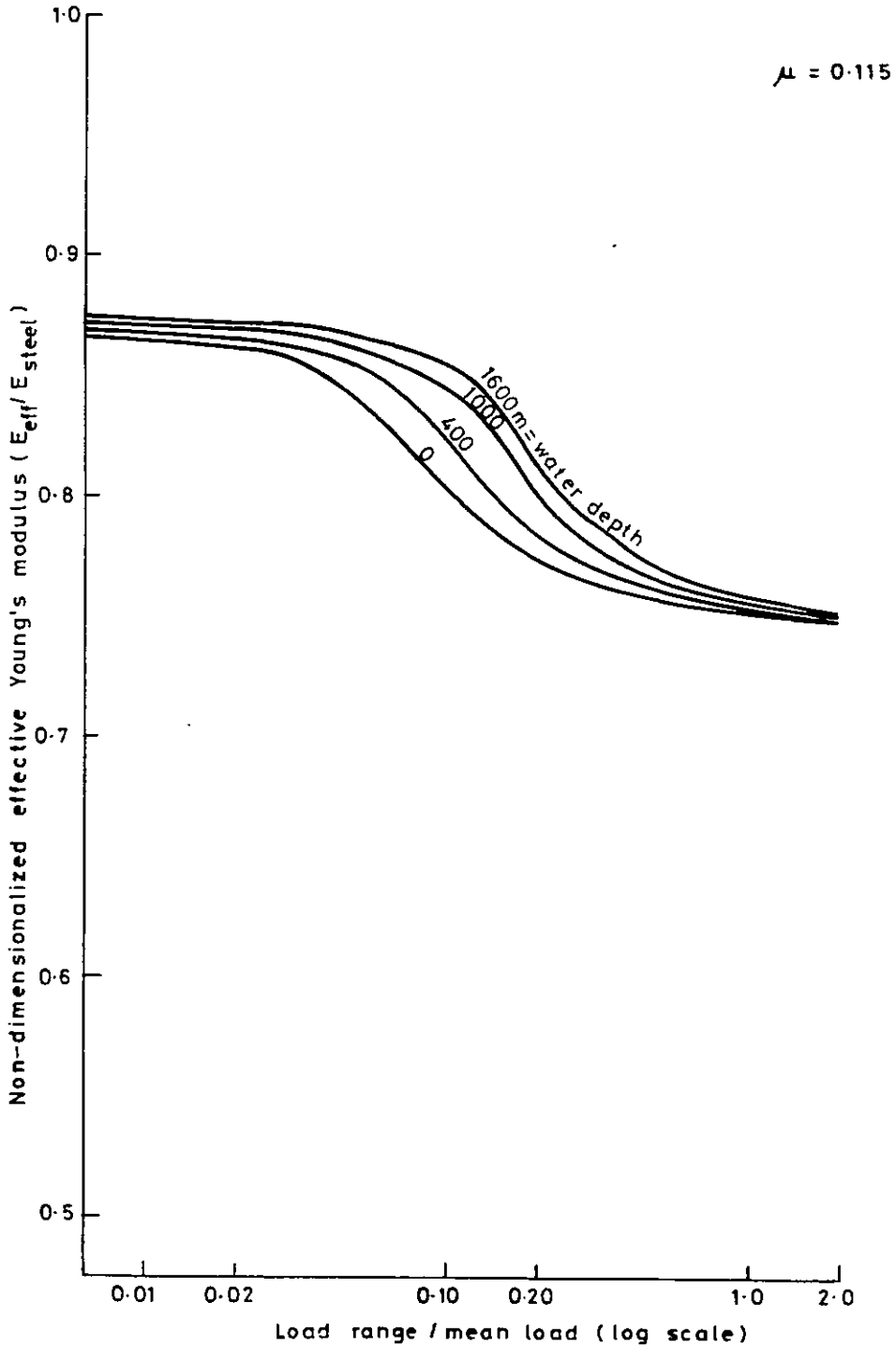

Fig 3·33 Variation of axial stiffness with water depth — 39 mm O·D strand

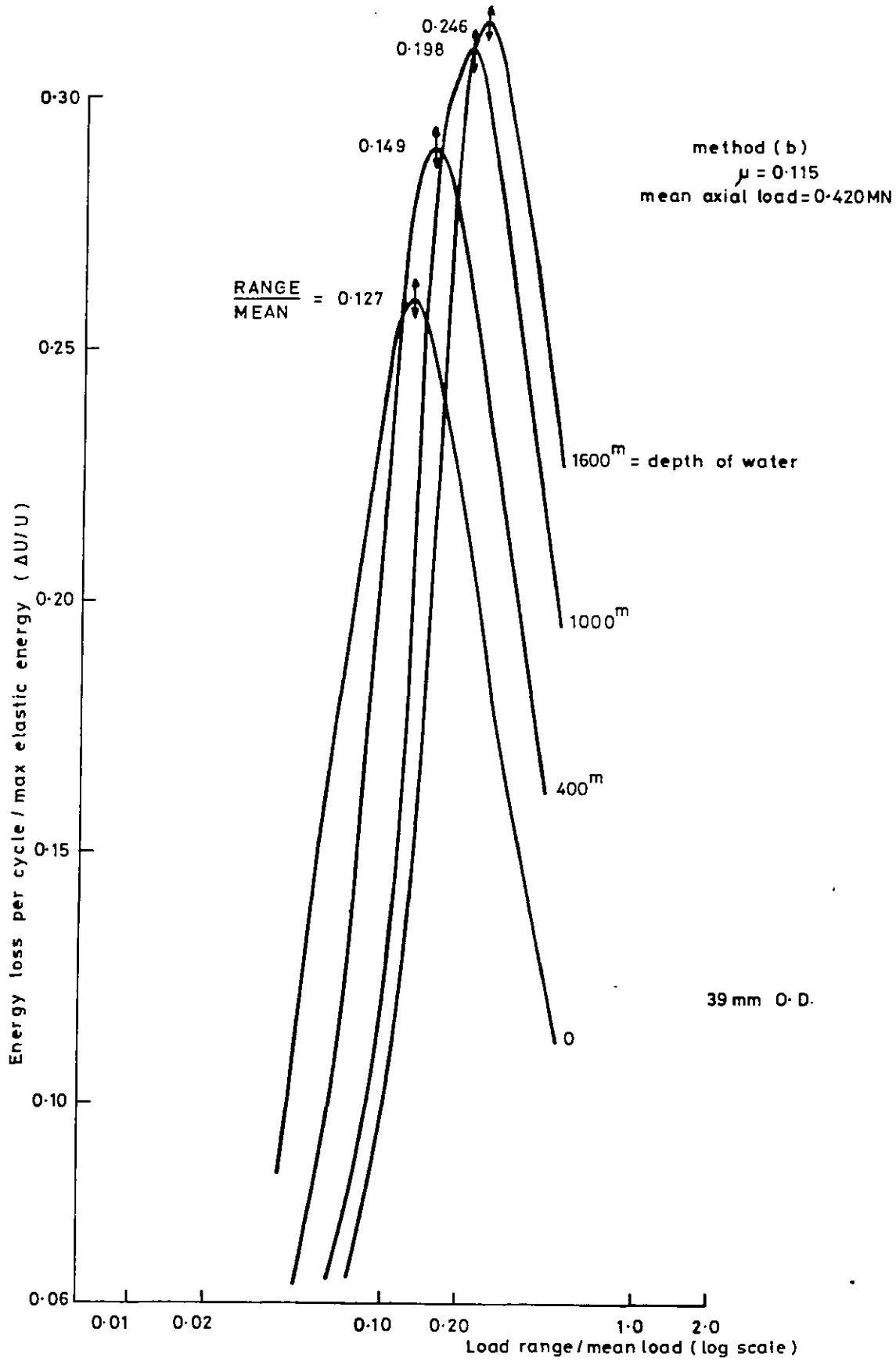

Fig 3·34 Theoretical axial energy dissipation in 39 mm O. D. strand as a function of water depth and range / mean of axial load

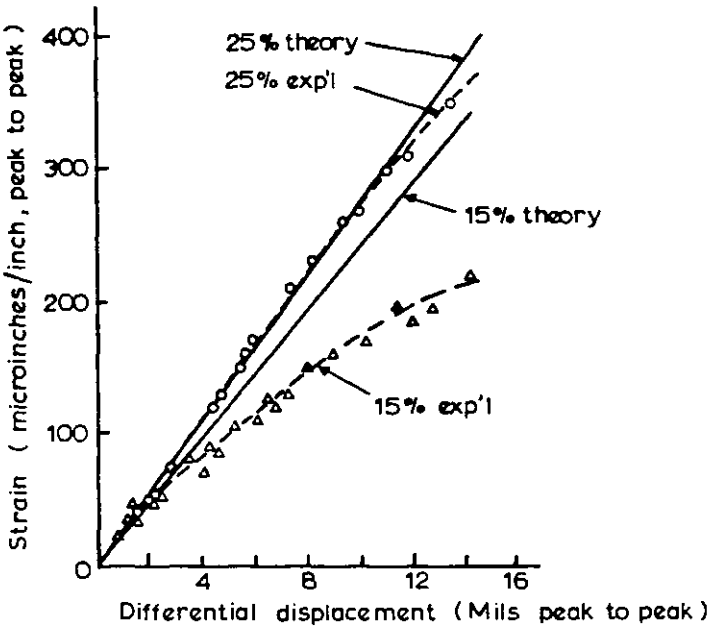

Fig (4.1) Experimental strain - displacement data at two tensions compared with theory After Ref(4.18)

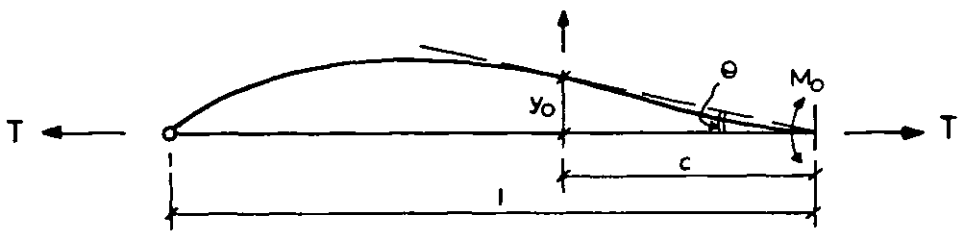

Fig (4.2)

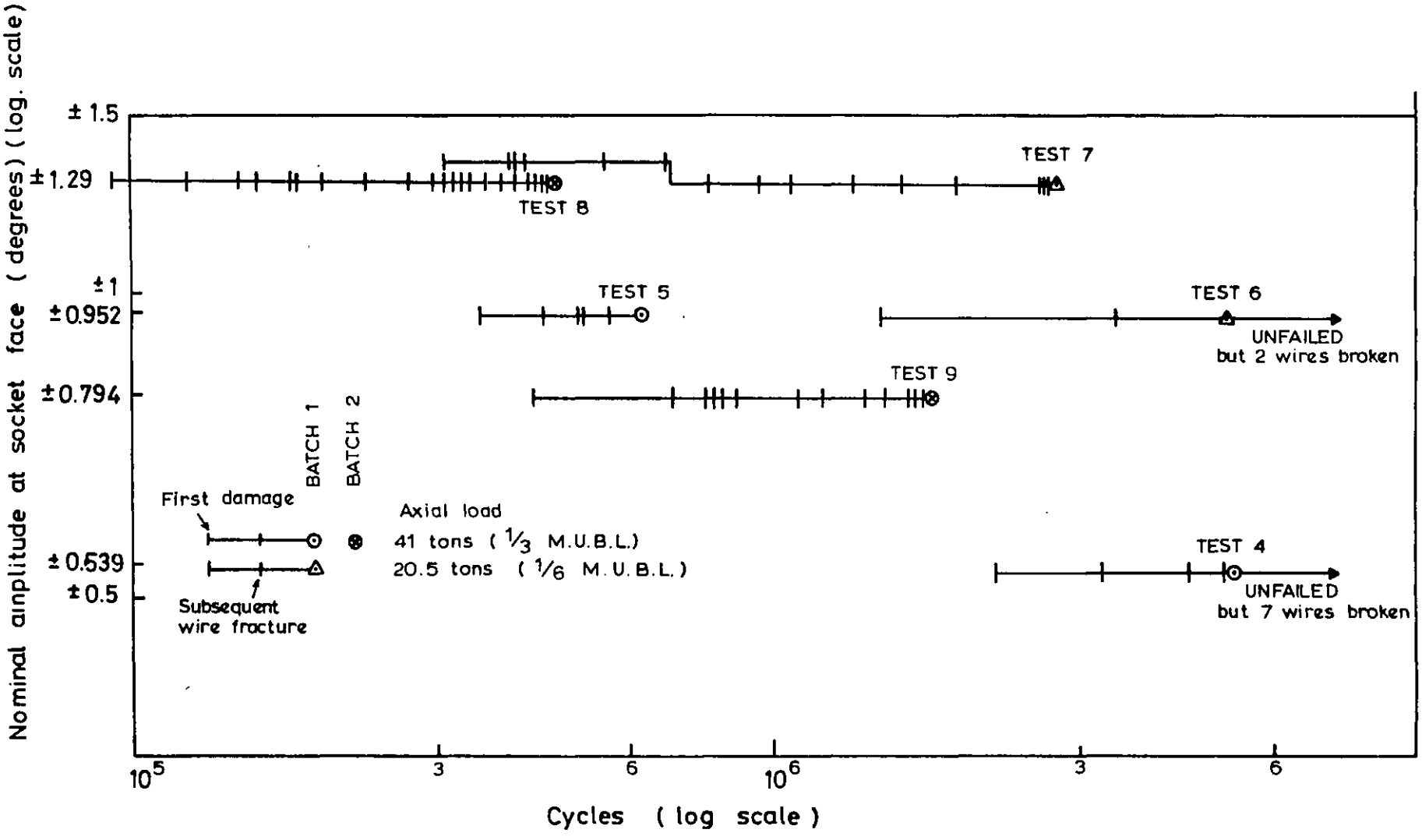

Fig (4.3) Life and earlier damage - Transverse tests
After Ref (2.53)

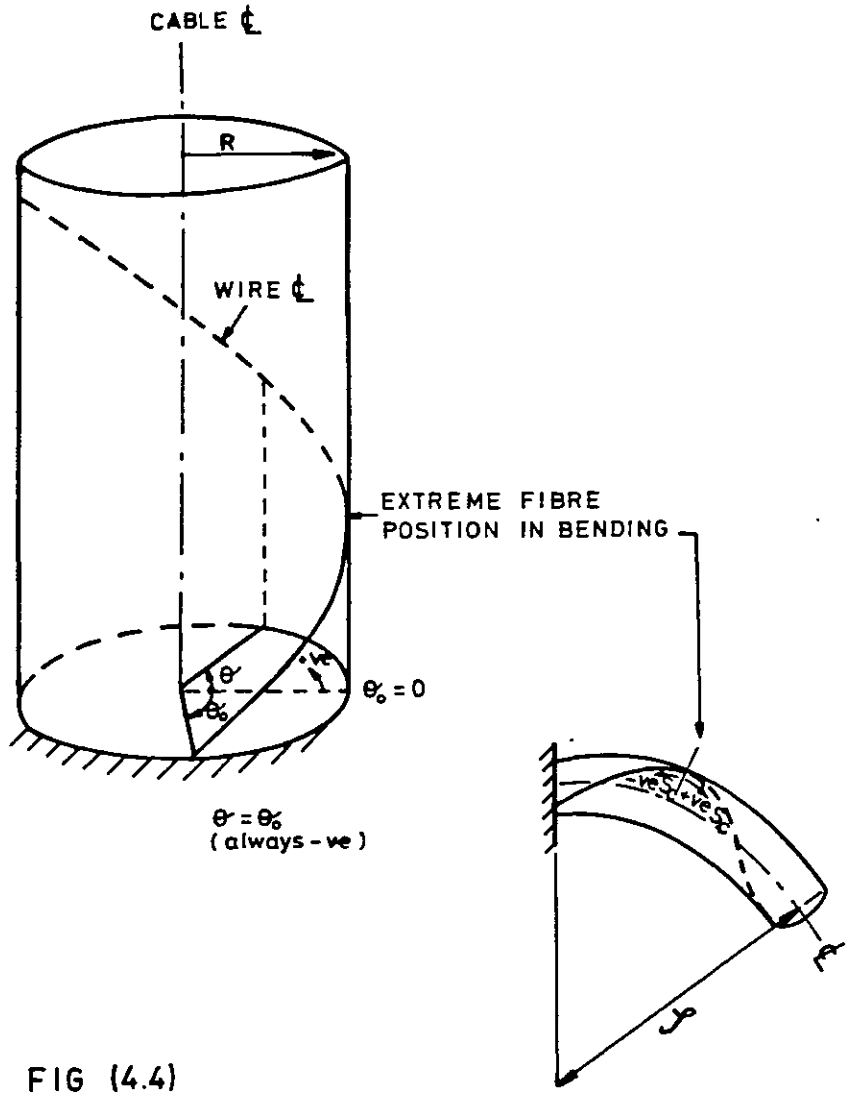

FIG (4.4)

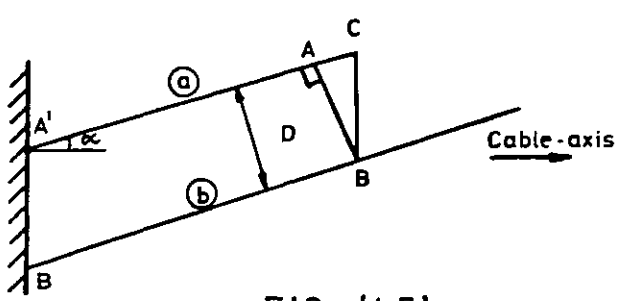

FIG (4.5)

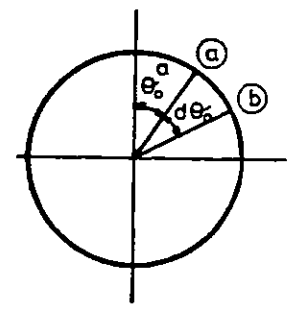

CABLE CROSS SECTION

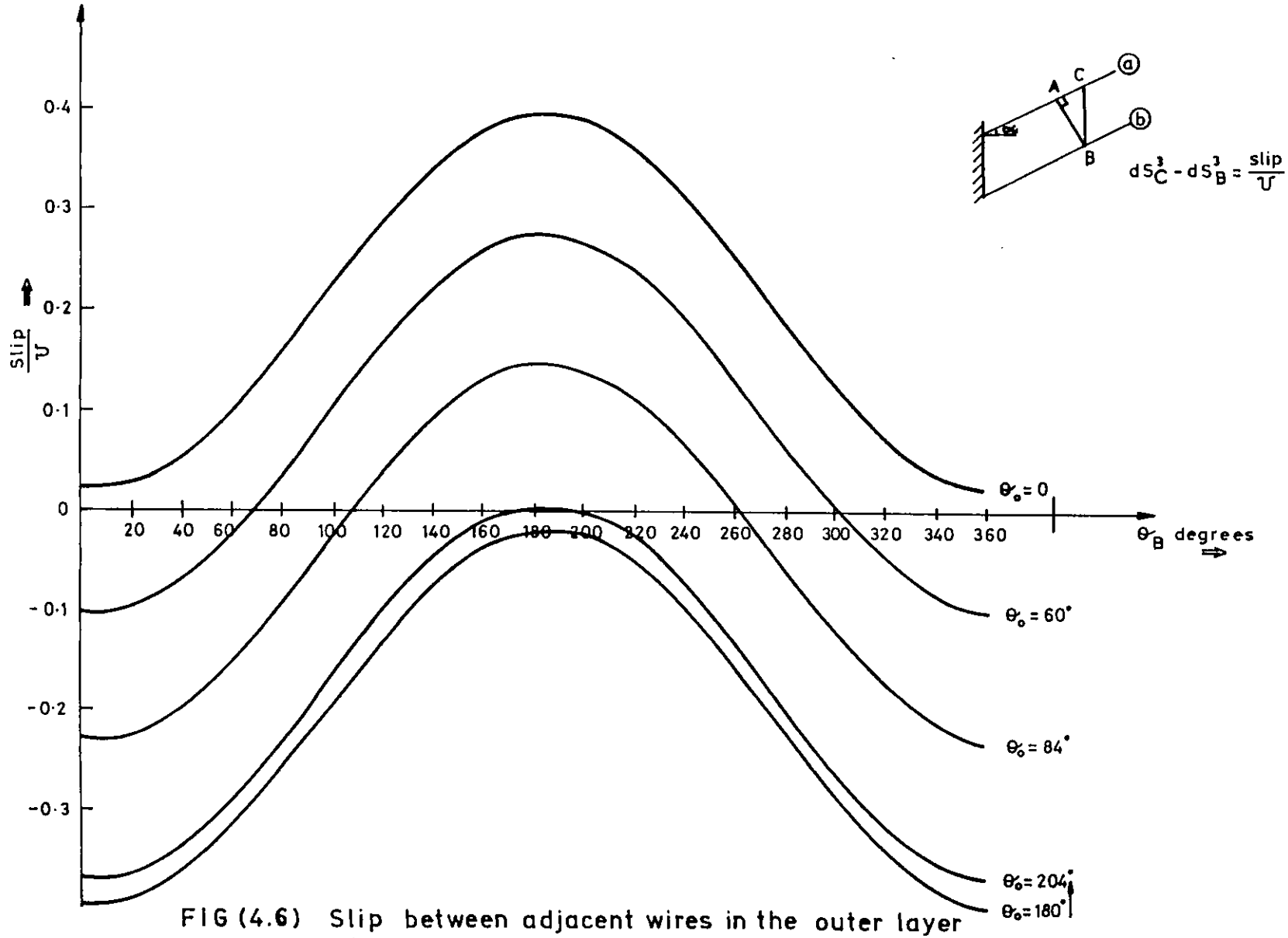

FIG (4.6) Slip between adjacent wires in the outer layer of the 39mm O·D strand subject to the plane–section bending

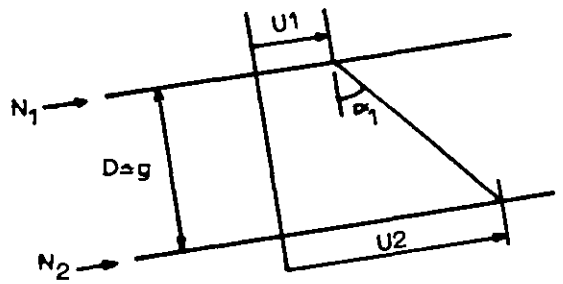

SHEAR DISPLACEMENT BETWEEN WIRES
IN LINE CONTACT

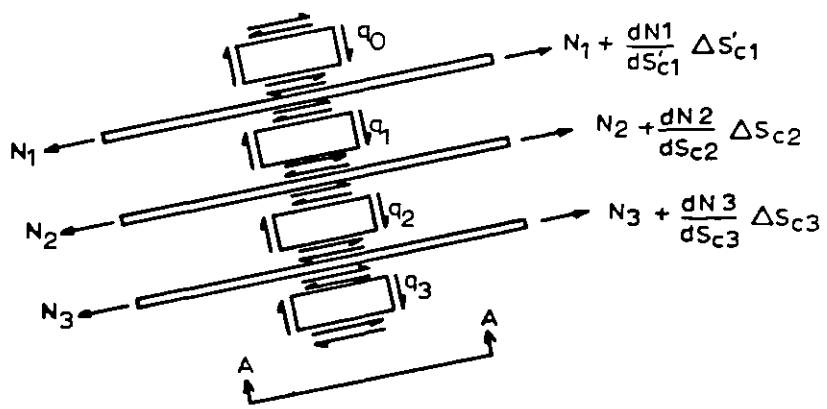

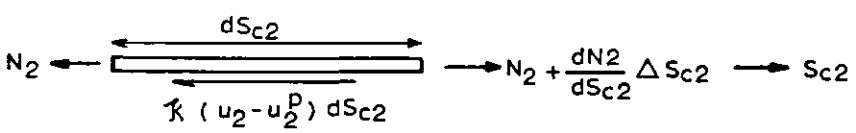

VIEW A-A OUTER WIRE CORE INTERACTION

Fig (4.7) Interwire shear interaction for the outer layer over a rigid core

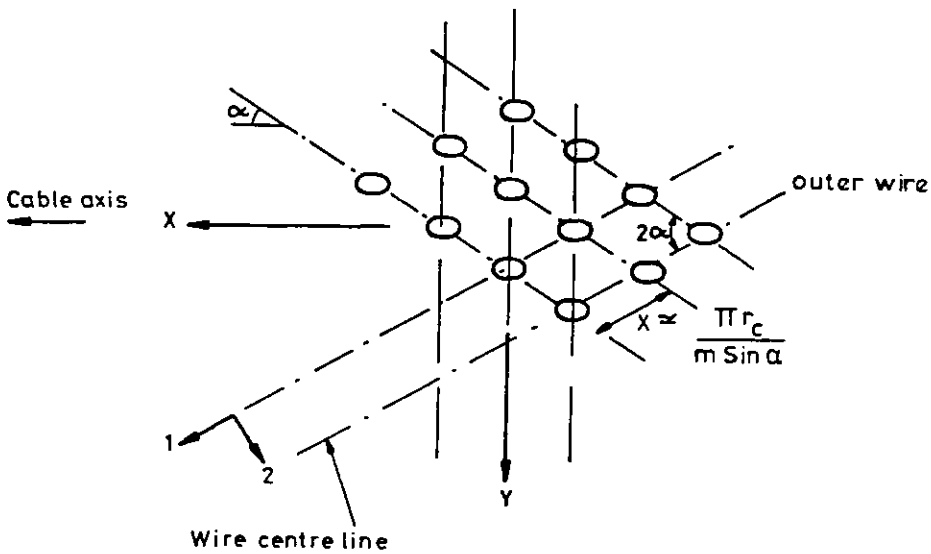

FIG (4.8) Contact pattern between the outer layer and the core

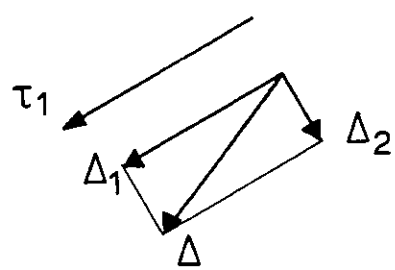

Fig.(4-9)

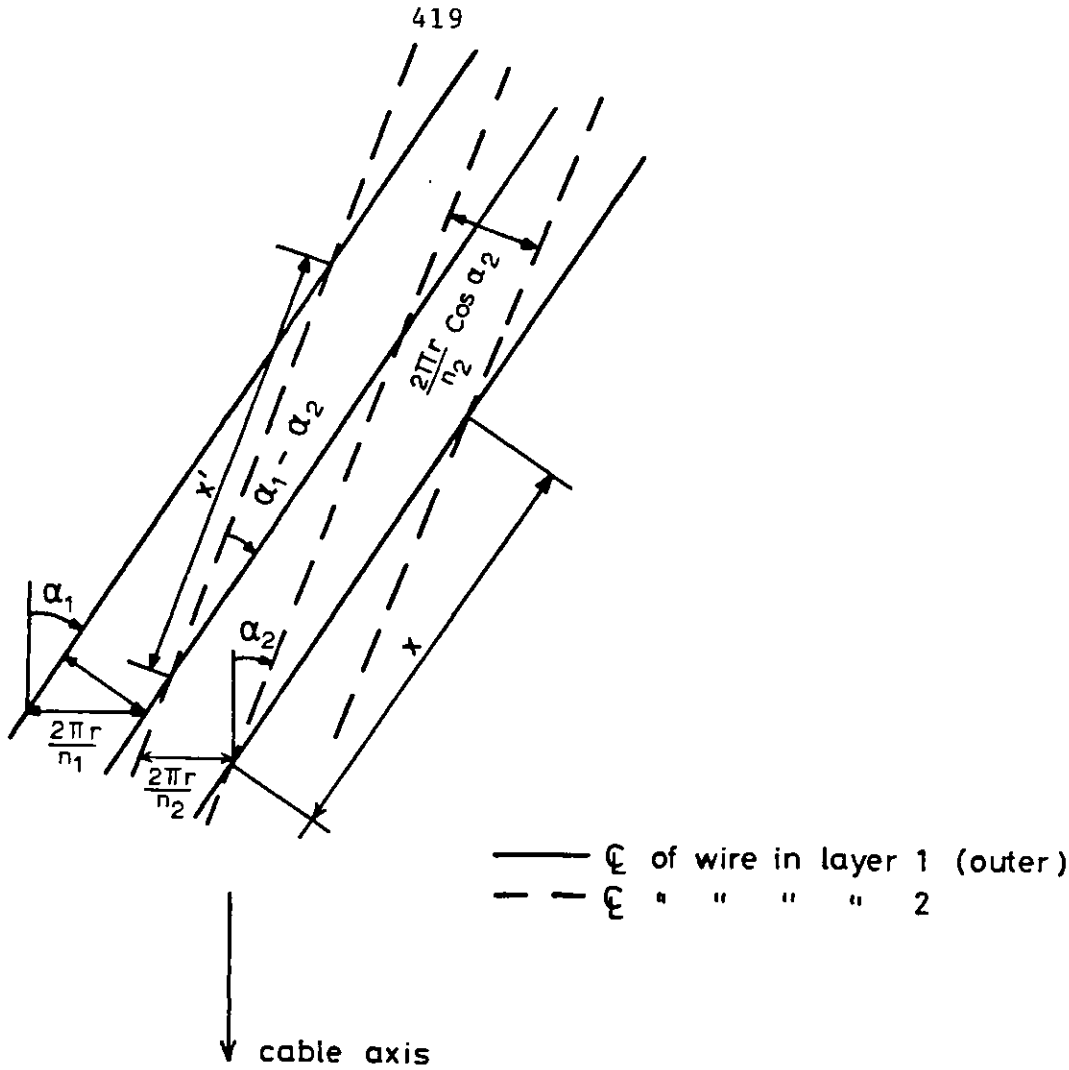

Fig. (4.10)

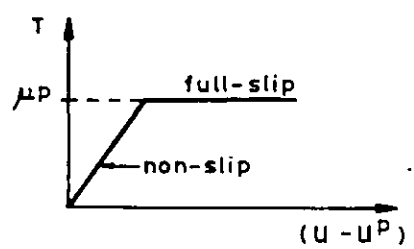

FIG (4.11) Ideal elastic - plastic model

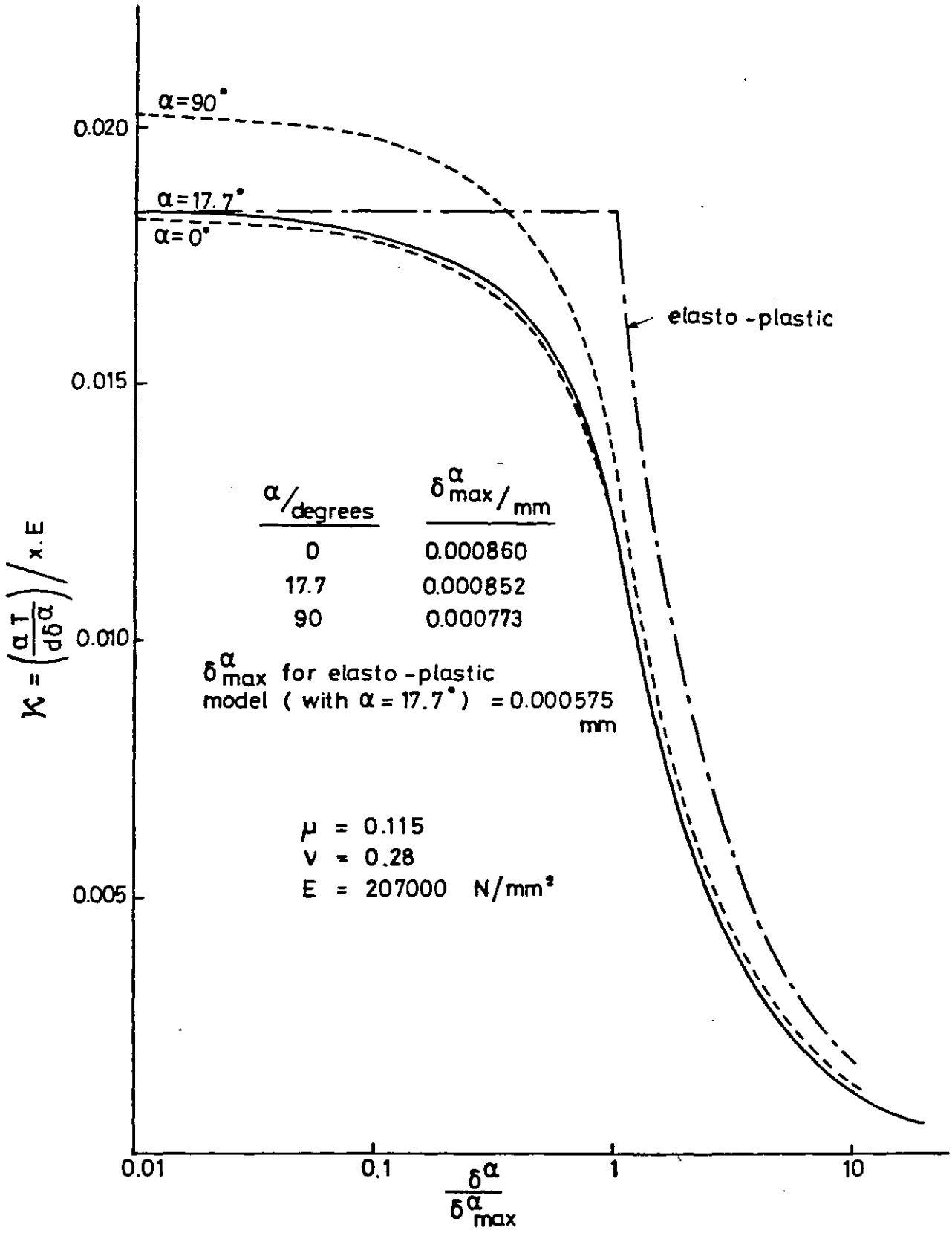

Fig(4.12)Theoretical plots of shear stiffness versus relative slip between the two outer layers of the 39 mm O.D. strand under a mean axial load of 0.410 MN

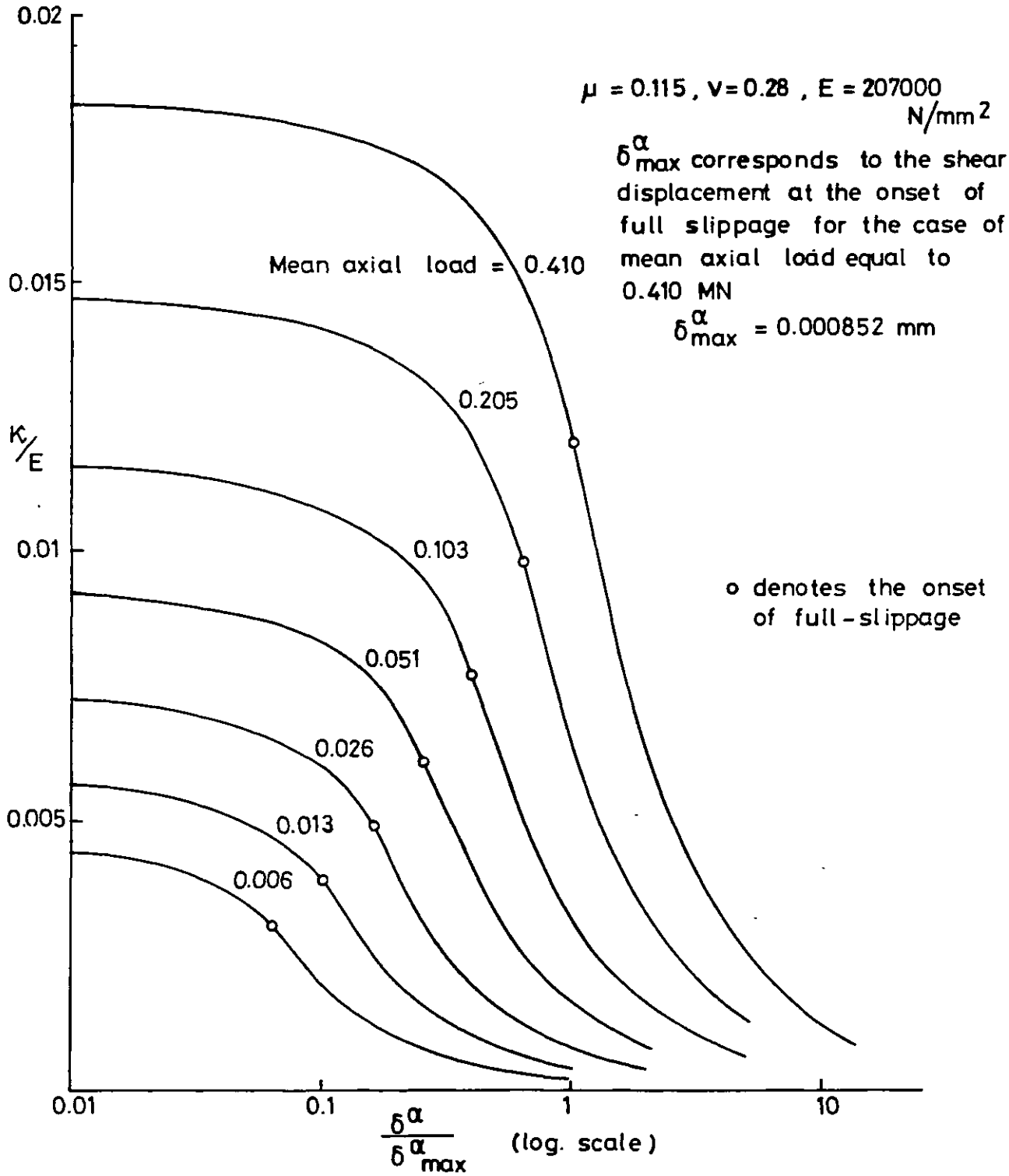

Fig(4.13) Theoretical plots of tangential stiffness between the outer wire and the core versus shear deformation for various mean axial loads on the 39 mm O.D. strand

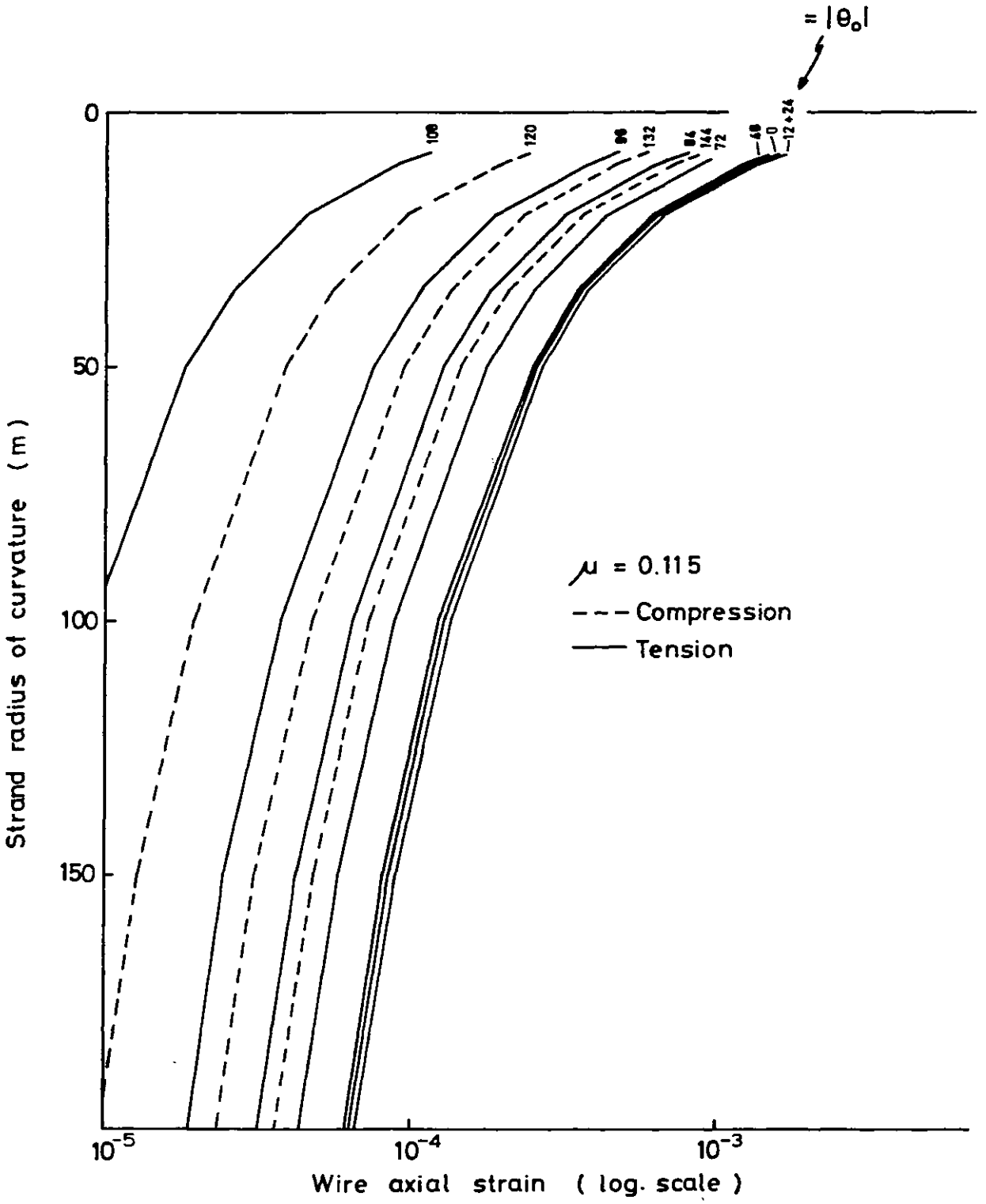

Fig. (4.14) Wire axial strains for position $\theta=\theta_o$ plotted as a function of the radius of curvature near the clamp (39 mm O.D. strand ; mean axial load = 0.420 MN)

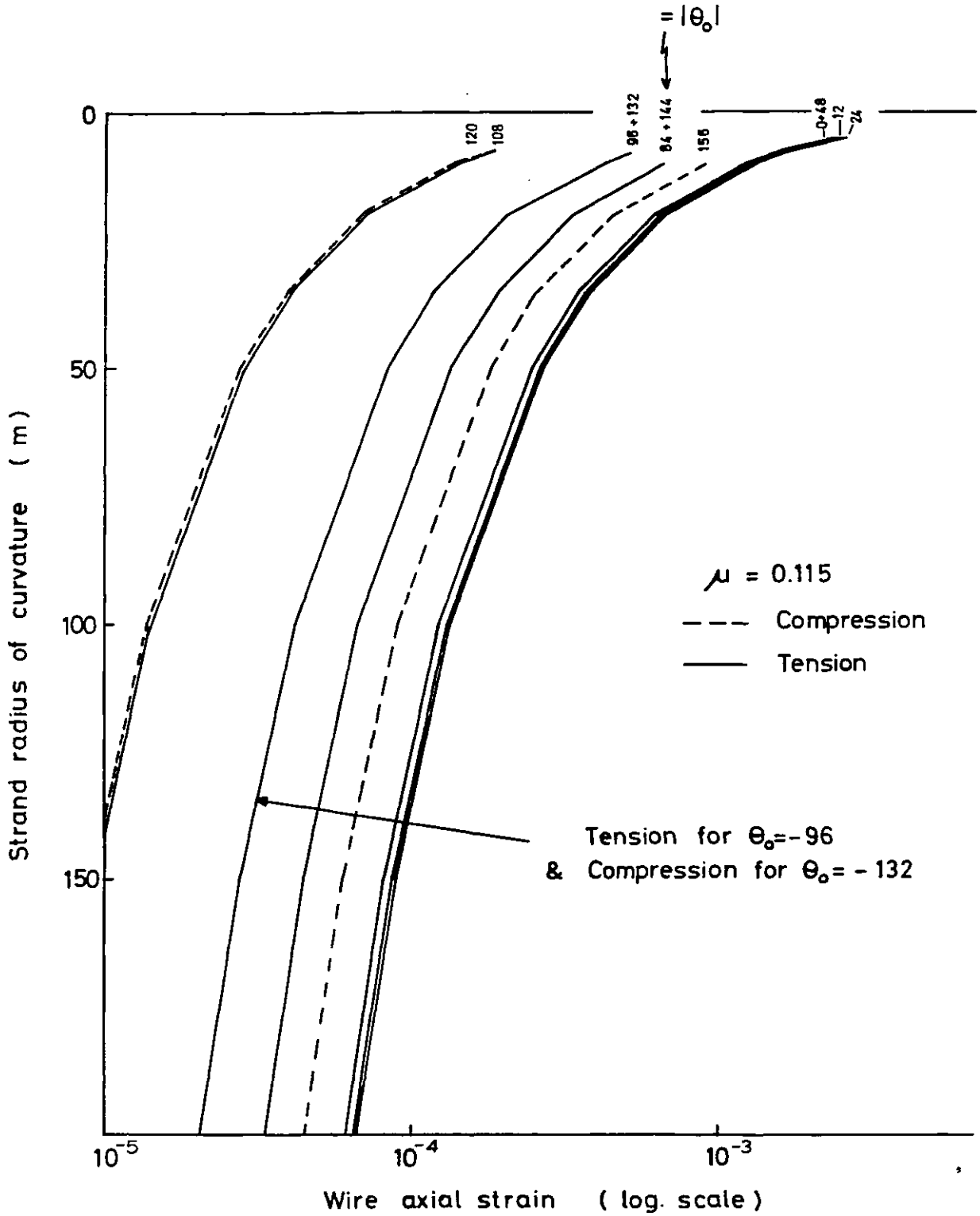

Fig.(4.15) Wire axial strains at position $\theta=\theta_o$ plotted as a function of the radius of curvature near the clamp (39 mm O.D. strand ; mean axial load = 0.205 MN)

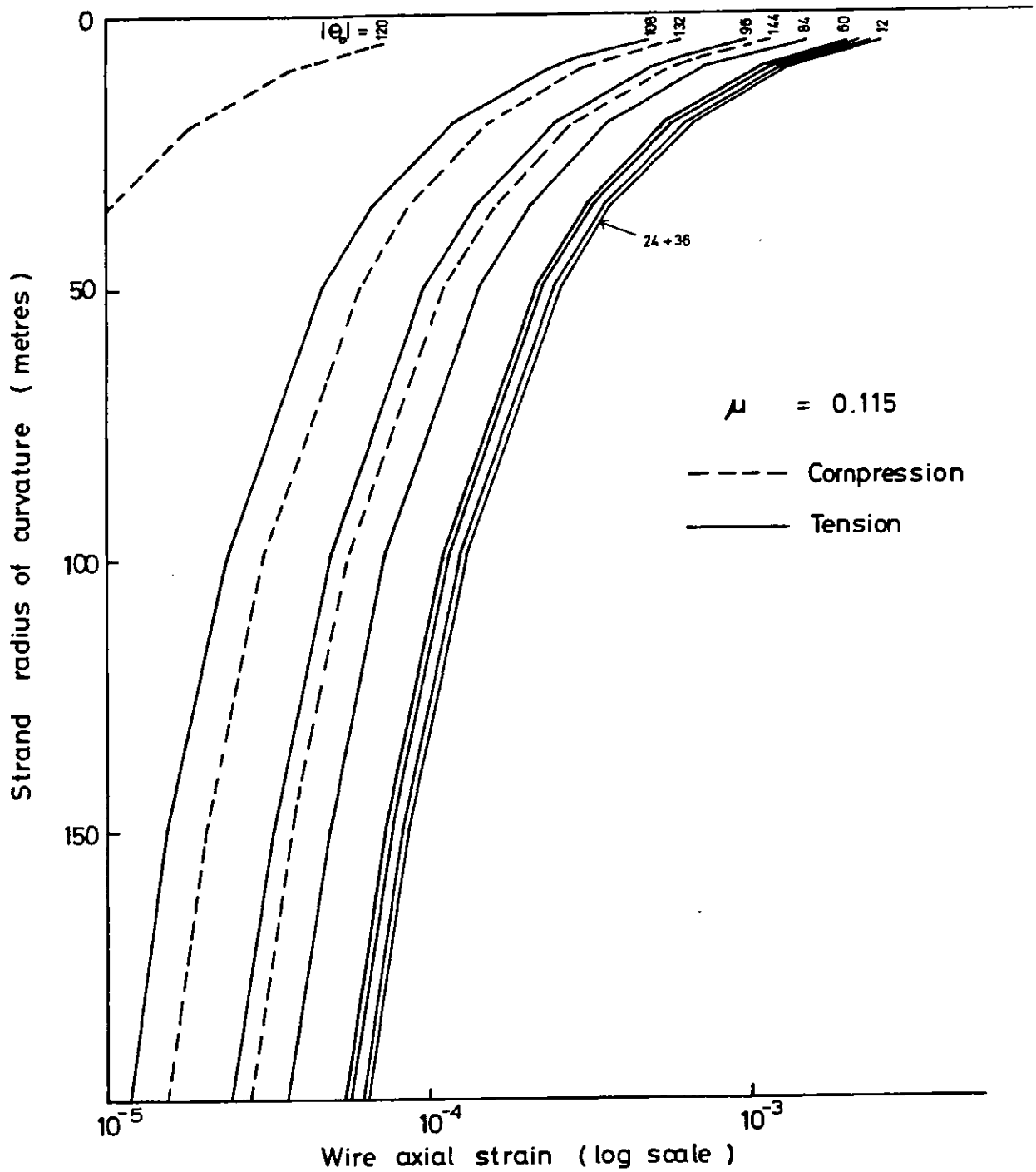

Fig.(4.16) Wire axial strains for position $\theta = \theta_0$ plotted as a function of the radius of curvature near the clamp (39 mm O.D. strand ; mean axial load = 0.050 MN)

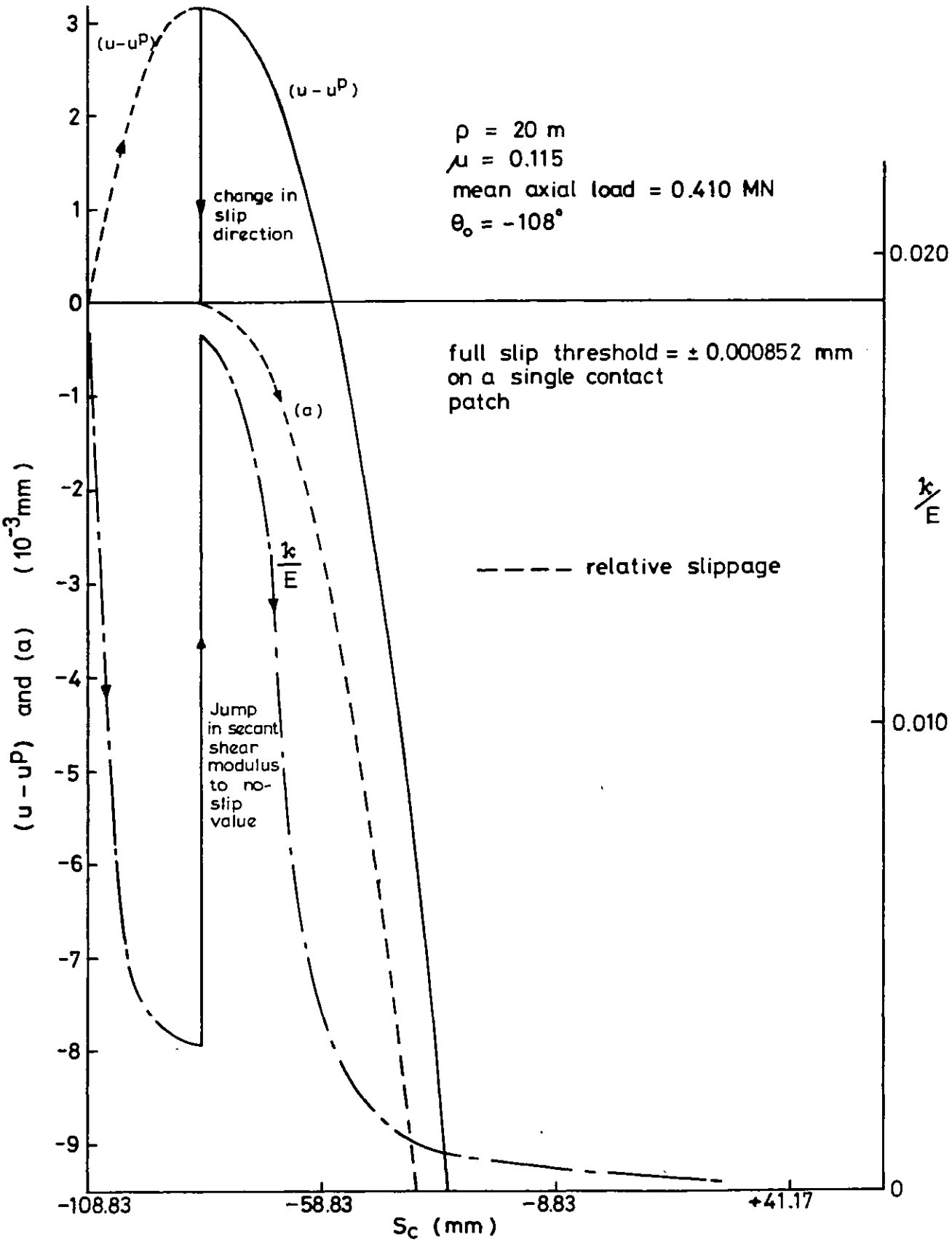

Fig (4.17) Theoretical plots of variation in relative slippage and shear stiffness along a wire in bending

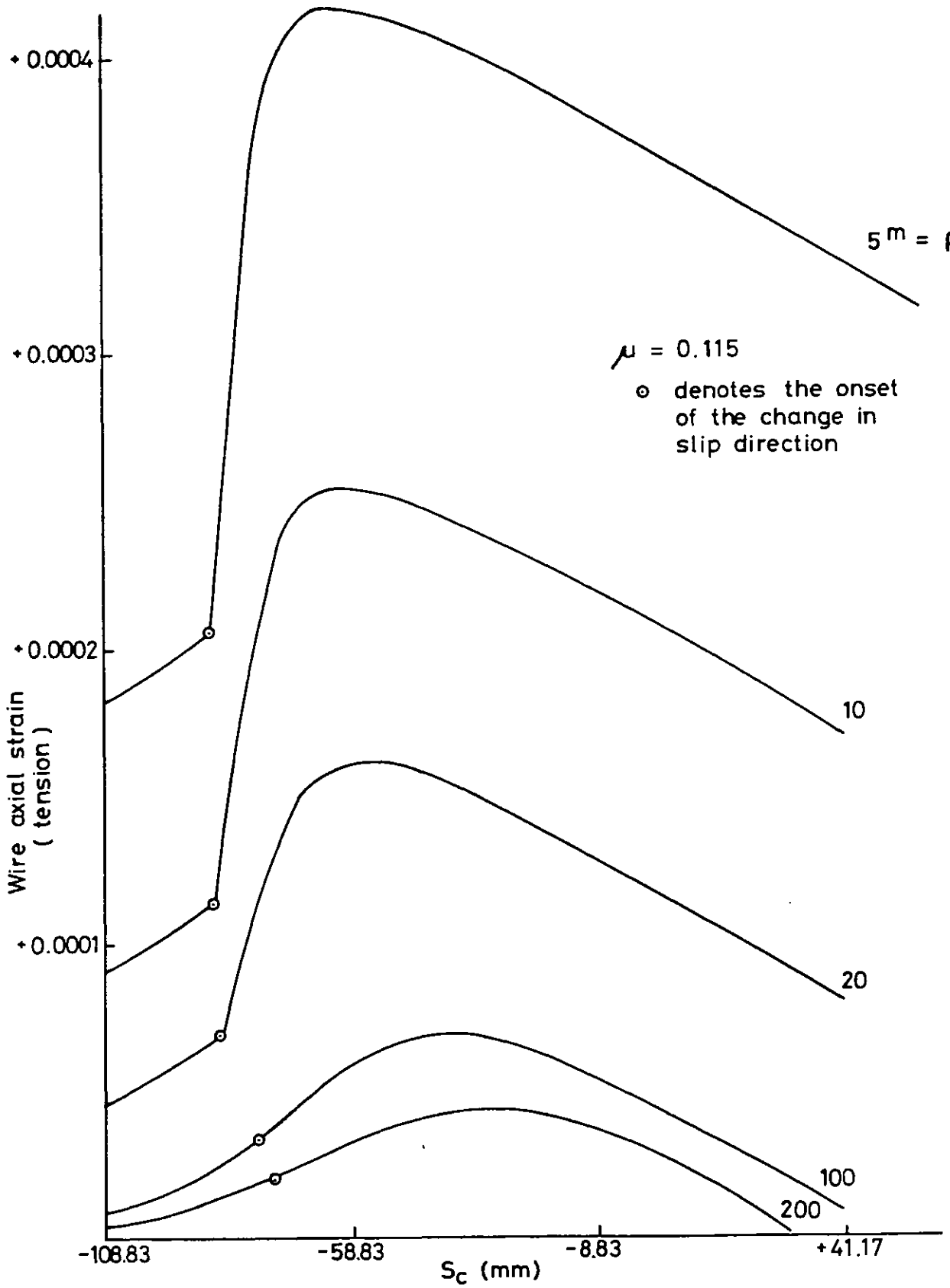

Fig (4.18) Plot of wire axial strain along the wire with $\theta_o = -108^\circ$ as a function of ρ (39 mm O.D. strand ; mean axial load = 0.420 MN)

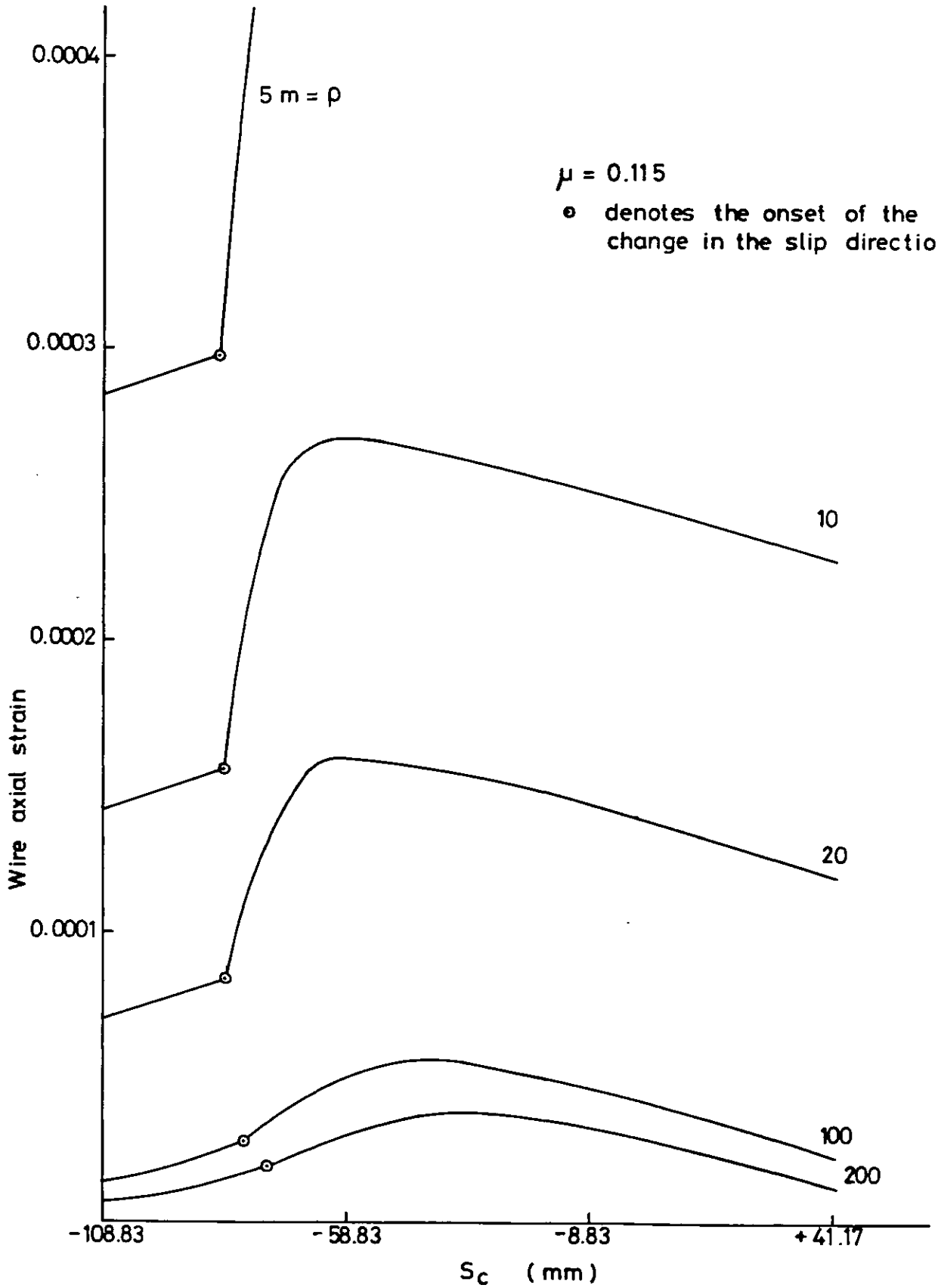

Fig.(4.19) Theoretical axial strain along the wire with $\theta_e = -108°$ as a function of ρ (39 mm O.D. strand ; mean axial load = 0.205 M

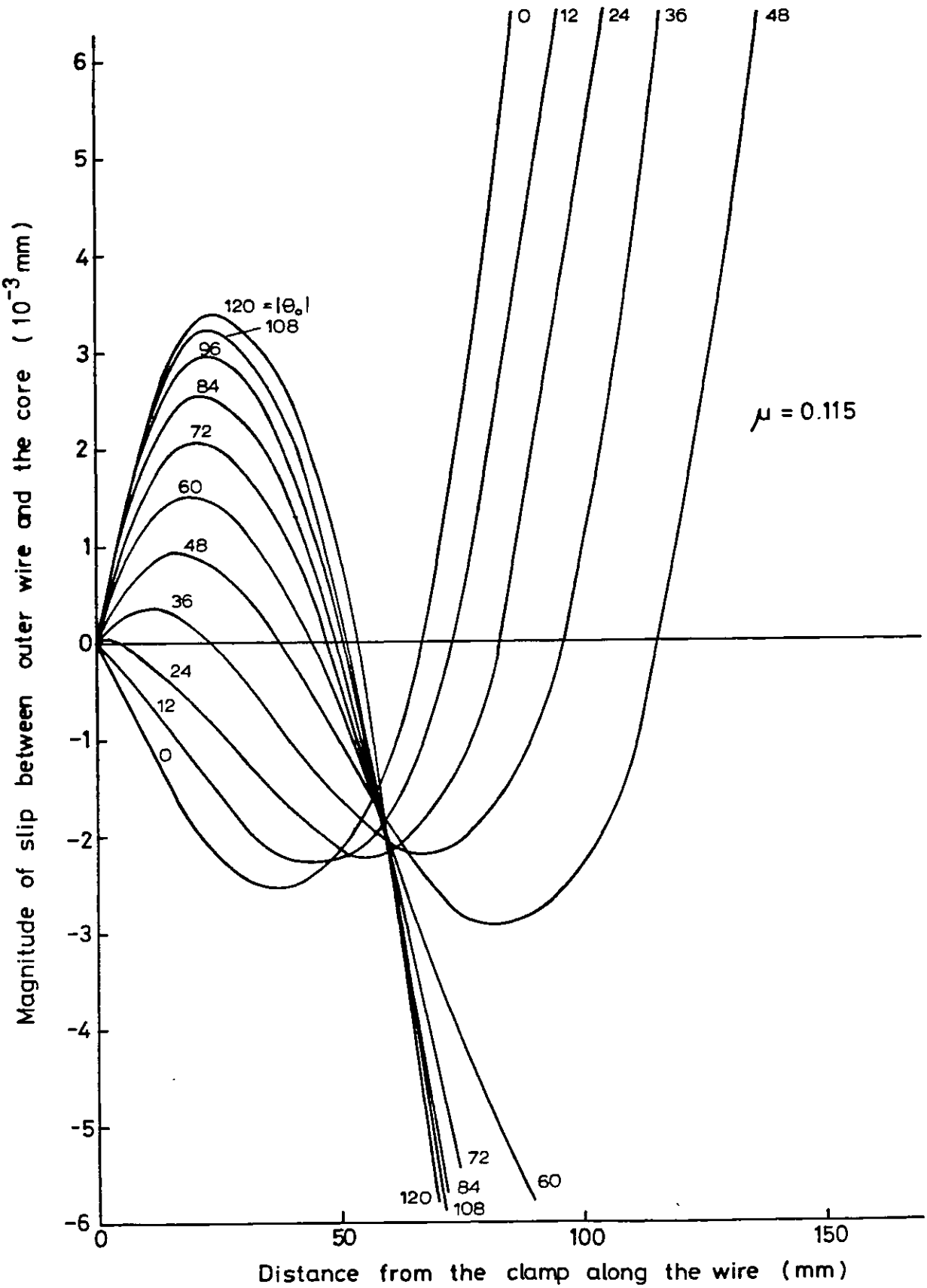

Fig (4.20) Slip between outer wires of the 39 mm OD strand and the core (ρ = 20 m ; mean axial load = 0.410 MN)

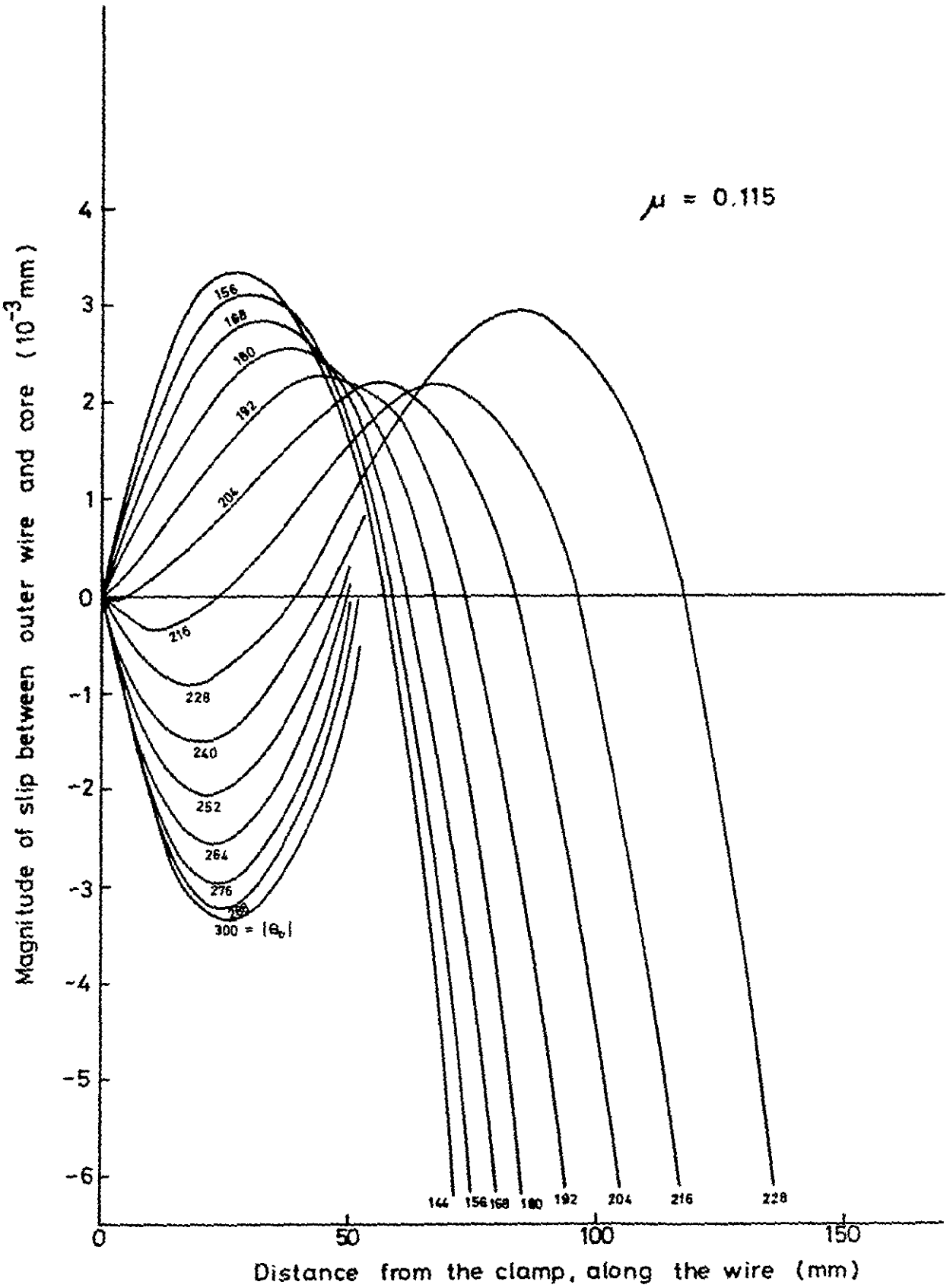

Fig. (4.21) Slip between outer wires of the 39 mm O.D. strand and the core (p = 20 m ; mean axial load = 0.0410 MN)

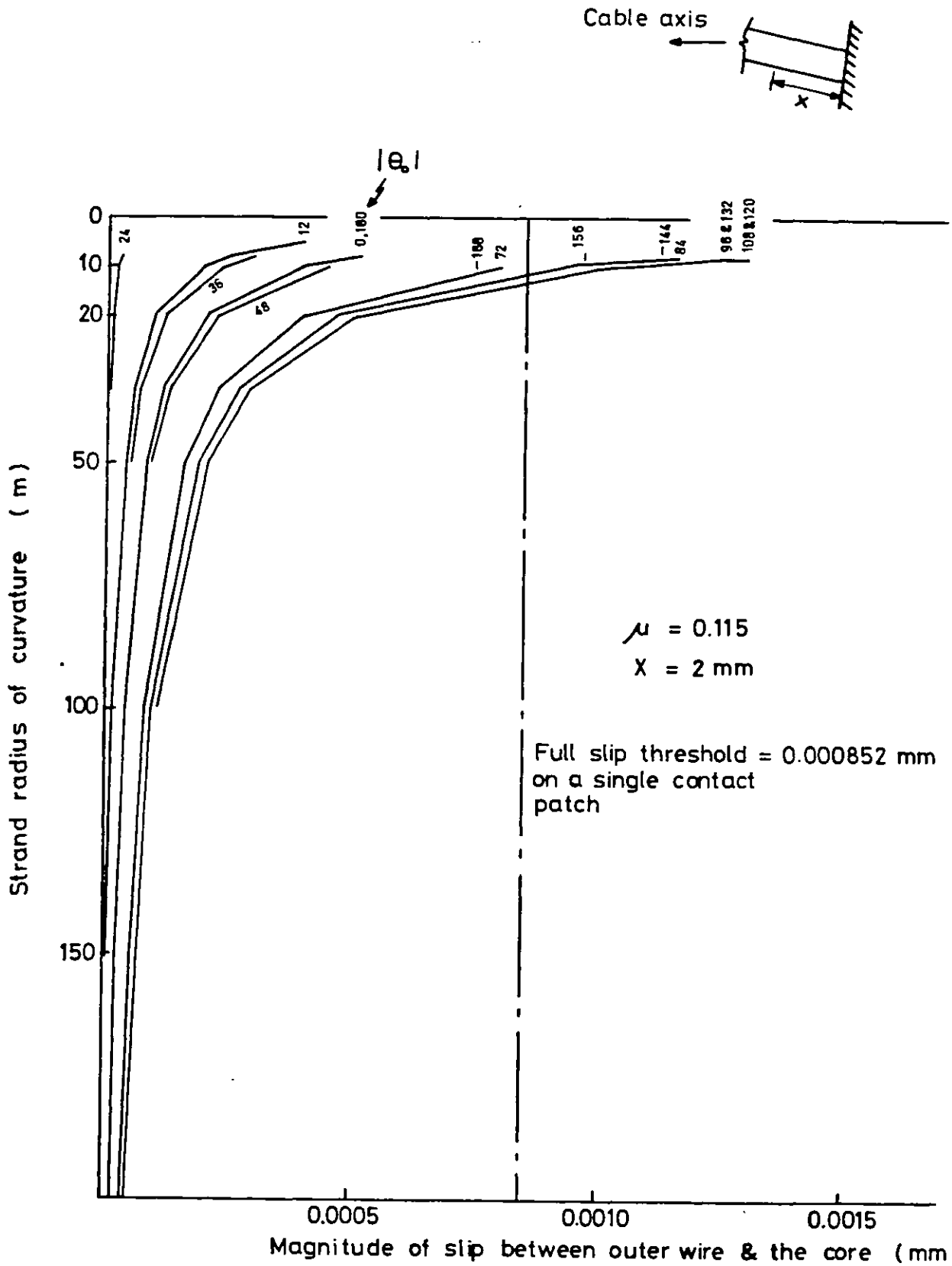

Fig. (4.22) Plot of $u-u^{P}$ between outer wires and the core at a distance of 2 mm along the wires from the clamp, versus ρ (39 mm O.D. strand; mean axial load = 0.410 MN)

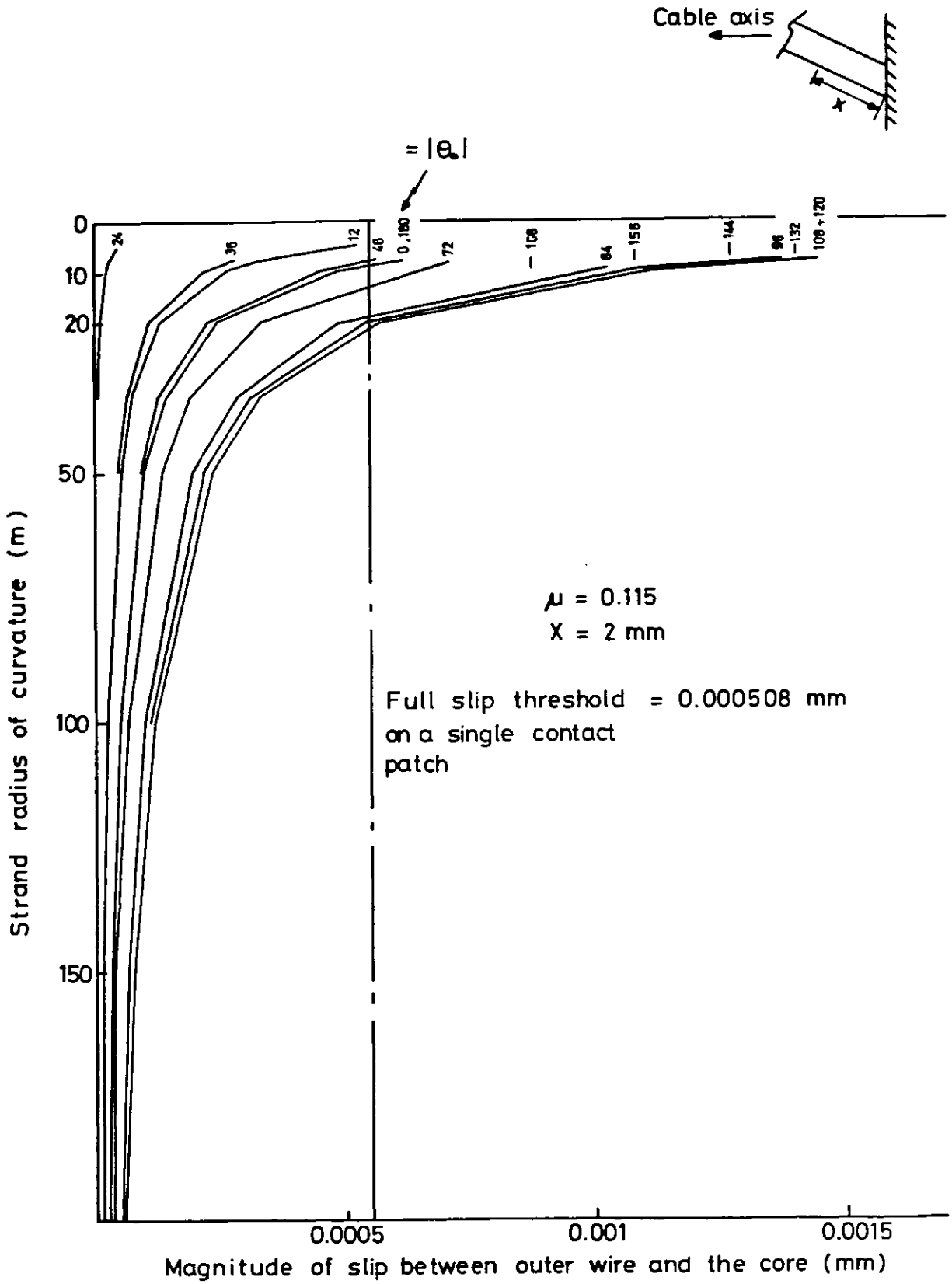

Fig. 4.23 Plot of $u-u^{p}$ between outer wires and the core at a distance of 2 mm along the wires from the clamp, versus ρ (39 mm O.D. strand ; mean axial load = 0.205 MN)

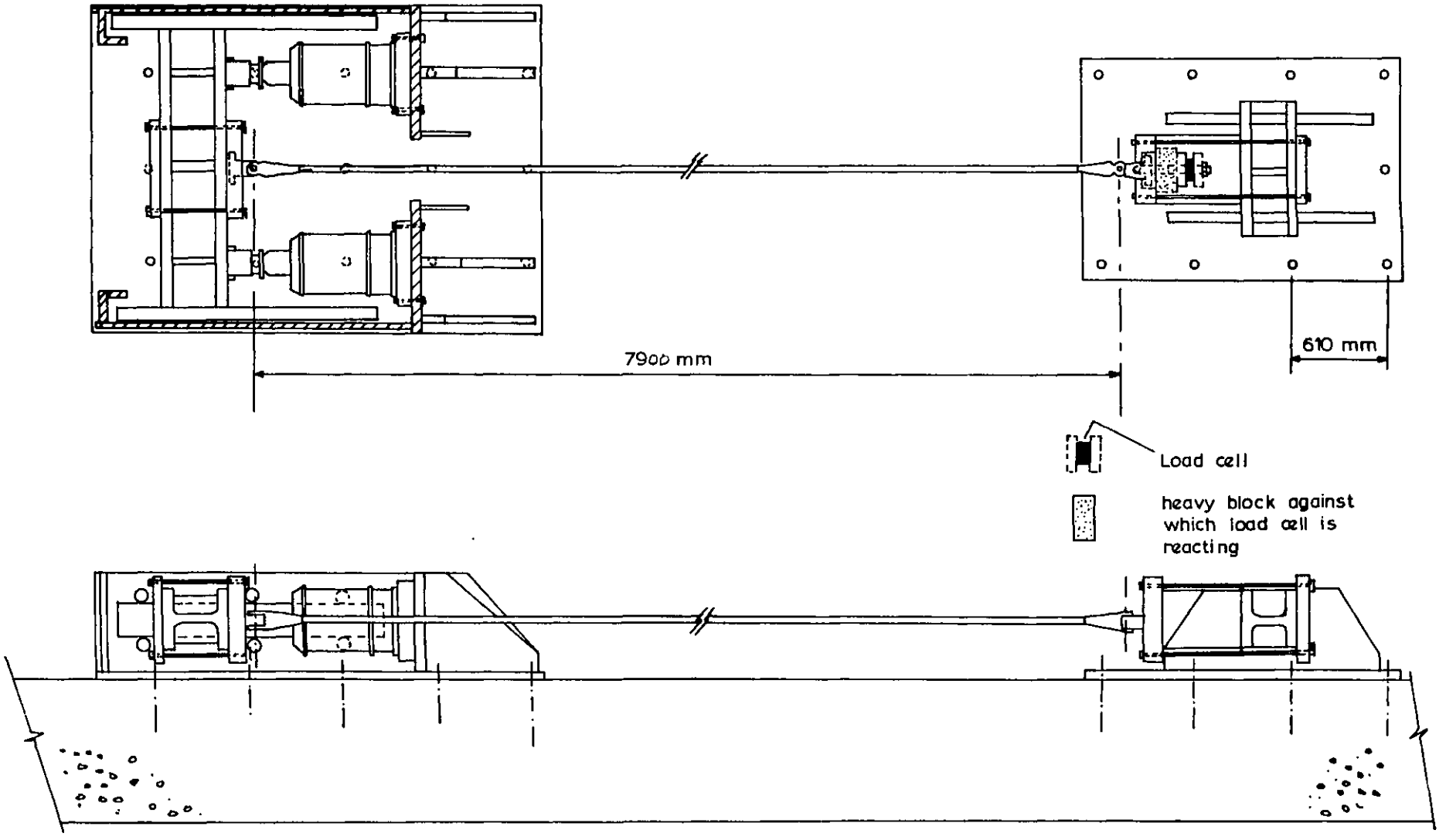

Fig (5.1) General arrangement of the test rig for axial tensioning

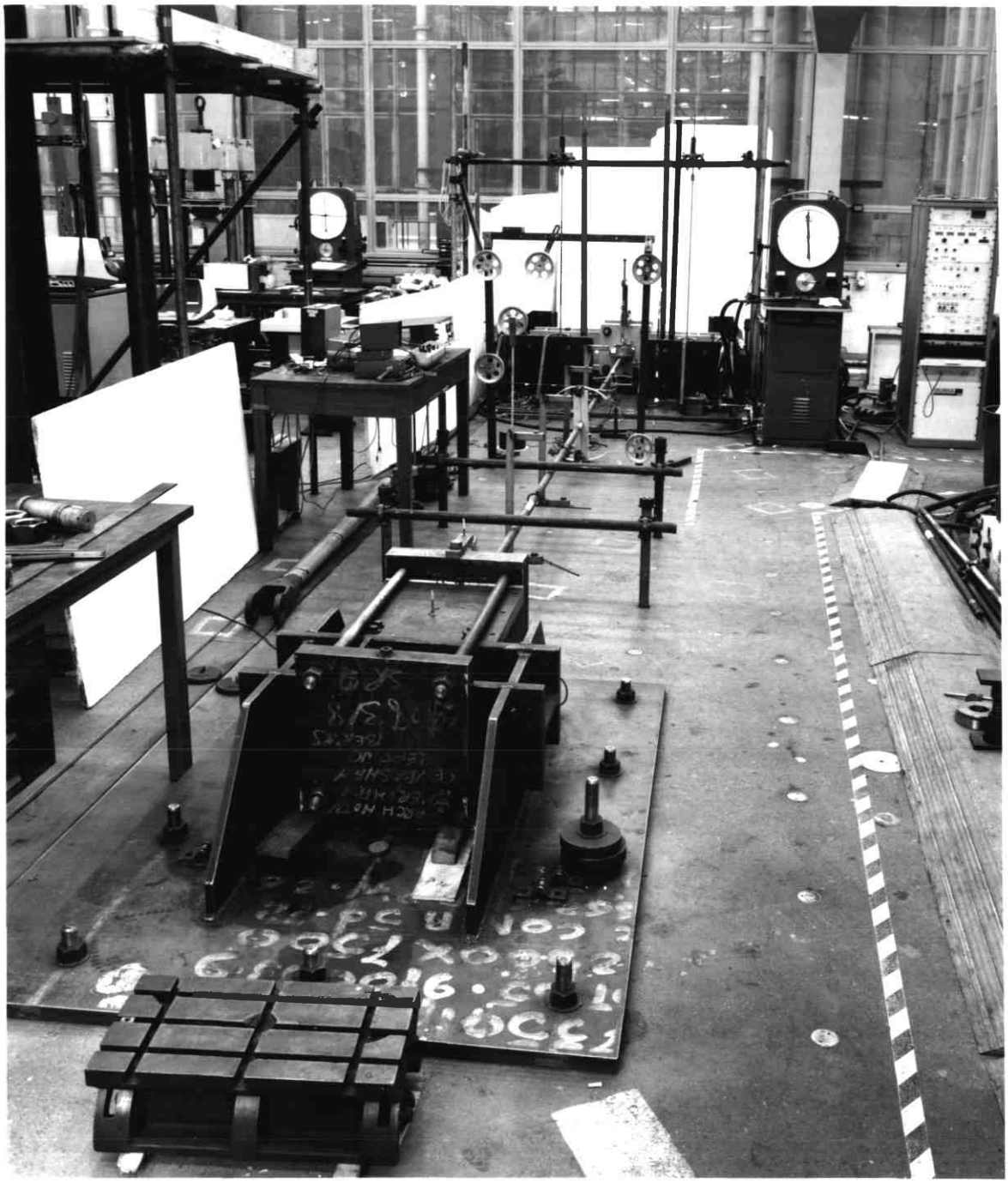

Fig. 5.2 General arrangement for axial tensioning of the cable and also the torsion set-up.

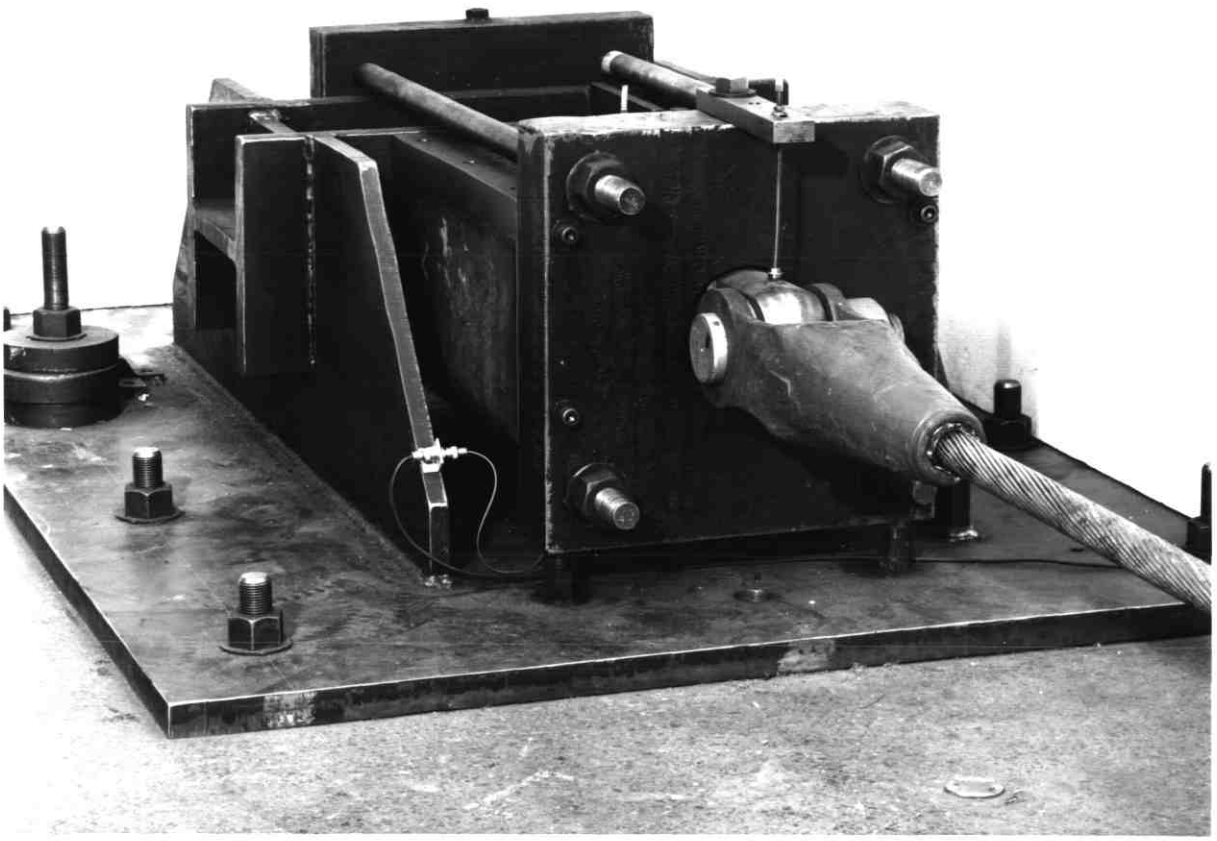

Fig. 5.3 Detail of the fixed hold-down with the housing for the load cell.

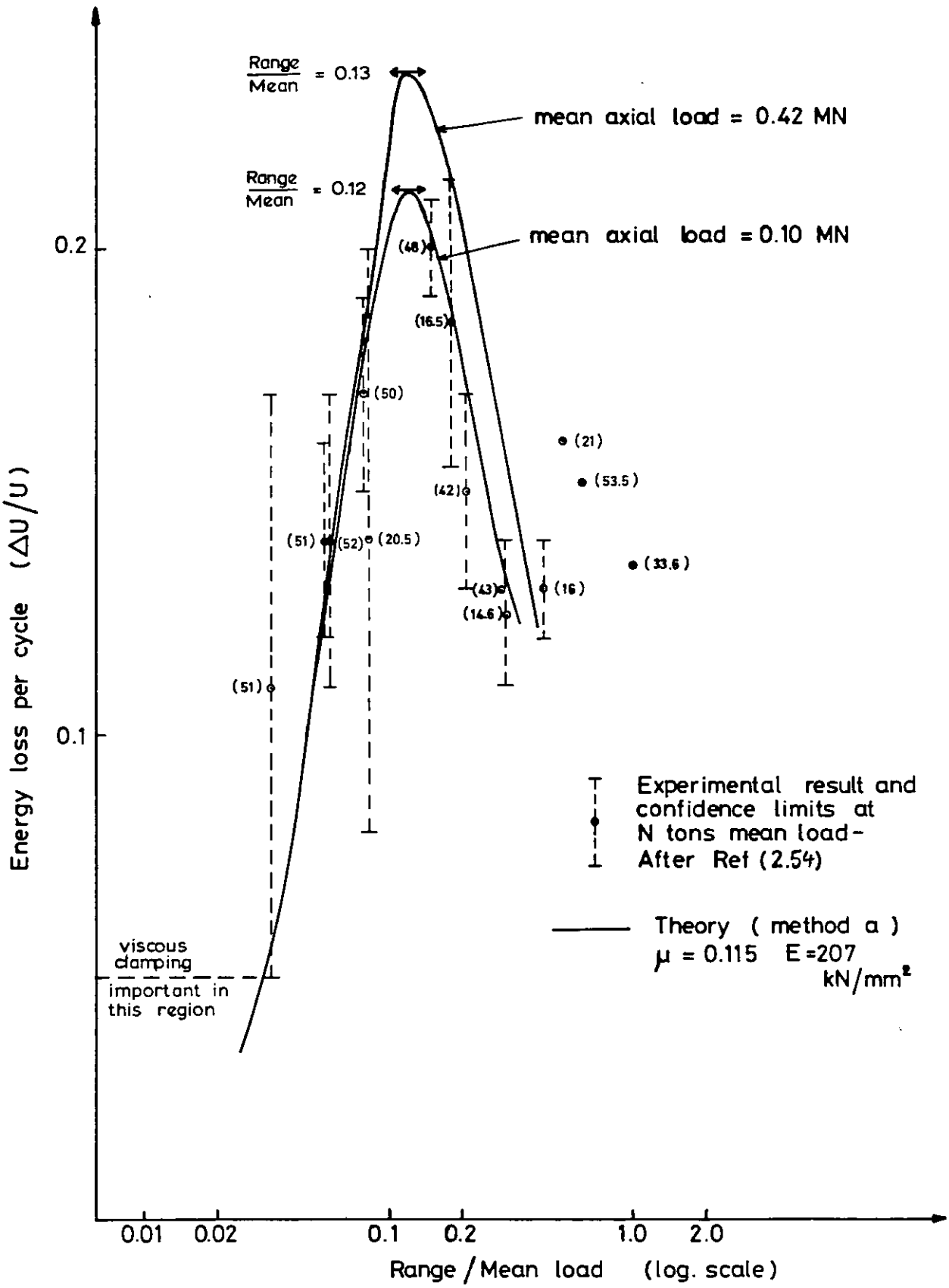

Fig. (5.4) Strand axial energy dissipation for various mean axial loads on 39 mm O.D. strand

$\varepsilon_c = 970 \times 10^{-6}$

(zero ε_c at 50 ton base load)

Near the termination

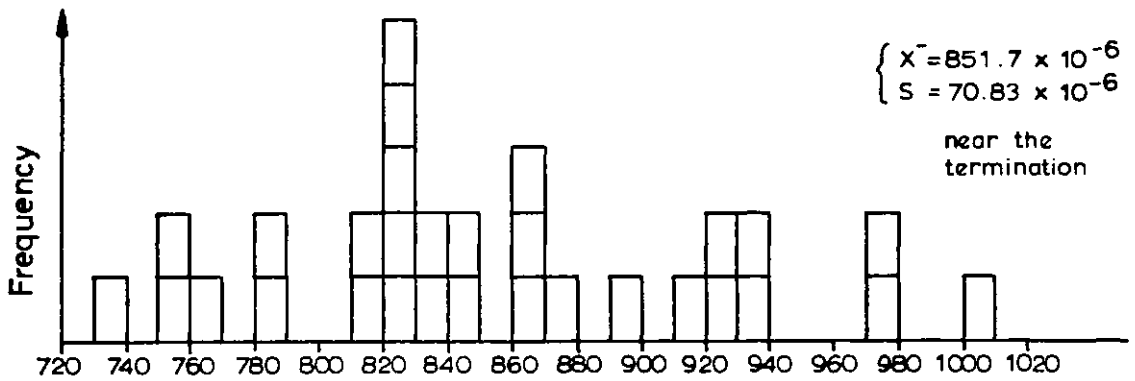

Away from the termination

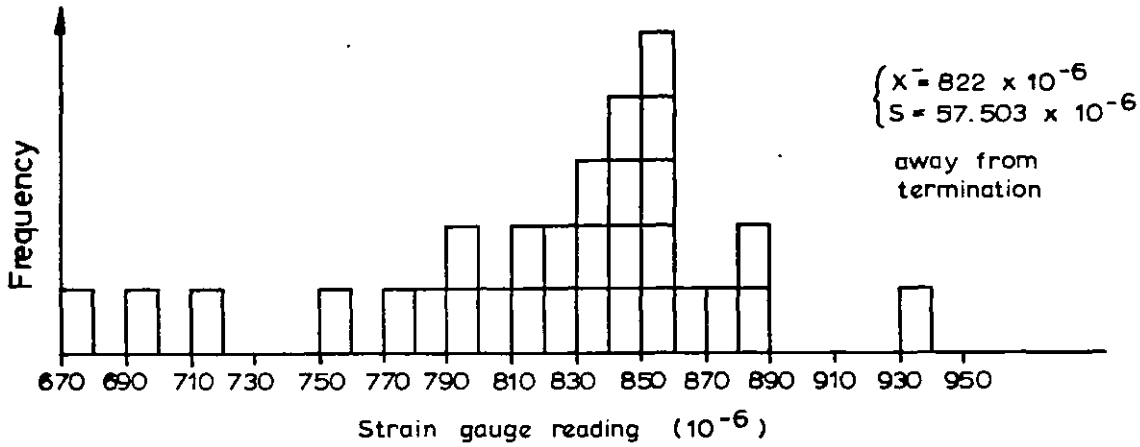

Fig(5.5) Scatter in the strain gauge readings for the axial test with minimum load of 0.50 MN

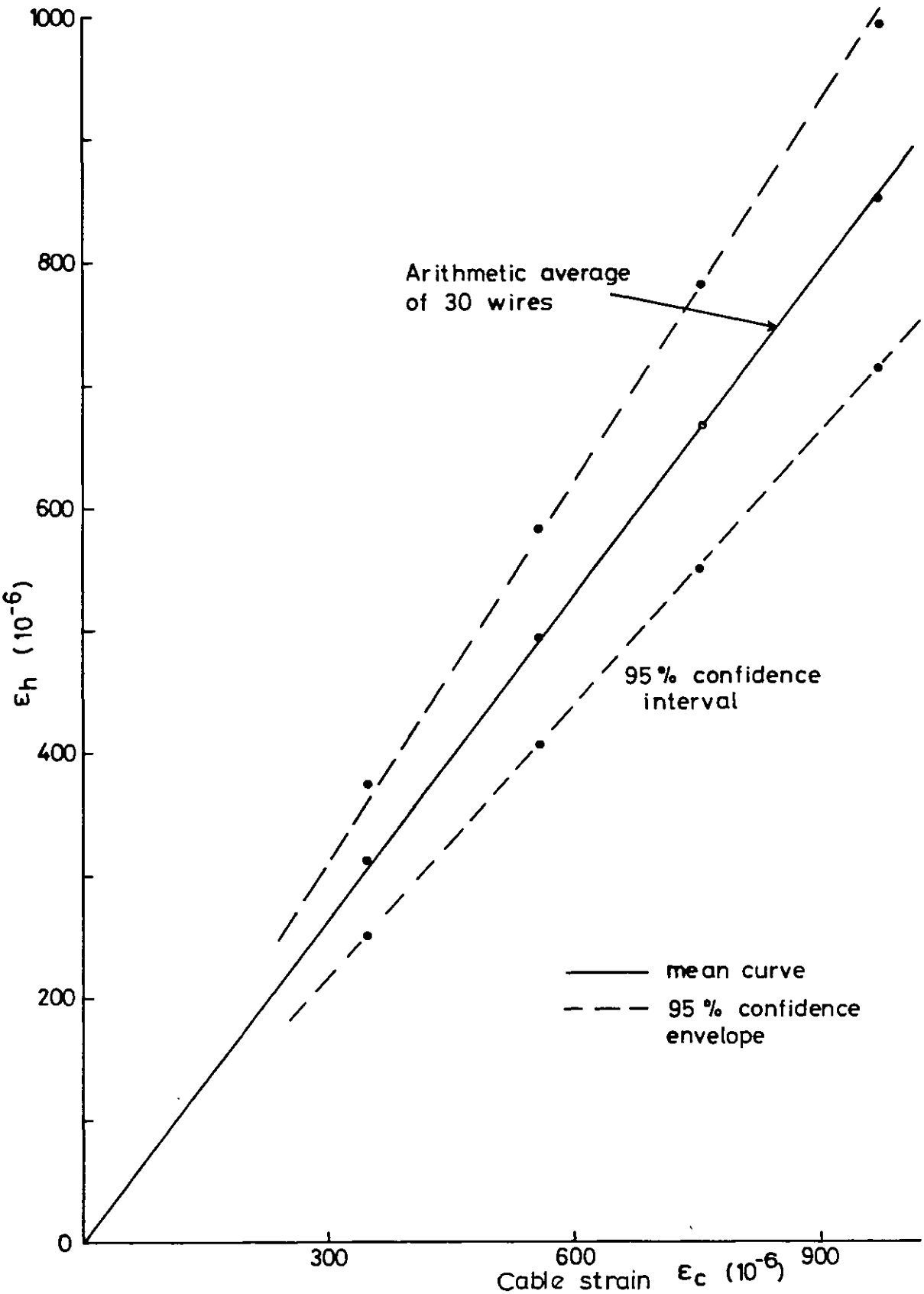

Fig (5.6) Strain gauge readings near the termination for the axial test (39 mm O.D. strand ; minimum load = 0.50 MN)

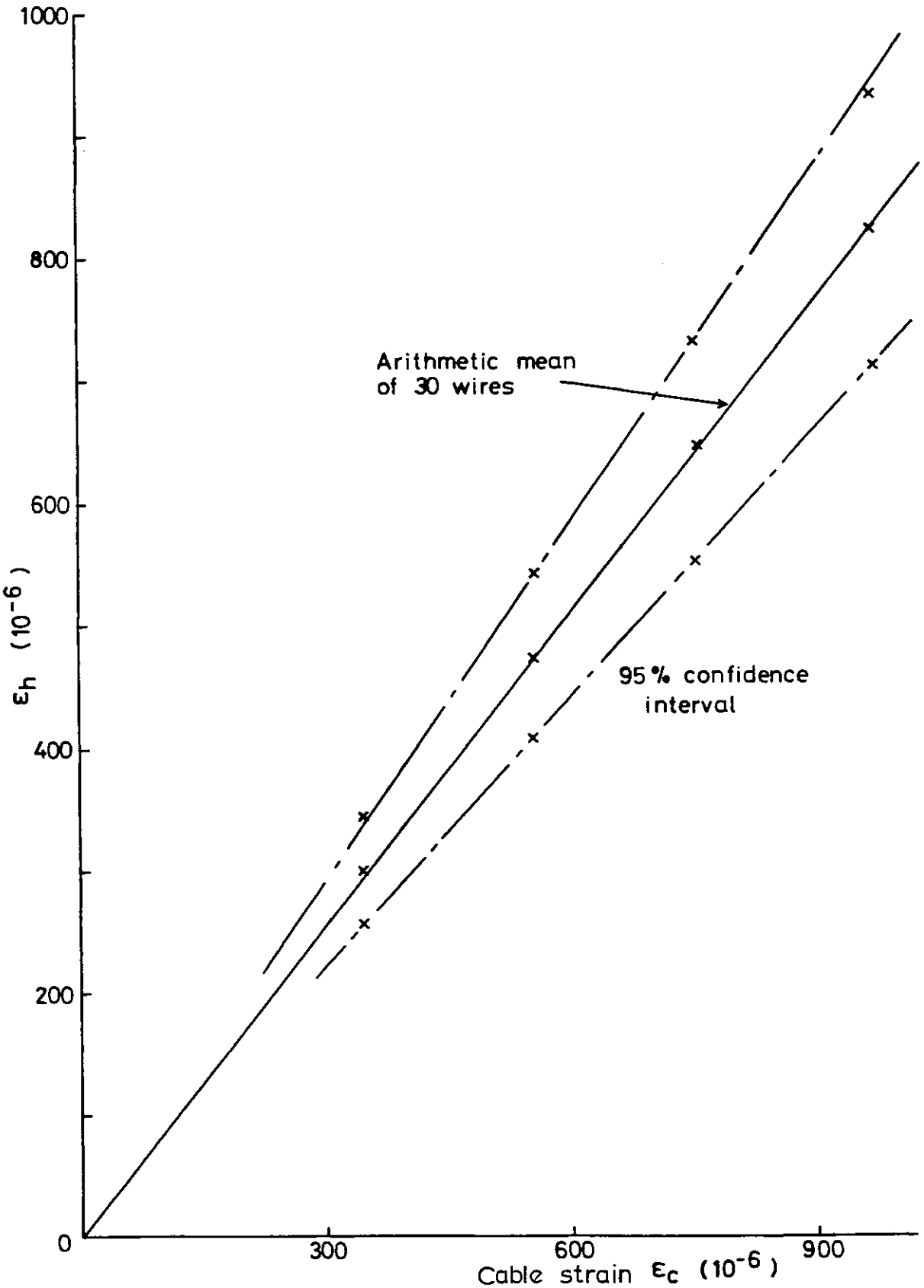

Fig(5.7) Strain gauge readings away from the termination for the axial test (39 mm O.D. strand ; minimum load = 0.50 MN)

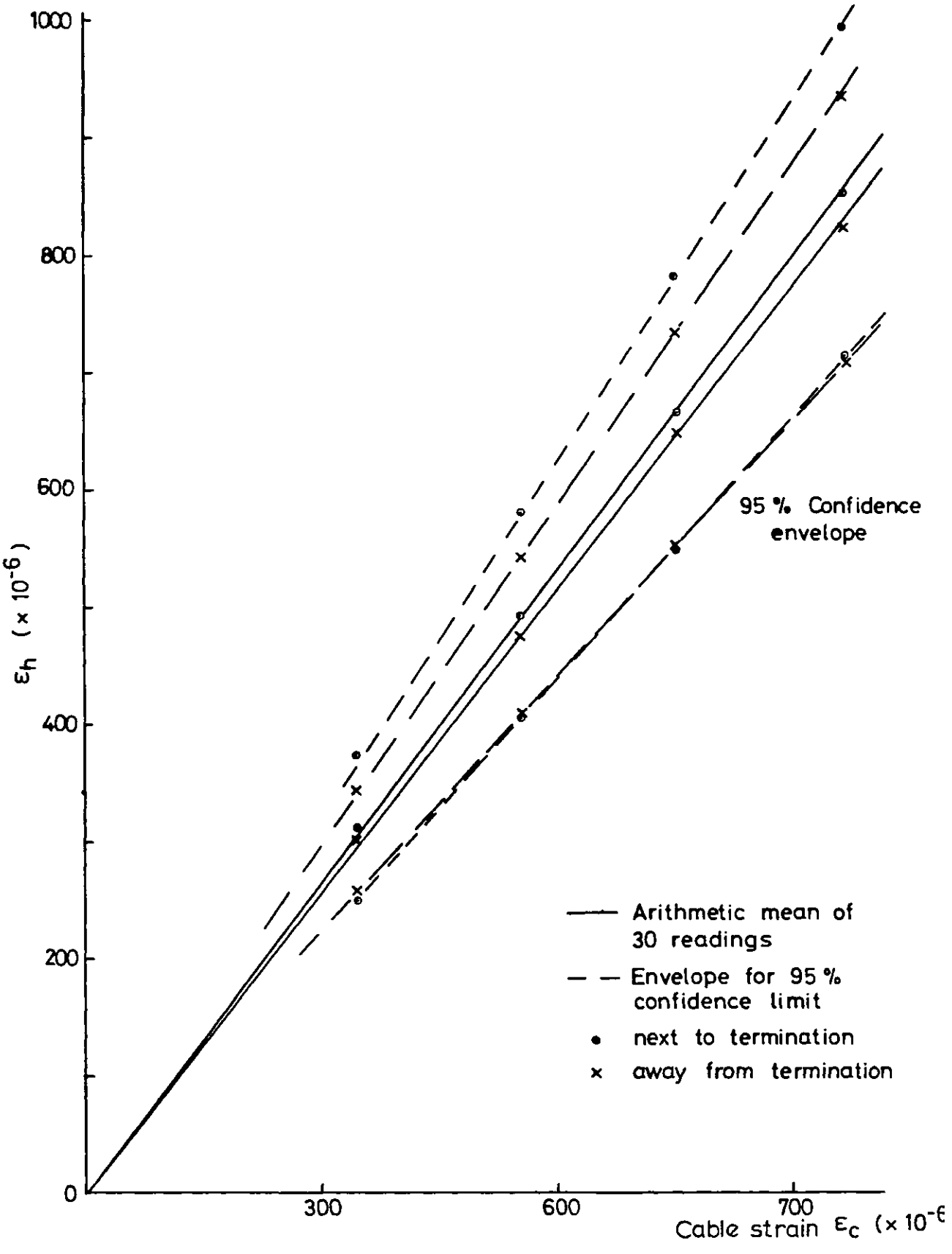

Fig (5.8) Comparison of strain gauge readings near the termination with those away from the termination, for the axial case

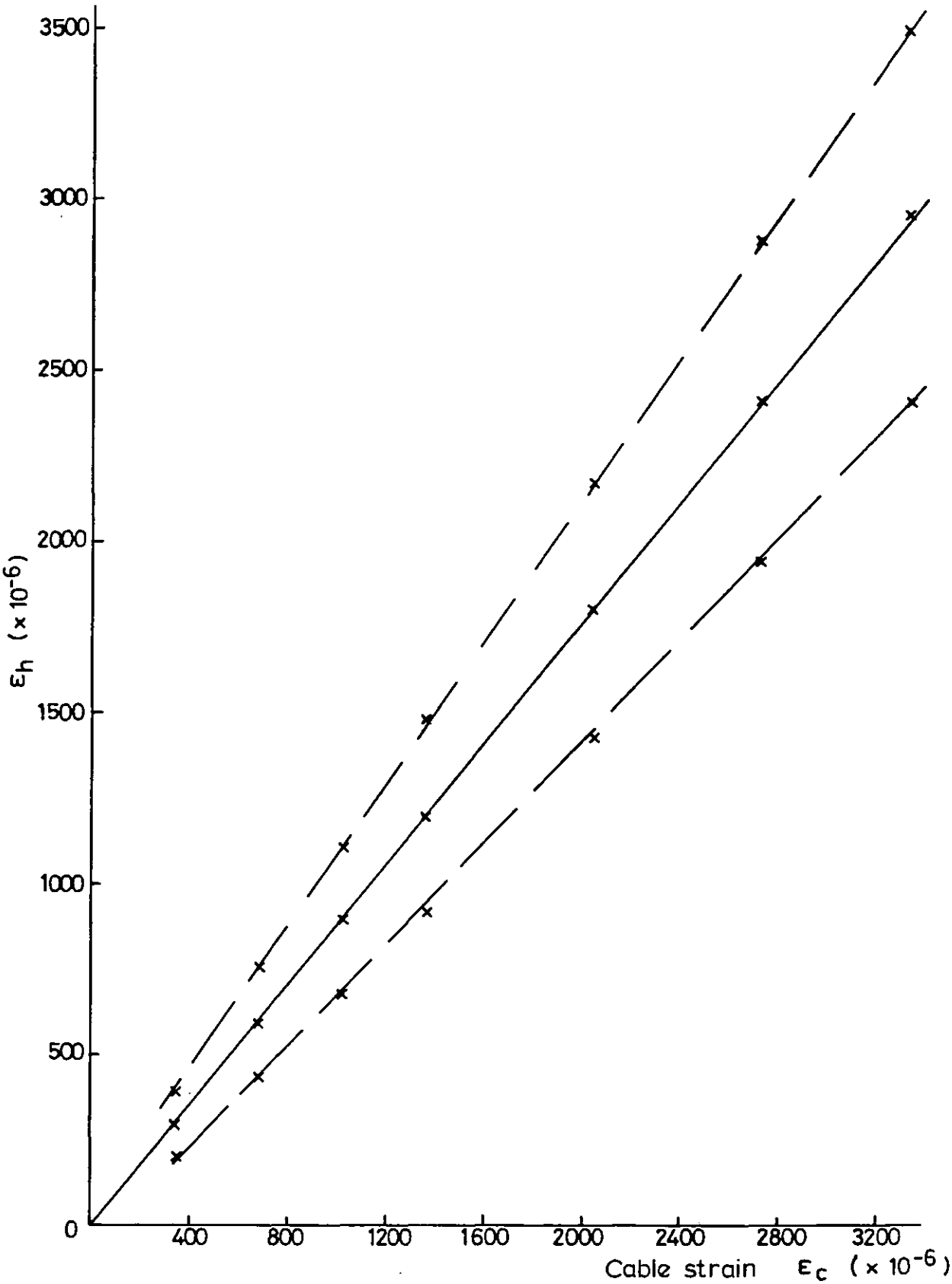

Fig(5.9) Strain gauge readings (for the axial case) away from the termination and with a base axial load of 0.15 MN

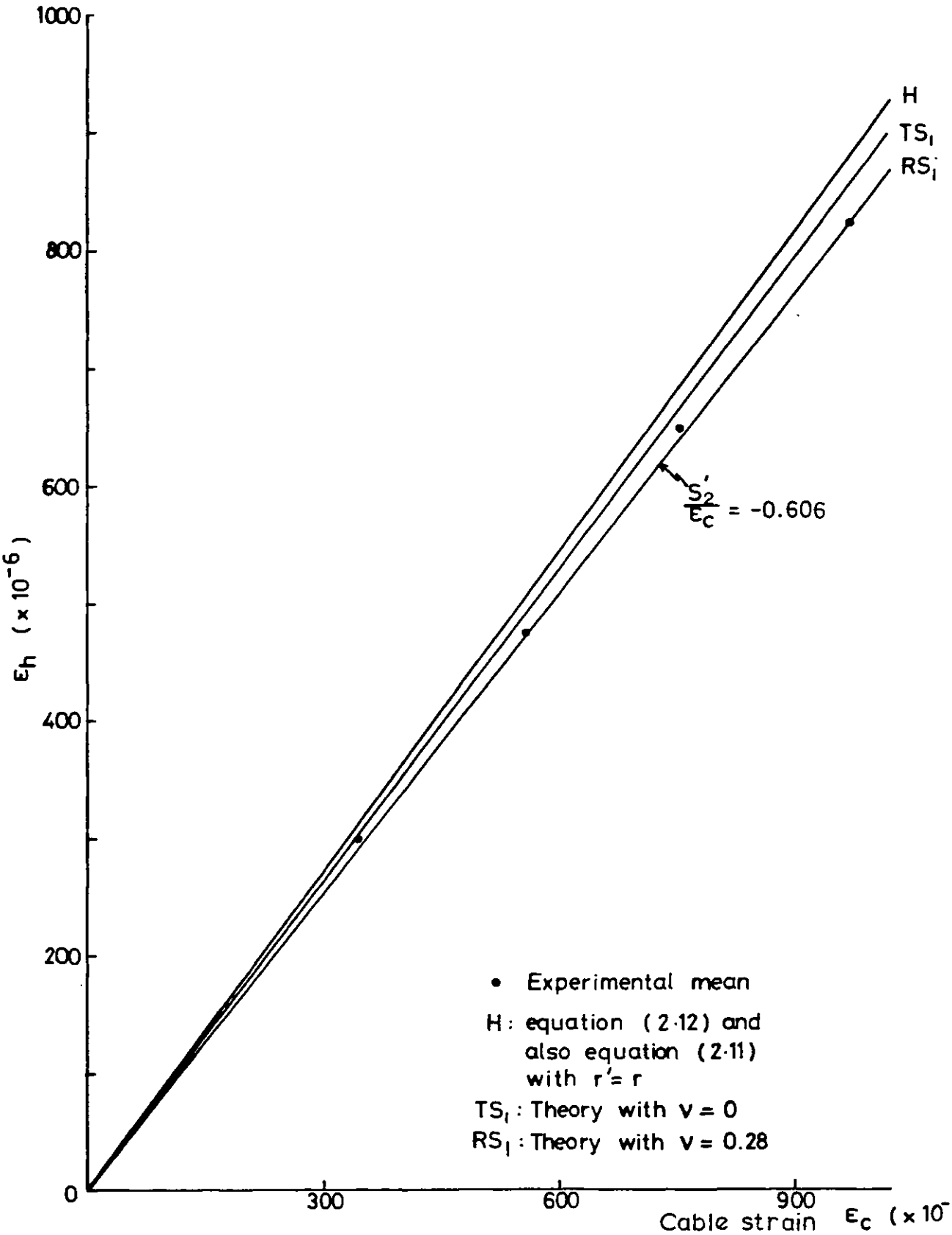

Fig (5.10) Comparison of the axial theory with arithmetic mean of experimental results away from the termination

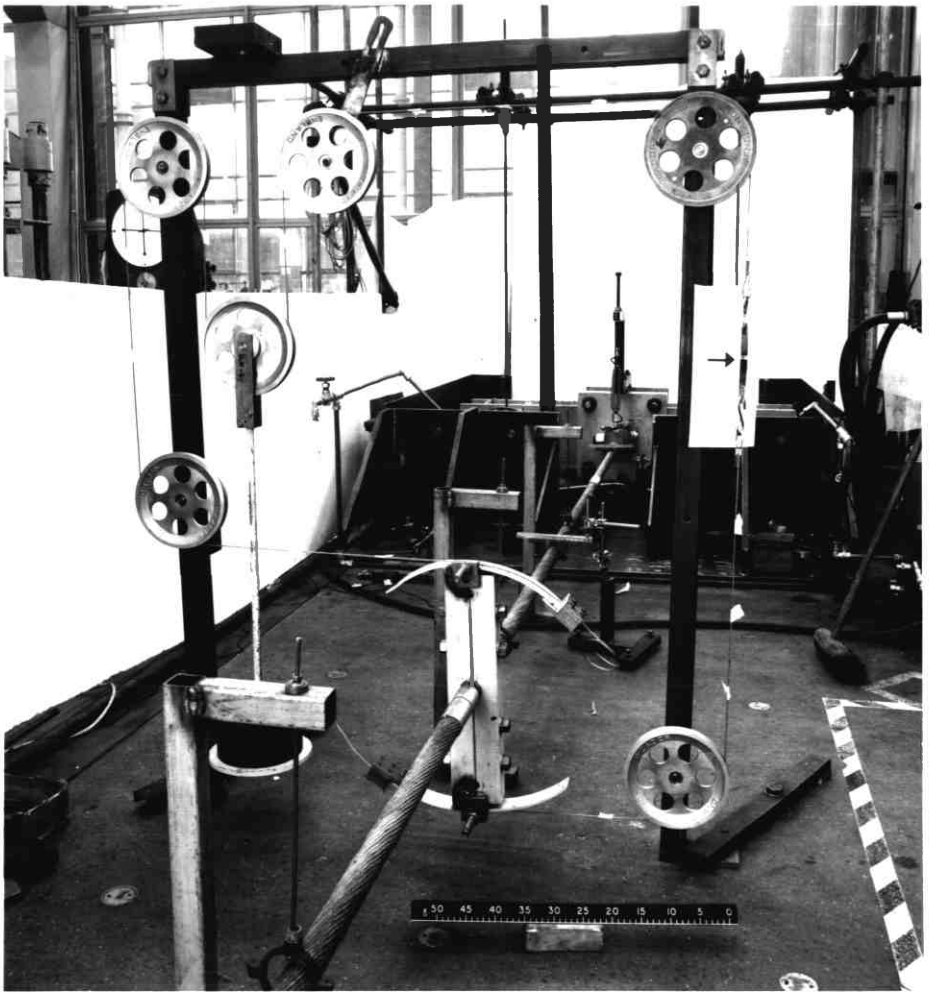

Fig. 5.11 A close view of the torsion frame including the soldered lap-joint (denoted by the arrow)

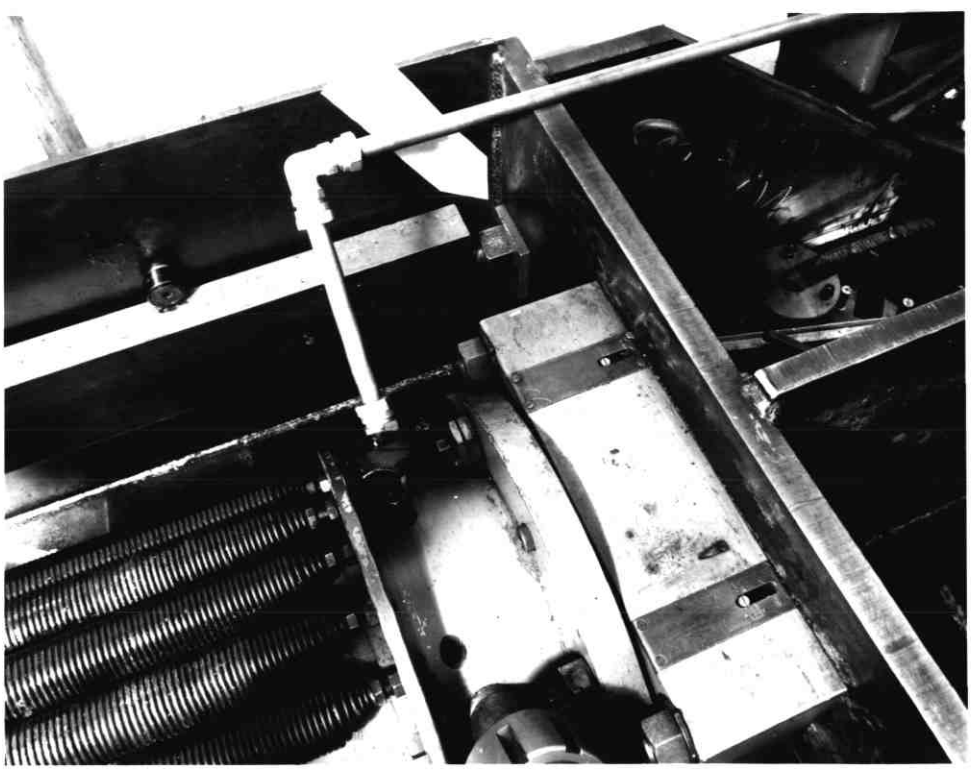

Fig. 5.12 Detail at the cross-head position where the cross-head is prestressed against the robust frame.

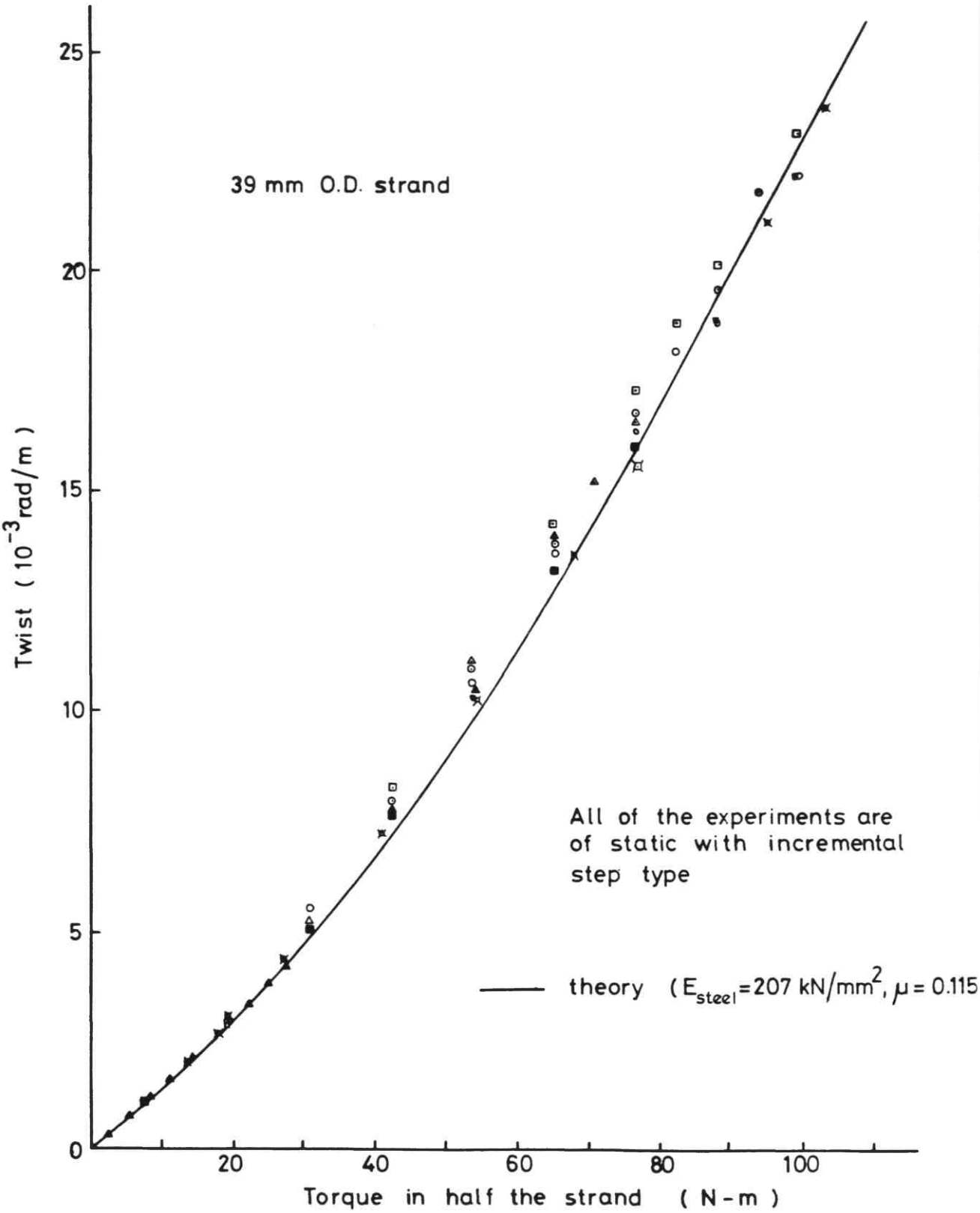

Fig (5.13) Experimental torque twist results with various degrees of axial - bedding , compared with theory (mean axial load = 0.414 MN)

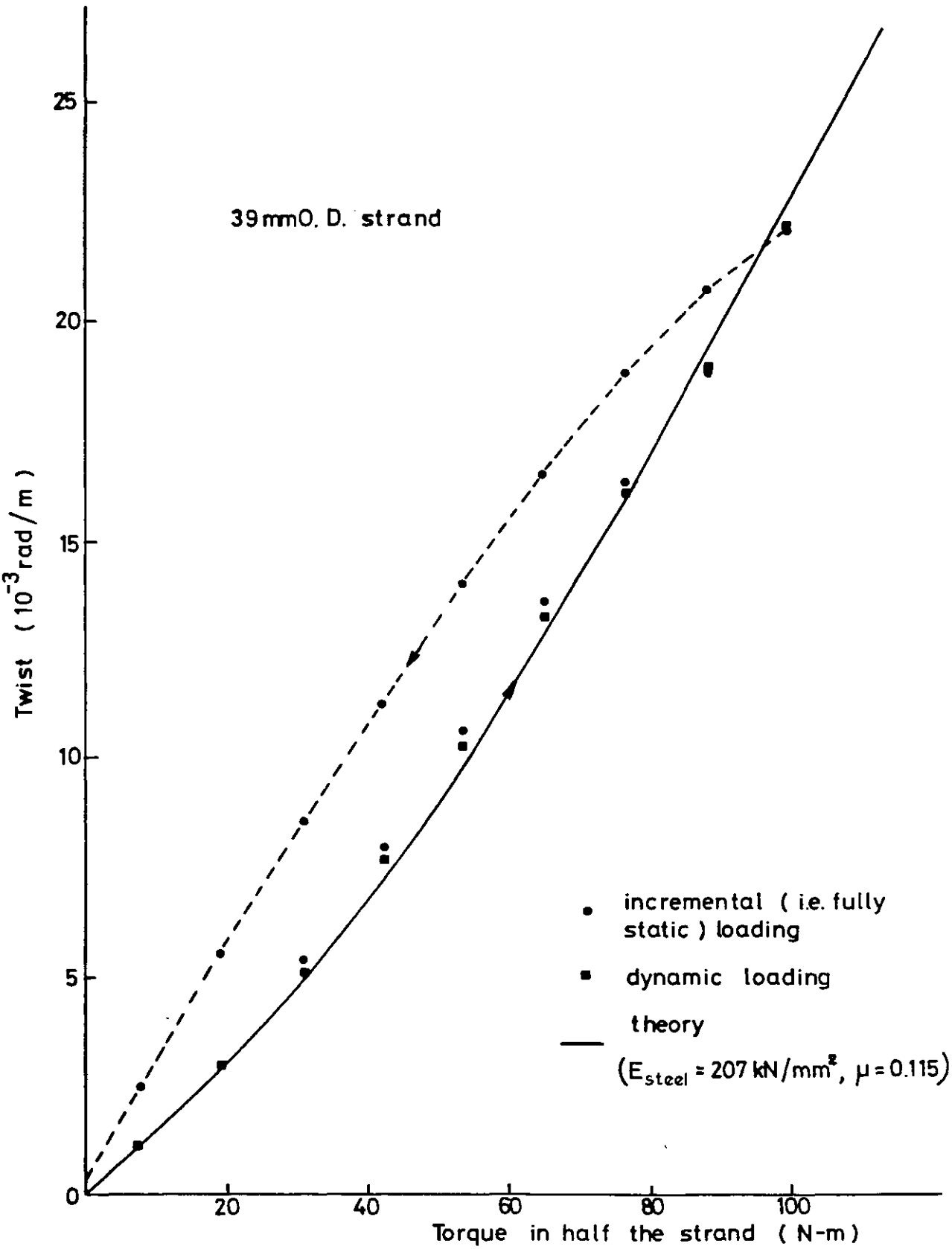

Fig (5.14) Torque – twist experiments compared with theory (mean axial load = 0.410 MN)

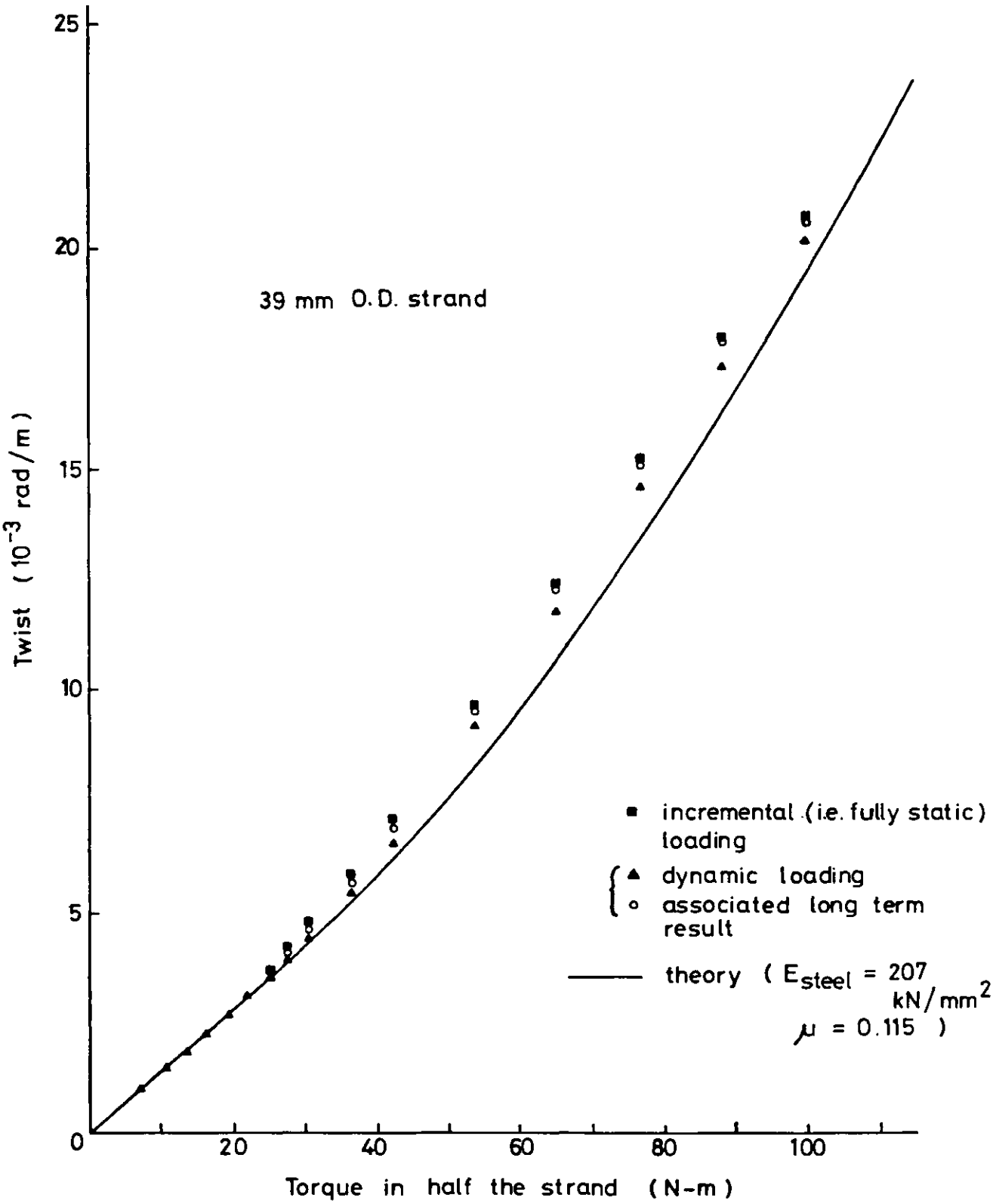

Fig (5.15) Experimental torque - twist results compared with theory (mean axial load = 0.590 MN)

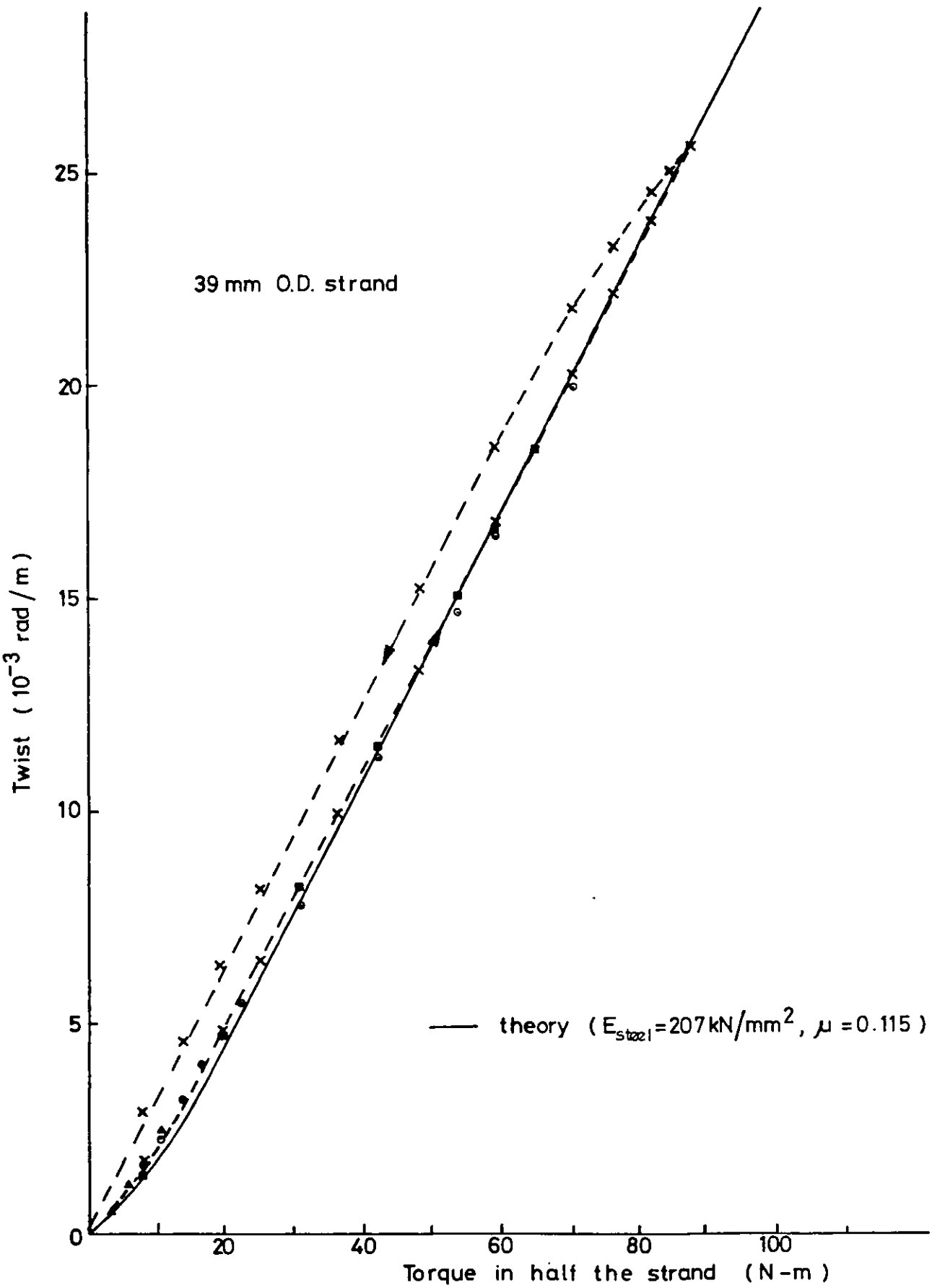

Fig(5.16)Static torque - twist experiments compared with theory
(mean axial load = 0.105 MN)

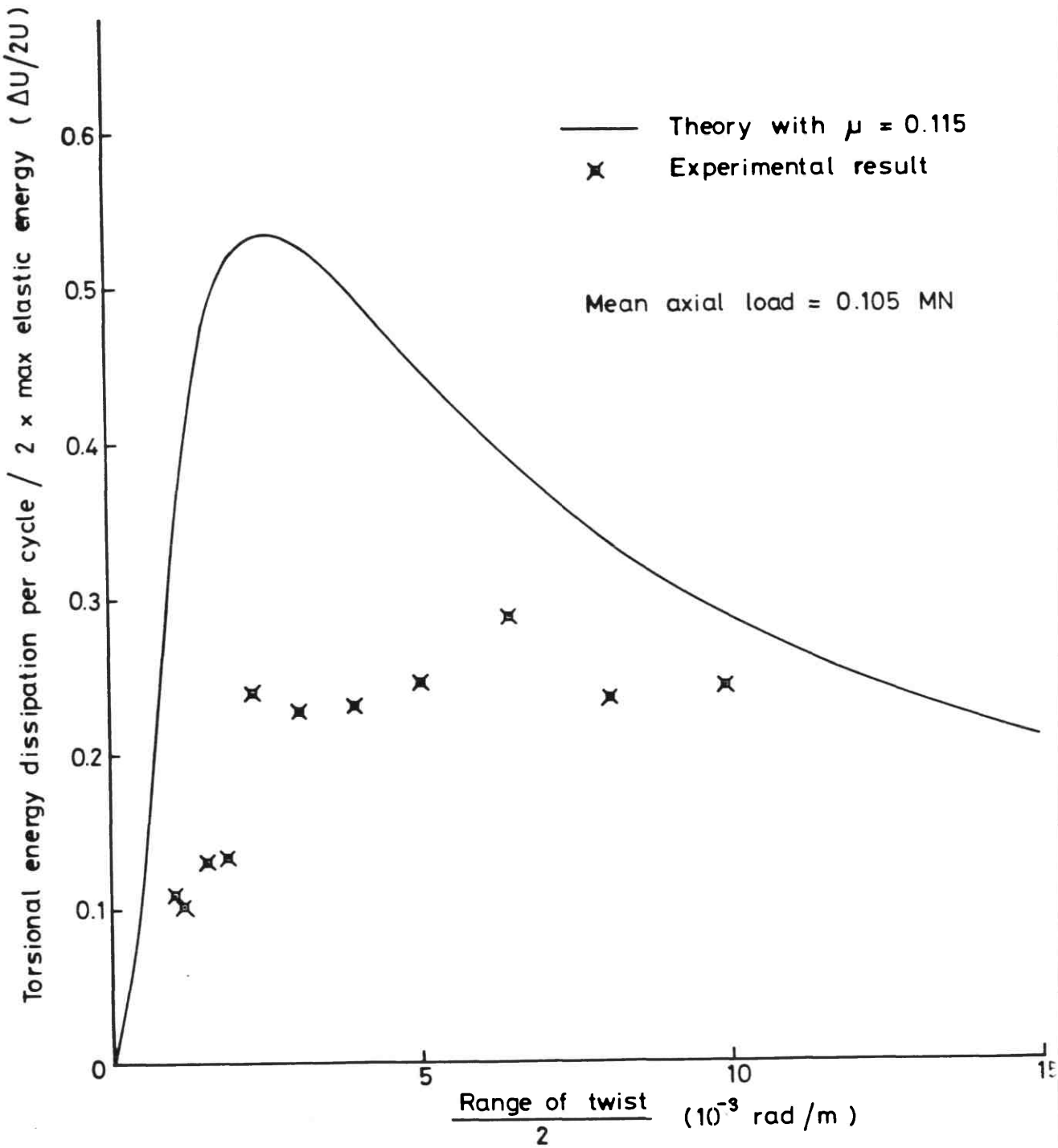

Fig (5.17) Comparison of theory and experiment for static torsional energy dissipation in 39 mm O.D. strand

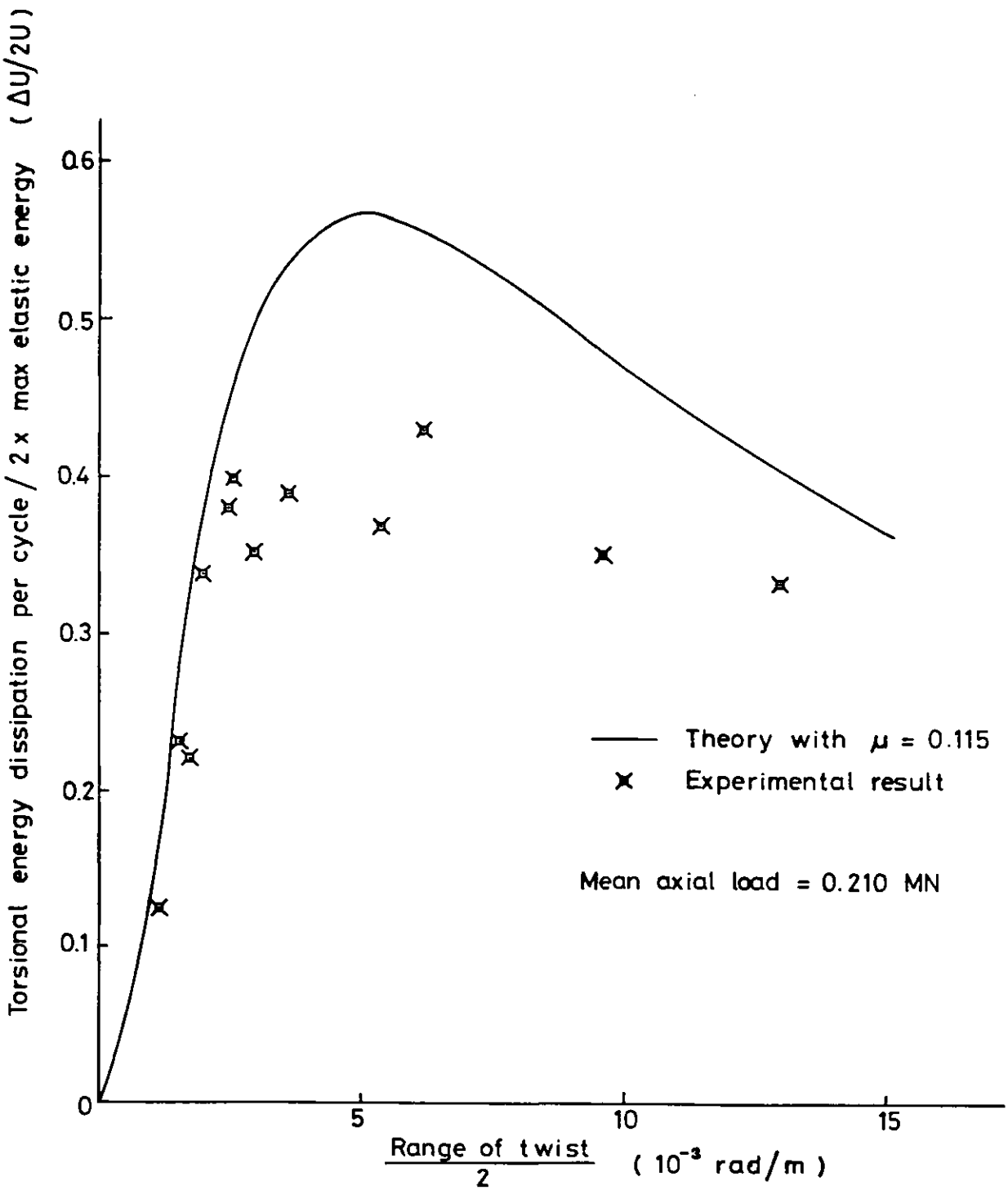

Fig(5.18) Comparison of theory and experiment for static torsional energy dissipation in 39 mm O.D. strand

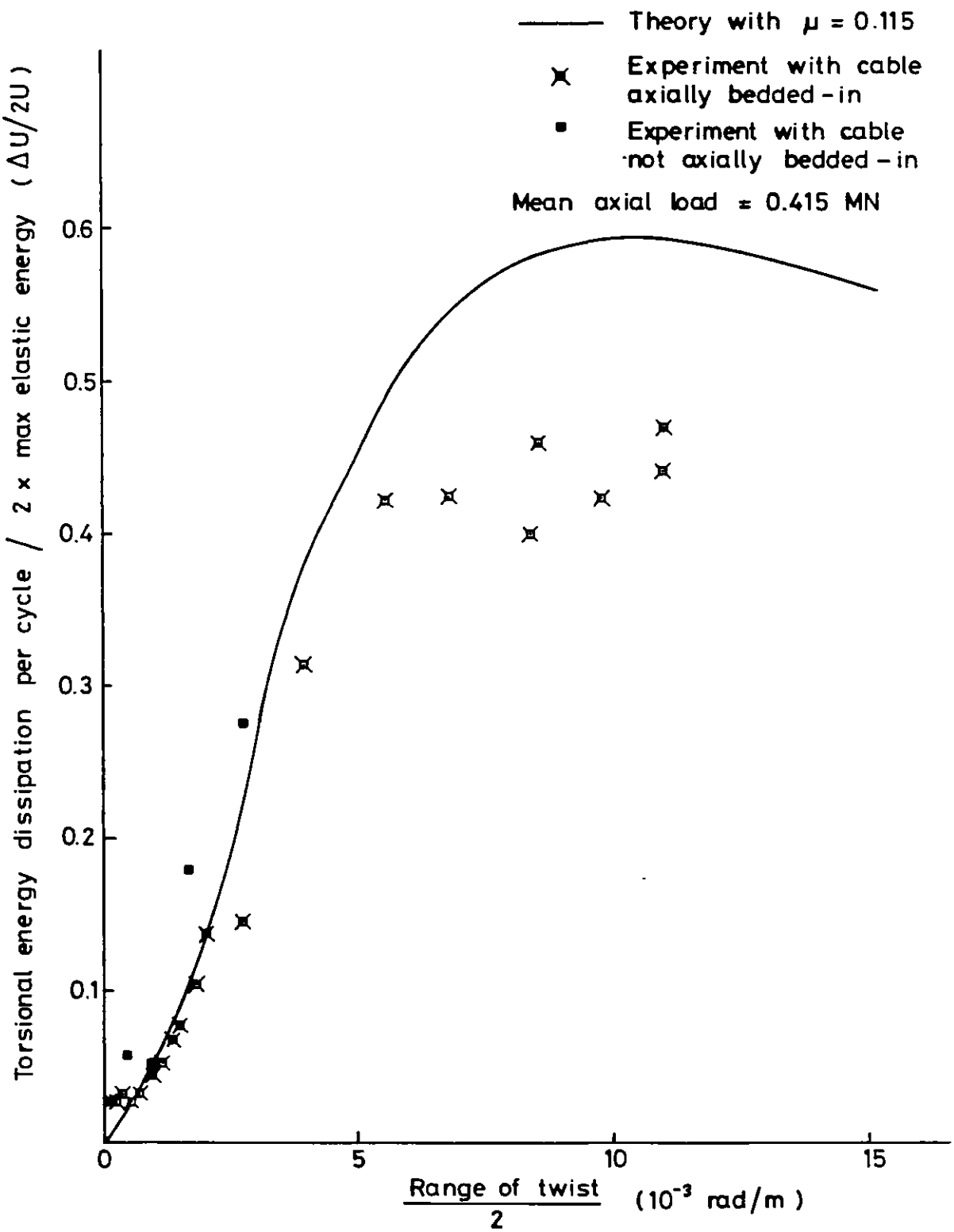

Fig (5.19) Comparison of theory and experiment for static torsional energy dissipation in 39 mm O.D. strand

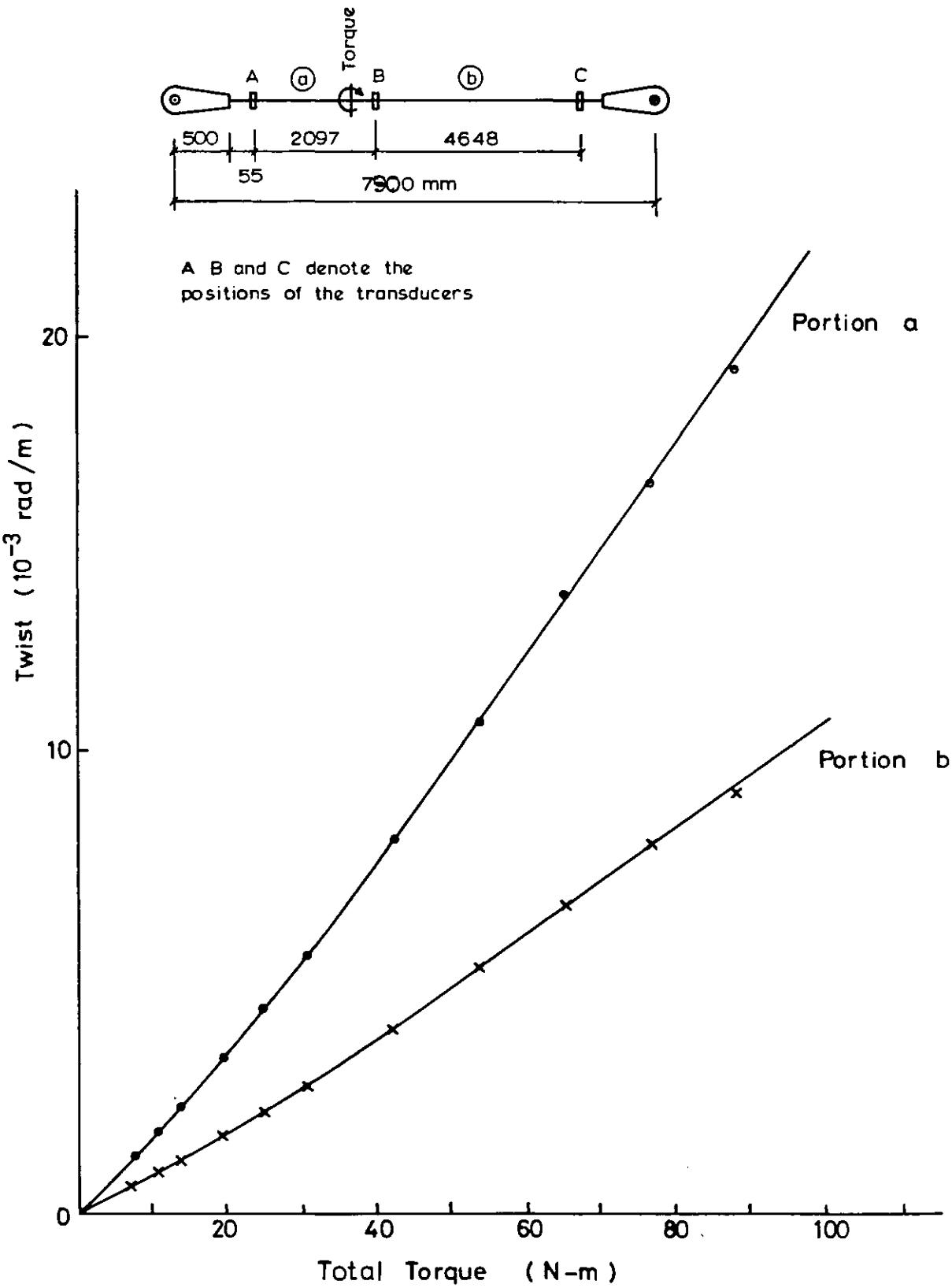

Fig (5.20) Torque – twist experimental results on the 39 mm O.D. strand with the external torque applied at the $^1/_3$ rd position (pin centre to pin centre)

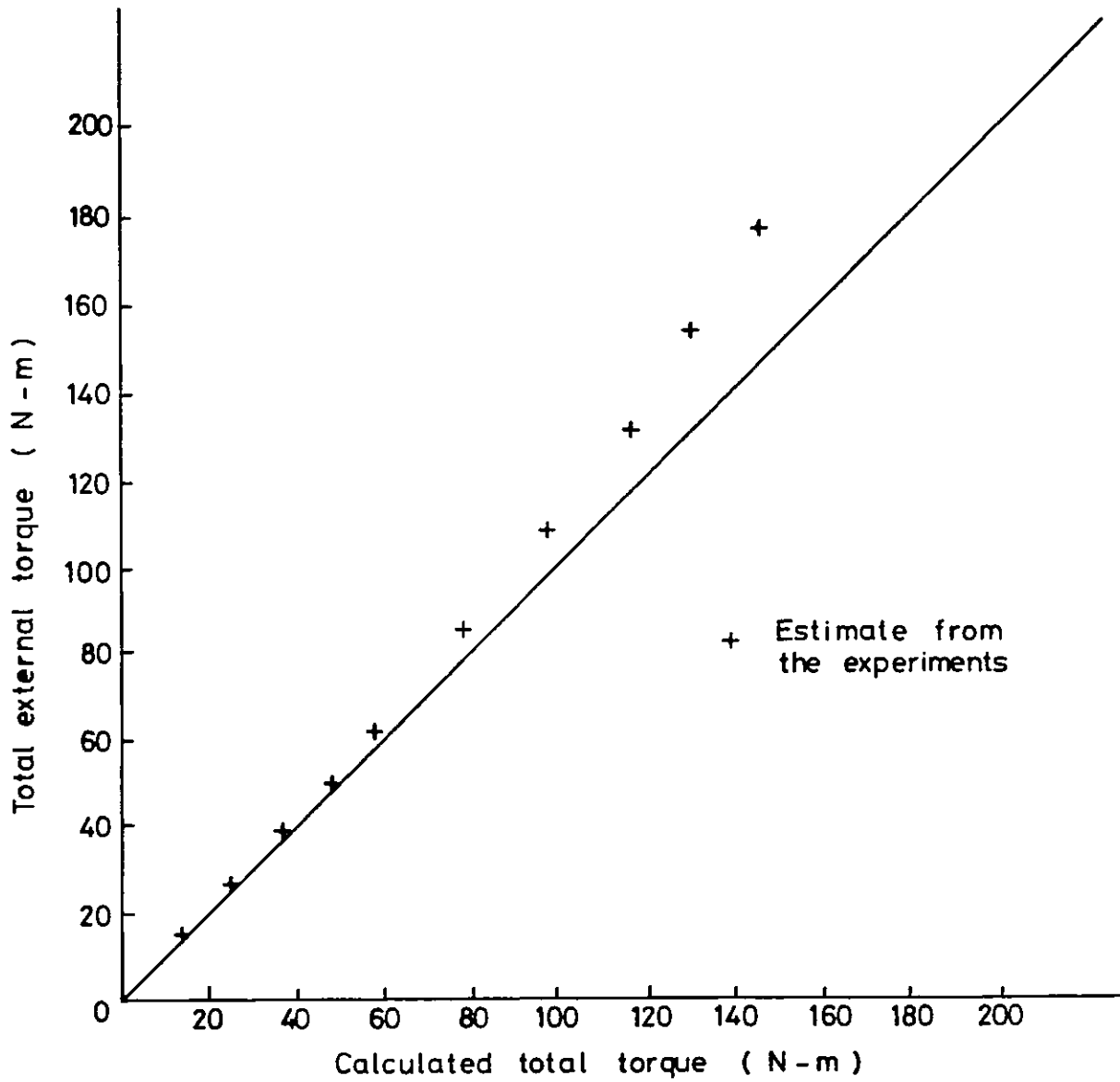

Fig. (5.21) Torque – twist result on the 39 mm O.D. strand with torque applied at the $^{1}/_{3}$ rd position

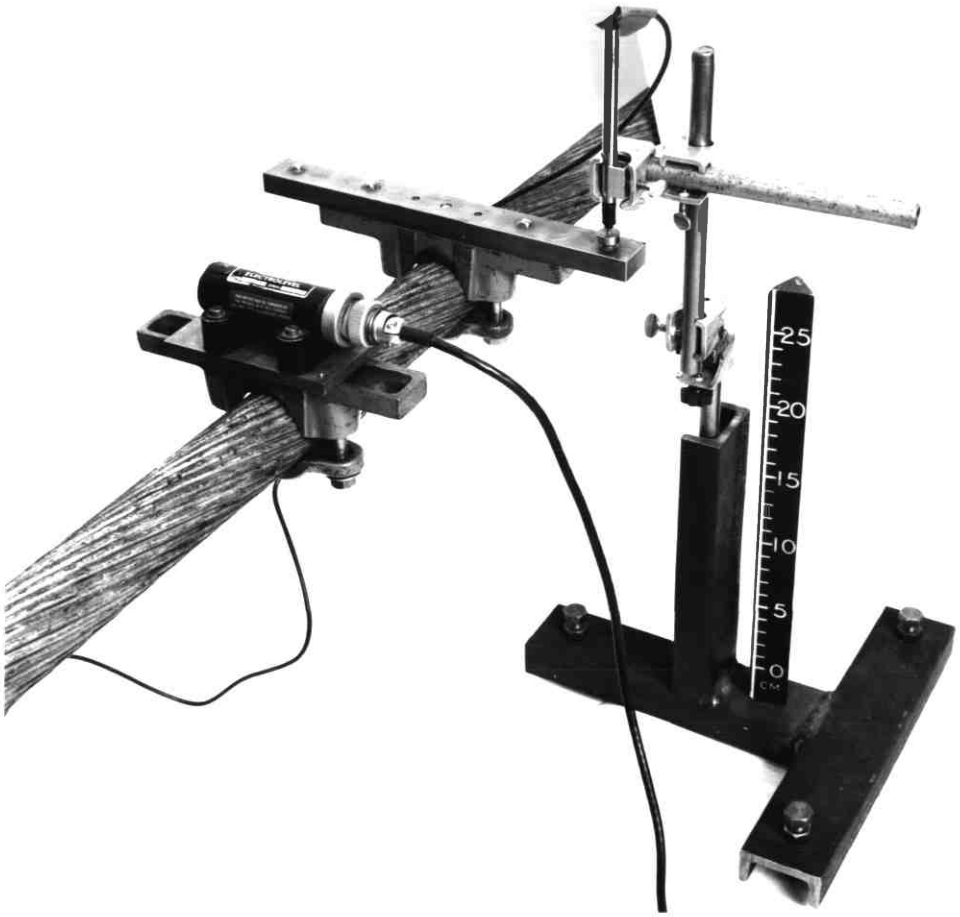

Fig. 5.22 Two alternative arrangements for measuring twist in the cable.

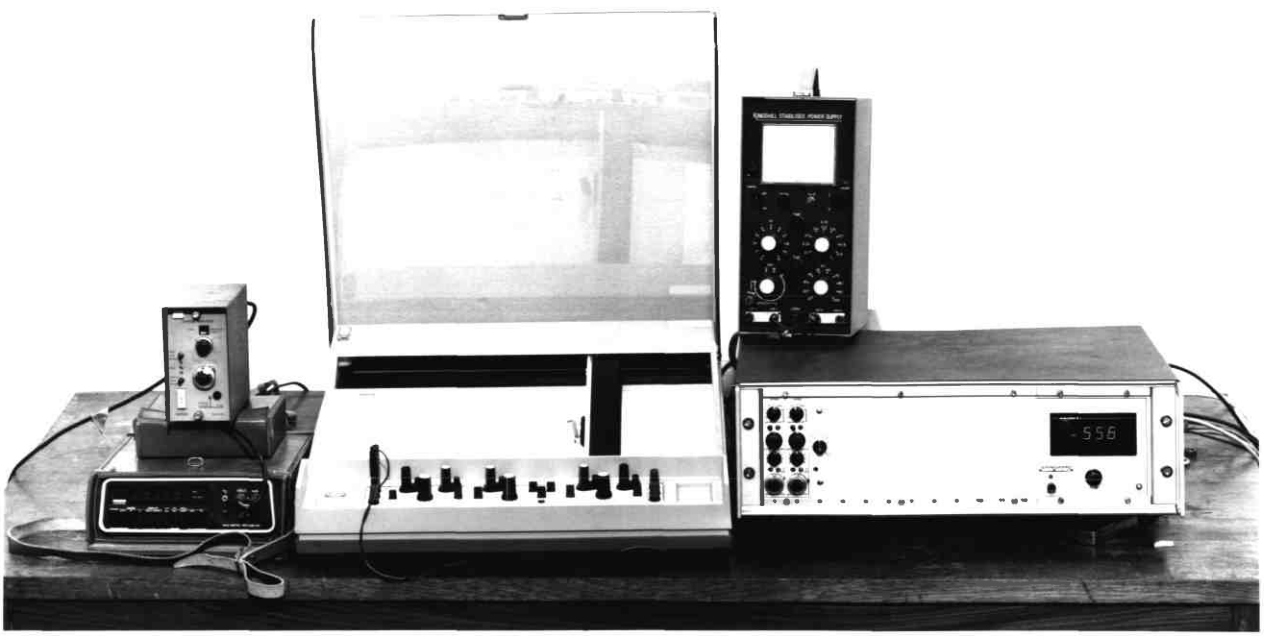

Fig. 5.23 Fast response x-y plotter with the load cell amplifier and digital voltmeter on the left, and the amplifier and function modules for displacement transducer signals, on the right.

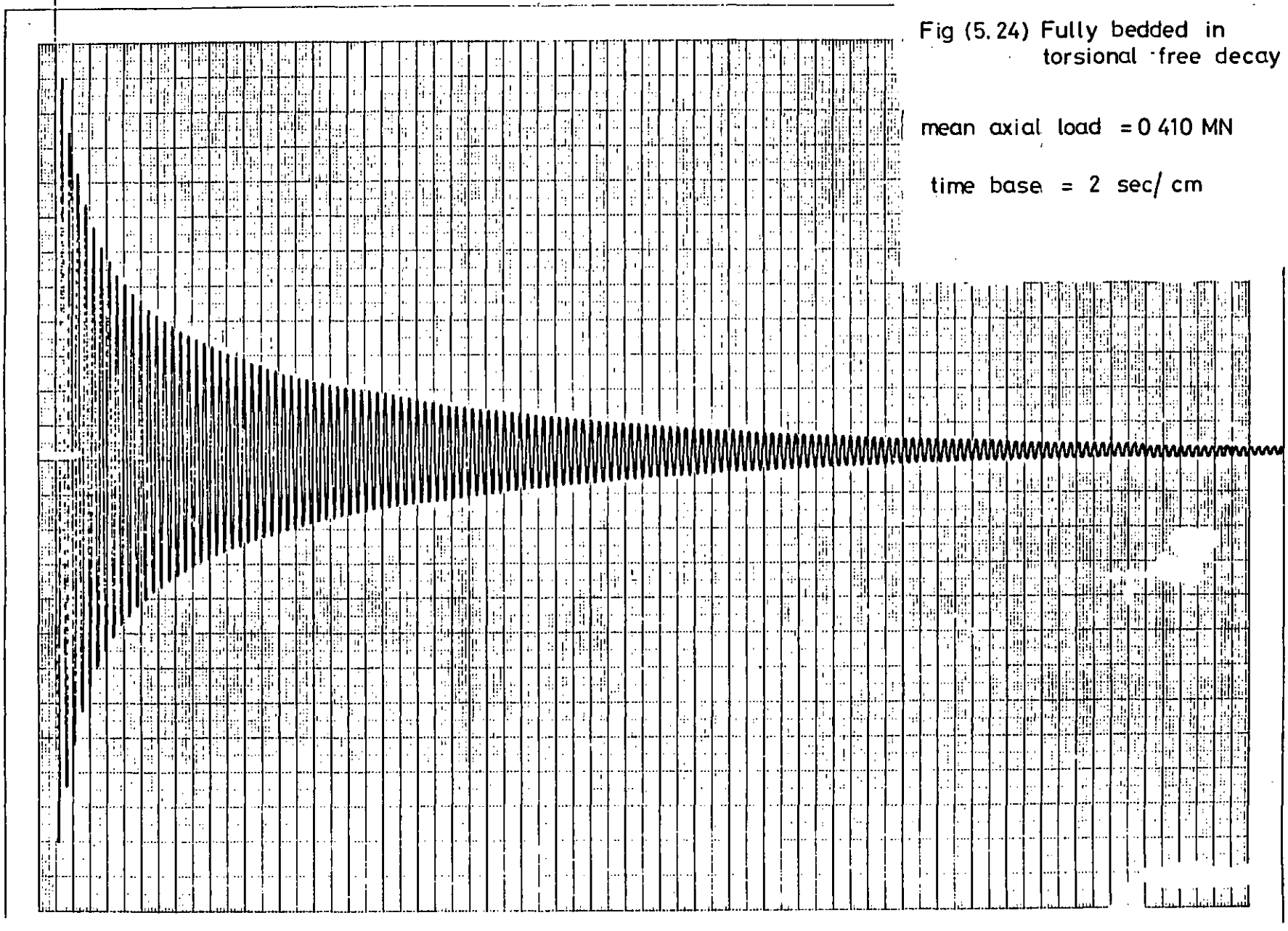

Fig (5.24) Fully bedded in torsional free decay

mean axial load = 0 410 MN

time base = 2 sec/ cm

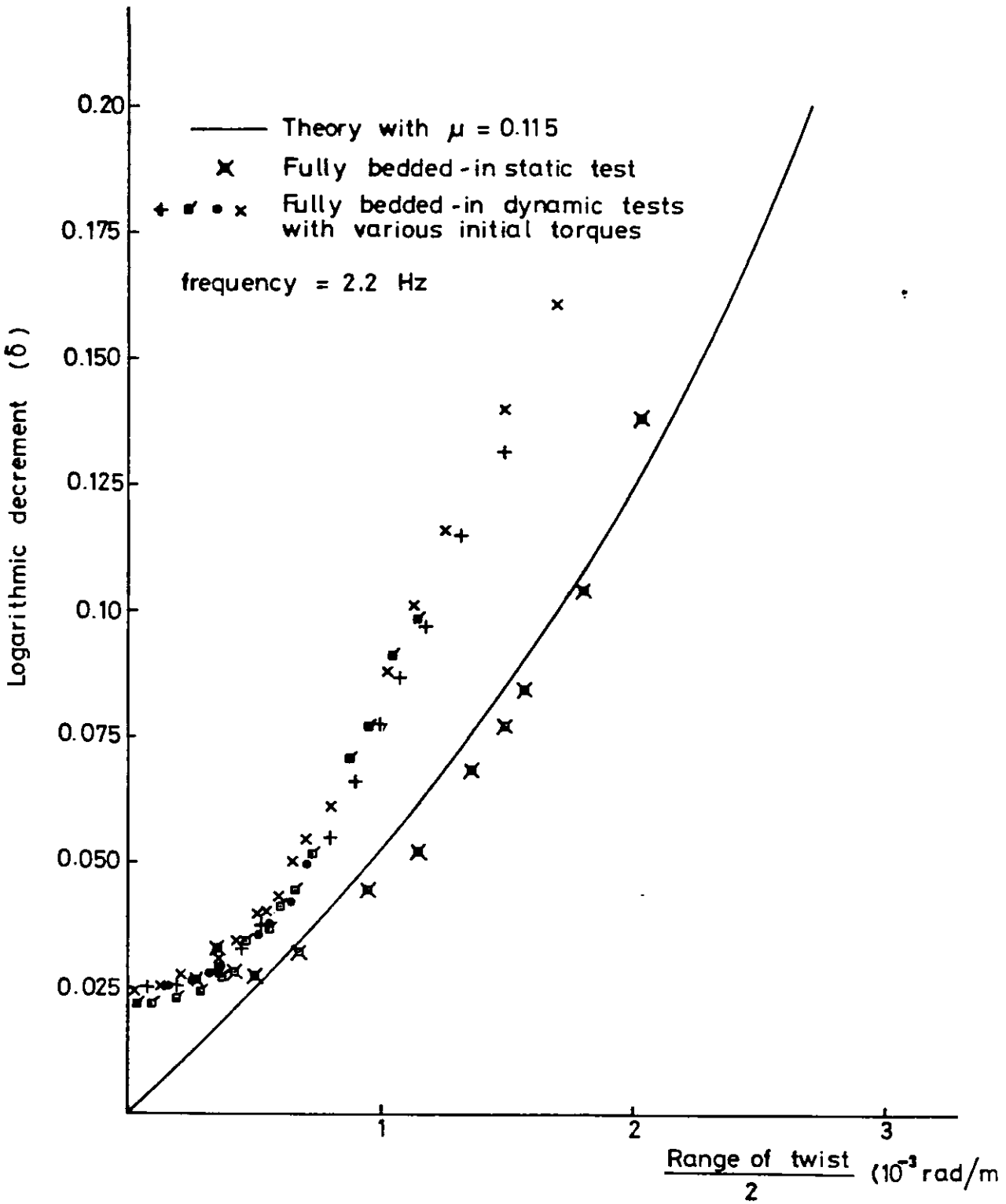

Fig(5.25)Plots of theoretical and experimental torsion log. dec. of the 39 mm O.D. strand , under mean axial load of 0.415 MN

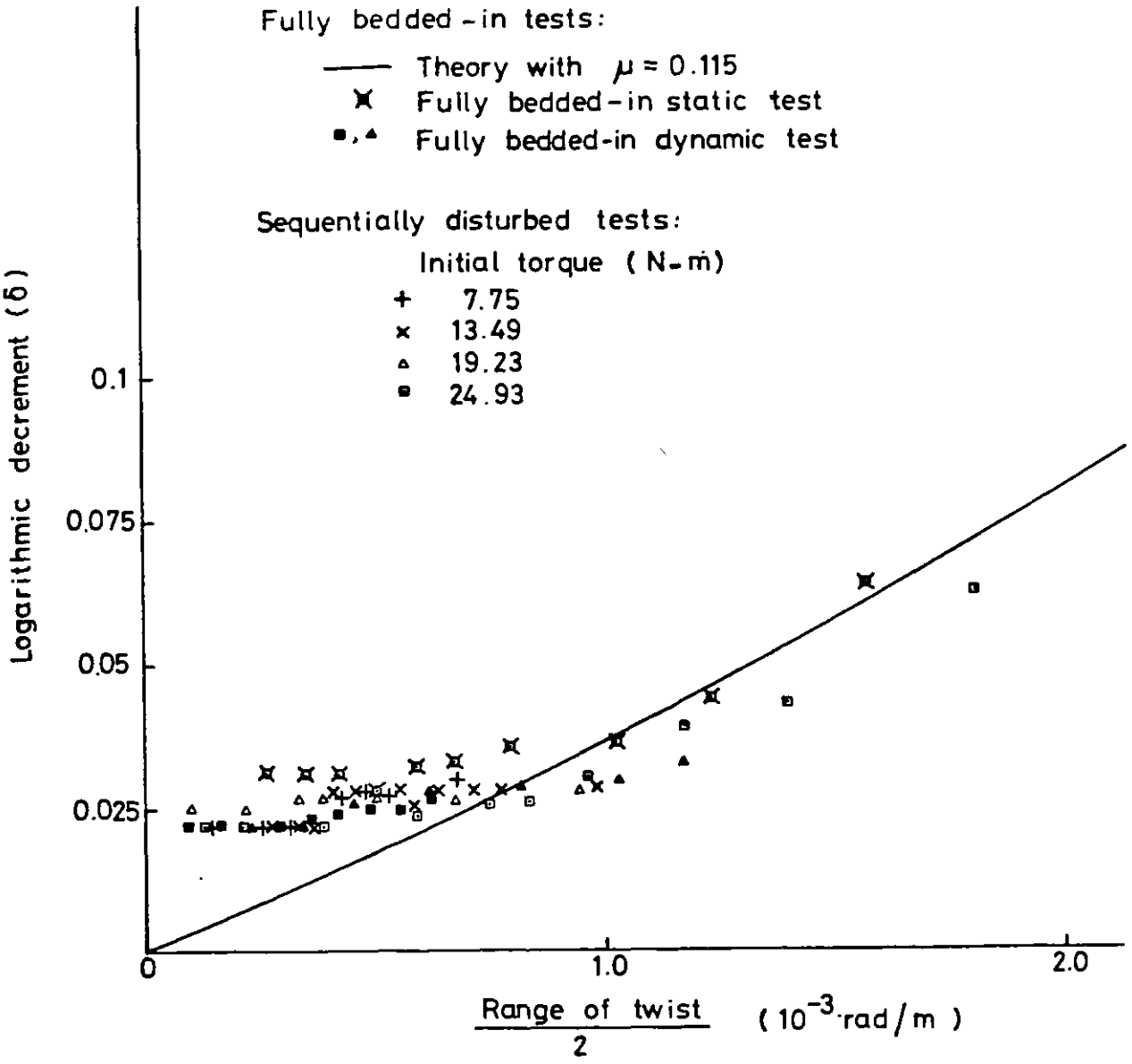

Fig (5.26) Plots of theoretical and experimental log. dec. of the 39 mm O.D. strand, under mean axial load of 0.590 MN

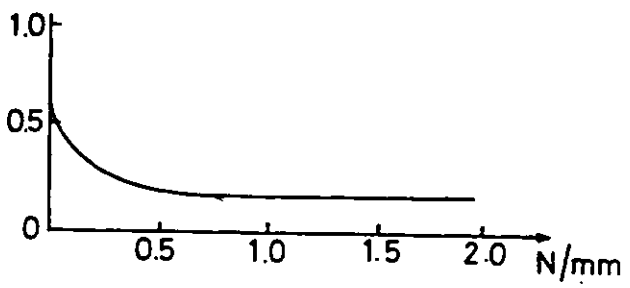

Fig (5 27) Coefficient friction versus linear pressure
After Ref. (5.2)

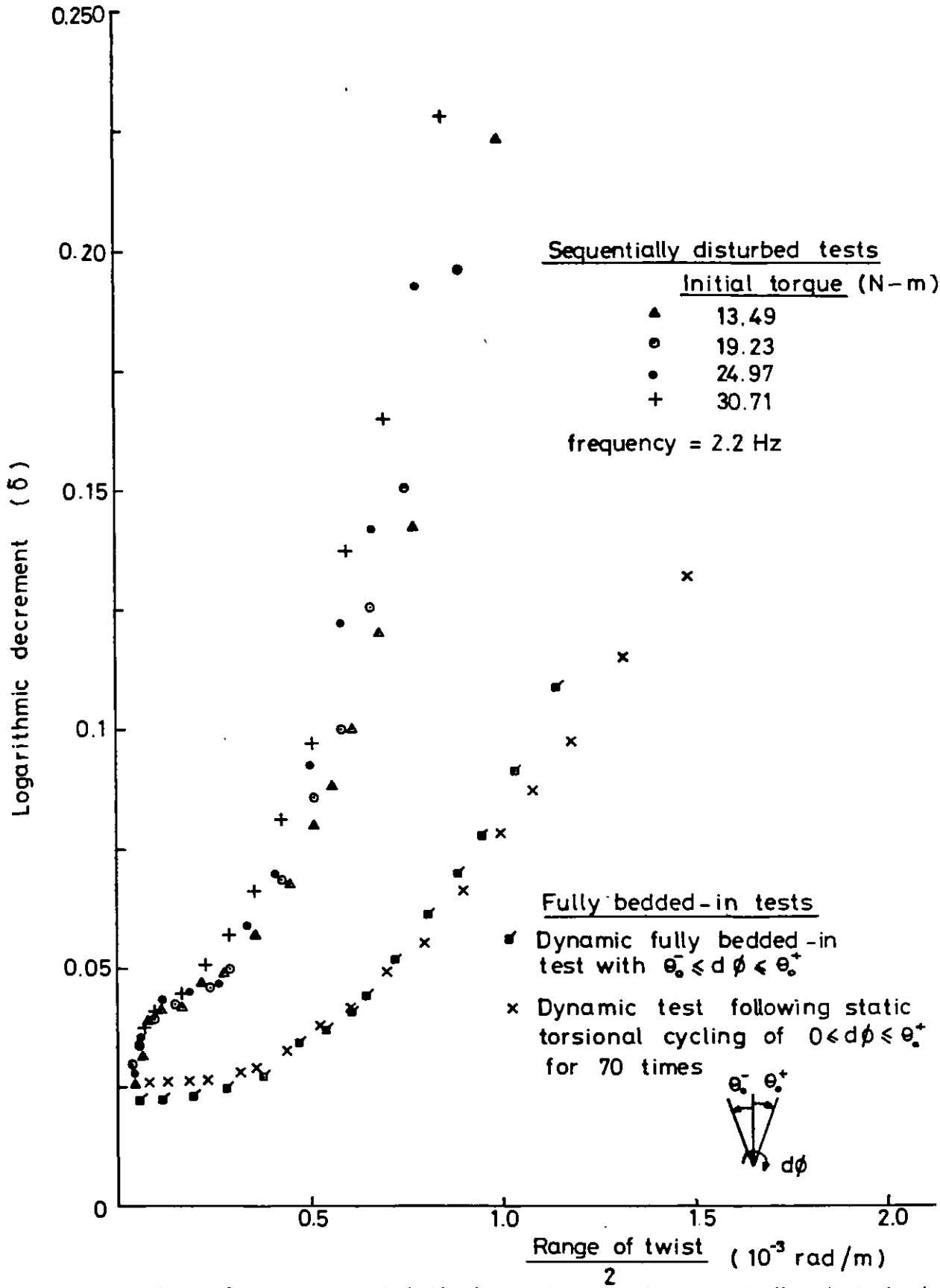

Fig (5.28) Comparison of fully bedded-in and sequentially disturbed dynamic torsion log.dec. for 39 mm OD strand, under mean axial load of 0.415 MN

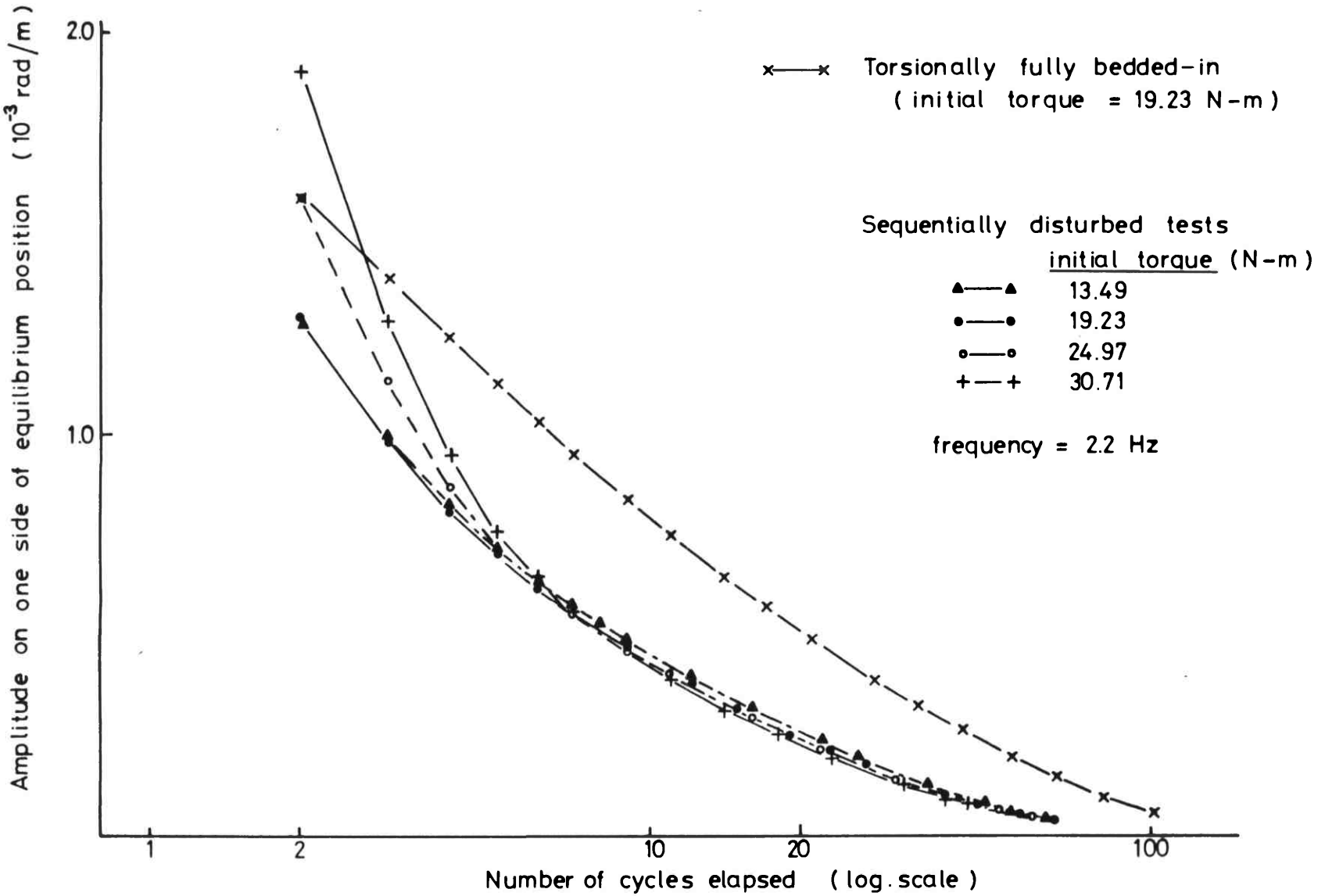

Fig (5.29) Experimental plots of decay in amplitude versus number of cycles for the 39 mm O D strand , under mean axial load of 0.415 MN

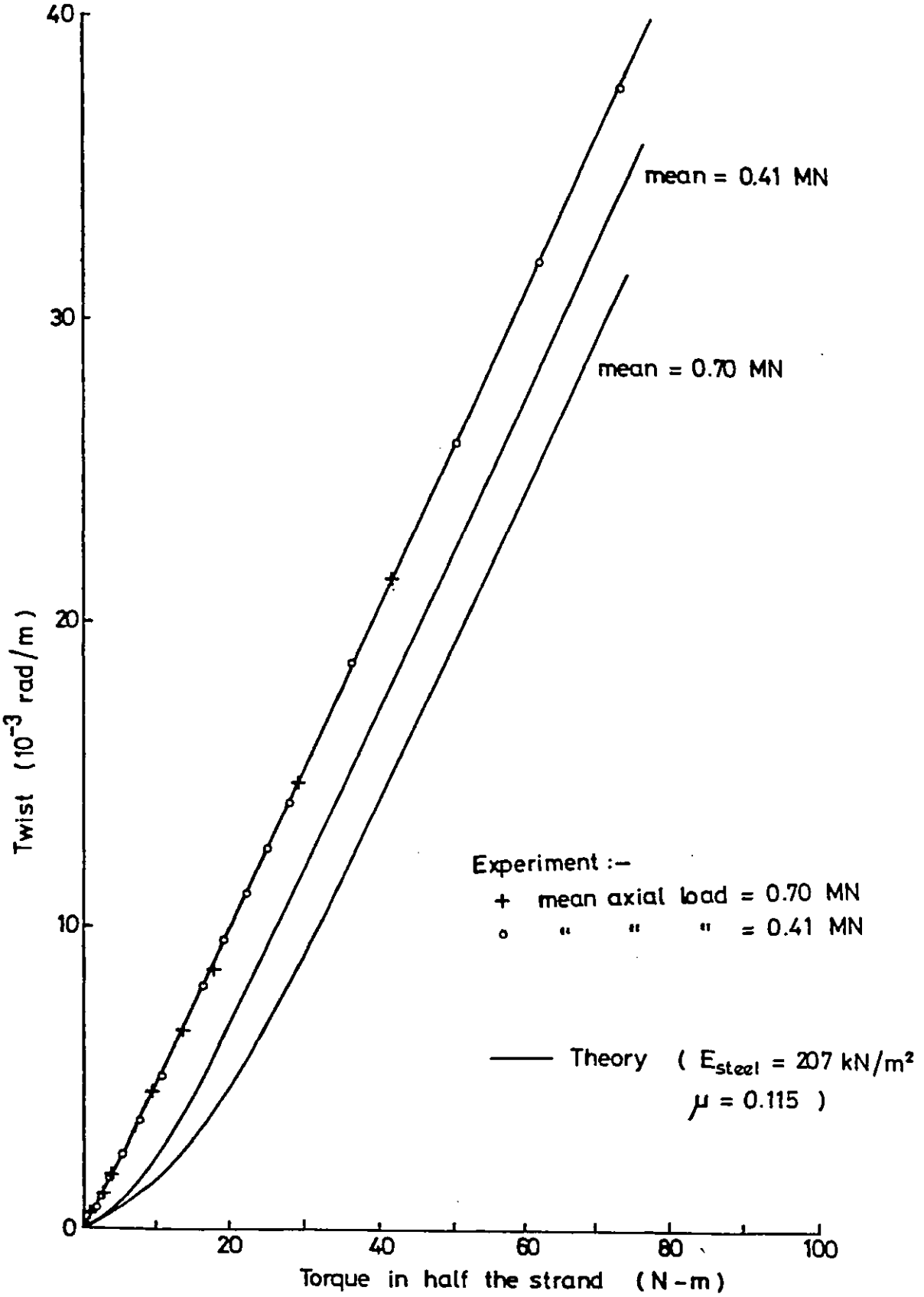

Fig (5.30) Comparison of experimental torque-twist results with theory for the new 41 mm O.D. strand

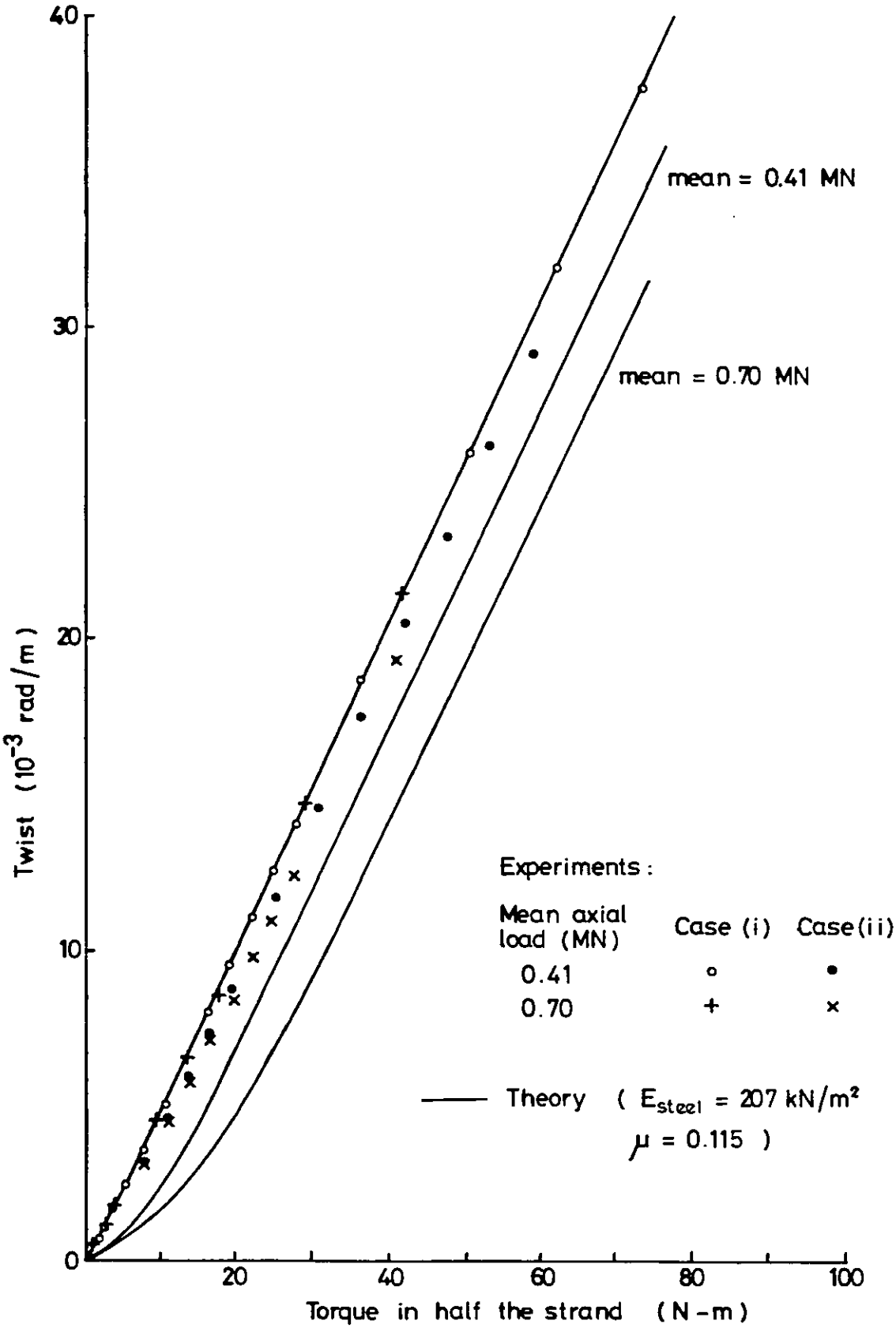

Fig (5.31) Comparison of torque - twist experiments after case (i) and case (ii) of axial bedding - in for the 41 mm O.D. strand

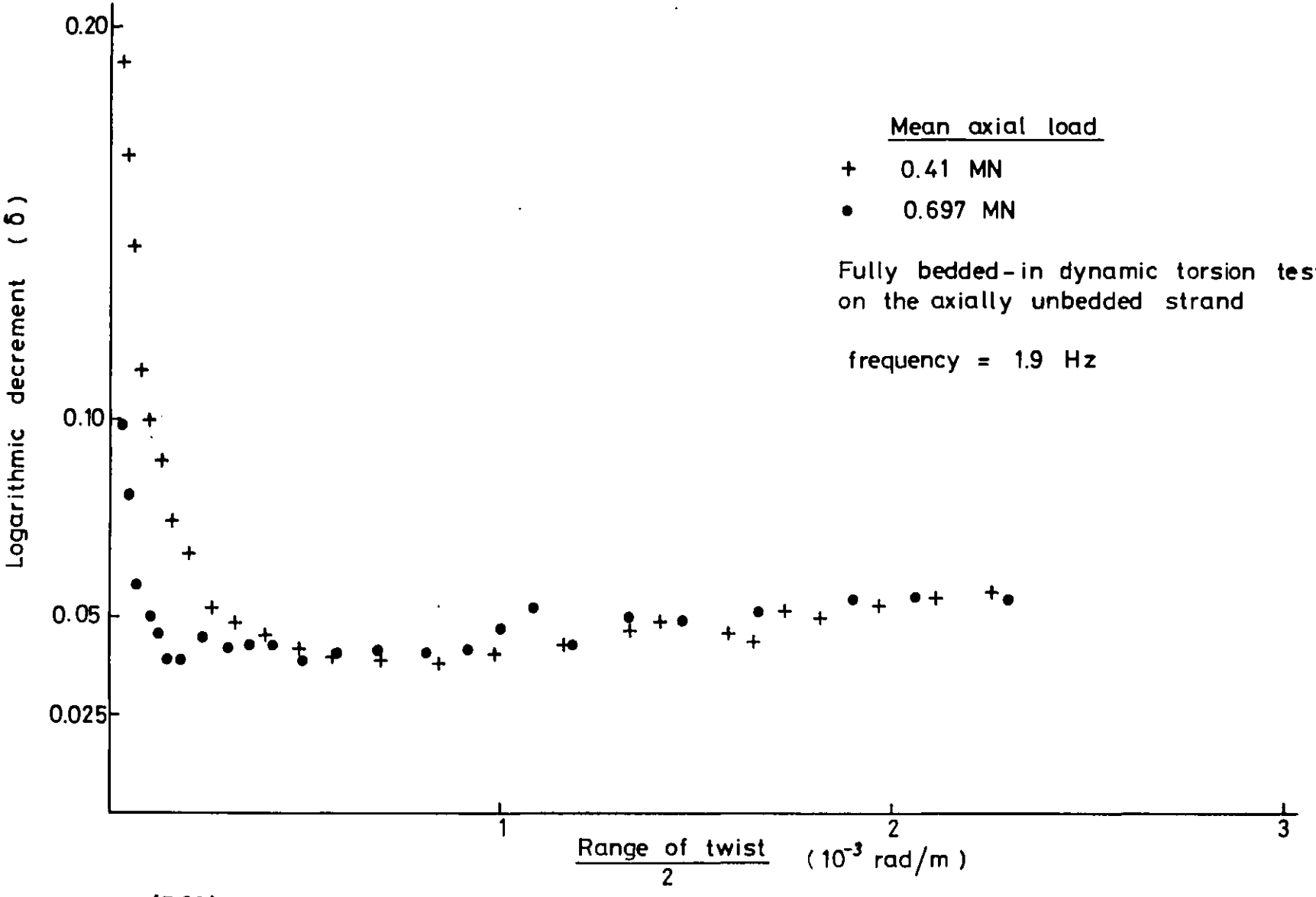

Fig (5.32) Plot of log. dec. from dynamic torsion tests on 41 mm O.D. strand under two different mean axial loads

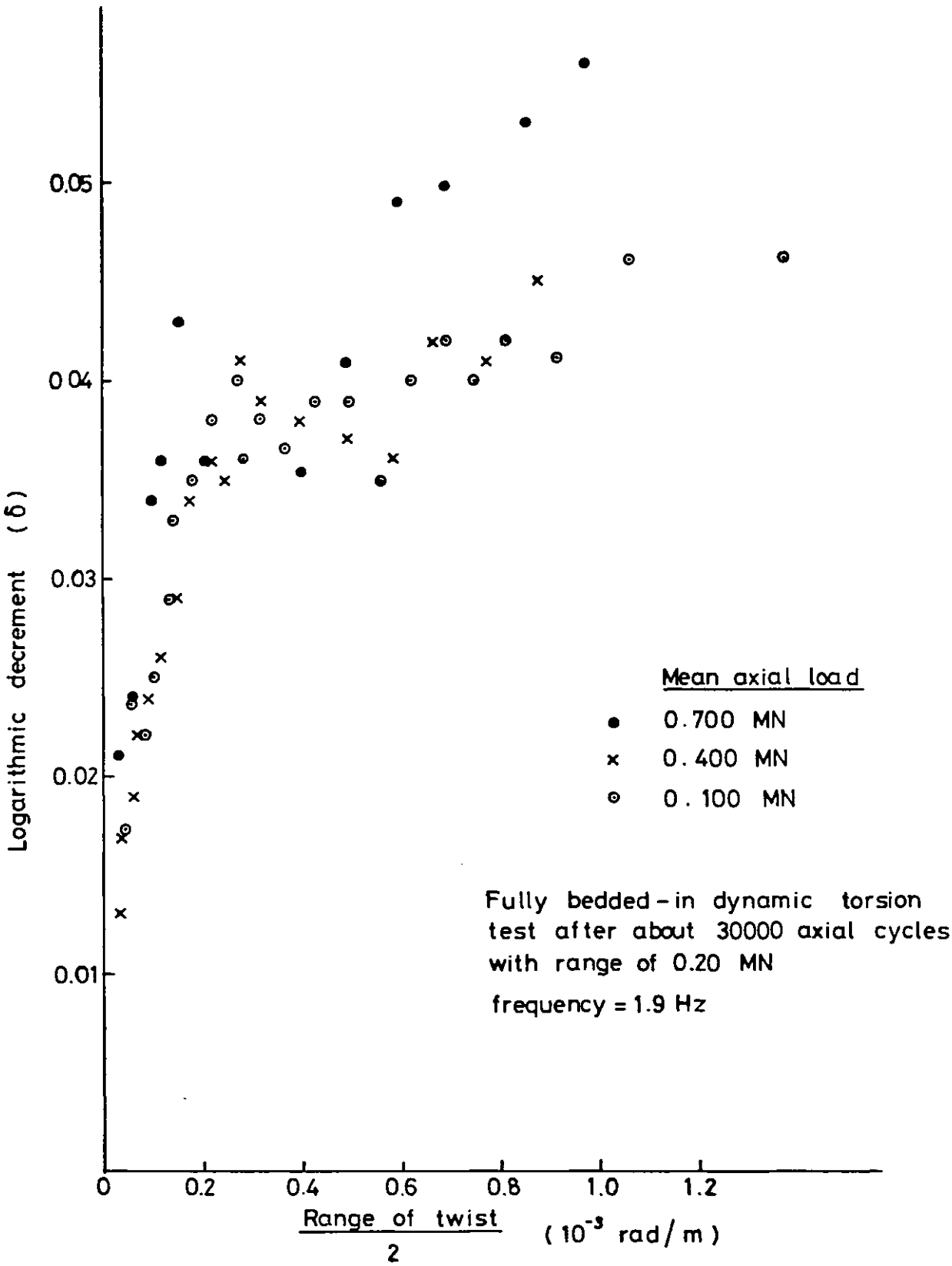

Fig (5.33)Plot of log. dec. from dynamic torsion tests on 41 mm O.D. strand under various mean axial loads

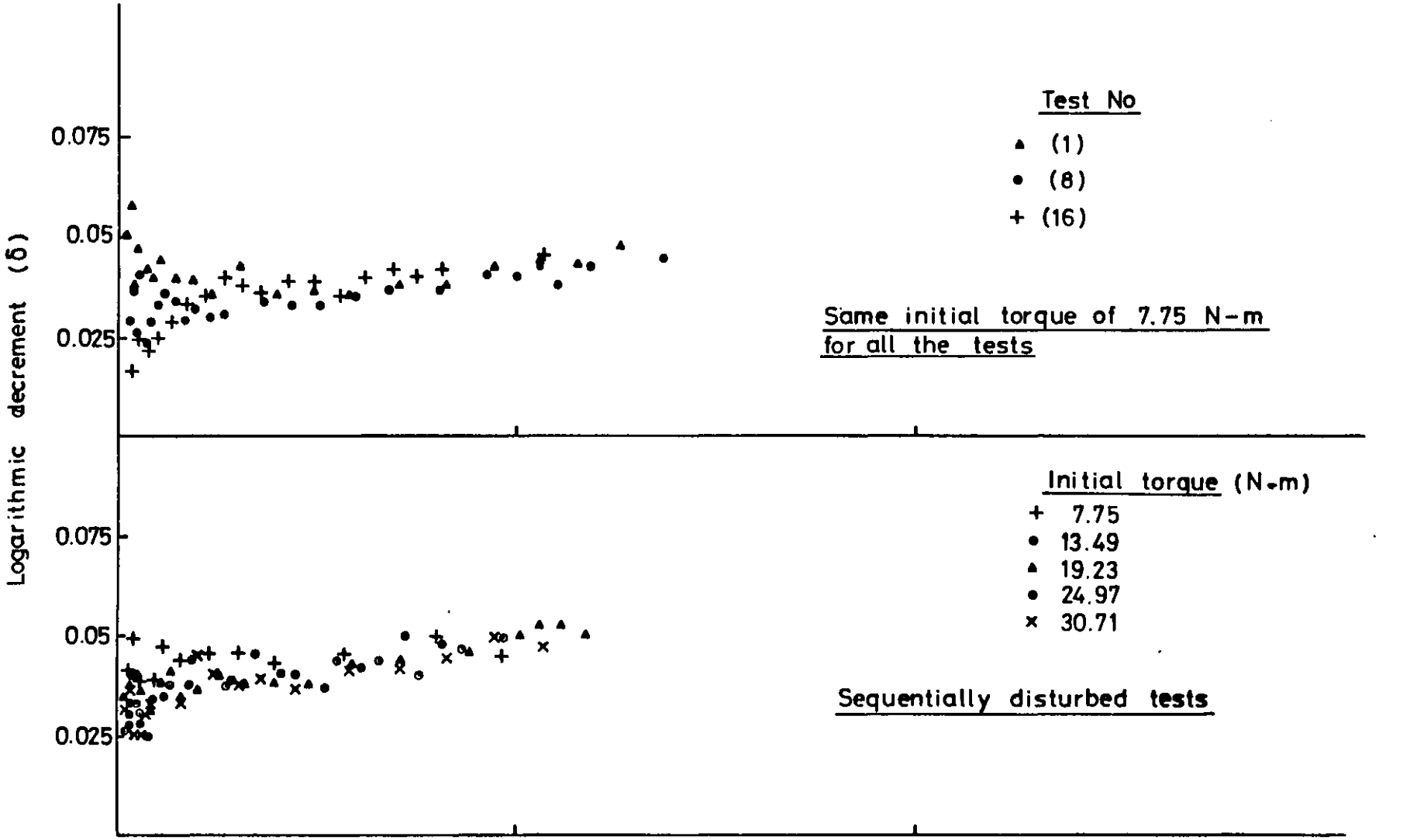

Fig(5.34)Plots of log dec from dynamic torsion tests on 41mm O.D. strand, under a mean axial load of 0.100 MN

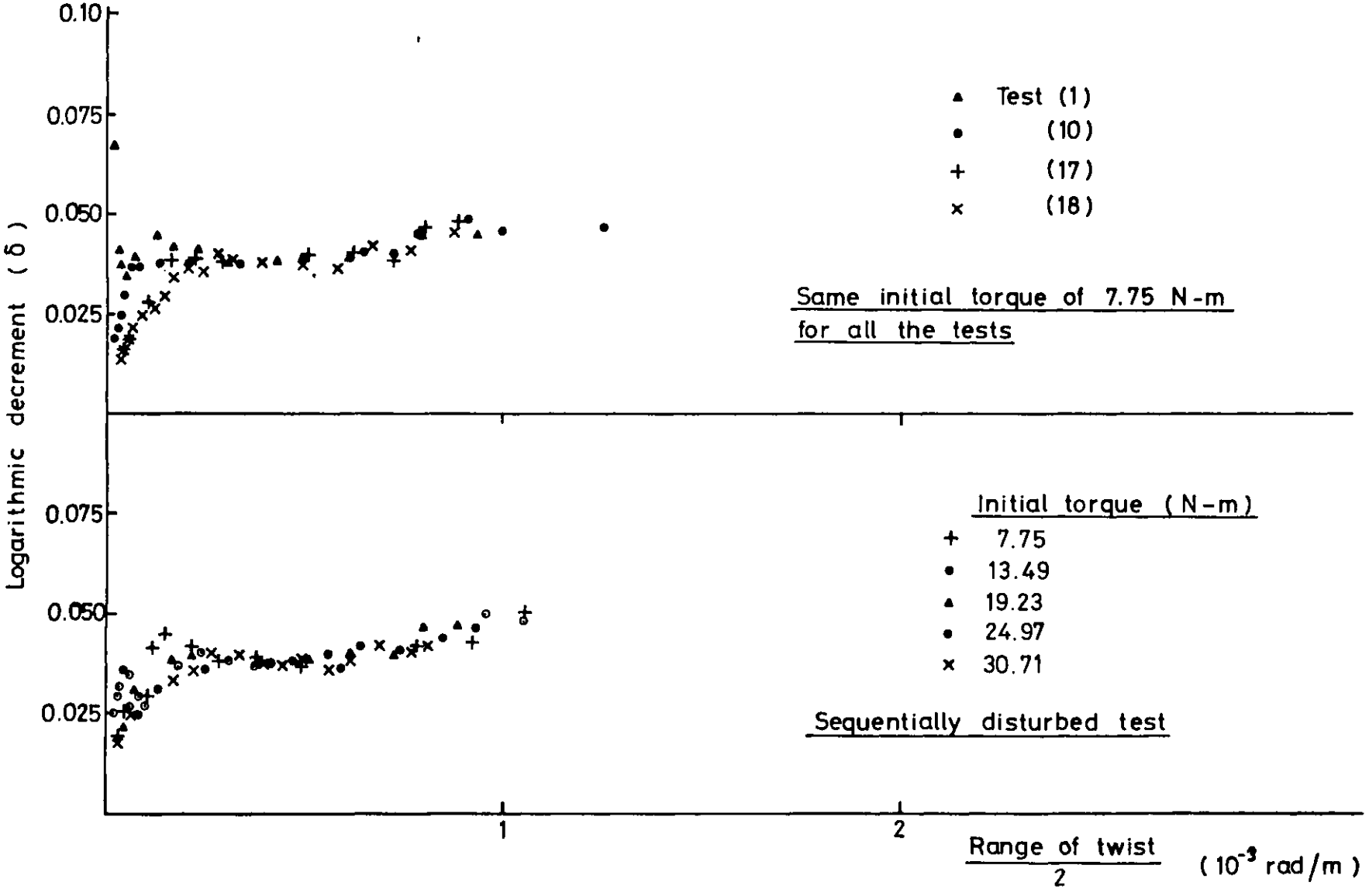

Fig (5.35) Plots of log dec from dynamic torsion tests on 41 mm OD strand under axial load of 0.400 MN

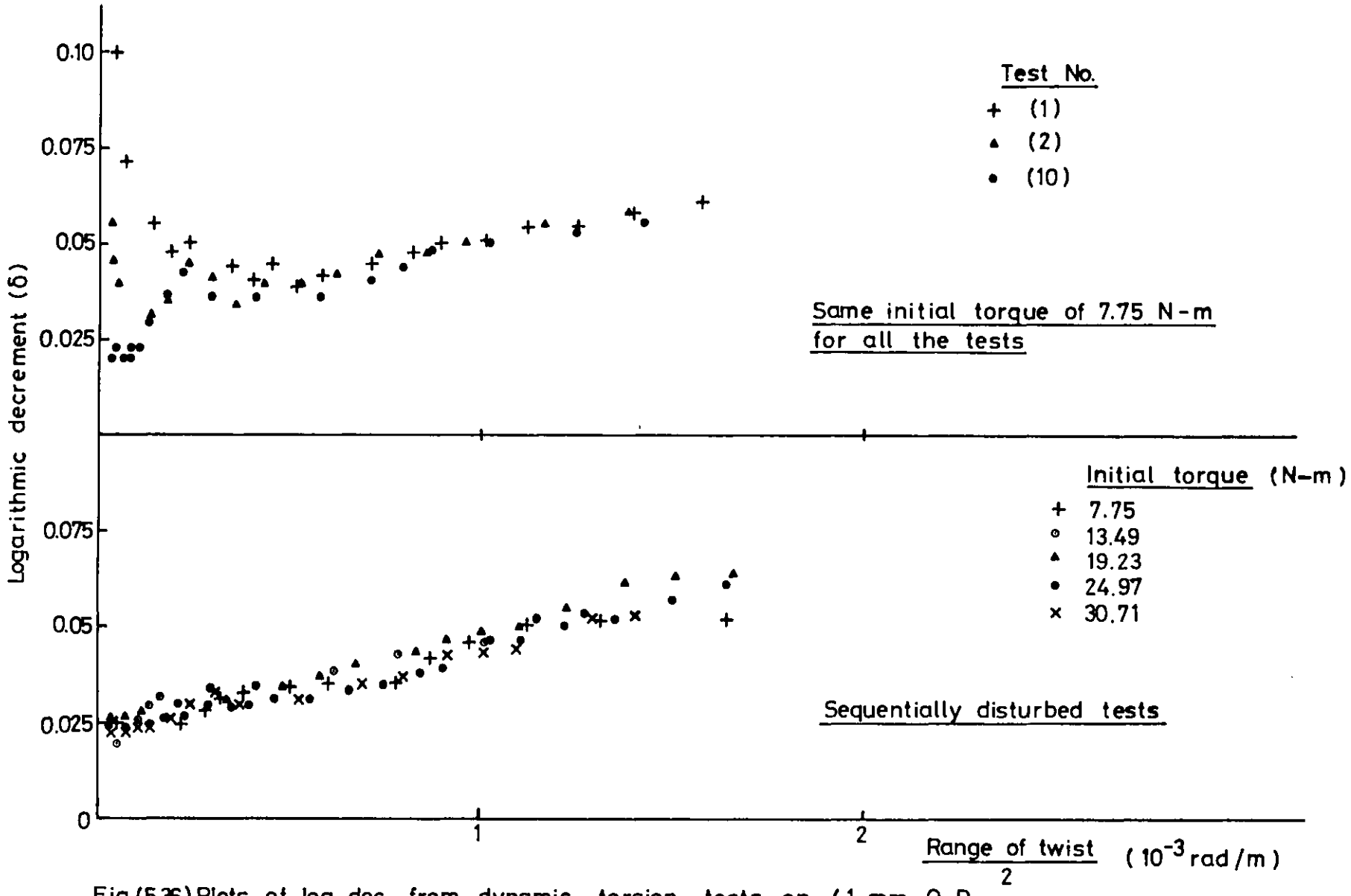

Fig (5.36) Plots of log. dec. from dynamic torsion tests on 41 mm O.D. strand, under a mean axial load of 0.700 MN

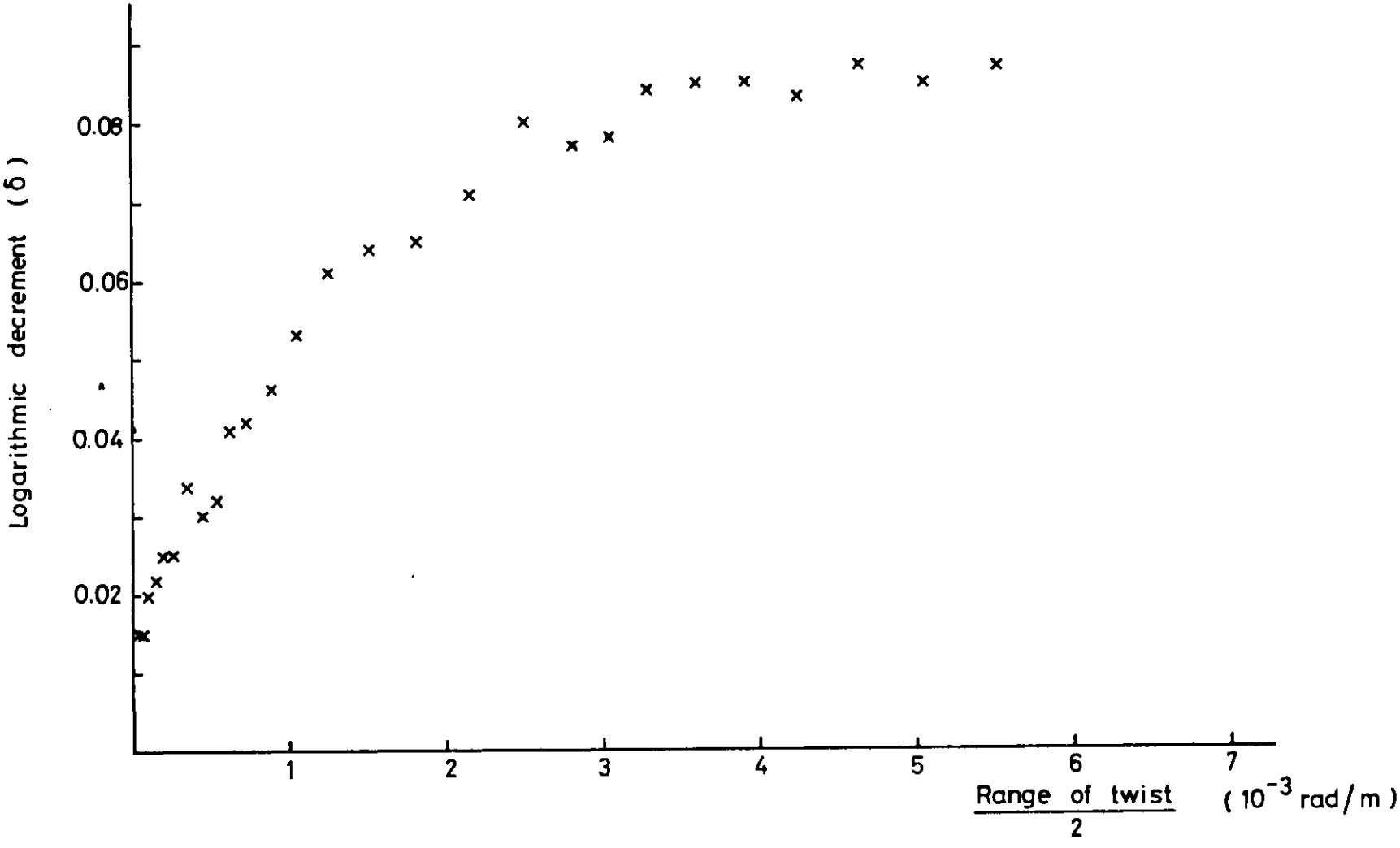

Fig (5.37) Plot of log. dec. from dynamic torsion tests on 41 mm O.D. strand under a mean axial load of 0.700 MN

$$\frac{d\phi}{dl} = 18.61 \times 10^{-6} \text{ rad/mm}$$

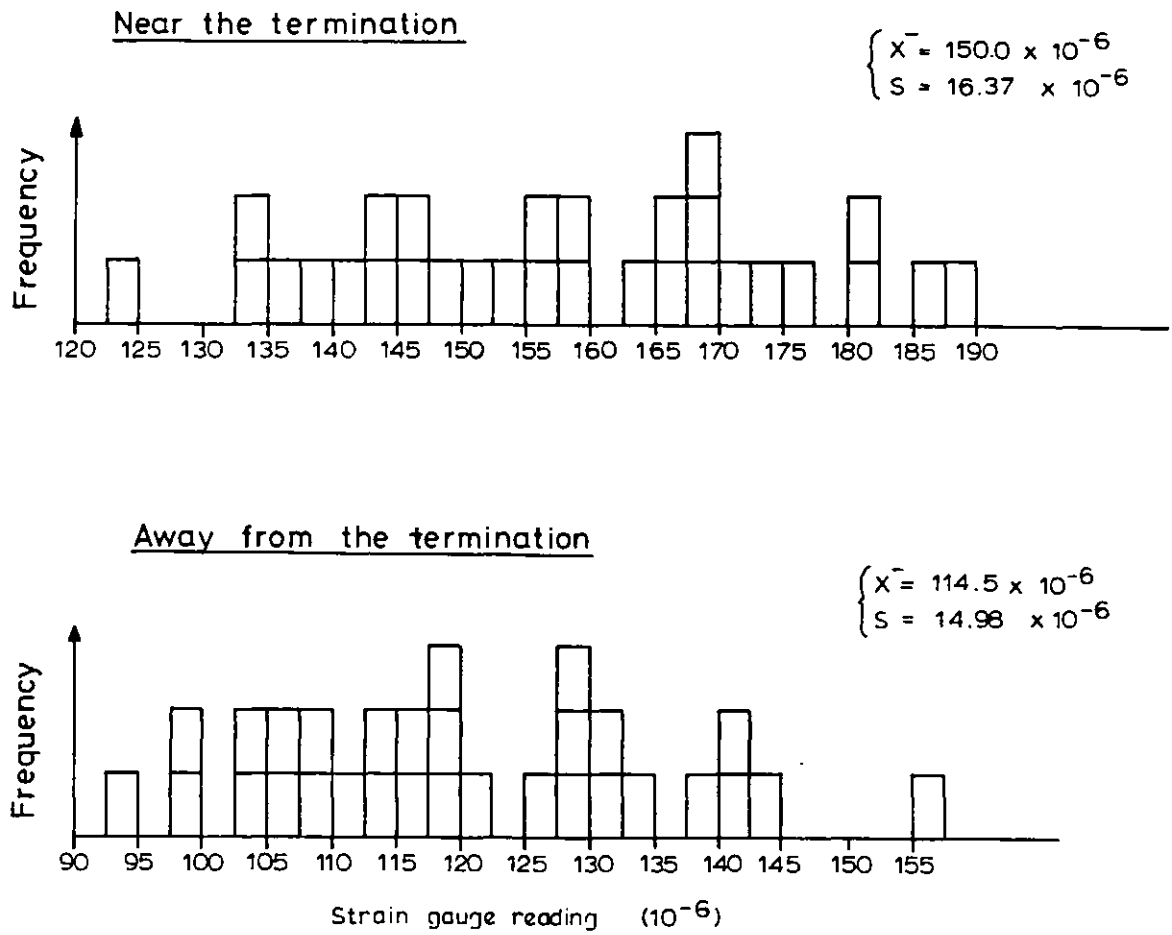

Fig(5.38)Scatter in the strain gauge readings for the torsion test

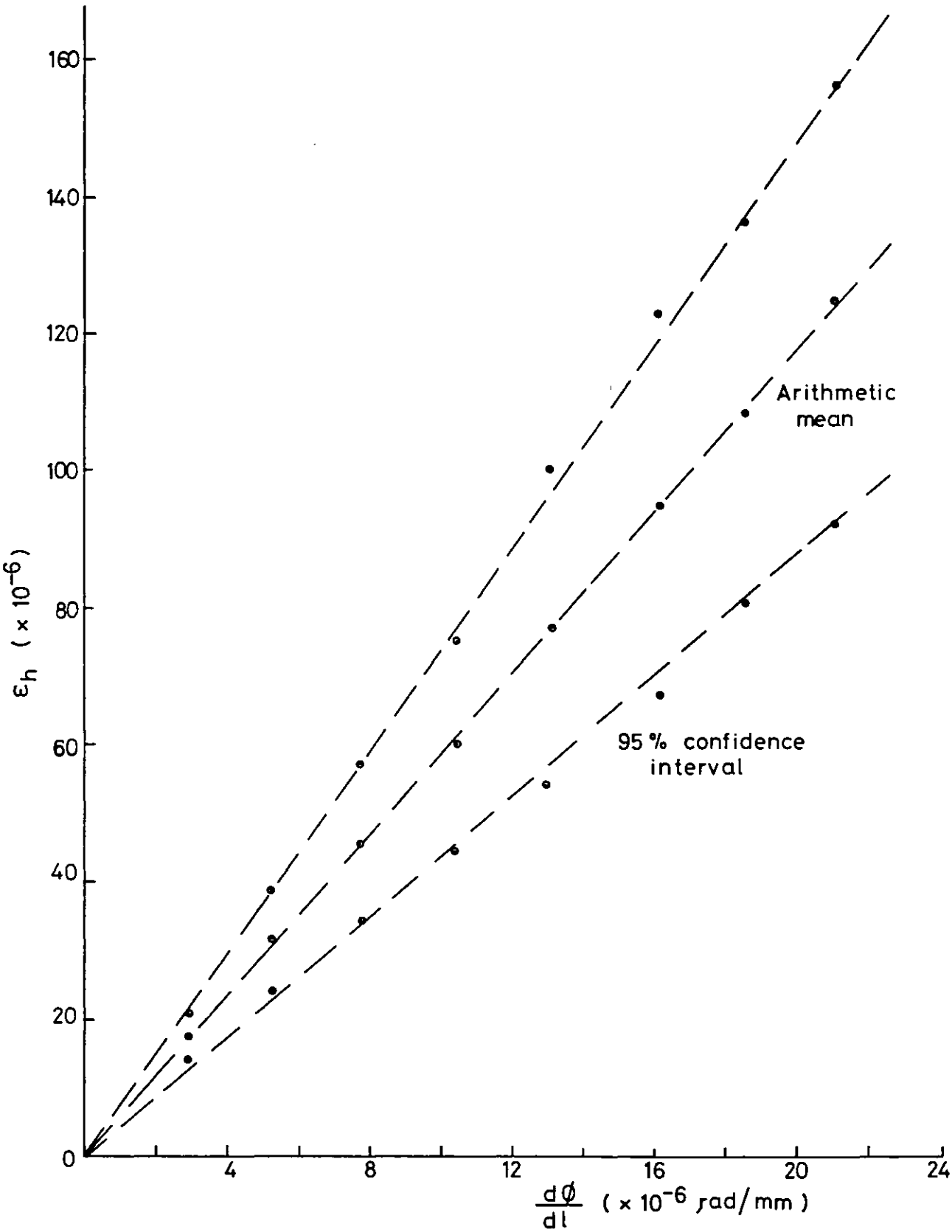

Fig (5.39) Strain gauge readings away from the terminations for the torsion test (39 mm O.D. strand ; mean axial load = 0.41 tons

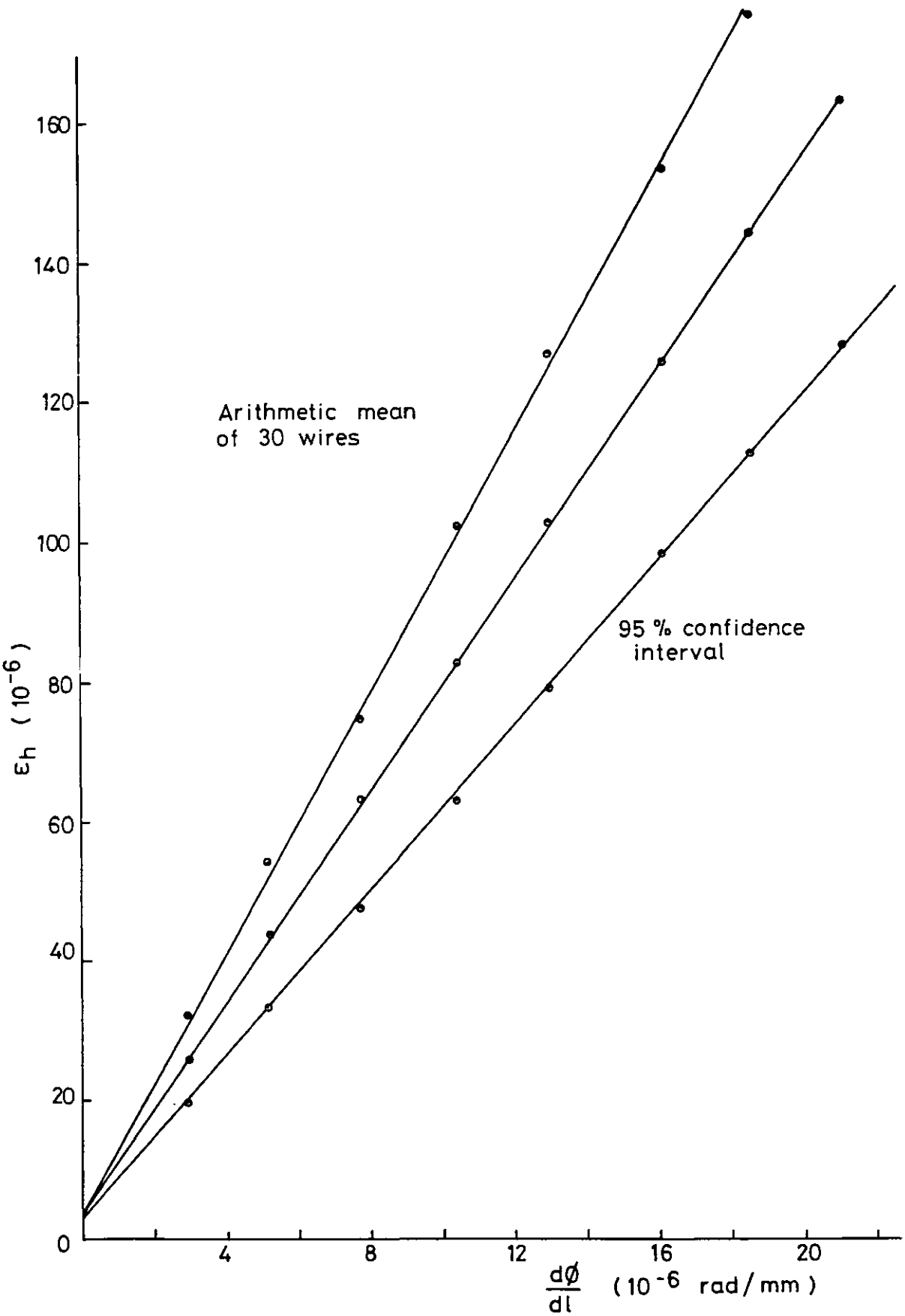

Fig (5.40) Strain gauge readings near the termination for the torsion test (39 mm O.D. strand mean axial load = 0.410 MN)

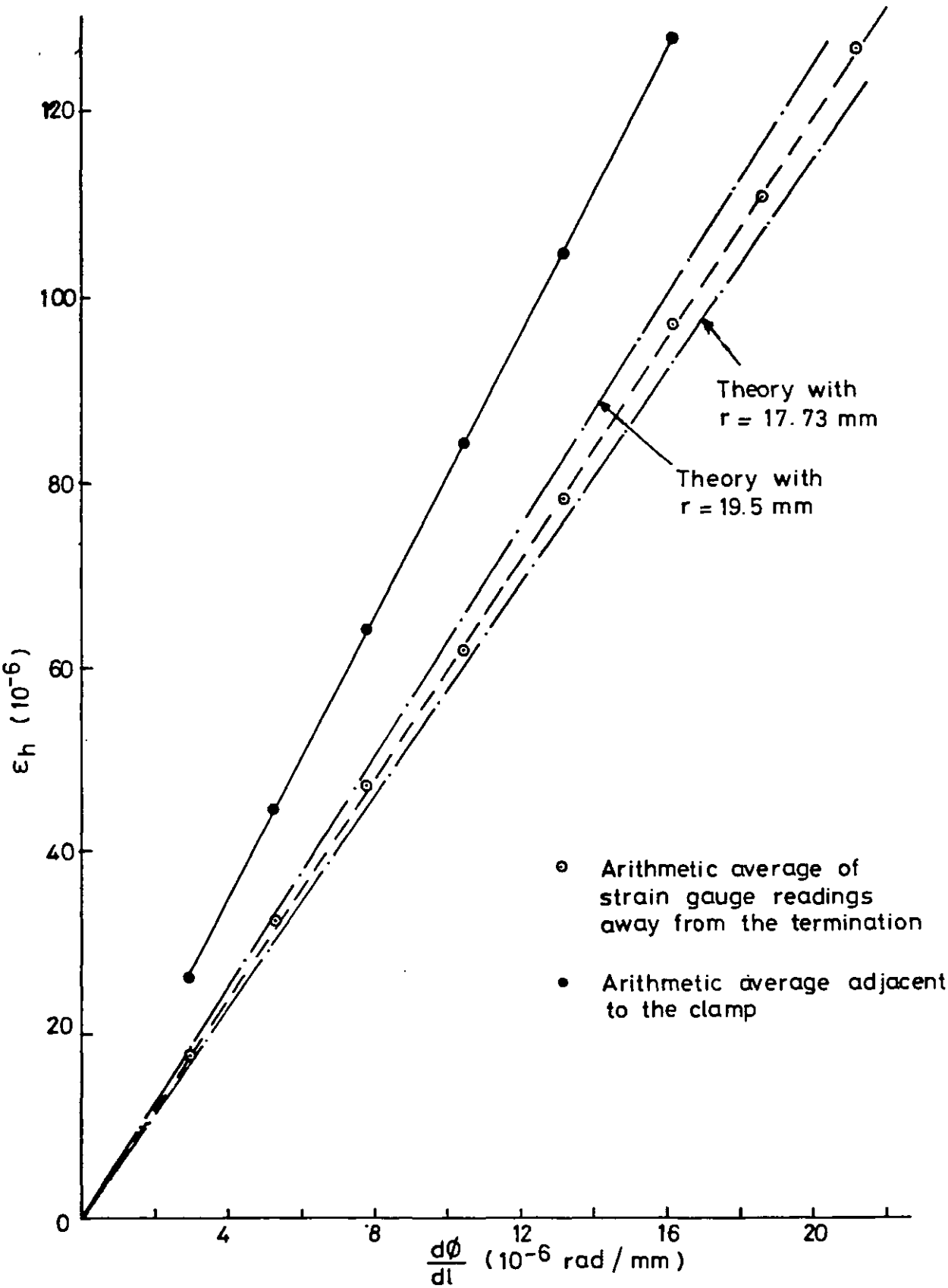

Fig(5.41) Comparison of theory and average of experimental results for the case of torsional loading (39 mm O.D.strand mean axial load = 0.410 MN

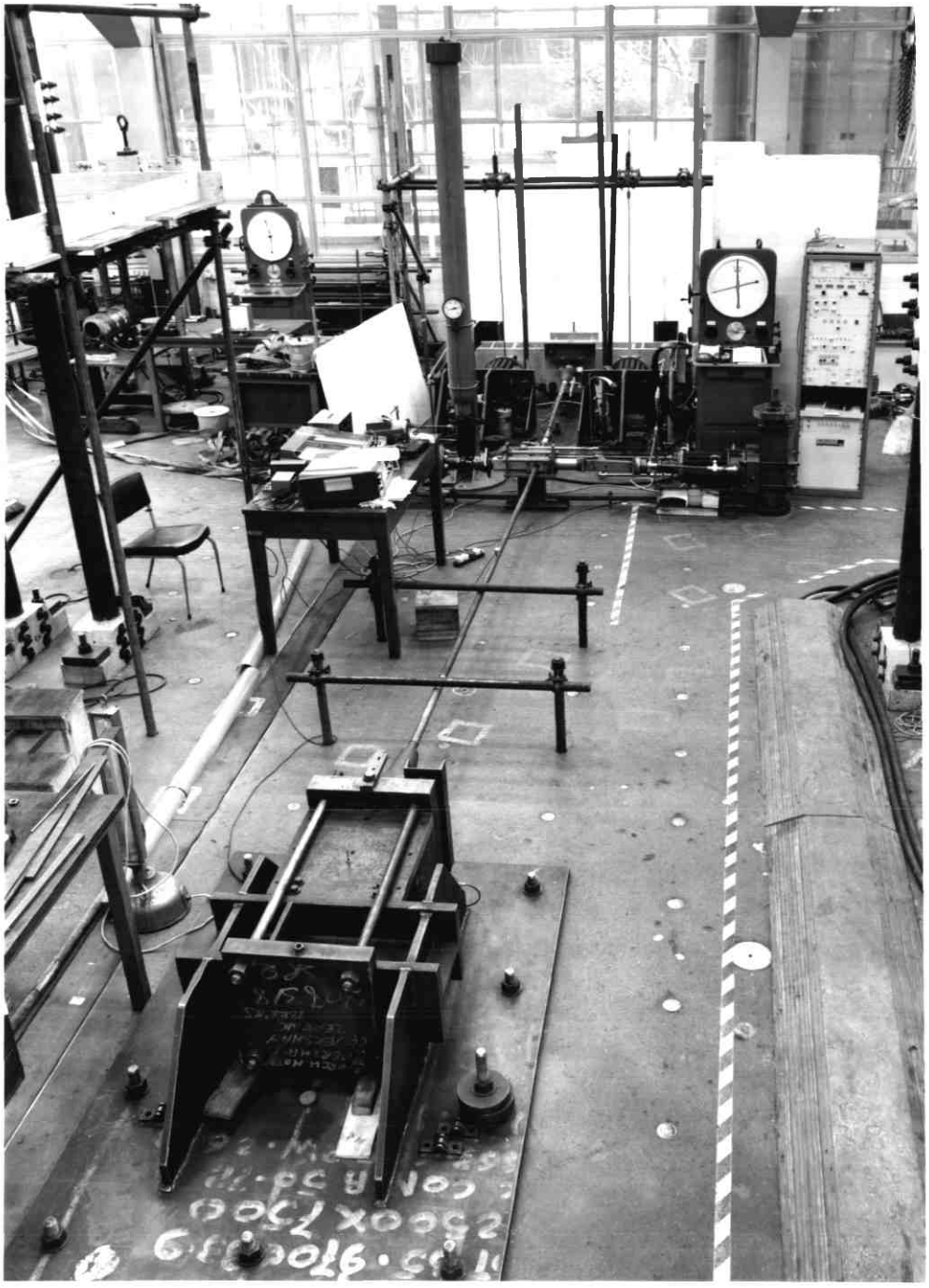

Fig. 5.42 General arrangement for free bending tests.

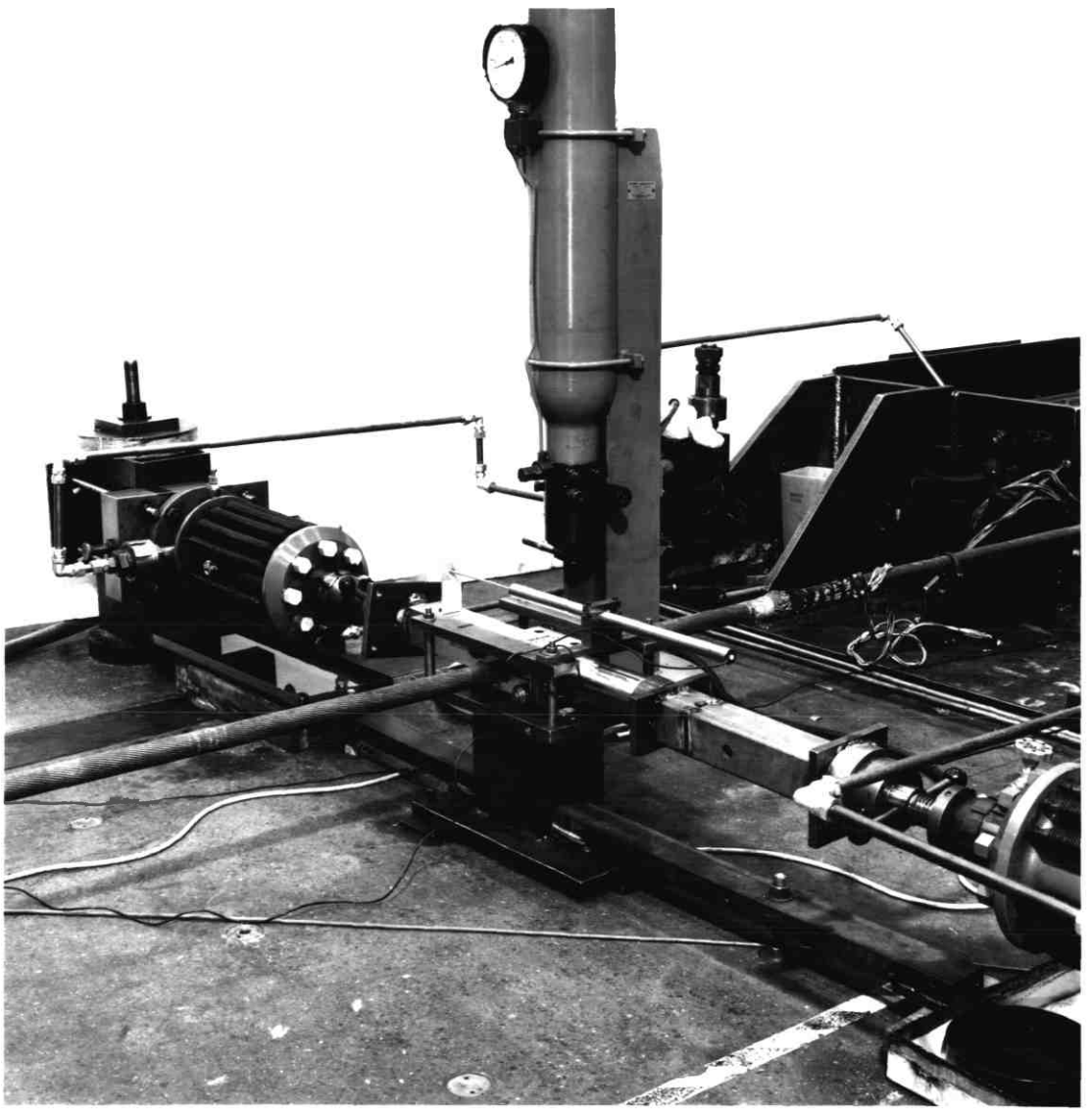

Fig. 5.43 General arrangement for controlling the lateral deflections in the cable.

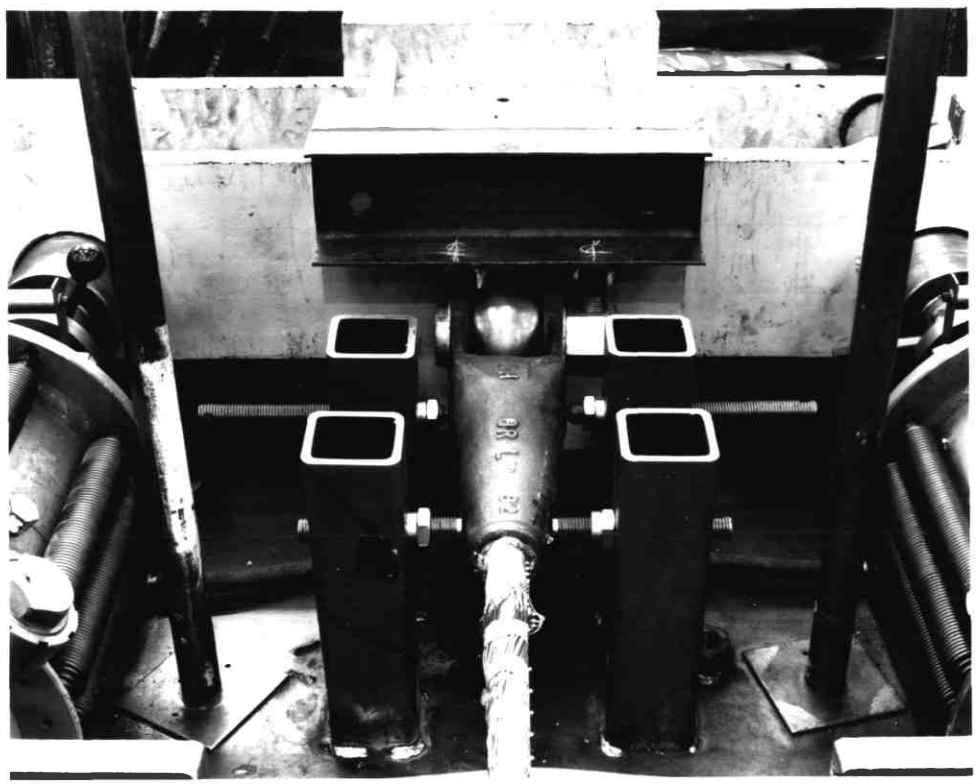

Fig. 5.44 Method of preventing the socket from lateral movements.

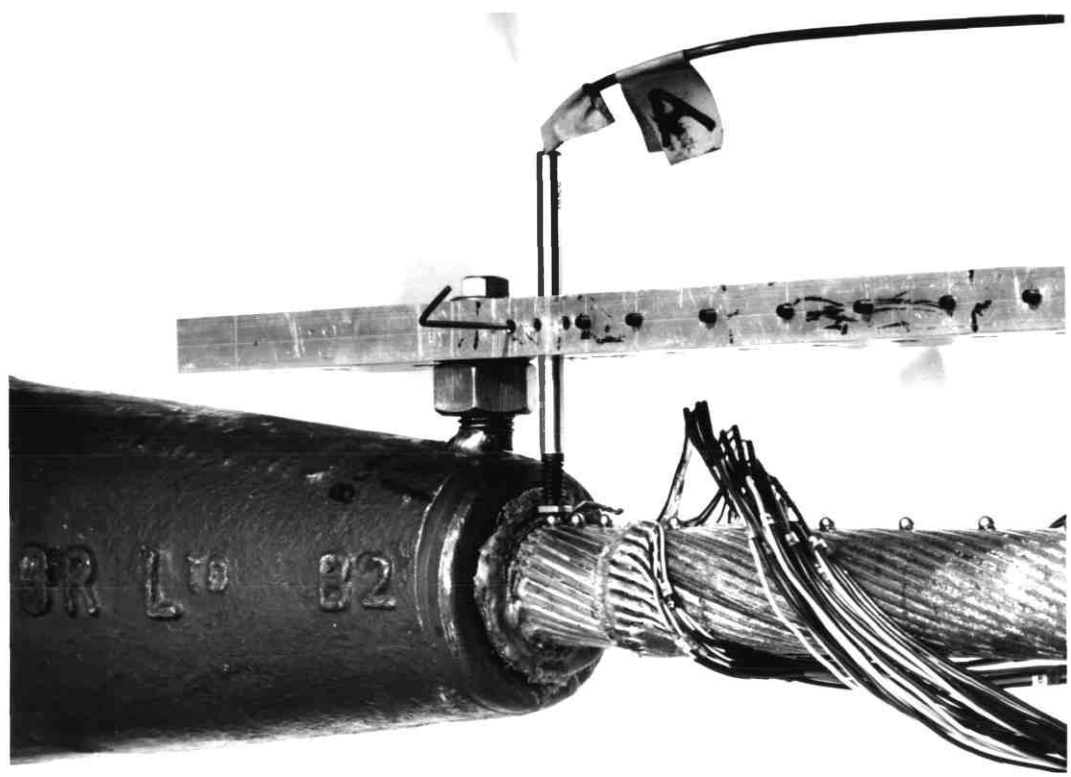

Fig. 5.45 Strain gauges on the individual wires at the mouth of the socket with the extended rigid bar and displacement transducer for differential (net) displacement measurements.

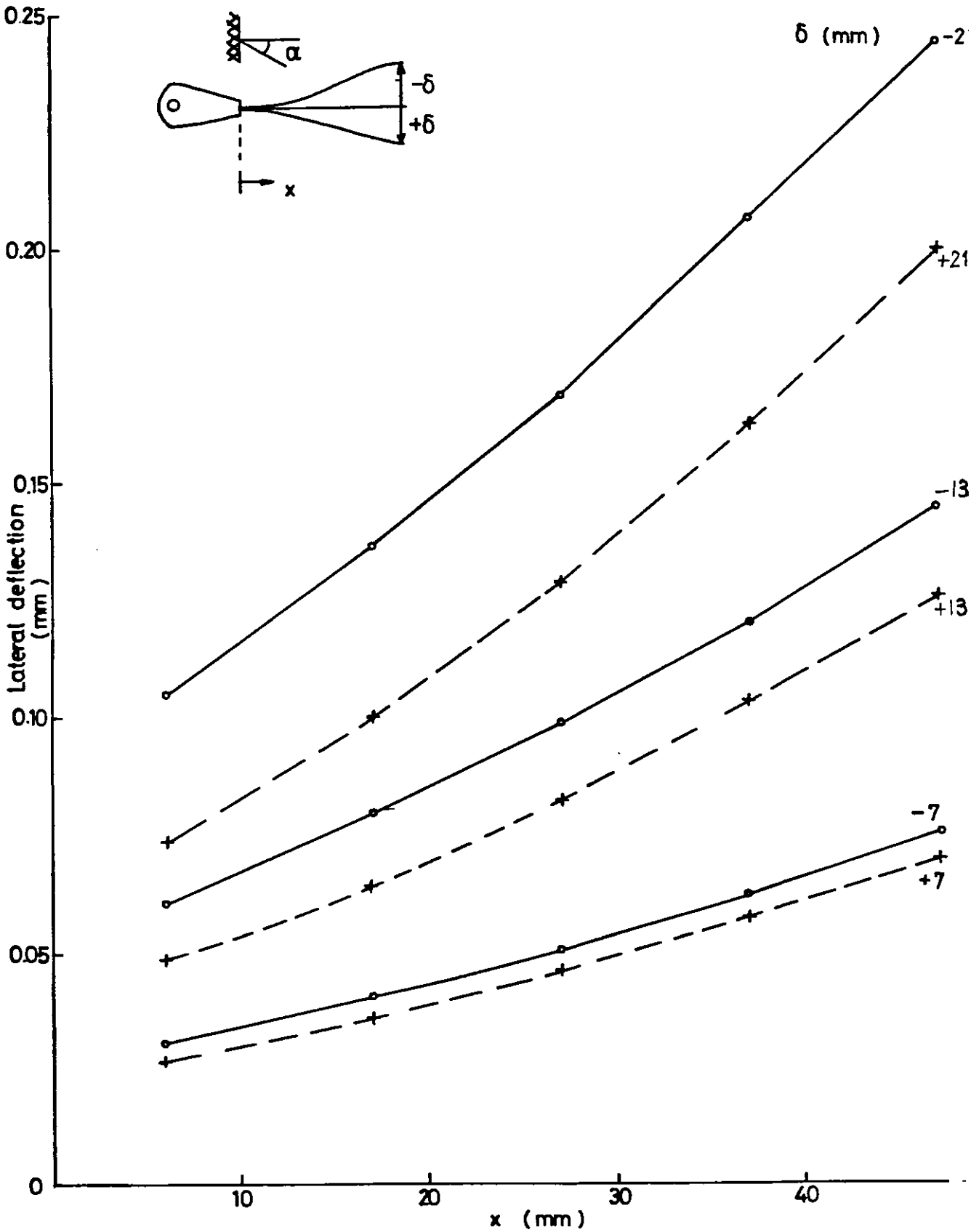

Fig (5.46) The net deflected shape of the cable at the termination as a function of the lateral deflection at jacking position (mean axial load = 0.410 MN)

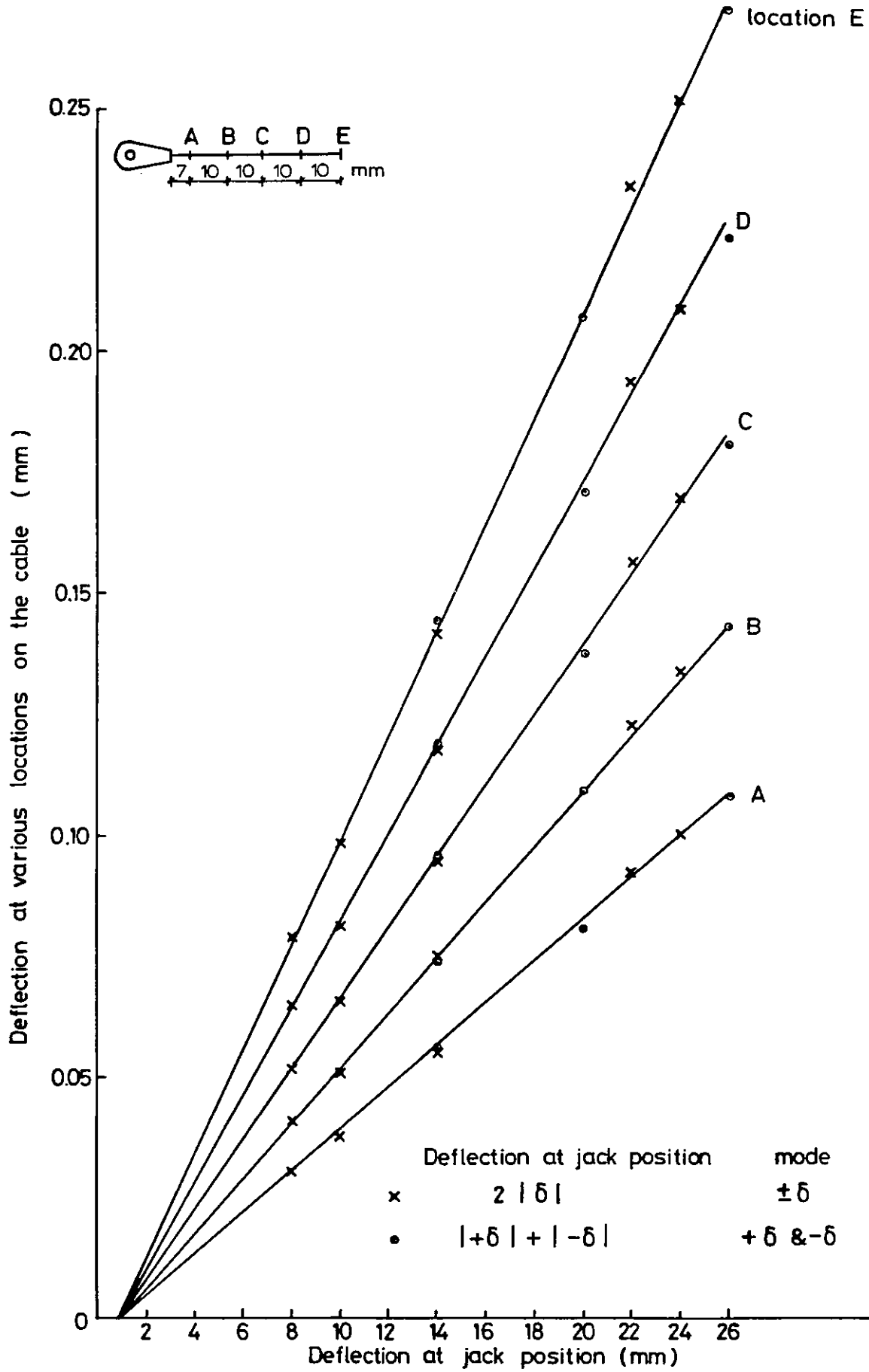

Fig (5.47) Net deflection at various locations on the cable near the socket as obtained by differential displacement method (mean axial load =0.410MN

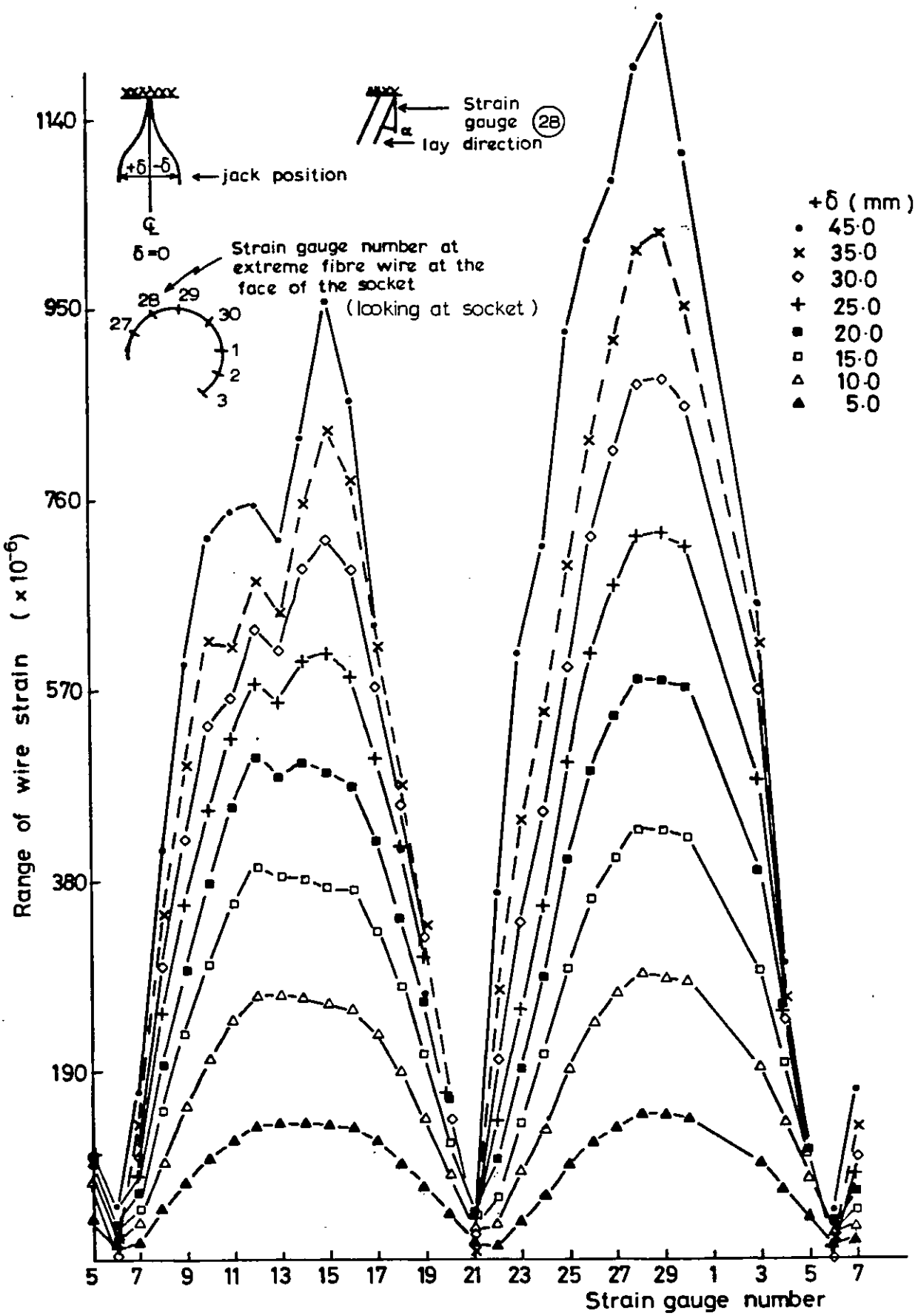

Fig (5.48) Variation of wire strain at the fixed end for various magnitudes of imposed lateral displacement, δ (mean axial load = 0.615 MN)

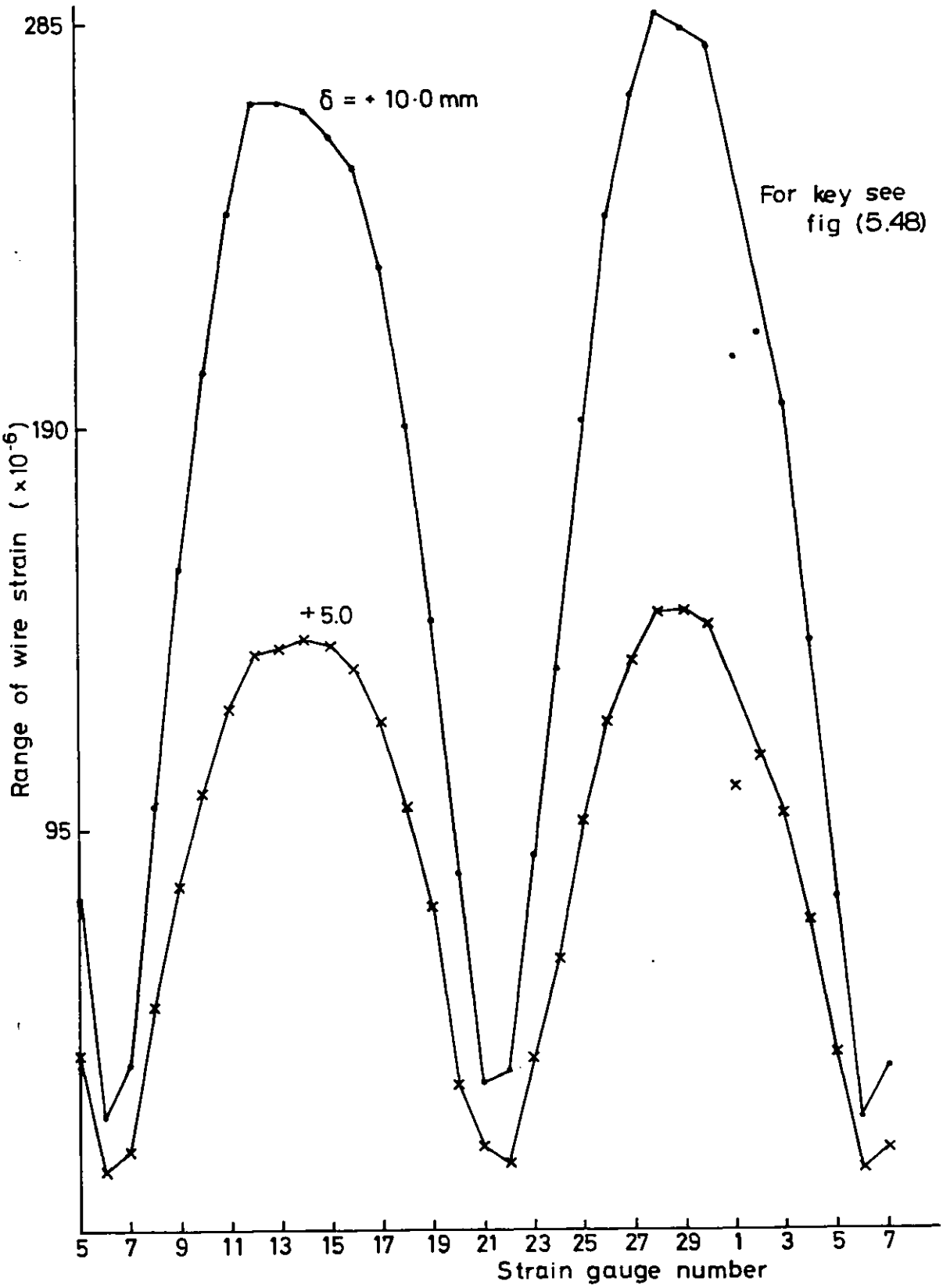

Fig (5.49) Variation of axial wire strain over the gauges at the fixed end for two levels of imposed lateral displacement δ (mean axial load = 0.615 MN)

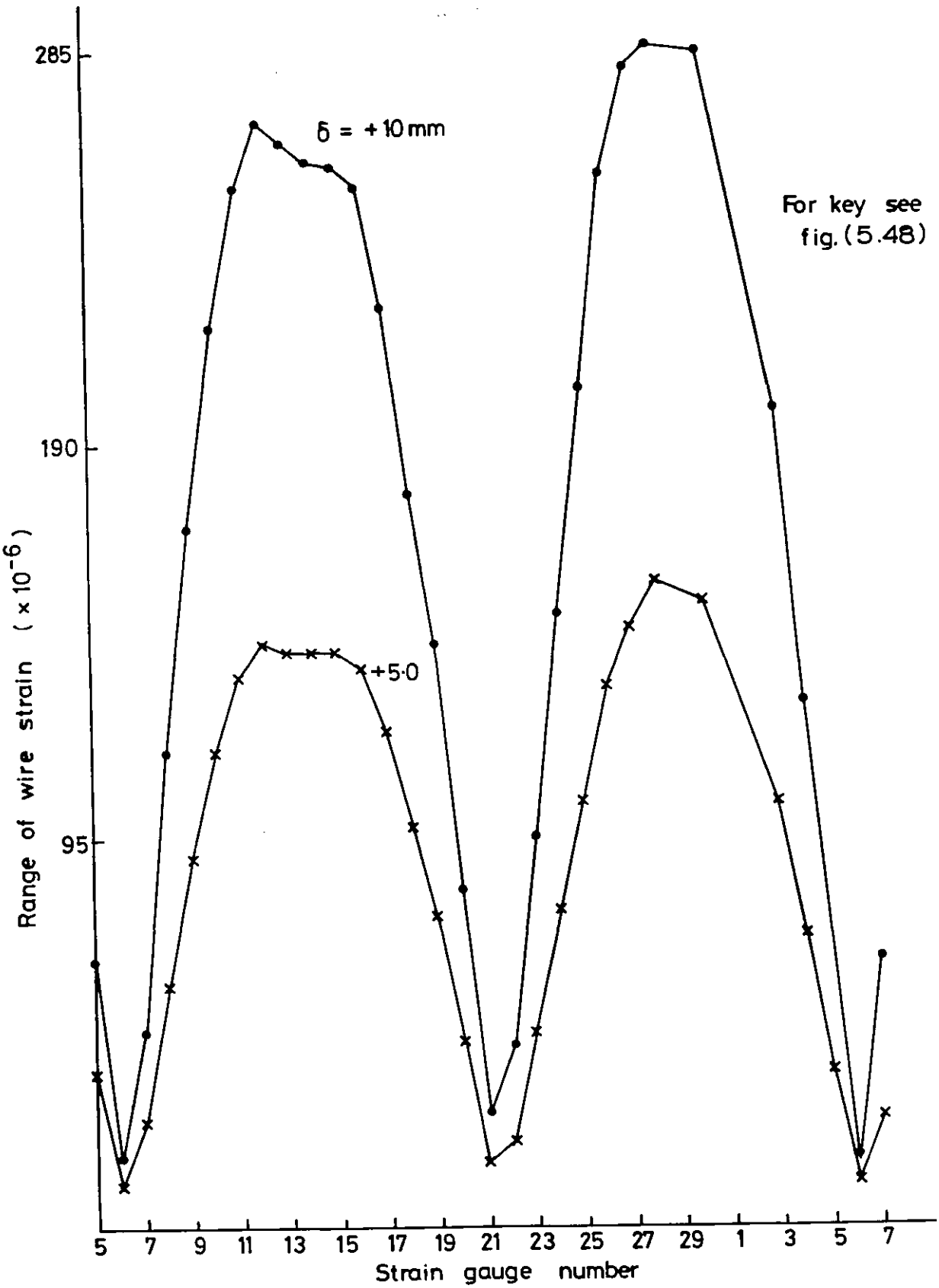

Fig(5.50) Variation of axial wire strain over the gauges at the fixed end for two levels of the imposed lateral displacement, δ (mean axial load = 0·410 MN)

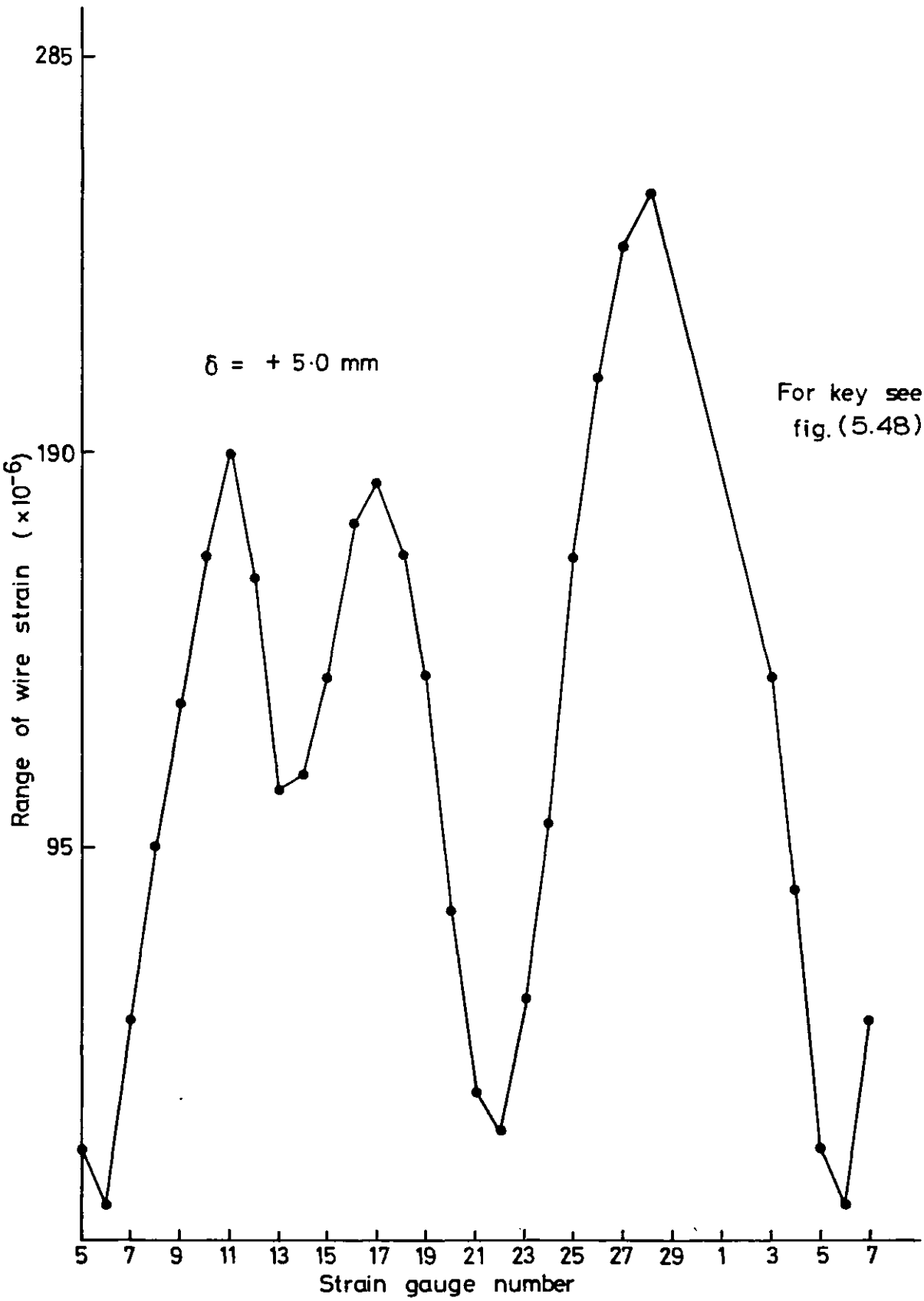

Fig (5.51) Variation of axial wire strain over the gauges at the fixed end for a given lateral displacement
(mean axial load = 0·205 MN)

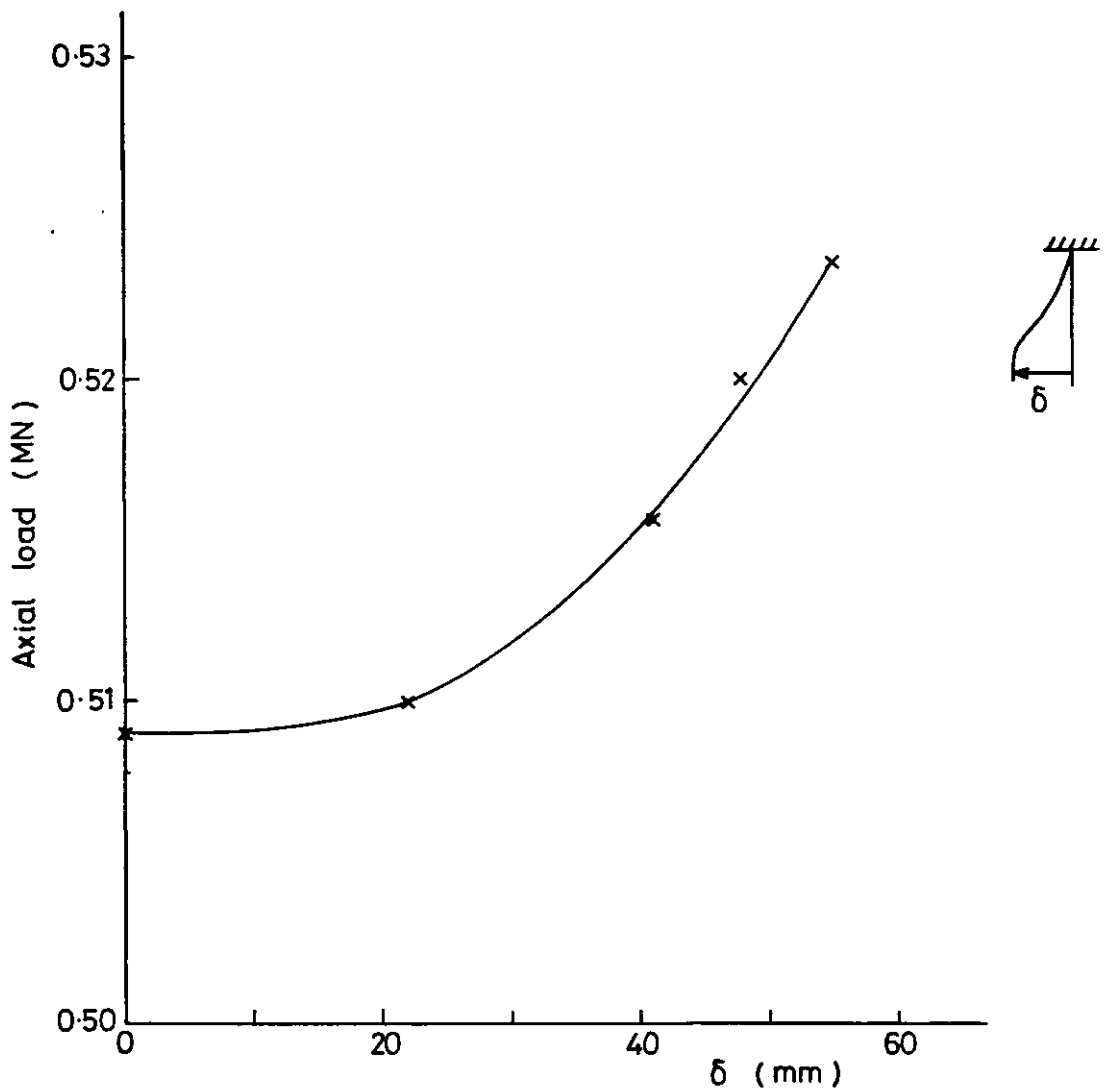

Fig (5.52) Variation of the axial load in the cable as a function of the imposed lateral displacement at the jack position, δ

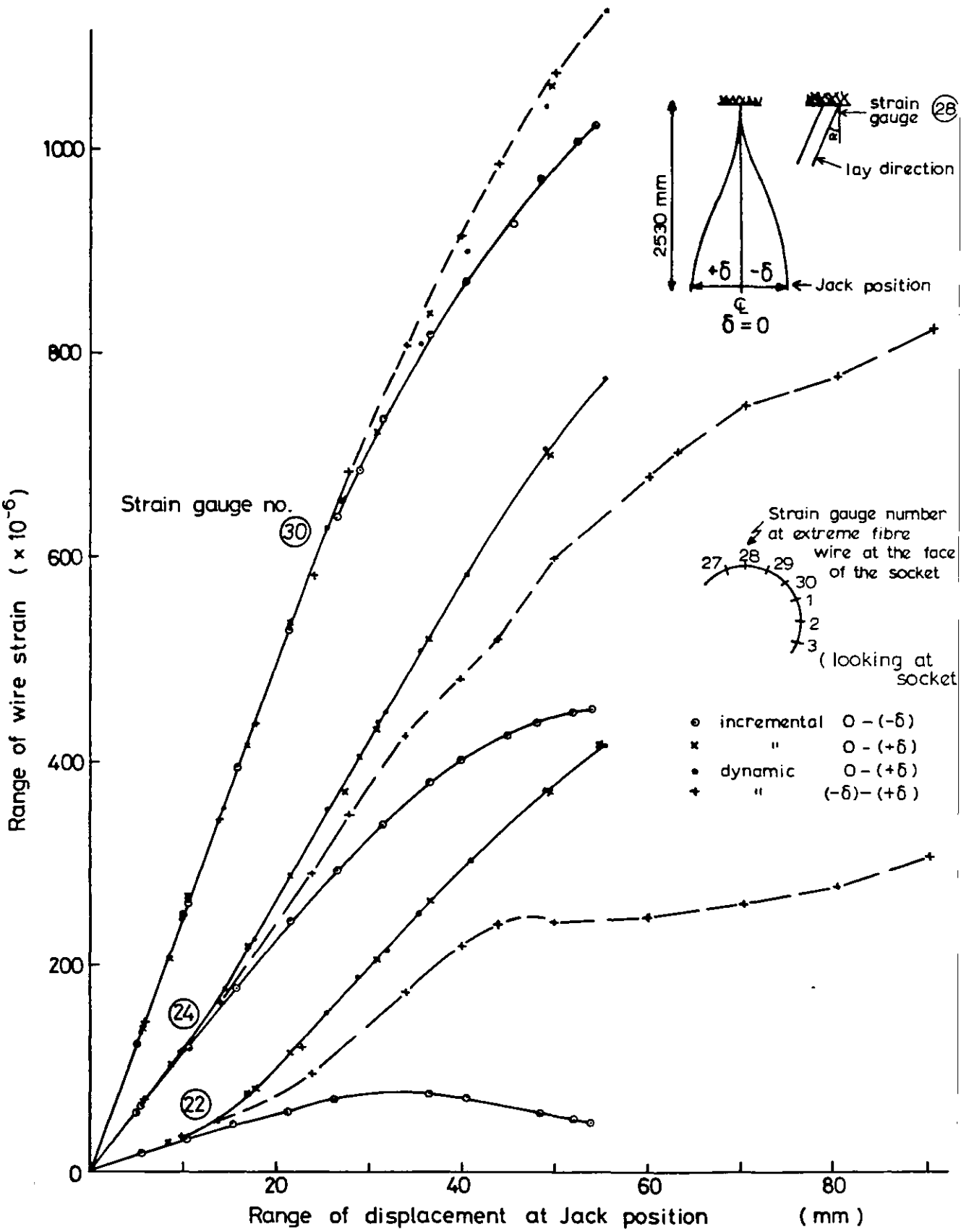

Fig (5.53a) Experimental plots of individual wire strains near the fixed end for the strand under bending (mean axial load = 0·410 MN)

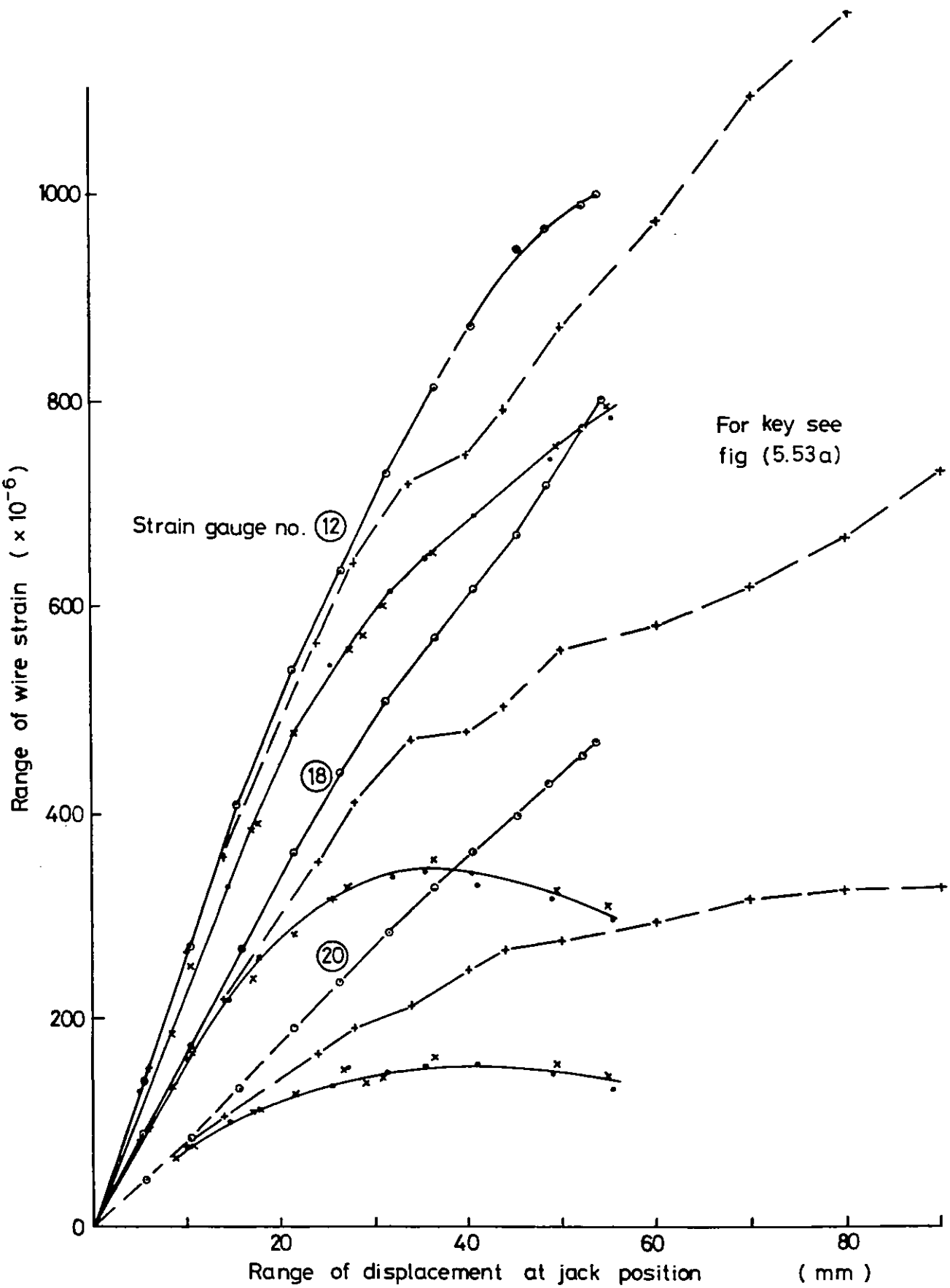

Fig (5.53 b) continuation of Fig (5.53 a)

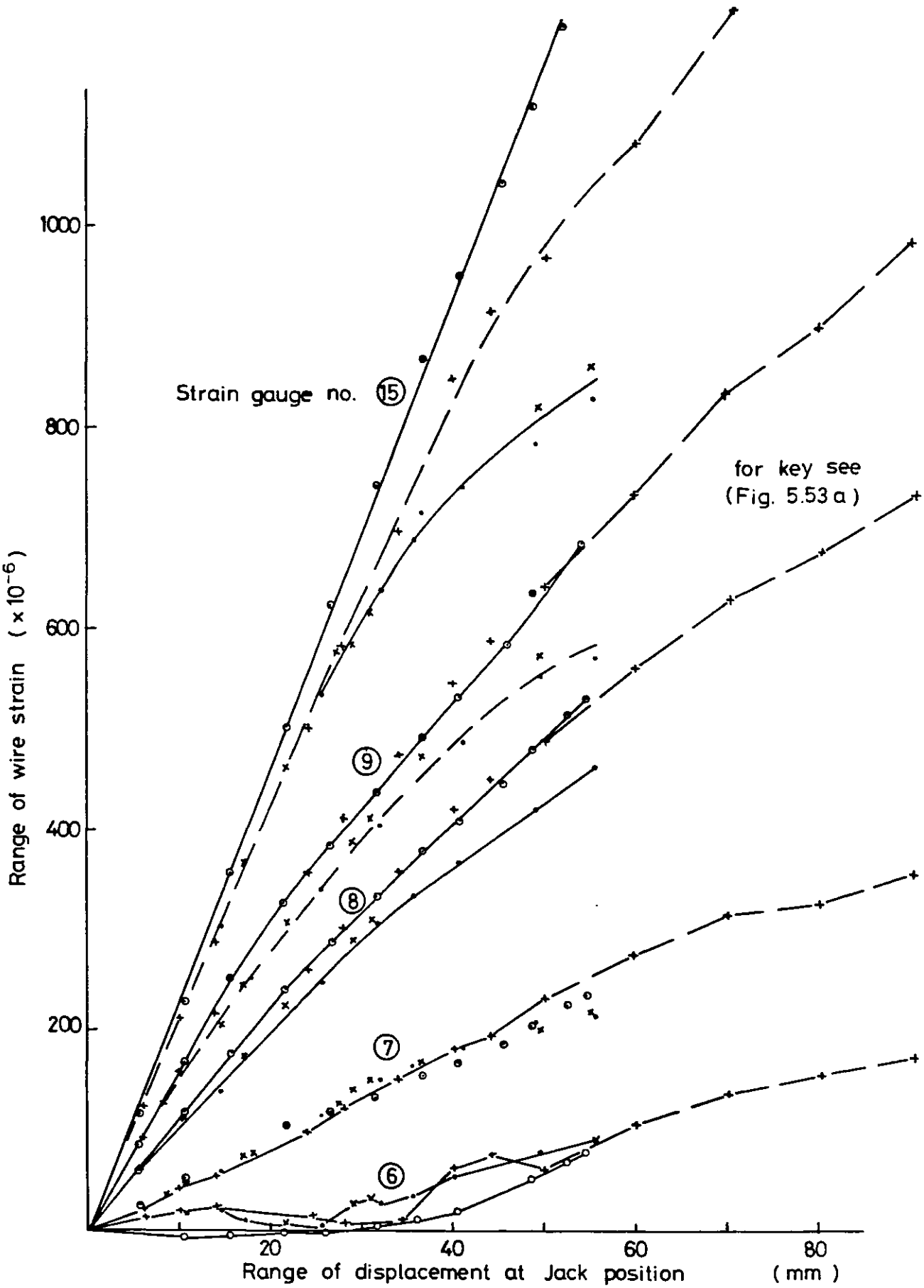

Fig. (5.53 c) continuation of Fig (5.53 b)

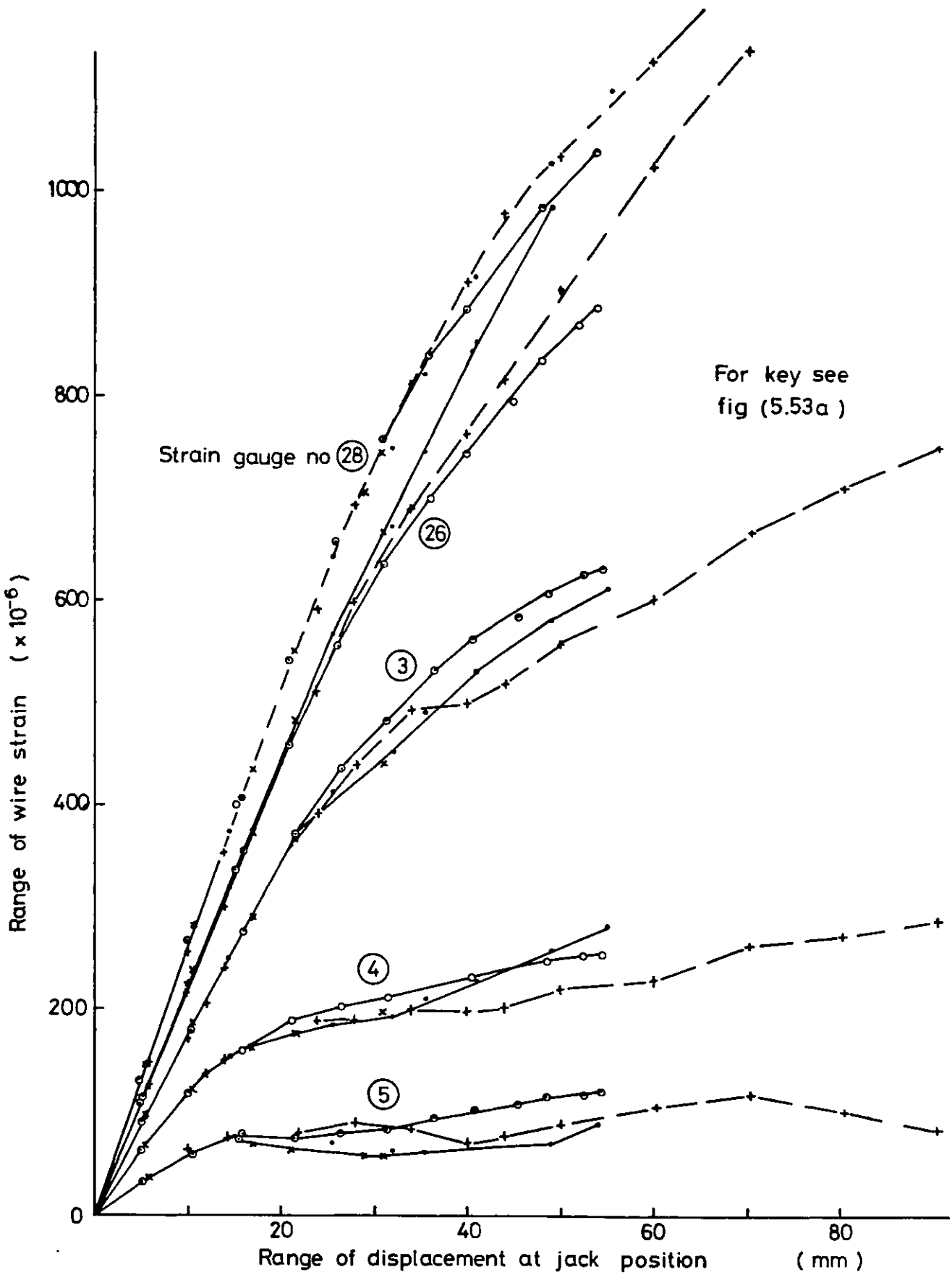

Fig (5.53d) continuation of Fig (5.53c)

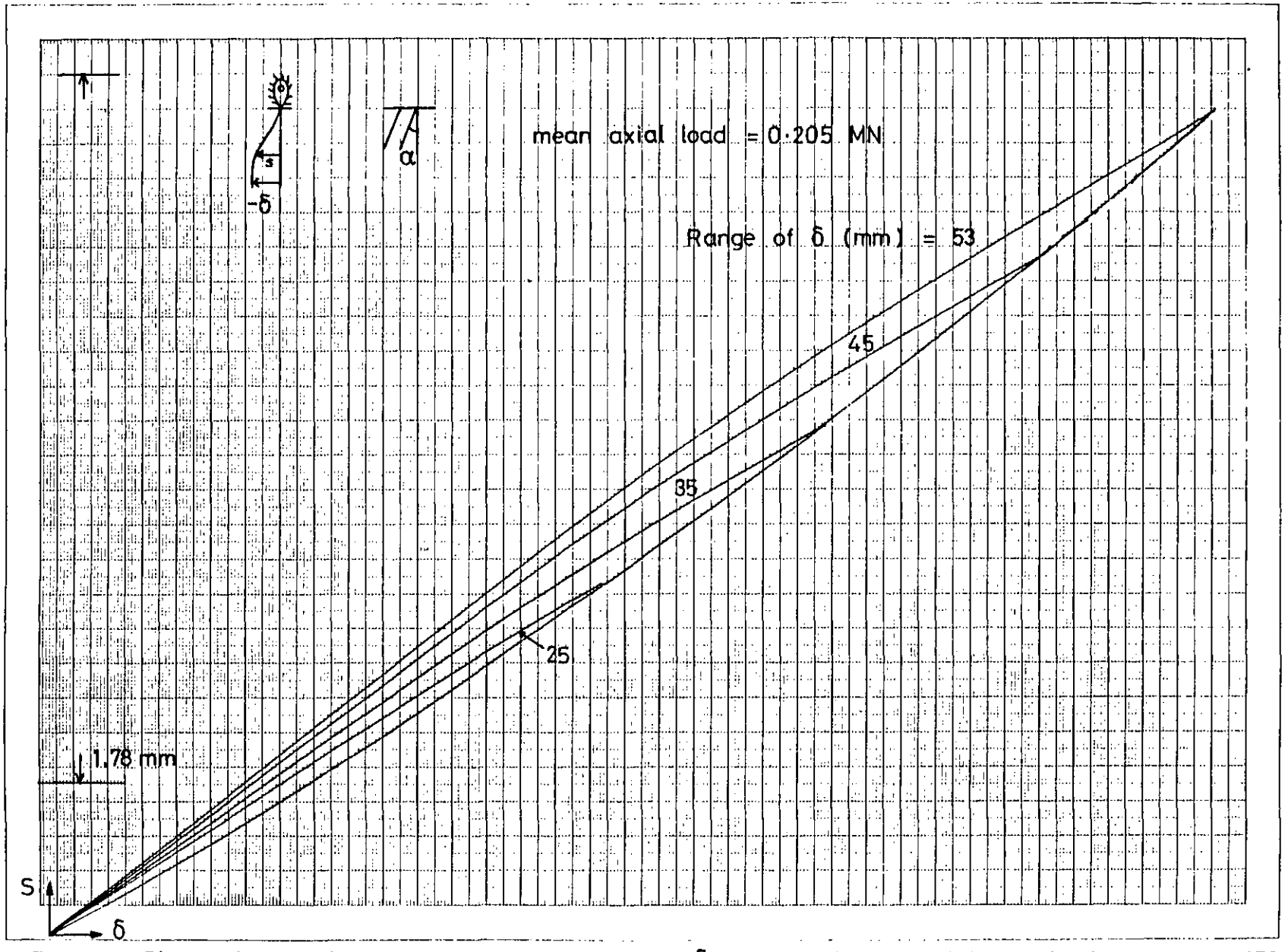

Fig (5.54) Plots of lateral deflection at jack position δ against differential (net) displacement at 150 mm from the face of the socket.

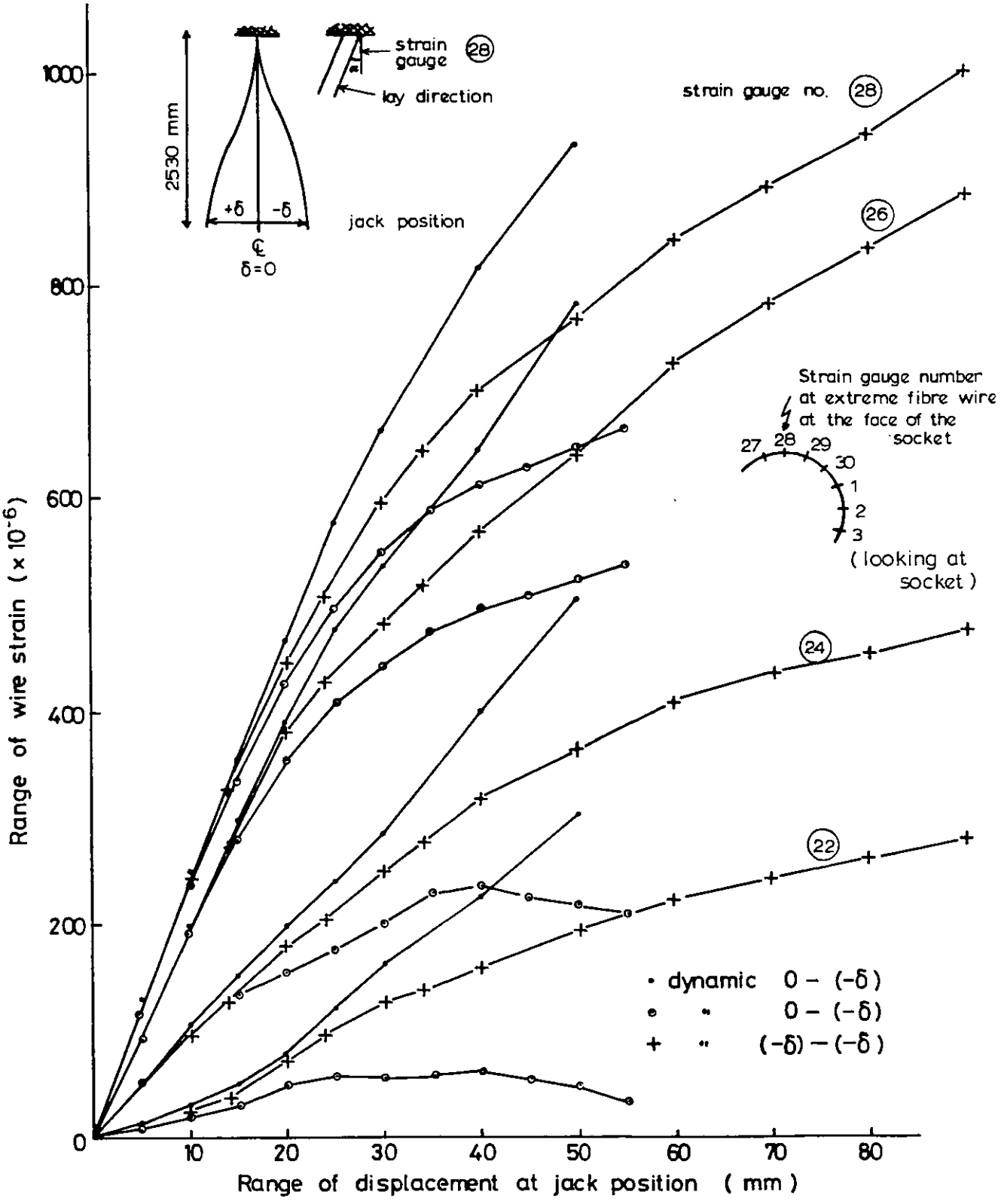

Fig (5.55a) Experimental plots of individual wire strains near the fixed end for the strand under bending (mean axial load = 0.205 MN)

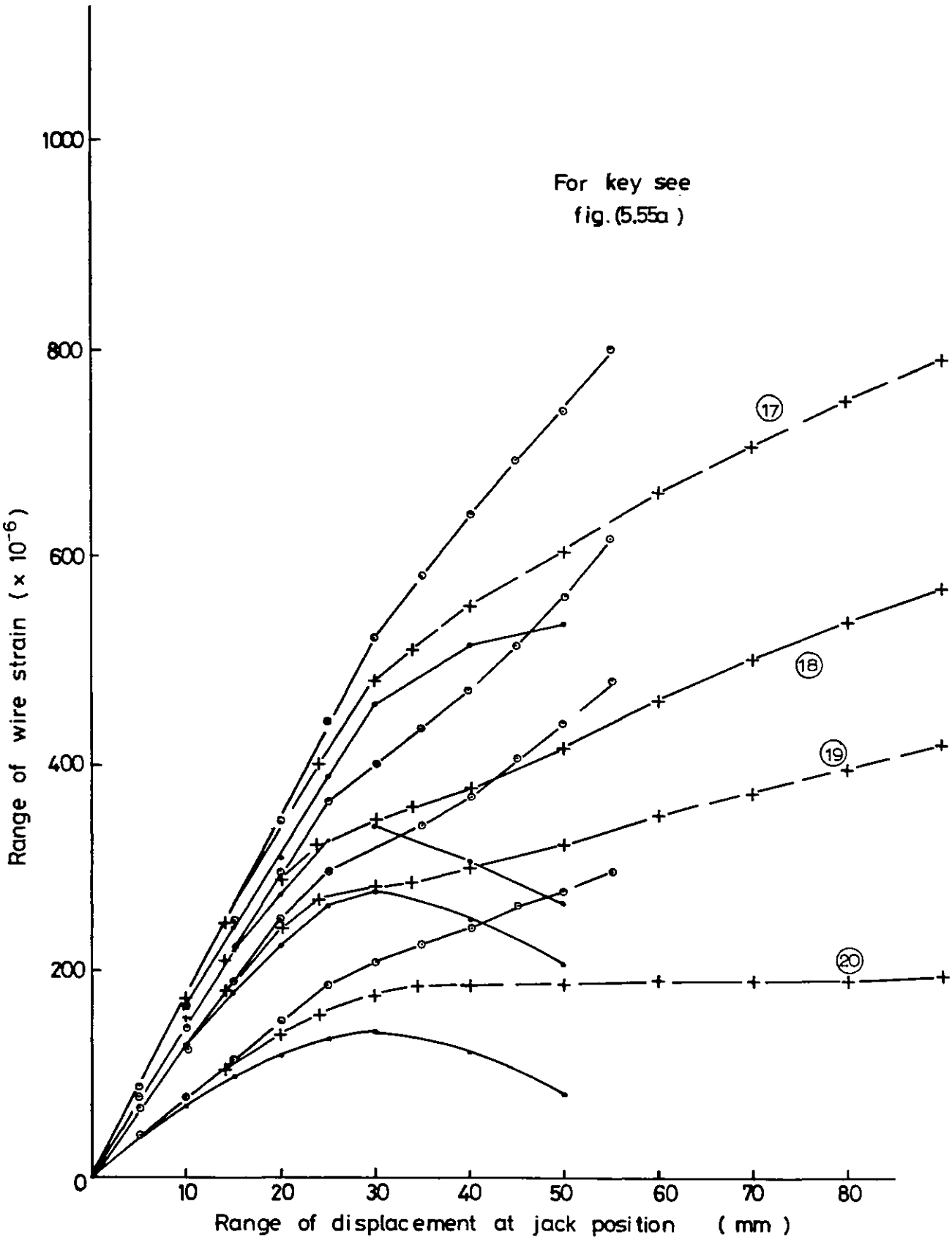

Fig.(5.55b) Continuation of fig. (5.55a)

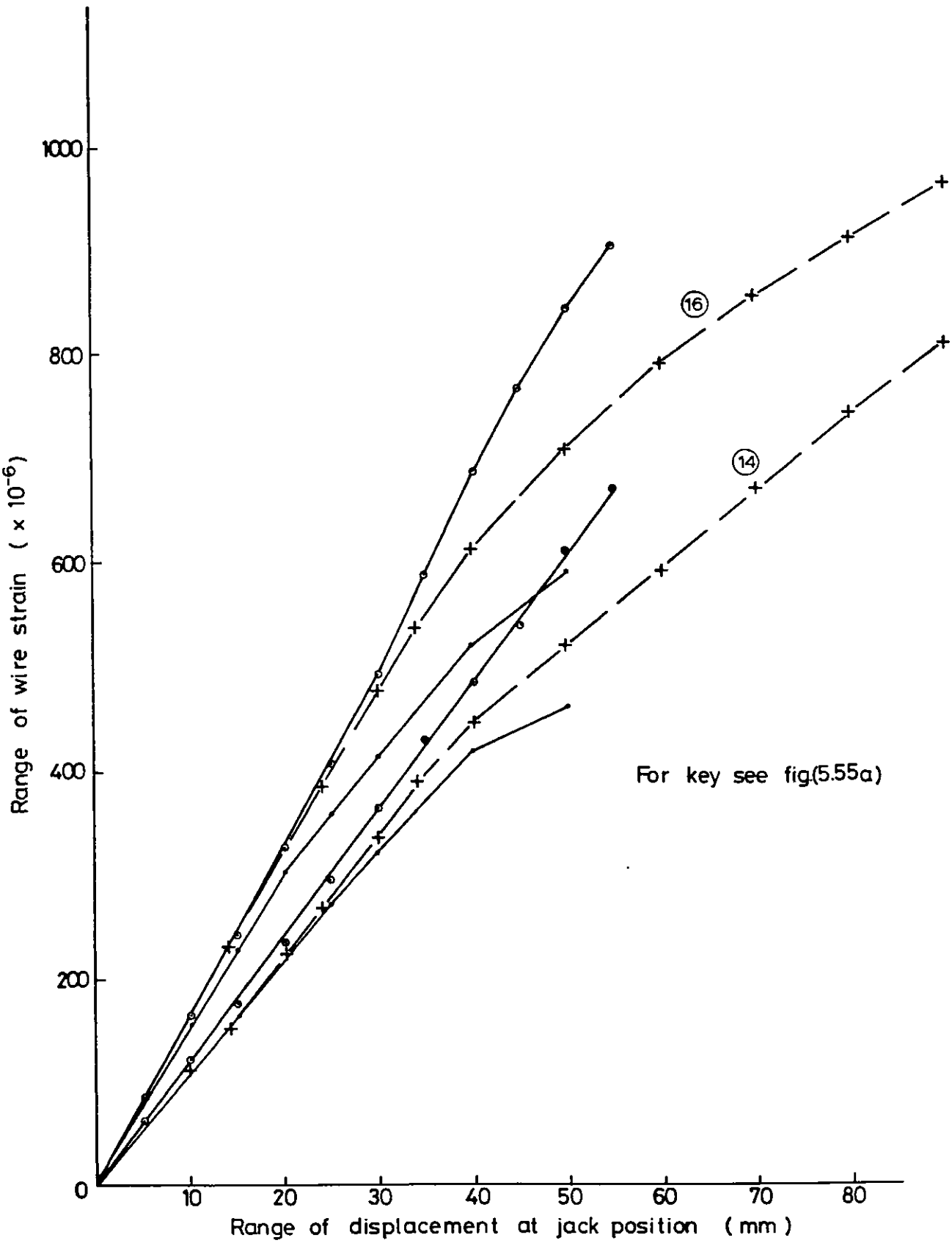

Fig. (5.55c) Continuation of fig. (5.55b)

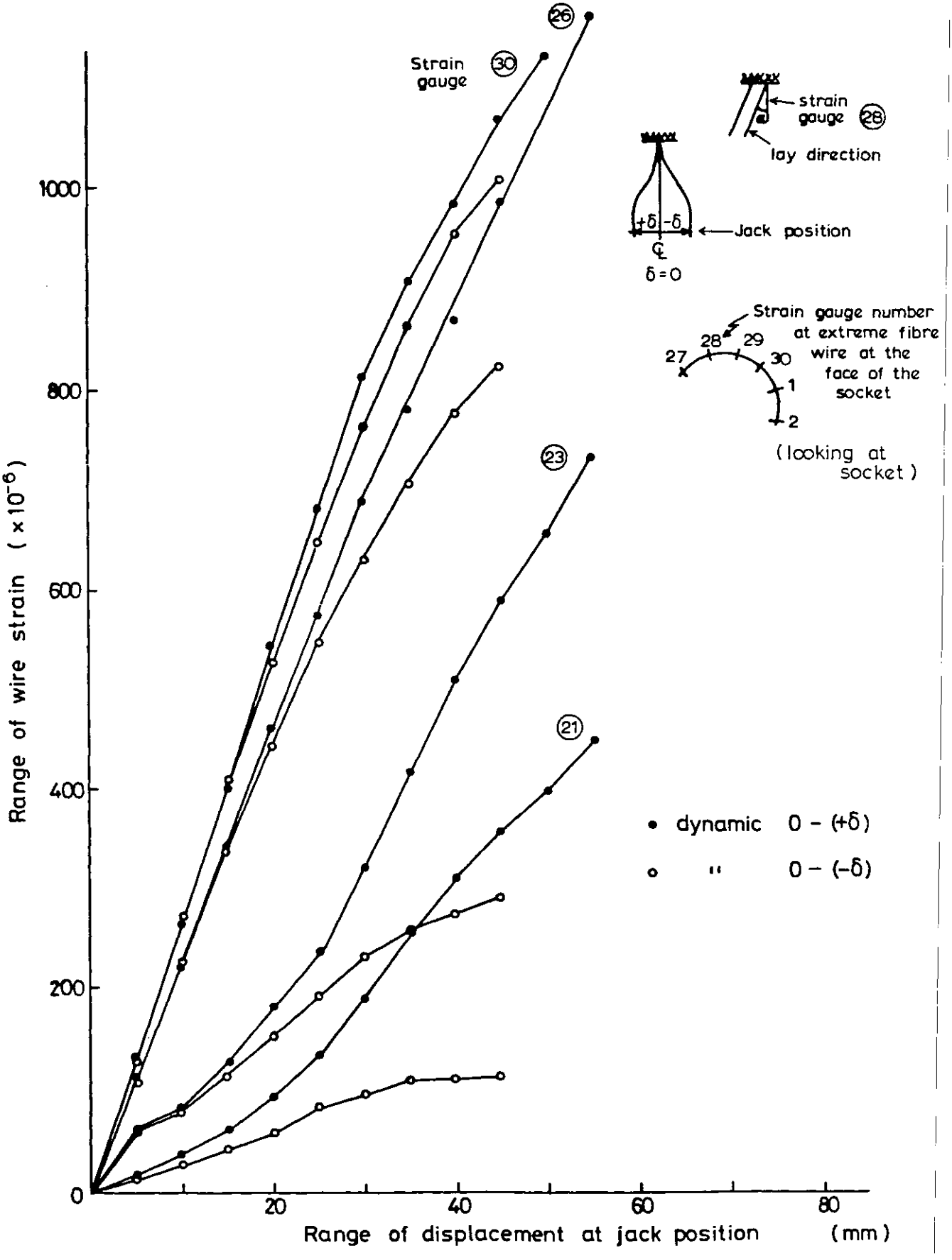

Fig (5.56a) Experimental plots of individual wire strains near the fixed end for the strand under bending (mean axial load = 0·615 MN)

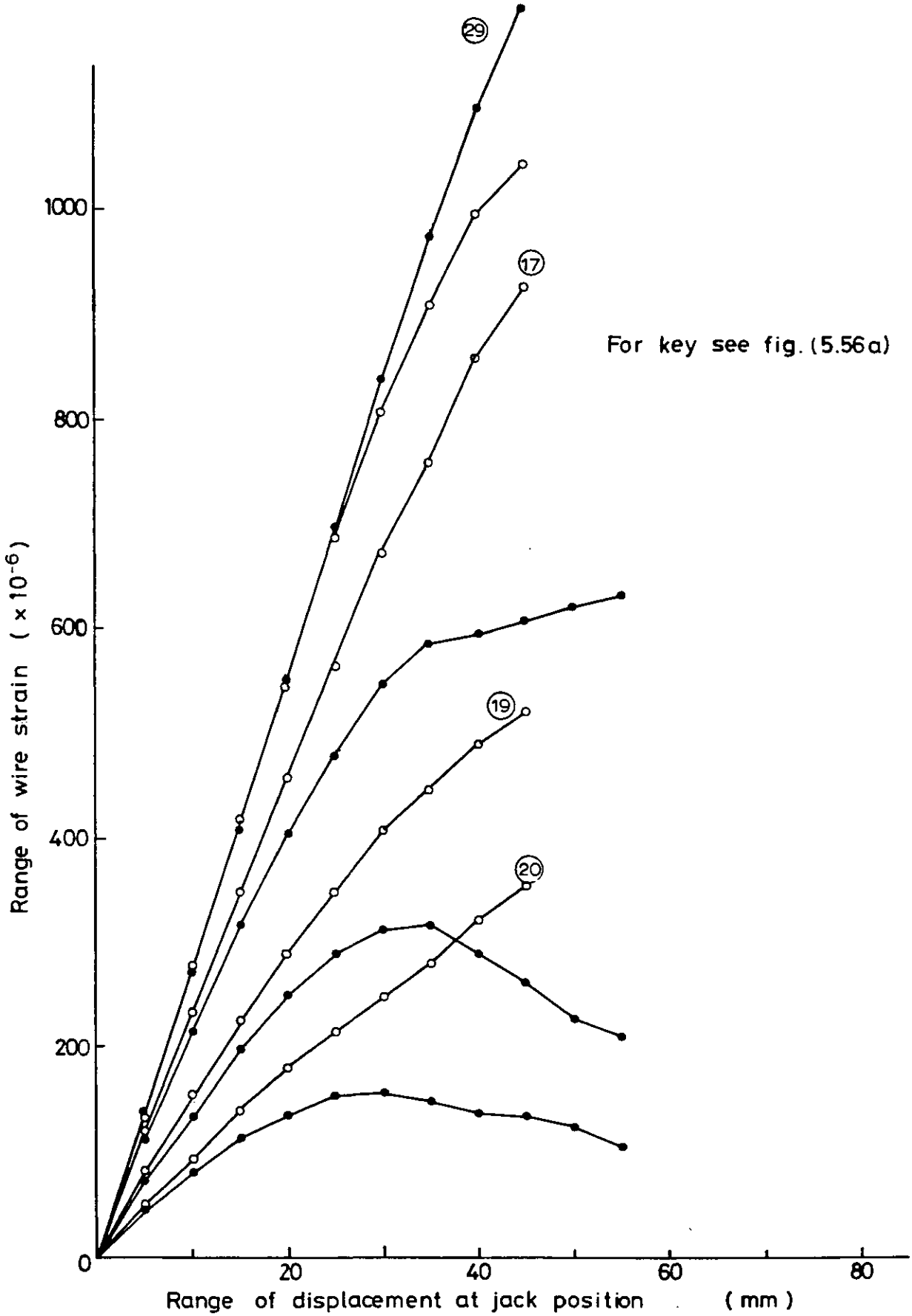

Fig (5.56b) Continuation of fig. (5 56a)

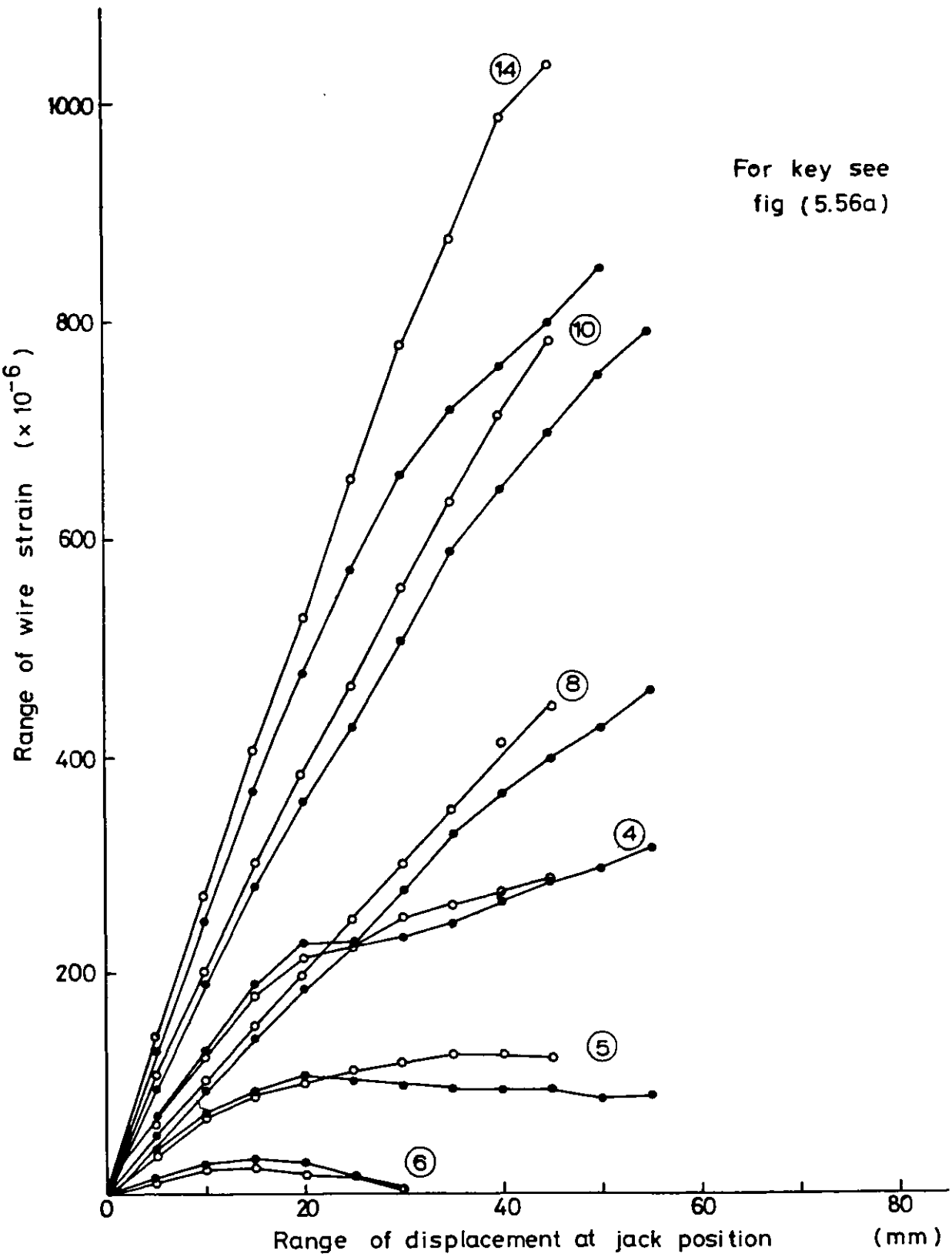

Fig.(5.56c)Continuation of fig (5.56b)

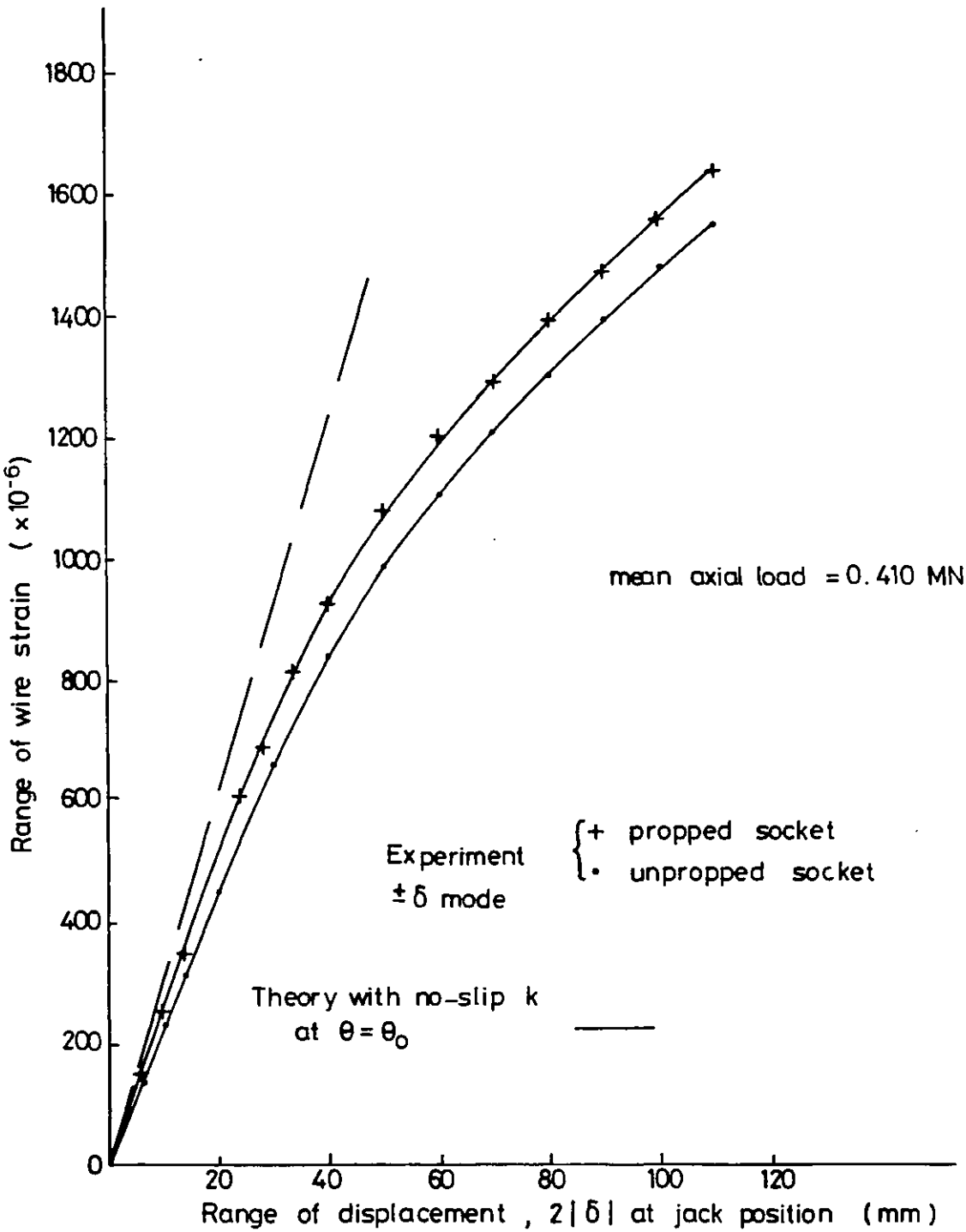

Fig(5.57) Effect of propping the socket against lateral movements on the experimental maximum wire strain at the face of the socket , plus a comparison with the theoretical prediction of the maximum wire strain at the inaccessible point of zero lateral deflection

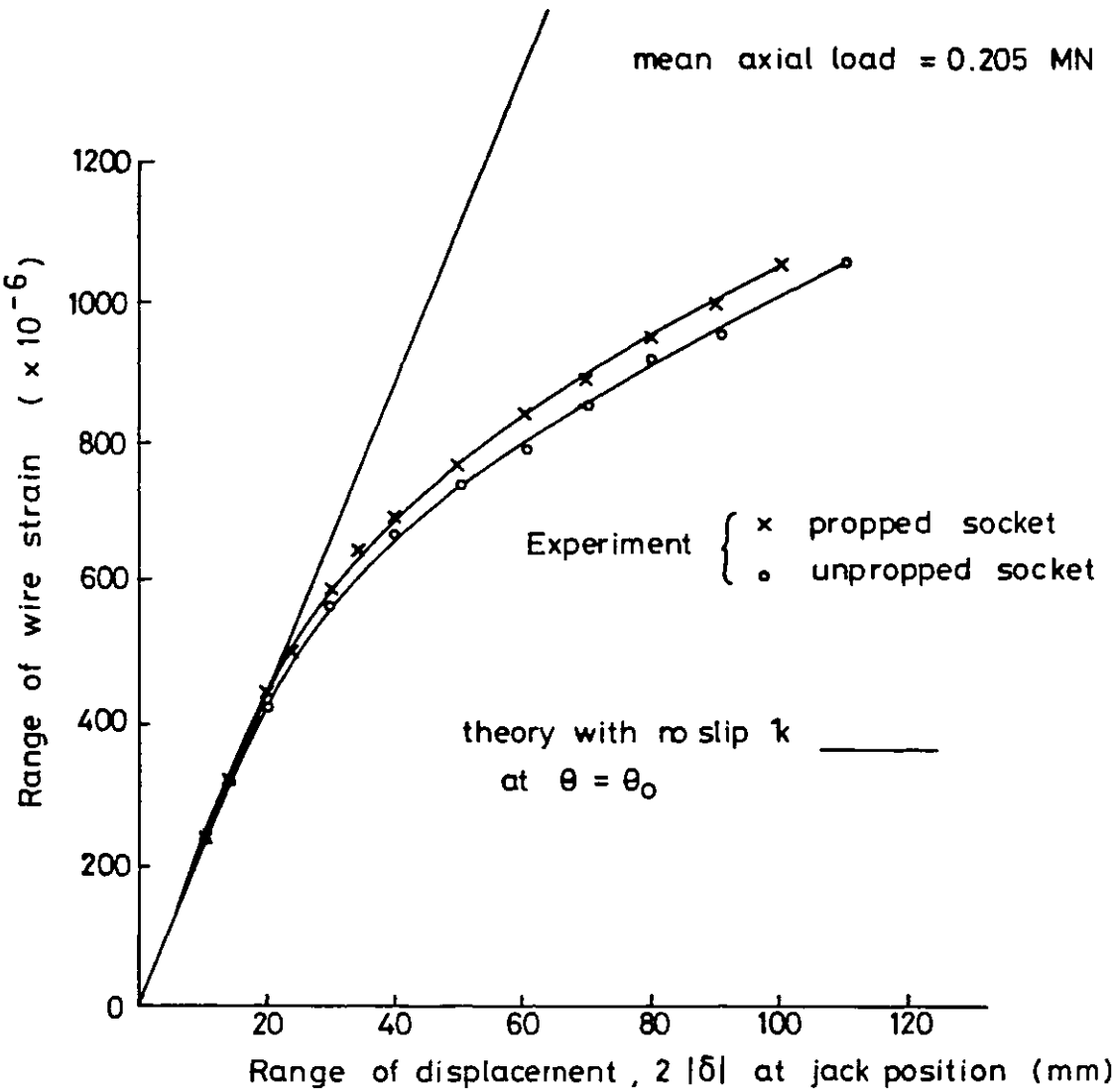

Fig (5.58) Effect of propping the socket against lateral movement on the experimental maximum wire strain at the face of the socket which is also compared with the theoretical prediction of the maximum wire strain at the inaccessible point of zero lateral deflection

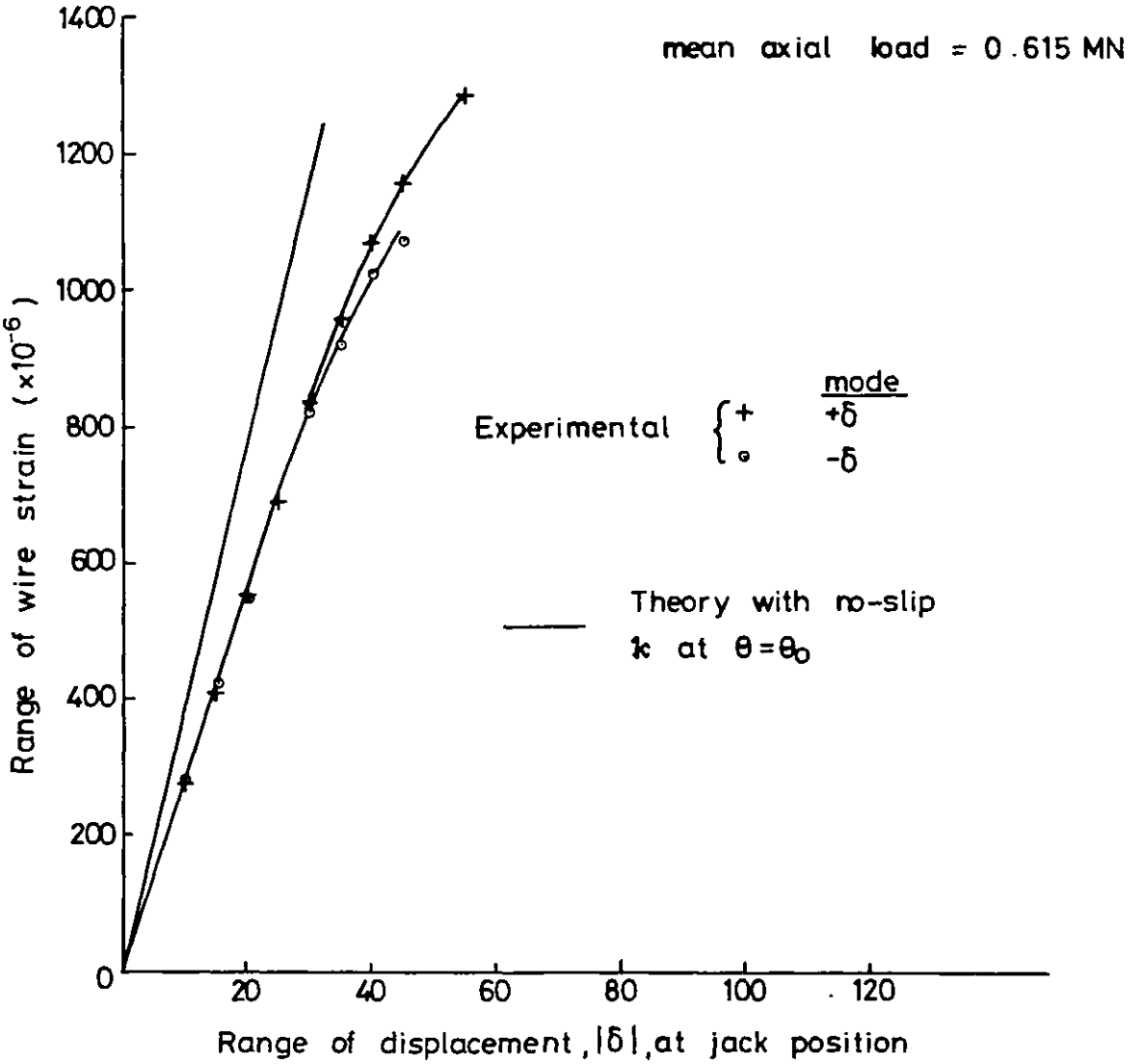

Fig (5.59) Comparison of experimental maximum wire strain measurements with the socket propped against lateral movements (under + δ and − δ mode) with the theoretical prediction of maximum wire strain at the inaccessible point of zero lateral deflection

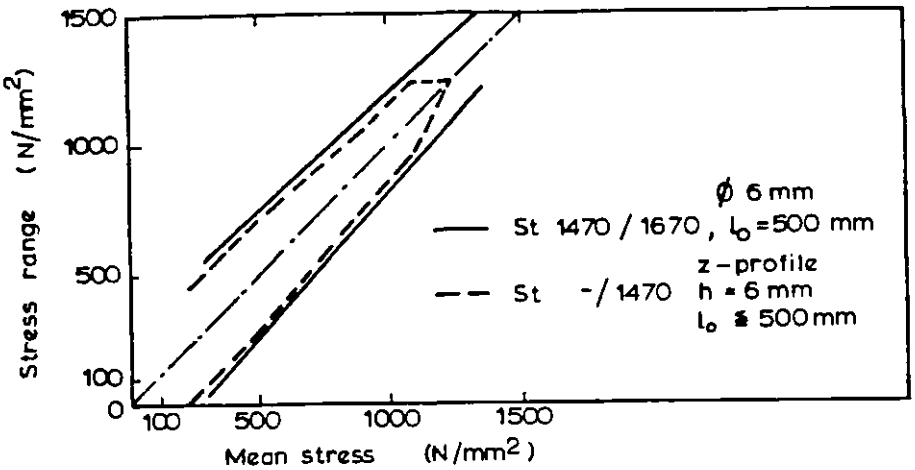

Fig 6.1 Fatigue strength diagrams according to Smith for prestressing steel and galvanised shaped wires for 2×10^6 cycles of fatigue life and $P_r = 5\%$
After Ref.(6.12)

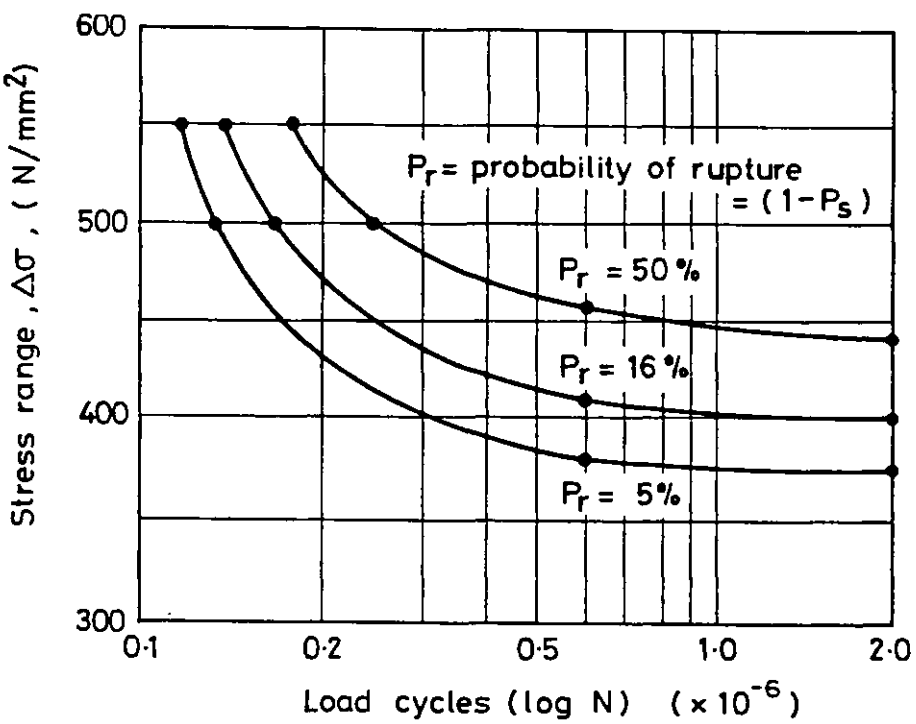

Fig 6.2 S-N axial fatigue curves for single 7 mm dia. plain wires at different P_r- values
After Ref. (6.10)

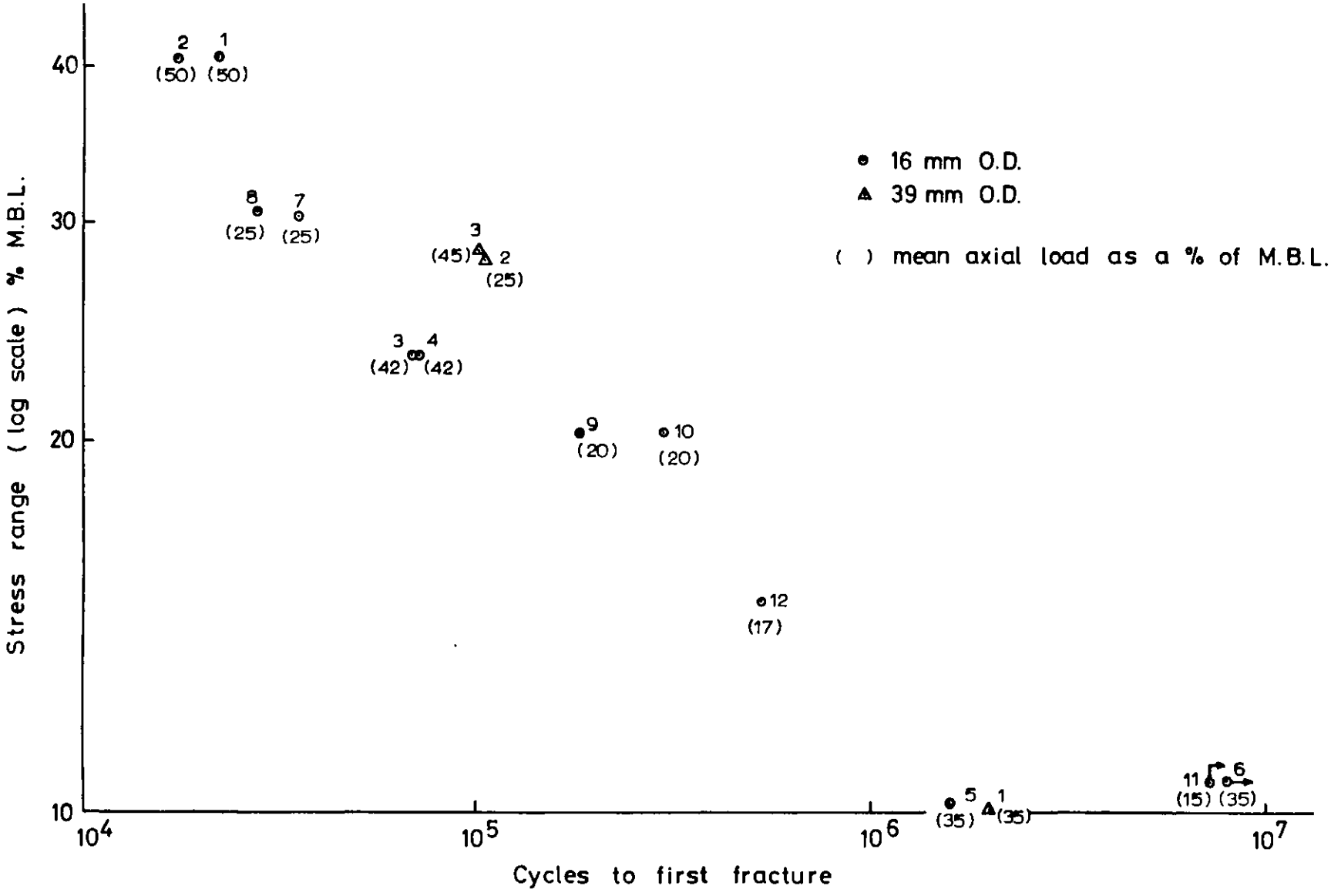

Fig 6.3 Plot of fatigue life for the 16 mm and 38 mm O.D. strands reported in Ref. (2·53), as a function of the range of stress

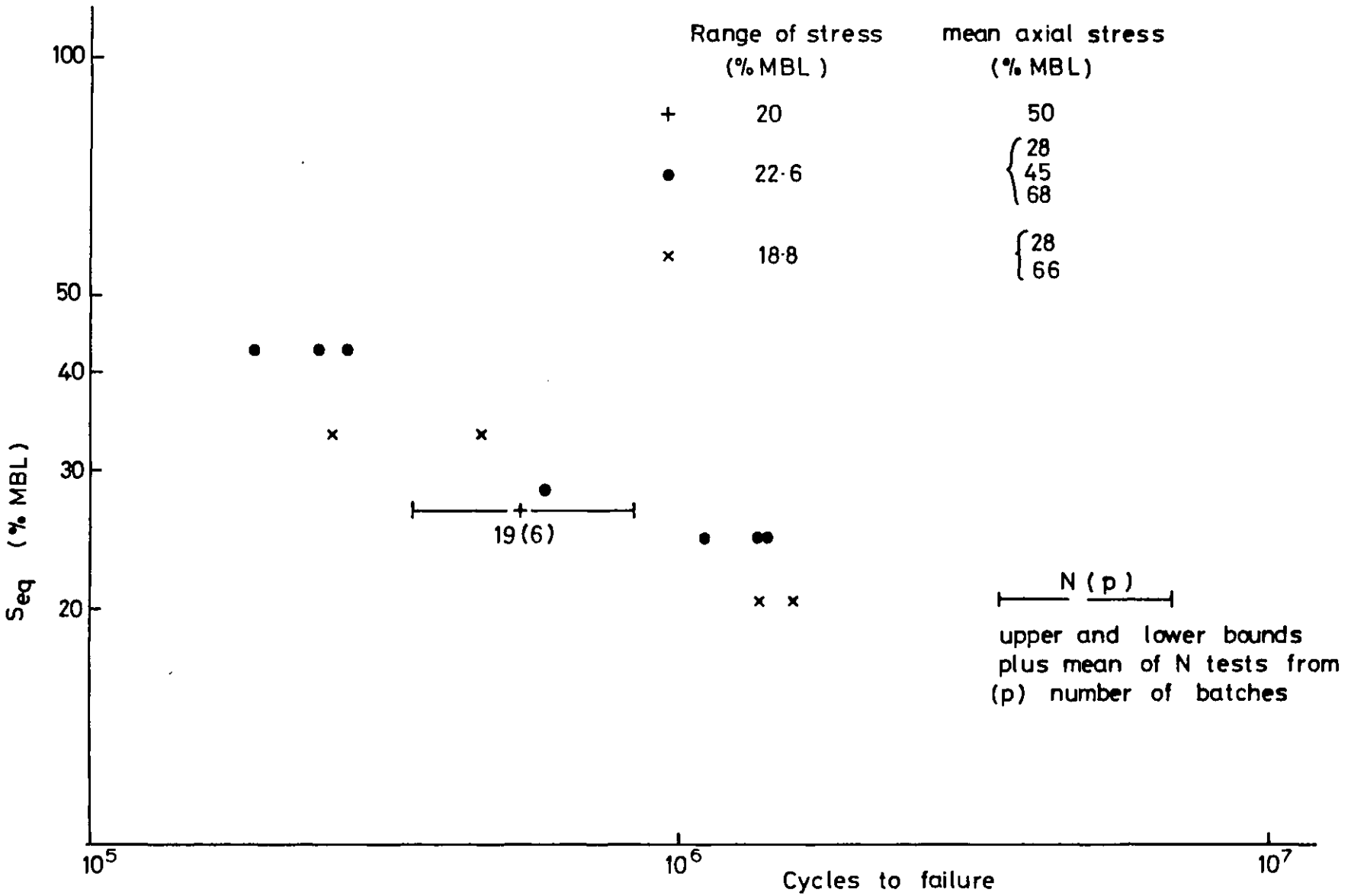

Fig 6·4 Plots of equivalent stress, S_{eq}, versus fatigue life to complete failure for a 32 mm 6 x 25 IWRC rope of right hand ordinary lay construction

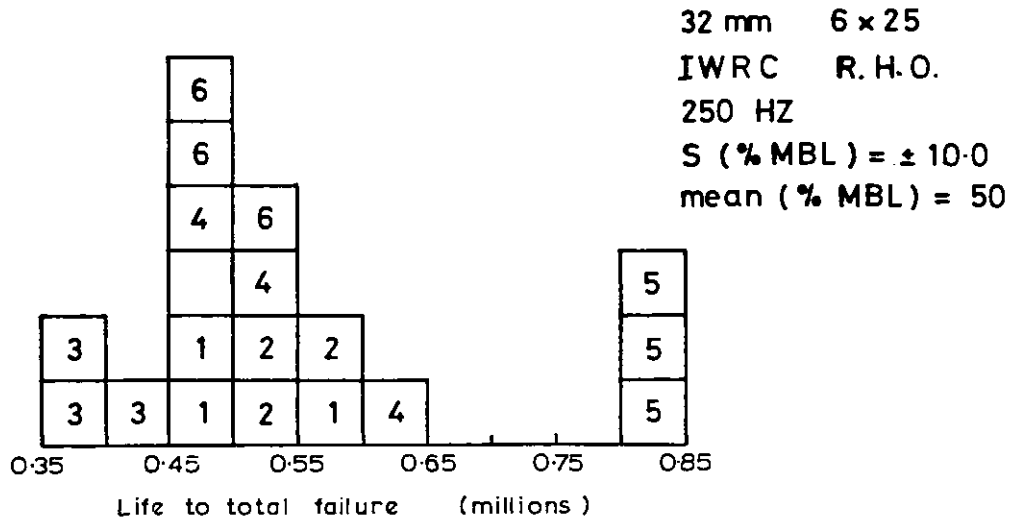

N : batch number

(a)

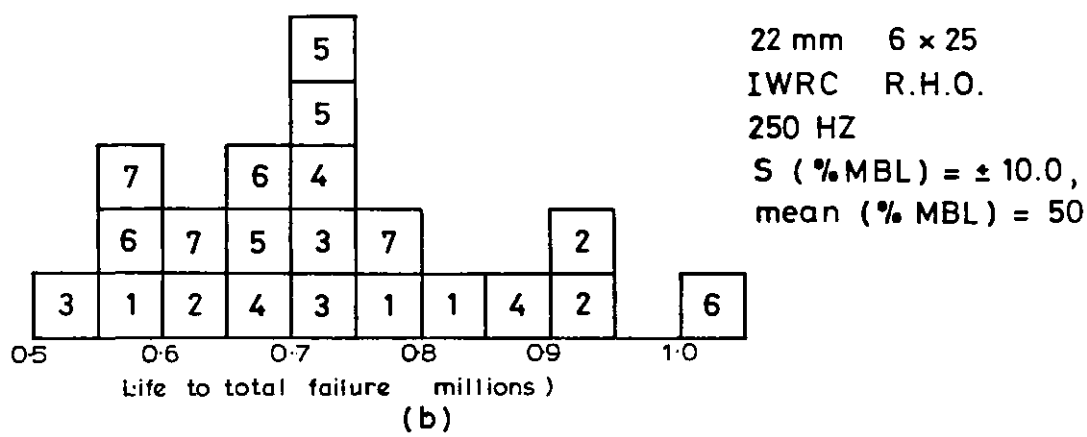

(b)

Fig 6·5 Scatter in the fatigue results to complete failure for various batches of two different wire rope constructions

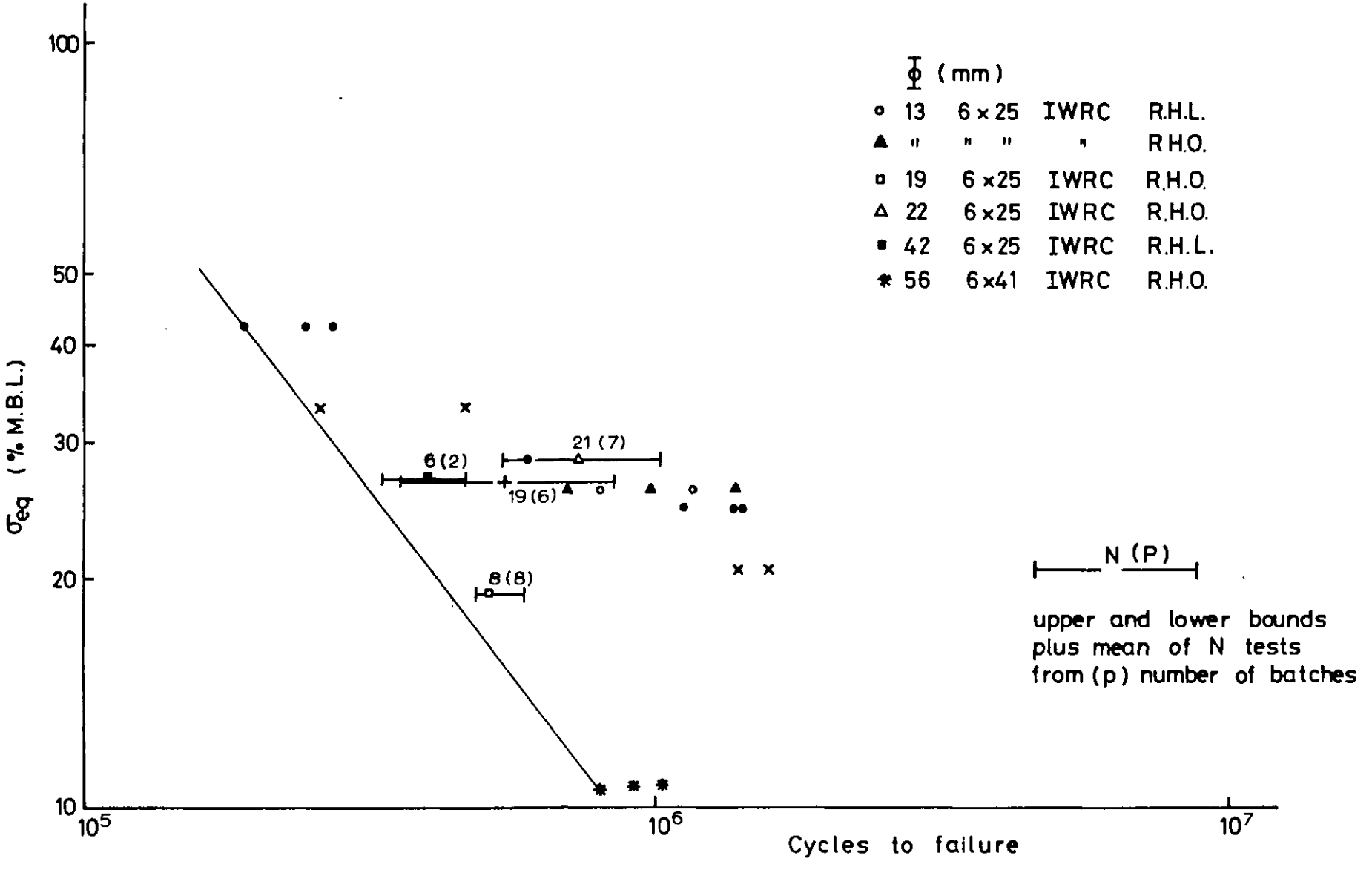

Fig. 6.6 Plot of equivalent stress σ_{eq} against fatigue life to complete failure for various rope constructions and batches

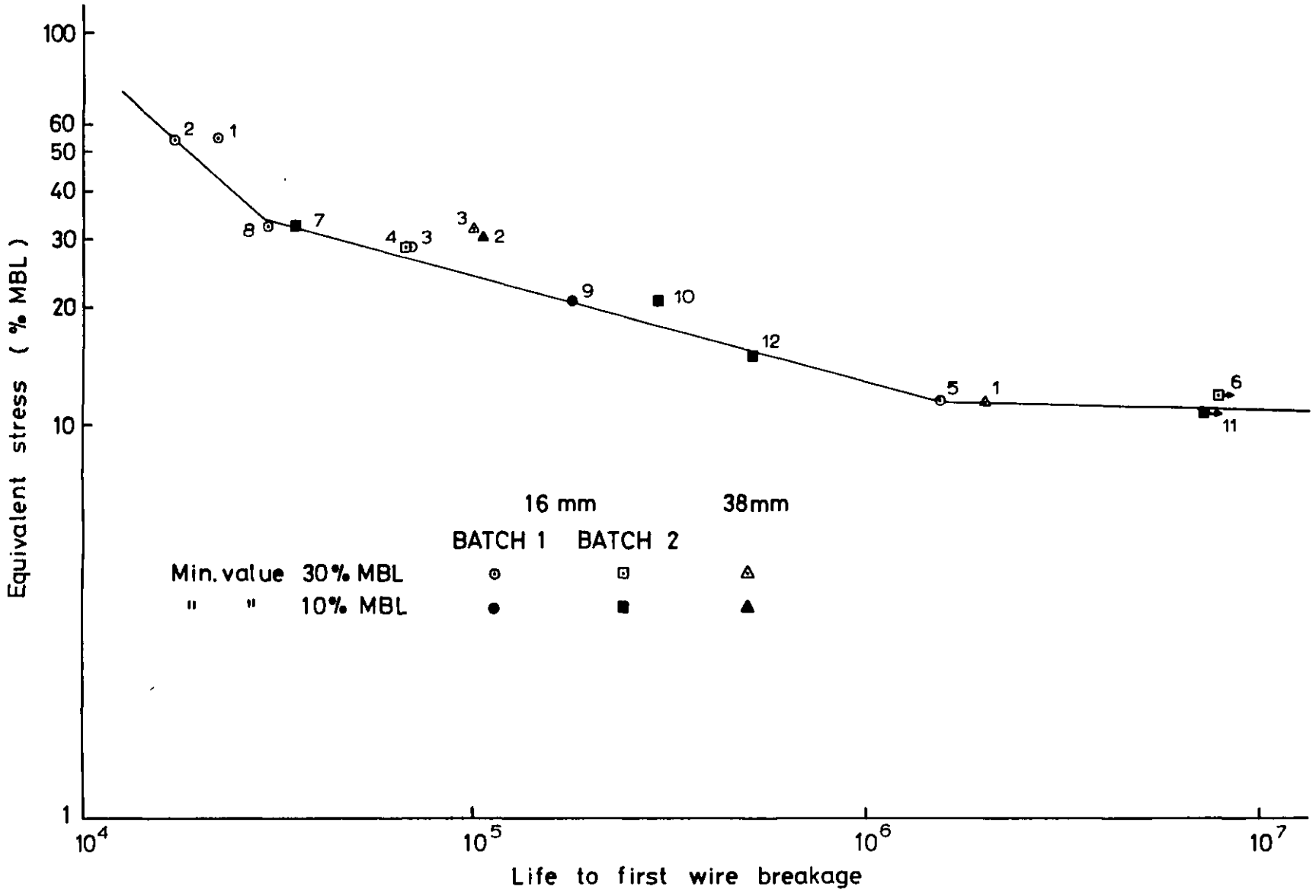

Fig. 6.7 Plots of axial fatique life to first wire breakage using the concept of equivalent stress (Basic data on 38 mm and 16 mm strands obtained from Ref (2.53))

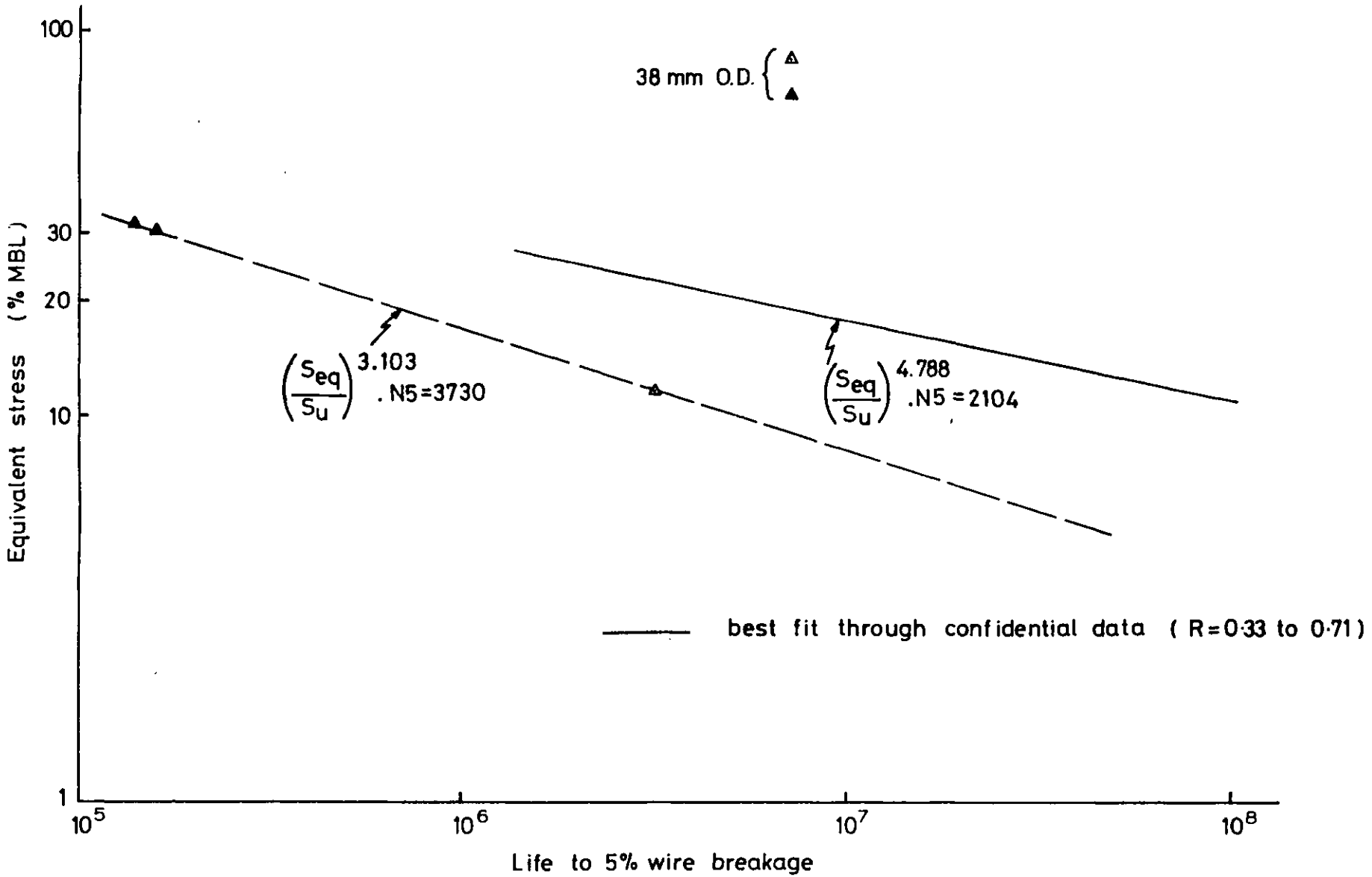

Fig 6.8 Plots of axial fatigue life to 5% wire breakage for 38 mm O.D. strands and also the confidential data for which only a regression line is given

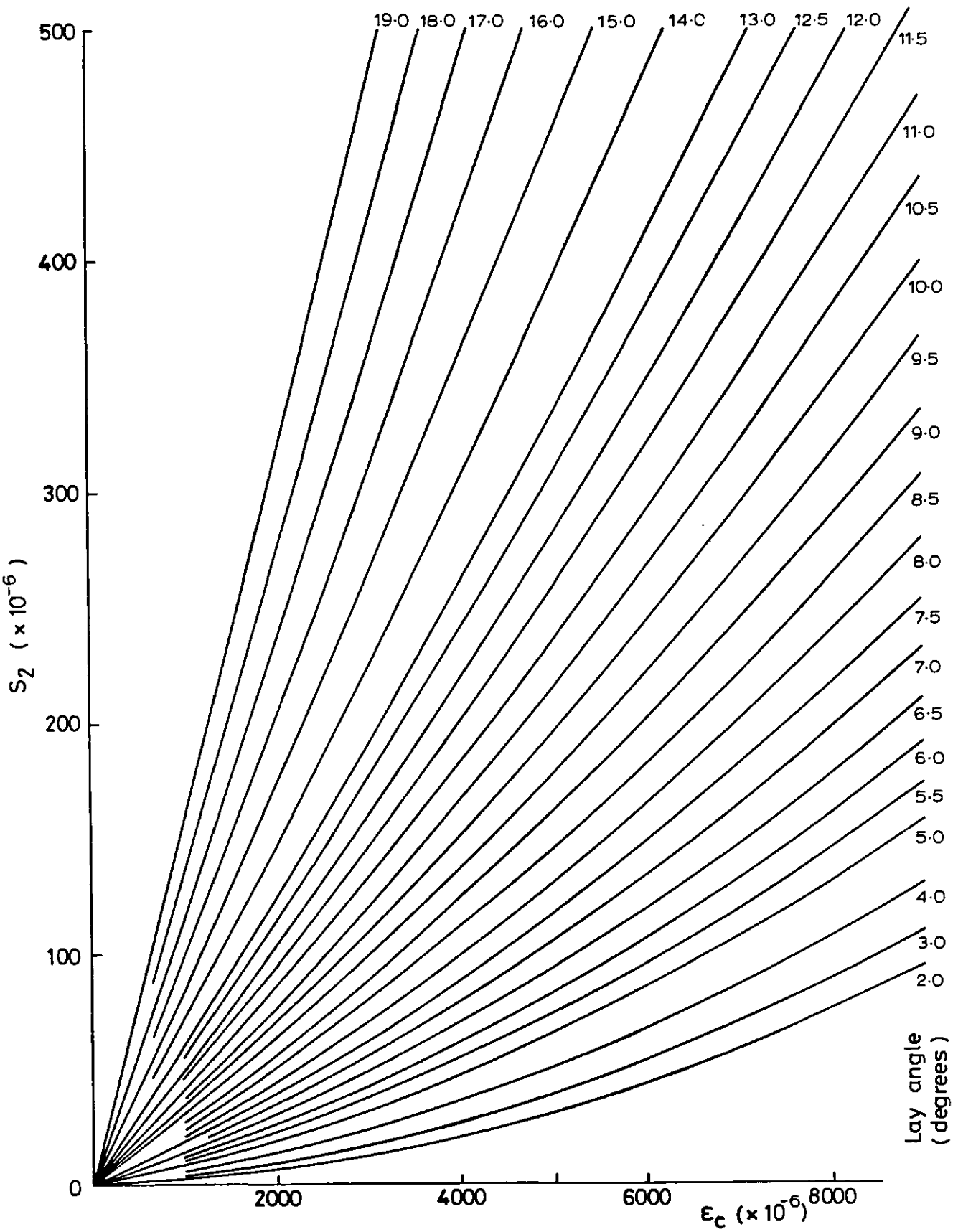

Fig 6.9 Theoretical plots of line contact strain, S_2, against strand axial strain, ε_c, for various magnitudes of lay angle, α

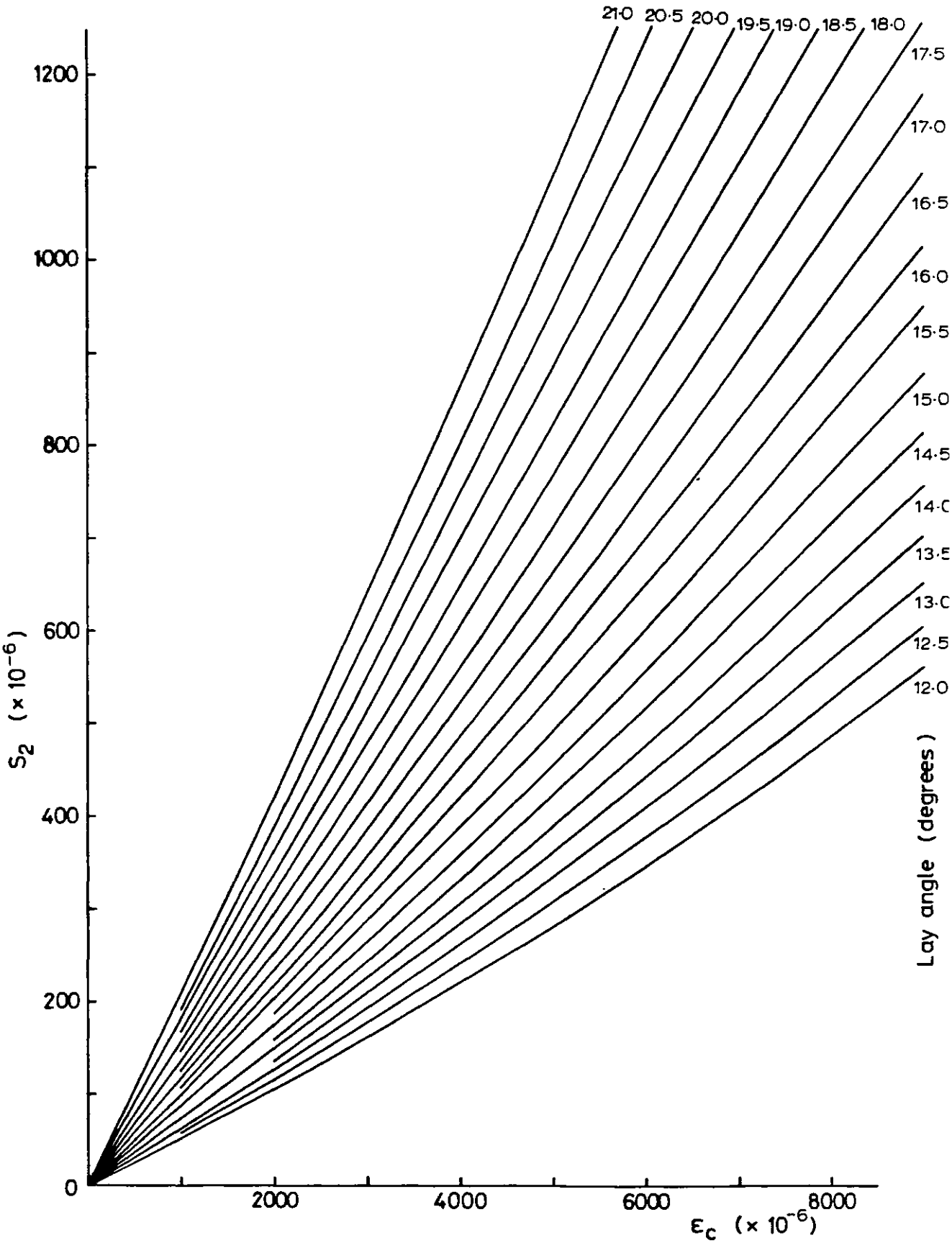

Fig. 6.10 Theoretical plots of line-contact strain, S_2, against strand axial strain, ε_c, for various magnitudes of lay angle, α

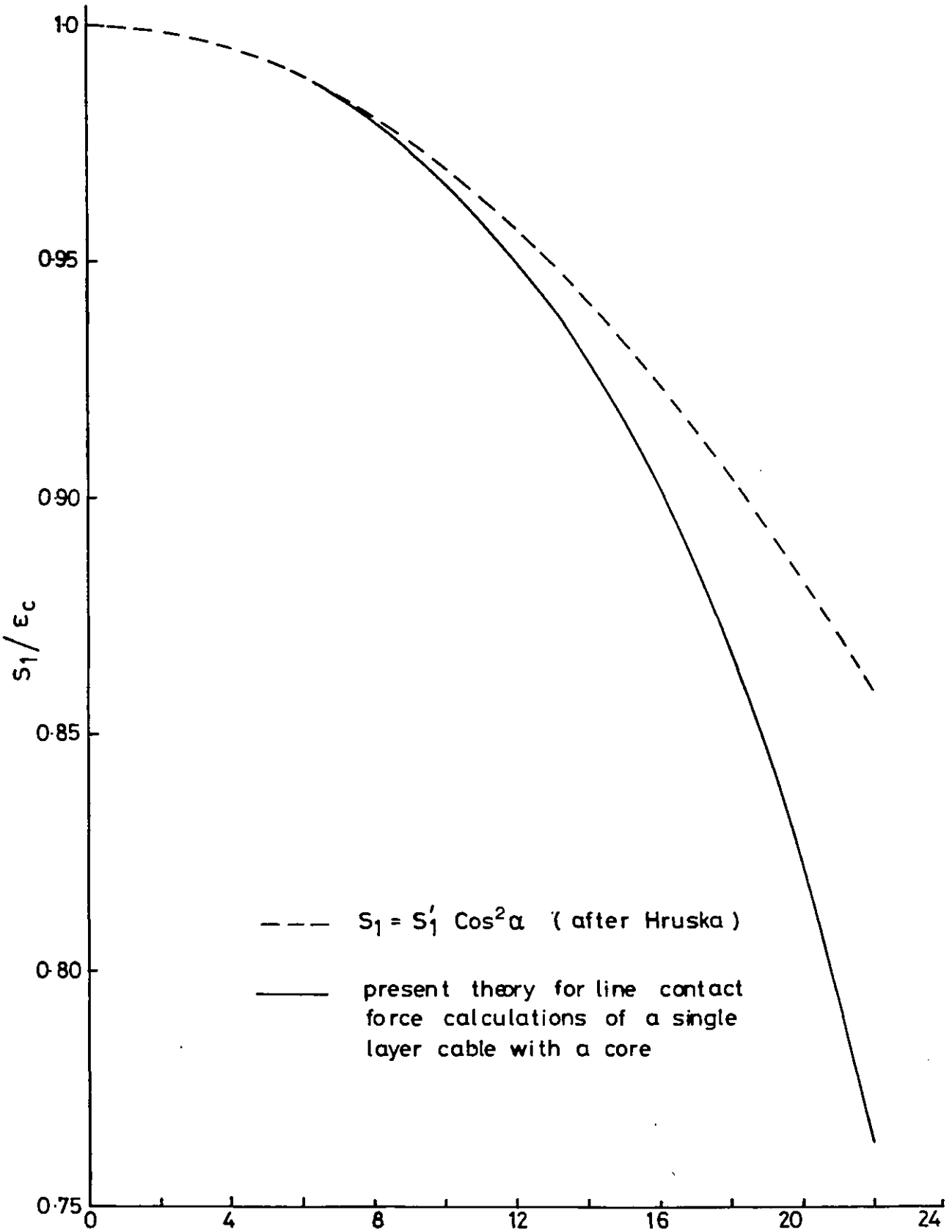

Fig. 6.11 Theoretical plot of wire axial strain , S_1 , as a function of the lay angle , α

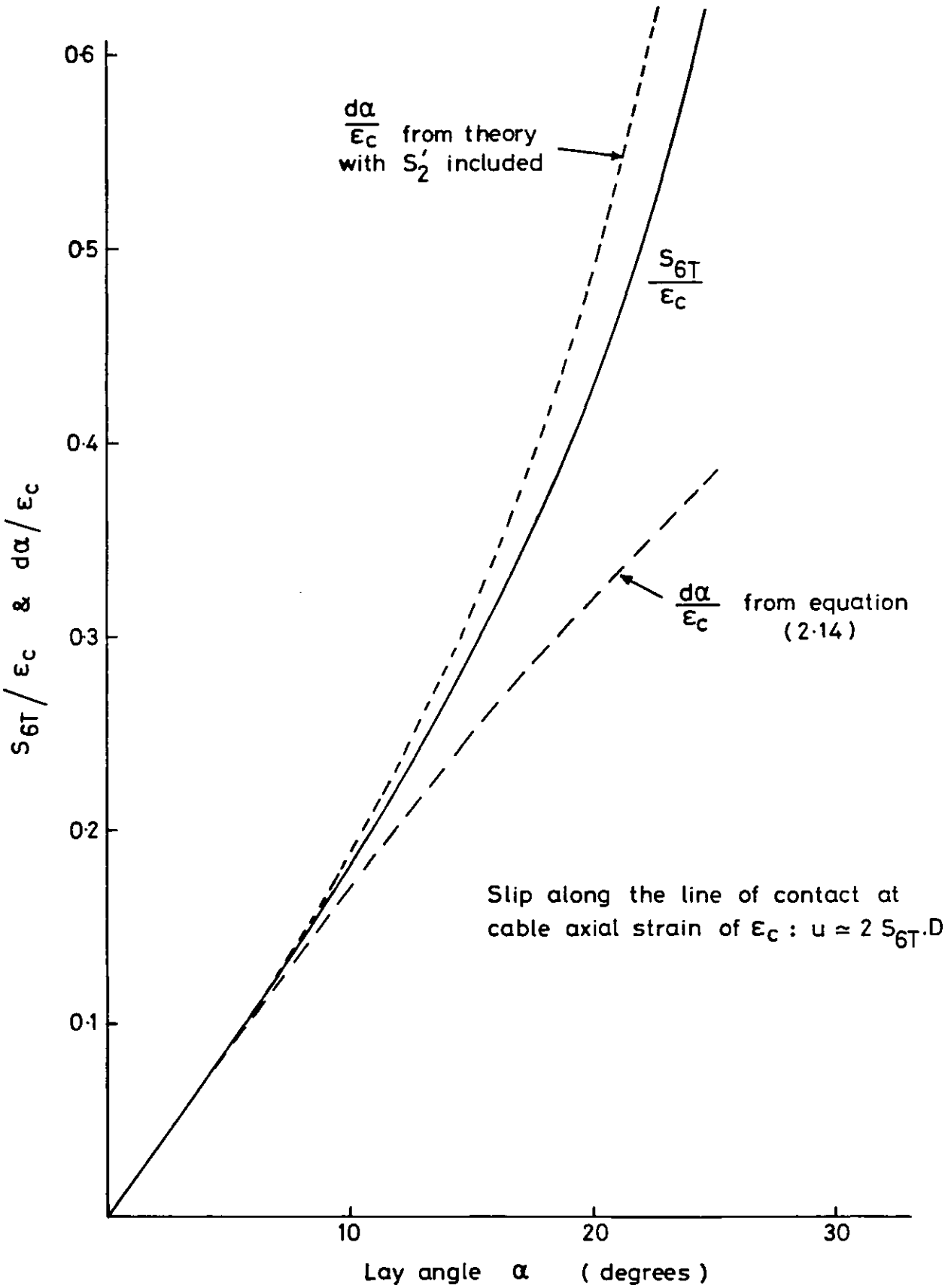

Fig. 6.12 Theoretical plot of tensorial shear strain, S_{6T} and changes in the lay angle, $d\alpha$, as a function of the lay angle, α, for large diameter strands

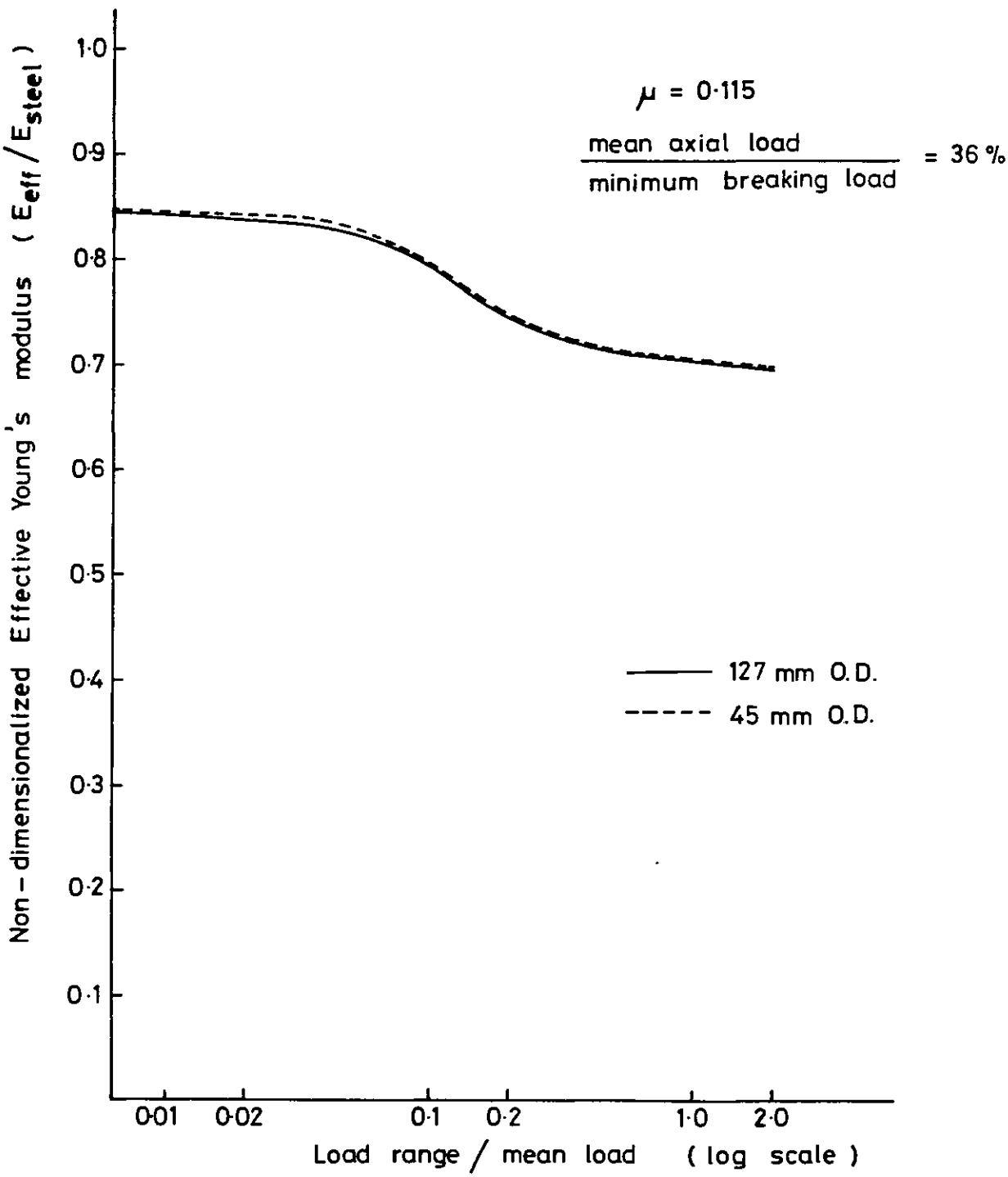

Fig. 6.13 Axial stiffness results for various cable constructions

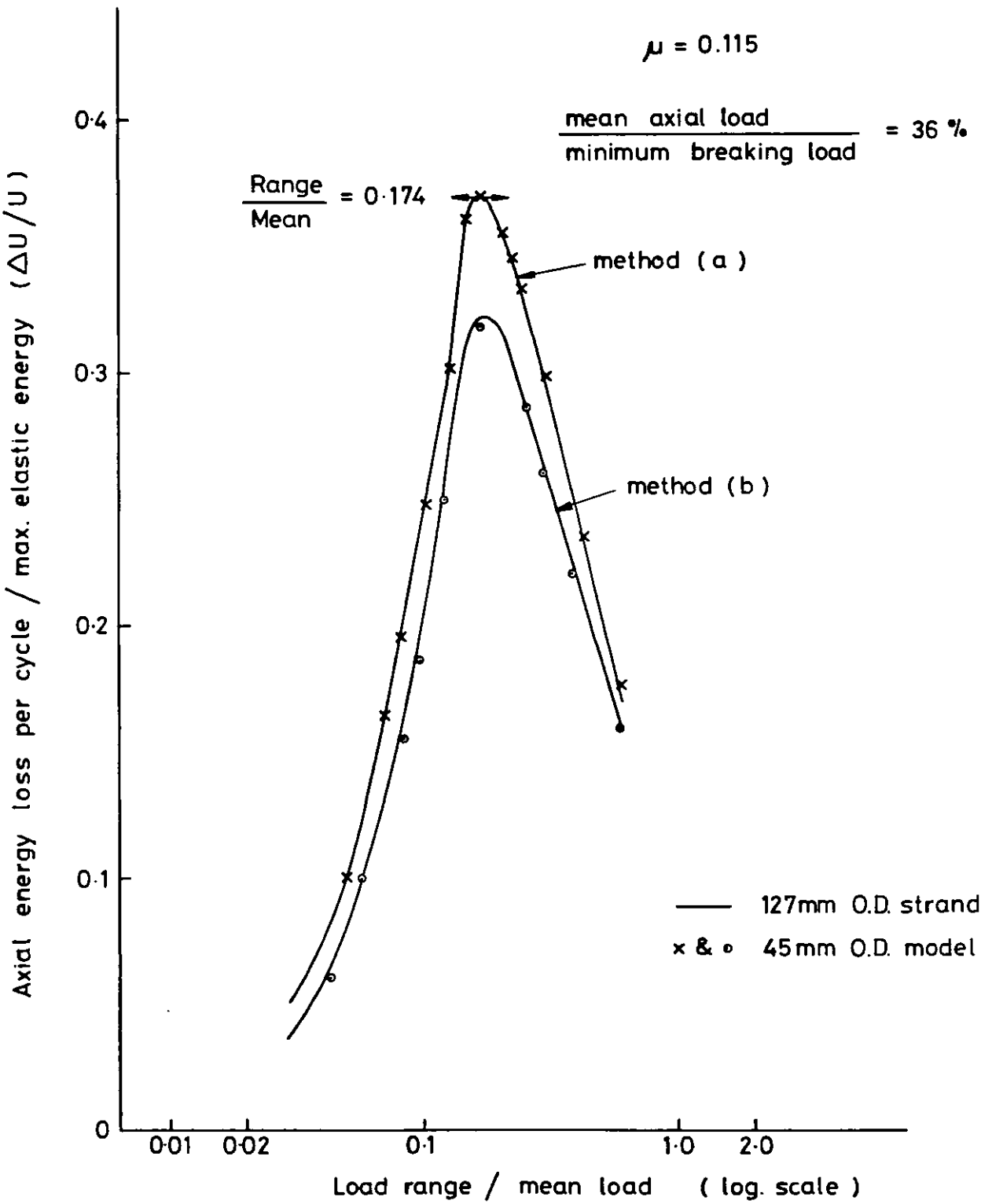

Fig. 6.14 Theoretical axial energy dissipation in 127 mm O.D strand and its corresponding small scale (45 mm O.D) model

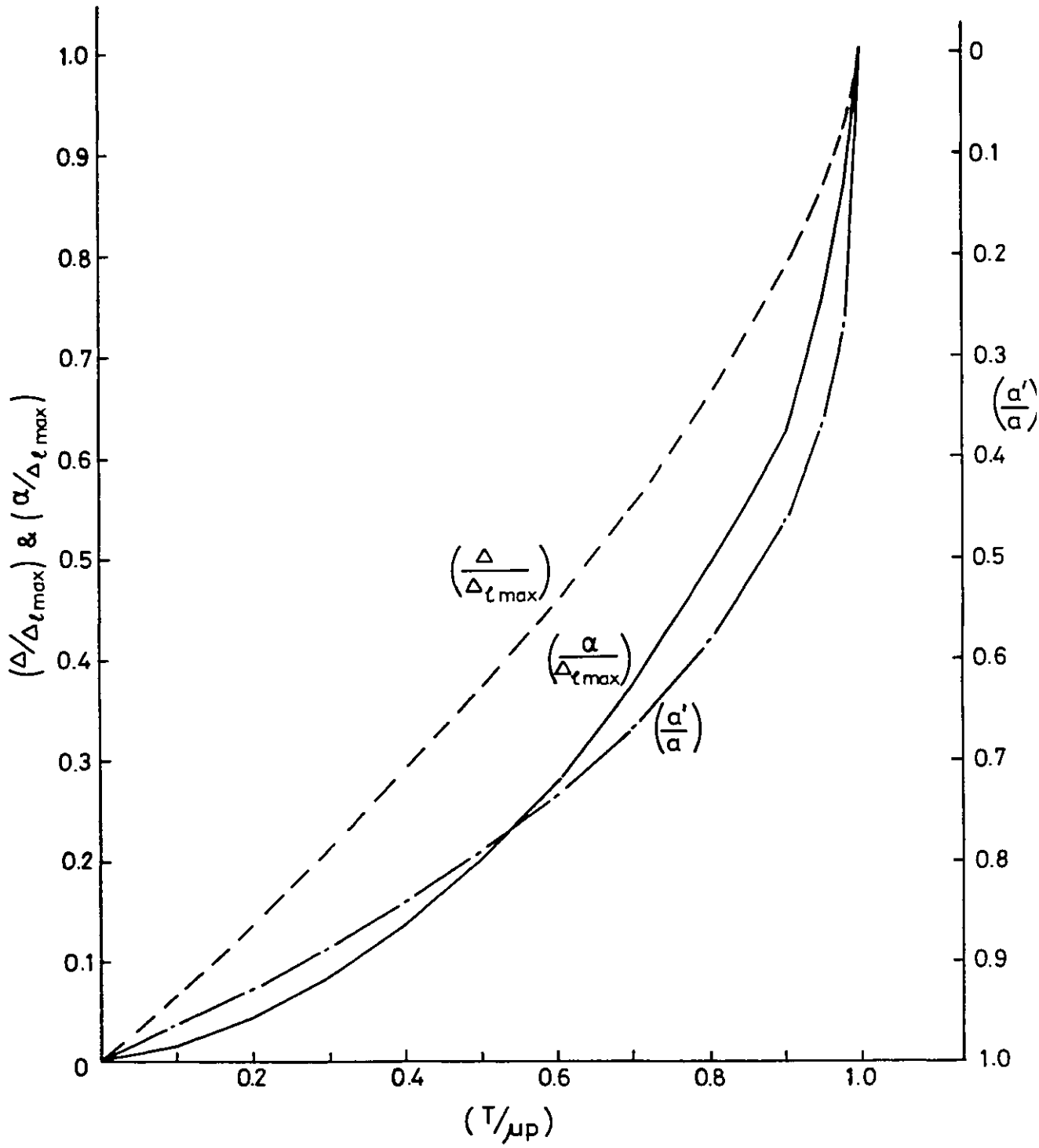

Fig 6.15 Theoretical plots of non-dimensionalized gross slippage, $\Delta/\Delta_{\ell max}$, micro-slippage at the outer periphery of the contact patch, $\alpha/\Delta_{\ell max}$, plus the manner in which size of no-slip regions, a'/a, vary as a function of $T/\mu p$

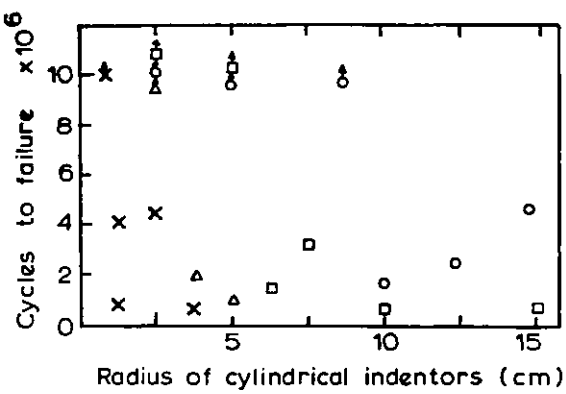

Fig. 6·16 Fatigue life plotted against indentor radius for four series of fatigue tests in each of which P/D was held constant

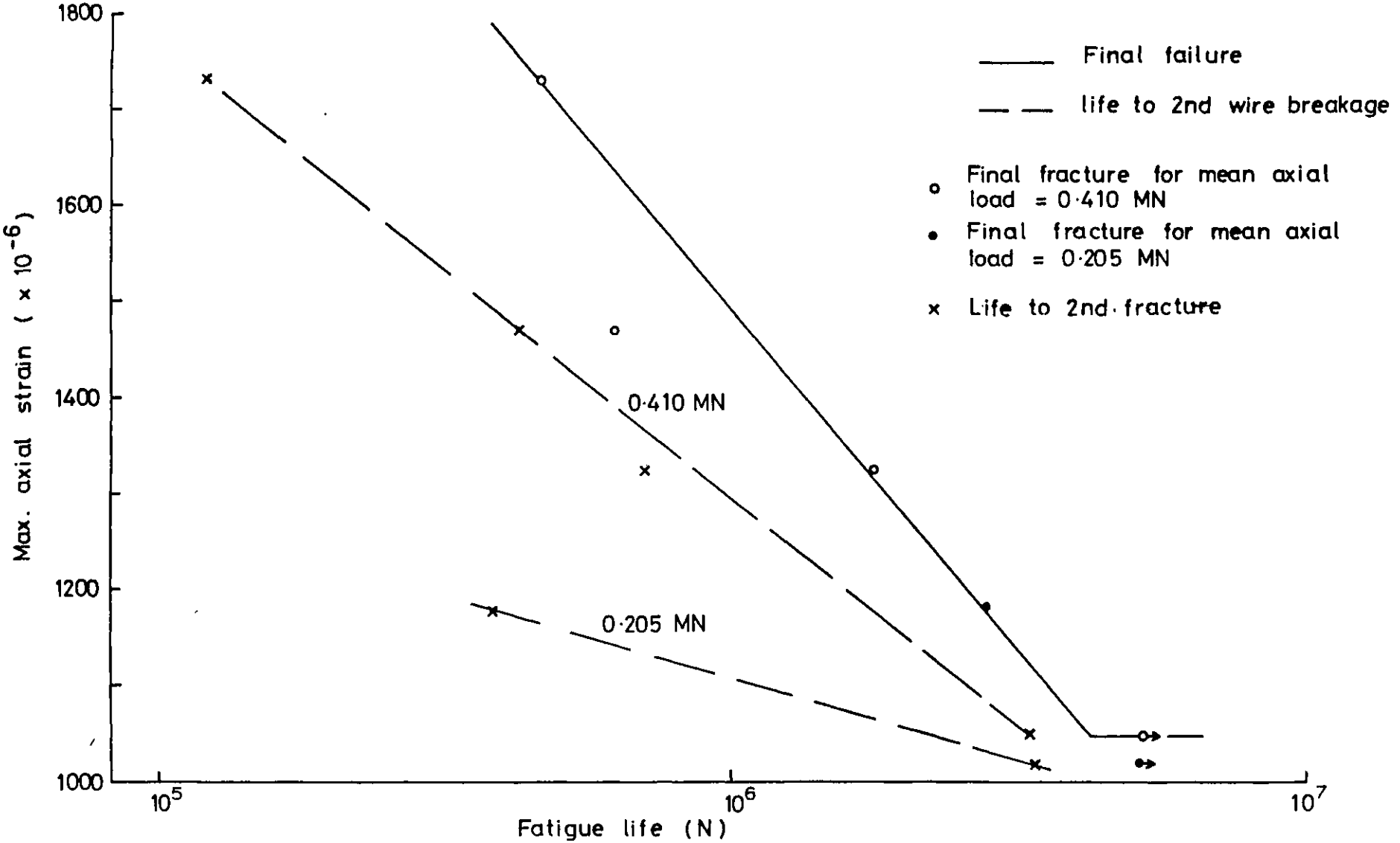

Fig 6·17 Free bending fatigue results for the 39 mm O.D. strand After Ref (2.53)